Universität Bremen

Kinetic Stabilization of Low Valent Main Group Compounds

Inaugural Dissertation

Towards the academic title Doctor Rerum Naturalium

(Dr. rer. nat.)

Submitted to the Department of Biology and Chemistry of the Universität Bremen

by

Daniel Duvinage

from Bremen

Bremen 2024

Begutachtung des schriftlichen Teils:
Prof. Dr. Jens Beckmann (Universität Bremen)
Prof. Dr. Anne Staubitz (Universität Bremen)
Prof. Dr. Axel Schulz (Universität Rostock)

Betreuer:
Prof. Dr. Jens Beckmann (Universität Bremen)

Datum des Promotionskolloquiums: 08.03.2024

Schriftliche Erklärung an Eides statt

Ich, Daniel Duvinage, erkläre, dass eine Promotion noch an keiner anderen Hochschule als der Universität Bremen, im Fachbereich Biologie und Chemie, versucht wurde.

Ich versichere an Eides statt durch meine Unterschrift, dass ich die vorgelegte Dissertation mit dem Titel

Kinetic Stabilization of Low Valent Main Group Compounds

selbstständig und ohne fremde Hilfe verfasst, nicht andere als die in ihr angegebenen Quellen oder Hilfsmittel benutzt und alle vollständig oder sinngemäß übernommenen Zitate als solche gekennzeichnet habe.

Ich versichere an Eides statt, dass ich die vorgenannten Angaben nach bestem Wissen und Gewissen gemacht habe und dass die Angaben der Wahrheit entsprechen und ich nichts verschwiegen habe.

Die Strafbarkeit einer falschen eidesstattlichen Versicherung ist mir bekannt, namentlich die Strafandrohung nach § 156 StGB bis zu drei Jahren Freiheitsstrafe oder Geldstrafe bei vorsätzlicher Begehung der Tat bzw. gemäß § 161 Abs. 1 StGB bis zu einem Jahr Freiheitsstrafe oder Geldstrafe bei fahrlässiger Begehung.

Diese Dissertation wurde in der vorliegenden oder einer ähnlichen Form noch bei keiner anderen in oder ausländischen Hochschule anlässlich eines Promotionsgesuches oder zu anderen Prüfungszwecken eingereicht.

_____ _____

Ort, Datum Daniel Duvinage

Schriftliche Erklärung zur elektronischen Version und Überprüfung der Dissertation

Ich, Daniel Duvinage, erkläre gemäß §7 Abs. 7, Punkt 4, dass die zu Prüfungszwecken vorgelegte elektronische Version meiner Dissertation identisch mit der abgegebenen gedruckten Version ist.

Ich bin mit der Überprüfung meiner Dissertation gemäß §6 Abs. 2, Punkt 4, mit qualifizierter Software im Rahmen der Untersuchung von Plagiatsvorwürfen einverstanden.

_____	_____
Ort, Datum	Daniel Duvinage

Acknowledgements

First and foremost, I want to acknowledge Prof. Dr. Jens Beckmann for the opportunity to prepare my PhD thesis under his supervision. As he loves to say, he gives us the sandbox with all his toys, and we design our own sand castles. With this, I want to thank him for providing me with all the freedom, advice and care needed to design this work. Without this, a lot of Ideas would not have been converted to publications.

I further want to thank him for the opportunity to start my scientific career as a first-year student in his workgroup. He believed in my enthusiasm and passion for chemistry and encouraged it.

I want to acknowledge Prof. Dr. Anne Staubitz for agreeing to be the second reviewer of this thesis and Prof. Dr. Axel Schulz for being the external reviewer. Also, I want to thank the committee, consisting of Prof. Dr. Boris Nachtsheim as the chairman, Dr. Emanuel Hupf, Marvin Janßen and Oliver Fincke.

Additionally, I want to thank every student I supervised during my PhD thesis. Special thanks to Yannick Naß and Marvin Janßen who did their master thesis under my supervision, which resulted in excellent theses and awesome publications. Marvin Janßen you are not only a great lab-mate, but also a became an awesome friend. I also want to acknowledge my friends Nils Clamor, Mattis Damrath and Julian Spils, who were under my supervision and who are still great friends to me, although working now in different fields.

I wish to thank especially Dr. Marian Olaru for the time we spent together. You inspired me and we were doing a lot of night and weekend shifts together, ate a lot of junk food and had great moments. Our ways went apart, but I hope you will keep the time we shared, in good memories.

I also would like to thank Dr. Enno Lork, our crystallographer. Thank you for teaching me X-ray structure refinements and for the great friendship we developed. You helped me in difficult times and topics. I am thankful that you always had an open ear for me.

Another person I am grateful for is Dr. Julius Kögel. Since you started as a post-doc, we did a lot of dangerous, but cool chemistry together and became awesome

friends. Probably we developed a good friendship because of all the toxic cyanide we handled and also the awesome evenings we had.

I also want to thank the former workgroup members Sebastian Holsten, Artem Schröder, Dr. Rasmus Stichauer, Dr. Farzin Mostaghimi, Dr. Julius Kögel and the current workgroup members Fabio Meyer, Marvin Janßen, Isabell Heuermann, Isabell Winkel, Dr. Pim Puylaert and Corina Stoian, Dr. Emanuel Hupf, Sarah Matz and Zaki Warsame for the great environment, the tremendous number of barbecues, themed evenings and also the amount of time we shared during work. Thank you for making this workplace so enjoyable!

Special thanks also to the people who proof-read this thesis even if I have mentioned them already: Thanks to Dr. Yannik Appiarius, Dr. Jonas Hoffmann, Sebastian Holsten, Fabio Meyer, Dr. Julius Kögel, Prof. Dr. Malte Fischer and Dr. Julius Kögel a second time. It had a tremendous effect in times when I lost the motivation and did not know how to handle this.

A special thanks goes to all my friends as well. To all the people who I shared a chapter of my life with and to all the people who are still a part of my life.

Last but not least I want to thank my family, my mother Andrea Duvinage and my brother Marcel Duvinage. You had to survive my moods, I know that it was not easy, but you made it. You were there at all times and I am thankful for that. Thank you very much!

Thank you all for the time!

List of Publications

Published Articles

D. Duvinage, F. Mostaghimi, M. Damrath, J. Spils, P. Komorr, D. S. Odintsov, M. Fedin, L. Shundrin, S. Mebs, J. Beckmann, 'Synthesis and Single-Electron Oxidation of Bulky Bis(*m*-terphenyl)chalcogenides: The Quest for Kinetically Stabilized Radical Cations' *Chem. Eur. J.* **2023**, e202203498.

D. Duvinage, L. Malaspina, S. Grabowsky, S. Mebs, J. Beckmann, 'Divalent Bis(*m*-terphenyl)element Cations $[(2,6\text{-}Mes_2C_6H_3)_2E]^+$ of Group 13 Revisited and Extended (E = B, Al, Ga, In, Tl)' *Eur. J. Inorg. Chem.* **2023**, *26*, e202200482.

D. Duvinage, M. Janssen, E. Lork, H. Grützmacher, S. Mebs, J. Beckmann, 'Kinetic Stabilization of Heavier Bis(*m*-terphenyl)pnictogen Phosphaethynolates' *Z. anorg. Allg. Chem.* **2022**, 648, e202200133.

D. Duvinage, M. Janssen, E. Lork, H. Grützmacher, S. Mebs, J. Beckmann, 'Heavier bis(*m*-terphenyl)element phosphaethynolates of group 13' *Dalton Trans*. **2022**, *51*, 7622-7629.

D. Duvinage, S. Mebs, J. Beckmann, 'Isolation of an Antiaromatic 9-Hydroxy Fluorenyl Cation' *Chem. Eur. J.* **2021**, *27*, 8105-8109.

D. Duvinage, A. Schröder, E. Lork, J. Beckmann, 'New crystal structures of alkali metal tetrakis(pentafluorophenyl)borates' *Main Group Met. Chem.* **2020**, *43*, 99-101.

M. Olaru, D. Duvinage, Y. Naß, L. A. Malaspina, S. Mebs, J. Beckmann, 'Intramolecular Reaction of Transient Phosphenium and Arsenium Ions Giving Rise to Isolable 9-Phospha- and 9-Arsena-Fluorenium Ions' *Angew. Chem. Int. Ed.* **2020**, *59*, 14414-14417.

M. Olaru, D. Duvinage, E. Lork, S. Mebs, J. Beckmann, 'Transient Phosphenium and Arsenium Ions versus Stable Stibenium and Bismuthenium Ions' *Chem. Eur. J.* **2019**, *25*, 14758-14761.

M. Olaru, D. Duvinage, E. Lork, S. Mebs, Jens Beckmann, 'Heavy Carbene Analogues: Donor-Free Bismuthenium and Stibenium Ions' *Angew. Chem. Int. Ed.* **2018**, *57*, 10080-10084.

Poster Presentations at Conferences

D. Duvinage, J. Beckmann, 'Sterically Encumbered Boron Compounds' 22nd Norddeutsches Doktorandenkolloquium 2019, Oldenburg, Germany.

List of Figures

List of Schemes

List of Abbreviations

°	degree(s)
°C	degree(s) Celsius
Å	Ångström
$AlOR^F$	tetrakis(perfluoro-*tert*-butoxy)aluminate
AN	acceptor number
Ar	aryl
BAr^F	tetrakis(3,5-bis(trifluoromethyl)phenyl)borate
br	broad
COSY	correlation spectroscopy
δ	chemical shift
d	doublet
D	deuterium
DFT	density functional theory
DCM	dichloromethane
Dur	duryl (2,3,5,6-tetramethylphenyl)
e.g.	*exempli gratia* (for example)
eq.	equivalent
ESI	electro spray ionization
EPR	electron paramagnetic resonance
et al.	*et alii* (and others)
g	gram(s)
h	hour(s)
HSQC	heteronuclear single quantum coherence
HMBC	heteronuclear multiple bond correlation
HRMS	high resolution mass spectrometry
i	*ipso*
LA	Lewis acid
LSA	Lewis superacid

MeCN	acetonitrile
MeOH	methanol
Mes	mesityl (2,4,6-trimethylphenyl)
mg	milligram(s)
min	minute(s)
mL	millilitre(s)
mmol	millimole(s)
m	*meta*
m	multiplet
NHC	N-heterocyclic carbene
NICS	nucleus independent chemical shift
NMR	nuclear magnetic resonance
o	*ortho*
p	*para*
$PerBAr^F$	tetrakis(pentafluorophenyl)borate
Ph	phenyl
Pmp	pentamethylphenyl
Per	pentamethylphenyl substituted *m*-terphenyl (2,6-Bis(2,3,4,5,6-pentamethyl)phenyl)
PTFE	polytetrafluoroethylene
q	quartet
r.t.	room temperature
sLSA	soft Lewis superacid
t	triplet
Ter	mesityl substituted *m*-terphenyl (2,6-bis(2,4,6-trimethylphenyl)phenyl)
THF	tetrahydrofuran
TMS	trimethylsilyl
VE	valence electron
WCA	weakly coordinating anion
Xyl	xylyl (2,6-dimethylphenyl)

Content

Abstract

Highly reactive species, such as cations and radicals, are often proposed as intermediates in reaction mechanisms. The stabilization and isolation of such species is an ongoing challenge in chemistry. One strategy is the use of sterically demanding substituents for the stabilization and isolation of highly reactive low valent main group compounds. A pioneer in this field is Philip P. Power, who investigated the mono and bis-substituted *meta*-terphenyl element compounds of group 14, which allows to activate small molecules, such as hydrogen. This led to a paradigm shift of main group compounds mimicking the behaviour of transition metal complexes, which gained the title “metallomimetics” by Holger Braunschweig.

The emphasis of this thesis is based on bis-substituted *m*-terphenyl element compounds of groups 13, 15 and 16, targeting the thermodynamically or kinetically stabilization of low valent compounds towards the activation of small molecules.

The reported bis(*m*-terphenyl)bismuth hydride Ter_2BiH and chloride Ter_2BiCl (Ter = 2,6-$Mes_2C_6H_3$) act as a starting material for the study of hydride or halide abstraction under the formation of low valent bis-substituted group 15 element compounds. Consequently, the bis(*m*-terphenyl)antimony chloride and hydride were synthesized. By abstraction of the halide or hydride with a trityl or triethylsilyl salt of a weakly coordinating anion, the first bismuthenium- and stibenium ion Ter_2Bi^+ and Ter_2Sb^+ were obtained and represent a novel compound class of kinetically stabilized group 15 six valence electron (6 VE) species.

The main part of this work is based on the synthesis of the lighter congeners of the bis-substituted *m*-terphenyl group 15 compounds. The introduction of the second *m*-terphenyl unit was rather challenging compared to the heavier homologues. By a halide-exchange to fluoride the second *m*-terphenyl unit was introduced, forming the bis-substituted *m*-terphenyl phosphorus and arsenic fluorides Ter_2EF (E = P, As). The abstraction of the fluoride led to transient phosphenium and arsenium species Ter_2E^+ (E = P, As), which reacted intramolecularly indicating the high Lewis acidity of the formed lighter pnictogenium ions. The attempt to block these positions and stabilize the pnictogenium ions by the more electron dense pentamethylphenyl

substituted *m*-terphenyl substituent Per (Per = 2,6-$(C_6(CH_3)_5)_2C_6H_3$) failed, which led again to a ring closure under methyl group migration forming stable arenium ions.

For group 13, the known bis(*m*-terphenyl)indium bromide was used, from which the selective abstraction of the bromide was achieved to obtain the first kinetically stabilized indinium ion Ter_2In^+. Also, in the case of boron, fluoride was used as a substituent for the synthesis of the bis-substituted *m*-terphenyl boron fluoride Ter_2BF and hydride Ter_2BH. The selective abstraction failed, indicating the degradation of the *m*-terphenyl unit, as well as the anion. This behaviour is also indicated by the high Lewis acidity as a four valence electron (4 VE) species.

In the case of group 16, the chalcogen tetrafluorides of sulfur, selenium and tellurium had to be used to employ two *m*-terphenyl substituents, forming the bis(*m*-terphenyl)chalcogenides Ter_2E (E = S, Se, Te). The single electron oxidation led, in the case of the bis(*m*-terphenyl)telluride Ter_2Te, to the first kinetically stabilized bis-substituted tellurenyl radical cation $Ter_2Te^{\cdot+}$, a seven valence electron (7 VE) species.

This work provides new synthetic methods for the introduction of multiple highly sterical demanding substituents leading to the stabilization of otherwise unstable novel low valent main group compounds of group 13, 15 and 16 elements.

1 Introduction

1.1 The Octet Rule

Amongst the first chemical concepts learned by students is the octet rule, which states that each main group element, except for hydrogen and helium, in a molecule tend to bond in a way that each atom is surrounded by eight valence electrons (8 VE).[1]

If the atom has less or more than eight valence electrons in a compound, a highly reactive species is formed in most cases, in particular for lighter main group elements. These low valent or hypervalent compounds are often proposed as reaction intermediates for instance in the nucleophilic substitution reactions S_N1 and S_N2, which propose a low valent species as intermediate (S_N1) or a hypervalent species as a transition state (S_N2) (**Scheme 1**).

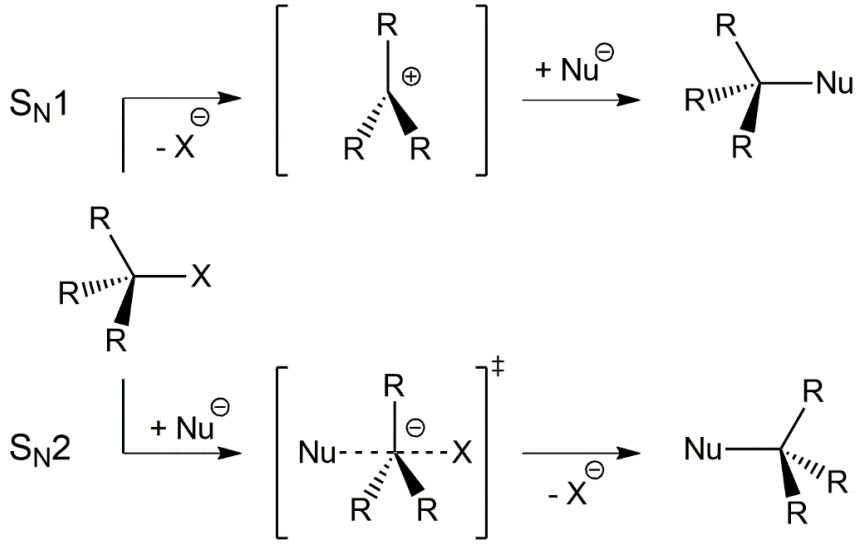

Scheme 1. S_N1 and S_N2 reaction advancing via a low valent species (top) or hypervalent transition state (bottom).

In the nucleophilic substitution reaction, a leaving group X is cleaved off from a carbon center substituted by a nucleophile Nu. For this reaction, two basic mechanisms are possible. The S_N1 reaction shows first the cleavage of the leaving group forming a carbocation as a low valent species. In case of the S_N2 reaction, the nucleophile attacks the carbon centre simultaneously as the leaving group is cleaved off, forming a pentacoordinated carbanion as a transition state, a

hypervalent species. Even in this simple reaction, the stabilization of the intermediate often determines the favored pathway. Tertiary and secondary alkyl halides or alcohols tend to react by the formation of a carbocation, due to electronic and steric stabilization of the carbocation, and primary and secondary alkyl halides and alcohols tend to undergo an S_N2 reaction due to lack of stabilization. [2]

The stabilization of such reactive intermediate is necessary to understand or to postulate a reaction mechanism and also to explain possible reactivities.[2] Therefore, the stabilization as well as the isolation of a reactive species in order to verify the reaction mechanism is most likely a task as long-known as chemistry itself. Strategies to achieve this goal include different methods such as thermodynamic or kinetic stabilization, in case of cationic species the choice of the corresponding anion is also crucial to inhibit cation-anion pairing.[3]

1.2 Low Valent Species

The stabilization of reactive species is a task that can be succeeded by the combination of various methods, including a suitable substituent, a weakly coordinating anion and a suitable formation agent in the right solvent. This can lead to the isolation of a reactive element compound. It is necessary to distinguish between predominately thermodynamic and kinetic stabilization. The stabilization by donor atoms can be useful for possible applications such as catalysis and the stability and lifetime of the cationic species, whereas the kinetic stabilization is often used for main-group element compounds that were unknown as stable species until then. A low valent species is formed by the formal abstraction of electrons. This removal of an electron is often accomplished by the cleavage of a substituent or by oxidation (fide supra). Due to this change in the electron count, each main group provides different structural motifs (**Fig. 1**).

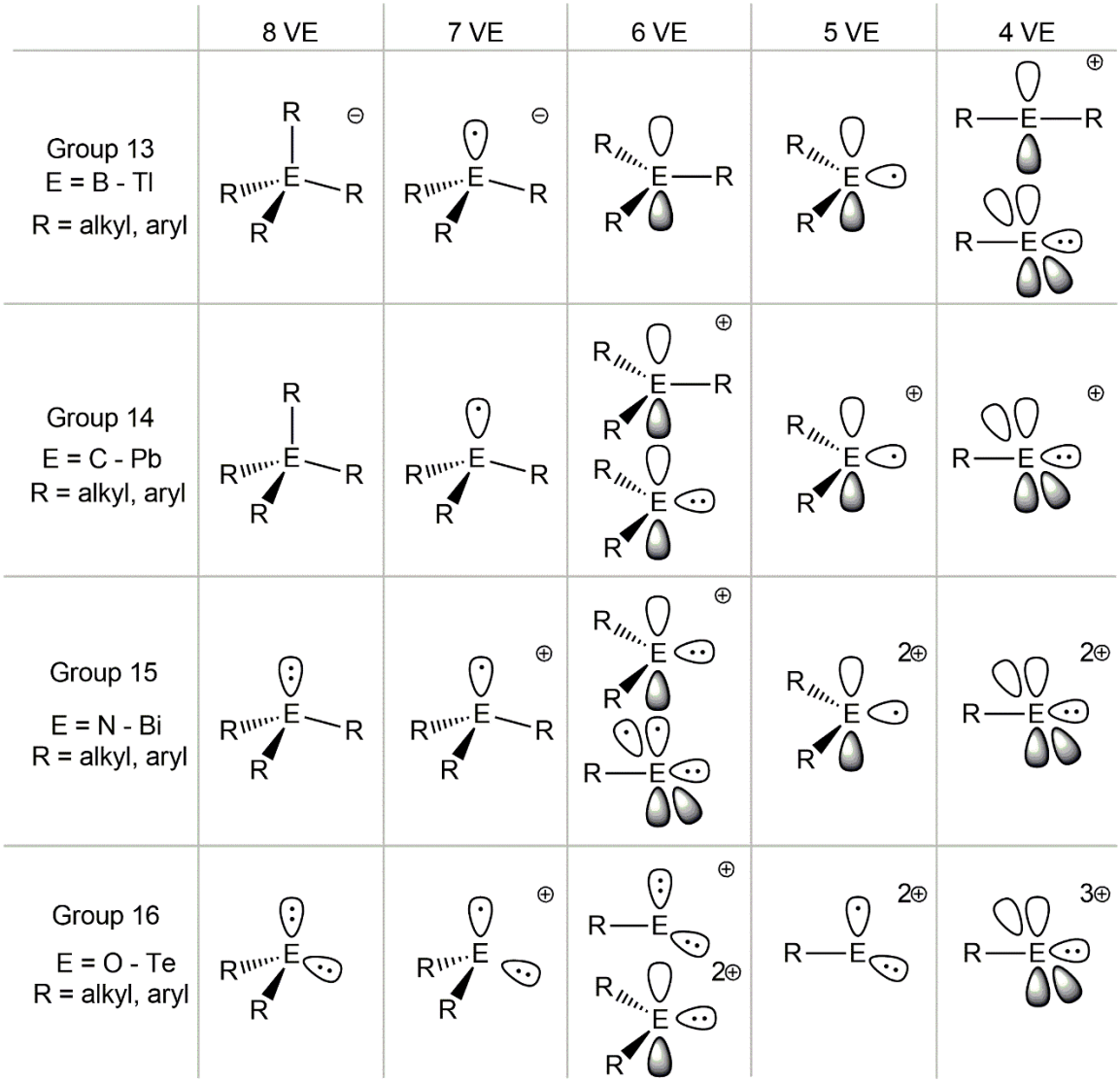

Figure 1. Overview of the theoretical structural motifs of the eight valence electron (8 VE) and the corresponding low valent species for group 13-16. The shown multiplicity is the estimated one in the ground state.

The stabilization of low valent cationic species has to be covered by the choice of the corresponding substituents as well as the weakly coordinating anion. This means there is no perfect substituent and no perfect anion and it can be fulfilled by several criteria. Also, the reaction medium and reactants are important as solvents tend to coordinate towards the reactive species and not all reactants form a reactive species. Exemplary, for highly electrophilic species, the abstraction of a substituent is usually achieved by a highly electrophilic reactant, for instance in the case of a halide abstraction with silylium ions. [4-5]

In general, it can be postulated, the higher the valence electron difference to the octet rule, the higher the reactivity. A tremendous amount of Lewis acids comprises group 13 elements, as they have a natural electron vacancy, being six valence electron species in their neutral form. Also, the number of substituents changes the reactivity drastically. Six valence electron group 14 element species were isolated as early as in the beginning of the 20th century[6] and are nowadays widely available and often used as electrophiles, whereas to the best of my knowledge no six valence electron group 15 cation has been reported to date. Group 15 low valent cations exhibit only two substituents compared to group 14 low valent cations, stabilized by three substituents (**Fig. 1**). This means that low valent species tend to be electrophilic, with increasing Lewis acidity if the electron difference to the eight valence electrons is higher. Two possible synthetic strategies in the stabilization of low valent species are by thermodynamic or kinetic stabilization.

1.3 Thermodynamic Stabilization

Thermodynamic stabilization is defined as the stabilization of a reactive species by coordination of electron pairs, often stemming from an atom with free lone pairs, like oxygen, nitrogen or phosphorus. This can either be accomplished by the coordination of molecules with donor atoms like solvents such as THF, Et_2O and DMSO, or by additional ligands like amines or phosphines for instance triphenylphosphine or pyridine. By the introduction of a donor atom in the target molecule an intramolecular stabilization can be achieved as well. In the work of Dostal *et al.*[7] a NCN Pincer-type ligand was used to stabilize antimony and bismuth in the rare oxidation state +1 for the first time (**Fig. 2**, **I**). Venugopal and coworkers[8] stabilized several cationic bismuth compounds with their NC ligand, which in theory provides a free coordination sphere on bismuth, that is occupied by a THF molecule, simultaneously demonstrating the synthetic difficulties, to obtain non-coordinating low valent group 15 cations (**Fig. 2**, **II**).

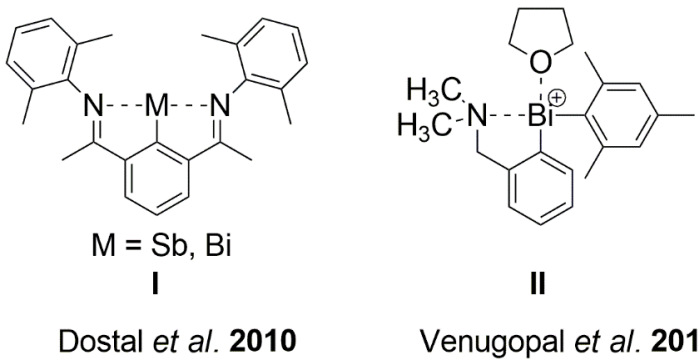

Figure 2. Thermodynamic stabilization **I** (intramolecular) and **II** (donor solvent (intermolecular) and intramolecular).[7-8]

An intermolecular thermodynamic stabilization can also occur by ion pairing, as the cationic center can be coordinated by the anion. This is often observed for small anions and can be avoided in many cases by the usage of weakly coordinating anions (see Chapter 1.5.2 weakly coordinating anions).

It has to be considered, that the addition of electrons to a low valent species saturating the valence electron shell lowers the reactivity like thermodynamic stabilization by donor atoms does. Thermodynamically stabilized cations are usually less reactive than their kinetically stabilized congeners. However, in case of weak intermolecular stabilization, e.g. weak donors like solvents, olefins or aromatic systems, a thermodynamically stabilized reactive species can still possess a high reactivity.[9-11]

Stephan and coworkers[12] have shown that the inhibition of coordination between Lewis acid and Lewis base can provide an increased reactivity, able to activate small molecules such as H_2. This generated a new research field and is coined by the term “frustrated Lewis pairs”. The Lewis acid and base are substituted by sterically demanding substituents, kinetically inhibiting the formation of a regular Lewis pair, but still providing the possibility to interact with a small molecule. The choice of the substituent is crucial as a preorganisation between Lewis acid and base is required to form a pocket in which the small molecule can be activated.

1.4 Kinetic Stabilization

Kinetic stabilization is provided by the size of the substituent, as it prevents an interaction between the reactive center and another atom (**Fig. 3**). These kinetically stabilized low valent species are often considered as “truly” low valent, as their valence electron shell is not filled up with electrons by donation of an electron pair by inter- or intramolecular coordination of donor atoms or ion pairing, to achieve noble gas valency.

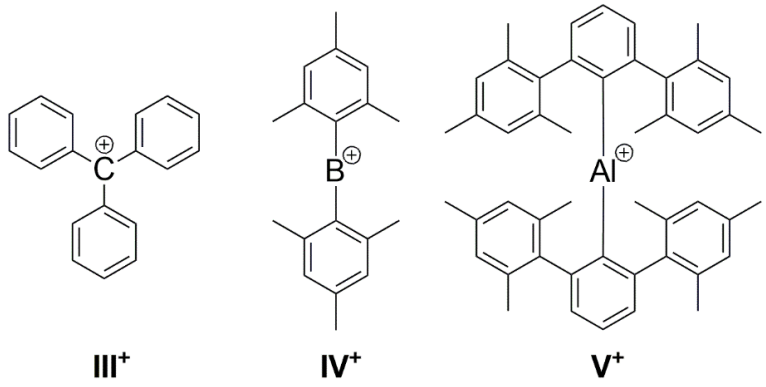

Figure 3. Kinetically stabilized cations from left to right with increased sterically encumbered ligands (**III**$^+$ = Ph, **IV**$^+$ = Mes[4], **V**$^+$ = Ter[13]).

However, due to the highly reactive central atom, even aryl systems can interact with it e.g. in a Menshutkin-type complex by π complexation. By close interaction of an aromatic system with the reactive element, it increases also the possibility of a bond activation, leading to a degradation of the ligand and the reactive element center forming an undesired species. [14-16]

The synthetic strategy for kinetic stabilization can be illustrated in the quest of isolating a purely three coordinated silicon cation. In 1993, the group of Lambert had a tremendous breakthrough, and set a milestone by the isolation of a free silyl cation. By the use of a weakly coordinating anion, namely tetrakis(pentafluorophenyl)borate $[B(C_6F_5)_4]^-$, and a non-nucleophilic solvent such as benzene or toluene, Lambert *et al.* were able to prepare $[Et_3Si(toluene)]^+[B(C_6F_5)_4]^-$ (**VI**$^+[B(C_6F_5)_4]^-$).[17] Within the crystal structure of **VI**$^+[B(C_6F_5)_4]^-$ no cation-anion interaction was observed, contrary to other attempts in the formation of silyl cations like the previously synthesized Me_3SiClO_4 and Ph_3SiClO_4 by Lambert and coworkers.[18] However it shows a distant coordination

of the cationic silicon atom towards one molecule of toluene (**Fig. 4**). The geometry of the toluene molecule is almost undistorted, which leads to the conclusion that only a very weak interaction between the Si and the C atom of the toluene molecule is present and therefore **VI**$^{+}$ can be regarded as a stable silylium ion with no coordination to the counter anion and only very weak solvent interaction.

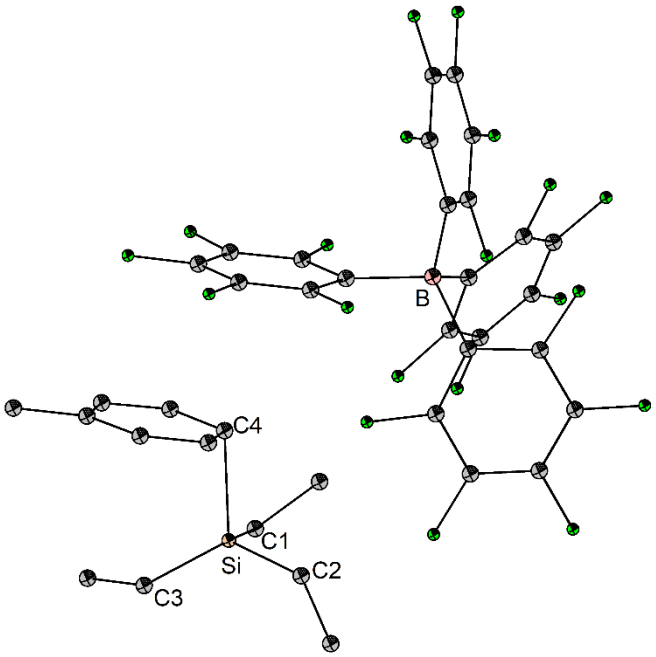

Figure 4. Molecular structure of $[Et_3Si\text{-}Tol]^+[B(C_6F_5)_4]^-$ **VI**$^{+}$$[B(C_6F_5)_4]^-$. Solvent and hydrogen atoms are omitted for clarity. Selected bond lengths (Å) and angles (°): Si-C1 1.858(1), Si-C2 1.864(4), Si-C3 1.834(1), Si-C4 2.195(4); C1-Si-C2 112.84(1), C2-Si-C3 113.67(1), C1-Si-C3 115.06(1) Σ = 341.5(1).[17]

This was debated by Pauling by consideration of the calculated bond order between silicon and the interacting carbon of a coordinated toluene molecule.[19] Olah *et al.* also stated that the experimentally observed ^{29}Si NMR resonance (δ = 92.3 ppm)[17] is shifted to higher fields in comparison to the calculated resonance of the planar free Et_3Si^+ cation, expected at the very low field (δ = 371.3 ppm).[20] This led to the conclusion that the solvent coordination masks the silylium ion.

The second milestone regarding silylium ions was achieved by Reed *et al.* by the synthesis of $[i\text{Pr}_3\text{Si}]^+[CB_{11}H_6Br_6]^-$ (**VII**$^{+}$$[CB_{11}H_6Br_6]^-$), realised by hydride abstraction of $i\text{Pr}_3\text{SiH}$ with $[Ph_3C]^+[CB_{11}H_6Br_6]^-$ in toluene also introducing a weakly coordinating anion, namely the carborane anion. The molecular structure reveals no interaction of the silicon atom with toluene, as it was visible for **VI**$^{+}$, but shows

weak interaction between the silicon atom and a bromine atom of the anion (**Fig. 4**). Overall, *i*Pr_3Si^+ (**VII$^+$**) was more deshielded than the ethyl congener (δ = 109.8 ppm (**VII$^+$**) vs. δ = 92.3 ppm (**VI$^+$**)) and exhibited a more planar geometry around the silicon atom in the solid state (351° (**VII$^+$**) vs. 342° (**VI$^+$**)) leading to the conclusion that **VII$^+$** is closer to a "free" silyl cation, providing the highest similarity to a "free" silylium ion.[21-22] Again, this was debated and Olah *et al.* stated that it is more related to a polarized silylbromonium zwitterion, as the Si-Br bond length is only 0.2 Å longer than a normal Si-Br bond and the ^{29}Si-NMR shift is far off from the calculated value.[19]

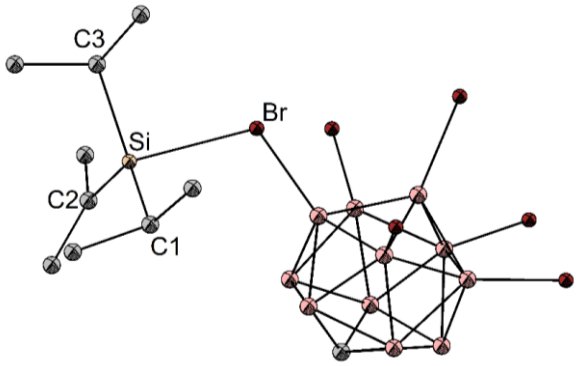

Figure 5. Molecular structure of $iPr_3Si^+[CB_{11}H_6Br_6]^-$ **VII$^+$**$[CB_{11}H_6Br_6]^-$. Hydrogen atoms are omitted for clarity. Selected bond lengths (Å) and angles (°): Si-C1 1.908(1), Si-C2 1.798(1), Si-C3 1.860(1); C1-Si-C2 119.55(1), C2-Si-C3 111.21(1), C1-Si-C3 120.15(1) Σ = 350.9(1).[21]

Reed *et al.* varied the alkyl substituents around the silicon atom and prepared several trialkylsilylium ions $R_3Si^+[CB_{11}H_6Br_6]^-$ (R_3Si^+ = Et_3Si^+, *t*Bu_2MeSi^+ and *t*Bu_3Si^+)[23] resulting in a similar coordination towards a bromine atom of the anion. Surprisingly, increasing the sterical hindrance from **VII$^+$** towards *t*Bu_3Si^+ did not increase the C-Si-C angle, nor elongate the Si-Br interaction. In additional studies they also introduced the hexachloro- and hexaiodocarborane as weakly coordinating anions and prepared the structurally related *i*$Pr_3Si^+[CB_{11}H_6X_6]^-$ (X = Cl or I) salts, to which the hexachlorocarborane derivative shows the highest similarity to a "free" silylium ion at that time (**Fig. 6**).[24]

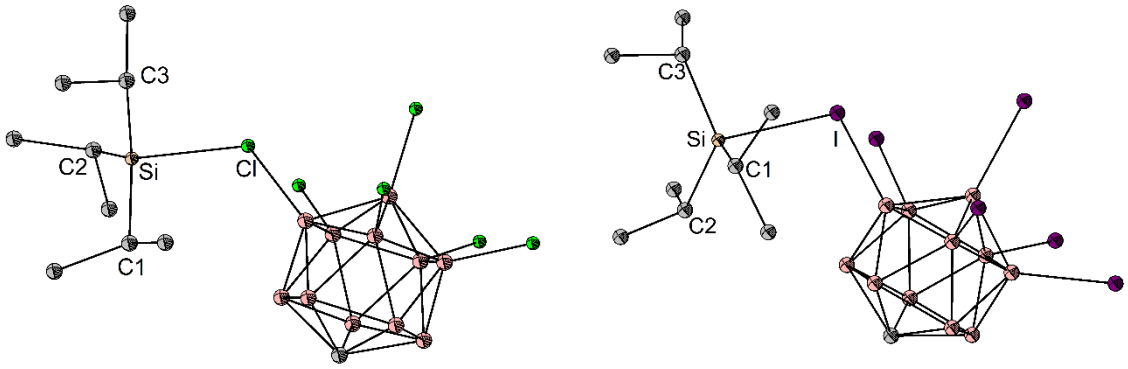

Figure 6. Molecular structures of iPr$_3$Si$^+$[CB$_{11}$H$_6$Cl$_6$]$^-$ (left) and iPr$_3$Si$^+$[CB$_{11}$H$_6$I$_6$]$^-$ (right). Hydrogen atoms are omitted for clarity. Selected bond lengths (Å) and angles (°): iPr$_3$Si$^+$[CB$_{11}$H$_6$Cl$_6$] - Si-C1 1.849(1), Si-C2 1.845(1), Si-C3 1.850(8), Si-Cl 2.322(3); C1-Si-C2 119.07(1), C2-Si-C3 115.40(1), C1-Si-C3 117.42(1) Σ = 351.9(1). iPr$_3$Si$^+$[CB$_{11}$H$_6$I$_6$] – Si-C1 1.877(1), Si-C2 1.901(1), Si-C3 1.872(1), Si-I 2.660(7); C1-Si-C2 113.21(1); C2-Si-C3 120.76(1); C1-Si-C3 112.78(1), Σ = 346.7(1).[24]

By the introduction of mesityl substituents, the experimental breakthrough was achieved by Lambert and coworkers, who prepared the trimesitylsilylium ion as tetrakis(pentafluorophenyl)borate salt Mes$_3$Si$^+$[B(C$_6$F$_5$)$_4$]$^-$ (**IX$^+$**[B(C$_6$F$_5$)$_4$]$^-$) by the allyl abstraction with Et$_3$Si(benzene)$^+$[B(C$_6$F$_5$)$_4$]$^-$ from allyltrimesitylsilane Mes$_3$Si-CH$_2$-CH=CH$_2$ **VIII** (**Scheme 2**).[5]

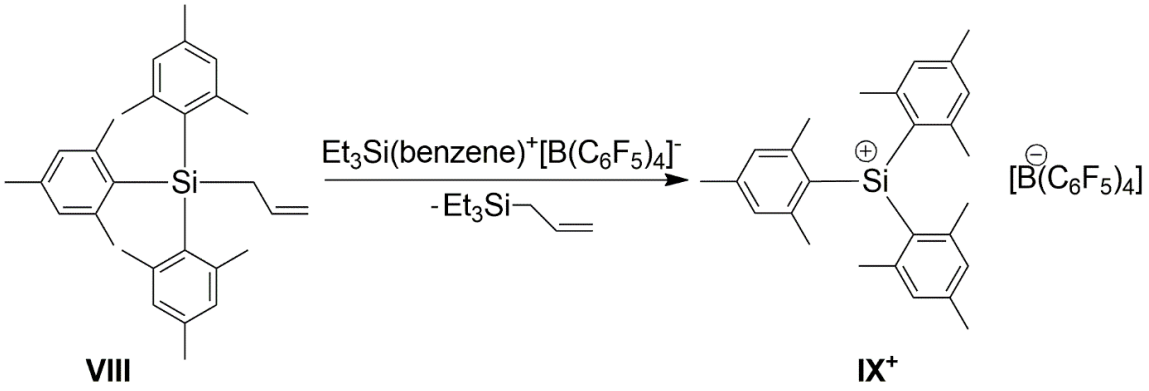

Scheme 2. Synthesis of the trimesitylsilylium cation by allyl abstraction.[5]

IX$^+$[B(C$_6$F$_5$)$_4$]$^-$ provides the same ^{29}Si NMR resonance in several aromatic solvents (δ = 225.5 ppm) indicating no solvation of the cation.[5] Due to the fact that [B(C$_6$F$_5$)$_4$]$^-$ salts often form oils, it was not possible for Lambert *et al.* to crystallize **IX$^+$**[B(C$_6$F$_5$)$_4$]$^-$. By the replacement of the anion by the carborane anion CB$_{11}$HMe$_5$Br$_6^-$ prepared by Reed *et al.*, **IX$^+$**[BC$_{11}$HMe$_5$Br$_6$]$^-$ could be prepared in a joined publication by Lambert and Reed, in which single crystal diffraction experiments revealed the trigonal-planar trimesitylsilylium ion, lacking any covalent

interaction with the anion or solvents, providing the first truly “free” silylium ion (**Fig. 7**).[25]

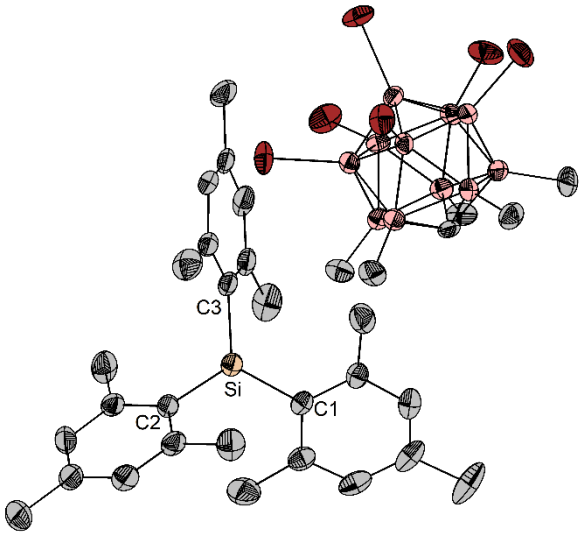

Figure 7. Molecular structure of $Mes_3Si^+[CB_{11}HMe_5Br_6]^-$ **IX**$^+[CB_{11}HMe_5Br_6]^-$. Solvent and hydrogen atoms are omitted for clarity. Selected bond lengths (Å) and angles (°): Si-C1 1.820(1), Si-C2 1.808(1), Si-C3 1.824(1); C1-Si-C2 120.5(2), C2-Si-C3 121.7(2), C1-Si-C3 117.7(2) Σ = 359.9(2).[25]

1.5 Sterically Demanding Substituents

The development of a synthetic route towards the first free silylium ion, described by Lambert and Reed [25] illustrates the need of substituents with increased steric demand. Alkyl substituents, such as *iso*-propyl[21, 24] or *tert*-butyl[23] were not able to prevent cation-anion interactions between silicon and the corresponding anion. Introduction of the bulkier mesityl substituent ultimately allowed to achieve the goal of a free silylium ion, proven by neither cation-anion interaction nor solvent interactions in the solid state. (**Fig. 7**) Also in solution, no interaction is visible, as the chemical shift of the ^{29}Si NMR resonance remains similar in several aromatic solvents and with different anions.[25]

The mesityl group proved to be a very versatile substituent in the realization of the first silylium ion, the first disilene and the first borinium ion.[4-5, 26] However, it has several limitations, particularly in the attempt to stabilize radicals and element compounds in low oxidation states. Mesityl substituents often lack sufficient sterical hindrance to inhibit oligomerization, exemplified by mesityl pnictogen hydrides, which form polypnictogens such as $(MesP)_5$, $(MesAs)_4$ and $(MesSb)_4$ *via*

dehydrocoupling.[27-29] Radical formation can also lead to intramolecular degradation, as the attempt to form heavier group 14 carbene analogues, such as a silylene and germylene, activate one of the methyl groups forming **XI** and **XIII** (**Scheme 3**).[30-31]

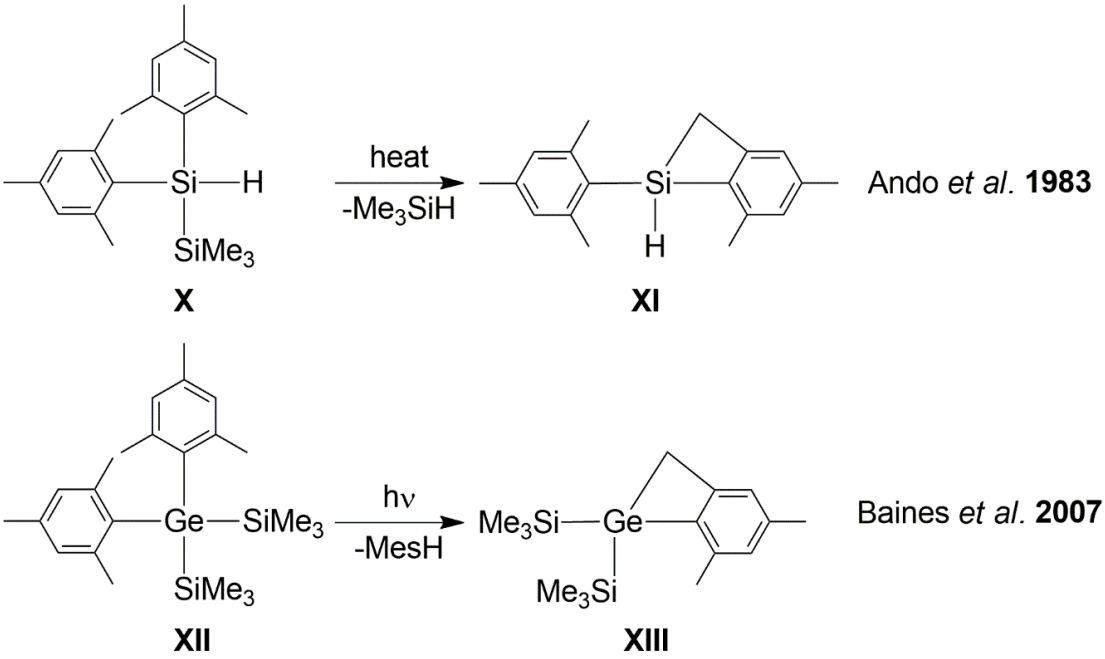

Scheme 3. Activation of the mesityl substituent by a transient heavier carbene analog. [30-31]

Consequently, bulkier substituents, such as Dipp (Dipp = 4,6-*i*Pr$_2$C$_6$H$_3$), Tripp (Tripp = 2,4,6-*i*Pr$_3$C$_6$H$_2$) and supermesityl Mes* (Mes* = 2,4,6-*t*Bu$_3$C$_6$H$_2$) were explored and used to stabilize several low valent element compounds, such as the first diphosphene Mes*P=PMes* **XIV** by Yoshifuji *et al*.[32] The diphosphene **XIV** shows a tendency to photolysis to form a transient triplet phosphinidene, which attacks the substituent leading to an intramolecular ring closure to form **XV** (**Scheme 4**).[33-34]

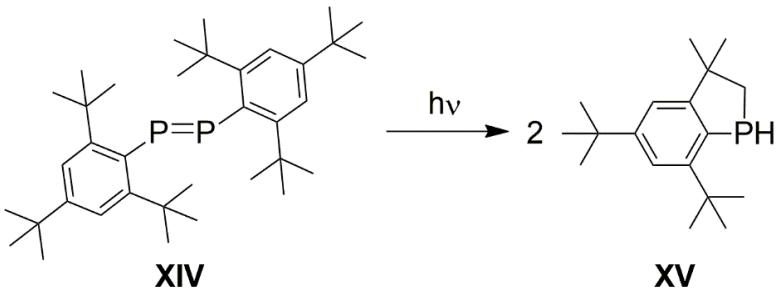

Scheme 4. Irradiation of diphosphene **XIV** leads to an intramolecular CH insertion. [33]

Using the even bulkier *m*-terphenyl substituent Ter (Ter = 2,6-$Mes_2C_6H_3$), Protasiewicz *et al.*[35] were able to synthesize the corresponding bis(*m*-terphenyl)diphosphene TerP=PTer by the reduction of the organophosphorus dichloride $TerPCl_2$ with magnesium. Power *et al.*[36] adopted this method and the authors were able to reduce the organopnictogen dichlorides $TerECl_2$ to the corresponding heavier dipnictenes TerE=ETer (E = As, Sb, Bi). The same formation of dipnictenes was also achieved by dehydrocoupling of the *m*-terphenylpnictogen dihydrides for arsenic and antimony.[28],[29] The formation of dipnictenes instead of pnictogenacycles indicates the increased steric demand of terphenyl systems compared to mesityl.

Power and coworkers were able to isolate a series of low valent element compounds by the use of the *m*-terphenyl system, such as Ter_2Cr_2[37], with a chromium chromium quintuple bond. The heavier tetrel element alkyne analogs Ter_2E_2 (E = Ge, Sn, Pb).[38-40] TerGa **XVI**, as a gallium (I) species, which is able to activate ammonia and hydrogen.[41] Also the heavier carbene analogs Ter_2E (E = Ge, Sn, Pb)[42-44] from which the germylene **XVIII** and stannylene **XX** are able to activate hydrogen (**Scheme 5**).

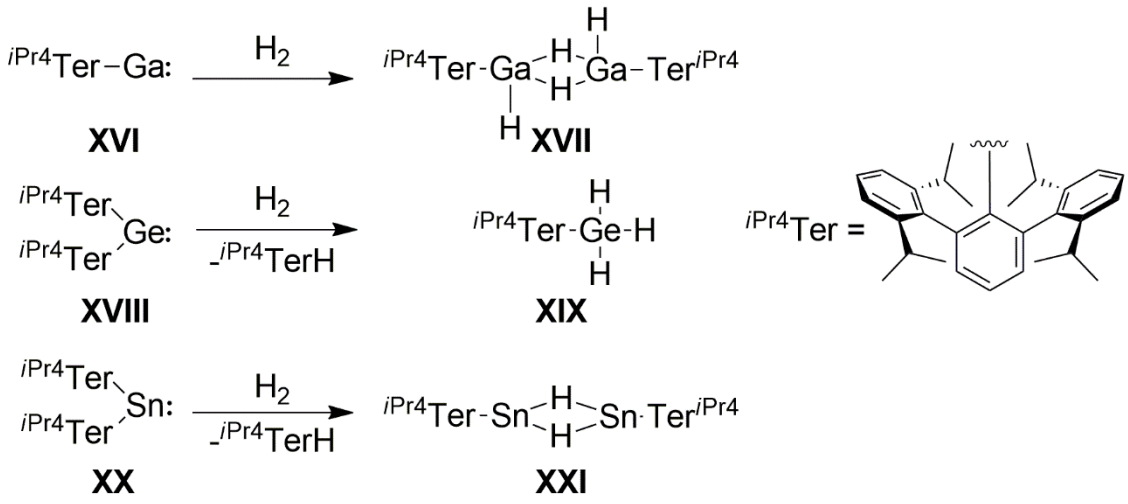

Scheme 5. Reactions of low valent *m*-terphenyl element compounds with hydrogen.

The advantage of *meta*-terphenyl systems stems from the flanking aryl substituents, which form a bowl-shaped cavity around the central atom and provide steric shielding. However, the aromatic rings can also interact with the central element, by donation of electron density to form a Menshutkin-like complex, which is also a form of thermodynamic stabilization, even though it is weaker than the

coordination by typical electron donor atoms (O, N, P, etc.).[15] Various types of *m*-terphenyl substituents have been designed and used over the last few decades to fine-tune steric and electronic properties.

This led to the development of a plethora of *m*-terphenyl element compounds. By decoration of the flanking aromatic rings with alkyl groups, such as methyl, *iso*propyl and *tert*butyl, the steric demand can be controlled (**Fig. 8**). Furthermore, the inductive effect of these alkyl groups increases the electron density in the aromatic rings, which potentially promotes the element···π interactions of the central atom, also leading to a thermodynamic stabilization of the low valent species.[36, 40]

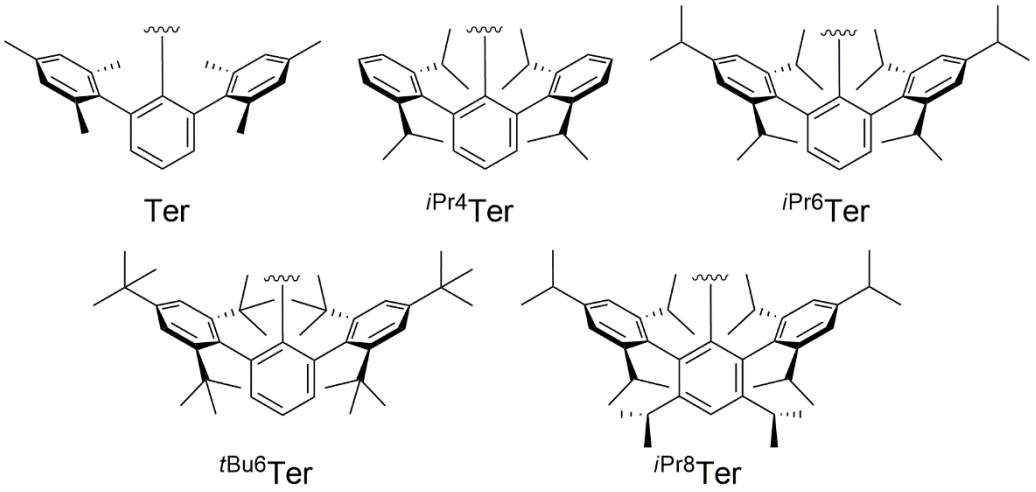

Figure 8. Commonly used *m*-terphenyl systems. Mesityl substituted Ter[45], di*iso*propylphenyl substituted $^{i\text{Pr4}}$Ter[46], tri*iso*propylphenyl substituted $^{i\text{Pr6}}$Ter[46] (top, l. to r.), supermesityl substituted $^{t\text{Bu6}}$Ter[47] and the octa*iso*propyl terphenyl system $^{i\text{Pr8}}$Ter[48] (bottom, l. to r).

The increased E···π interaction that induces a stabilization of silylium ions (R_3Si^+) was demonstrated by Siegel *et al.* The authors demonstrated that the substitution pattern increases the π electron density that is donated towards the silicon with increasing number of methyl groups as shown in **XXII$^+$** (**Fig. 9**, left). This is also shown in the ^{29}Si NMR shift (δ = 60.6 ppm (**XXII$^+$**)), which gets more deshielded with less methyl groups (δ = 80.1 ppm (^{Xyl}TerMe$_2$Si$^+$)).[49] To counter this effect electron poor flanking groups should reduce the E···π interaction, leading to a tricoordinate silicon cation. However, exchange of the methyl groups with halogens lead to the formation of penta-coordinated silicon cations, with close Si···X interactions (X = F, Cl), visible in **XXIII$^+$** (**Fig. 9**, right). This is also visible in solution

by the ^{29}Si shift (δ = 88.6 ppm (**XXIII$^+$**), 90.5 ppm ($^{o\text{-}F2}$TerMe$_2$Si$^+$), which is not enough deshielded to resemble a tricoordinated silyl cation. Additionally, a coupling between the fluorine and silicon nuclei is visible, verifying the interaction in solution.[50]

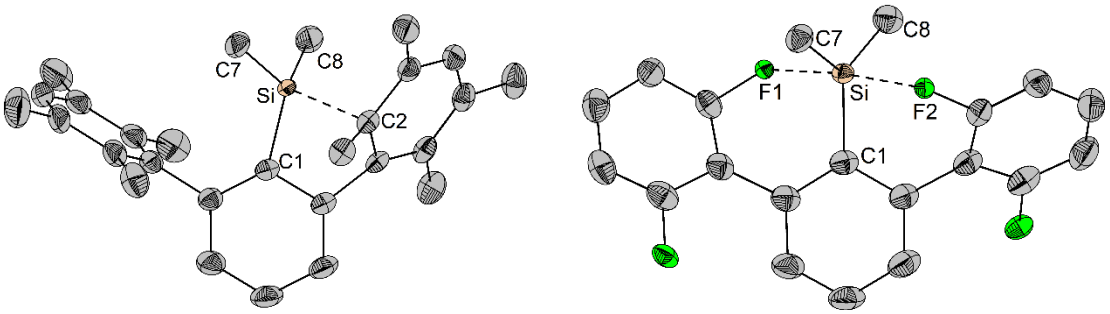

Figure 9. Molecular structures of ^{Dur}TerMe$_2$Si$^+$ **XXII$^+$**, $^{o\text{-}F2}$TerMe$_2$Si$^+$ **XXIII$^+$**.[49-50] Anions and hydrogen atoms were omitted for clarity. Dashed lines show the E··· π and E···F interactions.

Finally, Siegel *et al.* designed *m*-terphenyl substituents bearing one electron-rich flanking group, with methyl substituents, and one electron-poor flanking group, with fluorine substituents, to evaluate the contribution of E··· π and E···F interactions to the stabilization of E. A competition between E··· π and E···F interactions is visible, in which the less electron dense xylyl (**XXIV$^+$**) and mesityl substituents contribute less than the E···F interactions and the electron dense substituents duryl and pentamethylphenyl (**XXV$^+$**) substituents favour the E··· π interactions (**Fig. 10**), which is also reflected in the calculated and measured ^{29}Si NMR shifts, as the E··· π interaction produces a more shielded silicon nucleus (δ = 57.2 ppm (**XXIV$^+$**)), whereas the E···F interaction leads to a more highfield shifted resonance (δ = 101.3 ppm (**XXV$^+$**)) .[51]

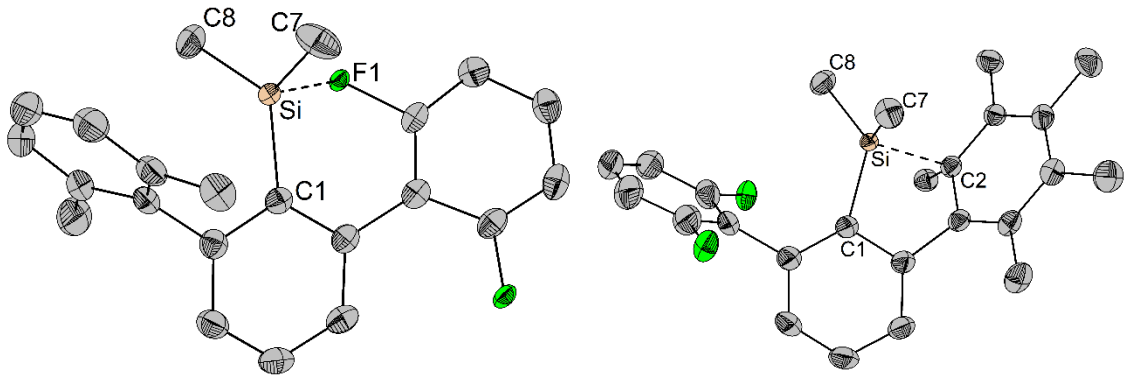

Figure 10. Molecular structures of the mixed $^{Xyl\text{-}o\text{-}F2}$TerMe$_2Si^+$ **XXIV$^+$** and $^{Me5\text{-}o\text{-}F2}$TerMe$_2Si^+$ **XXV$^+$**.[51] Anions and hydrogen atoms were omitted for clarity. Dashed lines show the E··· π and E···F interactions.

The central aromatic ring in *m*-terphenyl substituents can also be modified in *para* and *meta* position, leading to electronic and or steric effects on the central atom. Power *et al.* studied this influence in the context of the formation of digermynes and distannynes in 2010. The incorporation of a $SiMe_3$ group in *para* position of the central ring drastically increases the E-E triple bond length. In the original Ar-Sn-Sn-Ar, the Sn-Sn distance is 2.607 A, and the bond angle is 125.24(7)°, whereas in the modified 4-TMS-Ar-Sn-Sn-Ar-4-TMS, the Sn-Sn distance increased to 3.066(10) Å, and the Sn-Sn-C angle decreased to 99.25(14)°, which is 0.4 Å longer and 26° smaller than the unsubstituted reference system.[38,47] This introduction indicated a transformation of a Sn-Sn triple bond to a single bond. It is also reflected by the geometry of the molecule in the molecular structure. For the reference compound, it is visible that the central rings are in plane with the C-Sn-Sn-C unit, whereas the central rings in the TMS substituted species are perpendicular to the element-element bond, which is comparable to the previously published single-bonded lead derivative Ar-Pb-Pb-Ar.[40]

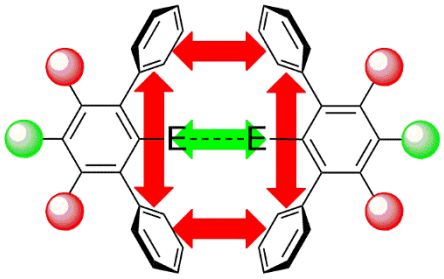

Figure 11. Influence of the substitution pattern in the central ring regarding electronic (green) and steric effects (red).

The introduction of *iso*-propyl groups in *meta* position at the central ring pushes the flanking groups closer to the protected element, leading to increased steric hindrance and also inhibiting a possible twisting of the flanking aryl rings. This leads to increased intermolecular element-element distances in hypothetical RE-ER compounds, which can inhibit a bond formation and therefore leads to monomeric species. In recent studies, Power *et al.* were able to isolate the first single substituted alanediyl species ^{i}Pr8TerAl: **XXVI** by reduction of the parent aluminium diiodide compound ^{i}Pr8TerAlI$_2$.[52] By the use of this alanediyl species in the reaction with *m*-terphenyl azide, the first iminoalane **XXVII** was formed and isolated by Power and coworkers, providing an almost linear C-Al-N angle

(172.5(3)°) and an Al-N bond length of 1.625(4) Å, which is the shortest one reported to date (**Fig. 12**). This agrees with the calculated Al-N bond lengths in HAlNH and MeAlNMe.[53-56]

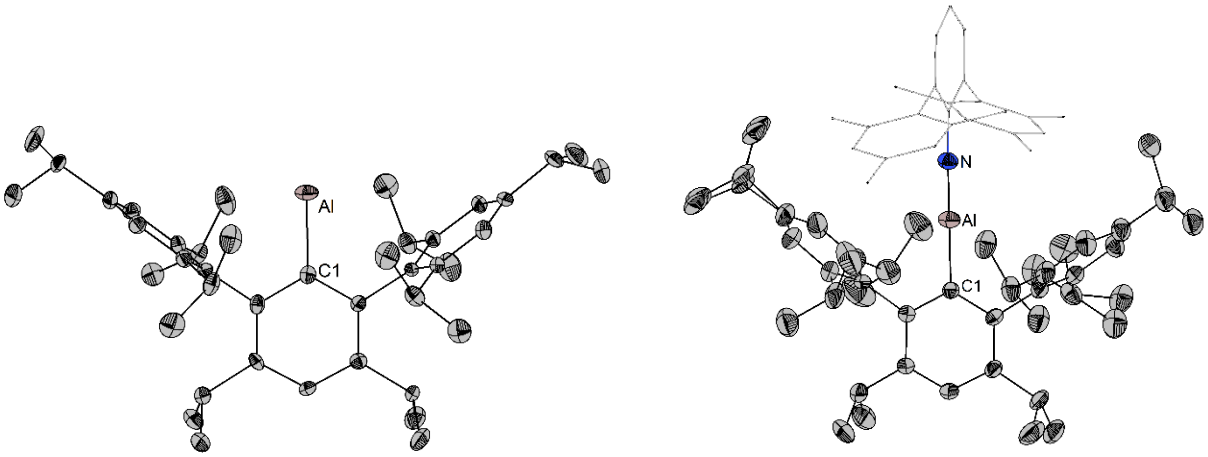

Figure 12. Molecular structures of ^{i}Pr8TerAl: **XXVI** (left)[52] and ^{i}Pr8TerAlNTer **XXVII** (right)[53]. The second terphenyl unit (right) was displayed as a stick model and hydrogen atoms were omitted for clarity.

1.6 The Nature of Cation and Anion

1.6.1 Cation Formation

Arguably, the first reported low valent cation was the trityl cation, reported by Norris and Kehrmann independently in 1902, who treated triphenylmethanol with concentrated sulfuric acid and by Adolf von Baeyer, who reacted triphenylmethyl chloride with aluminium trichloride. The authors obtained a deep yellow solution, which could be later identified as the triphenylmethyl cation Ph_3C^+, shortly trityl cation (**Scheme 6**).[6, 57-58]

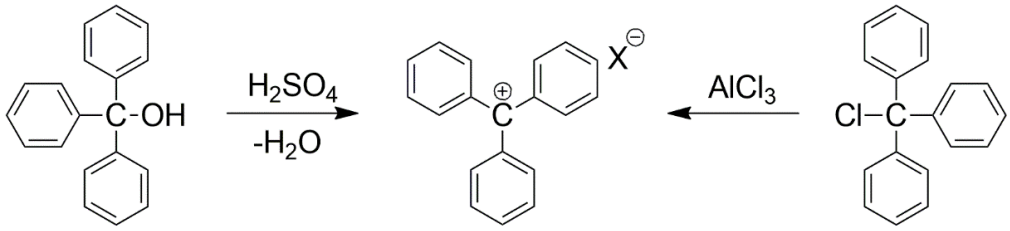

Scheme 6. Water elimination from triphenylmethanol, by the addition of a strong Brønsted acid to form a cation and halide abstraction from triphenylmethyl chloride by a strong Lewis acid.[6, 57-58]

By the abstraction of an anionic substituent from an element, a low valent species can be formed. In this example, the protonation of the hydroxy group was used to form water as elimination product as well as the abstraction of a chloride by the Lewis acid aluminium trichloride. The formed trityl cation, as the first example of a persistent carbenium ion, shows an extraordinary stability, which can be explained by a charge delocalization over each phenyl group.[59] The trityl cation is a strong hydride acceptor and can be used to abstract hydrides from element hydride compounds to generate an element cation.[13, 60-62]

As previously shown in the case of the alkylsilylium ions **VI**$^+$ and **VII**$^+$, the trityl cation can be used to generate e.g. silylium ions from silyl hydrides.[17, 49-51] The inhibition of cation-anion pairing make silylium cations extremely electrophilic. Therefore, they are often used for the abstraction of halides, especially fluorides, which is due to the high fluoride affinity of silicon.[17, 21]

Olah *et al.* have used similar methods, but harsher conditions, to generate alkylcarbenium ions, such as the *tert*butylcarbenium $(CH_3)_3C^+$ **XVIII**$^+$. By the use of antimony pentafluoride as a super Lewis acid, the *tert*butylcarbenium ion could be synthesized from isobutyl fluoride $(CH_3)_3CF$.[63] They were also able to show, that *iso*butane $(CH_3)_3CH$ reacts in super acidic conditions, by the use of fluorosulfonic acid and antimony pentafluoride, under the formation of the carbenium ion **XXVIII**$^+$ (**Scheme 7**). This reaction is possible, as the superacidic H^+ acts as a hydride acceptor and leads to the abstraction of a hydride under formation of hydrogen gas.[64] The used combination of fluorosulfonic acid and antimony pentafluoride was later coined by the term “magic acid”. By the synthesis and study of this carbocation and many others, such as the methanium ion CH_5^+[65], Olah set

multiple milestones in carbon chemistry and received in 1994 the noble price “for his contribution to carbocation chemistry”.[66]

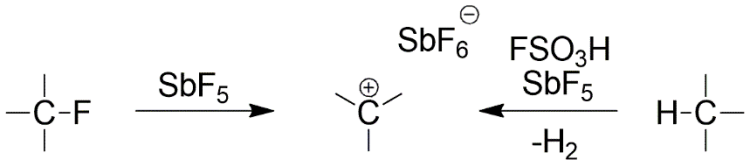

XXVIII⁺

Scheme 7. Formation of the *tert*butylcarbenium ion **XXVIII⁺** by abstraction of a fluoride with antimony pentafluoride as a super Lewis acid or by abstraction of a hydride by the Super acid FSO_3H-SbF_5.[63-64]

Also, alkaline metal and other metal salts can be used as electrophilic source, to generate element cations, due to salt formation with a high lattice energy as a strong driving force. In cases where the element halide bond is labile in solution, the lithium, sodium, potassium, silver and thallium salts of weakly coordinating anions are applicable.[3, 67-69] The silver cation is often used for halide abstraction as the lattice energy of silver halide salts is exceptionally high, but they also tend to be light sensitive and can act as oxidants.[70] Because of this, in some cases thallium salts are used as alternative, even though they have a high toxicity.[71]

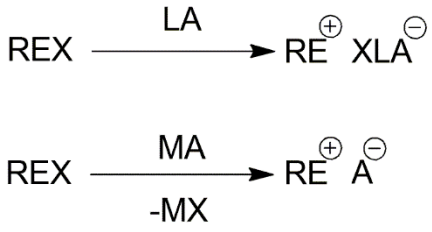

R = any substituent

LA = Lewis acid

M = Li^+, K^+, Ag^+, Tl^+, Ph_3C^+, R_3Si^+

A = WCA

X = halide, hydride, methide, ethide, allylide

Scheme 8. Generation of an element cation by the use of Lewis acids (top) or by use of electrophilic cation salts of weakly coordinating anions (bottom).

Furthermore, by the cleavage of an element carbon bond, an element cation can be generated. Common groups that can be abstracted are e.g. methide CH_3^-, ethide CH_2-CH_3^- or allylide CH_2-CH=CH_2^- groups either by trityl salts of weakly coordinating anions, e.g. in the generation of the silylium ion Mes_3Si^+ by Lambert and Reed or Lewis acids, such as tris(pentafluorophenyl)borane $B(C_6F_5)_3$.[25, 72-73]

The oxidizing power of silver salts can also be used in the formation of radical cations, as the silver cation can act as single electron oxidants under the formation of elemental silver.[74] Other common single electron oxidants that can be used are e.g. nitrosyl salts NO^+ and halogens or halogen equivalents, such as iodine I_2 or xenon difluoride XeF_2 with alkaline metal, silver or silylium salts of weakly coordinating anions (WCA) or Lewis acids (**Scheme 9**).[75-77]

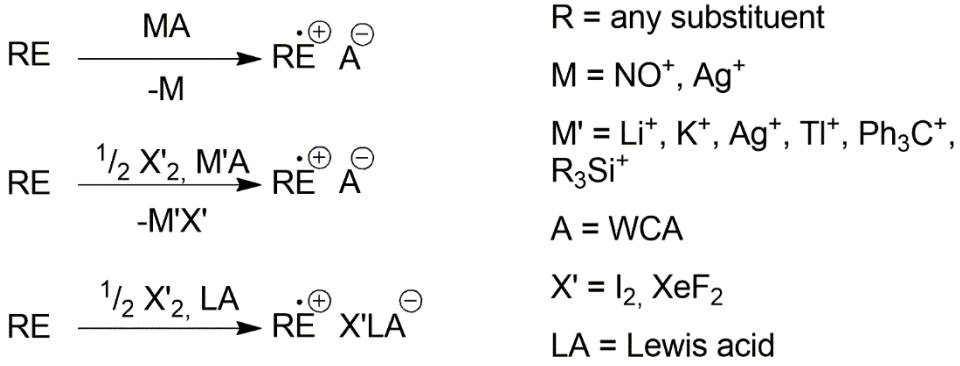

Scheme 9. Common single electron oxidation methods for the generation of radical cations.

In general, several methods can be applied to generate a low valent species, but in all cases, the charge separation by the introduction of a weakly coordinating anion is required.

1.6.2 Weakly Coordinating Anions

As increased steric bulk helps in the stabilization of cations, a similar strategy can be adapted for the anion to achieve a more balanced charge distribution and minimize the polarization to inhibit cation-anion interaction.[78] “Weakly coordinating anions” (WCAs) are designed for this purpose and paved a new research area over the last few decades (**Fig. 13**).

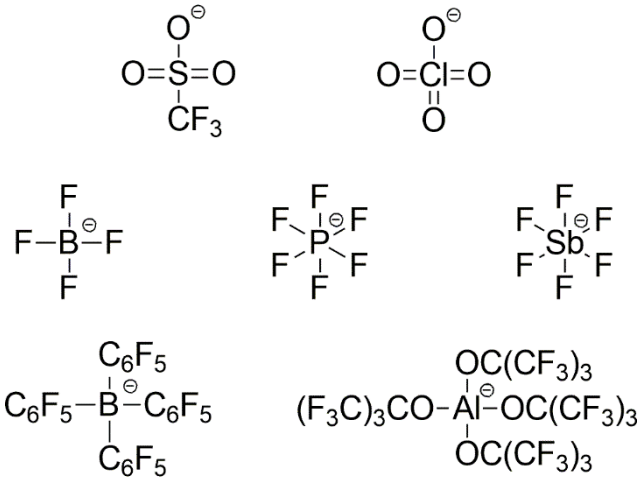

Figure 13. Examples of weakly coordinating anions, sorted by their coordinating ability in descending order (top to bottom).

According to the hard and soft acids and bases concept, it is best to choose a mismatching pair for the stabilization of highly reactive cations. A hard acid is stabilized best by a soft base and *vice versa*, due to minimal interaction between cation and anion.[79] The first generation of weakly coordinating anions included the conjugated bases of strong Brønsted acids like perchlorate, sulphate and nitrate, as these tend to have a delocalized charge over all oxygen atoms. Therefore, perchlorates and later hexafluoropnictogenates were often used in the early era of weakly coordinating anions, but showed coordination to the cation in several cases, such as the porphyrin iron(III) complexes with perchlorate **XXIX** or hexafluoroantimonate **XXX** as anion by Reed *et al.* (**Fig. 12**).[80-84]

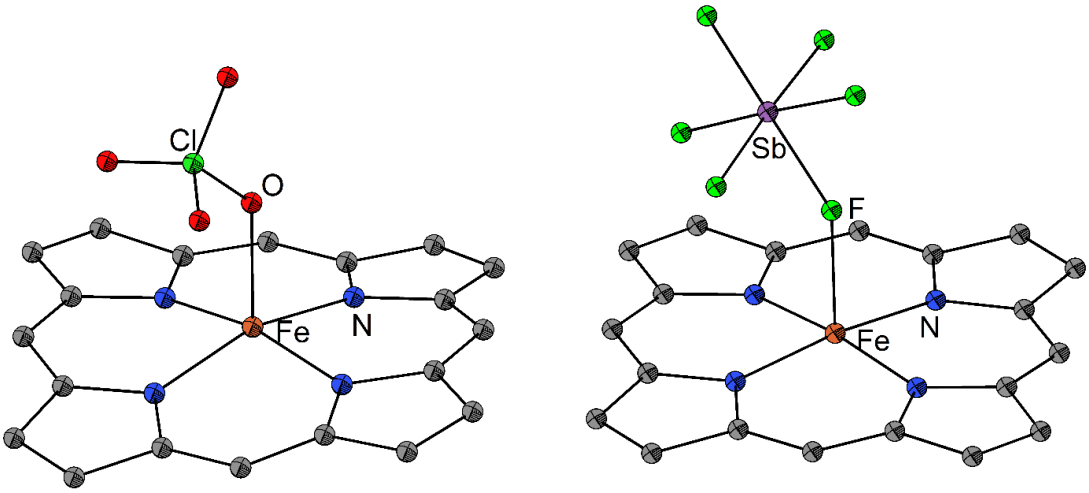

Figure 14. Molecular structures of the porphyrine iron(III) species presented by Reed *et al.* with perchlorate **XXIX** (left)[80] and hexafluoroantimonate **XXX** (right)[82] coordinating towards the metal center. Phenyl groups, hydrogen atoms and solvent are omitted for clarity.

In order to generate a weaker coordinating anion, the distribution of the charge has to be increased to inhibit cation-anion interaction and/or anion degradation. Furthermore, an increase in size of the anion leads to a better charge delocalization and a lower polarization on the surface of the molecule. Additionally, it is necessary that the anion comprises chemically robust groups, to ensure it withstands the reactivity the formed cation might provide, for instance a strong electrophilicity. By the combination of these aspects a variety of new weakly coordinating anions were designed and synthesized, from which the most frequently used classes are summarized in the next chapters.

1.6.2.1 Borates and Aluminates

One of the two major classes of weakly coordinating anions contain group 13 elements like boron or aluminium as the central atom. These are electron deficient in their neutral ER_3, due to an unoccupied p_z orbital. This species readily generates anions to fulfil the octet rule. The group 13 elements are often substituted by (per)fluorinated organic systems, which provide a high stability, as the C-F bond is considered as one of the strongest bonds, and the (per)fluorinated organic groups provide a high charge delocalization, due to the electron deficient substituents (**Fig. 15**).[69-70, 85]

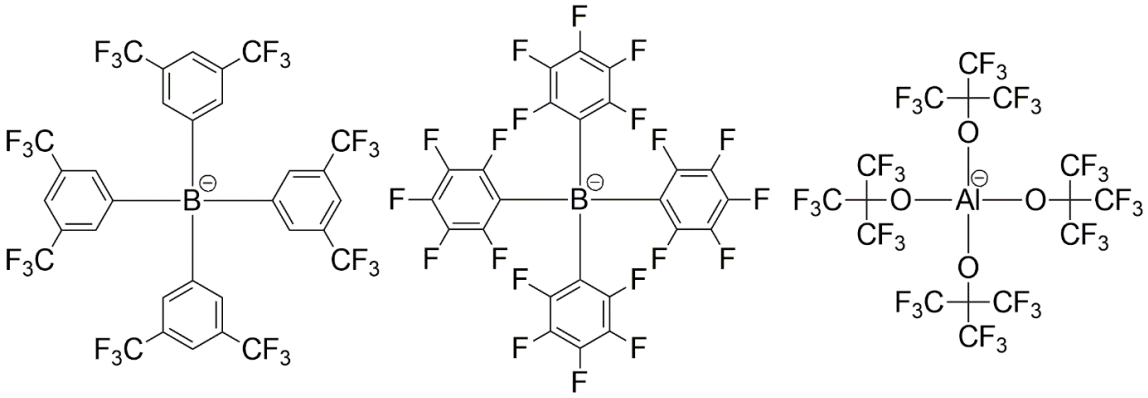

Figure 15. Examples of commonly used weakly coordinating anions, tetrakis(3,5-bis(trifluoromethyl)phenyl)borate BAr^F, tetrakis(pentafluorophenyl)borate $PerBAr^F$ and tetrakis(perfluoro-tert-butoxy)aluminate $AlOR^F$ (l. to r.).

Upon reaction of a group 13 halide or hydride with the corresponding organolithium or alkaline metal alcoholate, the anion formation is straightforward and can be prepared on a multigram scale providing a good source of weakly coordinating anions.[67, 86-88] Also bridged borates and aluminates have been reported, exhibiting a higher charge delocalization, but are often prone to dissociation or exchange reactions.[89-90]

A recently reported bridged anions is the aluminium based species $[((CF_3)_3CO)_3Al\text{-}F\text{-}Al(OC(CF_3)_3)_3]^-$, which was prepared by Krossing *et al.,* in 2018 (**Fig. 16**). The work group developed a reasonable synthesis of this bridged anion and demonstrated the stability due to the increased charge delocalization by the stabilization of several synthetically potent cations, namely Ag^+, NO^+ and Ph_3C^+ on a multigram scale.[89]

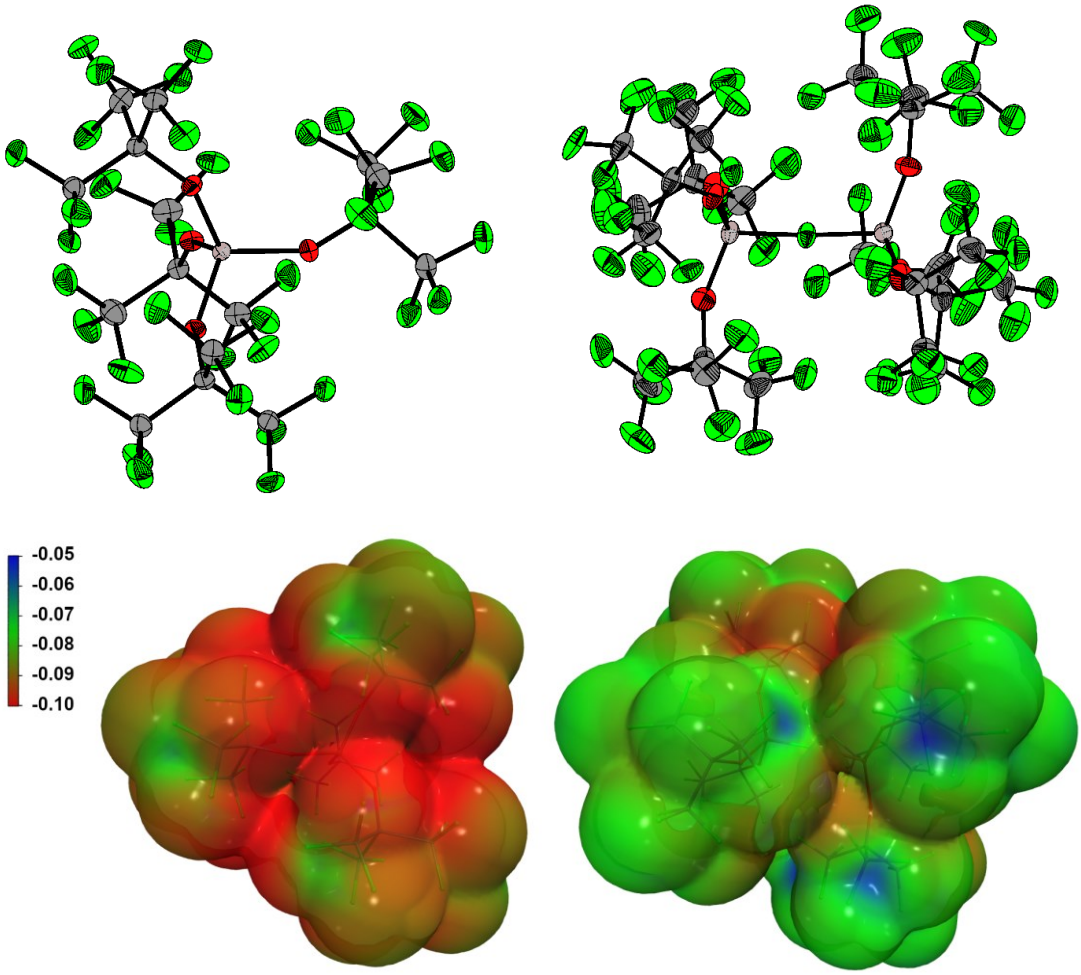

Figure 16. Molecular structures (top) and electrostatic potential (bottom) of the $AlOR^F$ anion $[Al(OC(CF_3)_3)_4]^-$ (left) and the bridged anion $[(F_3C)_3CO)Al\text{-}F\text{-}Al(OC(CF_3)_3)_4]^-$ (right).

Also similar bridged anions $[(C_6F_5)_3E\text{-}F\text{-}E(C_6F_5)_3]^-$ (E = Al, Ga) were prepared by Marks *et al.* by the reaction of the corresponding Lewis acids with trityl fluoride Ph_3CF. Interestingly, in the case of aluminium, even the dianionic species $[(C_6F_5)_3Al\text{-}F\text{-}Al(C_6F_5)_3\text{-}F\text{-}Al(C_6F_5)_3]^{2-}$ can be obtained by the adjustment of the stoichiometry.[90]

But the lighter congener $[(C_6F_5)_3B\text{-}F\text{-}B(C_6F_5)_3]^-$ is not known, due to sterical effects. However, the cyanide bridged $[(C_6F_5)_3B\text{-}CN\text{-}B(C_6F_5)_3]^-$ anion could be prepared by Bochmann and coworkers, by the reaction of the Lewis acid $B(C_6F_5)_3$ with potassium cyanide and cation exchange with trityl chloride afforded the trityl salt $[Ph_3C]^+[(C_6F_5)_3B\text{-}CN\text{-}B(C_6F_5)_3]^-$.[91]

1.6.2.2 Boron Based Clusters and Other Weakly Coordinating Anions

Another prominent class of weakly coordinating anions include borane clusters, with the charge being distributed over boron atoms in a three-dimensional cage-like structure. By substitution of these borane clusters and/or introduction of carbon atoms, a variety of weakly coordinating anions are available (**Fig. 17**).[68, 71] Frequently used are the *closo*-carborane $[CB_{11}H_{12}]^-$ and the dodecaborate cluster $[B_{12}H_{12}]^{2-}$ often providing a charge separation, due to delocalization of the charge over all boron molecules. In 1986 Reed *et al.* presented the $[CB_{11}H_{12}]^-$ cluster, revealing in the published work only a weak interaction between the *closo*-carborane and the iron(II) cation.[71] Modification of these anions include the halogenation by Stibr *et al.* and Reed *et al.* providing even weaker coordinating anions.[24, 92] Modifications by fluorination and trifluoromethylation were performed by Strauss *et al.* and Michl *et al.* providing the most likely weakest coordinating anions $[CHB_{11}F_{11}]^-$ and $[CB_{11}(CF_3)_{12}]^-$ with the latter one being explosive. Due to the fact that the synthesis needs handling of fluorine in anhydrous HF, the fluorinated anions are only used in niche applications.[93-94]

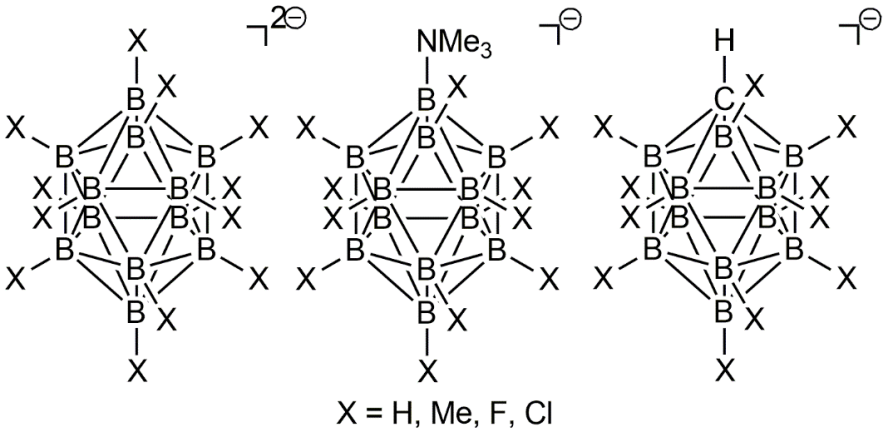

Figure 17. Commonly used dodecaborates, trimethylaminododecaborates and carboranes as anions (l. to r.).

Overall, the synthesis of carborane and dodecaborate clusters as anions is only achieved in expensive and time-consuming multi-step procedures, with the generation of large amounts of hydrogen, preventing an extensive use.

A rather new concept in the design of weakly coordinating anions include the class of teflates, in which formal fluoroelementates EF_n^-, such as BF_4^-, AsF_6^- and SbF_6^-, are substituted by the $OTeF_5$ motif, to increase the charge delocalization as used

in group 13 teflato elementates $E(OTeF_5)_4^-$ (E = B, Al)[95-96] and the hexa-coordinated group 15 teflato pnictogenates $E(OTeF_5)_6^-$ (E = As, Sb, Bi).[97]

The synthesis of the teflate anions is usually done by the reaction of an element salt with teflic acid $HOTeF_5$ as it is often used for the group 13 elementates. By transmetallation from $B(OTeF_3)_3$, the neutral pnictogen teflates can be obtained followed by the addition of a teflate salt to form the anion. Only in the case of antimony the oxidation to the anion is required as the Lewis acid $Sb(OTeF_5)_5$ is not stable at ambient temperatures. For this, xenon teflate $Xe(OTeF_5)_2$ is used, which indicates the immense stability towards oxidation.[95, 97]

1.7 Lewis Acidity

Due to the lack of electrons and non-fulfillment of the octet rule, low valent species are highly Lewis acidic. In order to determine and scale the Lewis acidity, several experimental and computational methods were developed.

From an experimental point of view, the Lewis acidity of reactive species can be examined by several experiments, which often rely on the chemical shift difference in NMR spectroscopic measurements of a Lewis base which is coordinated to a Lewis acidic species. A widely used strategy is the Gutmann-Beckett method, in which triethylphosphine oxide (Et_3PO) is used as the Lewis base. The chemical shift in the ^{31}P NMR spectrum of Et_3PO is highly sensitive towards coordinative interactions between the oxygen atom and a Lewis acid and therefore the shift will change depending on the strength of the dative bond. By application of a simple formula, the so-called “acceptor number” (AN) can be calculated and referenced against other benchmark values like the AN of $SbCl_5$, which is defined as 100 (δ = 86.1 ppm), and the AN of free Et_3PO, which is defined as 0 (δ = 41.0 ppm) (**Scheme 10**). The higher the acceptor number, the higher the Lewis acidity of the reactive species.[98-99]

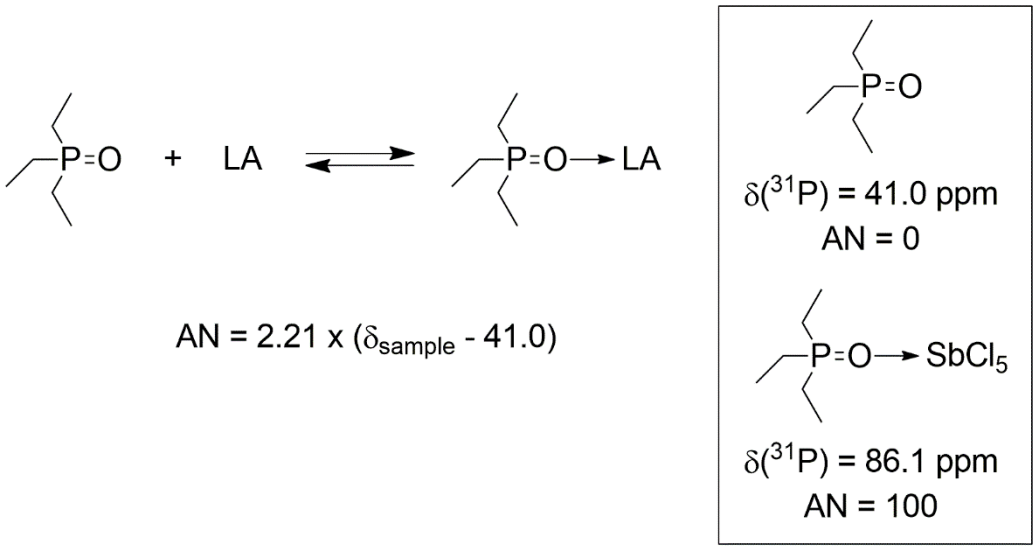

Scheme 10. Reaction and equation of the Gutmann-Beckett method with triethylphosphine oxide and triethylphosphine oxide antimony pentachloride adduct as reference.[98-99]

However, the correlation of Lewis acidity and the chemical shift can be problematic. For soft Lewis acids, according to the HSAB concept, the coordination to a hard Lewis base, like Et_3PO, is unfavoured. Therefore, the dative bond will not be as strong as for a hard Lewis acid. Secondly, the stoichiometry is highly important, as dissociation is possible and for heavier atoms two molecules of Et_3PO can coordinate. This can lead to a dynamic equilibrium resulting in an average shift.[100] Also the solvent can have an influence. It has been suggested to use an “aprotic unpolar solvent”, such as benzene, or DCM. But even these solvents have a tremendous effect on the Acceptor number, as Gutmann *et al.* stated. *n*-Hexane was used as a reference point for non-coordinated Et_3PO (AN = 0) and $SbCl_5$ as a reference for fully coordinated Et_3PO (AN = 100). Based on this scale the typically used solvents such as benzene (AN = 8.2) and CCl_4 (AN = 8.6), which is often substituted if possible by DCM (AN = 20.4) or chloroform (AN = 23.1), already show a coordination towards Et_3PO.[98] In general for strong Lewis acids this should not affect the measurement. A competing coordination with the solvent can affect the result, if the Lewis acid is soft or weak forming an adduct with an AN close to the used solvent, or if the coordination of Et_3PO is hindered due to steric effects.[100]

To overcome the problem of soft Lewis acids in the Gutmann-Beckett method Lichtenberg *et al.* introduced Me_3PS and Me_3PSe as soft Lewis bases, for a better understanding of the Lewis acidity of bismuth cations and used several common

Lewis acids for a scale similar to the original Gutmann-Beckett method. The GaI_3 adducts were used as a reference, with the highest achieved ^{31}P NMR shift (**Scheme 11**).[101]

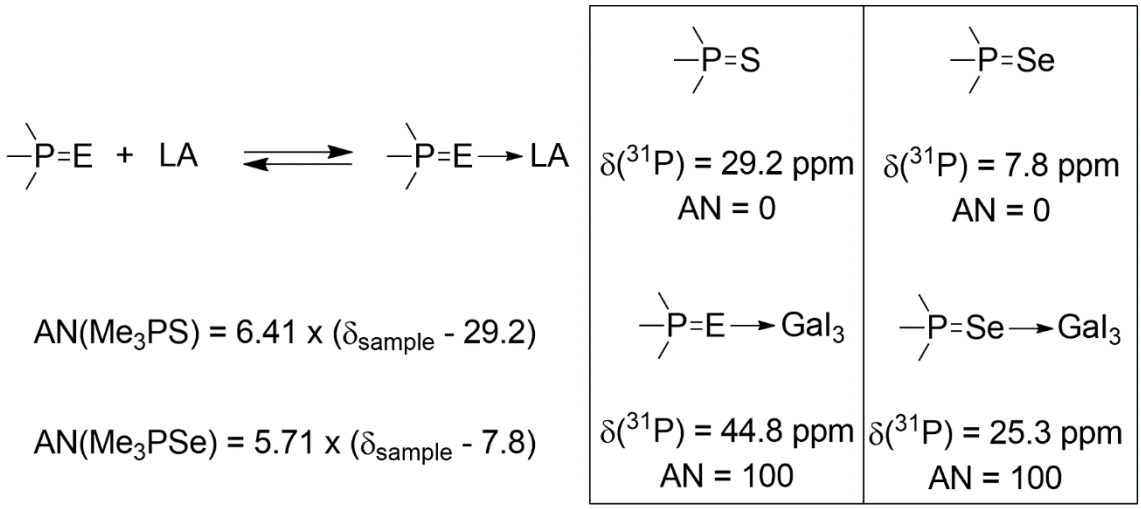

Scheme 11. Reaction and equation of the Lichtenberg-Gutmann-Beckett method with the soft Lewis bases trimethylphosphine sulfide and trimethylphosphine selenide and their corresponding GaI_3 adduct as reference.[101]

A similar approach for the Lewis acidity determination is Childs' method (**Scheme 12**), in which crotonaldehyde is used to coordinate the Lewis acid, which changes the chemical shifts in ^1H-NMR spectroscopy related to the Lewis acid strength. Especially the hydrogen atom in γ-position changes in a linear way with regard to the Lewis acidity. In this method, BBr_3 is assigned for the full coordination of crotonaldehyde giving the relative acidity (RA).[102]

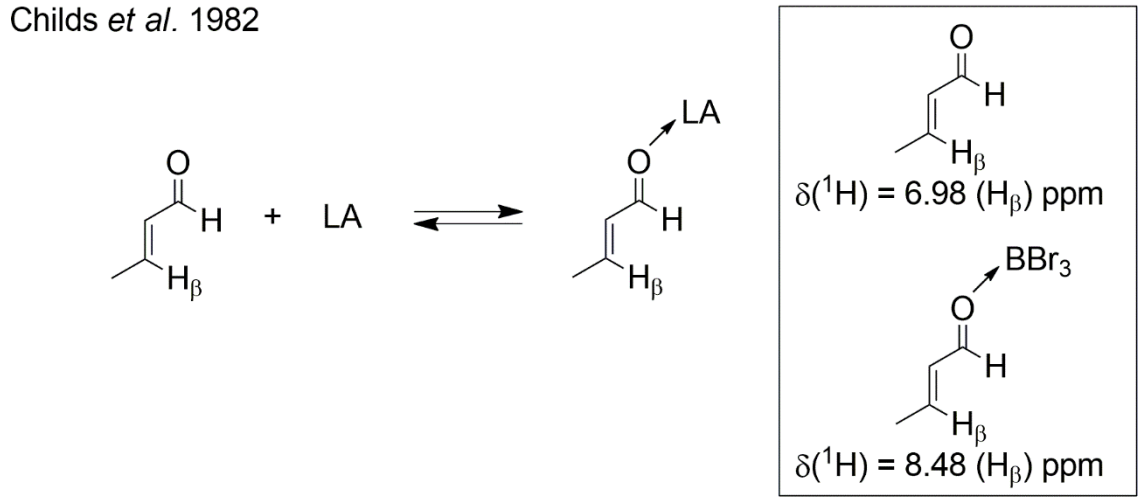

Scheme 12. Reaction of the Childs' method with crotonaldehyde and the crotonaldehyde boron tribromide Lewis adduct as reference.[102]

Similar to Childs' method is the method developed by Hilt *et al. (***Scheme 13**, top).[103] In which deuterated pyridine is used as a donor and the increasing shift difference can be correlated to the Lewis acidity by ^{2}H-NMR spectroscopy.

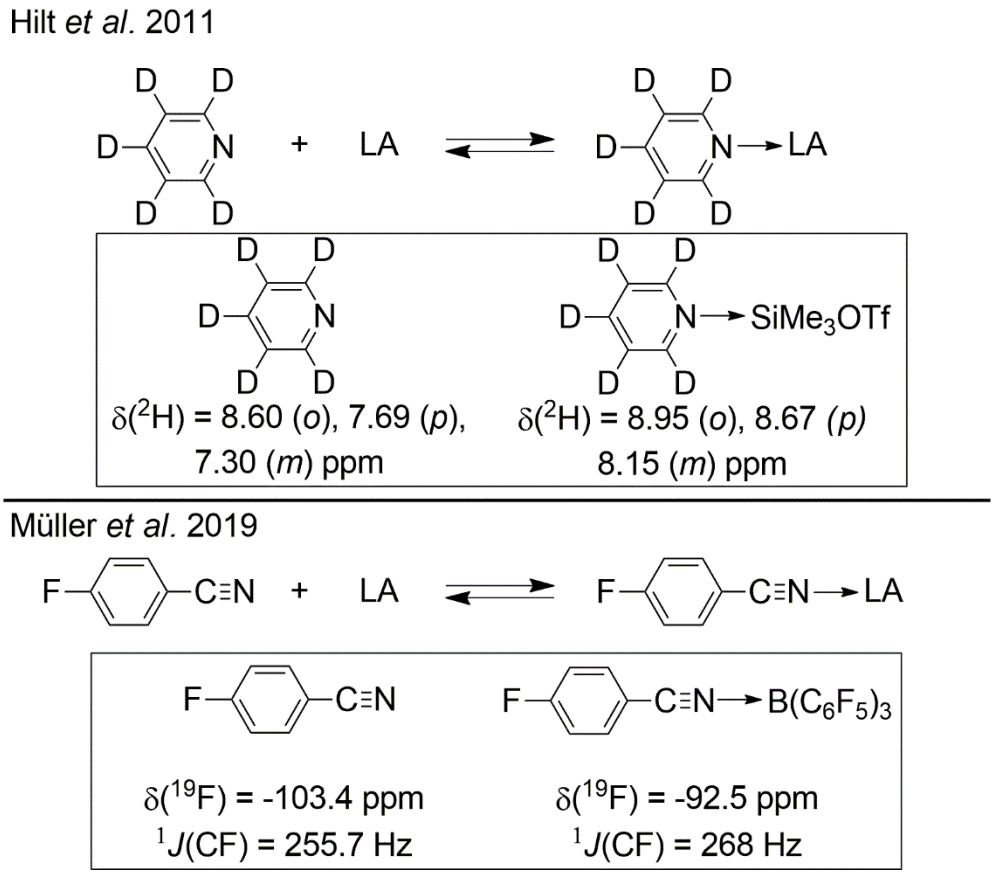

Scheme 13. Hilt's method and Müller's method for Lewis acidity determination. [103-104]

Additionally, Müller *et al.* developed a method to determine the Lewis acidity of intramolecular stabilized silyl cations based on *p*-fluorobenzonitrile (BFN) in 2019 (**Scheme 13**, bottom). By the use of the ^{19}F-NMR shift, as well as the C-F coupling constant, the Lewis acidity can be determined.[104]

Also, acetonitrile can be used as a sensitive Lewis base to determine the Lewis acidity. By coordination of the acetonitrile, a blue shift is observed for the C≡N stretching frequency, and for stronger Lewis acids, the shift difference compared to free MeCN becomes larger.[105] Timoshkin *et al.* have shown recently that the square root of the C≡N stretching frequency shift for 1:1 and 1:2 complexes with acetonitrile correlates with the strength of the donor-acceptor bond.[106]

Another method for the qualitative determination of the Lewis acidity is the abstraction of a fluoride from hexafluoroantimonate salts, as the abstraction indicates a higher fluoride ion affinity than antimony pentafluoride, which is considered as the Lewis superacid threshold. This method can determine if the used Lewis acid acts as a Lewis superacid in principle, but it does not allow for quantification.[107] As a drawback of this method, it is possible that the used LA is strong enough to abstract a fluoride from SbF_6^- but the generated SbF_5, which is a strong oxidant, can attack the solvent and the ligand backbone, generating different species.[108] The same concept can be used with other Lewis acid fluoride adducts, like salts of $[FB(C_6F_5)_3]^-$, BF_4^- and others.[109]

Overall, there are various methods to experimentally determine the Lewis acid strength, but each method relies on several factors and each has its own limitations. Soft Lewis acids will give different results as a consequence of oxygen coordination to Et_3PO using the Gutmann-Beckett-method compared to coordination to acetonitrile or para-fluorobenzonitrile than hard Lewis acids, which can mask the reactivity towards different Lewis bases. The introduction of Me_3PS and Me_3PSe as soft Lewis bases by Lichtenberg *et al.* introduces a similar scale for soft Lewis acids. Stronger Lewis acids might attack functional groups of the Lewis base as it can happen in Childs' method. Hilt's method uses deuterated pyridine and ^{2}H-NMR spectroscopy, which can diminish the availability of this method.

The best way to determine the Lewis acidity is to use a combination of methods and calculations, as Lewis acidity cannot be considered in a one-dimensional manner. Multiple variables contribute to it, such as polarizability, steric hindrance or element specific affinities. This becomes evident by the calculation of multiple ion affinities, as some elements have a higher affinity for softer Lewis bases than hard ones and *vice versa*.[110]

Most often the fluoride ion affinity (FIA) is rather calculated, than experimentally determined. It was used first, but not labelled as such, in 1955 for BF_3 as a Lewis acid.[111] The term was introduced by Haartz and McDaniel in 1973 by reporting the fluoride ion affinity to several inorganic Lewis acids, such as SiF_4, BF_3, PF_5, AsF_5.[112] In 2000 Christe *et al.* described a reliable isodesmic method for the

determination of the FIA and introducing the pF values, which represent the fluoride ion affinity in kcal/mol divided by 10. The FIA value calculation is based on the abstraction of fluoride from a model system of COF_3^-.[113] Even though the pF value is not used anymore, the calculation of the FIA value is still in use today. As more highly Lewis acidic species being synthesized, that show unusual behaviour, Krossing *et al.* defined the threshold for Lewis superacidity as the FIA of antimony pentafluoride, which is around 480 kJ/mol (**Fig. 18**).[107, 109, 114-116]

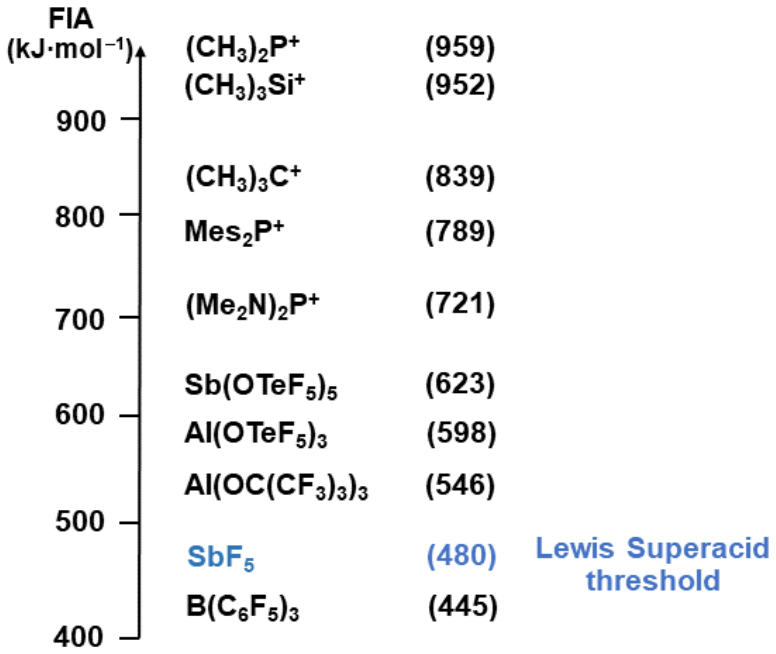

Figure 18. FIA scale of synthesized and theoretical Lewis acids and cations. All values are calculated in the gas phase.[117-118]

As it becomes evident by the the displayed fluoride ion affinities, (**Fig. 18**) low valent main group cations exhibit an extraordinarily high Lewis acidity. This can be explained by the positive charge leading to a high electrophilicity. Even though group 13 elements already provide a low valency, (*vide supra*) cationic species tend to be more electrophilic. In the solvated phase, in dichloromethane, these values often decrease. Exemplarily, the value for Me_2P^+ decreases from 959 kJ/mol to 535 kJ/mol.[118] For $Sb(OTeF_5)_5$, the change as dramatic and reduced from 623 to 416 kJ/mol and for SbF_5 it decreases from 496 kJ/mol to 362 kJ/mol.[117] Thus, a tendency is visible, in which the higher the Lewis acidity, the stronger the decrease of FIA in the condensed phase.

In 2020, Greb *et al.* described an improved method for the calculation of FIA values by the use $(CH_3)_3Si\text{-}F$ as a model system, due to less charge relation compared to the anionic COF_3^- model system, leading to more accurate values.[117] Also, Greb and Erdmann attempted to describe the multidimensionality of Lewis acidity. Several additional affinities were calculated such as the hydride ion affinity (HIA), chloride ion affinity (CIA), methide ion affinity (MIA) and additionally the water affinity (WA) and ammonia affinity (AA) (**Scheme 14**).[110]

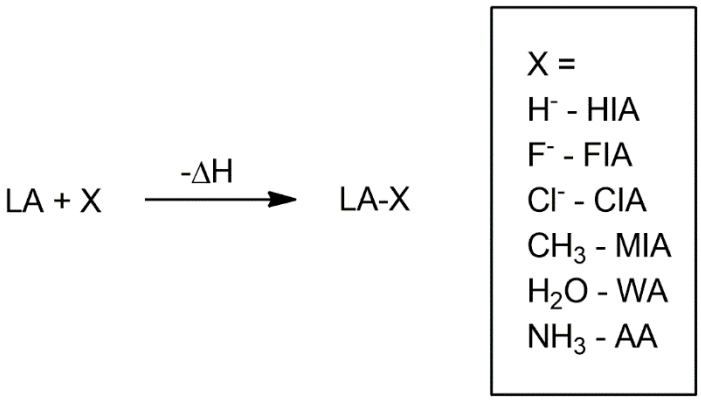

Scheme 14. Lewis acid base - adduct formation with common used Lewis bases for affinity calculations.[110]

These multiple affinities can be used to gain a more balanced view on the Lewis acidity. The hydride ion contributes as an easily polarizable small Lewis base, which provides additional information decreasing the sterical influence in Lewis acids, as the hydride is the smallest nucleophile. The fluoride, chloride and methide ion can lead to information regarding the steric contribution to the Lewis acidity and can also be seen as a variety of Lewis bases generating a broad spectrum of variation regarding the HSAB character and element specific affinities. Ammonia and water contribute as weaker donors, which can be useful for the formation of less stable Lewis adducts, whose formation is influenced by additional Lewis acid properties such as hydrogen bonding or dispersion effects. This also shows, that by definition tris(pentafluorophenyl)borane ($B(C_6F_5)_3$) is not a Lewis superacid (according to its FIA value), but by the HIA value it exceeds some of the common Lewis superacids. Thus, Greb classifies $B(C_6F_5)_3$ as a soft Lewis superacid (sLSA).[110, 119]

1.8 Motivation and Objectives

The strong Lewis acidity of Low valent main group species is often desired as it can be used in bond activation, for instance in small molecules such as H_2 and CO_2. Furthermore, the free coordination site and the altered geometry due to sterically demanding or coordinating substituents opens the area, that is normally covered by transition metals and their complexes. These have the unique situation of partially filled d-orbitals, providing a large range of oxidation states and electronic flexibility, leading to a high flexibility in coordination chemistry.[120-121] The exchange of transition metal complexes in catalytic chemistry and industrial application is of interest, as metals like platinum, palladium, rhodium and iridium are usually costly due to their scarcity and complex mining and extraction techniques, which are often environmentally problematic. Moreover, they are often toxic requiring special precautions and special treatments of waste in industrial processes.[122-123]

The characteristics of main group compounds behaving like transition metal complexes, was described by Power in 2010. The author states that the interest in the stabilization of otherwise unstable species led to multiple examples of main group element compounds showing transition metal like behaviour.[124]

Of high relevance are main group element compounds with E-E multiple bonds (e.g. **XXXI**), low valent species with a free coordination site (e.g. **XXXII**), molecules with a quasi-open coordination site due to a frustrated Lewis pair (e.g. **XXXIII**) as well as radicals and diradicaloids (**Fig. 19**).[125-131]

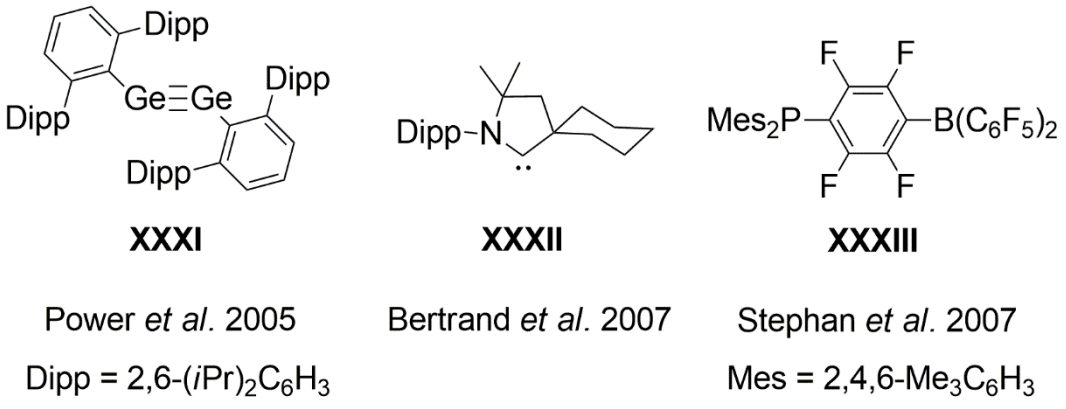

XXXI **XXXII** **XXXIII**

Power *et al*. 2005 Bertrand *et al*. 2007 Stephan *et al*. 2007

Dipp = 2,6-(iPr)$_2$C$_6$H$_3$ Mes = 2,4,6-Me$_3$C$_6$H$_3$

Figure 19. Molecules showing transition metal like behaviour.[12, 132-133]

The compounds **XXXI-XXXIII** are all able to activate H_2 as a small molecule at ambient conditions and are the first of their kind.[12, 132-133] Therefore, these compounds show transition metal like behaviour, which was named by Braunschweig *et al*.[134] as “metallomimetics”.

As it is a new research field, a plethora of potential metallomimetics were synthesized, characterized and studied regarding catalytic application and activation of small molecules over the last years. Also established compounds were studied regarding activation of small molecules as it was shown by Stephan *et al*.[135] for the borinium ion Mes_2B^+ **IV$^+$**, which is able to activate hydrogen (**Scheme 15**).

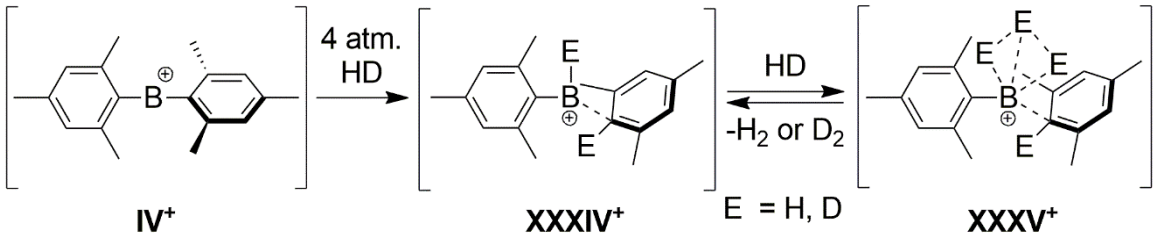

Scheme 15. Activation of hydrogen by the borinium cation Mes_2B^+ (**IV$^+$**). Anions are omitted for clarity.[135]

Inspired by the work of Power, Stephan and others, the focus of this thesis is the synthesis of novel cationic low valent main group element compounds and their study regarding metallomimetic behaviour in small molecule activation. Cationic Low valent species are a promising approach, as the abstraction of a substituent opens a coordination sphere and increases the electrophilicity. The stabilization of these highly reactive species is approached by the combination of sterically demanding substituents and weakly coordinating anions. The *m*-terphenyl substituent is ideal for the stabilization of bis substituted low valent species, as the *meta* substitution provides a 2-dimensional cavity and two ligands encapsulate the central atom (**Fig. 20**).

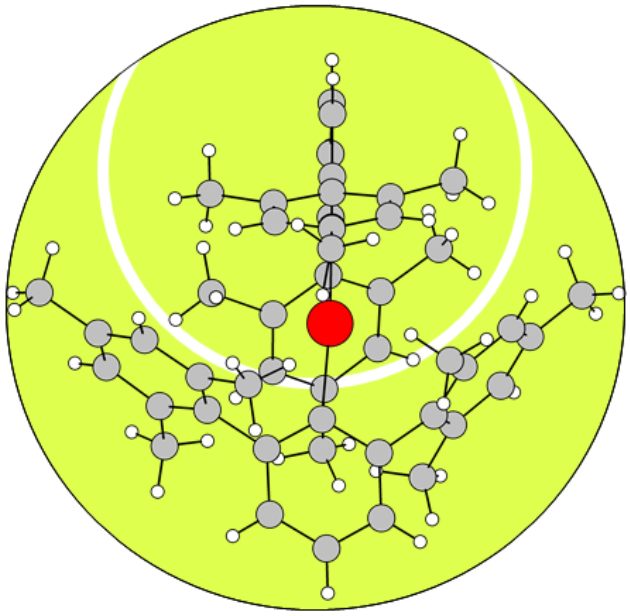

Figure 20. A bis(*m*-terphenyl)element cation in linear geometry. The *m*-terphenyl groups perpendicularly protect the element cation (red central atom) with four mesityl substituents.

The synthesis of most *m*-terphenyl species is achieved by the Hart-aryne synthesis, in which 1,3-dichlorobenzenes are lithiated in *ortho*-position, followed by the reaction with an excess of aryl Grignard reagents. It has been proposed that after the formation of an aryne species, the organomagnesium reagent reacts under oxidative addition to the formed triple bond twice under the formation of the *m*-terphenyl magnesium reagents. These can be reacted with an electrophile, such as iodine to isolate iodoterphenyl compounds as convenient stable precursors on a multigram scale (**Scheme 16**).[45, 136]

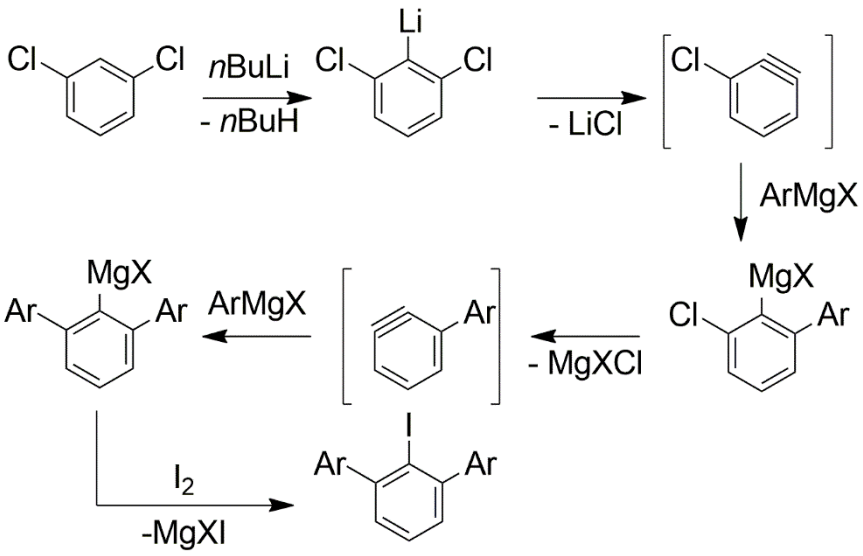

Scheme 16. Synthesis of *meta*-terphenyls *via* the Hart-aryne synthesis.

In this thesis, the mesityl *m*-terphenyl substituent will be used, as it showed encouraging outcomes in the Beckmann group's research. The substituent has demonstrated its kinetically stabilizing properties in the synthesis of mixed valent aryltellurenyl halides, diaryl dichalcogenide radical cations, defined tellurinic and stibonic acids, novel fluorosilanes, and a low valent bis(*m*-terphenyl)thallium cation.[75, 137-140]

Until now, only a limited number of bis(*m*-terphenyl)element cations of the group 13 is known. Wehmschulte *et al.*[13, 73] synthesized the bis(*m*-terphenyl)aluminium and gallium cations by abstraction of a hydride ion. Beckmann *et al.*[140] synthesized a bis(*m*-terphenyl)thallium cation by oxidation of the corresponding *m*-terphenylthallium(I) compound. To the best of my knowledge no bis(*m*-terphenyl) element cations of group 15 and 16 are reported yet. The challenge compared to group 14 chemistry, in which three substituents can stabilize the cation, is that only two substituents provide stabilization for low valent group 13, group 15 and group 16 species.

Two bis(*m*-terphenyl)element compounds have been reported, allowing for the generation of low valent species regarding group 13 and group 15 elements. Robinson *et al.* prepared bis(*m*-terphenyl)indium bromide[141] and bis(*m*-terphenyl)bismuth chloride and hydride were synthesized by Power *et al.*[142] Thus, these compounds provide a convenient option for investigating the abstraction of halides and hydrides, with the goal of forming low valent cationic species.

In summary, the target of this thesis consists of the synthesis of novel bis(*m*-terphenyl)element compounds of the groups 13, 15 and 16. These compounds will serve as starting materials for the formation of low valent main group species through the abstraction of a substituent or by single electron oxidation, concurrently incorporating a weakly coordinating anion. The generated low valent main group compounds will then be investigated for their Lewis acidity and their potential as metallomimetics in small molecule activation.

2 Results and Discussion

2.1 Heavy Carbene Analogues: Donor-Free Bismuthenium and Stibenium Ions

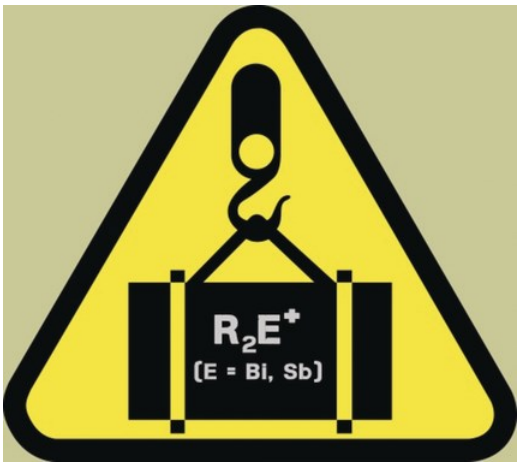

2.1.1 Synopsis

In this work the known compound bis(*m*-terphenyl)bismuth hydride[142] was used as an example for the abstraction of a substituent and formation of a bis(*m*-terphenyl)pnictogenium ion. By the abstraction of the hydride with trityl tetrakis(3,5-bis(trifluoromethyl)phenyl)borate the corresponding cation bis(*m*-terphenyl)-bismuthenium tetrakis(3,5-bis-(trifluoromethyl)phenyl)borate $[Ter_2Bi]^+[B(3,5\text{-}(CF_3)_2C_6H_3)_4]^-$ was isolated as a deep red solid, which allowed its characterization. Subsequently, the corresponding bis(*m*-terphenyl)antimony chloride and hydride were synthesized and the same reaction conditions with the corresponding hydride were tested, but were not successful. Consequently, the abstraction of the chloride from bis(*m*-terphenyl)antimony chloride was attempted and by the *in situ* preparation of triethylsilylium tetrakis(pentafluorophenyl)borate $[Et_3Si]^+[B(C_6F_5)_4]^-$, the abstraction was successful leading to

bis(*m*-terphenyl)stibenium tetrakis(pentafluorophenyl)borate $[Ter_2Sb]^+[B(C_6F_5)_4]^-$, which was isolated as a deep red solid. The new compounds namely Ter_2SbCl, Ter_2SbH, $[Ter_2Bi]^+[B(3,5\text{-}(CF_3)_2C_6H_3)_4]^-$ and $[Ter_2Sb]^+[B(C_6F_5)_4]^-$ were fully characterized by means of NMR, UV-Vis and IR spectroscopy as well as single crystal X-ray diffraction experiments. The low valency and bonding situations were studied by DFT calculations. Attempts for the activation of small molecules were made, but were not successful and thus were not included in the publication.

2.1.2 Scientific Contribution

In this project I developed the synthesis of the bis(terphenyl)antimony compounds and cations, fully characterized the new compounds and co-wrote the manuscript. M. Olaru did the bismuth counterpart co-wrote the manuscript. J. Beckmann was the principal investigator, designed the concept and co-wrote the manuscript. E. Lork did the X-ray crystallographic solution and refinement, S. Mebs executed the theoretical investigations contributing this publication.

Percentage of my contribution of the total workload:

Experimental concept and design: ca. 40%, experimental work and acquisition of experimental data: ca. 50%, data analysis and interpretation: ca. 50%, preparation of figures and tables: ca. 20%, drafting of the manuscript: ca. 10%.

The article was published in the journal “Angewandte Chemie International Edition“ in 2018 as a “Very Important Paper (VIP)” article and was also translated to German:

Marian Olaru, Daniel Duvinage, Enno Lork, Stefan Mebs*, Jens Beckmann*, *Angew. Chem. Int. Ed.* **2018**, *57*, 10080-10084.

Marian Olaru, Daniel Duvinage, Enno Lork, Stefan Mebs*, Jens Beckmann*, *Angew. Chem.* **2018**, *130*, 10237-10241.

International Edition: DOI: 10.1002/anie.201803160

German Edition: DOI: 10.1002/ange.201803160

The Supporting Information includes experimental procedures, NMR spectra, X-ray crystallographic data and structure refinement and computational data and is available free of charge on the journal′s website:

https://onlinelibrary.wiley.com/action/downloadSupplement?doi=10.1002%2Fanie.201803160&file=anie201803160-sup-0001-misc_information.pdf

GDCh Communications Angewandte International Edition Chemie

Check for updates

VIP Carbene Analogues Very Important Paper

International Edition: DOI: 10.1002/anie.201803160
German Edition: DOI: 10.1002/ange.201803160

Heavy Carbene Analogues: Donor-Free Bismuthenium and Stibenium Ions

Marian Olaru, Daniel Duvinage, Enno Lork, Stefan Mebs, and Jens Beckmann**

In memory of Chris Cornell

Abstract: *Kinetically stabilized congeners of carbenes, R_2C, possessing six valence electrons (four bonding electrons and two non-bonding electrons) have been restricted to Group 14 elements, R_2E ($E = Si, Ge, Sn, Pb$; $R =$ alkyl or aryl) whereas isoelectronic Group 15 cations, divalent species of type $[R_2E]^+$ ($E = P, As, Sb, Bi$; $R =$ alkyl or aryl), were unknown. Herein, we report the first two examples, namely the bismuthenium ion $[(2,6\text{-}Mes_2C_6H_3)_2Bi][BAr^F_4]$ (**1**; $Mes = 2,4,6\text{-}Me_3C_6H_2$, $Ar^F = 3,5\text{-}(CF_3)_2C_6H_3$) and the stibenium ion $[(2,6\text{-}Mes_2C_6H_3)_2Sb][B(C_6F_5)_4]$ (**2**), which were obtained by using a combination of bulky meta-terphenyl substituents and weakly coordinating anions.*

The octet rule states that main-group-element compounds are most stable when all atoms (except H) are surrounded by eight valence electrons (8 VE species). Compounds with main-group elements with lower valence-electron counts are substantially more reactive and are usually observed only as short-lived intermediates in chemical reactions. In Group 14, carbocations, $[R_3C]^+$ (**I**), and carbenes, R_2C (**II**; R = alkyl or aryl groups), as well as their heavier congeners possessing six valence electrons (6 VE species) are strong electrophiles, which seek to attract two additional electrons (Scheme 1).[1]

Over the last decades, tremendous efforts have been directed towards the isolation of kinetically stabilized 6 VE species **I** and **II** of the heavier Group 14 elements. Lambert and co-workers achieved the isolation of three-coordinate triarylsilyl and triarylstannyl cations $[Mes_3Si][HCB_{11}Me_5Br_6]$[2] ($Mes = 2,4,6\text{-}Me_3C_6H_2$) and $[Tipp_3Sn][B(C_6F_5)_4]$[3] ($Tipp = 2,4,6\text{-}iPr_3C_6H_2$) by using a combination of three bulky aryl substituents and weakly coordinating anions. Smaller organic substituents failed to provide sufficient steric protection, giving rise to significant cation–anion contacts.[4] The first stannylene and plumbylene, $[(Me_3Si)_2CH]_2E$ ($E = Sn, Pb$), were prepared by Lappert and co-workers by making use of the kinetic stabilization imparted by two bulky alkyl substituents. While these compounds are present as monomers in solution, they form dimers with significant E–E contacts ($E = Sn, Pb$) in the solid state.[5] This is due to the ambivalent nature of these species, possessing both an electron lone pair and electron deficiency, which renders them Lewis acidic and Lewis basic at the same time. The tendency to form dimers is most pronounced for the light Group 14 elements. West and co-workers photochemically generated the transient species dimesitylsilylene (Mes_2Si), which immediately underwent dimerization to give rise to tetramesityldisilene ($Mes_2Si)_2$, with a Si–Si double bond and a so-called *trans*-bent structure.[6] The first isolable dialkylsilylene, *cyclo*-$[H_2CC(SiMe_3)_2]_2Si$, which was reported by Kira and co-workers, comprises a shielded divalent Si atom incorporated into a five-membered ring structure.[7]

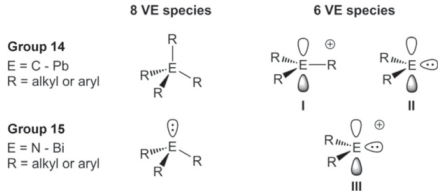

Scheme 1. 8 VE and 6 VE species of Group 14 and 15 elements.

Whereas the chemistry of the 6 VE species **I**[8] and **II**[9] of the heavier Group 14 elements is well advanced, very little is known about the organometallic cationic Group 15 element species **III**, which are also heavier analogues of carbenes and isoelectronic to **II** (Scheme 1). The difficulty of isolating such species is probably due to the fact that the combined challenges of **I** and **II** are encountered with **III**, namely a positive charge, an electron lone pair, as well as electron deficiency. Only two substituents are available to sterically protect compounds **III** from dimerization and coordination of the anion. Against these odds, we have now succeeded in the preparation of the first examples of species **III**, namely a bismuthenium ion and a stibenium ion, by using bulky *meta*-terphenyl substituents and weakly coordinating borate anions.

The reaction of bis(*meta*-terphenyl)bismuth hydride, $(2,6\text{-}Mes_2C_6H_3)_2BiH$,[10] with the hydride abstraction reagent $[Ph_3C][BAr^F_4]$ ($Ar^F = 3,5\text{-}(CF_3)_2C_6H_3$) under ambient conditions provided $[(2,6\text{-}Mes_2C_6H_3)_2Bi][BAr^F_4]$ (**1**) in 87% yield (Figure 1).[11] Attempts to apply the same strategy to the

[*] Dr. M. Olaru, D. Duvinage, Dr. E. Lork, Prof. Dr. J. Beckmann
Institut für Anorganische Chemie und Kristallographie
Universität Bremen
Leobener Straße 7, 28359 Bremen (Germany)
E-mail: j.beckmann@uni-bremen.de
Dr. S. Mebs
Institut für Experimentalphysik
Freie Universität Berlin
Arnimallee 14, 14195 Berlin (Germany)
E-mail: stebs@chemie.fu-berlin.de

Supporting information and the ORCID identification number(s) for the author(s) of this article can be found under: https://doi.org/10.1002/anie.201803160.

 © 2018 Wiley-VCH Verlag GmbH & Co. KGaA, Weinheim

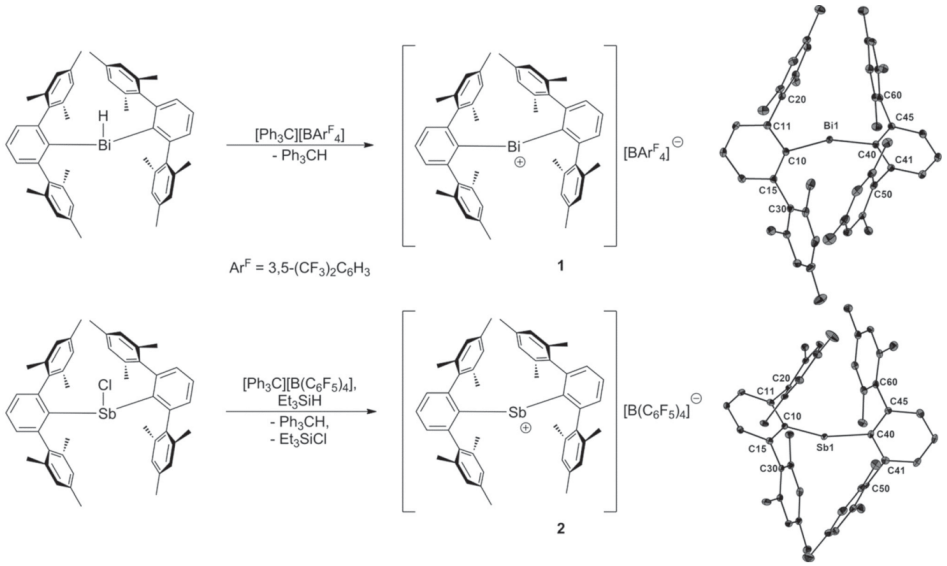

Figure 1. Synthesis of the bismuthenium ion **1** and the stibenium ion **2**. Molecular structures of $[(2,6\text{-}Mes_2C_6H_3)_2Bi]^+$ and $[(2,6\text{-}Mes_2C_6H_3)_2Sb]^+$.[25] Thermal ellipsoids set at 30% probability. Selected bond lengths [Å] and angles [°]: for **1**: Bi1–C10 2.274(3), Bi1–C40 2.277(2); C10-Bi1-C40 116.7(1); for **2**: Sb1–C10 2.176(3), Sb1–C40 2.182(3); C10-Sb1-C40 121.4(1).

reaction of the related compound bis(*meta*-terphenyl)antimony hydride, $(2,6\text{-}Mes_2C_6H_3)_2SbH$, and $[Ph_3C][BAr^F{}_4]$ failed to give the desired stibenium ion. Under ambient conditions, no reaction occurred, presumably because the Sb–H bond is stronger and better protected than the Bi–H bond. At elevated temperatures, the same reaction gave rise to a mixture of products, which were not assigned. However, the reaction of bis(*meta*-terphenyl)antimony chloride, $(2,6\text{-}Mes_2C_6H_3)_2SbCl$, with the chloride abstraction reagent $[Et_3Si(1,2\text{-}F_2C_6H_4)][B(C_6F_5)_4]$[12] (prepared in situ from $[Ph_3C][B(C_6F_5)_4]$ and Et_3SiH in 1,2-difluorobenzene) afforded $[(2,6\text{-}Mes_2C_6H_3)_2Sb][B(C_6F_5)_4]$ (**2**) in 82% yield (Figure 1).[13] The cationic carbene congeners **1** and **2** were obtained as air-sensitive, dark-colored, crystalline solids, which were soluble in reasonably polar solvents such as CH_2Cl_2 or 1,2-difluorobenzene.

The solid-state structures of **1** and **2** show that the divalent cations (Figure 1) are well separated from their counteranions. This is a unique feature compared to previously known diarylbismuth and diarylantimony salts, in which either coordination of the counteranion (e.g., $Ph_2BiO_3SCF_3$)[14] or inter- or intramolecular donor-atom coordination (e.g., $[Ph_2Bi(HMPA)_2]BF_4$; HMPA = hexamethylphosphoramide)[15–18] increase the number of valence electrons. The C-Bi-C bond angle of **1** (116.7(1)°) is only slightly larger than that of $(2,6\text{-}Mes_2C_6H_3)_2BiH$ (114.9(3)°),[10] but significantly larger than that of $(2,6\text{-}Mes_2C_6H_3)_2BiCl$ (98.4(2)°).[10] The C-Pb-C bond angle of the isoelectronic plumbylene $(2,6\text{-}Mes_2C_6H_3)_2Pb$ (114.5(6)°) is very similar.[19] In the asymmetric unit of **2**, two independent conformers of the stibenium ion are present. The C-Sb-C bond angles of **2** (121.4(1) and 122.8(1)°) are larger than those of $(2,6\text{-}Mes_2C_6H_3)_2SbH$ (117.5(1)°) and $(2,6\text{-}Mes_2C_6H_3)_2SbCl$ (103.4(1)°). The C-Sn-C bond angle of the isoelectronic stannylene $(2,6\text{-}Mes_2C_6H_3)_2Sn$ (114.7(2)°) is considerably smaller.[19] In the solid state, the C–Bi and C–Sb bonds are tilted towards one mesityl group, which is reflected in the C-C-Bi angles (102.5(2), 103.7(2)° vs. 133.9(2), 134.7(2)°) and in the C-C-Sb bond angles (101.9(2), 103.6(2)° vs. 133.8(2), 135.3(2)°). In this way, it seems that the Bi and Sb atoms interact with the
π-electrons of the mesityl groups. The shortest intramolecular $Bi\cdots C_{Mes}$ distances (2.799(3), 2.831(3) Å) and $Sb\cdots C_{Mes}$ distances (2.699(4), 2.819(4) Å) are significantly shorter than the sum of the van der Waals radii (3.90 and 3.76 Å). Notably, the isoelectronic plumbylene $(2,6\text{-}Mes_2C_6H_3)_2Pb$ and stannylene $(2,6\text{-}Mes_2C_6H_3)_2Sn$ show similar intramolecular contacts, with $Pb\cdots C_{Mes}$ (3.185(1) Å) and $Sn\cdots C_{Mes}$ (3.171(5) Å) distances that are somewhat longer.[19]

The formation of **1** and **2** was confirmed by NMR spectroscopy, where several key features were noted (see the Supporting Information). Common to both **1** and **2** is the presence of spectroscopic features indicating a relief of steric restraint associated with the flanking mesityl groups upon abstraction of the third substituent (i.e., H or Cl). In both starting materials, $(2,6\text{-}Mes_2C_6H_3)_2BiH$ and $(2,6\text{-}Mes_2C_6H_3)_2SbCl$, the *ortho* and *meta* hydrogen and carbon atoms of the mesityl groups are magnetically nonequivalent,

 © 2018 Wiley-VCH Verlag GmbH & Co. KGaA, Weinheim

which is due to sterically restricted rotation. As a result, three resonances are observed for the nonequivalent methyl groups in the aliphatic region of the ^{1}H NMR spectra as well as broad resonances assigned to the *meta* hydrogen atoms. The ^{13}C NMR spectra display six resonances in the aromatic region, which were assigned to the mesityl groups. Upon abstraction of the hydride or chloride substituent, the *ortho* and the *meta* positions of the mesityl groups become equivalent, which is consistent with their free rotation. This results in simplified ^{1}H and ^{13}C NMR spectra for **1** and **2**, with fewer resonances corresponding to the mesityl groups. Moreover, the abstraction of hydride by the trityl cation was evidenced by the loss of the resonance characteristic to the hydrogen atom attached to bismuth ($\delta = 19.6$ ppm, C_6D_6) and the formation of triphenylmethane ($\delta = 5.4$ ppm, C_6D_6). In the ^{13}C NMR spectrum of **1**, the signal assigned to the carbon atom attached to bismuth was found at a significantly higher chemical shift ($\delta = 246.0$ ppm, CD_2Cl_2) than that of the starting material ($\delta = 153.6$ ppm, C_6D_6). For compound **2**, this difference was less pronounced, with the chemical shift of the carbon atom bonded to antimony ($\delta = 156.4$ ppm, CD_2Cl_2) being less than 7 ppm downfield-shifted from that of (2,6-$Mes_2C_6H_3$)$_2$SbCl ($\delta = 149.7$ ppm, CD_2Cl_2). Intrigued by the observation that the Bi and Sb atoms engage in interactions with the π-electrons of the mesityl groups in the solid state, ^{1}H and ^{13}C NMR spectra were recorded at variable (low) temperatures in an effort to understand the importance of these interactions in solution. For both **1** and **2**, the ^{1}H and ^{13}C NMR spectra (CD_2Cl_2) recorded at room temperature were virtually identical to those measured at −70 °C and displayed sharp resonances, indicating either a lack of E···aryl interactions (E = Bi, Sb) or a weak coordination–dissociation process that is fast on the NMR timescale.

In an effort to shed light on the electronic structure of the neutral and cationic carbene congeners, density functional theory (DFT) calculations including complementary Hilbert space and real-space analyses were carried out (see the Supporting Information). For the series Ph_2E (E = Si, Ge, Sn, Pb) and $[Ph_2E]^+$ (E = P, As, Sb, Bi), the two possible multiplicities (M = 1 and 3) reflecting the different spin states were calculated. In all cases, the singlet state (M = 1) was the electronic ground state and energetically well-separated from the triplet state (M = 3). For the Group 14 elements, our results confirmed previous observations.[9] For the Group 15 elements, the results are consistent with the experimental NMR data showing no evidence for paramagnetism arising from unpaired electrons. Natural bond orbital (NBO) analysis[20] of [(2,6-$Mes_2C_6H_3$)$_2$E]$^+$ (E = P, As, Sb, Bi) and (2,6-$Mes_2C_6H_3$)$_2$E (E = Si, Ge, Sn, Pb) revealed almost fully occupied lone pair orbitals with predominant s character, which increased from E = P (70 %) to E = Bi (89 %) and from E = Si (81 %) to E = Pb (93 %; Figure 2a).

The electron localization indicator (ELI-D),[21] which is related to the electron pair density, comprises kidney-shaped lone pair basins, populated with about two electrons, next to the central atoms E for [(2,6-$Mes_2C_6H_3$)$_2$E]$^+$ (E = P, As, Sb, Bi) and (2,6-$Mes_2C_6H_3$)$_2$E (E = Si, Ge, Sn, Pb). The basin volumes (V_{eli}) vary between 12.4 Å^3 (E = P) and 21.4 Å^3 (E = Sn) without showing a clear periodic trend (Figure 2b).

A topological atoms in molecules (AIM) analysis[22] of [(2,6-$Mes_2C_6H_3$)$_2$E]$^+$ (E = P, As, Sb, Bi) and (2,6-$Mes_2C_6H_3$)$_2$E (E = Si, Ge, Sn, Pb) revealed bond paths for the primary E–C bonds, with typical bond properties at the bond critical points (bcp) for polar-covalent interactions (with an electron density, ED, $(\rho(r)_{bcp})$ between ca. 0.5 and 1.0 e Å^{-3}, a Laplacian of the ED $(\nabla^2\rho(r)_{bcp})$ close to zero, and high positive and negative

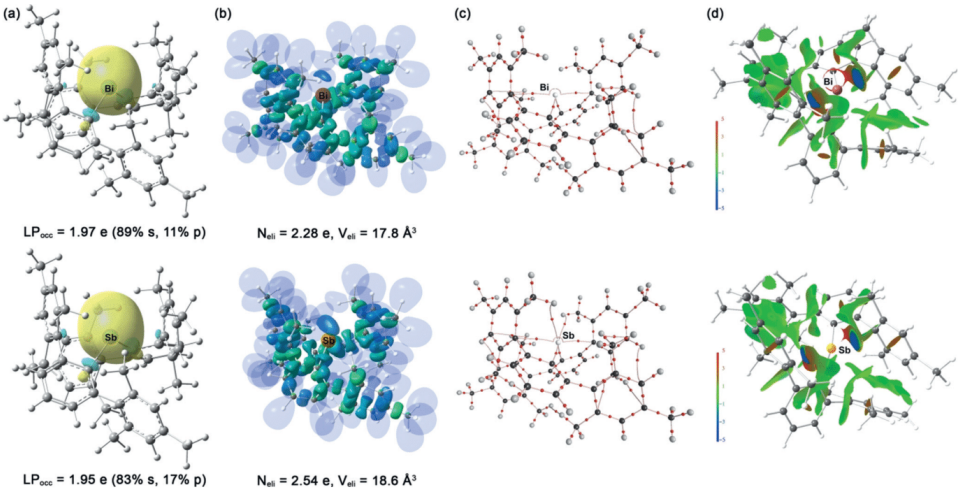

Figure 2. a) NBO depictions of the lone pairs, b) ELI-D, c) AIM bond topologies, and d) NCI indices of [(2,6-$Mes_2C_6H_3$)$_2$Bi]$^+$ (top) and [(2,6-$Mes_2C_6H_3$)$_2$Sb]$^+$ (bottom).

 © 2018 Wiley-VCH Verlag GmbH & Co. KGaA, Weinheim

kinetic and total energy density over ED ratios, $G/\rho(r)_{bcp}$ and $H/\rho(r)_{bcp}$). In addition, bond paths for secondary intramolecular interactions involving the 2,6-$Mes_2C_6H_3$ substituents were observed (Figure 2c). The heavier cations $[(2,6\text{-}Mes_2C_6H_3)_2E]^+$ (E = As, Sb, Bi) display bond paths associated with E···C contacts, which were absent for the lightest member (E = P) and the neutral Group 14 compounds $(2,6\text{-}Mes_2C_6H_3)_2E$ (E = Si, Ge, Sn, Pb). Both compound classes show additional bond paths related to E···H contacts (E = Si, Ge, Sn, Pb, P, As, Sb). Together, these E···C and E···H contacts are indicative of electrostatic and London dispersion interactions, which are generally operative within reactive species stabilized by *meta*-terphenyl substituents.[23] This finding was reinforced by inspection of the non-covalent interaction index (NCI),[24] which revealed attractive contact areas where these interactions occur (Figure 2d). Particularly noteworthy are the attractive (in blue) contact patches for the short Bi···C and Sb···C interactions of $[(2,6\text{-}Mes_2C_6H_3)_2E]^+$ (E = Sb, Bi). This is in line with the observation that only for these two compounds, the molecular orbital (MO) that constitutes the Bi or Sb atomic lone pair is energetically stabilized by 19.8 and 6.3 kJ mol^{-1} with respect to the highest occupied molecular orbital (HOMO). For all other carbene analogues, the corresponding lone-pair MO is the HOMO.

In conclusion, the first divalent Group 15 element analogues of carbenes, namely the bismuthenium ion $[(2,6\text{-}Mes_2C_6H_3)_2Bi]^+$ and the stibenium ion $[(2,6\text{-}Mes_2C_6H_3)_2Sb]^+$, have been obtained by using bulky *meta*-terphenyl substituents in combination with weakly coordinating borate anions. The divalent nature of both cations was inferred from NMR spectroscopy and confirmed by X-ray crystallography. DFT calculations, including Hilbert space (MO, NBO) and real-space (AIM, ELI-D, NCI) analyses, uniformly showed that virtually fully occupied lone-pair orbitals with predominant s character are located on the Bi and Sb atoms. The kinetic stabilization relies on the shielding of the central Bi and Sb atoms as well as intramolecular electrostatic and London dispersion interactions of these central atoms with the *meta*-terphenyl substituent.

Acknowledgements

We thank Dr. Ole Mallow for performing the elemental analyses. The Deutsche Forschungsgemeinschaft (DFG) is gratefully acknowledged for financial support.

Conflict of interest

The authors declare no conflict of interest.

Keywords: bismuthenium · carbene analogues · divalency · *meta*-terphenyl · stibenium

How to cite: *Angew. Chem. Int. Ed.* **2018**, *57*, 10080–10084
Angew. Chem. **2018**, *130*, 10237–10241

[1] G. Bertrand, *Science* **2004**, *305*, 783–785.
[2] K. C. Kim, C. A. Reed, D. W. Elliot, L. J. Mueller, F. Tham, L. Lin, J. B. Lambert, *Science* **2002**, *297*, 825–827.
[3] J. B. Lambert, L. Lin, S. Keinan, T. Müller, *J. Am. Chem. Soc.* **2003**, *125*, 6022–6023.
[4] I. Zharov, T.-C. Weng, A. M. Orendt, D. H. Barich, J. Penner-Hahn, D. M. Grant, Z. Havlas, J. Michl, *J. Am. Chem. Soc.* **2004**, *126*, 12033–12046.
[5] P. J. Davidson, D. H. Harris, M. F. Lappert, *J. Chem. Soc. Dalton Trans.* **1976**, 2268–2274.
[6] R. West, M. J. Fink, J. Michl, *Science* **1981**, *214*, 1343–1344.
[7] M. Kira, S. Ishida, T. Iwamoto, C. Kabuto, *J. Am. Chem. Soc.* **1999**, *121*, 9722–9723.
[8] T. A. Engesser, M. R. Lichtenthaler, M. Schleep, I. Krossing, *Chem. Soc. Rev.* **2016**, *45*, 789–899.
[9] Y. Mizuhata, T. Sasamori, N. Tokitoh, *Chem. Rev.* **2009**, *109*, 3479–3511.
[10] N. J. Hardman, B. Twamley, P. P. Power, *Angew. Chem. Int. Ed.* **2000**, *39*, 2771–2773; *Angew. Chem.* **2000**, *112*, 2884–2886.
[11] Synthesis of **1**: 1,2-Difluorobenzene (3 mL) was added to a solid mixture of $(2,6\text{-}Mes_2C_6H_3)_2BiH$ (0.125 g, 0.15 mmol) and $[Ph_3C][BAr^F{}_4]$ (0.165 g, 0.15 mmol) at room temperature. The reaction mixture was stirred for 5 h; a dark green-brown solution was obtained. All volatile components were removed at reduced pressure, and the solid residue was washed with hexane (3 × 25 mL) and then dried at reduced pressure. Compound **1** was obtained as a black solid (0.220 g, 87%).
[12] Given the reaction conditions (see below), it is reasonable to assume that $[Et_3Si(1,2\text{-}F_2C_6H_4)][B(C_6F_5)_4]$ was generated in situ. For more information regarding the synthesis of $[Et_3Si(solvent)][B(C_6F_5)_4]$ and $[Et_3Si\text{-}H\text{-}SiEt_3][B(C_6F_5)_4]$, see: a) S. J. Connelly, W. Kaminsky, D. M. Heinekey, *Organometallics* **2013**, *32*, 7478–7481; b) M. Nava, C. A. Reed, *Organometallics* **2011**, *30*, 4798–4800.
[13] Synthesis of **2**: A solution of Et_3SiH (0.035 g, 0.30 mmol) in 1,2-difluorobenzene (1.2 mL) was added to a mixture of $(2,6\text{-}Mes_2C_6H_3)_2SbCl$ (0.235 g, 0.30 mmol) and $[Ph_3C][B(C_6F_5)_4]$ (0.277 g, 0.30 mmol) in 1,2-difluorobenzene (3 mL) at room temperature. The reaction mixture was stirred at room temperature for 14 h. A dark red-brown solution was obtained. The product was triturated with hexane (45 mL); the solid was separated by decantation, subsequently washed with hexane (3 × 15 mL), and then dried at 70 °C (1×10^{-3} mbar). Compound **2** was obtained as a dark green-brown solid (0.352 g, 82%).
[14] J. Beckmann, J. Bolsinger, A. Duthie, P. Finke, E. Lork, C. Lüdtke, O. Mallow, S. Mebs, *Inorg. Chem.* **2012**, *51*, 12395–12406.
[15] C. J. Carmalt, L. J. Farrugia, N. C. Norman, *J. Chem. Soc. Dalton Trans.* **1996**, 443–454.
[16] N. L. Kilah, S. Petrie, R. Stranger, J. W. Wielandt, A. C. Willis, S. B. Wild, *Organometallics* **2007**, *26*, 6106–6113.
[17] L. Dostál, R. Jambor, A. Růžička, R. Jirásko, A. Lyčka, J. Beckmann, S. Ketkov, *Inorg. Chem.* **2015**, *54*, 6010–6019.
[18] R. Kannan, S. Kumar, A. P. Andrews, E. D. Jemmis, A. Venugopal, *Inorg. Chem.* **2017**, *56*, 9391–9395.
[19] R. S. Simons, L. Pu, M. M. Olmstead, P. P. Power, *Organometallics* **1997**, *16*, 1920–1925.
[20] a) J. P. Foster, F. Weinhold, *J. Am. Chem. Soc.* **1980**, *102*, 7211–7218; b) A. E. Reed, L. A. Curtiss, F. Weinhold, *Chem. Rev.* **1988**, *88*, 899–926.
[21] a) M. Kohout, *Int. J. Quantum Chem.* **2004**, *97*, 651–658; b) M. Kohout, F. R. Wagner, Y. Grin, *Theor. Chem. Acc.* **2008**, *119*, 413–420.
[22] R. F. W. Bader, *Atoms in Molecules: A Quantum Theory*, Oxford University Press, Oxford UK, **1990**.
[23] D. J. Liptrot, P. P. Power, *Nat. Rev. Chem.* **2017**, https://doi.org/10.1038/s41570-016-0004.

 © 2018 Wiley-VCH Verlag GmbH & Co. KGaA, Weinheim

[24] a) E. R. Johnson, S. Keinan, P. Mori-Sanchez, J. Contreras-García, A. J. Cohen, W. Yang, *J. Am. Chem. Soc.* **2010**, *132*, 6498 – 6506; b) J. Contreras-García, E. Johnson, S. Keinan, R. Chaudret, J.-P. Piquemal, D. Beratan, W. Yang, *J. Chem. Theory Comput.* **2011**, *7*, 625 – 632.

[25] CCDC 1823886 (**1**) and 1823887 (**2**) contain the supplementary crystallographic data for this paper. These data can be obtained free of charge from The Cambridge Crystallographic Data Centre.

Manuscript received: March 15, 2018
Accepted manuscript online: April 12, 2018
Version of record online: May 9, 2018

 © 2018 Wiley-VCH Verlag GmbH & Co. KGaA, Weinheim

2.2 Transient Phosphenium and Arsenium Ions versus Stable Stibenium and Bismuthenium Ions

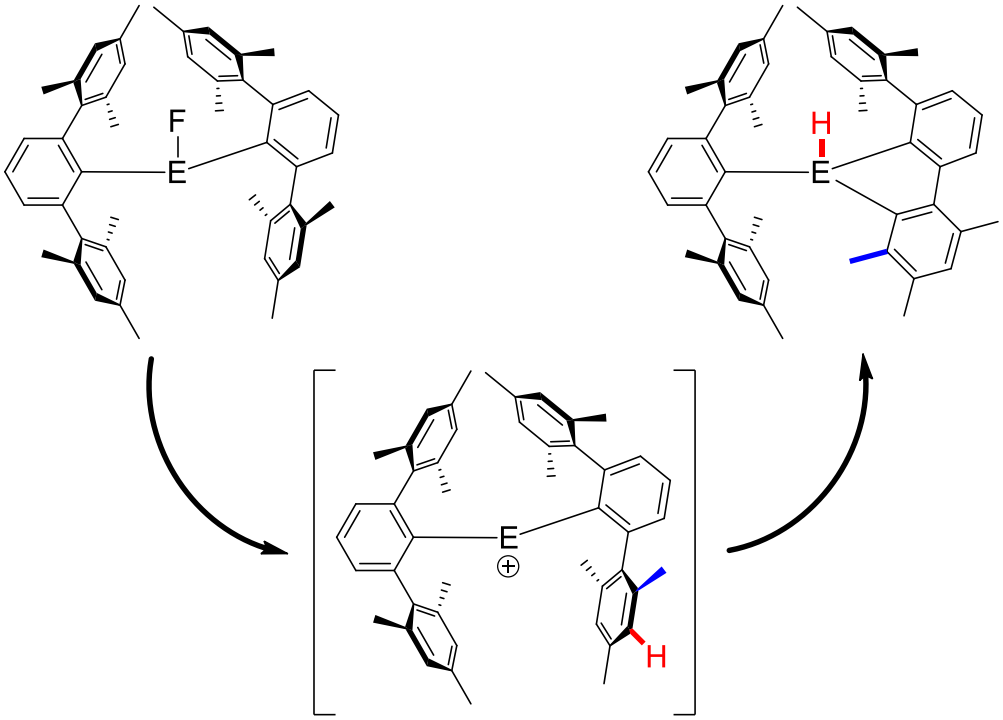

E = P, unstable at T > –80°C
E= As, unstable at T > –20°C

2.2.1 Synopsis

After the successful synthesis of the two bis(*m*-terphenyl)pnictogenium ions $[Ter_2Sb]^+[B(C_6F_5)_4]^-$ and $[Ter_2Bi]^+[B(3,5\text{-}(CF_3)_2C_6H_3)_4]^-$ the synthesis of the lighter homologues was attempted. Due to the unsuccessful attempts for the preparation of the corresponding chlorides, a new attempt was made by *in situ* fluorination of the corresponding *m*-terphenylpnictogen dichloride with caesium fluoride and further reaction with a second equivalent of *m*-terphenyllithium. By this one-pot reaction, the bis(*m*-terphenyl)pnictogen fluorides Ter_2AsF and Ter_2PF were accessible. The abstraction of this fluoride was attempted with multiple Lewis acids and electrophilic abstraction agents. The reaction of Ter_2PF with $[Et_3Si]^+[B(C_6F_5)_4]^-$ led to the donor acceptor adduct $[Ter_2P(F)SiEt_3]^+[B(C_6F_5)_4]^-$, which was published by our workgroup in an independent publication.[143] Also, tris(pentafluorophenyl)borane was used as a strong Lewis acid, but showed no reaction. With $EtAlCl_2$, as a weaker but also smaller Lewis acid, the fluoride was removed from Ter_2PF leading to a deep red reaction mixture at -80 °C, which undergoes a color change to yellow at higher temperatures. The abstraction of the

fluoride from Ter_2AsF was attempted at -40 °C with $[Et_3Si]^+[B(C_6F_5)_4]^-$ leading also to a dark red reaction mixture, which changes color above -20 °C. Unlike the heavier homologues, the formed pnictogenium ions were not stable and underwent an intramolecular reaction with one of the mesityl groups of a *m*-terphenyl substituent. In the case of phosphorus, the intermediate could be isolated and was identified as 1,2,4-trimethyl-6-mesityl-5-*m*-terphenyl-benzo[*b*]phospholium ion by NMR spectroscopy. The formation was also visible in the case of arsenic, but formed multiple products at ambient temperatures after a short period of time. Therefore, similar to phosphorus, the reaction mixture was quenched with triethylamine as a base to deprotonate the cationic pnictogonium ion to obtain the neutral pnictol species. The arsole and phosphole were isolated and characterized by means of NMR spectroscopy and single crystal X-ray diffraction experiments. This proved the intramolecular electrophilic attack of the transient pnictogenium ion on one of the mesityl rings, inducing a 1,2-methyl shift. The mechanism of the rearrangement was proposed by DFT calculations, verifying the energetic minima for phosphorus and arsenic in comparison to antimony and bismuth and also proposing a short-lived arenium ion as transient intermediate.

2.2.2 Scientific Contribution

In this project I developed the synthesis of the bis(terphenyl)arsenic compounds and cations and fully characterized the obtained compounds. M. Olaru did the phosphorus counterpart. M. Olaru and me co-wrote the manuscript. E. Lork perfored the crystallographic structure refinements. S. Mebs did the computational part contributing to this publication. J. Beckmann was the principal investigator, designed the concept and co-wrote the manuscript.

Percentage of my contribution of the total workload:

Experimental concept and design: ca. 40%, experimental work and acquisition of experimental data: ca. 50%, data analysis and interpretation: ca. 50%, preparation of figures and tables: ca. 40%, drafting of the manuscript: ca. 20%.

The article was published in the journal “Chemistry – A European Journal“ in 2019 as an Open Access Communication:

Marian Olaru, Daniel Duvinage, Enno Lork, Stefan Mebs*, Jens Beckmann*, *Chem. Eur. J.* **2019**, *25*, 14758-14761.

DOI: 10.1002/chem.201902520

The Supporting Information includes experimental procedures, NMR spectra, X-ray crystallographic data and computational data and is available free of charge on the journal′s website:

https://chemistry-europe.onlinelibrary.wiley.com/action/downloadSupplement?doi=10.1002%2Fchem.201902520&file=chem201902520-sup-0001-misc_information.pdf

ChemPubSoc Europe

DOI: 10.1002/chem.201902520

CHEMISTRY A European Journal Communicatio

Organometallic Chemistry |*Hot Paper*|

Transient Phosphenium and Arsenium Ions versus Stable Stibenium and Bismuthenium Ions

Marian Olaru,[a] Daniel Duvinage,[a] Enno Lork,[a] Stefan Mebs,*[b] and Jens Beckmann*[a]

Dedicated to Professor Konrad Seppelt on the occasion of his 75th birthday

Abstract: Fluoride abstraction from bis-*m*-terphenylelement fluorides (2,6-$Mes_2C_6H_3)_2EF$ (E = P, As) generated the highly reactive phosphenium ion $[(2,6\text{-}Mes_2C_6H_3)_2P]^+$ and the arsenium ion $[(2,6\text{-}Mes_2C_6H_3)_2As]^+$, which immediately underwent intramolecular electrophilic substitution and formation of an 1,2,4-trimethyl-6-mesityl-5-*m*-terphenyl-benzo[*b*]phospholium ion and an 1,2,4-trimethyl-6-mesityl-5-*m*-terphenyl-benzo[*b*]arsolium ion, respectively. The formation of the latter involved a methyl group migration from the *ortho*-position of a flanking mesityl group to the *meta*-position. This reactivity of $[(2,6\text{-}Mes_2C_6H_3)_2E]^+$ (E = P, As) is in sharp contrast to the related stibenium ion $[(2,6\text{-}Mes_2C_6H_3)_2Sb]^+$ and bismuthenium ion $[(2,6\text{-}Mes_2C_6H_3)_2Bi]^+$, which have been recently isolated and fully characterized (*Angew. Chem. Int. Ed.* 2018, **57**, 10080–10084). On the basis of DFT calculations, a mechanism for the rearrangement of the phosphenium and arsenium ions into the phospholium and arsolium ions is proposed, which is not feasible for the stibenium and bismuthenium ions.

Divalent phosphenium ions, $[R_2P]^+$, and arsenium ions, $[R_2As]^+$, are six-valence electron species, containing an electron lone pair as well as a vacant *p*-orbital, which consequently possess Lewis amphoteric properties.[1] Compared to the neutral isoelectronic group 14 carbene analogues, R_2E (E = Si, Ge),[2] the cationic group 15 analogues $[R_2E]^+$ (E = P, As, Sb, Bi) are much stronger electrophiles. In fact, the simplest donor-free dialkyl- and diarylphosphenium ions, $[Me_2P]^+$ and $[Ph_2P]^+$ are predicted to be strong Lewis super acids in the gas phase.[3] Therefore, the vast majority of phosphenium and arsenium ions known in condensed phase are intra- or intermolecularly stabilized by substituents or ligands that compensate the electron deficiency by conjugation with donor atoms possessing electron lone pairs, which dramatically reduces the Lewis acidity and reactivity.[1] Since the seminal work of Dimroth and Hoffmann, published in 1964,[4] many of these electron-rich, donor-stabilized phosphenium[5] and arsenium ions[6] have been reported. The only disputable exception seems to be the bis(ferrocenyl)phosphenium ion $[Fc_2P]^+$, reported by Cowley et al. in 1981, which, however, was never structurally characterized.[7] The fact that other main group cations containing ferrocenyl groups, such as $[FcPh_2C]^+$[8] and $[Fc(Me)tBuSi]^+$,[9] show significant intramolecular Fe···E (E = C, Si) interaction, casts doubt on the claim that $[Fc_2P]^+$ is a donor-free phosphenium ion and suggests that a similar Fe···P interaction might be present.[10] The preparation of divalent phosphenium and arsenium ions from neutral trivalent precursors involves the abstraction of one substituent and replacement by a weakly coordinating anion. This is exemplified in the reaction of Ph_2PCl with $GaCl_3$ or $[Me_3Si][FAl(OR^F)_3]$ respectively, providing a phosphino-phosphonium ion $[Ph_2PPPh_2Cl]A$ (A = $GaCl_4$,[11] or $F[Al(OR^F)_3]_2$;[12] $R^F = C(CF_3)_3$), which can be regarded as a donor–acceptor complex between the elusive Lewis acid $[Ph_2P]^+$ and Lewis base Ph_2PCl. These examples raise the question whether bulky substituents are able to prevent the formation of such dinuclear donor–acceptor complexes.

In this work we describe the fluoride abstraction from (2,6-$Mes_2C_6H_3)_2PF$[13] and (2,6-$Mes_2C_6H_3)_2AsF$ that proceeded most likely with the formation of the transient phosphenium ion $[(2,6\text{-}Mes_2C_6H_3)_2P]^+$ [**1a**]$^+$ and the arsenium ion $[(2,6\text{-}Mes_2C_6H_3)_2As]^+$ [**1b**]$^+$, whereby two bulky *m*-terphenyl substituents prevent the formation of dinuclear donor–acceptor complexes. Using a similar strategy, we have been recently able to isolate the heavier stibenium ion $[(2,6\text{-}Mes_2C_6H_3)_2Sb]^+$ [**1c**]$^+$ and the bismuthenium ion $[(2,6\text{-}Mes_2C_6H_3)_2Bi]^+$ [**1d**]$^+$ (Scheme 1).[14]

Unlike the indefinitely stable [**1c**]$^+$ and [**1d**]$^+$, the transient [**1a**]$^+$ and [**1b**]$^+$, immediately undergo intramolecular electrophilic substitution and formation of the 1,2,4-trimethyl-6-mesityl-5-*m*-terphenyl-benzo[*b*]phospholium ion, [**2a**]$^+$, and the 1,2,4-trimethyl-6-mesityl-5-*m*-terphenyl-benzo[*b*]arsolium ion, [**2b**]$^+$, respectively. The formation of these protonated 9-phospha- and 9-arsena-fluorenes [**2a**]$^+$ and [**2b**]$^+$ involved a 1,2-methyl shift in one of the flanking mesityl groups of the *m*-ter-

[a] Dr. M. Olaru, D. Duvinage, Dr. E. Lork, Prof. Dr. J. Beckmann
Institut für Anorganische Chemie und Kristallographie
Universität Bremen
Leobener Straße 7, 28359 Bremen
(Germany)
E-mail: j.beckmann@uni-bremen.de

[b] Dr. S. Mebs
Institut für Experimentalphysik
Freie Universität Berlin
Arnimallee 14, 14195 Berlin (Germany)
E-mail: stebs@chemie.fu-berlin.de

Supporting information and the ORCID identification number(s) for the author(s) of this article can be found under: https://doi.org/10.1002/chem.201902520.

© 2019 The Authors. Published by Wiley-VCH Verlag GmbH & Co. KGaA. This is an open access article under the terms of the Creative Commons Attribution License, which permits use, distribution and reproduction in any medium, provided the original work is properly cited.

ChemPubSoc Europe

CHEMISTRY A European Journal Communication

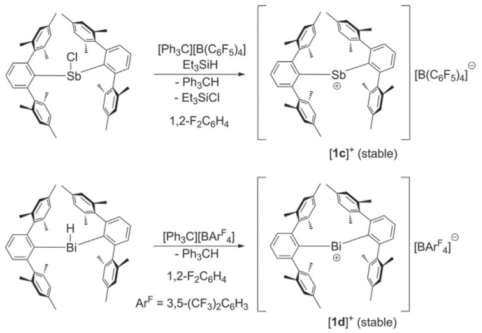

Scheme 1. Synthesis of the stibenium ion [**1 c**]$^+$ and the bismuthenium ion [**1 d**]$^+$.

phenyl substituent, for which a mechanism is proposed on the basis of DFT calculations.

The starting materials (2,6-$Mes_2C_6H_3$)$_2$EF (E = P, As) were prepared in a one pot reaction from 2,6-$Mes_2C_6H_3$Li, ECl_3 and CsF, as recently communicated already for the phosphorus compound (Figure 1).[14] Unlike many other examples of this compound class, (2,6-$Mes_2C_6H_3$)$_2$EF (E = P, As) show no sign for spontaneous redistribution.[14,15] In solution, they are characterized by ^{19}F NMR chemical shifts (CD_2Cl_2) of $\delta = -197.6$ (E = P) and -209.7 ppm (E = As). Comparison of the molecular structure reveals that the C–P–C bond angle (106.1(1)°) is slightly smaller than the C–As–C bond angle (112.8(1)°). The attempted fluoride abstraction of (2,6-$Mes_2C_6H_3$)$_2$PF with the strong electrophile [Et_3Si(toluene)][$B(C_6F_5)_4$] gave rise to the formation of the donor acceptor complex [R_2(F)P$SiEt_3$][$B(C_6F_5)_4$] only.[14] Interestingly, fluoride abstraction was achieved using an excess of the weaker electrophiles $EtAlCl_2$ or $AlCl_3$ in CH_2Cl_2 and/or

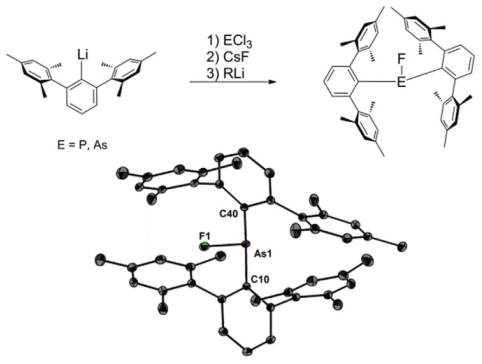

Figure 1. Synthesis of the bis(*m*-terphenyl)element fluorides. Molecular structure of (2,6-$Mes_2C_6H_3$)$_2$AsF showing 50% probability ellipsoids and the essential atom numbering Scheme. Selected bond parameters [Å, °]: As1–F1 1.764(1), As1–C10 1.992(1), As1–C40 1.993(1), C10-As1-C40 112.8(1).

heptane. Due to the higher solubility of $EtAlCl_2$ in most organic solvents the results were better than with $AlCl_3$.

Thus, the reaction of (2,6-$Mes_2C_6H_3$)$_2$PF with $EtAlCl_2$ at -90 °C provided a dark solution, reminiscent of the color of solutions containing the stibenium ion [(2,6-$Mes_2C_6H_3$)$_2$Sb]$^+$, [**1 c**]$^+$ or the bismuthenium ion [(2,6-$Mes_2C_6H_3$)$_2$Bi]$^+$, [**1 d**]$^+$.[14] Above -80 °C, the dark color rapidly faded away to give a yellow solution, which contained the 1,2,4-trimethyl-6-mesityl-5-*m*-terphenyl-benzo[*b*]phospholium ion, [**2 a**]$^+$ as the major product (Figure 2). In solution, this protonated 9-phospha-fluorene [**2 a**]$^+$ is characterized by a ^{31}P NMR chemical shift (CD_2Cl_2) of $\delta = -15.0$ (E = P) and a $^1J(^1H\text{-}^{31}P)$ coupling of 501 Hz. Under inert conditions, solution of [**2 a**]$^+$ are stable for at least

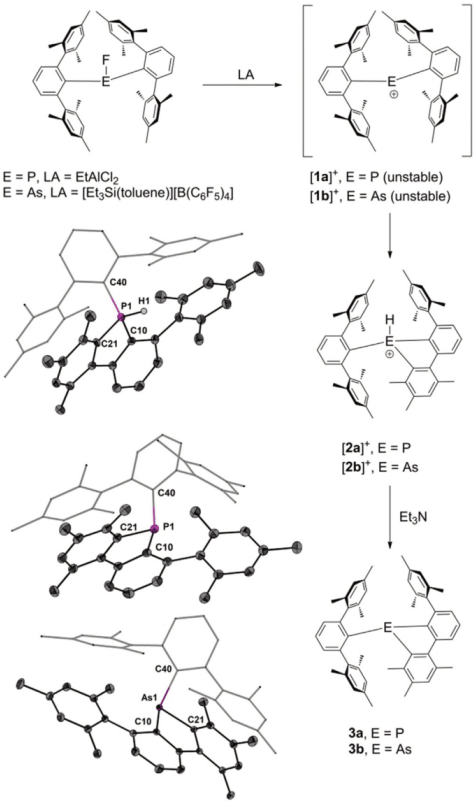

Figure 2. Fluoride abstraction of bis(*m*-terphenyl)element fluorides. Molecular structures of [**2 a**]$^+$, **3 a**, and **3 b** showing 50% probability ellipsoids and the essential atom numbering Scheme. Selected bond parameters [Å, °] of [**2 a**]$^+$: P1–H1 1.31(3), P1–C10 1.793(2), P1–C21 1.788(2), P1–C40 1.809(2), C10-P1-C40 123.4(1), C21-P1-C10 94.6(1), C21-P1-C40 110.9(1). Selected bond parameters [Å, °] of **3 a**: P1–C10 1.838(2), P1–C21 1.832(2), P1–C40 1.871(2), C10-P1-C21 89.48(7), C10-P1-C40 104.51(6), C21-P1-C40 107.26(6). Selected bond parameters [Å, °] of **3 b**: As1–C10 1.957(1), As1–C21 1.954(1), As1–C40 2.002(1), C10-As1-C21 85.68(5), C10-As1-C40 107.76(5), C21-As1-C40 99.43(5).

 © 2019 The Authors. Published by Wiley-VCH Verlag GmbH & Co. KGaA, Weinheim

ChemPubSoc Europe

CHEMISTRY A European Journal Communication

several days. Unfortunately, all attempts to isolate or crystallize [**2a**]$^+$ as aluminate salt from these solutions failed. We therefore added triethylamine to induce deprotonation of [**2a**]$^+$, which provided the related neutral phosphole **3a** as crystalline solid (Figure 2). In solution, 9-phospha-fluorene **3a** gives rise to a ^{31}P NMR chemical shift (CD_2Cl_2) of $\delta = -25.2$ ppm. Re-protonation of **3a** using HCl/Na[BAr^F_4] eventually afforded [**2a**]$^+$ as crystalline [BAr^F_4]$^-$ salt (Figure 2, Ar^F = 3,5-$(CF_3)_2C_6H_3$). We note in passing that [**2a**]$^+$ does not react further with excess $EtAlCl_2$ unlike **3a**, which readily undergoes oxidative addition[16] with $EtAlCl_2$ in CH_2Cl_2 to give 5-(chloromethyl)-5-*m*-terphenyl-6-mesityl-1,2,4-trimethyl-benzo[*b*]-phospholium salt [**4**][$AlCl_4$] as major species (see the Supporting Information). Inspection of the molecular structures of [**2a**]$^+$ and **3a** revealed that the initially formed phosphenium ion had undergone an intramolecular electrophilic attack of a flanking mesityl groups at one of the *m*-terphenyl substituents. This attack occurred in *ortho*-position of the mesityl group and proceeded with cleavage of the methyl group, which migrated to the *meta*-position. Unlike (2,6-$Mes_2C_6H_3)_2$PF, the fluoride abstraction of (2,6-$Mes_2C_6H_3)_2$AsF was achieved with [Et_3Si(toluene)][$B(C_6F_5)_4$] at −40 °C to give initially the arsenium cation [**1b**]$^+$, which, however, rearranged into the 1,2,4-trimethyl-6-mesityl-5-*m*-terphenyl-benzo[*b*]arsolium ion, [**2b**]$^+$ above −20 °C (Figure 1). NMR inspection showed that solutions of [**2b**]$^+$ are unstable and give multiple products after a short period of time. We therefore also added triethylamine to induce deprotonation of [**2b**]$^+$. In this way, the related neutral arsole **3b** was obtained as crystalline solid (Figure 2). Similar as for [**2a**]$^+$ and **3a**, the molecular structure of **3b** revealed that an 1,2-methyl shift in one of the mesityl groups had taken place (Figure 2). We note that Wehmschulte et al. had previously observed the formation of 9-phospha- and 9-arsafluorenes from *m*-terphenyldichlorophosphines and -arsenes; however, these involved no methyl group migration.[17]

The fluoride abstraction from (2,6-$Mes_2C_6H_3)_2$PF with [Et_3Si]$^+$ was impaired by the exothermic formation (ΔE = −241.0 kJ mol^{-1}) of the stable donor–acceptor complex [(2,6-$Mes_2C_6H_3)_2$(F)PSiEt_3]$^+$.[13,18] The hypothetical elimination of Et_3SiF and formation of [(2,6-$Mes_2C_6H_3)_2$P]$^+$ [**1a**]$^+$ was found to be endothermic (ΔE = +40.1 kJ mol^{-1}).[13,18] In comparison, the fluoride abstraction from (2,6-$Mes_2C_6H_3)_2$AsF with [Et_3Si]$^+$ might also form a thermodynamically donor–acceptor complex [(2,6-$Mes_2C_6H_3)_2$(F)AsSiEt_3]$^+$ (ΔE = −128.3 kJ mol^{-1}); however, the competing elimination into Et_3SiF and formation of [(2,6-$Mes_2C_6H_3)_2$As]$^+$ [**1b**]$^+$ was calculated to be thermodynamically more feasible (ΔE = −133.0 kJ mol^{-1}), which is fully consistent with the experimental observations.[13,18] With the substantially weaker electrophile $EtAlCl_2$, both the complex formation (2,6-$Mes_2C_6H_3)_2$P(F)AlEtCl_2 (ΔE = 33.08 kJ mol^{-1}) and the fluoride abstraction to give [(2,6-$Mes_2C_6H_3)_2$P]$^+$ [**1a**]$^+$ and [$EtAlCl_2F$]$^-$ (ΔE = 210.9 kJ mol^{-1}) are predicted to be endothermic. We therefore hypothesized that the active electrophile might have been [EtAlCl]$^+$ or [$AlCl_2$]$^+$, which were formed from $EtAlCl_2$ through autoionization. Notably, the autoionization of the $AlCl_3$ in donor solvents to give solvated [$AlCl_2$]$^+$ and [$AlCl_4$]$^-$ is well established.[19] The complex formation between (2,6-$Mes_2C_6H_3)_2$PF and [EtAlCl]$^+$ or [$AlCl_2$]$^+$ was indeed calculated to be exothermic (ΔE = −343.4 and −448.7 kJ mol^{-1}, respectively); however, the fluoride abstraction to give [(2,6-$Mes_2C_6H_3)_2$P]$^+$ [**1a**]$^+$, EtAlClF (ΔE = 44.2 kJ mol^{-1}) and $AlCl_2F$ (ΔE = 51.5 kJ mol^{-1}), respectively, was still calculated to be endothermic, which does not verify our hypothesis conclusively.

To this end, it remains unclear as to why the weak Lewis acid $EtAlCl_2$ is able to abstract fluoride from (2,6-$Mes_2C_6H_3)_2$PF.

In an effort to understand why the phosphenium ion [(2,6-$Mes_2C_6H_3)_2$P]$^+$ [**1a**]$^+$ and the arsenium ion [(2,6-$Mes_2C_6H_3)_2$As]$^+$ [**1b**]$^+$ undergo rearrangement into the phospholium and arsolium ions [**2a**]$^+$ and [**2b**]$^+$, whereas the stibenium ion [(2,6-$Mes_2C_6H_3)_2$Sb]$^+$ [**1c**]$^+$ and bismuthenium ion [(2,6-$Mes_2C_6H_3)_2$Bi]$^+$ [**1d**]$^+$ are stable, we calculated a conceivable mechanism for the 1,2-methyl shift for all heteroelements (Scheme 2). The energy of the pnictogenium ions [**1a**]$^+$–[**1d**]$^+$

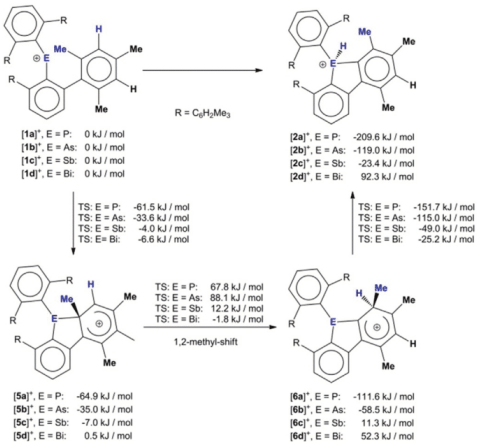

Scheme 2. Mechanism of the rearrangement from pnictogenium ions [**1a**]$^+$–[**1d**]$^+$ to the protonated 9-pnictogena-fluorene ions [**2a**]$^+$–[**2d**]$^+$.

was arbitrarily set to 0 kJ mol^{-1}. Compared to these references, the conversion is strongly exothermic for [**2a**]$^+$ (−209.6 kJ mol^{-1}) and [**2b**]$^+$ (−119.0 kJ mol^{-1}), weakly exothermic for **2c**]$^+$ (−23.4 kJ mol^{-1}) and endothermic for [**2d**]$^+$ (92.3 kJ mol^{-1}). The intramolecular electrophilic attack of [**1a**]$^+$–[**1d**]$^+$ gives rise to the formation of arenium ions [**5a**]$^+$–[**5d**]$^+$, followed by the 1,2-methyl shift and the formation of other arenium ions [**6a**]$^+$–[**6d**]$^+$ and a subsequent proton transfer to give the protonated 9-pnictogena-fluorene ions [**2a**]$^+$–[**2d**]$^+$ (Scheme 2). The formation of both types of arenium ions [**5a**]$^+$–[**5d**]$^+$ is exothermic for phosphorus and arsenic, but only very weakly exothermic or endothermic for antimony and bismuth (Scheme 2). The highest transition state energies were found for the migration of the methyl groups from the *ortho*-positions to the *meta*-positions. Overall, the energy pathways are consistent with the observed rearrangement of

 © 2019 The Authors. Published by Wiley-VCH Verlag GmbH & Co. KGaA, Weinheim

ChemPubSoc Europe

CHEMISTRY A European Journal Communication

the phosphenium ion $[(2,6\text{-}Mes_2C_6H_3)_2P]^+$ $[\mathbf{1a}]^+$ and the arsenium ion $[(2,6\text{-}Mes_2C_6H_3)_2As]^+$ $[\mathbf{1b}]^+$ into the protonated 9-phospha- and 9-arsena-fluorenes $[\mathbf{2a}]^+$ and $[\mathbf{2b}]^+$ and the observed stability of the stibenium ion $[(2,6\text{-}Mes_2C_6H_3)_2Sb]^+$, $[\mathbf{1c}]^+$ or the bismuthenium ion $[(2,6\text{-}Mes_2C_6H_3)_2Bi]^+$, $[\mathbf{1d}]^+$.[14]

The fluoride abstraction from the bis(*m*-terphenyl)element fluorides $(2,6\text{-}Mes_2C_6H_3)_2EF$ (E = P, As) using the Lewis acids $EtAlCl_2$ and $[Et_3Si(toluene)]^+$, respectively, provided the transient phosphenium ion $[(2,6\text{-}Mes_2C_6H_3)_2P]^+$ $[\mathbf{1a}]^+$ and the arsenium ion $[(2,6\text{-}Mes_2C_6H_3)_2As]^+$ $[\mathbf{1b}]^+$, which rearrange into protonated 9-phospha- and 9-arsena-fluorenes $[\mathbf{2a}]^+$ and $[\mathbf{2b}]^+$. The mechanism of the rearrangement involves an intramolecular electrophilic attack, a methyl group migration in one of the flanking mesityl groups and proton transfer to phosphorus and arsenic. This mechanism suggests to avoid reactive hydrogen atoms in the *m*-terphenyl substituents, for example, by using permethylated phenyl groups in the flanking positions, which is now being investigated in our laboratory. For the stable stibenium ion $[(2,6\text{-}Mes_2C_6H_3)_2Sb]^+$, $[\mathbf{1c}]^+$ and the bismuthenium ion $[(2,6\text{-}Mes_2C_6H_3)_2Bi]^+$, $[\mathbf{1d}]^+$[14] the same mechanism is not feasible on thermodynamic grounds.

Acknowledgements

The Deutsche Forschungsgemeinschaft (DFG) is gratefully acknowledged for financial support.

Conflict of interest

The authors declare no conflict of interest.

Keywords: arsenium ion · fluoride abstraction · Lewis acid · *m*-terphenyl · phosphenium ion

[1] Reviews: a) A. H. Cowley, R. A. Kemp, *Chem. Rev.* **1985**, *85*, 367–382; b) M. Sanchez, M.-R. Mazières, L. Lamandé, R. Wolf in *Multiple Bonds and Low Coordination in Phosphorus Chemistry* (eds. M. Regitz, O. J. Scherer), Chapter D1: *Phosphenium Cations*, Georg Thieme Verlag, Stuttgart, New York **1990**, 129–148; c) D. Gudat, *Coord. Chem. Rev.* **1997**, *163*, 71–106; d) N. Burford, P. J. Ragogna, *Dalton Trans.* **2002**, 4307–4315; e) N. Burford, P. J. Ragogna in *Modern Aspects of Main Group Chemistry* (ed. M. Lattman et al.), Chapter 20: *Coordination Chemistry of Phosphorus(III) as a Lewis Acceptor*. ACS Symposium Series, Washington, DC, **2005**; f) A. P. M. Robertson, P. A. Gray, N. Burford, *Angew. Chem. Int. Ed.* **2014**, *53*, 6050–6069; *Angew. Chem.* **2014**, *126*, 6162–6182.

[2] a) Y. Mizuhata, T. Sasamori, N. Tokitoh, *Chem. Rev.* **2009**, *109*, 3479–3511; b) M. Asay, C. Jones, M. Driess, *Chem. Rev.* **2011**, *111*, 354–396; c) P. Bag, S. U. Ahmad, S. Inoue, *Bull. Chem. Soc. Jpn.* **2017**, *90*, 255–271; d) M.-X. Wang, *Acc. Chem. Res.* **2012**, *45*, 182–195.

[3] a) B. D. Ellis, P. J. Ragogna, C. L. B. Macdonald, *Inorg. Chem.* **2004**, *43*, 7857–7867; b) J. M. Slattery, S. Hussein, *Dalton Trans.* **2012**, *41*, 1808–1815.

[4] K. Dimroth, P. Hoffmann, *Angew. Chem. Int. Ed. Engl.* **1963**, *2*, 621; *Angew. Chem.* **1963**, *75*, 860.

[5] a) N. Kuhn, J. Fahl, D. Bläser, R. Boese, *Z. Anorg. Allg. Chem.* **1999**, *625*, 729–734; b) M. B. Abrams, B. L. Scott, R. T. Baker, *Organometallics* **2000**, *19*, 4944–4956; c) D. Gudat, A. Haghverdi, H. Hupfer, M. Nieger, *Chem. Eur. J.* **2000**, *6*, 3414–3425; d) N. Burford, D. E. Herbert, P. J. Ragogna, R. McDonald, M. J. Ferguson, *J. Am. Chem. Soc.* **2004**, *126*, 17067–17073; e) P. Kilian, A. M. Z. Slawin, *Dalton Trans.* **2007**, 3289–3296; f) J. J. Weigand, S. D. Riegel, N. Burford, A. Decken, *J. Am. Chem. Soc.* **2007**, *129*, 7969–7976; g) S. Burck, D. Gudat, *Inorg. Chem.* **2008**, *47*, 315–321; h) A. L. Brazeau, C. A. Caputo, C. D. Martin, N. D. Jones, P. J. Ragogna, *Dalton Trans.* **2010**, *39*, 11069–11073; i) A. Kraft, J. Beck, I. Krossing, *Chem. Eur. J.* **2011**, *17*, 12975–12980; j) C. Hering, A. Schulz, A. Villinger, *Inorg. Chem.* **2013**, *52*, 5214–5225; k) L. Liu, D. A. Ruiz, F. Dahcheh, G. Bertrand, *Chem. Commun.* **2015**, *51*, 12732–12735; l) Y. Wang, H. P. Hickox, Y. Xie, P. Wie, D. Cui, M. R. Walter, H. F. Schaefer, G. H. Robinson, *Chem. Commun.* **2016**, *52*, 5746–5748; m) E. R. Clark, A. M. Borys, K. Pearce, *Dalton Trans.* **2016**, *45*, 16125–16129; n) S. Volodarsky, R. Dobrovetsky, *Chem. Commun.* **2018**, *54*, 6931–6934; o) B. Rao, C. C. Chong, R. Kinjo, *J. Am. Chem. Soc.* **2018**, *140*, 652–656.

[6] a) K. A. Porter, A. C. Willis, J. Zank, S. B. Wild, *Inorg. Chem.* **2002**, *41*, 6380–6386; b) R. J. Wiacek, J. N. Jones, C. L. B. Macdonald, A. H. Cowley, *Can. J. Chem.* **2002**, *80*, 1518–1523; c) N. Burford, P. J. Ragogna, K. Sharp, R. McDonald, M. J. Ferguson, *Inorg. Chem.* **2005**, *44*, 9453–9460; d) N. L. Kilah, M. L. Weir, S. B. Wild, *Dalton Trans.* **2008**, 2480–2486; e) M. L. Weir, I. A. Cade, N. L. Kilah, X. Zhou, S. B. Wild, *Inorg. Chem.* **2009**, *48*, 7482–7490; f) C. Hering, J. Rothe, A. Schulz, A. Villinger, *Inorg. Chem.* **2013**, *52*, 7781–7790; g) J. W. Dube, Y. Zheng, W. Thiel, M. Alcarazo, *J. Am. Chem. Soc.* **2016**, *138*, 6869–6877.

[7] a) S. G. Baxter, R. L. Collins, A. H. Cowley, S. F. Sena, *J. Am. Chem. Soc.* **1981**, *103*, 714–715; b) S. G. Baxter, R. L. Collins, A. H. Cowley, S. F. Sena, *Inorg. Chem.* **1983**, *22*, 3475–3479.

[8] U. Behrens, *J. Organomet. Chem.* **1979**, *182*, 89–98.

[9] K. Müther, R. Fröhlich, C. Mück-Lichtenfeld, S. Grimme, M. Oestreich, *J. Am. Chem. Soc.* **2011**, *133*, 12442–12444.

[10] a) J. Beckmann: Invited lecture IL9c "Donor-free carbene analogues of group 15 elements" *Intern. Conf. Heteroatom Chem.* 30.6.-5.7. 2019, Prague, Czech Republic. Book of abstracts p. 48; b) M. Olaru, A. Mischin, S. Mebs, L. Malaspina, J. Beckmann, manuscript in preparation.

[11] N. Burford, P. J. Ragogna, R. McDonald, M. J. Ferguson, *J. Am. Chem. Soc.* **2003**, *125*, 14404–14410.

[12] J. Possart, A. Martens, M. Schleep, A. Ripp, H. Scherer, D. Kratzert, I. Krossing, *Chem. Eur. J.* **2017**, *23*, 12305–12310.

[13] M. Olaru, A. Schröder, L. Albers, D. Duvinage, S. Mebs, J. Beckmann, *Chem. Eur. J.* **2019**, *25*, 9861–9865.

[14] M. Olaru, D. Duvinage, S. Mebs, J. Beckmann, *Angew. Chem. Int. Ed.* **2018**, *57*, 10080–10084; *Angew. Chem.* **2018**, *130*, 10237–10241.

[15] N. Fey, M. Garland, J. P. Hopewell, C. L. McMullin, S. Mastroianni, A. G. Orpen, P. G. Pringle, *Angew. Chem. Int. Ed.* **2012**, *51*, 118–122; *Angew. Chem.* **2012**, *124*, 122–126.

[16] H. Bock, U. Lechner-Knoblauch, *J. Organomet. Chem.* **1985**, *294*, 295–304.

[17] A. A. Diaz, J. D. Young, M. A. Khan, R. J. Wehmschulte, *Inorg. Chem.* **2006**, *45*, 5568–5575.

[18] Energies at zero Kelvin were calculated using density functional theory (DFT) at the B3PW91/6–311+G* level of theory. For the heavier atoms fully relativistic effective core potentials (Sb: ECP28MDF; Bi: ECP60MDF) and corresponding cc-pVTZ basis sets were utilized. See the Supporting Information for details.

[19] a) D. W. Grattan, P. H. Plesch, *J. Chem. Soc. Dalton Trans.* **1977**, 1734–1744; b) J. Derouault, M. T. Forel, *Inorg. Chem.* **1977**, *16*, 3207–3213; c) I. Beattie, P. J. Jones, J. A. K. Howard, L. E. Smart, C. J. Gilmore, J. W. Akitt, *J. Chem. Soc. Dalton Trans.* **1979**, 528–535; d) N. C. Means, C. M. Means, S. G. Bott, J. L. Atwood, *Inorg. Chem.* **1987**, *26*, 1466–1468; e) R. Sluka, M. Nečas, P. Šindelár, *Acta Crystallogr. Sect. E* **2004**, *60*, m447–m448.

Manuscript received: June 2, 2019
Accepted manuscript online: August 12, 2019
Version of record online: October 24, 2019

 © 2019 The Authors. Published by Wiley-VCH Verlag GmbH & Co. KGaA, Weinheim

2.3 Intramolecular Reaction of Transient Phosphenium and Arsenium Ions Giving Rise to Isolable 9-Phospha- and 9-Arsena-Fluorenium Ions

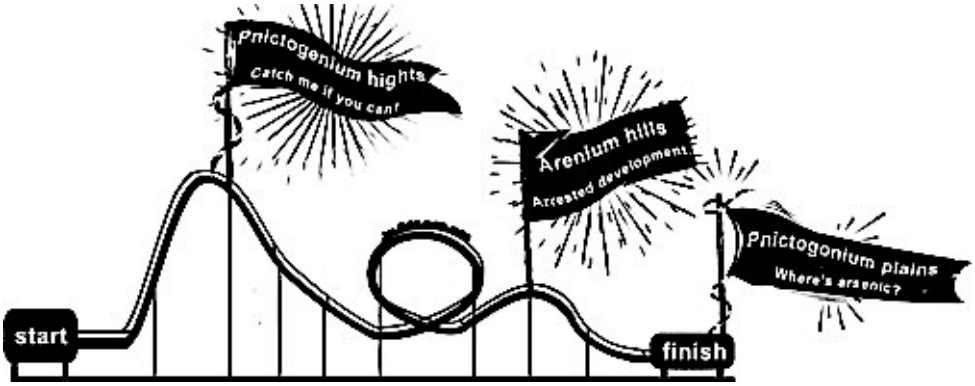

2.3.1 Synopsis

It was shown that the transient pnictogenium ions Ter_2E^+ (E = P, As) react in an intramolecular 1,2-methyl shift from the *ortho* to the *meta* position under proton migration to the pnictogenium ion. A short-lived transient arenium intermediate was proposed by DFT calculations. Because of this, permethylated phenyl groups as flanking groups were introduced providing the pentamethylphenyl substituted *m*-terphenyl substituent (Per). By this, the presence of reactive hydrogen atoms in the *m*-terphenyl system are avoided and the electron inductive effect of the permethylated system makes the substituent more electron-rich in an attempt to stabilize the low valent central atom. In a similar approach to the previously used terphenyl system, the one-pot procedure for the synthesis of Per_2PF and Per_2AsF was used providing both starting materials, which were fully characterized. For the fluoride abstraction, $EtAlCl_2$ for Per_2PF and $AlCl_3$ for Per_2AsF were used, because previously it was shown that these weaker Lewis acids can be used for highly sterically demanding element fluorides. Both reaction mixtures turn immediately deep red similar to the heavier bis(*m*-terphenyl)pnictogenium ions. Two isomers were identified by NMR analysis and one of the isomers was identified by single-crystal X-ray experiments. The identity of the second isomer was identified by NMR analysis. The reaction proceeds under ring closure including a methyl migration the pnicta-fluorenium ions, in which the isomers are differing in the position of the methyl group migration. In both isomers, the methyl group migrated to the *meta* position with regard to the central element. Over the course of a month in DCM solution, the phospha-fluorenium ion reacts intramolecularly, in which the methyl

group migrates to the phosphol forming a phospholium ion. The arsenic congener does not exhibit this behaviour and is stable in solution over the course of at least 6 months and also at elevated temperatures of 80 °C. No methyl group migration is visible by means of NMR spectroscopy. In THF both pnicta-fluorenium ions are deprotonated at the methyl group in para position to the dimethyl group. The deprotonation by THF indicates the high acidity of the system due to the Wheland complex. This reaction is quasi-reversible as removal of the solvent under reduced pressure formed the pnicta-fluorenium ions, but also side products are visible by NMR spectroscopy. Due to the complex reaction mechanism and the newly observed 1,3-methyl shift instead of a 1,2-methyl shift, DFT calculations were used to elucidate the mechanism of the rearrangement. It was found that the energy gain is even higher compared to the mesityl substituted terphenyl system, which might be related to the higher susceptibility for electrophilic attacks on the permethylated phenyl substituents due to increased electron density.

2.3.2 Scientific Contribution

In this project I carried out the synthesis and full characterization of the arsenic compounds with the support of the co-author Yannick Naß, who developed the synthesis of the arsenic compounds under my supervision during his master thesis. M. Olaru developed the synthesis of the phosphorus compounds and M. Olaru and me co-wrote the manuscript. L. A. Malaspina performed the X-ray crystallographic part and the computational part with S. Mebs. J. Beckmann was the principal investigator, designed the concept and co-wrote the manuscript.

Percentage of my contribution of the total workload:

Experimental concept and design: ca. 40%, experimental work and acquisition of experimental data: ca. 40%, data analysis and interpretation: ca. 50%, preparation of figures and tables: ca. 20%, drafting of the manuscript: ca. 10%.

The article was published in the journal “Angewandte Chemie International Edition“ in 2020 as an open access communication and was also translated to german:

Marian Olaru, Daniel Duvinage, Yannik Naß, Lorraine A. Malaspina, Stefan Mebs, Jens Beckmann*, *Angew. Chem. Int. Ed.* **2020**, *59*, 14414-14417.

Marian Olaru, Daniel Duvinage, Yannik Naß, Lorraine A. Malaspina, Stefan Mebs, Jens Beckmann*, *Angew. Chem.* **2020**, *59*, 14414-14417.

International Edition: DOI: 10.1002/anie.202006728

German Edition: DOI: 10.1002/ange.202006728

The Supporting Information includes experimental procedures, NMR spectra, X-ray crystallographic data and computational data and is available free of charge on the journal′s website:

https://onlinelibrary.wiley.com/action/downloadSupplement?doi=10.1002%2Fanie.202006728&file=anie202006728-sup-0001-misc_information.pdf

GDCh Communications Angewandte International Edition Chemie

Check for updates

How to cite: *Angew. Chem. Int. Ed.* **2020**, *59*, 14414–14417
International Edition: doi.org/10.1002/anie.202006728
German Edition: doi.org/10.1002/ange.202006728

Pnictogenium ions

Intramolecular Reaction of Transient Phosphenium and Arsenium Ions Giving Rise to Isolable 9-Phospha- and 9-Arsena-Fluorenium Ions

*Marian Olaru, Daniel Duvinage, Yannik Naß, Lorraine A. Malaspina, Stefan Mebs, and Jens Beckmann**

In memory of Professor Robert R. Holmes

Abstract: *Transient phosphenium and arsenium ions, generated by fluoride abstraction from bis(m-terphenyl)fluoropnictogens, underwent intramolecular electrophilic attack prior to methyl group migration and gave rise to isolable 9-phospha- and 9-arsena-fluorenium ions.*

Arenium ions are well-recognized key intermediates of electrophilic aromatic substitution reactions.[1] Although often referred to as Wheland intermediates due to his seminal theoretical publication of 1942,[2] the interest in arenium ions dates back earlier to pioneering experimental work by Pfeiffer and Wizinger, published already in 1928.[3] Over the years a number of arenium ions have been isolated and fully characterized (Scheme 1). For instance, the protonation of benzene provided the parent benzenium ion $[C_6H_7]^+$ (**I**).[4] Starting from hexamethylbenzene, substituted hexamethylbenzenium ions $[C_6Me_6R]^+$ (**II**, R = Me,[5] Cl,[6] Br[7]) were obtained. Attempts to afford silyl cations $[R_3Si]^+$ have led to the isolation of silyl-substituted toluenium ions $[C_6H_5MeSiR_3]^+$ (**III**, R = Me, Et).[8]

In their native form, phosphenium ions $[R_2P]^+$ and arsenium ions $[R_2As]^+$ are highly reactive six-valence-electron species that have never been isolated without the support of electron-rich ligands.[9] Our efforts to prepare kinetically stabilized pnictogenium ions $[(2,6\text{-}Mes_2C_6H_3)_2E]^+$[10] by fluoride abstraction from bis-*m*-terphenylpnictogen fluorides $(2,6\text{-}Mes_2C_6H_3)_2EF$ (E = P, As) yielded 1,2,4-trimethyl-6-mesityl-5-*m*-terphenylbenzo[b]phospholium and -arsolium ions instead.[11] The formation of these protonated phosphole and arsole structures involved a methyl group migration from the *ortho*-position of a flanking mesityl group to the *meta*-position prior to a hydrogen transfer from that position to phosphorus and arsenic. For the mechanism of this rearrangement we proposed transient short-lived arenium ions. We further concluded that reactive hydrogen atoms need to be avoided in the *m*-terphenyl substituents in order to isolate kinetically stabilized phosphenium and arsenium ions by this route.[11]

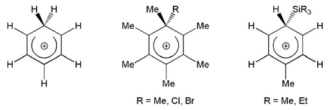

Scheme 1. Examples of previously known arenium ions.

We have therefore adjusted our strategy and turned our attention to a related *m*-terphenyl substituent in which the two flanking aryl groups are permethylated. Starting from 2,6-$(Me_5C_6)_2C_6H_3Li$[12] and ECl_3 (E = P, As), we have now prepared the bis(*m*-terphenyl)fluoropnictogens (2,6-$\{Me_5C_6\}_2C_6H_3)_2EF$ (**1a**, E = P; **1b**, E = As). The synthesis, solution NMR, and solid-state structural features of **1a** and **1b** resemble those of $(2,6\text{-}Mes_2C_6H_3)_2EF$ (E = P,[13] As[11]) reported previously. In solution, **1a** and **1b** are characterized by ^{19}F NMR chemical shifts (CD_2Cl_2) at $\delta = -200.3$ (E = P) and −216.0 ppm (E = As), while **1a** gives a ^{31}P NMR signal at $\delta = 193.8$ ppm. Fluoride ion abstraction from **1a** and **1b** using $EtAlCl_2$ and $AlCl_3$, respectively, in CH_2Cl_2 proceeded in virtually quantitative yield to afford two-isomer mixtures of phospha-fluorenium ions $[\mathbf{5a}]^+$ and $[\mathbf{7a}]^+$ (ca. 0.65:0.35 molar ratio) and arsa-fluorenium ions $[\mathbf{5b}]^+$ and $[\mathbf{7b}]^+$ (ca. 0.70:0.30 molar ratio), species isolated as dark-red crystalline solids (Figure 1). The ^{31}P NMR spectrum (CD_2Cl_2) showing two close resonances at $\delta = -26.9$ ppm for $[\mathbf{5a}]^+$ and −22.2 ppm for $[\mathbf{7a}]^+$ confirmed that phosphorus was in a very similar coordination environment for both isomers. The ^1H NMR spectra of these mixtures were complex; as a consequence of complete desymmetrization of the molecules, each species displayed six signals assigned to the aromatic protons and individual resonances for all methyl groups in the aliphatic area which only overlapped by chance. The similar distribution pattern of the resonances and of the coupling constants indicated that the major and minor species were closely related isomers. In both the phosphorus and arsenic cases, the ^1H NMR spectra displayed sharp signals with virtually no change when measured at lower temperatures, signaling

[*] Dr. M. Olaru, D. Duvinage, Y. Naß, Dr. L. A. Malaspina, Prof. Dr. J. Beckmann
Institut für Anorganische Chemie und Kristallographie
Universität Bremen
Leobener Straße 7, 28359 Bremen (Germany)
E-mail: j.beckmann@uni-bremen.de
Dr. S. Mebs
Institut für Experimentalphysik, Freie Universität Berlin
Arnimallee 14, 14195 Berlin (Germany)

Supporting information and the ORCID identification number(s) for the author(s) of this article can be found under: https://doi.org/10.1002/anie.202006728.

© 2020 The Authors. Published by Wiley-VCH Verlag GmbH & Co. KGaA. This is an open access article under the terms of the Creative Commons Attribution License, which permits use, distribution and reproduction in any medium, provided the original work is properly cited.

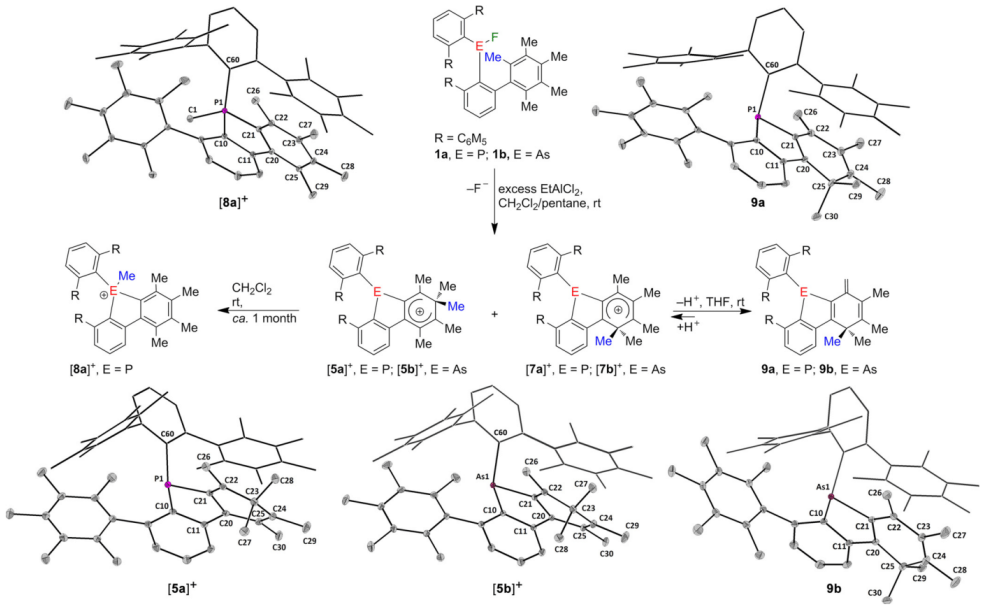

Figure 1. Fluoride abstraction from bis(*m*-terphenyl)element fluorides **1a** and **1b** and subsequent reactions of arenium ions $[\mathbf{5a}]^+$ and $[\mathbf{5b}]^+$ as well as $[\mathbf{7a}]^+$ and $[\mathbf{7b}]^+$. Molecular structures of $[\mathbf{5a}]^+$, $[\mathbf{5b}]^+$, $[\mathbf{8a}]^+$, **9a**, and **9b** showing 30% probability ellipsoids and the essential atom numbering scheme. For clarity, the counter ions of $[\mathbf{5a}]^+$ ($[0.75\cdot AlCl_4 + 0.25\cdot EtAlCl_3]^-$), $[\mathbf{5b}]^+$ ($[AlCl_4]^-$), and $[\mathbf{8a}]^+$ ($[AlCl_4]^-$) were omitted from both the reaction scheme and structure depictions. Selected bond parameters [Å, °] of $[\mathbf{5a}]^+$: P1-C10 1.831(2), P1-C21 1.836(2), P1-C60 1.861(2), C20-C21 1.432(3), C21-C22 1.359(3), C22-C23 1.500(3), C24-C23 1.499(3), C25-C24 1.370(3), C20-C25 1.429(3), C10-P1-C21 88.40(8), C10-P1-C60 104.77(8), C21-P1-C60 107.63(8), C28-C23-C27 108.69(16). Selected bond parameters [Å, °] of $[\mathbf{5b}]^+$: As1-C10 1.950(1), As1-C21 1.956(1), As1-C60 1.982(1), C20-C21 1.432(2), C20-C25 1.436(2), C21-C22 1.362(2), C22-C23 1.499(2), C24-C23 1.499(2), C25-C24 1.376(2), C10-As1-C21 84.64(5), C10-As1-C60 103.21(5), C21-As1-C60 104.80(5), C27-C23-C28 109.12(11). Selected bond parameters [Å, °] of $[\mathbf{8a}]^+$: P1-C1 1.7962(9), P1-C10 1.7997(8), P1-C21 1.7825(8), P1-C60 1.8269(8), C21-P1-C1 110.38(4), C21-P1-C10 93.86(4), C1-P1-C10 109.84(4), C21-P1-C60 114.40(4), C1-P1-C60 114.96(4), C10-P1-C60, 111.45(4). Selected bond parameters [Å, °] of **9a**: C10-P1 1.836(2), C21-P1 1.824(2), C60-P1 1.865(2), C20-C21 1.352(3), C21-C22 1.459(3), C22-C26 1.340(3), C22-C23 1.469(3), C23-C24 1.348(3), C24-C25 1.518(3), C20-C25 1.520(3) C21-P1-C10 89.78(9), C21-P1-C60 105.15(8), C10-P1-C60 111.59(8), C29-C25-C30 109.17(17). Selected bond parameters [Å, °] of **9b**: As1-C10 1.970(1), As1-C21 1.946(2), As1-C60 2.004(1), C21-C20 1.356(2), C21-C22 1.465(2), C22-C26 1.360(2), C22-C23 1.460(2), C23-C24 1.352(3), C25-C24 1.518(3), C20-C25 1.522(2), C21-As1-C60 103.53(6), C21-As1-C10 85.58(6), C10-As1-C60 106.33(6), C29-C25-C30 110.6(1).

configurationally stable structures. NOESY spectra did not reveal any exchange between the major and the minor species in either phosphorus or arsenic cases, even at very short mixing times (see the Supporting Information).[15] The identities of the major phosphole $[\mathbf{5a}]^+$ and arsole $[\mathbf{5b}]^+$ components of the mixtures were confirmed by single-crystal X-ray diffraction (Figure 1),[14] and after the full NMR assignment it was clear that the solid-state structures were retained in solution. The molecular structures of $[\mathbf{5a}]^+$ and $[\mathbf{5b}]^+$ reveal that after abstraction of the fluoride ion, the corresponding pnictogenium ions $[(2,6\text{-}\{Me_5C_6\}_2C_6H_3)_2E]^+$ ($[\mathbf{2a}]^+$, E = P; $[\mathbf{2b}]^+$, E = As) immediately underwent intramolecular electrophilic substitution, which caused the displacement of one of the original *ortho*-methyl groups of a flanking C_6Me_5 group and formation of arenium ions. This is reminiscent of similarly behaving unstable cations $[(2,6\text{-}Mes_2C_6H_3)_2E]^+$ (E = P, As), which were previously shown to undergo a 1,2-methyl shift, resulting in formation of protonated phospholium and arsolium ions.[11] The molecular structures of $[\mathbf{5a}]^+$ and $[\mathbf{5b}]^+$ compare well with those of the related phospholes and arsoles,[11] with very similar bond lengths and angles around the pnictogen atoms. The dearomatized rings in $[\mathbf{5a}]^+$ and $[\mathbf{5b}]^+$ contain two single C–C bonds (C22,24–C23 1.499(3) Å for both $[\mathbf{5a}]^+$ and $[\mathbf{5b}]^+$) while the rest of the C–C bond lengths range between 1.359(3) Å (C21–C22, $[\mathbf{5a}]^+$) and 1.436(2) Å (C20–C25, $[\mathbf{5b}]^+$). Despite significant efforts we could not obtain suitable single crystals of $[\mathbf{7a}]^+$ and $[\mathbf{7b}]^+$ but the solution structures were unambiguously inferred from NMR spectroscopy and identified as positional isomers resulting from the migration of the displaced methyl group in a position *ortho* relative to the central aromatic ring.

In dichloromethane solution the mixture of $[\mathbf{5a}]^+$ and $[\mathbf{7a}]^+$ underwent a slow reaction in which a methyl group migrated to phosphorus, over the course of ca. one month, yielding $[\mathbf{8a}]^+$ as the major product.[16] Such a reaction did not

 © 2020 The Authors. Published by Wiley-VCH Verlag GmbH & Co. KGaA, Weinheim

take place for $[\mathbf{5b}]^+$ and $[\mathbf{7b}]^+$ even after six months. The methyl-phospholium ion $[\mathbf{8a}]^+$ gave a ^{31}P NMR resonance signal at $\delta = 21.7$ ppm. Inspection of its molecular structure reveals that upon methylation of phosphorus, the C_6Me_4 ring rearomatized. The coordination geometry around the phosphorus atom is disordered tetrahedral with bond lengths and angle values that are remarkably close to those of the simplest congener 2,2′-biphenylenemethylphenylphosphonium iodide despite the steric bulk of the substituents in $[\mathbf{8a}]^+$.[17] With tetrahydrofuran, mixtures of $[\mathbf{5a}]^+$ and $[\mathbf{7a}]^+$, as well as $[\mathbf{5b}]^+$ and $[\mathbf{7b}]^+$, reacted within minutes to afford **9a** and **9b**, respectively, as the major species, as a result of a methyl group deprotonation in *trans*-position of the dimethyl group.[18] This transformation took place in a seemingly complex equilibrium; the reversal of the reaction by evaporation of THF gave, aside from $[\mathbf{5a}]^+$ and $[\mathbf{7a}]^+$, as well as $[\mathbf{5b}]^+$ and $[\mathbf{7b}]^+$, a complex mixture of by-products. In solution, **9a** is characterized by a ^{31}P NMR chemical shift ($[D_8]$THF) of $\delta = -24.2$ ppm. The molecular structure of neutral species **9a** (and similarly that of **9b**) shows that the dearomatized C20–C25 ring contains two parallel double bonds (C23–C24 1.348(3) and C21–C20 1.352(3) Å) and four single bonds with C–C distances ranging between 1.459(3) (C21–C22) and 1.520(3) Å (C20–C25). The C22–C26 distance (**9a**: 1.340-(3) Å; **9b**: C22–C26 1.360(2) Å) is consistent with a double bond character.

From the very different structures of the targeted pnictogenium ions $[\mathbf{2a}]^+$ and $[\mathbf{2b}]^+$ and the actually isolated 9-pnictogena-fluorenium ions $[\mathbf{5a}]^+$ and $[\mathbf{5b}]^+$ it becomes obvious that the mechanism of the rearrangement involved unobserved cationic intermediates. In an effort to shed some light on the possible mechanism of the rearrangement, DFT calculations were carried out at the B3PW91/6-311 + G(d) level of theory, whereby the relative energies of the isolated arenium ions $[\mathbf{5a}]^+$ and $[\mathbf{5b}]^+$ were arbitrarily set to 0 kJ mol^{-1} (Figure 2). The energetically least favorable cation is the initially formed phosphenium ion $[\mathbf{2a}]^+$, which is 90.9 kJ mol^{-1} higher in energy. Notably, all attempts to geometrically optimize the arsenium ion $[\mathbf{2b}]^+$ failed and gave the product of the electrophilic attack at the *ortho*-position, namely, the arenium ion $[\mathbf{3b}]^+$, which is 3.7 kJ mol^{-1} more stable than the isolated $[\mathbf{5b}]^+$. The related arenium ion $[\mathbf{3a}]^+$ is 82.4 kJ mol^{-1} more stable than the phosphenium ion $[\mathbf{2a}]^+$, but 8.5 kJ mol^{-1} less stable than reference $[\mathbf{5a}]^+$. From the arenium ions $[\mathbf{3a}]^+$ and $[\mathbf{3b}]^+$, formal 1,2-, 1,3-, 1,4-, and 1,5-methyl shifts give rise to the conceivable arenium ions $[\mathbf{4a}]^+$ and $[\mathbf{4b}]^+$ (not observed), $[\mathbf{5a}]^+$ and $[\mathbf{5b}]^+$ (observed), $[\mathbf{6a}]^+$ and $[\mathbf{6b}]^+$ (not observed), as well as $[\mathbf{7a}]^+$ and $[\mathbf{7b}]^+$ (observed), whereby the

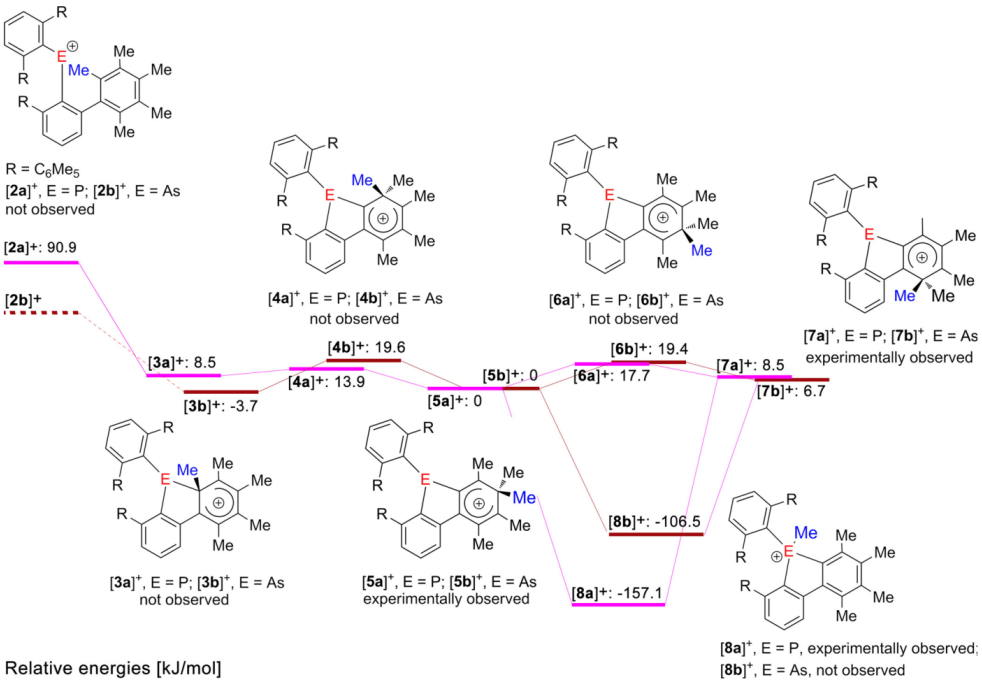

Figure 2. Suggested mechanism of the rearrangement, including relative energies of the pnictogenium ions $[\mathbf{2a}]^+$, the 9-pnictogena-fluorenium ions $[\mathbf{5a}]^+$ and $[\mathbf{5b}]^+$ as well as $[\mathbf{7a}]^+$ and $[\mathbf{7b}]^+$ and the phospholium ion $[\mathbf{8a}]^+$. Attempts to optimize $[\mathbf{2b}]^+$ always resulted in the conversion into $[\mathbf{3b}]^+$.

 © 2020 The Authors. Published by Wiley-VCH Verlag GmbH & Co. KGaA, Weinheim

relative energies correctly reflect the experimental observations. Mechanistically, the circumambulation of the methyl groups might involve intermediate bicycle[3.1.0]hexenyl cations as suggested by Childs and Winstein for the parent heptamethylbenzenium ions $[C_6Me_7]^+$.[19] This might also explain why the global energetic minimum, the phospholium ion $[\mathbf{8a}]^+$, which is 57.1 kJ mol^{-1} more stable than the reference $[\mathbf{5a}]^+$, is not immediately formed from $[\mathbf{3a}]^+$, despite the fact that the volatile methyl group is already in close proximity to the phosphorus atom. In the same context it is surprising that the related arsonium ion $[\mathbf{8b}]^+$ is not experimentally observed, although the energy gain relative to reference $[\mathbf{5b}]^+$ would be 106.5 kJ mol^{-1}. In light of these energy values, the observed slow transfer of the methyl group to the phosphorus might occur by an intermolecular transfer mechanism, perhaps involving traces of aluminum species as transfer reagents. Overall, the rearrangement of the phosphenium ion $[\mathbf{2a}]^+$ to the methyl-phospholium ion $[\mathbf{8a}]^+$ is energetically favored by 248.0 kJ mol^{-1}. This might be explained by the fact that the permethylphenyl group is electron-richer than the mesityl group, which makes it more susceptible to an electrophilic attack. Therefore, this value even exceeds the energy gain (209.6 kJ mol^{-1}) associated with the rearrangement of the previously studied $[(2,6\text{-}Mes_2C_6H_3)_2P]^+$ into the related protonated 9-phospha-fluorene.[11]

In summary, attempts to prepare the kinetically stabilized phosphenium and arsenium ions $[(2,6\text{-}\{Me_5C_6\}_2C_6H_3)_2E]^+$ (**2a**, E = P; **2b**, E = As) lead to the isolation of two-isomer mixtures of phospha-fluorenium ions $[\mathbf{5a}]^+$ and $[\mathbf{7a}]^+$ (ca. 0.65:0.35 molar ratio) and arsena-fluorenium ions $[\mathbf{5b}]^+$ and $[\mathbf{7b}]^+$ (ca. 0.70:0.30 molar ratio), respectively. Compared to the methyl-phospholium ion $[\mathbf{8a}]^+$, the arenium ions $[\mathbf{5a}]^+$ and $[\mathbf{7a}]^+$ are high-energy species; their conversion is slow enough (ca. one month) on the laboratory time scale, which enabled their full characterization. Although thermodynamically also favored, the conversion of the arsena-fluorenium ions $[\mathbf{5b}]^+$ and $[\mathbf{7b}]^+$ into the elusive methyl-arsolium ion $[\mathbf{8b}]^+$ is not observed.

Acknowledgements

The Deutsche Forschungsgemeinschaft (DFG) is gratefully acknowledged for financial support. We thank Johannes Stelten for his help with the acquisition of some NMR data. Open access funding enabled and organized by Projekt DEAL.

Conflict of interest

The authors declare no conflict of interest.

[1] D. Lenoir, *Angew. Chem. Int. Ed.* **2003**, *42*, 854 – 857; *Angew. Chem.* **2003**, *115*, 880 – 883.
[2] G. W. Wheland, *J. Am. Chem. Soc.* **1942**, *64*, 900 – 908.
[3] P. Pfeiffer, R. Wizinger, *Liebigs Ann. Chem.* **1928**, *461*, 132 – 154.
[4] a) C. A. Reed, K.-C. Kim, E. S. Stoyanov, D. Stasko, F. S. Tham, L. J. Mueller, P. D. W. Boyd, *J. Am. Chem. Soc.* **2003**, *125*, 1796 – 1804; b) F. Scholz, D. Himmel, L. Eisele, W. Unkrig, I. Krossing, *Angew. Chem. Int. Ed.* **2014**, *53*, 1689 – 1692; *Angew. Chem.* **2014**, *126*, 1715 – 1718.
[5] N. C. Baenziger, A. D. Nelson, *J. Am. Chem. Soc.* **1968**, *90*, 6602 – 6607.
[6] R. Rathore, J. Hecht, J. K. Kochi, *J. Am. Chem. Soc.* **1998**, *120*, 13278 – 13279.
[7] A. V. Vasilyev, S. V. Lindeman, J. K. Kochi, *New J. Chem.* **2002**, *26*, 582 – 592.
[8] a) J. B. Lambert, S. Zhang, C. Stern, J. Huffman, *Science* **1993**, *260*, 1917 – 1918; b) M. F. Ibad, P. Langer, A. Schulz, A. Villinger, *J. Am. Chem. Soc.* **2011**, *133*, 21016 – 21027.
[9] a) A. H. Cowley, R. A. Kemp, *Chem. Rev.* **1985**, *85*, 367 – 382; b) D. Gudat, *Coord. Chem. Rev.* **1997**, *163*, 71 – 106; c) N. Burford, P. J. Ragogna, *Dalton Trans.* **2002**, 4307 – 4315; d) A. P. M. Robertson, P. A. Gray, N. Burford, *Angew. Chem. Int. Ed.* **2014**, *53*, 6050 – 6069; *Angew. Chem.* **2014**, *126*, 6162 – 6182; e) M. Olaru, A. Mischin, L. A. Malaspina, S. Mebs, J. Beckmann, *Angew. Chem. Int. Ed.* **2020**, *59*, 1581 – 1584; *Angew. Chem.* **2020**, *132*, 1597 – 1600.
[10] M. Olaru, D. Duvinage, S. Mebs, J. Beckmann, *Angew. Chem. Int. Ed.* **2018**, *57*, 10080 – 10084; *Angew. Chem.* **2018**, *130*, 10237 – 10241.
[11] M. Olaru, D. Duvinage, E. Lork, S. Mebs, J. Beckmann, *Chem. Eur. J.* **2019**, *25*, 14758 – 14761.
[12] S. Hino, M. M. Olmstead, J. C. Fettinger, P. P. Power, *J. Organomet. Chem.* **2005**, *690*, 1638 – 1644.
[13] M. Olaru, A. Schröder, L. Albers, D. Duvinage, S. Mebs, J. Beckmann, *Chem. Eur. J.* **2019**, *25*, 9861 – 9865.
[14] Deposition numbers 1993654 (**1a**), 1993655 $[\mathbf{5a}]^+$, 1993656 $[\mathbf{5b}]^+$, 1993657 $[\mathbf{8a}]^+$, 1993658 (**9a**), and 1993659 (**9b**) contain the supplementary crystallographic data for this paper. These data are provided free of charge by the joint Cambridge Crystallographic Data Centre and Fachinformationszentrum Karlsruhe Access Structures service
[15] This observation is in contrast to the heptamethylbenzenium ion $[C_6Me_7]^+$, which undergoes a methyl shift making all seven methyl groups equivalent at sufficiently high temperatures. B. H. Meier, R. R. Ernst, *J. Am. Chem. Soc.* **1979**, *101*, 6441 – 6442.
[16] The reaction appeared to be faster and cleaner when the solution was exposed to sunlight. A control reaction that was ran in parallel, in complete darkness, was significantly slower (see the Supporting Information).
[17] P. Adkine, T. Cantat, E. Deschamps, L. Ricard, N. Mézailles, P. Le Floch, M. Geoffroy, *Phys. Chem. Chem. Phys.* **2006**, *8*, 862 – 868.
[18] The same regioselectivity was observed for the deprotonation of heptamethylbenzenium ion and the protonation of 4-methylene-1,1,2,3,5,6-hexamethylcyclohexadiene-2,5; a) W. von Doering, M. Saunders, H. G. Boyton, H. W. Earhart, E. F. Wadley, W. R. Edwards, G. Laber, *Tetrahedron* **1958**, *4*, 178 – 185; b) H. Hart, P. M. Collins, A. J. Waring, *J. Am. Chem. Soc.* **1966**, *88*, 1005 – 1013; c) M. Attina, F. Cacece, G. de Petris, S. Fornarini, P. Giacomello, *J. Am. Chem. Soc.* **1985**, *107*, 2297 – 2302.
[19] R. F. Childs, S. Winstein, *J. Am. Chem. Soc.* **1974**, *96*, 6409 – 6417.

Keywords: arenium ions · arsoles · *m*-terphenyl compounds · phospholes · pnictogenium ions

Manuscript received: May 9, 2020
Accepted manuscript online: May 27, 2020
Version of record online: July 6, 2020

 © 2020 The Authors. Published by Wiley-VCH Verlag GmbH & Co. KGaA, Weinheim

2.4 New crystal structures of alkali metal tetrakis(pentafluorophenyl)borates

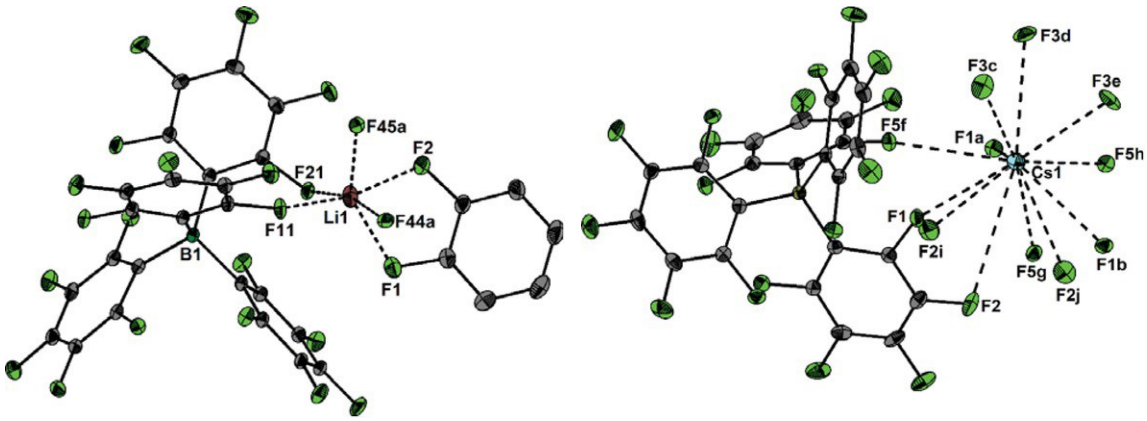

2.4.1 Synopsis

During the work with tetrakis(pentafluorophenyl)borate salts as abstraction agents for halides and hydrides, the crystal structures of a lithium tetrakis-(pentafluorophenyl)borate) 1,2-difluorobenzene adduct $[Li(DFB)]^+[B(C_6F_5)_4]^-$ and the solvent free caesium tetrakis(pentafluorophenyl)borate $Cs^+[B(C_6F_5)_4]^-$ were obtained. Both compounds were synthesized by either dissolving solvent free lithium tetrakis(pentafluorophenyl)borate in 1,2-difluorobenzene or by ion exchange of lithium tetrakis(pentafluorophenyl)borate with caesium fluoride in 1,2-difluorobenzene and subsequent diffusion of *n*-hexane into the solution. Interestingly both compounds provide a large amount of E···F close contacts in the solid state. $[Li(DFB)]^+[B(C_6F_5)_4]^-$ has six Li···F contacts and no π-interactions, which is visible in electron rich solvate molecules such as $[Li(C_6H_6)]^+[B(C_6F_5)_4]^-$ made by Bolte *et al.*[144] or $[Li(CH_3C_6H_5)]^+[B(C_6F_5)_4]^-$ made by Kuprat *et al.*[145] The solvent free $Cs^+[B(C_6F_5)_4]^-$ has twelve Cs···F contacts. Both compounds are useful sources for the tetrakis(pentafluorophenyl)borate anion, without the need for introducting typical donor solvents like Et_2O or THF. In the case of the lithium salt, it also provides a higher solubility than the solvent free $Li^+[B(C_6F_5)_4]^-$.

2.4.2 Scientific contribution

In this publication I developed the synthesis of the lithium compound and fully characterized it. Furthermore, I found a reliable synthesis for the cesium compound and co-wrote the manuscript. A. Schröder prepared the cesium compound. E. Lork

provided the X-ray crystallographical part and J. Beckmann was principal investigator, designed the concept and co-wrote the manuscript.

Percentage of my contribution of the total workload:

Experimental concept and design: ca. 90%, experimental work and acquisition of experimental data: ca. 95%, data analysis and interpretation: ca. 90%, preparation of figures and tables: ca. 80%, drafting of the manuscript: ca. 40%.

The article was published in the journal “Main Group Metal Chemistry“ in 2020 as an open access article:

Daniel Duvinage, Artem Schröder, E. Lork, J. Beckmann*, *Main Group Met. Chem.* **2020**, *43*, 99-101.

DOI: 10.1515/mgmc-2020-0011

DE GRUYTER Main Group Met. Chem. 2020; 43: 99–101

Short Communication **Open Access**

Daniel Duvinage, Artem Schröder, Enno Lork and Jens Beckmann*

New crystal structures of alkali metal tetrakis(pentafluorophenyl)borates

https://doi.org/10.1515/mgmc-2020-0011
Received March 01, 2020; accepted May 12, 2020.

Abstract: The crystal structures of the salts $[Li(1,2\text{-}F_2C_6H_4)][B(C_6F_5)_4]$ (**1**) and $Cs[B(C_6F_5)_4]$ (**2**) comprise six Li···F contacts (1.965(3) – 2.312(3) Å) and twelve Cs···F contacts (3.0312(1) – 3.7397(2) Å), respectively, which are significantly shorter than the sum of van der Waals radii (3.29 and 4.90 Å).

Keywords: lithium; caesium; boron; borate ion; weakly coordinating anion

Polyfluorinated tetraarylborate ions, such as $[B\{3,5\text{-}(CF_3)_2C_6H_3\}_4]^-$ "BAr^F" and $[B(C_6F_5)_4]^-$ (Scheme 1), have received numerous applications as weakly coordinating anions (Krosssing and Raabe, 2004; Riddlestone et al., 2018), which also stimulated research into their alkali metal salts. Very recently, for the former, the crystal structures of $[Li(H_2O)][B\{3,5\text{-}(CF_3)_2C_6H_3\}_4]$, $M[B\{3,5\text{-}(CF_3)_2C_6H_3\}_4]$ (M = Na, K) were described (Martínez-Martínez and Weller, 2019). For the latter, the crystal structures of $[Li(C_6H_6)][B(C_6F_5)_4]$·benzene (Bolte et al., 2005), $[Li(MeC_6H_5)][B(C_6F_5)_4]$·toluene, $[Li(Et_2O)_4][B(C_6F_5)_4]$, $[Li(Et_2O)_4][B(C_6F_5)_4]$·$CH_2Cl_2$ (Kuprat et al., 2010; Martin et al., 2010), $[Li(MeCN)_4][B(C_6F_5)_4]$ (Zhang et al., 2012) and $K[B(C_6F_5)_4]$ (Protchenko et al., 2016) were reported. In this work we convey two new crystal structures of the same anion.

Crystals of $[Li(1,2\text{-}F_2C_6H_4)][B(C_6F_5)_4]$ (**1**) were obtained by recrystallization of $[Li(Et_2O)_4][B(C_6F_5)_4]$ from 1,2-difluorobenzene. The key feature of **1** (Figure 1) is the presence of six Li···F contacts (1.965(3) - 2.312(3) Å) that are significantly shorter than the sum of van der Waals radii (3.29 Å) and the absence of π-interactions between cation the electron poor aromatic rings. By contrast, in the crystal structure of $[Li(C_6H_6)][B(C_6F_5)_4]$·benzene (Bolte et al., 2005) and $[Li(MeC_6H_5)][B(C_6F_5)_4]$·toluene (Kuprat et al., 2010), the cations show also π-interactions with the electron rich solvate molecules. The cesium salt $Cs[B(C_6F_5)_4]$ (**2**) crystallized in the rare cubic space group $I\bar{4}3d$ (a = 19.213(1) Å). It is isostructural with the previously known thallium compound $Tl[B(C_6F_5)_4]$ (a = 19.10(1) Å) (Parvez et al., 2005). The cell volume of **2** (V = 7092(1) $Å^3$) is smaller than that of $Tl[B(C_6F_5)_4]$ (V = 6962(8) $Å^3$), which can be attributed to the smaller ion radius of cesium (1.67 Å) compared to thallium (1.5 Å). The key feature of **2** (Figure 2) is the presence of twelve Cs···F contacts (3.0312(1)-3.7397(2) Å), respectively, which are significantly shorter than the sum of van der Waals radii (4.90 Å). These distances are consistent with those observed for $Cs[H_2NB_2(C_6F_5)_6]$, which shows even sixteen Cs···F contacts (Pollak et al., 2016).

1 X-ray crystallography

Single crystals of **1** were obtained by drying $[Li(Et_2O)_4][B(C_6F_5)_4]$ in high vacuum ($5{\cdot}10^{-3}$ bar) at 140°C for 24 h and recrystallization from 1,2-difluorobenzene and *n*-hexane (Romanato et al., 2010). Single crystals of **2** were obtained by ion exchange of **1** in 1,2-difluorobenzene with Cesium fluoride followed by filtration and addition of *n*-hexane (Mon et al., 2013). Intensity data were collected on a Bruker Venture D8 diffractometer with graphite-monochromated Mo-Kα (0.7107 Å) radiation. The structure was solved by direct methods and difference Fourier synthesis with subsequent Full-matrix least-squares refinements on F^2, using all data (Dolomanov, 2009). All non-hydrogen atoms were refined using anisotropic displacement parameters. Hydrogen atoms attached to carbon atoms were included in geometrically calculated positions using a riding model. Crystal and refinement data are collected in Table 1. Figures were created using DIAMOND (Brandenburg and Putz, 2006). Crystallographic data for the structural analysis has been deposited with the Cambridge Crystallographic Data Centre, CCDC numbers 1974618 (**1**) and 1974619 (**2**).

*** Corresponding author: Jens Beckmann,** Institut für Anorganische Chemie und Kristallographie, Universität Bremen, Leobener Straße 7, 28359 Bremen, Germany, e-mail: j.beckmann@uni-bremen.de
Daniel Duvinage, Artem Schröder and Enno Lork, Institut für Anorganische Chemie und Kristallographie, Universität Bremen, Leobener Straße 7, 28359 Bremen, Germany

Open Access. © 2020 Duvinage et al., published by De Gruyter. This work is licensed under the Creative Commons Attribution alone 4.0 License.

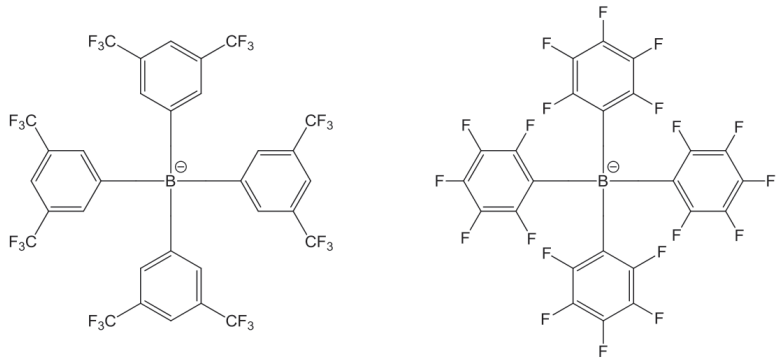

Scheme 1: Weakly coordinating polyfluorinated tetraarylborate "BArF" ions.

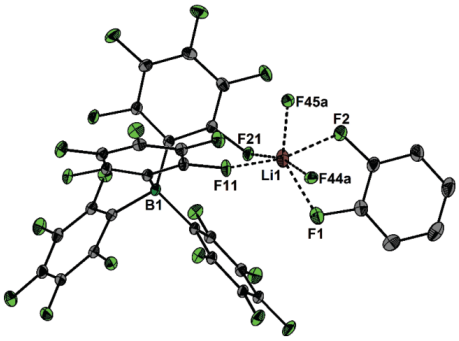

Figure 1: Crystal structure of [Li(1,2-$F_2C_6H_4$)][$B(C_6F_5)_4$] (**1**) showing 50% probability ellipsoid and the essential atomic numbering. Cation anion contacts [Å]: Li1-F1 2.053(3), Li1-F2 2.090(3), Li1-F11 1.968(3), Li1-F21 1.965(3), Li1-F44a 2.312(3), Li1-F45a 2.018(3).

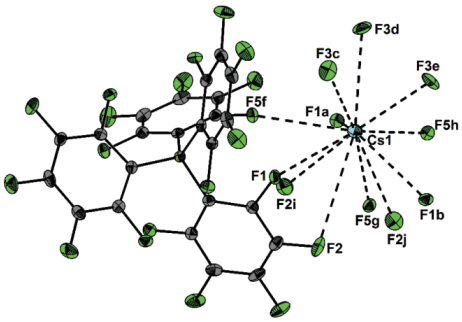

Figure 2: Crystal structure of Cs[$B(C_6F_5)_4$] (**2**) showing 50% probability ellipsoid and the essential atomic numbering. Cation anion contacts [Å]: Cs1-F1 3.0312(1), Cs1-F2 3.7397(2), Cs1-F3 3.1943(1), Cs1-F5 3.3292(1).

Table 1: Crystal data and structure refinement of [Li(1,2-$F_2C_6H_4$)$B(C_6F_5)_4$] (**1**) and [Cs$B(C_6F_5)_4$] (**2**).

	1	**2**
Formula	$C_{30}H_4BF_{22}Li$	$C_{24}BCsF_{20}$
Formula weight, g mol^{-1}	800.08	394.74
Crystal system	monoclinic	cubic
Crystal size, mm	0.5 × 0.5 × 0.4	0.3 × 0.3 × 0.3
Space group	$P2_1/n$	$I\bar{4}3d$
a, Å	13.9256(5)	19.213(1)
b, Å	12.4375(5)	19.213(1)
c, Å	15.9947(5)	19.213(1)
α, °	90	90
β, °	92.016(1)	90
γ, °	90	90
V, Å^3	2768.6(2)	7092(1)
Z	4	12
ρ_{calcd}, Mg m^{-3}	1.920	2.281
T, K	100	100
m (Mo $K\alpha$), mm^{-1}	0.215	1.741
F(000)	1560	4608
θ range, deg	2.20 to 33.23	2.60 to 30.43
Index ranges	−21 ≤ h ≤ 21	−27 ≤ h ≤ 23
	−18 ≤ k ≤ 19	−27 ≤ k ≤ 23
	−24 ≤ l ≤ 24	−20 ≤ l ≤ 27
No. of reflns collected	108154	23264
Completeness to θ_{max}	99.9%	99.9%
No. indep. Reflns	10630	1805
No. obsd reflns with ($I>2\sigma(I)$)	8391	1695
No. refined params	487	105
GooF (F^2)	1.037	1.110
R_1 (F) ($I > 2\sigma(I)$)	0.0444	0.0277
wR_2 (F^2) (all data)	0.1272	0.0749
$(\Delta/\sigma)_{max}$	< 0.001	< 0.001
Largest diff peak/hole, e Å^{-3}	0.706 / −0.505	0.514 / −0.632

Copies of this information may be obtained free of charge from The Director, CCDC, 12 Union Road, Cambridge CB2 1EZ, UK (Fax: +44-1223-336033; e-mail: deposit@ccdc.cam.ac.uk or http://www.ccdc.cam.ac.uk).

Conflict of interest: One of the authors (Jens Beckmann) is a member of the Editorial Board of Main Group Metal Chemistry.

References

Bolte M., Ruderfer I., Müller T., Lithium-tetrakis(pentafluorophenyl) borate-benzene (1/1/2). Acta Crystallogr. 2005, E61, m1581-m1582.

Brandenburg K., Putz H., DIAMOND V3.1d. Crystal Impact GbR, 2006.

Dolomanov O.V., Bourhis L.J., Gildea R.J., Howard A.K., Puschmann H., OLEX2: a complete structure solution, refinement and analysis program. J. Appl. Crystallogr., 2009, 42, 339-341.

Krossing I., Raabe I., Noncoordinating anions-fact or fiction? A survey of likely candidates. Angew. Chem. Int. Ed., 2004, 43, 2066-2090.

Kuprat M., Lehmann M., Schulz A., Villinger A., Synthesis of Pentafluorophenyl Silver by Means of Lewis Acid Catalysis: Structure of Solver Solvent Complexes. Organometallics, 2010, 29, 1421-1427.

Martin E., Hughes D.L., Lancaster S.J., The composition and structure of lithium tetrakis(pentafluorophenyl)borate diethyletherate. Inorg. Chim. Acta, 2010, 363, 275-278.

Martínez-Martínez A.J., Weller A.S., Solvent-free anhydrous Li^+, Na^+ and K^+ salts of $[B(3,5\text{-}(CF_3)_2C_6H_3)_4]^-$, $[BArF_4]^-$. Improved synthesis and solid-state structures. Dalton Trans., 2019, 48, 3551-3554.

Mon I., Jose D.A., Vidal-Ferran A., Bis(phosphite) Ligands with Distal Regulation: Application in Rhodium-mediated Asymmetric Hydroformylations. Chem. Eur. J., 2013, 19, 2720-2725.

Parvez M., Piers W.E., Ghesner I., Thallium tetrakis(pentafluorophenyl) borate. Acta Cryst., 2005, E61, m1801-m1803.

Pollak D., Goddard R., Pörschke K.-R., $Cs[H_7NB_2(C_6F_5)_6]$ Featuring an Unequivocal 16-Coordinate Cation. J. Am. Chem. Soc., 2016, 138, 9444-9451.

Protchenko A.V., Bates J. I., Saleh L.M.A., Blake M.P., Schwarz A.D., Kolychev E.L., et al., Enabling and probing oxidative addition and reductive elimination at a Group 14 metal center: cleavage and functionalization of E-H bonds by a bis(boryl)stannylene. J. Am. Chem. Soc., 2016, 138, 4555-4564.

Riddlestone I.M., Kraft A., Schaefer J., Krossing I., Taming the Cationic Beast: Novel Developments in the Synthesis and Application of Weakly Coordinating Anions. Angew. Chem. Int. Ed., 2018, 57, 13982-14024.

Romanato P., Duttwyler S., Linden A., Baldridge K.K., Siegel J.S., Intramolecular Halogen Stabilization of Silylium Ions Directs Gearing Dynamics. J. Am. Chem. Soc., 2010, 132, 7828-7829.

Zhang B., Köberl M., Pöthig A., Cokoja M., Herrmann W.A., Kühn F.E., Synthesis and Characterization of Imidazolium Salts with the Weakly Coordinating $[B(C_6F_5)_4]^-$ Anion. Z. Naturforsch., 2012, 67b, 1030-1036.

2.5 Isolation of an Antiaromatic 9-Hydroxy Fluorenyl Cation

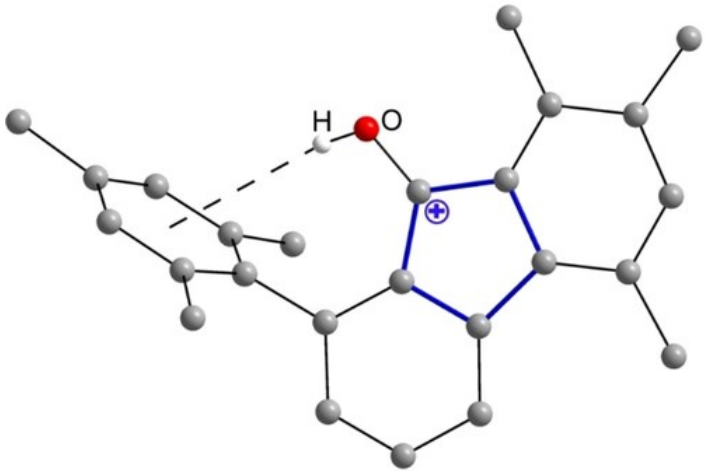

2.5.1 Synopsis

The bis(*m*-terphenyl)carbon motif is an attractive target, as it can form kinetically stabilized carbenium ions and carbenes. Especially in the case of the carbene, it is interesting, as the sterically demanding substituents can alter the geometry, enabling space for the triplet ground state. For this, the reported carboxylic acid chloride was synthesized by a modified procedure according to the literature.[146] The introduction of a second *m*-terphenyl substituent was attempted by the addition of *m*-terphenyllithium to the corresponding acyl chloride. Similar to previous approaches, the chloride was exchanged to a fluoride, which remained still unsuccessful for the introduction of a second substituent. Due to this, the abstraction of the fluoride was attempted to provide a kinetically stabilized acylium ion, which can be described by its mesomeric form as TerC≡O^+. A small number of acylium ions are reported in the literature, but often exhibit ion-pairing. It is remarkable that known acylium ions provide a C-O triple bond and can be seen as a carboxonium ion. [147-148] By abstraction of the fluoride from TerC(O)F with an excess of $AlCl_3$ a deep red solution is formed from which dark brown single crystals were obtained. Through single crystal X-ray diffraction experiments the compound could be identified as 9-hydroxy-1-mesityl-5,7,8-trimethylfluorenylium tetrachloroaluminate. The compound is stable in solution for a few days and in solid state for a few weeks under inert conditions. The formation of this compound can be explained by an intramolecular Friedel-Crafts reaction, providing a 1,2-methyl shift under the migration of a proton to the CO moiety. The formed hydroxyfluorenyl cation should exhibit antiaromaticity according to the Hückel rule as it possesses

four π electrons. This was examined by the use of NICS calculations showing that a certain degree of antiaromaticity is present but it is compensated by the two annulated phenyl rings and the hydroxy group. Additionally, the mechanism was also postulated by DFT calculations.

By deprotonation with sodium hydroxide, the corresponding 9-fluorenone was obtained. This compound exhibits a strong yellow fluorescence at λ = 512 nm. It was also tested if the fluorenone shows antibacterial properties similar to other fluorenones.[149] Against E. Coli, it shows no antibacterial properties and therefore it was not included in the publication.

2.5.2 Scientific Contribution

In this publication, I designed the concept and synthesized and fully characterized all compounds. Furthermore, I did the X-ray structure determination and wrote the supporting information and co-wrote the manuscript. S. Mebs did the computational part and J. Beckmann was the principal investigator and co-wrote the publication.

Percentage of my contribution of the total workload:

Experimental concept and design: ca. 100%, experimental work and acquisition of experimental data: ca. 100%, data analysis and interpretation: ca. 100%, preparation of figures and tables: ca. 80%, drafting of the manuscript: ca. 50%.

The article was published in the journal “Chemistry – A European Journal“ in 2021 as an open access communication:

Daniel Duvinage, Stefan Mebs*, Jens Beckmann*, *Chem. Eur. J.* **2021**, *27*, 8105-8109.

DOI: 10.1002/chem.202100786

The Supporting Information includes experimental procedures, NMR spectra, X-ray crystallographic data and structure refinement and computational data and is available free of charge on the journal's website:

https://chemistry-europe.onlinelibrary.wiley.com/action/downloadSupplement?doi=10.1002%2Fchem.202100786&file=chem202100786-sup-0001-misc_information.pdf

Chemistry–A European Journal | Communication
doi.org/10.1002/chem.202100786
Chemistry Europe
European Chemical Societies Publishing

Isolation of an Antiaromatic 9-Hydroxy Fluorenyl Cation

Daniel Duvinage,[a] Stefan Mebs,*[b] and Jens Beckmann*[a]

Dedicated to Herbert W. Roesky on the occasion of his 85th birthday.

Abstract: Fluorenyl cations are textbook examples of 4π electron antiaromatic five-membered ring systems. So far, they were reported only as short-lived intermediates generated under superacidic conditions or by flash photolysis. Attempts to prepare a *m*-terphenyl acylium cation by fluoride abstraction from a benzoyl fluoride gave rise to an isolable 9-hydroxy fluorenyl cation that formed by an intramolecular electrophilic attack at a flanking mesityl group prior to a 1,2-methyl shift and proton transfer to oxygen.

Carbocations are key intermediates in numerous organic reactions. Groundbreaking work by Olah in the 1970s demonstrated that many of these transient carbocations can be detected at low temperatures under superacidic conditions. However, most attempts to isolate these highly reactive species were impaired by decomposition at the time.[1] With the introduction of new powerful Lewis acids and weakly coordinating anions, the situation gradually changed and in recent years the isolation and full characterization of many carbocations was achieved including a non-classical 2-norbornyl cation,[2] the benzenium ion,[3] hexahalobenzene radical cations,[4] the hexamethylbenzene dication[5] and cationic ring systems.[6]

Acylium ions play a significant role as intermediates in Friedel-Crafts reactions. In the solid state most acylium ions form ion pairs with their counterions.[7] This observation prompted us to attempt the synthesis of a kinetically-stabilized *m*-terphenylacylium ion, in which two flanking mesityl groups were supposed to prevent the coordination of the counterion. Surprisingly, the desired acylium ion immediately underwent an intramolecular Friedel-Crafts reaction with one of the mesityl groups giving rise to an unexpectably stable 9-hydroxy fluorenyl cation that was isolated and fully characterized in this work.

Fluorenyl cations comprise a central antiaromatic 4π electron five-membered ring with two annelated benzene rings (Scheme 1). Motivated by the debate[8] that the antiaromaticity[9] might be compensated by the two benzene rings, serveral attempts were made to spectroscopically characterize or even isolate fluorenyl cations. In 1980, Olah *et al.* obtained several 9-fluorenyl cations under superacidic conditions including the 9-hydroxy fluorenyl cation that was generated by protonation of 9-fluorenone with HSO_3F/SbF_5 ("magic acid") in SO_2ClF solution at −78 °C.[10] All attempts to isolate these species failed and provided only ill-defined polymeric materials instead. As the bulk synthesis of 9-fluorenyl cations deemed impossible, all latter work focused on the photolysis of appropriate precursors, such as 9-fluorenol or 9-diazofluorene, in solution and amorphous water ice / neon matrices, respectively.[11]

We have now found that fluoride abstraction from the benzoyl fluoride 2,6-$Mes_2C_6H_3C(O)F$ (**1**)[12] with an excess $AlCl_3$ provided 9-hydroxy-1-mesityl-5,7,8-trimethyl fluorenylium tetrachloroaluminate (**2**) as deep brown crystals in 91% yield (Figure 1). The fluorenyl cation **2** is stable in chlorinated NMR solvents for a short period of time, but slowly degrades over the course of one day. In donor solvents (e.g. THF, Et_2O) it turns immediately yellow. Even as a solid under inert conditions, it slowly degrades to become a yellow powder over the course of a few weeks at room temperature. Controlled deprotonation of **2** with NaOH afforded the related 9-fluorenone **3** as bright yellow crystals in quantitiatve yield. The identity of **1–3** was inferred by the full assignment of the ^1H and ^{13}C NMR spectra and confirmed by X-ray structure determination (Figure 1).[13] In solution, **1** is characterized by its ^{19}F NMR chemical shift ($CDCl_3$) of $\delta = 52.2$ ppm. It reveals a doublet in the ^{13}C NMR spectrum for the *ipso* carbon atom at $\delta = 157.7$ ppm with a coupling constant of $^1J(^{13}C–^{19}F) = 357.2$ Hz. Upon fluoride abstraction, the ^{13}C spectrum (CD_2Cl_2) of **2** shows a more strongly deshielded singlet at $\delta = 200.6$ ppm for the *ipso* carbon atom. Furthermore, a new broad signal in the ^1H NMR spectrum (CD_2Cl_2) became

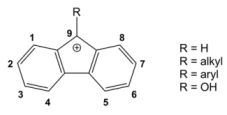

Scheme 1. 9-Fluorenyl cations.

[a] D. Duvinage, Prof. Dr. J. Beckmann
Institut für Anorganische Chemie und Kristallographie
Universität Bremen
Leobener Straße 7, 28359 Bremen (Germany)
E-mail: j.beckmann@uni-bremen.de
[b] Dr. S. Mebs
Institut für Experimentalphysik
Freie Universität Berlin
Arnimallee 14, 14195 Berlin (Germany)
E-mail: stebs@fu-berlin.de

Supporting information for this article is available on the WWW under https://doi.org/10.1002/chem.202100786

© 2021 The Authors. Published by Wiley-VCH GmbH. This is an open access article under the terms of the Creative Commons Attribution License, which permits use, distribution and reproduction in any medium, provided the original work is properly cited.

Chemistry–A European Journal | Communication doi.org/10.1002/chem.202100786 | Chemistry Europe European Chemical Societies Publishing

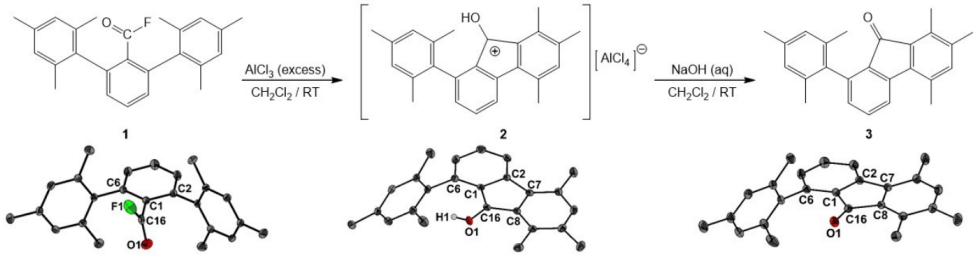

Figure 1. Fluoride abstraction from **1** afforded the 9-hydroxy fluorenylium tetrachloroaluminate **2**. Base hydrolysis of **2** gave the 9-fluorenone **3**. Molecular structures of **1**, **2** (counter ion omitted for clarity) and **3** showing 50% probability ellipsoids and the atom numbering scheme. Selected bond lengths [Å] of **1**: C1-C2 1.4026(16), C1-C16 1.4894(17), C2-C7 1.4983(16), C7-C8 1.4042(17), O1-C16 1.2009(17), F1-C16 1.3308(16). Selected bond lengths [Å] of **2**: C1-C2 1.416(3), C1-C16 1.442(3), C2-C7 1.487(3), C7-C8 1.418(3), C8-C16 1.444(3), O1-C16 1.287(2). Selected bond lengths [Å] of **3**: C1-C2 1.406(3), C1-C16 1.496(3), C2-C7 1.484(3), C7-C8 1.414(3), C8-C16 1.501(3), O1-C16 1.209(3).

visible at $\delta = 9.71$ ppm, which was assigned to the hydroxyl group in 9-position being involved in hydrogen bonding with the π-system of the mesityl ring. This value is significantly less deshielded than that observed for the parent 9-hydroxy fluorenylium ion ($\delta = 12.75$ ppm), reported by Olah *et al.*[10] According to their work, the relative deshielding of this proton is a measure for the charge density residing on the oxygen atom. Following along this argument, **2** possess a rather low positive charge density there.[14] In **3**, the ^{13}C NMR ($CDCl_3$) resonance shows a nearly unchanged singlet at $\delta = 195.3$ ppm. A UV/vis spectrum of **2** in CH_2Cl_2 (50 μM) shows a broad absorption maximum at $\lambda_{max} = 421$ nm, which is also present in **3**. In addition, **3** shows also two absorptions at $\lambda_{max} = 333$ and 346 nm and shows a green-yellow luminescence with an excitation maximum of $\lambda_{max} = 320$ nm and an emission maximum at $\lambda_{max} = 512$ nm.

The molecular structures[13] of **2** and **3** reveal the presence of fluorene scaffolds and indicate that a methyl group migration had taken place. In both five-membered ring structures, the C2-C7, C1-C16 and C8-C16 bond lengths are considerably longer than C1-C2 and C7-C8, which are shared with the annelated benzene rings. In the fluorenyl cation **2**, the C–O bond length (1.287(2) Å) is significantly longer than in the fluorenone **3** (1.209(3) Å). Both values closely resemble those of protonated cyclopentanone (1.266(3) Å) and cyclopentanone (1.211(2) Å).[15] In **2**, the hydroxyl group points towards the π-electrons of the remaining mesityl group. In an effort to shed some light on the mechanism that led to the formation of **2**, DFT calculations were carried out at the B3PW91/6-311+G* level of theory (Figure 2). The relative energy of the assumed initial product of the fluoride abstraction, namely the *m*-terphenylacylium ion, $[2,6\text{-}Mes_2C_6H_3CO]^+$ (**A**) was arbitrarily set to zero. The acylium ion **A** undergoes an electrophilic attack at the *ortho*-position of one flanking mesityl group. The product of this attack, the arenium ion **C** is by 30 kJ mol^{-1} energetically less favoured. Next, a 1,2-methyl shift takes place, which gave the arenium ion **E**, which is by 36.8 kJ mol^{-1} energetically even less favoured than the acylium ion **A**. Only the last step is by −114 kJ mol^{-1} energetically favoured. It entails a proton transfer from **E** to the fluorenyl cation **G** (the cation of **2**). This last step involves the largest activation barrier, as the transition state **F**$^{\#}$ is 154.2 kJ mol^{-1} higher in energy than **A**. In a future study it should be taken into consideration if the proton transfer might as well be mediated by the $[AlCl_4]^-$ ion.

In order to qualitatively monitor the processes of bond formation and rapture along the proposed reaction coordinate, the Atoms-In–Molecules (AIM)[16] and non-covalent interactions index (NCI)[17] methods were applied to the DFT models **A**–**G** (Figure 3 and Figures S1–S3). The former provides a molecular graph exceeding the Lewis picture of chemical bonding, whereas the latter provides contact patches even for very weak interactions which not necessarily form a bond critical point (bcp) in AIM. The AIM graph of the transition state **B**$^{\#}$ (electrophilic attack) closely resembles that of the intermediate **C** in that the CO-fragment is considerably bent and a C(O)···C_{ortho} bcp is already formed despite the large C···C distance of 1.942 Å (Figure 3a). The O atom, now closer to the mesityl part on the opposite side, forms a weak O···H–C hydrogen bond, which is also visible in the NCI together with even weaker H···H contacts. In the transition state of the subsequent 1,2-methyl shift (**D**$^{\#}$) the methyl C atom is still somewhat closer to the *ortho*-position (1.873 Å) than to the *meta*-position (1.880 Å). Accordingly, the AIM bond path, which approaches the C_{ortho}-C_{meta} bcp, bends away and finally connects the methyl C atom with the *ortho* C atom, resulting in a quasi T-shaped bonding scenario (Figure 3b). It might be stated, however, that **D**$^{\#}$ is closer to the educt (intermediate **C**) than to the product (intermediate **E**). In the latter a second O···H–C hydrogen bond is then established. The energy demanding proton transfer (transition state **F**$^{\#}$) shows that the proton in *meta*-position is still topologically connected to the mesityl ring despite a long C–H distance of 1.381 Å (Figure 3c). The out-of-plane bending (C_{ortho}-C_{meta}-C_{methyl} angle; $C_{ortho'}$ is the *ortho* C atom on the

 © 2021 The Authors. Published by Wiley-VCH GmbH

Chemistry–A European Journal | Communication doi.org/10.1002/chem.202100786 | Chemistry Europe European Chemical Societies Publishing

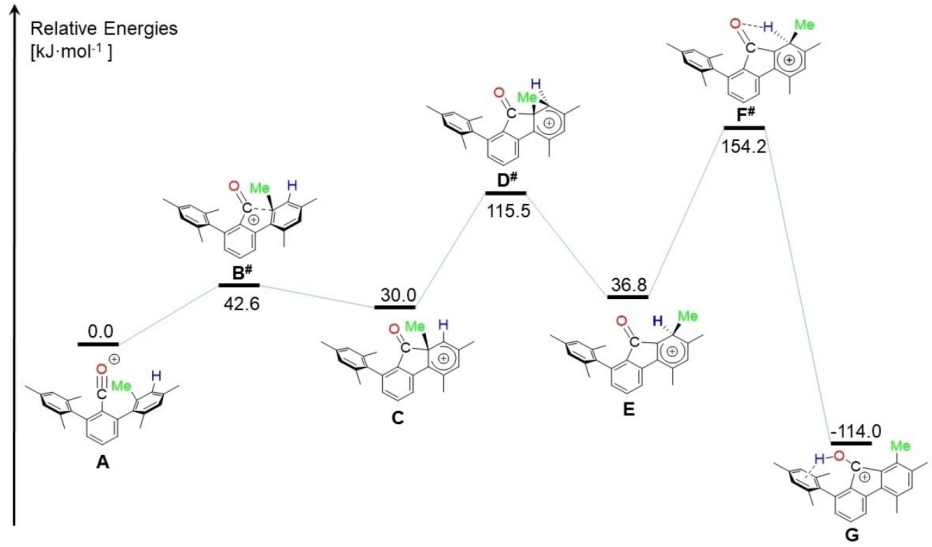

Figure 2. Suggested mechanism of the rearrangement the presumed initial acylium ion **A** into the 9-hydroxy fluorenyl cation **G** (the cation of **2**). Transition states are marked by superscripted #.

opposite side of the mesityl ring) of the methyl group is reduced from 128° (intermediate **C**) to 152° (**F#**), which is half way to the value of 178° found in the final compound **G**. It is noted that the experimentally observed intramolecular hydrogen bridge is also present in the optimized structure of **G**, which suggests that it possesses a stabilizing effect to some extent. The NCI proves that non-covalent interactions are of minor importance for the reaction steps. Notably, transition states which are closer to the product are lower in energy than those which are closer to the starting compound in the current study.

The cyclopentadienyl cation as well as the central five-membered ring in the fluorenyl cation formally possess 4π electrons and according to the Hückel rule are antiaromatic, but it is still unclear what influence the two annelated aromatic benzene rings and the hydroxyl group in 9-position pose on the central five-membered ring.[8] In an effort to address this question, we calculated nuclear-independent chemical shifts (NICS) for a number of aromatic and antiaromatic parents compounds (Figure 4).[18] The NICS(0)$_{iso}$ values of benzene and the cyclopentadienyl cation, determined at the ring critical points (rcp) are −8.08 and −13.14, whereas the NICS(1)$_{iso}$ values, referring to points perpendicular to the ring, 1 Å above the rcps are −10.21 and −10.45.[19] Compared to these clearly aromatic benchmarks, the anti-aromatic cyclopentadienyl cation shows the largest deviation with NICS(0)$_{iso}$ and NICS(1)$_{iso}$ values of 88.96 and 67.45. Introduction of the hydroxyl group in 9-position dramatically reduces these values to 25.89 and 16.25. Going from the cyclopentadienyl cation to the fluorenyl cation has about the same effect as the values of the 5-membered ring decrease to 30.03 and 20.11. In turn, the NICS(0)$_{iso}$ and NICS(1)$_{iso}$ values of the two annelated aromatic benzene rings increase to 10.85 and 5.55 when compared to benzene. Both effects are accumulated in the 9-hydroxyfluorenyl cation with NICS(0)$_{iso}$ and NICS(1)$_{iso}$ values of 18.70 and 11.75 for the central five-membered ring. These values are very close to those calculated for **G** (Table S2). Thus, the two annelated aromatic benzene rings and the 9-hydroxy group outweigh the antiaromatic character, which provides a reasonable explanation as to why it was possible to isolate **2**.

In summary, attempts to prepare a kinetically stabilized *m*-terphenyl acylium ion by fluoride abstraction from the benzoyl fluoride **1** gave the 9-hydroxy-1-mesityl-5,7,8-trimethyl fluorenyl cation **2** instead. The rearrangement was rationalized by an intramolecular electrophilic attack (Friedel Crafts reaction) of the initially formed *m*-terphenylacylium ion, $[2,6\text{-}Mes_2C_6H_3CO]^+$ at a flanking mesityl group, prior to a 1,2-methyl shift and a proton transfer to oxygen. This rearrangement is strongly reminiscent of the reaction between 2,6-(4-*t*-BuC_6H_4)C_6H_3Li with $Cl_2BH{\cdot}SMe_2$, which gave 9-bora-fluorene rather than the expected bis(*m*-terphenyl)borane.[20] It also resembles our previous attempts to prepare stable bis(*m*-terphenyl)-phosphenium ions by fluoride abstraction from (2,6-$Mes_2C_6H_3)_2$PF and $[2,6\text{-}(Me_5C_6)_2C_6H_3]_2$PF, which gave a (protonated) 9-phospha-fluorene[21] and isomeric 9-phospha-fluorenium ions instead.[22] The latter two reactions also involved

 © 2021 The Authors. Published by Wiley-VCH GmbH

Chemistry–A European Journal | Communication doi.org/10.1002/chem.202100786 | Chemistry Europe European Chemical Societies Publishing

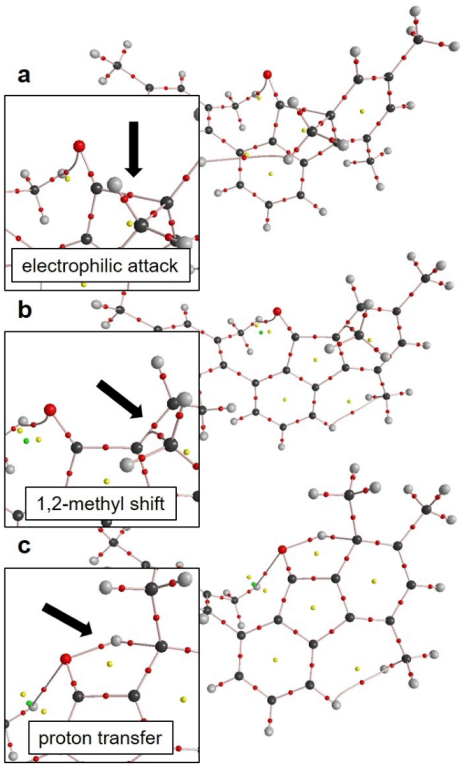

Figure 3. AIM bond topology of the transition states $\mathbf{B}^{\#}$, $\mathbf{D}^{\#}$, and $\mathbf{F}^{\#}$. Color code atoms: dark grey – C, light gray – H, ref – O. Color code AIM critical points: red – bond critical point (bcp), yellow – ring critical point (rcp), green – cage critical point (ccp). Regions of electrophilic attack, 1,2-methyl shift, and proton transfer are magnified and highlighted by black arrows.

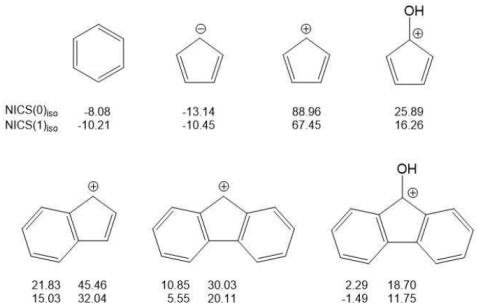

Figure 4. NICS values of aromatic and antiaromatic parent compounds.

methyl group migrations. The 9-hydroxy fluorenyl cation **2** comprises a central five-membered ring with formally 4π electron, thus fulfilling the Hückel rule for antiaromaticity. The calculation of NICS values suggest that the antiaromatic character is compensated by the accumulative effect of the two annelated benzene rings and the hydroxyl group in 9-position.

Acknowledgements

The Deutsche Forschungsgemeinschaft (DFG) is gratefully acknowledged for financial support. We thank Nils Clamor for the fluorescence measurement of **3**. Open access funding enabled and organized by Projekt DEAL.

Conflict of Interest

The authors declare no conflict of interest.

Keywords: acylium ion · antiaromaticity · carbocation · electrophilic substitution · fluorenyl ion

[1] a) G. A. Olah, *J. Am. Chem. Soc.* **1972**, *94*, 808–820; b) G. A. Olah, *Angew. Chem. Int. Ed.* **1995**, *34*, 1393–1405; *Angew. Chem.* **1995**, *107*, 1519–1532; c) G. A. Olah, *J. Org. Chem.* **2001**, *66*, 5943–5957; d) R. R. Nardela, D. A. Klumpp, *Chem. Rev.* **2013**, *113*, 6905–6948.
[2] F. Scholz, D. Himmel, F. W. Heinemann, P. v. R. Schleyer, K. Meyer, I. Krossing, *Science* **2013**, *341*, 62–64.
[3] F. Scholz, D. Himmel, L. Eisele, W. Unkrig, I. Krossing, *Angew. Chem. Int. Ed.* **2014**, *53*, 1689–1692; *Angew. Chem.* **2014**, *126*, 1715–1718.
[4] a) H. Shorafa, D. Mollenhauer, B. Paulus, K. Seppelt, *Angew. Chem. Int. Ed.* **2009**, *48*, 5845–5847; *Angew. Chem.* **2009**, *121*, 5959–5961; b) M. J. Molski, D. Mollenhauer, S. Gohr, B. Paulus, M. A. Khanfar, H. Shorafa, S. H. Strauss, K. Seppelt, *Chem. Eur. J.* **2012**, *18*, 6644–6654.
[5] M. Malischewski, K. Seppelt, *Angew. Chem. Int. Ed.* **2017**, *56*, 368–370; *Angew. Chem.* **2017**, *129*, 374–376.
[6] a) A. Martens, M. Kreuzer, A. Ripp, M. Schneider, D. Himmel, H. Scherer, I. Krossing, *Chem. Sci.* **2019**, *10*, 2821–2829; b) S. M. Rupf, P. Pröhm, M. Malischewski, *Chem. Commun.* **2020**, *56*, 9834–9837; c) S. Nees, T. Kupfer, A. Hofmann, H. Braunschweig, *Angew. Chem. Int. Ed.* **2020**, *59*, 18809–18815; *Angew. Chem.* **2020**, *132*, 18971–18978.
[7] a) F. P. Boer, *J. Am. Chem. Soc.* **1966**, *88*, 1572–1574; b) B. Chevrier, J.-M. Le Carpentier, R. Weiss, *J. Am. Chem. Soc.* **1972**, *94*, 5718–5723; c) M. G. Davlieva, S. V. Lindeman, I. S. Neretin, J. K. Kochi, *J. Org. Chem.* **2005**, *70*, 4013–4021; d) Y. K. Loh, M. A. Fuentes, P. Vasko, S. Aldridge, *Angew. Chem. Int. Ed.* **2018**, *57*, 16559–16563; *Angew. Chem.* **2018**, *130*, 16797–16801.
[8] A. D. Allen, T. T. Tidwell, *Chem. Rev.* **2001**, *101*, 1333–1348.
[9] a) T. L. Amyes, J. P. Richard, M. Novak, *J. Am. Chem. Soc.* **1992**, *114*, 8032–8041; b) H. Jiao, R. v. R. Schleyer, Y. Mo, M. A. McAllister, T. T. Tidwell, *J. Am. Chem. Soc.* **1997**, *119*, 7075–7083; c) N. S. Mills, *J. Am. Chem. Soc.* **1999**, *121*, 11690–11696; d) B. J. Dahl, N. S. Mills, *Org. Lett.* **2008**, *10*, 5605–5608; e) N. S. Mills, S. P. McClintock, *Chem. Commun.* **2012**, *48*, 8099–8101; f) A. Simita, M. Gasonoo, K. J. Boblak, T. Ohwada, D. A. Klumpp, *Chem. Eur. J.* **2017**, *23*, 2566–2570.
[10] G. A. Olah, G. K. S. Prakash, G. Liang, P. W. Westerman, K. Kunde, J. Chandrasekhar, P. v. R. Schleyer, *J. Am. Chem. Soc.* **1980**, *102*, 4485–4492.
[11] a) S. L. Mecklenburg, E. F. Hilinski, *J. Am. Chem. Soc.* **1989**, *111*, 5471–5472; b) R. A. McClelland, N. Mathivanan, S. Steenken, *J. Am. Chem. Soc.* **1990**, *112*, 4857–4861; c) P. Costa, I. Trosten, M. Fernandez-Oliva, E. Sanchez-Garcia, W. Sander, *Angew. Chem. Int. Ed.* **2015**, *23*, 2656–2660; *Angew. Chem. Int. Ed.* **2015**, *127*, 2694–2698; d) J. Fulara, A. Chakraborty, J. P. Maier, *Angew. Chem. Int. Ed.* **2016**, *55*, 3424–3427; *Angew. Chem.* **2016**, *128*, 3485–3488.

 © 2021 The Authors. Published by Wiley-VCH GmbH

Chemistry–A European Journal | Communication doi.org/10.1002/chem.202100786 | Chemistry Europe European Chemical Societies Publishing

[12] The starting material **1** was obtained by exchange of chlorine in 2,6-$Mes_2C_6H_3C(O)Cl$ by fluorine. E. S. Akturk, S. J. Scappaticci, R. N. Seals, M. P. Marshak, *Inorg. Chem.* **2017**, *56*, 11466–11469.
[13] Deposition Number 2063417 (for **1**), 2063418 (for **2**), and 2063419 (for **3**) contain; the supplementary crystallographic data for this paper. These data are provided free of charge by the joint Cambridge Crystallographic Data Centre and Fachinformationszentrum Karlsruhe Access Structures service www.ccdc.cam.ac.uk/structures.
[14] G. A. Olah, D. H. O'Brien, M. Calin, *J. Am. Chem. Soc.* **1967**, *94*, 3586–3590.
[15] D. Stuart, S. D. Wetmore, M. Gerken, *Angew. Chem. Int. Ed.* **2017**, *56*, 16380–16384; *Angew. Chem.* **2017**, *129*, 16598–16602.
[16] R. F. W. Bader, *Atoms in Molecules: A Quantum Theory*, Oxford University Press, Oxford UK, **1990**.
[17] E. R. Johnson, S. Keinan, P. Mori-Sanchez, J. Contreras-García, A. J. Cohen, W. Yang, *J. Am. Chem. Soc.* **2010**, *132*, 6498–6506.
[18] a) P. V. R. Schleyer, C. Maerker, A. Dransfeld, H. Jiao, N. J. R. van Eikema Hommes, *J. Am. Chem. Soc.* **1996**, *118*, 6317–6318; b) Z. Chen, C. S. Wannere, C. Corminboeuf, R. Puchta, P. v. R. Schleyer, *Chem. Rev.* **2005**, *105*, 3842–3888; c) H. Fallah-Bagher-Shaidaei, C. S. Wannere, C. Corminboeuf, P. v. R. Schleyer, *Org. Lett.* **2006**, *8*, 863–866.
[19] M. Hedja, D. Duvinage, E. Lork, R. Jirásko, A. Lyčka, S. Mebs, L. Dostál, J. Beckmann, *Organometallics* **2020**, *39*, 1202–1212.
[20] R. Wehmschulte, A. A. Diaz, M. A. Khan, *Organometallics* **2003**, *22*, 83–92.
[21] M. Olaru, D. Duvinage, E. Lork, S. Mebs, J. Beckmann, *Chem. Eur. J.* **2019**, *25*, 14758–14761.
[22] M. Olaru, D. Duvinage, Y. Naß, L. A. Malaspina, S. Mebs, J. Beckmann, *Angew. Chem. Int. Ed.* **2020**, *59*, 14414–14417; *Angew. Chem.* **2020**, *132*, 14520–14524.

Manuscript received: March 3, 2021
Accepted manuscript online: April 9, 2021
Version of record online: May 6, 2021

 © 2021 The Authors. Published by Wiley-VCH GmbH

2.6 Divalent Bis(*m*-terphenyl)element Cations [(2,6-$Mes_2C_6H_3)_2E]^+$ of Group 13 Revisited and Extended (E = B, Al, Ga, In, Tl)

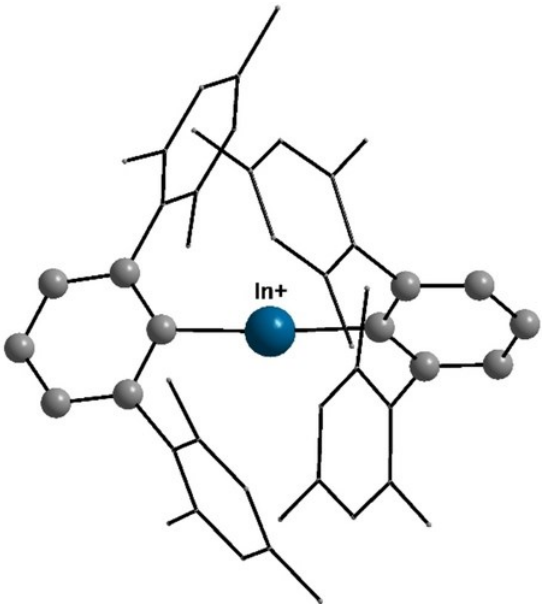

2.6.1 Synopsis

Switching from diorganopnictogenium ions, possessing six valence electrons to diorgano group 13 cations, which possess four valence electrons, increases the Lewis acidity, therefore the cations are highly interesting regarding metallomimetic behaviour. The synthetic focus of this publication is based on boron and indium, as Wehmschulte *et al.* synthesized the bis(*m*-terphenyl)aluminium and gallium cations[13],[150] and Beckmann *et al.* synthesized the bis(*m*-terphenyl)thallium cation.[140] As a starting point the reported bis(*m*-terphenyl)indium bromide was used.[141] By the abstraction of the bromide with potassium tetrakis(pentafluorophenyl)borate $K^+[B(C_6F_5)_4]^-$, the bis(*m*-terphenyl)indinium tetrakis(pentafluorophenyl)borate $[Ter_2In]^+[B(C_6F_5)_4]^-$ was synthesized and fully characterized by means of NMR and UV-Vis spectroscopy, mass spectrometry as well as single crystal X-ray diffraction experiments. Regarding boron, *m*-terphenyllithium was reacted with BF_3OEt_2 forming *m*-terphenylboron difluoride $TerBF_2$, which could be isolated as a colorless solid. This was reacted with another equivalent of *m*-terphenyllithium to obtain bis(*m*-terphenyl)boron fluoride Ter_2BF. Additionally, by reduction with lithium aluminium hydride and methyl iodide the corresponding hydride Ter_2BH was formed. These bis(*m*-terphenyl)boron compounds were used as the starting materials for the attempt to form the

bis(*m*-terphenyl)borinium ion. Unfortunately, a variety of Lewis acids and abstraction agents, namely $AlCl_3$, $B(C_6F_5)_3$, $Al[OC(C_6F_5)_3]_3$, $[Ph_3C]^+[B(C_6F_5)_4]^-$, $[Me_3Si\text{-}H\text{-}SiMe_3]^+[B(C_6F_5)_4]^-$ and $[Me_3Si(Tol)]^+[B(C_6F_5)_4]^-$ did not induce the selective formation of the borinium ion Ter_2B^+. In the case of $AlCl_3$, the *m*-terphenylboron dichloride was isolated, which indicates that a *m*-terphenyl substituent was cleaved. With the hydrogen bridged $[Me_3Si\text{-}H\text{-}SiMe_3]^+[B(C_6F_5)_4]^-$ as fluoride abstraction agent an F-H exchange was visible forming Ter_2BH. This indicates that the borinium cation has a high hydride affinity, which explains also that no reaction of Ter_2BH with $[Ph_3C]^+[B(C_6F_5)_4]^-$ occurred. Also in the case of the Lewis acids $B(C_6F_5)_3$ and $Al[OC(C_6F_5)_3]_3$, no reaction took place. Ter_2BF reacts with $[Me_3Si(Tol)]^+[B(C_6F_5)_4]^-$ giving multiple signals in the ^{11}B- and ^{19}F-NMR spectra, which indicates a degradation of the bis(*m*-terphenyl)boron moiety as well as the degradation of the anion. Regarding the Lewis acidity of the group 13 cationic species, the FIA value was calculated, leading to the result, that all R_2E^+ (E = B, Al, Ga, In, Tl) tend to be above the Lewis superacid threshold, the highest shown by R_2B^+ (725 kJ/mol). This can explain the failed attempts of the isolation of the borinium ion, as the FIA value is even higher than that of Ter_2P^+ (701 kJ/mol) and Ter_2As^+ (657 kJ/mol), which react intramolecularly under quenching of the pnictogenium ion. The Indinium cation R_2In^+ (577 kJ/mol) and thallium cation R_2Tl^+ (520 kJ/mol) have a decreased FIA value. which can be explained by the half shell occupation providing a certain stabilization, as well as the linear adopted geometry.

2.6.2 Scientific contribution

In this project I developed the synthesis of the compounds and fully characterized the provided compounds. Furthermore, I wrote the Supporting Information and co-wrote the manuscript. L. Malaspina performed the Hirshfeld Atom Refinement, S. Mebs executed theoretical calculations contributing to this publication. S. Grabowsky co-wrote the manuscript and J. Beckmann was the principal investigator and co-wrote the manuscript.

Percentage of my contribution of the total workload:

Experimental concept and design: ca. 90%, experimental work and acquisition of experimental data: ca. 90%, data analysis and interpretation: ca. 80%, preparation of Figures and Tables: ca. 40%, drafting of the manuscript: ca. 40%.

The article was published in the journal “European Journal of Inorganic Chemistry“ in 2023 as a “Very Important Paper (VIP)” Open Access article.

Daniel Duvinage, Lorraine A. Malaspina, Simon Grabowsky, Stefan Mebs, Jens Beckmann, *Eur. J. Inorg. Chem.* **2023**, *26*, e202200482.

DOI: 10.1002/ejic.202200482

The Supporting Information includes NMR and UV-Vis spectra, X-ray crystallographic data and structure refinement and computational data and is available free of charge on the journal′s website:

https://chemistry-europe.onlinelibrary.wiley.com/action/downloadSupplement?doi=10.1002%2Fejic.202200482&file=ejic202200482-sup-0001-misc_information.pdf

Check for updates

EurJIC
European Journal of Inorganic Chemistry

Research Article
doi.org/10.1002/ejic.202200482

Chemistry Europe
European Chemical Societies Publishing

www.eurjic.org

VIP *Very Important Paper*

Lewis Superacidic Divalent Bis(*m*-terphenyl)element Cations $[(2,6\text{-}Mes_2C_6H_3)_2E]^+$ of Group 13 Revisited and Extended (E=B, Al, Ga, In, Tl)

Daniel Duvinage,[a] Lorraine A. Malaspina,[b] Simon Grabowsky,*[b] Stefan Mebs,*[c] and Jens Beckmann*[a]

Dedicated to Professor Klaus Jurkschat on the occasion of his 70th birthday.

In a combined experimental and computational study, the molecular and electronic structures of the divalent bis(*m*-terphenyl)element cations $[(2,6\text{-}Mes_2C_6H_3)_2E]^+$ of group 13 (**1**, E=B; **2**, E=Al; **3**, E=Ga; **4**, E=In; **5**, E=Tl) were investigated. The preparation and characterization of **2**, **3** and **5** were previously reported by Wehmschulte's (*Organometallics* **2004**, *23*, 1965–1967; *J. Am. Chem. Soc.* **2003**, *125*, 1470–1471) and our groups (*Organometallics* **2009**, *28*, 6893–6901). The indinium ion **4** was prepared and fully characterized for the first time. Attempts to prepare the borinium ion **1** by fluoride or hydride abstraction were unsuccessful. The electronic structures of **1**–**5** and the stabilization by the bulky *m*-terphenyl substituents were analyzed using quantum chemical calculations and compared to the divalent bis(*m*-terphenyl)pnictogenium ions $[(2,6\text{-}Mes_2C_6H_3)_2E]^+$ of group 15 (**6**, E=P; **7**, E=As; **8**, E=Sb; **9**, E=Bi) previously investigated by our group (*Angew. Chem. Int. Ed.* **2018**, *57*, 10080–10084). The calculated fluoride ion affinities (FIA) of **1**–**9** are higher than that of SbF_5, which classifies them as Lewis superacids.

Introduction

Borinium ions[1] and their heavier group 13 analogs[2] have received tremendous interest over the years, but the first truly two-coordinate borinium ion, $[Mes_2B]^+$, was only recently reported by Shoji *et al.*[3] The interest in these four-valence-electron (4 VE) species stems from their high Lewis acidity and applications in bond activation chemistry and catalysis deriving therefrom.[1]

The present work revisits and extends a series of bulky bis(*m*-terphenyl) element cations $[(2,6\text{-}Mes_2C_6H_3)_2E]^+$ (**1**, E=B; **2**, E=Al;[4] **3**, E=Ga;[5] **4**, E=In; **5**, E=Tl[6]), for which three examples were already reported by Wehmschulte *et al.*[4,5] and our group.[6] Here we describe the analogous $[(2,6\text{-}Mes_2C_6H_3)_2In]^+$ (**4**), which represents the first donor-free, two-coordinate indinium ion. By contrast, all previously known related indenium cations, such as $[(Me_3SiCH_2)_2In(THF)_3]^+$ and $[Mes_2In]^+[BF_4]^-$, possess saturated hypercoordinate indium atoms due to solvation or ion pairing.[7] We also report on our failed attempts to prepare the related borinium ion $[(2,6\text{-}Mes_2C_6H_3)_2B]^+$ (**1**) by fluoride and hydride abstraction.[3]

Complementing the experimental results, the electronic structures of **1**–**5** were investigated by density functional theory (DFT) calculations and real space bond indicator (RSBI) analyses. RSBIs comprise bond topology according to the Atoms-In-Molecules (AIM)[8] theory, intramolecular contact patches according to the noncovalent interactions (NCI)[9] index, and bonding and lone-pair basins according to the electron localizability indicator (ELI–D).[10] The results of group 13 are compared to a complementary series of group 15 cations $[(2,6\text{-}Mes_2C_6H_3)_2E]^+$ (**6**, E=P; **7**, E=As;[11] **8**, E=Sb; **9**, E=Bi[12]), possessing six valence electrons (6 VE) which were either assigned as transient species in fluoride abstraction reactions[11] or isolated and fully characterized by us previously.[12]

Results and Discussion

Attempted preparation of the borinium ion $[(2,6\text{-}Mes_2C_6H_3)_2B]^+$ (1)

The reaction of *m*-terphenyllithium, 2,6-$Mes_2C_6H_3Li$,[13] with an excess of boron trifluoride etherate, $BF_3{\cdot}OEt_2$, provided the mono-substituted product 2,6-$Mes_2C_6H_3BF_2$ (**10**) in 66% yield (Scheme 1). After isolation of **10**, the reaction with 2,6-$Mes_2C_6H_3Li$ afforded the di-substituted product $(2,6\text{-}Mes_2C_6H_3)_2BF$ (**11**) in 82% yield (Scheme 1). Efforts were made

[a] D. Duvinage, Prof. Dr. J. Beckmann
Institut für Anorganische Chemie und Kristallographie,
Universität Bremen
Leobener Straße 7, 28359 Bremen, Germany
E-mail: j.beckmann@uni-bremen.de
[b] Dr. L. A. Malaspina, PD Dr. S. Grabowsky
Departement für Chemie, Biochemie und Pharmazie,
Universität Bern
Freiestrasse 3, 3012 Bern, Switzerland
E-mail: simon.grabowsky@unibe.ch
[c] Dr. S. Mebs
Institut für Experimentalphysik, Freie Universität Berlin
Arnimallee 14, 14195 Berlin, Germany
E-mail: stefan.mebs@fu-berlin.de

Supporting information for this article is available on the WWW under https://doi.org/10.1002/ejic.202200482

© 2022 The Authors. European Journal of Inorganic Chemistry published by Wiley-VCH GmbH. This is an open access article under the terms of the Creative Commons Attribution License, which permits use, distribution and reproduction in any medium, provided the original work is properly cited.

© 2022 The Authors. European Journal of Inorganic Chemistry published by Wiley-VCH GmbH

EurJIC
European Journal of Inorganic Chemistry

Research Article
doi.org/10.1002/ejic.202200482

Chemistry Europe
European Chemical Societies Publishing

10990682, 2023, 1, Downloaded from https://chemistry-europe.onlinelibrary.wiley.com/doi/10.1002/ejic.202200482 by Staats- und Universitätsbibliothek, Wiley Online Library on [20/09/2023]. See the Terms and Conditions (https://onlinelibrary.wiley.com/terms-and-conditions) on Wiley Online Library for rules of use; OA articles are governed by the applicable Creative Commons License

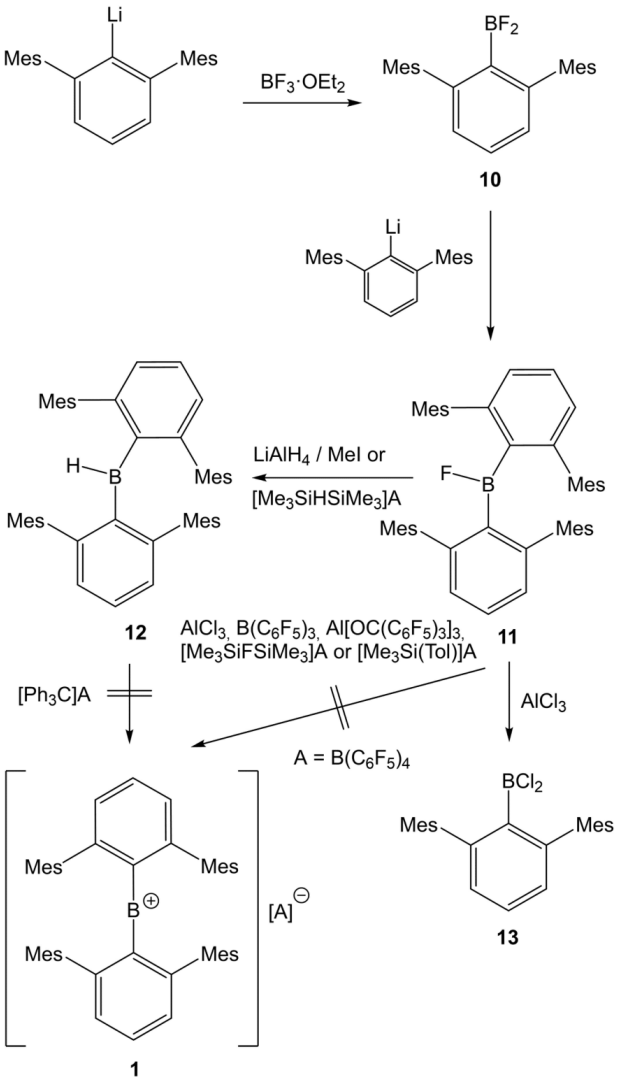

Scheme 1. Synthesis of mono- and di-substituted *m*-terphenyl boranes **10**, **11** and **12** and attempted preparation of the borinium ion **1**.

to prepare **11** in a one-pot procedure; however, it was noted that the second equivalent of 2,6-$Mes_2C_6H_3Li$ attacks the ether molecule under these Lewis acidic conditions. Both *m*-terphenylboron fluorides could be readily distinguished by heteronuclear NMR spectroscopy. The ^{11}B NMR spectra (CD_2Cl_2) of **10** and **11** show broad signals at $\delta = 25.3$ ($W_{1/2} = 1500$ Hz) and 51.4 ppm ($W_{1/2} = 1600$ Hz), respectively. The ^{19}F NMR spectra (CD_2Cl_2) of **10** and **11** reveal very different signals at $\delta = -70.9$ and 17.5 ppm. The reduction of **11** with $LiAlH_4$ (after workup with MeI) produced the corresponding bis(*m*-terphenyl)boron hydride (2,6-$Mes_2C_6H_3)_2BH$ (**12**) in 96% yield (Scheme 1). The ^{11}B NMR spectrum (CD_2Cl_2) of **12** shows a broad signal at $\delta =$

© 2022 The Authors. European Journal of Inorganic Chemistry published by Wiley-VCH GmbH

EurJIC
European Journal of Inorganic Chemistry

Research Article
doi.org/10.1002/ejic.202200482

Chemistry Europe
European Chemical Societies Publishing

10990682c, 2023, 1, Downloaded from https://chemistry-europe.onlinelibrary.wiley.com/doi/10.1002/ejic.202200482 by Staats- und Universitätsbibliothek, Wiley Online Library on [20/06/2023]. See the Terms and Conditions (https://onlinelibrary.wiley.com/terms-and-conditions) on Wiley Online Library for rules of use; OA articles are governed by the applicable Creative Commons License

74.3 ppm. The IR spectrum (ATR, neat) of **12** exhibits a peak at $\tilde{\nu} = 2580\ cm^{-1}$, which was assigned to the terminal B–H stretching vibration.

The bis(*m*-terphenyl)boranes **11** and **12** were used for the attempted preparation of the borinium ion **1**. The attempted fluoride abstraction of (2,6-$Mes_2C_6H_3)_2BF$ (**11**) with $AlCl_3$ gave rise to mixture of products, from which only the previously known mono-substituted product 2,6-$Mes_2C_6H_3BCl_2$ (**13**)[14] was isolated by crystallization in low yields (Scheme 1). In the remaining dark oil, only the parent *m*-terphenyl ligand 2,6-$Mes_2C_6H_4$ was identified. The reaction of **11** with the milder Lewis acid $EtAlCl_2$ occurred at slower pace, but it also gave multiple products. No reactivity was observed between **11** and the bulkier Lewis acids $B(C_6F_5)_3$[15] and $Al[OC(C_6F_5)_3]_3$.[16] The reaction of **11** with the disguised silylium ion $[Me_3Si–H–SiMe_3][B(C_6F_5)_4]$[17] proceeded with a smooth H/F exchange and afforded (2,6-$Mes_2C_6H_3)_2BH$ (**12**) and the previously known fluorine-bridged species $[Me_3Si–F–SiMe_3][B(C_6F_5)_4]$.[18] With $[Me_3Si\cdot toluene][B(C_6F_5)_4]$, prepared *in situ* from $[Me_3Si–H–SiMe_3][B(C_6F_5)_4]$ and toluene,[17] multiple signals were observed by ^{11}B and ^{19}F NMR spectroscopy, which tentatively suggests that the bis(*m*-terphenyl)borane moiety as well as the borate anion had degraded. Similar observations were made by Wehmschulte[19] and Power.[14] The attempted hydride abstraction of (2,6-$Mes_2C_6H_3)_2BH$ (**12**) with the trityl salt $[Ph_3C][B(C_6F_5)_4]$[20] gave no reaction (Scheme 1).

The molecular structures of **10** and **13** are shown in Figure 1. Selected bond parameters of the series 2,6-$Mes_2C_6H_3BX_2$ (**10**, X=F; **13**, X=Cl and X=Br[14]) are collected in Table 1. The spatial arrangements of **10** and **13**, like the previously studied 2,6-$Mes_2C_6H_3BBr_2$, are slightly distorted trigonal planar.[14] As anticipated, the B–X bond length increases from **10** (1.307(2), 1.314(2) Å for X=F) to **13** (1.750(1) Å for X=Cl) and 2,6-$Mes_2C_6H_3BBr_2$ (1.903(1) Å for X=Br), whereas the other bond parameters (B–C bond lengths, X–B–X, X–B–C bond angles) show little variance.

The molecular structures of **11** and **12** are shown in Figure 2. Selected bond parameters of the series (2,6-$Mes_2C_6H_3)_2BX$ (**11**, X=F; **12**, X=H) and Mes_2BF[21] are collected in Table 2. Unlike Mes_2BF, the geometries of **11** and **12** strongly deviate from an ideal trigonal planar arrangement. Due to the repulsion of the bulky *m*-terphenyl substituents, the C–B–C bond angles of **11** (142.0(1)°) and **12** (136.6(1)°) are dramatically enlarged as compared to that of Mes_2BF (125.4(1)°). In turn, the X–B–C bond angles of **11** (107.1(1) and 110.9(1)°) and **12** (111.7(1)°) are significantly compressed in comparison to that of Mes_2BF[21] (116.8(1) and 117.8(1)°). The B–F bond lengths of **11** and Mes_2BF (1.339(2) Å) are identical within the experimental error and slightly longer than in **10** (1.307(2) and 1.314(2) Å). The B–C bond length increases from Mes_2BF[21] (1.568(2) and 1.570(2) Å) to **12** (1.573(1) Å) and **11** (1.586(2) and 1.599(2) Å) reflecting the bulk of the three substituents. We speculate that the slight elongation of the B–C bonds in **11** might be the reason why the cleavage of the second *m*-terphenyl substituent occurs in the reaction with $AlCl_3$ (see above).

Table 1. Selected bond lengths in Å and angles in ° of **10**, **13** and 2,6-$Mes_2C_6H_3BBr_2$.[14]

	10 (X=F)	**13** (X=Cl)	2,6-$Mes_2C_6H_3BBr_2$
B–X	1.307(2), 1.314(2)	1.750(1)[a]	1.903(1)[a]
B–C	1.560(2)	1.558(2)	1.565(1)
X–B–X	115.4(1)	116.4(1)	116.3(1)
X–B–C	122.2(1), 122.4(1)	121.8(1)	121.8(1)

[a] The two chlorine and two bromine atoms are crystallographically equivalent.

Table 2. Selected bond lengths in Å and angles in ° of **11**, **12** and Mes_2BF.[21]

	11 (X=F)	**12** (X=H)	Mes_2BF
B–X	1.339(2)	1.203(4)	1.339(2)
B–C	1.586(2), 1.599(2)	1.573(1)	1.568(2), 1.570(2)
X–B–C	107.1(1), 110.9(1)	111.7(1)	116.8(1), 117.8(1)
C–B–C	142.0(1)	136.6(1)	125.4(1)

The structure of **12** was subject to a Hirshfeld atom refinement (HAR),[22] which allows the precise and accurate determination of E–H bonds from X-ray data.[23] The B–H bond length of **12** (1.203(4) Å) can be compared to the other four existing HAR-refined terminal B–H bond length values in the literature, whereas neutron-diffraction references are missing in the literature. The B–H bond length in **12** is identical within the experimental error with those of *closo*-borane $(NH_4)_2[B_6H_6]$[24] and the terminal ones in the copper(I) complex $[(Ph_3P)_2Cu][BH_4]$[23] despite the different coordination numbers of the boron atoms. In contrast, the terminal B–H bonds in diborane $(BH_3)_2$[23] and the cobalt(II) complex $Co(Bm^{Me})_2$ (Bm^{Me} = bis(2-mercapto-1-methylimidazolyl)borate)[25] are significantly shorter at 1.170(7)/1.168(6) Å and 1.174(13) Å, respectively.

Figure 1. Molecular structures of the mono-substituted *m*-terphenylboron difluoride **10** and dichloride **13** showing 50% probability ellipsoids.

© 2022 The Authors. European Journal of Inorganic Chemistry published by Wiley-VCH GmbH

EurJIC
European Journal of Inorganic Chemistry

Research Article
doi.org/10.1002/ejic.202200482

Chemistry Europe
European Chemical Societies Publishing

10990682, 2023, 1, Downloaded from https://chemistry-europe.onlinelibrary.wiley.com/doi/10.1002/ejic.202200482 by Staats- und Universitätsbibliothek, Wiley Online Library on [20/06/2023]. See the Terms and Conditions (https://onlinelibrary.wiley.com/terms-and-conditions) on Wiley Online Library for rules of use; OA articles are governed by the applicable Creative Commons License

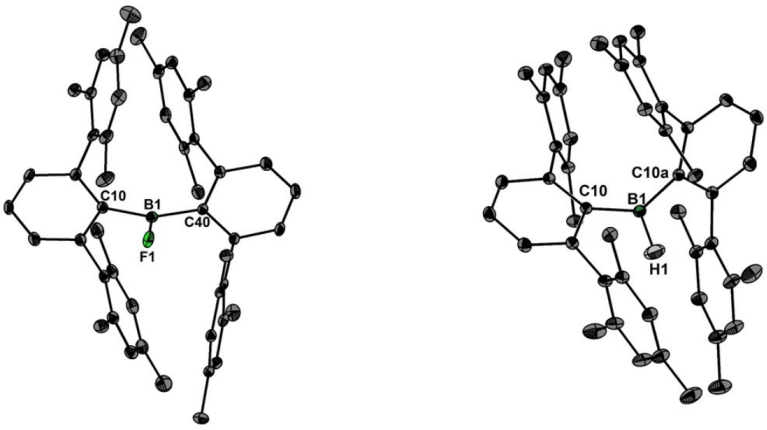

Figure 2. Molecular structure of the di-substituted *m*-terphenylboron fluoride **11** and hydride **12** (derived from Hirshfeld atom refinement (HAR)) showing 50% probability ellipsoids.

Preparation of the indinium cation 4

The indinium cation **4** was synthesized by bromide abstraction from (2,6-$Mes_2C_6H_3$)$_2$InBr[26] using $K[B(C_6F_5)]_4$[27] and obtained as orange crystals in 91% yield (Scheme 2). In solution, **4** reveals the typical set of *m*-terphenyl signals by ^{1}H NMR spectroscopy. In ^{13}C NMR spectroscopy, the influence of the positive charge is best visible in the shift of the *ipso* carbon atom, which shows a signal at $\delta = 156.92$ ppm, about 20 ppm downfield shifted compared to (2,6-$Mes_2C_6H_3$)$_2$InBr.[26]

The molecular structure of **4** is shown in Figure 3. Selected bond parameters of the series $[(2,6\text{-}Mes_2C_6H_3)_2E]^+$ (E=Al (**2**),[4] Ga (**3**),[5] In (**4**) and Tl (**5**)[6]) are collected in Table 3. The C–In-C angle is nearly linear (176.2(1)°), which is by about 20° larger than in the starting material. The value compares well with those of **3** (175.7(1)°) and **5** (177.4(3)°), but differs from that of **2** (159.2(1)°), which is attributed to the stronger intramolecular interactions between the Al atom and the flanking mesityl groups (see computational analysis below). The In–C bond lengths of **4** (2.092(2) and 2.089(2) Å) are considerably shorter than in the starting material (2.171(3) and 2.166(3) Å). In fact, they seem to be the shortest known In–C bond lengths, which usually fall in the range between 2.11 Å (Me_2InBr) and 2.24 Å (K[$InMe_4$]).[28]

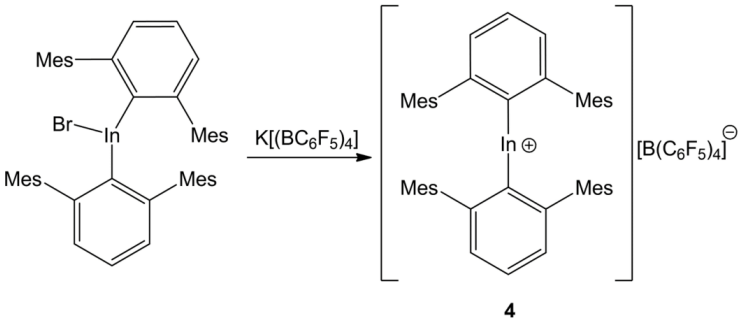

Scheme 2. Synthesis of the bis(*m*-terphenyl)indinium ion **4**.

© 2022 The Authors. European Journal of Inorganic Chemistry published by Wiley-VCH GmbH

EurJIC
European Journal of Inorganic Chemistry

Research Article
doi.org/10.1002/ejic.202200482

Chemistry Europe
European Chemical Societies Publishing

10990682c, 2023, 1, Downloaded from https://chemistry-europe.onlinelibrary.wiley.com/doi/10.1002/ejic.202200482 by Staats- und Universitätsbibliothek, Wiley Online Library on [20/06/2023]. See the Terms and Conditions (https://onlinelibrary.wiley.com/terms-and-conditions) on Wiley Online Library for rules of use; OA articles are governed by the applicable Creative Commons License

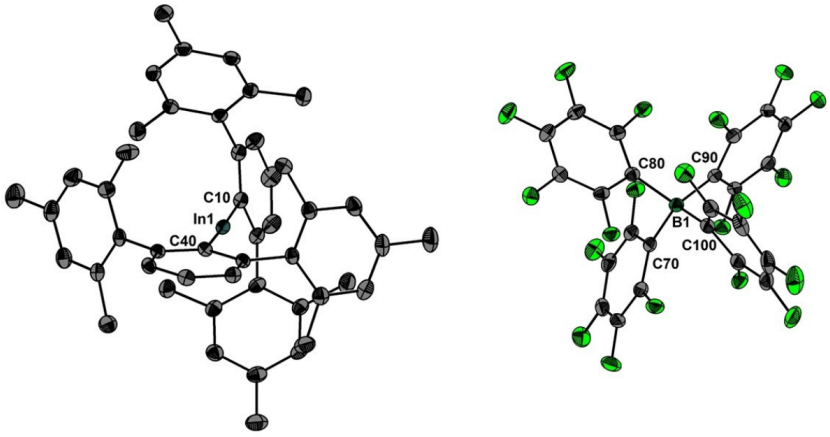

Figure 3. Molecular structure of **4** (left) and the counter anion (right) showing 50% probability ellipsoids.

Table 3. Selected bond lengths in Å and angles in ° of $[(2,6\text{-}Mes_2C_6H_3)_2E]^+$ (**2**, E=Al;[4] **3**, E=Ga;[5] **4**, E=In; **5** E=Tl[6]).

	2 (E=Al)	**3** (E=Ga)	**4** (E=In)	**5** (E=Tl)
E–C	1.938(1)	1.913(1)	2.092(2)	2.126(9)
	1.941(1)	1.915(1)	2.089(2)	2.127(9)
C–E–C	159.2(1)	175.7(1)	176.2(1)	177.4(3)

Density functional theory (DFT) and real space bond indicator (RSBI) analyses

The electronic structures in the bis(*m*-terphenyl)element cations $[(2,6\text{-}Mes_2C_6H_3)_2E]^+$ of group 13 (**1**, E=B; **2**, E=Al; **3**, E=Ga; **4**, E=In; **5**, E=Tl) were studied computationally by means of density functional theory (DFT) and real-space bonding indicator (RSBI) analysis. For this purpose, all five structures were fully optimized as isolated molecules (see ESI for details). The calculated molecular geometries match those obtained experimentally by X-ray crystallography very well. Topological and integrated bond parameters of the primary and secondary E–C interactions of **1**–**5** are collected in Table 4. AIM atomic and fragmental charges of **1**–**5** are listed in Table 5.[8] The AIM bond topology[8] as well as NCI[9] and ELI–D *iso*-surfaces[10] of **1** and **2** are shown in Figure 4 and Figure 5 (for **3**–**5**, see ESI).

The short B–C bond of **1** is dominated by covalent bonding aspects, which is reflected in a high electron density (ED, $\rho(\mathbf{r})_{bcp}$) at the bond critical point (bcp) of 1.5 eÅ^{-3}, a negative value of the Laplacian of the ED ($\nabla^2\rho(\mathbf{r})_{bcp} = -10.2$ eÅ^{-5}) and the total energy density over ED ratio also being significantly negative ($H/\rho(\mathbf{r})_{bcp} = -1.18$ a.u.). However, ionic bond contributions cannot be neglected, resulting in a considerably positive kinetic energy density over ED ratio ($G/\rho(\mathbf{r})_{bcp} = 0.71$ a.u.) and a Raub-Jansen Index (RJI)[29] of 82%, indicating that more than 80% of the electron populations of the ELI–D B–C bonding basins ($N_{ELI} = 2.78$ e) are located in the C atomic AIM basins, suggesting a perceivable bond polarity.

The longer E–C bonds of **2**–**5** (E=Al–Tl) show properties of typical polar-covalent interactions in which neither bonding

Table 4. Topological and integrated AIM and ELI–D properties of the primary E–C bonds and secondary E···C_π contacts in $[(2,6\text{-}Mes_2C_6H_3)_2E]^+$ of group 13 (**1**, E=B; **2**, E=Al; **3**, E=Ga; **4**, E=In; **5**, E=Tl).

	Contact or basin	d [Å]	$\rho(\mathbf{r})_{bcp}$ [eÅ^{-3}]	$\nabla^2\rho(\mathbf{r})_{bcp}$ [eÅ^{-5}]	ε	$G/\rho(\mathbf{r})_{bcp}$ [a.u.]	$H/(\mathbf{r})_{bcp}$ [a.u.]	N_{ELI} [e]	V_{ELI} [Å^3]	γ_{ELI}	RJI [%]
1	B–C	1.476	1.52	−10.2	0.14	0.71	−1.18	2.78	10.4	1.99	81.5
2	Al–C	1.938	0.63	6.4	0.07	1.12	−0.40	2.42	9.9	1.98	89.6
3	Ga–C	1.925	0.87	2.5	0.07	0.73	−0.52	2.61	10.7	1.68	63.0
4	In–C	2.094	0.77	2.9	0.08	0.69	−0.43	2.16	10.4	1.64	72.7
5	Tl–C	2.110	0.85	1.6	0.08	0.59	−0.46	1.84	7.0	1.56	72.7
2	Al···C_π	2.362	0.23	1.5	1.94	0.71	−0.26				
3	Ga···C_π	2.575	0.21	1.6	1.79	0.66	−0.11				

For all bonds, d is the geometric contact distance, $\rho(\mathbf{r})_{bcp}$ is the electron density at the bcp, $\nabla^2\rho(\mathbf{r})_{bcp}$ is the corresponding Laplacian, ε is the bond ellipticity, $G/\rho(\mathbf{r})_{bcp}$ and $H/\rho(\mathbf{r})_{bcp}$ are the kinetic and total energy density over $\rho(\mathbf{r})_{bcp}$ ratios, N_{ELI} and V_{ELI} are electron populations and volumes of related ELI–D basins, γ_{ELI} is the ELI–D value at the attractor position, RJI is the Raub-Jansen Index. Values are averaged over similar bonds (see Table S3 for all bonds).

© 2022 The Authors. European Journal of Inorganic Chemistry published by Wiley-VCH GmbH

EurJIC
European Journal of Inorganic Chemistry

Research Article
doi.org/10.1002/ejic.202200482

Chemistry Europe
European Chemical Societies Publishing

10990682, 2023, 1, Downloaded from https://chemistry-europe.onlinelibrary.wiley.com/doi/10.1002/ejic.202200482 by Staats- und Universitätsbibliothek, Wiley Online Library on [20/06/2023]. See the Terms and Conditions (https://onlinelibrary.wiley.com/terms-and-conditions) on Wiley Online Library for rules of use; OA articles are governed by the applicable Creative Commons License

Table 5. AIM atomic and fragmental charges of $[(2,6\text{-}Mes_2C_6H_3)_2E]^+$ of group 13 (**1**, E=B; **2**, E=Al; **3**, E=Ga; **4**, E=In; **5**, E=Tl) in e.[a]

Q_{AIM}	R_2B^+	R_2Al^+	R_2Ga^+	R_2In^+	R_2Tl^+
R	−0.46	−0.61	−0.17	−0.12	−0.01
R′	−0.46	−0.61	−0.15	−0.12	−0.01
E	1.92	2.22	1.35	1.25	1.02
Σ	1.00	1.00	1.02	1.00	0.99

[a] R, R′ = 2,6-$Mes_2C_6H_3$.

aspect – covalent or ionic – prevails. The ED varies between 0.63 and 0.87 eÅ^{-3}, the Laplacian is positive but close to zero, and the absolute value of $G/\rho(\mathbf{r})_{bcp}$ exceeds that of $H/\rho(\mathbf{r})_{bcp}$. RJI varies between 63% in **3** and 90% in **2**. Notably, **2** and **3** (but not **1**, **4** and **5**) exhibit additional secondary E···C_π bond paths and bcps to the 2,6-$Mes_2C_6H_3$ substituents (Figure 5a and Figure S25a), which are reminiscent of similar contacts in related group 15 cations $(2,6\text{-}Mes_2C_6H_3)_2E^+$ (E=As, Sb, Bi).[12] Such kinetic stabilization via E···C_π London-dispersive/electrostatic-type interactions was not observed for the borinium or phosphenium ions, $[(2,6\text{-}Mes_2C_6H_3)_2B]^+$ or $[(2,6\text{-}Mes_2C_6H_3)_2P]^+$, both of which could not be isolated despite significant efforts. With ED values below 0.25 eÅ^{-3}, strong $G/\rho(\mathbf{r})_{bcp}$ and small negative $H/\rho(\mathbf{r})_{bcp}$ values, these Al/Ga···C_π contacts are clearly dominated by ionic bond contributions. This is supported by the NCI *iso*-surfaces, which show localized, blue-colored NCI basins for the secondary Al/Ga···C_π contacts, whereas all other weak secondary contacts, such as π···π, H···H, etc. cause the formation of extended flat, green-colored NCI basins (Figure 4b, Figure 5b and Figures S25b-S27b). (Polarized) covalent bonds do not lead to the formation of NCI basins at the commonly chosen *iso*-value of 0.5. AIM atomic and fragmental charges disclose that charge separation between group 13 element E and the *m*-terphenyl substituents increases in the order Al > B > Ga ≈ In > Tl (Table 5).

A common method to assess the relative strength of isolated Lewis acids on the basis of DFT entails the calculation of the fluoride ion affinity (FIA).[30] The FIA values calculated for the divalent bis(*m*-terphenyl)element cations $[(2,6\text{-}Mes_2C_6H_3)_2E]^+$ of group 13 (**1**, E=B; **2**, E=Al; **3**, E=Ga; **4**, E=In; **5**, E=Tl) and group 15 (**6**, E=P; **7**, E=As; **8**, E=Sb; **9**, E=Bi) are collected in Figure 6. In addition, series of calculations were conducted on small Lewis acids for comparison at three levels of theory (B3PW91, BP86, and MP2 on the structures optimized at the B3PW91 level), which are given in the ESI (Tables S6–S8). For the group 13 compounds, the FIA values fall in the rather wide range between 725 (**1**) and 520 (**5**), whereas the group 15

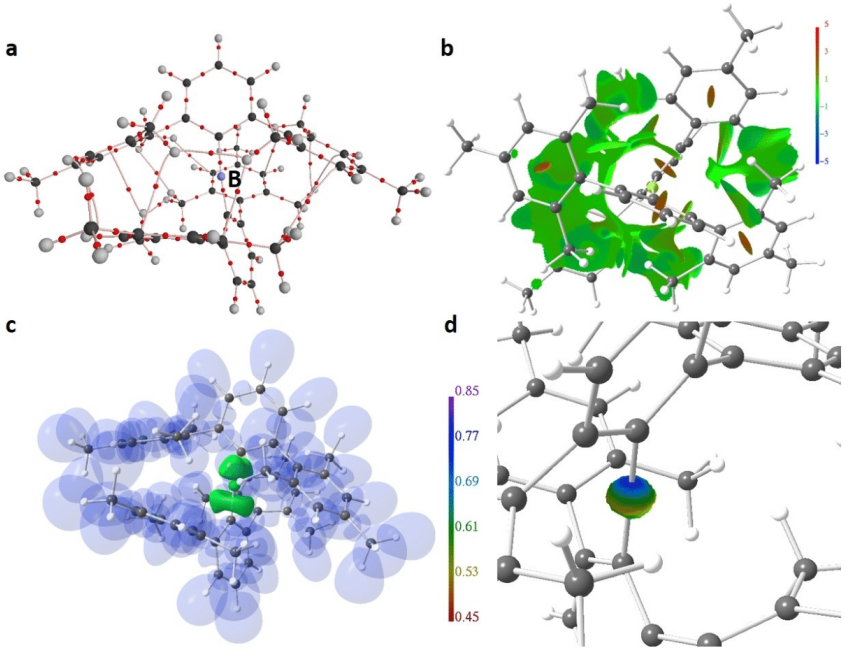

Figure 4. RSBI analysis of **1**: (a) AIM bond paths motif, (b) NCI *iso*-surface at s(**r**) = 0.5 colour coded with sign(λ_2)•ρ, (c) ELI–D localization domain representation at *iso*-value of 1.3, (d) ELI–D distribution mapped on the B atom ELI–D core basin.

© 2022 The Authors. European Journal of Inorganic Chemistry published by Wiley-VCH GmbH

EurJIC
European Journal of Inorganic Chemistry

Research Article
doi.org/10.1002/ejic.202200482

Chemistry Europe
European Chemical Societies Publishing

10990682c, 2023, 1, Downloaded from https://chemistry-europe.onlinelibrary.wiley.com/doi/10.1002/ejic.202200482 by Staats- und Universitätsbibliothek, Wiley Online Library on [20/06/2023]. See the Terms and Conditions (https://onlinelibrary.wiley.com/terms-and-conditions) on Wiley Online Library for rules of use; OA articles are governed by the applicable Creative Commons License

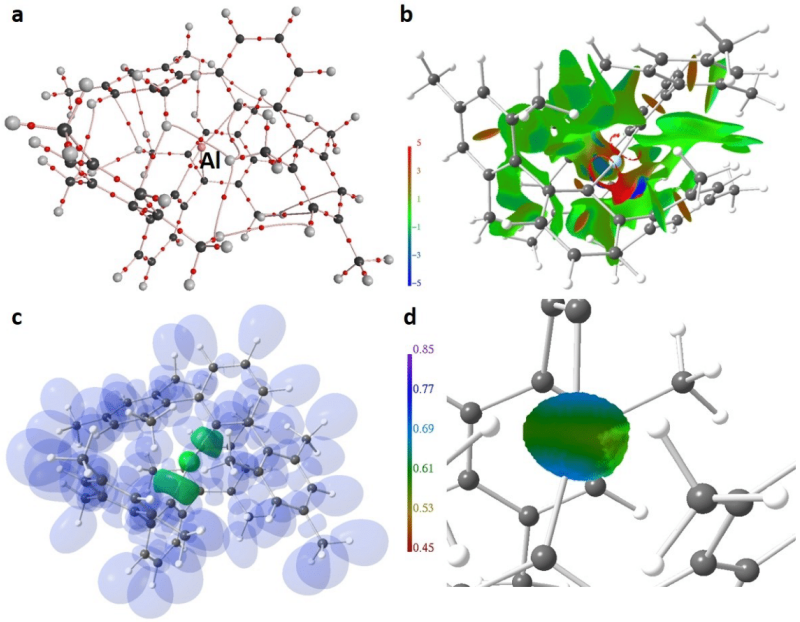

Figure 5. RSBI analysis of **2**: (a) AIM bond paths motif, (b) NCI *iso*-surface at s(**r**) = 0.5 colour coded with sign(λ_2)•ρ, (c) ELI–D localization domain representation at *iso*-value of 1.3, (d) ELI–D distribution mapped on the Al atom ELI–D core basin.

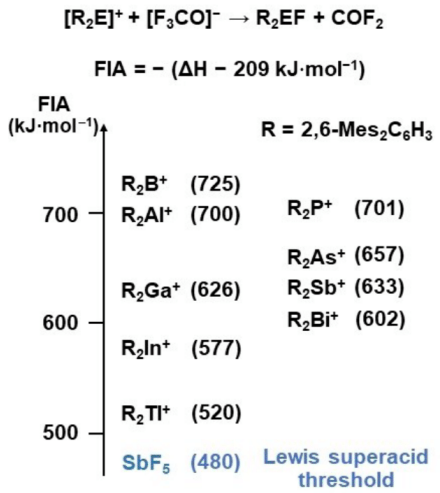

Figure 6. Calculated fluoride ion affinity (FIA) of $[(2,6\text{-}Mes_2C_6H_3)_2E]^+$ of group 13 (**1**, E=B; **2**, E=Al; **3**, E=Ga; **4**, E=In; **5**, E=Tl) and group 15 (**6**, E=P; **7**, E=As; **8**, E=Sb; **9**, E=Bi).

compounds cover the smaller range from 701 (**6**) to 602 (**9**). All of these values are smaller than those of the silyl cations $[Et_3Si]^+$ (808) and $[Mes_3Si]^+$ (778), but larger than that of SbF_5 (480), which qualifies **1**–**9** as Lewis superacids.

Conclusions

The first donor-free divalent indinium cation $[(2,6\text{-}Mes_2C_6H_3)_2In]^+$ (**4**) was obtained using sterically demanding *m*-terphenyl substituents in combination with a weakly coordinating anion, namely tetrakis(pentafluorophenyl)borate. Calculated fluoride anion affinity (FIA) qualifies **4** as Lewis superacid. Attempts to prepare the related borinium ion $[(2,6\text{-}Mes_2C_6H_3)_2B]^+$ (predicted to be an even stronger Lewis superacid) by fluoride or hydride abstraction from appropriate precursors failed on all accounts.

Experimental Procedures

General information

Unless otherwise stated, all reactions and manipulations were performed under inert atmosphere (argon) using anhydrous

© 2022 The Authors. European Journal of Inorganic Chemistry published by Wiley-VCH GmbH

EurJIC
European Journal of Inorganic Chemistry

Research Article
doi.org/10.1002/ejic.202200482

Chemistry Europe
European Chemical Societies Publishing

10990682, 2023, 1, Downloaded from https://chemistry-europe.onlinelibrary.wiley.com/doi/10.1002/ejic.202200482 by Staats- und Universitätsbibliothek, Wiley Online Library on [20/06/2023]. See the Terms and Conditions (https://onlinelibrary.wiley.com/terms-and-conditions) on Wiley Online Library for rules of use; OA articles are governed by the applicable Creative Commons License

solvents. The starting materials 2,6-$Mes_2C_6H_3Li$ (Mes = 2,4,6-$Me_3C_6H_2$)[13] (2,6-$Mes_2C_6H_3)_2InBr$,[26] $K[B(C_6F_5)_4]$[27] $[Ph_3C][B(C_6F_5)_4]$[20] and $[Me_3Si{-}H{-}SiMe_3][B(C_6F_5)_4]$[19] were prepared following the published procedures. The reagents $BF_3{\cdot}Et_2O$, $AlCl_3$, $EtAlCl_2$ (0.9 M in hexanes), $LiAlH_4$, MeI, and $InBr_3$ were obtained commercially and were used as received. Anhydrous dichloromethane, hexane, tetrahydrofurane and toluene were collected from an SPS800 mBraun solvent purification system and stored over 4 Å molecular sieves. Et_2O was dried by refluxing it over Na/benzophenone under argon atmosphere. Deuterated solvents were degassed and dried over 4 Å molecular sieves under argon.

Unless otherwise noted, NMR spectra were recorded at room temperature on a Bruker Avance 600 MHz spectrometer. ^1H, $^{13}C\{^1H\}$, ^{11}B, $^{11}B\{^1H\}$ and ^{19}F NMR spectra are reported on the δ scale (ppm) and are referenced against $SiMe_4$. ^1H and $^{13}C\{^1H\}$ chemical shifts are reported relative to the residual peak of the solvent ($CDHCl_2$ 5.32 ppm for CD_2Cl_2, C_6D_5H for C_6D_6 and *o*-$C_6D_3HCl_2$ for *o*-$C_6D_4Cl_2$) in the ^1H NMR spectra, and to the peak of the deuterated solvent (CD_2Cl_2 53.84 ppm, C_6D_6 128.39 ppm) in the $^{13}C\{^1H\}$ NMR spectra. The assignment of the ^1H and $^{13}C\{^1H\}$ resonance signals was made in accordance with the COSY, HSQC and HMBC spectra. The labelling schemes are attached to the ^1H and ^{13}C spectra.

The ESI HRMS spectra were measured on a Bruker Impact II spectrometer. Acetonitrile or dichloromethane/acetonitrile solutions ($c = 1{\cdot}10^{-5}$ mol·L^{-1}) were injected directly into the spectrometer at a flow rate of 3 µL·min^{-1}. Nitrogen was used both as a drying gas and for nebulization with flow rates of approximately 5 L·min^{-1} and a pressure of 5 psi. Pressure in the mass analyzer region was usually about $1{\cdot}10^{-5}$ mbar. Spectra were collected for 1 min and averaged. The nozzle-skimmer voltage was adjusted individually for each measurement.

IR spectra were recorded on a *Nicolet* Thermo iS10 scientific spectrometer with a diamond ATR unit. The absorption bands are reported in cm^{-1} with indicated relative intensities: s (strong, 0–33 % T); m (medium, 34–66 % T), w (weak, 67–100 % T), and br (broad). The UV-Vis spectra were recorded on a Varian Cary 50 Scan UV-Visible spectrophotometer.

Synthesis and characterization of $Mes_2C_6H_3BF_2$ (10). A solution of 2,6-$Mes_2C_6H_3Li$ (3.20 g, 10.0 mmol, 1.00 eq.) in Et_2O (50 mL) is added over a solution of $BF_3{\cdot}OEt_2$ (2.00 mL, 15.8 mmol, 1.58 eq.) in Et_2O (50 mL) at 0 °C over the course of 20 minutes. The reaction mixture s stirred for 2 hours at room temperature and the solvent is removed under reduced pressure. The remaining solid is extracted with DCM and filtered through a pad of celite. Afterwards the solvent is removed under vacuum and the residue washed with MeCN (3×10 mL) and *n*-hexane (3×10 mL). The remaining solid is dried under reduced pressure to obtain the title compound as a colourless solid (2.37 g, 66 %).

^1H NMR (600 MHz, CD_2Cl_2): $\delta = 7.64$ (t, $^3J(^1H{-}^1H) = 7.65$ Hz, 1H, H4), 7.16 (d, $^3J(^1H{-}^1H) = 7.65$ Hz, 2H, H3 and H5), 6.97 (s, 4H, H9 and H11), 2.34 (s, 6H, H14), 2.03 (s, 12H, H13 and H15) ppm. **$^{13}C\{^1H\}$ NMR (151 MHz, CD_2Cl_2):** $\delta = 146.94$ (s, C2 and C6), 138.85 (s, C7), 137.79 (s, C10), 136.39 (s, C8 and C12), 132.26 (s, C4), 128.59 (s, C9 and C11), 128.15 (s, C3 and C5), 21.41 (s. C14), 20.77 (s, C13 and C15) ppm. **$^{11}B\{^1H\}$ NMR (CD_2Cl_2, 193 MHz):** $\delta = 25.32$ ppm. **$^{19}F\{^1H\}$ NMR (CD_2Cl_2, 565 MHz):** $\delta = -70.89$ ppm. **HRMS ESI (m/z):** $[M+F]^-$ calculated. for $C_{24}H_{25}BF_3$, 381.20069; found, 381.20086.

Synthesis and characterization of (2,6-$Mes_2C_6H_3)_2BF$ (11). A Schlenk tube is charged with **10** (1.81 g, 5.00 mmol, 1.00 eq.) and 2,6-$Mes_2C_6H_3Li$ (1.60 g, 5.00 mmol, 1.00 eq.) before *n*-hexane (40 mL) is added. The reaction mixture is stirred for 72 h and monitored by ^{19}F-NMR spectroscopy. Then the solvent is removed under reduced pressure, the residue extracted with CH_2Cl_2 (40 mL) and filtered off from any insoluble materials. The solvent is removed under vacuum and the remaining solid washed with MeCN (3 × 10 mL) and *n*-hexane (3 × 10 mL). The residual solid is dried at 80 °C/$5{\cdot}10^{-3}$ mbar to obtain **11** as off-white solid (2.98 g, 82 %).

^1H NMR (600 MHz, CD_2Cl_2): $\delta = 7.22$ (t, $^3J(^1H{-}^1H) = 7.60$ Hz, 1H, H4), 6.80 (s, 4H, H9 and H11), 6.68 (d, $^3J(^1H{-}^1H) = 7.60$ Hz, 2H, H3 and H5), 2.32 (s, 6H, H14), 1.61 (s, 12H, H13 and H15) ppm. **$^{13}C\{^1H\}$ NMR (151 MHz, CD_2Cl_2):** $\delta = 147.71$ (d, $^3J(^{13}C{-}^{19}F) = 4.70$ Hz, C2 and C6), 140.88 (s, C7), 137.45 (s, C8 and C12), 136.69 (s, C10), 130.61 (s, C3 and C5), 129.84 (s, C4), 128.66 (s, C9 and C11), 22.29 (s, C13 and C15), 21.38 (s, C14) ppm. **$^{11}B\{^1H\}$ NMR (193 MHz, CD_2Cl_2):** $\delta = 51.48$ (s, br) ppm. **$^{19}F\{^1H\}$ NMR (565 MHz, CD_2Cl_2):** $\delta = 17.53$ (s). **HRMS ESI (m/z):** no signal in negative and positive mode.

Synthesis and characterization of (2,6-$Mes_2C_6H_3)_2BH$ (12). A Schlenk tube is charged with **11** (656 mg, 1.00 mmol, 1.00 eq.) and $LiAlH_4$ (80.0 mg, 2.00 mmol, 2.00 eq.) and cooled with an ice bath to 0 °C. Diethylether (12 mL) is added slowly. The reaction mixture is stirred for 48 h. Then, the solvent is removed under reduced pressure and the residue is dried at 60 °C/$5{\cdot}10^{-3}$ mbar. The remaining solid is dissolved in THF (12 mL) and to this methyl iodide (0.20 mL, 3.22 mmol, 8.46 eq.) is added. During the addition effervescence is visible. After 1 h of stirring the solvent is removed under reduced pressure and the residual solid is dried at 80 °C/$5{\cdot}10^{-3}$ mbar. Afterwards *n*-hexane (12 mL) is added and the reaction mixture is warmed up to 60 °C and the suspension is filtered. The solvent is removed under reduced pressure to yield **12** as colourless solid (613 mg, 96 %).

^1H NMR (600 MHz, C_6D_6): $\delta = 6.97$ (t, $^3J(^1H{-}^1H) = 7.60$ Hz, 1H, H4), 6.87 (s, 4H, H9 and H11), 6.74 (d, $^3J(^1H{-}^1H) = 7.60$ Hz, 2H, H3 and H5), 2.19 (s, 6H, H14) 1.91 (s, 12H, H13 and H15) ppm. H6 is not visible in a range of −50 to +50 ppm, which might be due to extreme broadening and splitting of the signal. **$^{13}C\{^1H\}$ NMR (151 MHz, C_6D_6):** $\delta = 148.59$ (s, C2 and C6), 141.40 (s, C7), 136.30 (s, C8 and C12), 135.95 (s, C10), 131.04 (s, C4), 129.50 (s, C3 and C5), 128.83 (s, C9 and C11), 22.90 (s, C13 and C15), 21.21 (s, C14) ppm. **^{11}B NMR (193 MHz, C_6D_6):** $\delta = 74.27$ (s, br) ppm. **HRMS ESI (m/z):** no signal in negative and positive mode. **IR (ATR, neat):** (B–H) = 2580 (m) cm^{-1}.

Attempted Synthesis of [(2,6-$Mes_2C_6H_3)_2B$][$B(C_6F_5)_4$] from [$Me_3SiHSiMe_3$][$B(C_6F_5)_4$]. A Schlenk tube is charged with **11** (65.6 mg, 0.10 mmol, 1.00 eq.) and $[Me_3SiHSiMe_3][B(C_6F_5)_4]$ (82.6 mg, 0.10 mmol, 1.00 eq.) and cooled with an ice bath to 0 °C. Then, CH_2Cl_2 (4 mL) is slowly added to the solids. The solution is stirred for an hour and monitored by ^{19}F- and ^{11}B

© 2022 The Authors. European Journal of Inorganic Chemistry published by Wiley-VCH GmbH

EurJIC
European Journal of Inorganic Chemistry

Research Article
doi.org/10.1002/ejic.202200482

Chemistry Europe
European Chemical Societies Publishing

10990682c, 2023, 1, Downloaded from https://chemistry-europe.onlinelibrary.wiley.com/doi/10.1002/ejic.202200482 by Staats- und Universitätsbibliothek, Wiley Online Library on [20/06/2025]. See the Terms and Conditions (https://onlinelibrary.wiley.com/terms-and-conditions) on Wiley Online Library for rules of use; OA articles are governed by the applicable Creative Commons License

NMR spectroscopy. The solution is carefully layered with *n*-hexane (20 mL) to allow slow diffusion. The product **12** is obtained as a colourless crystalline solid (53.4 mg, 84%). The remaining oil is identified by means of ^{29}Si and ^{19}F NMR spectra as $[Me_3SiFSiMe_3][B(C_6F_5)_4]$.[18]

^{1}H NMR (600 MHz, C_6D_6): $\delta = 6.97$ (t, $^3J(^1H^{-1}H) = 7.60$ Hz, 1H, H4), 6.87 (s, 4H, H9 and H11), 6.74 (d, $^3J(^1H^{-1}H) = 7.60$ Hz, 2H, H3 and H5), 2.19 (s, 6H, H14) 1.91 (s, 12H, H13 and H15) ppm. H6 is not visible in a range of −50 to +50 ppm, which might be due to extreme broadening and splitting of the signal. **^{13}C{^{1}H} NMR (151 MHz, C_6D_6)**: $\delta = 148.59$ (s, C2 and C6), 141.40 (s, C7), 136.30 (s, C8 and C12), 135.95 (s, C10), 131.04 (s, C4), 129.50 (s, C3 and C5), 128.83 (s, C9 and C11), 22.90 (s, C13 and C15), 21.21 (s, C14) ppm. **^{11}B NMR (193 MHz, C_6D_6)**: $\delta = 74.27$ (s, br) ppm. **HRMS ESI (m/z)**: no signal in negative and positive mode. **IR (ATR, neat)**: $\tilde{\nu}$(B–H) = 2580 (m) cm^{-1}.

Attempted Synthesis of $[(Mes_2C_6H_3)_2B][B(C_6F_5)_4]$ from $[Me_3Si\cdot toluene][B(C_6F_5)_4]$ and $(Mes_2C_6H_3)_2BF$. $[Me_3SiHSiMe_3][B(C_6F_5)_4]$ (82.6 mg, 0.10 mmol, 1.00 eq.) is placed in a Schlenk tube. To this, toluene (2 mL) is added. After 2 hours the solvent of the suspension is removed under reduced pressure and (2,6-$Mes_2C_6H_3)_2BF$ (65.6 mg, 0.10 mmol, 1.00 eq.) is added. To this, 1,2-difluorobenzene (4 mL) is added and the reaction mixture is stirred for 18 hours at room temperature, leading to a dark brown solution. The solution is layered with *n*-hexane (20 mL). After complete diffusion the solvent is removed by decantation and the remaining solid is dried under reduced pressure. NMR spectra are measured in CD_2Cl_2.

^{1}H NMR (600 MHz, CD_2Cl_2): $\delta = 7.71$ (m), 7.62 (m), 7.49 (t, $^3J(^1H^{-1}H) = 7.58$ Hz, 2H), 7.16 (m), 7.12 (dd, $^3J(^1H^{-1}H) = 7.58$ Hz, $^4J(^1H^{-1}H) = 1.54$ Hz, 4H)*, 7.05 (s), 6.89 (s), 6.87 (s), 6.95 (s, 5H)*, 6.91 (t, $^4J(^1H^{-1}H) = 1.54$ Hz, 1H)*, 4.69 (s), 4.65 (s), 2.34 (s, 3H), 2.33 (s, 9H), 2.06 (s, 18H)*, 2.03 (m, 6H)* ppm. All signals marked with * are assigned to 2,6-$Mes_2C_6H_4$.

^{11}B{^{1}H} NMR (193 MHz, CD_2Cl_2): $\delta = 54.57$ (s), 41.10 (s), 28.39 (s), 25.90 (s), −16.63 (s) ppm.

Attempted Synthesis of $[(2,6\text{-}Mes_2C_6H_3)_2B][B(C_6F_5)_4]$ from $[Ph_3C][B(C_6F_5)_4]$ and $(Mes_2C_6H_3)_2BH$ (12). A Young NMR tube is charged with **12** (6.4 mg, 0.01 mmol, 1.00 eq.) and $[Ph_3C][B(C_6F_5)_4]$ (9.2 mg, 0.01 mmol, 1.00 eq.) and 1,2-$Cl_2C_6D_4$ (0.5 mL) is added. The reaction is monitored by means of ^{1}H-, ^{11}B- and ^{11}B-{^{1}H}-NMR spectroscopy. At room temperature and 60 degrees no reaction occurred. By heating to 80 °C over the course of 12 hours the starting material got completely consumed by means of ^{11}B-NMR spectroscopy and the solution turned deep brown. The ^{1}H-NMR spectrum reveals multiple $Mes_2C_6H_3$ species.

^{1}H NMR (600 MHz, $C_6D_4Cl_2$): $\delta = .7.84$ (t (br), 2H), 7.49 (t (br), 4H), 7.40 (t (br), 1H), 7.34 (s, 2H), 7.33 (s, 2H), 7.12 (t (br), 1H), 7.05 (d (br), 2H), 7.02 (d (br), 2H), 6.81 (s, 4H), 6.72 (s, 1H), 2.24 (s, 10H), 2.02 (s, 16H) ppm. Due to broadness of the signals no coupling constants could be measured. For Integration, the signal with the lowest integral in the aromatic region was chosen and set to an Integral of ^{1}H. **^{11}B{^{1}H} NMR (193 MHz, CD_2Cl_2)**: $\delta = -16.19$ ($B(C_6F_4)^-$) ppm. No further signal in the range of +200 to −200 ppm visible.

Attempted Synthesis of $[(2,6\text{-}Mes_2C_6H_3)_2B][AlCl_4]$ from $(2,6\text{-}Mes_2C_6H_3)_2BF$ (11). A Schlenk tube is charged with **12** (65.6 mg, 0.10 mmol, 1.00 eq.) and $AlCl_3$ (133 mg, 1.00 mmol, 10.0 eq.). Then, CH_2Cl_2 (4 mL) is added. After stirring for 18 hours at room temperature, a dark red solution is obtained. The solution is layered with *n*-hexane (20 mL). After complete diffusion $Mes_2C_6H_3BCl_2$ (**13**) is obtained as a crystalline solid (19.2 mg, 48%). The analytical data is according to the literature.[14]

Any attempts to isolate the corresponding aluminium compound led to a mixture of undefined and insoluble products.

Attempted Synthesis of $[(2,6\text{-}Mes_2C_6H_3)_2B][EtAlCl_3]$. A Schlenk tube is charged with 12 (118 mg, 0.18 mmol, 1.00 eq.). Then, CH_2Cl_2 (4 mL) is added. The solution is cooled down to −78 °C and $EtAlCl_2$ (2.0 mL, 1.80 mmol, 10.0 eq.) is added. After stirring for 18 hours at room temperature, a dark brown solution is obtained. The solvent is removed under reduced pressure and the residue is washed several times with *n*-hexane to remove excess $EtAlCl_2$. The remaining solid is dissolved in CH_2Cl_2 (4 mL) crashed out by addition of *n*-hexane (20 mL). The solvent is decanted of and the residue is dried under reduced pressure to obtain a dark brown oil which was analysed by NMR spectroscopy in CD_2Cl_2.

All attempts to grow crystals suitable for X-ray diffraction measurements from the different solvents (CH_2Cl_2/*n*-hexane, 1,2-difluorobenzene/*n*-hexane, hot toluene, CH_2Cl_2/toluene) failed.

Synthesis and characterization of $[(Mes_2C_6H_3)_2In][B(C_6F_5)_4]$ (4). A Schlenk tube is charged with $(2,6\text{-}Mes_2C_6H_3)_2InBr$ (82.0 mg, 0.10 mmol, 1.00 eq.) and $K[B(C_6F_5)_4]$ (71.8 mg, 0.10 mmol, 1.00 eq.). Then, CH_2Cl_2 (4 mL) is added. After stirring for 30 minutes at 20 °C the solution is layered with *n*-hexane (20 mL). After complete diffusion the solvent is removed by decantation and the remaining solid is dried under reduced pressure to yield 4 as orange crystalline solid (129 mg, 91%).

^{1}H NMR (600 MHz, CD_2Cl_2): $\delta = 7.61$ (t, $^3J(^1H^{-1}H) = 7.59$ Hz, 1H, H4), 7.25 (d, $^3J(^1H^{-1}H) = 7.59$ Hz, 2H, H3 and H5), 7.06 (s, 4H, H9 and H11), 2.30 (s, 6H, H14), 1.73 (s, 12H, H13 and H15) ppm. **^{13}C{^{1}H} NMR (151 MHz, CD_2Cl_2)**: $\delta = 156.92$ (s, C1), 147.49 (s, C2 and C6), 140.95 (s, C10), 139.92 (s, C7), 136.56 (s, C8 and C12), 134.01 (s, C4), 130.90 (s, C9 and C11), 129.16 (s, C3 and C5), 21.53 (s, C13 and C15), 21.40 (s, C14) ppm. **^{11}B{^{1}H} NMR (193 MHz, CD_2Cl_2)**: δ =-16.65 (s) ppm. **^{19}F NMR (565 MHz, CD_2Cl_2)**: $\delta = -133.39$ (s), −163.76 (t, $^3J(^{19}F^{-19}F) = 20.37$ Hz), −167.59 (t, $^3J(^{19}F^{-19}F) = 17.77$ Hz) ppm. **HRMS ESI (m/z)**: $[M]^+$ calculated. for $C_{48}H_{50}In$, 741.29458; found, 741.29441. **UV-VIS (DCM, 100 μM)**: λ(abs) = 435 nm.

X-ray diffraction studies

Single crystals of **4**, **10** and **13** were grown by slow diffusion of n-hexane into CH_2Cl_2 solutions. Single crystals of **11** and **12** were grown by crystallization from hot *n*-hexane. Single crystal X-ray diffraction data were collected at 100 K using an open flow nitrogen stream on a Bruker Venture D8 diffractometer

© 2022 The Authors. European Journal of Inorganic Chemistry published by Wiley-VCH GmbH

EurJIC
European Journal of Inorganic Chemistry

Research Article
doi.org/10.1002/ejic.202200482

Chemistry Europe
European Chemical Societies Publishing

10990682, 2023, 1, Downloaded from https://chemistry-europe.onlinelibrary.wiley.com/doi/10.1002/ejic.202200482 by Staats- und Universitätsbibliothek, Wiley Online Library on [20/06/2023]. See the Terms and Conditions (https://onlinelibrary.wiley.com/terms-and-conditions) on Wiley Online Library for rules of use; OA articles are governed by the applicable Creative Commons License

with a Photon 100 detector in shutterless mode using a microfocus source (Mo$K\alpha$ = 0.71073 Å). All structures were solved using the dual-space algorithm in ShelXT[31] and refined against F^2 with the use of SHELXL[31] (Independent Atom Model – IAM) within the WinGX[32] and OLEX2[33] program package. All non-hydrogen atoms were refined using anisotropic displacement parameters. Hydrogen atoms were located from the Fourier difference map and had their positions and isotropic displacement parameter refined freely. Crystal and refinement data are collected in Table S1.

The geometry of **12** obtained from the IAM provided the initial model used as input for a subsequent Hirshfeld Atom Refinement (HAR)[22] performed using the Gaussian-HAR method with the lamaGOET[34] interface at the B3LYP/def2-TZVP level of theory. A surrounding self-consistent cluster charge field of 8 Å radius around the central formula unit was used in the iterative quantum chemical calculation step in order to simulate the crystal environment influence over the theoretical electron densities. HAR was performed against F using a merged set of reflections, whereby negative $|F|^2$ reflections, $|F| < 4.0$ sigma($|F|$) and all systematic absences were pruned. All H atoms were refined freely and anisotropically within HAR. Ortep-type figures were created using DIAMOND.[35]

Deposition Numbers 2177924 (for **4**), 2177925 (for **10**), 2177926 (for **11**), 2177927 (for **12**), and 2177928 (for **13**) contain the supplementary crystallographic data for this paper. These data are provided free of charge by the joint Cambridge Crystallographic Data Centre and Fachinformationszentrum Karlsruhe Access Structures service www.ccdc.cam.ac.uk/structures.

Computational Studies

Starting from the solid-state molecular geometries density functional theory (DFT) computations were performed in the gas-phase at the B3PW91/6-311+G(2df,p)[36] level of theory using Gaussian09.[37] For the In and Tl atoms, effective core potentials (ECP28MDF, ECP60MDF)[38] and corresponding cc-pVTZ basis set[38] were utilized. Dispersion was taken account for by the empirical dispersion correction of Grimme.[39] Subsequent normal mode analysis had to be skipped as it exceeded computational capacities. The wavefunction files were used for a topological analysis of the electron density according to the Atoms-In-Molecules space-partitioning scheme[8] using AIM2000,[40] whereas DGRID[41] was used to generate and analyze the Electron-Localizability-Indicator (ELI–D)[10] related real-space bonding descriptors applying a grid step size of 0.05 a.u. (0.12 a.u. for visualization). The NCI[9] grids were computed with NCIplot (0.1 a.u. grids).[42] Bond paths are displayed with AIM2000, ELI–D and NCI figures are displayed with MolIso,[43] AIM provides a bond paths motif, which resembles and exceeds the Lewis picture of chemical bonding, disclosing all types and strengths of interactions. Additionally, it provides atomic volumes and charges. Analyses of the reduced density gradient, $s(\mathbf{r}) = [1/(3\pi^2)^{1/3}]|\nabla\rho|/\rho^{4/3}$, according to the NCI method is used to visualize non-covalent bonding aspects. An estimation of different non-covalent contact types according to steric/repulsive ($\lambda_2 > 0$), van der Waals-like ($\lambda_2 \approx 0$), and attractive ($\lambda_2 < 0$) is facilitated by mapping the ED times the sign of the second eigenvalue of the Hessian (sign(λ_2)ρ) on the *iso*-surfaces of s(**r**). AIM and NCI are complemented by the ELI–D, which provides electron populations and volumes of bonding and lone-pair basins and is especially suitable for the analysis of (polar-)covalent bonding aspects.

Acknowledgements

The Deutsche Forschungsgemeinschaft (DFG) is gratefully acknowledged for financial support. Open Access funding enabled and organized by Projekt DEAL.

Conflict of Interest

The authors declare no conflict of interest.

Data Availability Statement

The data that support the findings of this study are available from the corresponding author upon reasonable request.

Keywords: Boron · Indium · Indinium cations · Lewis acids · Superacids

[1] a) W. E. Piers, S. C. Bourke, K. D. Conroy, *Angew. Chem. Int. Ed.* **2005**, *44*, 5016–5036; *Angew. Chem.* **2005**, *117*, 5142–5163; b) X. Tan, H. Wang, *Chem. Soc. Rev.* **2022**, *51*, 2583–2600.
[2] S. Dagorne, D. A. Atwood, *Chem. Rev.* **2008**, *108*, 4037–4071.
[3] Y. Shoji, N. Tanaka, K. Mikami, M. Uchiyama, T. Fukushima, *Nat. Chem.* **2014**, *6*, 498–503.
[4] J. D. Young, M. A. Khan, R. J. Wehmschulte, *Organometallics* **2004**, *23*, 1965–1967.
[5] R. J. Wehmschulte, J. M. Steele, J. D. Young, M. A. Khan, *J. Am. Chem. Soc.* **2003**, *125*, 1470–1471.
[6] S. U. Ahmad, J. Beckmann, *Organometallics* **2009**, *28*, 6893–6901.
[7] a) I. Peckermann, D. Robert, U. Englert, T. P. Spaniol, J. Okuda, *Organometallics* **2008**, *27*, 4817–4820; b) F. Gahlmann, B. Neumüller, *Z. Anorg. Allg. Chem.* **1994**, *620*, 847–850.
[8] R. W. F. Bader, *Atoms in Molecules: A Quantum Theory* (Cambridge University Press: Oxford U. K., **1991**).
[9] E. R. Johnson, S. Keinan, P. Mori-Sanchez, J. Contreras-García, A. J. Cohen, W. Yang, *J. Am. Chem. Soc.* **2010**, *132*, 6498–6506.
[10] M. Kohout, F. R. Wagner, Y. Grin, *Theor. Chem. Acc.* **2008**, *119*, 413–420.
[11] M. Olaru, D. Duvinage, E. Lork, S. Mebs, J. Beckmann, *Chem. Eur. J.* **2019**, *25*, 14758–14761.
[12] M. Olaru, D. Duvinage, S. Mebs, J. Beckmann, *Angew. Chem. Int. Ed.* **2018**, *57*, 10080–10084; *Angew. Chem.* **2018**, *130*, 10237–10241.
[13] K. Ruhlandt-Senge, J. J. Ellison, R. J. Wehmschulte, F. Pauer, P. P. Power, *J. Am. Chem. Soc.* **1993**, *115*, 11353–11357.
[14] W. J. Gribsy, P. P. Power, *J. Am. Chem. Soc.* **1996**, *118*, 7981–7988.
[15] a) A. G. Massey, A. J. Park, *J. Organomet. Chem.* **1964**, *2*, 245–250; b) M. Kuprat, M. Lehmann, A. Schulz, A. Villinger, *Organometallics* **2010**, *29*, 1421–1427.
[16] J. F. Kögel, A. Y. Timoshkin, A. Schröder, E. Lork, J. Beckmann, *Chem. Sci.* **2018**, *9*, 8178–8183.
[17] J. B. Lambert, S. Zhang, S. M. Ciro, *Organometallics* **1994**, *13*, 2430–2443.

© 2022 The Authors. European Journal of Inorganic Chemistry published by Wiley-VCH GmbH

EurJIC
European Journal of Inorganic Chemistry

Research Article
doi.org/10.1002/ejic.202200482

Chemistry Europe
European Chemical Societies Publishing

10990682c, 2023, 1, Downloaded from https://chemistry-europe.onlinelibrary.wiley.com/doi/10.1002/ejic.202200482 by Staats- und Universitätsbibliothek, Wiley Online Library on [20/06/2023]. See the Terms and Conditions (https://onlinelibrary.wiley.com/terms-and-conditions) on Wiley Online Library for rules of use; OA articles are governed by the applicable Creative Commons License

[18] M. Lehmann, A. Schulz, A. Villinger, *Angew. Chem. Int. Ed.* **2009**, *48*, 7444–7447; *Angew. Chem.* **2009**, *121*, 7580–7583.
[19] R. J. Wehmschulte, A. A. Diaz, M. A. Kahn, *Organometallics* **2003**, *22*, 83–92.
[20] J. C. W. Chien, W.-M. Tsai, M. D. Rausch, *J. Am. Chem. Soc.* **1991**, *113*, 8570–8571.
[21] S. M. Cornet, K. B. Dillon, C. D. Entwistle, M. A. Fox, A. E. Goeta, H. P. Goodwin, T. B. Marder, A. L. Thompson, *Dalton Trans.* **2003**, 4395–4405.
[22] a) D. Jayatilaka, B. Dittrich, *Acta Crystallogr.* **2008**, *A64*, 383–393; b) S. C. Capelli, H.-B. Bürgi, B. Dittrich, S. Grabowsky, D. Jayatilaka, *IUCrJ* **2014**, *1*, 361–379.
[23] M. Woińska, S. Grabowsky, P. M. Dominiak, K. Woźniak, D. Jayatilaka, *Sci. Adv.* **2016**, *2*, e1600192.
[24] F. Kleemiss, O. V. Dolomanov, M. Bodensteiner, N. Peyerimhoff, L. Midgley, L. J. Bourhis, A. Genoni, L. A. Malaspina, D. Jayatilaka, J. L. Spencer, F. White, B. Grundkötter-Stock, S. Steinhauer, D. Lentz, H. Puschmann, S. Grabowsky, *Chem. Sci.* **2021**, *12*, 1675–1692.
[25] E. Damgaard-Møller, L. Krause, H. Lassen, L. A. Malaspina, S. Grabowsky, H. Bamberger, J. McGuire, H. N. Miras, S. Sproules, J. Overgaard, *Inorg. Chem.* **2020**, *59*, 13190–13200.
[26] X.-W. Li, G. H. Robinson, W. T. Pennington, *Main Group Chem.* **1996**, *1*, 301–307.
[27] P. Romanato, S. Duttwyler, A. Linden, K. K. Baldridge, J. S. Siegel, *J. Am. Chem. Soc.* **2010**, *132*, 7828–7829.
[28] a) H. D. Hausen, K. Mertz, J. Weidlein, W. Schwarz, *J. Organomet. Chem.* **1975**, *93*, 291–296; b) K. Hoffmann, E. Weiss, *J. Organomet. Chem.* **1973**, *50*, 17–24; c) B. Cordero, V. Gómez, A. E. Platero-Prats, M. Revés, J. Echeverria, E. Cremades, F. Barragán, S. Alvarez, *Dalton Trans.* **2008**, *21*, 2832–2838.
[29] S. Raub, G. A. Jansen, *Theor. Chem. Acc.* **2001**, *106*, 223–232.
[30] P. Erdmann, J. Leitner, J. Schwarz, L. Greb, *ChemPhysChem* **2020**, *21*, 987–994.
[31] G. M. Sheldrick, *Acta Crystallogr.* **2015**, *C71*, 3–8.
[32] L. J. Farrugia, *J. Appl. Crystallogr.* **2012**, *45*, 849–854.
[33] O. V. Dolomanov, L. J. Bourhis, R. J. Gildea, J. A. Howard, H. Puschmann, *J. Appl. Crystallogr.* **2009**, *42*, 339–341.
[34] L. A. Malaspina, A. Genoni, S. Grabowsky, *J. Appl. Crystallogr.* **2021**, *54*, 987–995.
[35] K. Brandenburg, *Diamond*, Version 4.0.4, Crystal Impact GbR: Bonn, Germany, **2012**.
[36] a) A. D. Becke, *J. Chem. Phys.* **1993**, *98*, 5648–5652; b) J. P. Perdew, J. A. Chevary, S. H. Vosko, K. A. Jackson, M. R. Pederson, D. J. Singh, C. Fiolhais, *Phys. Rev.* B **1992**, *46*, 6671–6687.
[37] M. J. Frisch, G. W. Trucks, H. B. Schlegel, G. E. Scuseria, M. A. Robb, J. R. Cheeseman, G. Scalmani, V. Barone, G. A. Petersson, H. Nakatsuji, X. Li, M. Caricato, A. V. Marenich, J. Bloino, B. G. Janesko, R. Gomperts, B. Mennucci, H. P. Hratchian, J. V. Ortiz, A. F. Izmaylov, J. L. Sonnenberg, D. Williams-Young, F. Ding, F. Lipparini, F. Egidi, J. Goings, B. Peng, A. Petrone, T. Henderson, D. Ranasinghe, V. G. Zakrzewski, J. Gao, N. Rega, G. Zheng, W. Liang, M. Hada, M. Ehara, K. Toyota, R. Fukuda, J. Hasegawa, M. Ishida, T. Nakajima, Y. Honda, O. Kitao, H. Nakai, T. Vreven, K. Throssell, J. A. Montgomery, Jr., J. E. Peralta, F. Ogliaro, M. J. Bearpark, J. J. Heyd, E. N. Brothers, K. N. Kudin, V. N. Staroverov, T. A. Keith, R. Kobayashi, J. Normand, K. Raghavachari, A. P. Rendell, J. C. Burant, S. S. Iyengar, J. Tomasi, M. Cossi, J. M. Millam, M. Klene, C. Adamo, R. Cammi, J. W. Ochterski, R. L. Martin, K. Morokuma, O. Farkas, J. B. Foresman, D. J. Fox, Gaussian, Inc., Wallingford CT, **2016**.
[38] a) K. A. Peterson, *J. Chem. Phys.* **2003**, *119*, 11099; b) K. A. Peterson, D. Figgen, E. Goll, H. Stoll, M. Dolg, *J. Chem. Phys.* **2003**, *119*, 11113–11123.
[39] S. Grimme, J. Anthony, S. Ehrlich, H. Krieg, *J. Chem. Phys.* **2010**, *132*, 154104.
[40] F. Biegler-König, J. Schönbohm, D. Bayles, *J. Comput. Chem.* **2001**, *22*, 545–559.
[41] M. Kohout, *DGRID*-4.6 Radebeul, **2015**.
[42] J. Contreras-García, E. Johnson, S. Keinan, R. Chaudret, J.-P. Piquemal, D. Beratan, W. Yang, *J. Chem. Theory Comput.* **2011**, *7*, 625–632.
[43] C. B. Hübschle, P. Luger, *J. Appl. Crystallogr.* **2006**, *39*, 901–904.

Manuscript received: July 27, 2022
Revised manuscript received: August 17, 2022
Accepted manuscript online: August 19, 2022

© 2022 The Authors. European Journal of Inorganic Chemistry published by Wiley-VCH GmbH

2.7 Heavier Bis(*m*-terphenyl)element Phosphaethynolates of Group 13

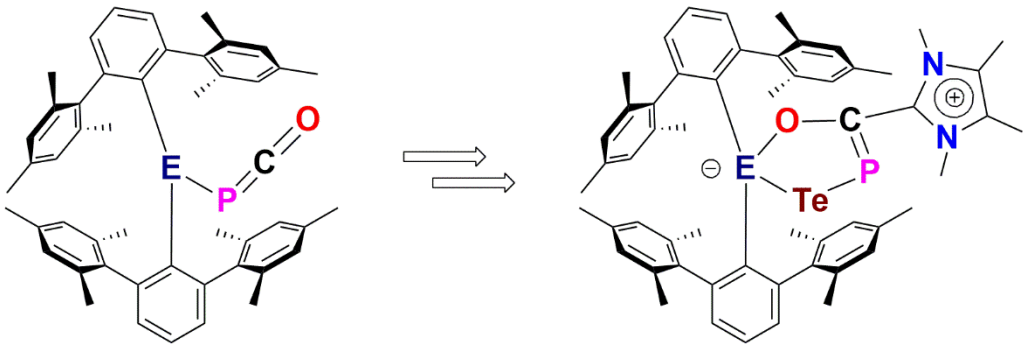

2.7.1 Synopsis

The phosphaethynolate ion PCO^- is of ambiphilic nature, similar to its lighter homologue the cyanate ion. The ambiphilicity can be described by its mesomeric forms.

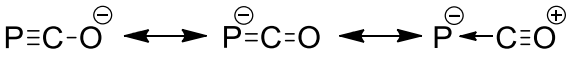

Scheme 17. Mesomeric forms of the phosphaethynolate anion.

This implies it can coordinate *via* the oxygen atom forming oxyphosphaalkene compounds (M-OCP) or by phosphorus, forming phosphaketenes (M-PCO). In accordance with the HSAB concept, the coordination pattern is dependent on the metal center, if it is hard and highly electropositive or soft and easily polarisable. Regarding the possible coordination, especially the coordination of the metal by the phosphorus atom exhibits a unique property, as it can be described as a phosphinidene stabilized by carbon monoxide (**Scheme 16**, right). Upon irradiation with UV-A light (λ = 365 nm), the phosphorus carbon bond is cleaved forming a phosphinidene and carbon monoxide.

Due to the sheer variety of bis(*m*-terphenyl)element halides that were synthesized in this thesis, the reaction of bis(*m*-terphenyl)indium bromide with sodium phosphaethynolate (NaOCP) was attempted, providing bis(*m*-terphenyl)indium phosphaethynolate. By this result, also the lighter bis(*m*-terphenyl)element halides of group 13 were synthesized, from which bis(*m*-terphenyl)gallium chloride reacted with sodium phosphaethynolate providing an isolable bis(*m*-terphenyl)gallium phosphaethynolate. These phosphaethynolates were tested regarding their

reactivity. Upon irradiation with UV-light, phosphinidenes as low valent species were formed, but reacted quickly under unselective decomposition. Because of this, the phosphaethynolates were reacted with a N-heterocyclic carbene, namely 1,2,3,4-tetramethylimidazolin-2-ylidene IMe_4, attempting to trap the formed phosphinidene. This led to the coordination of the NHC on the carbon atom of the phosphaethynolate unit, visible by NMR spectroscopy and single crystal X-ray diffraction experiments. Because of the natural electron vacancy of group 13 elements, the phosphaethynolate became bidentate and coordinates to the metal center *via* phosphorus and oxygen. The NHC adducts are stable towards irradiation with UV light, which can be attributed to the bidentate behaviour of the PCO entity. Furthermore, the reaction of the formed heterocycles with chalcogenes was investigated, from which tellurium selectively formed stable compounds, which was indicated by ^{31}P NMR spectroscopy. By single crystal X-ray diffraction experiments the insertion of tellurium in the E-P bond is visible forming an ETePCO heterocycle. The ionic character of the E-P and E-O bonds was studied by DFT calculation and showed that the ionicity is drastically reduced by coordination of the NHC to the PCO unit.

2.7.2 Scientific Contribution

In this project I developed and fully characterized the synthesis of the bis(*m*-terphenyl)indium phosphaethynolate. Under my supervision M. Janßen developed the synthesis of the gallium compound and the NHC adducts and fully characterized them during his master thesis. I co-wrote the publication and contributed the X-ray crystallographic part together with E. Lork. H. Grützmacher co-wrote the publication. S. Mebs provided the theoretical calculations and J. Beckmann was the principal investigator and co-wrote the publication.

Percentage of my contribution of the total workload:

Experimental concept and design: ca. 90%, experimental work and acquisition of experimental data: ca. 50%, data analysis and interpretation: ca. 80%, preparation of figures and tables: ca. 80%, drafting of the manuscript: ca. 50%.

The article was published in the journal “Dalton Transactions“ in 2022 as an article:

Daniel Duvinage, Marvin Janssen, Enno Lork, Hansjörg Grützmacher, Stefan Mebs*, Jens Beckmann*, *Dalton Trans.* **2022**, *51*, 7622-7629.

DOI: 10.1039/D2DT00907B

The Supporting Information includes experimental procedures, NMR data, X-ray crystallographic data and structure refinement and computational data and is available free of charge on the journal′s website:

https://www.rsc.org/suppdata/d2/dt/d2dt00907b/d2dt00907b2.pdf

Dalton Transactions

ROYAL SOCIETY OF CHEMISTRY

PAPER

View Article Online
View Journal | View Issue

Check for updates

Cite this: *Dalton Trans.*, 2022, **51**, 7622

Heavier bis(*m*-terphenyl)element phosphaethynolates of group 13†

Daniel Duvinage, ‡[a] Marvin Janssen, ‡[a] Enno Lork, [a] Hansjörg Grützmacher, [b] Stefan Mebs *[c] and Jens Beckmann *[a]

Received 24th March 2022,
Accepted 27th April 2022

DOI: 10.1039/d2dt00907b

rsc.li/dalton

The synthesis and reactivity of the heavier group 13 phosphaketene complexes (2,6-$Mes_2C_6H_3)_2$EPCO (**1**, E = Ga; **2**, E = In) were reported. The reaction of **1** and **2** with 1,2,3,4-tetramethylimidazolin-2-ylidene, IMe_4, gave rise to the formation of (2,6-$Mes_2C_6H_3)_2$EP(O)C(IMe_4) (**3**, E = Ga; **4** E = In; Mes = mesityl). Subsequent addition of elemental tellurium proceeded *via* insertion into the E–P bond and provided (2,6-$Mes_2C_6H_3)_2$ETeP(O)C(IMe_4) (**5**, E = Ga; **6**, E = In) comprising five-membered ETePCO-heterocycles. Compounds **1–6** were fully characterized by X-ray crystallography and heteronuclear NMR spectroscopy. The electronic structures of **1–6** were studied by DFT calculations and analyses of a complementary set of real-space bonding indicators (AIM, ELI-D, NCI) derived from the electron and pair densities, with focus on the bond characteristics of the PCO fragment.

Published on 28 April 2022. Downloaded by Universitat Bremen on 6/19/2023 6:36:17 AM.

Introduction

The coordination chemistry of the phosphaethynolate ion, $[PCO]^-$, now covers a great number of different elements across the periodic table.[1,2] Due to its ambiphilic nature it may coordinate *via* the phosphorus or oxygen atoms to give rise to either metal phosphaketene complexes, M–P=C=O or oxyphosphaalkyne complexes M–O–C≡P, respectively.[3] In group 13, the lighter and harder elements boron and aluminum seem to prefer the coordination *via* oxygen,[4–6] whereas heavier and softer gallium apparently favors phosphorus; that is the HSAB principle applies in this case.[6,7] However, reference data from group 13 is still very scarce, which holds particularly true for organometallic species of the heavier elements. There are only very few inorganic gallium species **I** and **II** in the literature, in which the inherent Lewis acidity was compensated by donor ligands (Scheme 1).[6,7]

In this work, we describe bis(*m*-terphenyl)gallium and -indium phosphaethynolates, ($Mes_2C_6H_3)_2$EPCO (**1**, E = Ga; **2** E = In), in which the group 13 elements are tricoordinate. The reaction of **1** and **2** with an N-heterocyclic carbene (NHC), namely, 1,2,3,4-tetramethylimidazolin-2-ylidene, IMe_4, afforded the complexes ($Mes_2C_6H_3)_2$EP(O)C(IMe_4) (**3**, E = Ga; **4**, E = In), which are reminiscent of the recently reported group 15 complexes $Ph_2E(I^iPr_2Me_2)PCO$ (E = Sb, Bi; $I^iPr_2Me_2$ = 1,3-diisopropyl-4,5-dimethylimidazolin-2-ylidene).[8] The reaction of **3** and **4** with tellurium powder occurred with insertion into the E–P bonds affording (2,6-$Mes_2C_6H_3)_2$ETeP(O)C(IMe_4) (**5**, E = Ga; **6**, E = In; Mes = mesityl) possessing unprecedented five-membered ETePCO-ring structures. Extended density functional theory (DFT) calculations on the target molecules were conducted to extract energetic differences between different PCO coordination modes (phosphaketene *vs.* oxyphosphaalkyne), PCO dissociation energies, as well as electronic bond characteristics of the PCO-fragment within its different chemical environments. The latter is based on analysis of the calculated electron and electron pairs densities and derived real-space bonding indicators (RSBI).

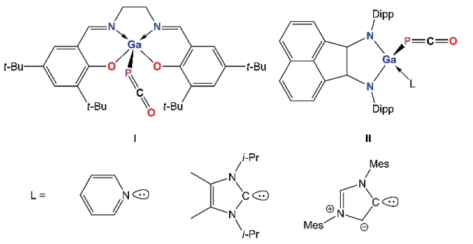

Scheme 1 Examples of known inorganic gallium phosphaethynolates.[6,7]

[a]*Institut für Anorganische Chemie und Kristallographie, Universität Bremen, Leobener Straße 7, 28359 Bremen, Germany. E-mail: j.beckmann@uni-bremen.de*
[b]*Department of Chemistry and Applied Biosciences, ETH Zürich, Vladimir-Prelog Weg 1, Hönggerberg, 8093 Zürich, Switzerland*
[c]*Institut für Experimentalphysik, Freie Universität Berlin, Arnimallee 14, 14195 Berlin, Germany. E-mail: stefan.mebs@fu-berlin.de*

† Electronic supplementary information (ESI) available: Experimental data, NMR spectra; crystal and refinement data; computational details (PDF, XYZ). CCDC 2105254–2105259. For ESI and crystallographic data in CIF or other electronic format see DOI: https://doi.org/10.1039/d2dt00907b

‡ These authors contributed equally to this work.

This journal is © The Royal Society of Chemistry 2022

View Article Online
Dalton Transactions Paper

Published on 28 April 2022. Downloaded by Universitat Bremen on 6/19/2023 6:36:17 AM.

Results and discussion

Synthesis and characterization

The salt metathesis reaction of the bis(*m*-terphenyl)element halides, $(2,6\text{-}Mes_2C_6H_3)_2GaCl$[9] and $(2,6\text{-}Mes_2C_6H_3)_2InBr$,[10] with solvated sodium phosphaethynolate, [Na(1,4-dioxane)$_{2.5}$][PCO],[11] provided the bis(*m*-terphenyl)element-phosphaethynolates, $(2,6\text{-}Mes_2C_6H_3)_2EPCO$ (**1**, E = Ga; **2**, E = In), as yellow solids in yields of 82 and 83%, respectively (Scheme 2).

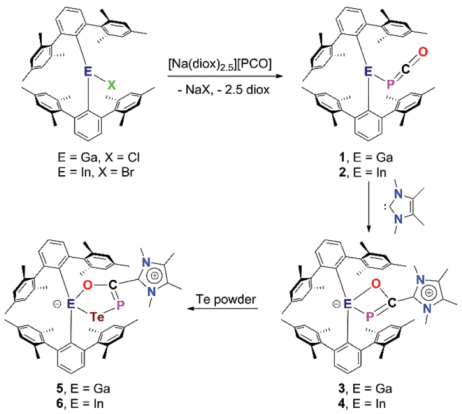

Scheme 2 Synthesis of **1**–**6**.

Efforts were made to obtain also lighter bis(*m*-terphenyl) element phosphaethynolates of group 13, however, the treatment of $(2,6\text{-}Mes_2C_6H_3)_2BF$ with [Na(1,4-dioxane)$_{2.5}$][PCO] gave no reaction, even under forcing conditions, whereas the reaction of $(2,6\text{-}Mes_2C_6H_3)_2AlCl$ with [Na(1,4-dioxane)$_{2.5}$][PCO] gave multiple products that could not be separated. In solution, **1** and **2** are characterized by ^{31}P NMR chemical shifts (C_6D_6) of δ = −283.3 and δ = −336.2 ppm, which accounts for less shielding compared to the free $[PCO]^-$ ion in water (δ = −396.4 ppm)[12] and the salen gallium phosphaethynolate **I** (δ = −376.9 ppm).[7] The ^{13}C NMR resonance of the PCO-moiety of **1** (186.5 ppm) and **2** (182.7 ppm) as well as the related $^1J(^{31}P\text{–}^{13}C)$ coupling of **1** (99.8 Hz) and **2** (96.0 Hz) are fully consistent with the phosphaketene coordination mode.[3] The molecular structures of **1** and **2** reveal the phosphaketene coordination mode, *e.g. via* Ga–P and In–P bonds (Fig. 1). Typically, the M–P–C angles are *ca.* 90° and the P–C–O angle is nearly 180°. The coordination mode is consistent with asymmetric PCO stretching vibration observed in the IR spectra of **1** and **2** at 1898 and 1880 cm^{-1}. The Ga–P and In–P bond lengths of **1** (2.361(1) Å) and **2** (2.573(1) Å) are close to the sum of the covalent radii (2.35 Å and 2.53 Å). The P–C bond length of **1** (1.567(5) Å) is significantly shorter than in **2** (1.636(2) Å), whereas in turn, the C–O bond length of **1** (1.224(5) Å) is significantly longer than in **2** (1.174(2) Å).

The reaction of **1** and **2** with a small NHC, namely, 1,2,3,4-tetramethylimidazolin-2-ylidene, IMe_4,[13] produced the complexes $(2,6\text{-}Mes_2C_6H_3)_2EP(O)C(IMe_4)$ (**3**, E = Ga; **4**, E = In), as

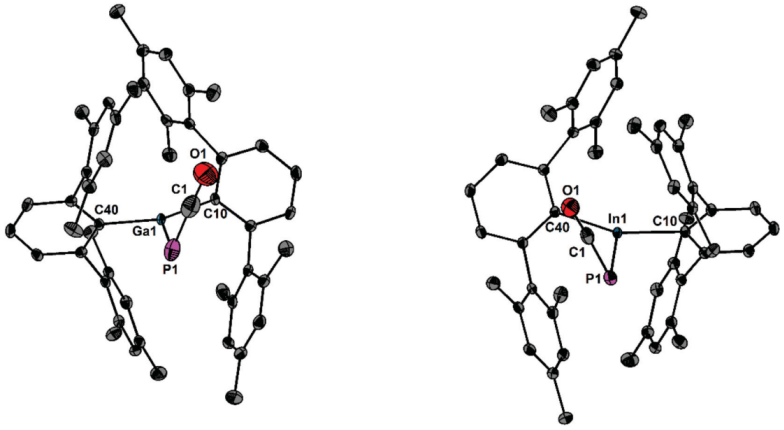

Fig. 1 Molecular structures of **1** (left) and **2** (right) showing 50% probability ellipsoids and the essential numbering scheme. Hydrogen atoms are omitted. Selected bond parameters of **1** [Å, °]: Ga1–P1 2.361(1), Ga1–C10 2.004(3), Ga1–C40 2.005(3), P1–C1 1.567(5), C1–O1 1.224(5), P1–Ga1–C10 111.76(8), P1–Ga1–C40 106.51(8), C10–Ga1–C40 141.7(1), C1–P1–Ga1 87.8(2), O1–C1–P1 175.5(4). Selected bond parameters of **2** [Å, °]: In1–P1 2.573(1), In1–C10 2.183(1), In1–C40 2.189(1), P1–C1 1.636(2), C1–O1 1.174(2), P1–In1–C10 105.28(4), P1–In1–C40 110.56(3), C10–In1–C40 144.14 (5), C1–P1–In1 85.76(6), O1–C1–P1 176.0(2).

View Article Online
Paper Dalton Transactions

Published on 28 April 2022. Downloaded by Universitat Bremen on 6/19/2023 6:36:17 AM.

yellow solids in 73 and 71% yield, respectively (Scheme 2). The IMe_4 attacks at the carbon atom of the phosphaethynolate moieties rather than Lewis acidic gallium and indium atoms.[8] The overall structural motif of **3** and **4** resembles those of the recently reported group 15 complexes $Ph_2E(I^iPr_2Me_2)PCO$ (E = Sb, Bi; $I^iPr_2Me_2$ = 1,3-diisopropyl-4,5-dimethylimidazolin-2-ylidene).[8] The formation of **3** and **4** is accompanied by a large change of the ^{31}P NMR resonances by more than 500 ppm and the ^{31}P NMR spectra (CD_2Cl_2) of **3** and **4** show signals at δ = 245.4 and 219.7 ppm. The molecular structures of **3** and **4** are shown in Fig. 2.

The P–C–O linkages now adopt acute angles to accommodate the 4-membered chelate rings containing gallium and indium atoms. Compared to **1** and **2**, the Ga–P bond length of **3** (2.406(2) Å) increased slightly, whereas the In–P bond length **4** (2.554(3) Å) slightly decreased. The Ga–O and In–O bond lengths of **3** (1.999(3) Å) and **4** (2.222(5) Å) are slightly longer than the sum of covalence radii (1.87 and 2.05 Å).[14] The bidentate coordination mode is in slight contrast to those of the group 15 complexes $Ph_2E(I^iPr_2Me_2)PCO$ (E = Sb, Bi; $I^iPr_2Me_2$ = 1,3-diisopropyl-4,5-dimethylimidazolin-2-ylidene), in which the oxygen atoms neither bond to antimony nor bismuth.[8] The C–C bond lengths that define the coordination of the NHCs to the PCO moieties of **3** (1.489(6) Å) and **4** (1.462(8) Å) are somewhat shorter than those of $Ph_2E(I^iPr_2Me_2)PCO$ for E = Sb (1.529(7) Å) and E = Bi (1.515(1) Å), which is tentatively attributed to stronger C–C bonding in the former complexes.

The reaction of **3** and **4** towards chalcogens was investigated, which gave sole products only for tellurium, which inserted in the Ga–P and In–P bonds giving rise to the formation of the products $(2,6\text{-}Mes_2C_6H_3)_2ETeP(O)C(IMe_4)$ (**5**, E = Ga; **6**, E = In) that were isolated as red and orange solids in 80 and 81% yield, respectively (Scheme 2). The reaction of **3** and **4** with sulfur provided a product mixture that gave rise to ^{31}P NMR spectra with more than five signals in each case. The reaction of **3** and **4** with red selenium resulted in reaction mixtures that showed only one ^{31}P NMR signal at δ = 173.5 and 202.4 ppm, respectively. Both signals showed satellites indicating $^1J(^{77}Se–^{31}P)$ couplings of 418 and 389 Hz, respectively. No ^{77}Se NMR signals were observed. ^1H and ^{13}C NMR spectra showed several sets of signals (in different integral ratios). All attempts to isolate pure products by fractional crystallization failed. As a result of this insertion, the ^{31}P NMR spectra (THF-d_8) of **5** and **6** show signals at δ = 171.9 and 122.3 ppm with tellurium satellites. The ^{125}Te NMR spectra (THF-d_8) of **5** and **6** exhibit doublets centered at δ = −414.4 and −544.4 ppm. The $^1J(^{125}Te–^{31}P)$ coupling constants of **5** (840 Hz) and **6** (683 Hz) are in a typical area of Te–P single bonds.[15]

The molecular structures of **5** and **6** are shown in Fig. 3. They comprise planar five-membered ETePCO-heterocycles (E = Ga, In). We note that **5** is an especially remarkable heterocycle in the sense that it comprises elements of group 13 (Ga), 14 (C), 15 (P) and 16 (O, Te) as well as at least one element from period 2 (C,O), 3 (P), 4 (Ga), and 5 (Te). The spatial arrangement of the gallium and indium atoms remains nearly unchanged, however, the divalent phosphorus atoms of **3** and **4** are replaced by the right-angled divalent tellurium atoms in **5** and **6**. The Ga–Te and In–Te bond lengths of **5** (2.6296(5) Å) and **6** (2.8331(3) Å) are in good agreement with the sum of covalent radii (2.60 and 2.78 Å).[14] The Ga–O and In–O bond lengths of **5** (1.916(3) Å) and **6** (2.167(2) Å) are only slightly shorter than in **3** and **4**. The Te–P bond lengths of **5** (2.407(1)

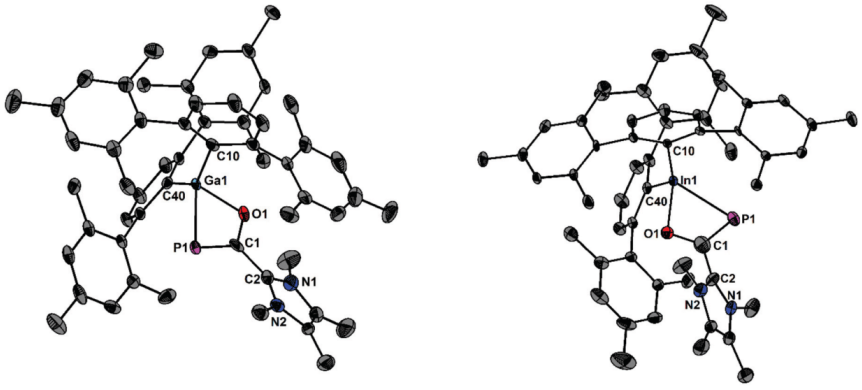

Fig. 2 Molecular structures of **3** (left) and **4** (right) showing 50% probability ellipsoids and the essential numbering scheme. Hydrogen atoms are omitted. Selected bond parameters for **3** [Å, °]: Ga1–P1 2.406(2), Ga1–O1 1.999(3), Ga1–C10 2.035(4), Ga1–C40 2.042(4), P1–C1 1.710(5), C1–O1 1.322(5), C1–C2 1.489(6), P1–Ga1–O1 73.2(1), P1–Ga1–C10 104.5(1), P1–Ga1–C40 115.2(1), O1–Ga1–C10 109.1(2), O1–Ga1–C40 96.5(1), C10–Ga1–C40 137.6(2), P1–C1–O1 121.0(3). Selected bond parameters for **4** [Å, °]: In1–P1 2.554(3), In1–O1 2.222(5), In1–C10 2.223(4), In1–C40 2.213(4), P1–C1 1.731(6), C1–O1 1.347(8), C1–C2 1.462(8), P1–In1–O1 68.6(2), P1–In1–C10 114.0(1), P1–In1–C40 107.4(1), O1–In1–C10 94.4(2), O1–In1–C40 109.6(2), C10–In1–C40 137.5(2), P1–C1–O1 122.5(5).

 This journal is © The Royal Society of Chemistry 2022

View Article Online
Dalton Transactions Paper

Published on 28 April 2022. Downloaded by Universitat Bremen on 6/19/2023 6:36:17 AM.

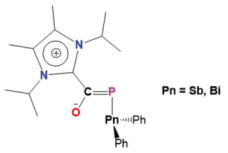

Fig. 3 Lewis formula of $Ph_2E(I^iPr_2Me_2)PCO$ (E = Sb, Bi).[8]

Å) and **6** (2.4480(8) Å) account for a single bond character (Fig. 4).[15]

Computational analysis

Density functional theory (DFT) calculations were used to obtain relaxed gas-phase geometries and energies of the whole series of group 13 bis(*m*-terphenyl)element phosphaethynolates for the phosphaketene coordination mode (2,6-$Mes_2C_6H_3)_2$EPCO as well as the oxyphosphaalkyne coordination mode (2,6-$Mes_2C_6H_3)_2$EOCP (E = B, Al, Ga, In, Tl) For all elements, the phosphaketene coordination mode is energetically favoured over the oxyphosphaalkyne mode (Table S2†). For Ga (−53.0 kJ mol^{-1}), In (−65.5 kJ mol^{-1}) and Tl (−61.3 kJ mol^{-1}), the energy difference is considerably larger than for B (−7.7 kJ mol^{-1}) and Al (−22.7 kJ mol^{-1}). Starting from the experimental structures of **3** and **5**, relaxed gas-phase geometries and energies for (2,6-$Mes_2C_6H_3)_2$EP(O)C(IMe_4) and (2,6-$Mes_2C_6H_3)_2$ETeP(O)C(IMe_4) were carried out (E = B, Al, Ga, In, Tl). The converged minima matched the overall experimental geometries well (Tables S3 and S4†). Real-space bonding indicator (RSBI) analyses were applied to **1–6** in order to qualitatively and quantitatively determine the electronic characteristics of the P–C and C–O bonds of the $[PCO]^-$ ion, as well as the E–P, E–O, E–Te, and Te–P bonds (E = Ga, In). The bond topology according to the Atoms-In-Molecules (AIM) theory,[16] intramolecular contact patches according to the noncovalent interactions index (NCI),[17] and bonding and lone-pair basins according to the electron localizability indicator (ELI-D)[18] altogether form a comprehensive picture of chemical bonding in real-space. Common AIM and ELI-D parameters are collected in Table 1, whereas the AIM topology as well as suitable NCI and ELI-D iso-surfaces are shown for the Ga compounds **1**, **3** and **5** in Fig. 5 and for the In compounds **2**, **4** and **6** in Fig. S25–S27.† The AIM topology confirms that in **1** and **2**, an E–P bond is formed, which is slightly weakened in **3** and **4** due to the formation of an E–O bond and finally replaced in **5** and **6** by a Te–P bond (Fig. 5a, e, i and Fig. S25a–S27a†). The C–O bond in the complexes **1** and **2** is a textbook case for a chemical interaction with both strong covalent and ionic contributions. The former is reflected by a strongly negative ratio of the total energy density (H) and the electron density ($\rho(r)$, ED) at the bond critical point (bcp): $H/\rho(r)_{bcp}$, whereas the latter causes an equally strong positive ratio of the kinetic energy density (G) and the ED: $G/\rho(r)_{bcp}$ (Table 1). Both together result in a Laplacian of the ED ($\nabla^2\rho(r)_{bcp}$) close to zero in case of the free PCO anion (in free CO it is positive as $G/\rho(r)_{bcp}$ = 2.17 a.u. dominates over $H/\rho(r)_{bcp}$ = −1.94 a.u.: $\nabla^2\rho(r)_{bcp}$ = 11 e $Å^{-5}$; we follow the most common sign notation, according to which the Laplacian is negative for covalent and positive for ionic atom-atom interactions[19]). Accordingly, the Raub–Jansen Index (RJI),[20] a tool for estimating the bond polarity, is about 80%. For homo-polar covalent bonds, the RJI approaches 50% (electron sharing), whereas it is larger than 90% for ionic and dative bonds, in which the electron density of the ELI-D bonding basin is located almost completely in the AIM atom being more electronegative. In contrast, the P–C bonds in **1–4** are dominated by ionic bond contributions ($|G/\rho(r)_{bcp}| > |H/$

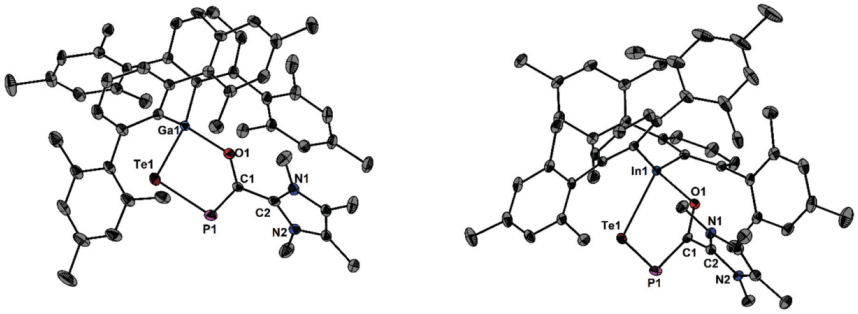

Fig. 4 Molecular structures of **5** (left) and **6** (right) showing 50% probability ellipsoids and the essential numbering scheme. Hydrogen atoms and co-crystallized toluene are omitted. Selected bond parameters for **5** [Å, °]: Ga1–Te1 2.6296(5), Ga1–O1 1.916(3), Ga1–C10 2.031(4), Ga1–C40 2.023 (4), P1–Te1 2.407(1), P1–C1 1.729(4), O1–C1 1.323(5), C2–C1 1.473(5), Te1–Ga1–O1 93.48(8), Te1–Ga1–C10 115.9(1), Te1–Ga1–C40 108.3(1), O1–Ga1–C10 110.1(1), O1–Ga1–C40 109.8(1), C10–Ga1–C40 116.7(2), Ga1–Te1–P1 89.02(3), P1–C1–O1 128.2(3). Selected bond parameters for **6** [Å, °]: In1–Te1 2.8331(3), In1–O1 2.167(2), In1–C10 2.205(2), In1–C40 2.216(2), P1–Te1 2.4480(8), P1–C1 1.717(3), O1–C1 1.303(3), C1–C2 1.492(4), Te1–In1–O1 87.05(5), Te1–In1–C10 101.72(6), Te1–In1–C40 113.57(6), O1–In1–C10 108.66(8), O1–In1–C40 89.33(8), C10–In1–C40 141.22(9), In1–Te1–P1 89.65(2), P1–C1–O1 132.9(2).

Published on 28 April 2022. Downloaded by Universitat Bremen on 6/19/2023 6:36:17 AM.

Table 1 Topological and integrated AIM and ELI-D properties of relevant interactions

	Contact or basin	D [Å]	$\rho(r)_{bcp}$ [e Å^{-3}]	$\nabla^2\rho(r)_{bcp}$ [e Å^{-5}]	ε	$G/\rho(r)_{bcp}$ [a.u.]	$H/\rho(r)_{bcp}$ [a.u.]	N_{ELI} [e]	V_{ELI} [Å^3]	γ_{ELI}	RJI
$[PCO]^-$	C–O	1.195	2.90	−1.3	0.00	1.80	−1.83	2.18	2.3	1.49	80.8
1	C–O	1.165	3.11	3.9	0.01	1.96	−1.87	2.53	3.7	1.53	81.6
2	C–O	1.169	3.08	0.7	0.01	1.88	−1.86	2.47	3.4	1.53	81.6
3	C–O	1.316	2.26	−15.7	0.07	1.15	−1.64	1.57	1.3	1.56	76.2
4	C–O	1.303	2.33	−15.5	0.07	1.20	−1.66	1.62	1.4	1.56	76.1
5	C–O	1.304	2.27	−12.0	0.08	1.28	−1.65	1.56	1.3	1.56	77.7
6	C–O	1.292	2.34	−12.5	0.08	1.30	−1.67	1.61	1.4	1.55	77.1
3	C–C	1.456	1.90	−19.0	0.13	0.29	−0.99	2.62	5.7	1.96	64.0
4	C–C	1.465	1.87	−18.3	0.12	0.29	−0.97	2.59	5.8	1.97	64.7
5	C–C	1.463	1.87	−18.1	0.13	0.29	−0.96	2.56	5.7	1.95	63.3
6	C–C	1.468	1.85	−17.6	0.12	0.29	−0.96	2.56	5.8	1.95	63.9
$[PCO]^-$	P–C	1.619	1.22	13.7	0.00	1.67	−0.88	2.47	8.4	1.53	95.5
1	P–C	1.641	1.18	10.9	0.21	1.54	−0.89	3.31	11.3	1.63	92.9
2	P–C	1.645	1.18	11.6	0.22	1.57	−0.88	3.25	11.0	1.64	93.3
3	P–C	1.724	1.17	3.8	0.20	1.19	−0.96	2.91	7.8	1.74	86.5
4	P–C	1.730	1.16	3.4	0.24	1.16	−0.96	2.86	7.6	1.74	86.6
5	P–C	1.721	1.20	2.1	0.43	1.11	−0.99	2.99	8.4	1.75	85.2
6	P–C	1.728	1.19	1.6	0.44	1.08	−0.99	2.92	8.2	1.76	85.3
3	Ga–O	2.032	0.52	6.8	0.02	1.18	−0.27	2.01	3.7	1.61	93.9
4	In–O	2.281	0.39	5.6	0.01	1.11	−0.10				
5	Ga–O	1.964	0.58	9.0	0.03	1.32	−0.23	2.16	3.7	1.60	93.5
6	In–O	2.203	0.44	7.1	0.03	1.22	−0.09	2.32	4.4	1.61	96.9
1	Ga–P	2.375	0.50	0.2	0.01	0.48	−0.44	1.64	7.4	1.58	62.4
2	In–P	2.579	0.41	1.3	0.01	0.52	−0.29	2.82	25.8	1.80	84.9
3	Ga–P	2.416	0.49	0.1	0.03	0.45	−0.44	2.13	10.3	1.78	72.2
4	In–P	2.592	0.42	1.1	0.06	0.49	−0.30	1.97	10.7	1.72	77.3
5	Te–P	2.409	0.65	−0.9	0.17	0.35	−0.45	1.75	5.1	1.50	58.7
6	Te–P	2.419	0.64	−0.9	0.15	0.34	−0.44	1.72	5.0	1.50	58.1
5	Te–Ga	2.689	0.38	0.3	0.08	0.41	−0.35	1.93	9.9	1.42	68.5
6	In–Te	2.842	0.34	1.0	0.10	0.46	−0.25	1.67	9.4	1.37	77.3

For all bonds, d is the geometric contact distance, $\rho(r)_{bcp}$ is the electron density at the bcp, $\nabla 2\rho(r)_{bcp}$ is the corresponding Laplacian, ε is the bond ellipticity, $G/\rho(r)_{bcp}$ and $H/\rho(r)_{bcp}$ are the kinetic and total energy density over $\rho(r)_{bcp}$ ratios, N_{ELI} and V_{ELI} are electron populations and volumes of related ELI-D basins, γ_{ELI} is the ELI-D value at the attractor position, RJI is the Raub–Jansen Index.

$\rho(r)_{bcp}|$), causing a positive Laplacian and a RJI above 90%, *i.e.* more than 90% of the ED in the ELI-D P–C bonding basin is located inside the AIM C atomic basin. The $[PCO]^-$ coordination to the $[(2,6\text{-}Mes_2C_6H_3)_2E]^+$ moieties slightly strengthens the C–O and weakens the P–C bond, thus affecting only little the respective electronic bond characteristics. Significant changes to these bonds, however, are observed for the formation of a C–C bond between PCO moiety and the IMe_4 (Table 1). The C–O (P–C) bond becomes about 0.13 Å (0.08 Å) longer, resulting in decreased accumulation of ED at the bcp (C–O) and inside both ELI-D bonding basins. Notably, the weakening of these bonds exclusively goes to the expense of ionic bond contributions, thereby increasing the role of covalent bonding aspects. This is visible in the Laplacian becoming negative (C–O) or considerably less positive (P–C) due to changed relative importance of kinetic and total energy densities, as well as diminished RJI values. The E–P, E–O, E–Te, and Te–P bonds are expectedly longer and weaker than the P–C and C–O bonds, resulting in $\rho(r)_{bcp}$ below one and smaller $G/\rho(r)_{bcp}$ and $H/\rho(r)_{bcp}$ values (E = Ga, In). Disregarding the lower absolute numbers, the trends are still the same. The E–O bonds are dominated by ionic bond contributions ($|G/\rho(r)_{bcp}| \gg |H/\rho(r)_{bcp}|$, RJI > 90%), whereas the E–P, E–Te, and Te–P bonds are constituted by both bonding aspects ($|G/\rho(r)_{bcp}| \approx |H/\rho(r)_{bcp}|$, RJI < 85%). The NCI displays (extended) regions in space in which non-covalent bonding aspects are relevant, thereby complementing the AIM approach of localized atom-atom contacts (Fig. 5b, f, j and Fig. S25b–S27b†). Flat, green-colored areas within the molecule disclose considerable van der Waals interactions between the ligands, some of which even give rise to the formation of bond path and a bcp in AIM.

The E–P, E–O, and Te–P bond axes are enclosed by thin ring-shaped and red-colored NCI basins, indicating minor non-covalent bond contributions, whereas a thicker (still ring – not yet disc-shaped) and blue-colored NCI basin encloses the E–Te bond axes, indicating non-negligible non-covalent bond contributions (E = Ga, In). ELI-D and NCI show spatial complementary suggesting at least partial spatial separation of covalent and non-covalent bonding aspects (Fig. 5b, f, g–c, g, k and Fig. S25b, c–S27b, c†).[21–23] The localization domain rep-

 This journal is © The Royal Society of Chemistry 2022

Published on 28 April 2022. Downloaded by Universitat Bremen on 6/19/2023 6:36:17 AM.

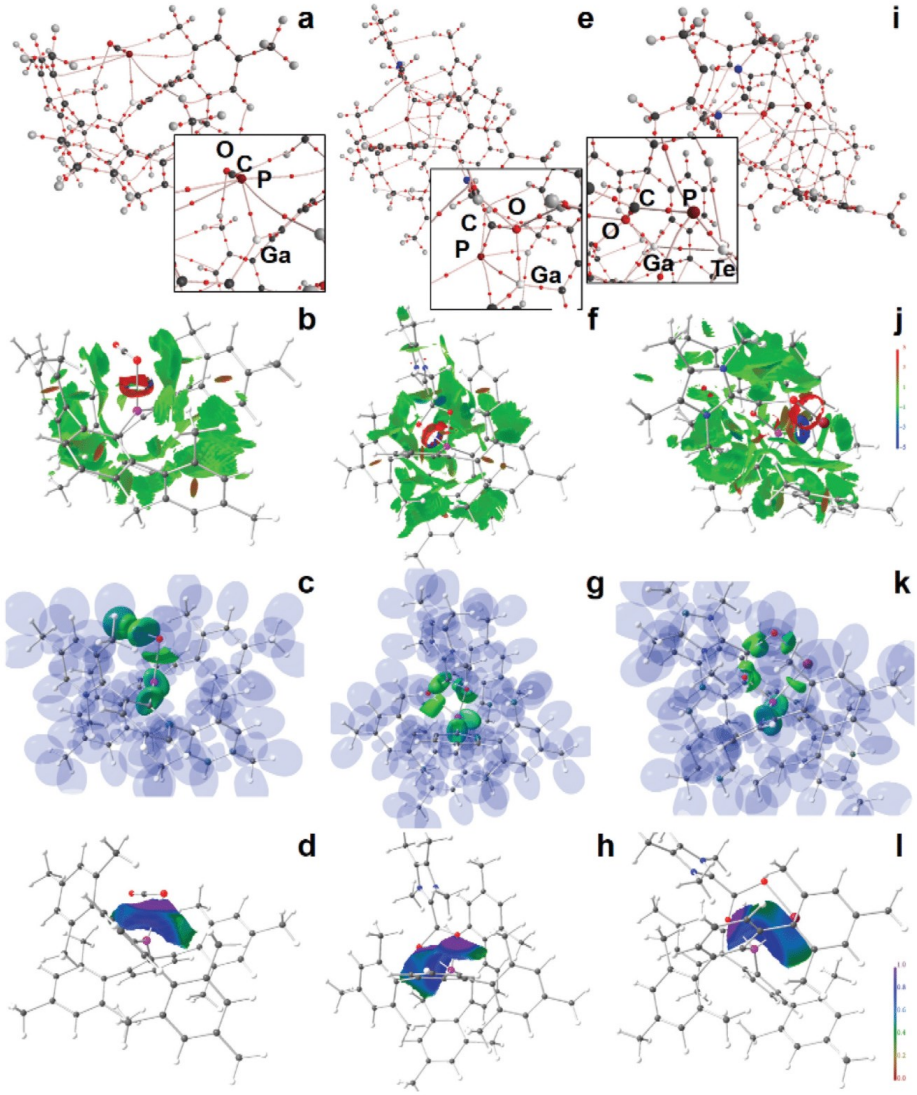

Fig. 5 RSBI analysis of **1**, **3**, and **5** (left, middle, right) AIM bond paths motif, (a, e and i) NCI iso-surface at $s(r)$ = 0.5, (b, f and j) ELI-D localization domain representation at iso-value of 1.3, (c, g and k) ELI-D distribution mapped on the Ga–P, Ga–O, and Ga–Te ELI-D basins (d, h and l).

resentations of the ELI-D (Fig. 5c, g, k and Fig. S25c–S27c†) and the ELI-D distribution mapped on the E–P, E–O, and E–Te bonding basins (Fig. 5d, h, l and Fig. S25d–S27d†) uncover their origin as formerly non-bonding lone-pairs of the P, O and Te atoms. At an iso-value of 1.3 they are still topologically connected to the remaining lone-pair basins in case of the P and O atoms, but already separated in case of the Te atom. In **4**, no distinct In–O bonding basin is formed in the ELI-D

Published on 28 April 2022. Downloaded by Universitat Bremen on 6/19/2023 6:36:17 AM.

Table 2 Atomic and fragmental AIM charges (in e)

	CO	$[PCO]^-$	1	2	3	4	5	6
E			1.25	1.18	1.35	1.25	1.37	1.27
R			−0.39	−0.33	−0.49	−0.45	−0.50	−0.44
R′			−0.40	−0.34	−0.49	−0.43	−0.50	−0.44
ERR′			0.46	0.51	0.37	0.37	0.37	0.39
P		0.19	0.39	0.40	0.25	0.21	0.50	0.47
C	1.20	0.07	0.33	0.29	0.04	0.08	0.05	0.10
O	−1.20	−1.26	−1.17	−1.18	−1.21	−1.20	−1.22	−1.21
PCO		−1.00	−0.46	−0.49	−0.92	−0.91	−0.67	−0.64
IMe_4					0.56	0.55	0.57	0.56
Te							−0.25	−0.28
Σ	0.00	0.00	0.01	0.01	0.01	0.01	0.02	0.02

E = Ga, In; R, R′ = 2,6-$Mes_2C_6H_3$.

(Table 1), presumably because the In–O bond is the weakest of all E–O bonds (E = Ga, In). The spatial requirements of the E–P, E–O, and E–Te bonding basins is also disclosed in Fig. 5d, h, l. Only small (purple) regions of increased localizability are visible towards the Ga and In atoms confirming the weakness of these bonds (see also Fig. S25d–S27d†). Charge redistribution *via* adduct formation was monitored by determination of suitable atomic and fragmental AIM charges (Q_{AIM}), which are collected together with CO and the isolated $[PCO]^-$ ion (Table 2).

The strongly electronegative O atom typically tends to show pronounced negative AIM charges, which are only little affected by chemical changes in the environment. Accordingly, the AIM charges of the O atom only varies between −1.17 and −1.26*e* for all compounds. So it can be surmised that the negative charge of −1 in the $[PCO]^-$ ion causes the P and C atoms *not* to be positively charged considerably, although being adjacent to the O atom. There is no effective difference between compounds containing Ga or In. The $[(2,6\text{-}Mes_2C_6H_3)_2E]^+$ and $[PCO]^-$-fragments partially compensate opposing charges in that the C and P atoms of PCO (each by about 0.2*e*) and the O atom (less than 0.1*e*) release charge density towards the $[(2,6\text{-}Mes_2C_6H_3)_2E]^+$ upon formation of **1** and **2**. The addition of IMe_4 reduces this effect, since the $[PCO]^-$-fragment withdraws significant amounts of ED (about 0.55*e*) from the NHC-fragment, resulting in atomic charges for the PCO moiety being very much the same as in the isolated $[PCO]^-$ ion, although being significantly bent in **3** and **4**. The insertion of Te atoms into the E–P bonds has only a local effect on the adjacent P atom, which it is bound to, and from which it withdraws about 0.25*e*. The remaining parts of **5** and **6** are basically not affected in terms of AIM charge redistribution.

Conclusions

Heavier bis(*m*-terphenyl)element phosphaethynolates, $(2,6\text{-}Mes_2C_6H_3)_2EPCO$ (**1**, E = Ga; **2**, E = In) of group 13 were prepared and the reactivity was studied. Compared to organometallic phosphaethynolates of group 14 and 15, such as Ph_3EPCO (E = Ge, Sn)[3] and Ph_2EPCO (E = Sb, Bi),[8] **1** and **2** are thermally stable, which is attributed to the kinetic stabilization of the two bulky *m*-terphenyl substituents. The reaction of **1** and **2** with 1,2,3,4-tetramethylimidazol-2-ylidene, IMe_4, provided the complexes $(2,6\text{-}Mes_2C_6H_3)_2EP(O)C(IMe_4)$ (**3**, E = Ga; **4** E = In), which reacted with tellurium to give the complexes $(2,6\text{-}Mes_2C_6H_3)_2ETeP(O)C(IMe_4)$ (**5**, E = Ga; **6**, E = In) comprising five-membered ETePCO-heterocycles. Considerable ionic and covalent bond contributions are obtained for the C–O bonds in the PCO fragments, whereas the P–C bonds are dominated by ionic contributions. Remarkably, for both bonds, the ionic bond contributions are significantly reduced after addition of the N-heterocyclic carbene IMe_4 to the central electrophilic carbon center of the PCO unit.

Author contributions

D. D. and M. J. contributed equally to this work.

Conflicts of interest

There are no conflicts to declare.

Acknowledgements

The Deutsche Forschungsgemeinschaft (DFG) is gratefully acknowledged for financial support.

Notes and references

1 J. M. Goicoechea and H. Grützmacher, *Angew. Chem., Int. Ed.*, 2018, **57**, 16968–16994.
2 L. Weber, *Eur. J. Inorg. Chem.*, 2018, **20–21**, 2175–2227.
3 D. Heift, Z. Benkő and H. Grützmacher, *Dalton Trans.*, 2014, **43**, 5920–5928.
4 D. W. N. Wilson;, A. Hinz and J. M. Goicoecha, *Angew. Chem., Int. Ed.*, 2018, **57**, 2188–2193.

 This journal is © The Royal Society of Chemistry 2022

Published on 28 April 2022. Downloaded by Universitat Bremen on 6/19/2023 6:36:17 AM.

5 D. W. N. Wilson, M. P. Franco, W. K. Myers, J. E. McGrady and J. M. Goicoechea, *Chem. Sci.*, 2020, **11**, 862–869.
6 D. W. N. Wilson, W. K. Meyers and J. M. Goicoecha, *Dalton Trans.*, 2020, **49**, 15249–15255.
7 Y. Mei, J. E. Borger, D.-J. Wu and H. Grützmacher, *Dalton Trans.*, 2019, **48**, 4370–4374.
8 J. E. Walley, L. S. Warring, E. Kertész, G. Wang, D. A. Dickie, Z. Benkő and R. J. Gillard, *Inorg. Chem.*, 2021, **60**, 4733–4743.
9 X.-W. Li, W. T. Pennington and G. H. Robinson, *Organometallics*, 1995, **14**, 2109–2111.
10 X.-W. Li, G. Robinson and W. T. Pennington, *Main Group Chem.*, 1996, **1**, 301–307.
11 R. E. Schreiber and J. M. Goicoecha, *Angew. Chem., Int. Ed.*, 2021, **60**, 3759–3767.
12 F. F. Puschmann, D. Stein, D. Heift, C. Hendriksen, Z. A. Gal, H. F. Grützmacher and H. Grützmacher, *Angew. Chem., Int. Ed.*, 2011, **50**, 8420–8423.
13 A. J. Arduengo III, H. V. R. Dias, R. L. Harlow and M. Kline, *J. Am. Chem. Soc.*, 1992, **114**, 5530–5534.
14 B. Cordero, V. Gómez, A. E. Platero-Prats, M. Revés, J. Echeverría, E. Cremades, F. Barragán and S. Alvarez, *Dalton Trans.*, 2008, **21**, 2832–2838.
15 A. Nordheider, J. D. Woollins and T. Chivers, *Chem. Rev.*, 2015, **115**, 10378–10406.
16 R. W. F. Bader, *Atoms in molecules. A quantum theory*, Cambridge University Press, Oxford U.K., 1991.
17 E. R. Johnson, S. Keinan, P. Mori-Sanchez, J. Contreras-García, A. J. Cohen and W. Yang, *J. Am. Chem. Soc.*, 2010, **132**, 6498–6506.
18 M. A. Kohout, *Int. J. Quantum Chem.*, 2004, **97**, 651–658.
19 D. Stalke, *Chem. – Eur. J.*, 2011, **17**, 9264–9278.
20 S. Raub and G. Jansen, *Theor. Chem. Acc.*, 2001, **106**, 223–232.
21 N. Gillet, R. Chaudret, J. Contreras-García and W. Yang, *J. Chem. Theory Comput.*, 2012, **8**, 3993–3997.
22 P. de Silva and C. Corminboeuf, *J. Chem. Theory Comput.*, 2014, **10**, 3745–3756.
23 S. Mebs, *Chem. Phys. Lett.*, 2016, **651**, 172–177.

2.8 Kinetic Stabilization of Heavier bis(*m*-terphenyl)pnictogen phosphaethynolates

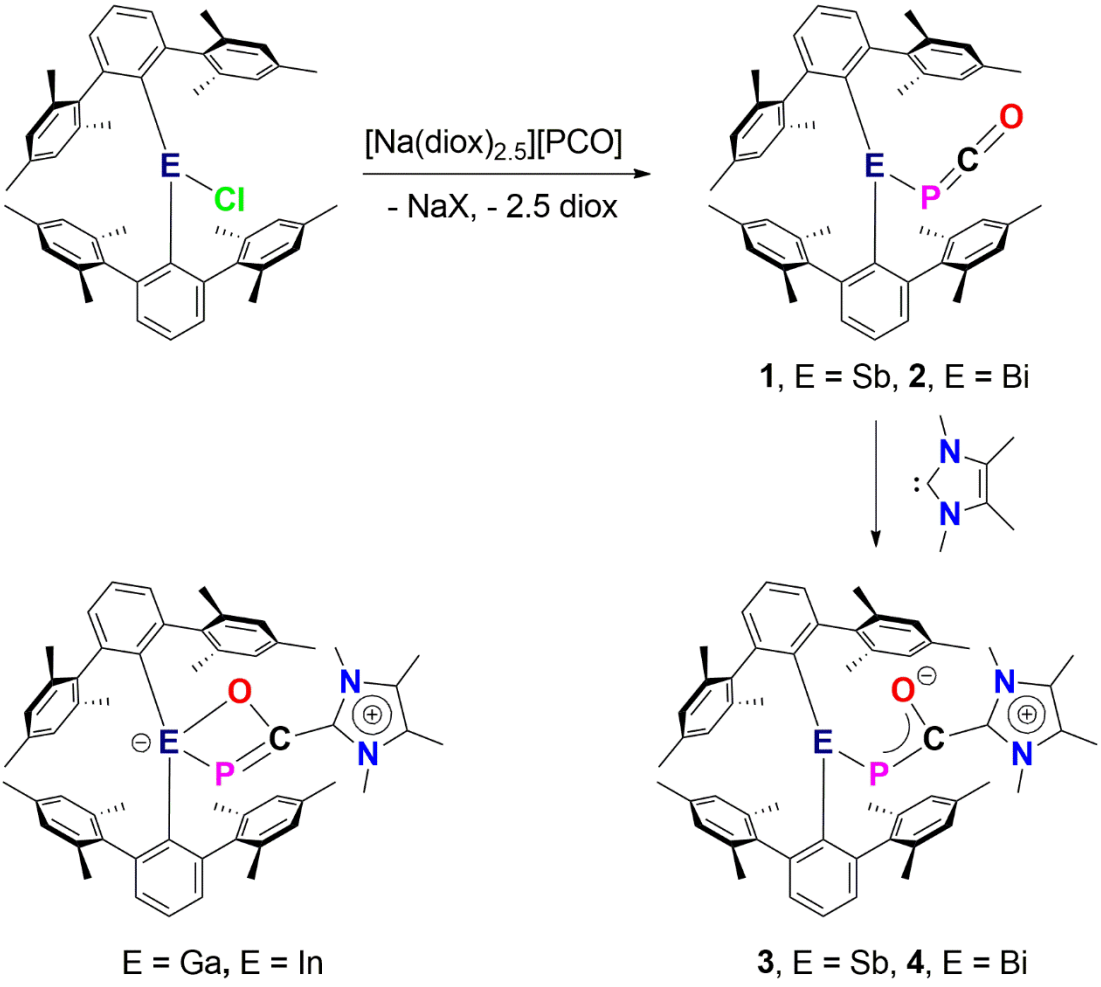

2.8.1 Synopsis

Similar to the group 13 phosphaethynolates, the obtained bis(*m*-terphenyl)pnictogen halides were reacted with sodium phosphaethynolate, from which bis(*m*-terphenyl)antimony phosphaethynolate Ter_2SbPCO and bis(*m*-terphenyl)bismuth phosphaethynolate Ter_2BiPCO formed stable products that could be isolated. The irradiation of the phosphaethynolates by UV-A light (λ = 365 nm) led to a transient species, which decomposes unselectively over the course of several minutes which could be monitored by NMR spectroscopy. Similar to the group 13 phosphaethynolates, 1,2,3,4-tetramethylimidazolin-2-ylidene IMe_4 was used as an NHC for scavenging the formed phosphinidene. The NHC again coordinates to the carbon atom of the PCO moiety, but contrary to group 13, the oxygen does not coordinate to the pnictogen center. This is visible by means of

^{31}P NMR spectroscopy and single crystal X-ray diffraction analysis. The NHC adducts of the group 15 element phosphaethynolates are more sensitive than the group 13 congeners, which can be attributed to the monodentate PCO moiety. Especially the bismuth phosphaethynolate NHC adduct decomposes in solution over the course of a day at ambient light. This decomposition leads to the formation of dibismuthene TerBi=BiTer and unidentified side products, which indicates a terphenyl migration. The formed NHC adducts showed also no reaction with chalcogenes. By DFT calculations, the interaction and ionic character is compared to the group 13 congeners, showing the substantially higher preference for the PCO coordination in group 15 compared to group 13. Again, coordination of the NHC drastically reduces the ionic interactions in the PCO moiety.

2.8.2 Scientific Contribution

In this project, M. Janßen developed the synthesis of the compounds under my supervision. M. Janßen and I did the full characterization of the shown compounds. I co-wrote the publication and contributed the X-ray crystallographic part with E. Lork. H. Grützmacher co-wrote the publication. S. Mebs provided the theoretical calculations and co-wrote the manuscript and J. Beckmann was principal investigator and co-wrote the publication.

Percentage of my contribution of the total workload:

Experimental concept and design: ca. 90%, experimental work and acquisition of experimental data: ca. 40%, data analysis and interpretation: ca. 90%, preparation of figures and tables: ca. 80%, drafting of the manuscript: ca. 60%.

The article was published in the journal “Zeitschrift für anorganische und allgemeine Chemie“ in 2022 as an open access article:

Daniel Duvinage, Marvin Janssen, Enno Lork, Hansjörg Grützmacher, Stefan Mebs*, Jens Beckmann*, *Z. Anorg. Allg. Chem.* **2022**, *648, e202200133.*

DOI: 10.1002/zaac.202200133

The Supporting Information includes experimental procedures, NMR data, X-ray crystallographic data and structure refinement and computational data and is available free of charge on the journal′s website:

https://onlinelibrary.wiley.com/action/downloadSupplement?doi=10.1002%2Fzaac.202200133&file=zaac202200133-sup-0001-misc_information.pdf

Journal of Inorganic and General Chemistry
ZAAC
Zeitschrift für anorganische und allgemeine Chemie
www.zaac.wiley-vch.de
RESEARCH ARTICLE

DOI: 10.1002/zaac.202200133

Kinetic Stabilization of Heavier Bis(*m*-terphenyl)pnictogen Phosphaethynolates

Daniel Duvinage[+],[a] Marvin Janssen[+],[a] Enno Lork,[a] Hansjörg Grützmacher,[b] Stefan Mebs,*[c] and Jens Beckmann*[a]

Dedicated to Professor Cameron Jones on the occasion of his 60th birthday

Kinetic stabilization using bulky *m*-terphenyl substituents is the key to the isolation of the diarylantimony and diarylbismuth phosphaethynolates (2,6-$Mes_2C_6H_3$)$_2$EPCO and the related N-heterocyclic carbene complexes (2,6-$Mes_2C_6H_3$)$_2$EP(O)C(IMe_4) (E = Sb, Bi; IMe_4 = 1,3,4,5-tetramethylimidazol-2-ylidene), which have been fully characterized crystallographically and spectroscopically. The experimental characterization was augmented by a DFT based real space bond indicator analysis of the electron density, including AIM, NCI, and ELI-D methods.

Introduction

The phosphaethynolate ion, $[PCO]^-$, a heavier congener of the cyanate ion $[NCO]^-$, has proven to be a versatile building block in synthetic main group element chemistry.[1,2] In light of one of its significant resonance structures which may be written as $[P{-}C{\equiv}O]^-$, it can be viewed as synthon for the $[P]^-$ ion, which has been used for the (photochemical) preparation of phosphinidenes and phospha-heterocycles formed upon decarbonylation. Recently developed synthetic procedures now allow the convenient preparation of the $[PCO]^-$ ion on a multi-gram scale.[3] In coordination chemistry, efforts were made to explore the ambiphilic nature of the $[PCO]^-$ ion, which may coordinate via their phosphorus or oxygen atoms giving rise to metal phosphaketenes, M–P=C=O, or their oxyphosphaalkyne analogues M–O–C≡P. While such compounds have been established where the OCP unit is bound to an element from group 13 or 14, the preparation of compounds with heavier elements from group 15 is challenging.

Very recently, Benkő and Gilliard et al. reported on the salt metathesis reaction of Na[OCP] with Ph_2SbCl and Ph_2BiCl, respectively, aimed to allow for the complexes Ph_2EPCO, but producing the tetraphenyldipnictines Ph_2EEPh_2 and ill-defined precipitates instead (E = Sb, Bi).[4] They also found that the reaction of the related N-heterocyclic carbene (NHC) complexes $Ph_2E(I^iPr_2Me_2)Cl$ with Na[OCP] proceeded with NaCl elimination without yielding the desired metathesis products Ph_2E-($I^iPr_2Me_2$)PCO (E = Sb, Bi; $I^iPr_2Me_2$ = 1,3-diisopropyl-4,5-dimethylimidazol-2-ylidene), which might have formed only as transient intermediate that rapidly rearrange into complexes $Ph_2EP(O)C(I^iPr_2Me_2)$ having the same elemental composition (Scheme 1). The rearrangement may be rationalized by the migration of the NHC from the pnictogen atom to the carbon atom of the PCO moiety, for which a mechanism was proposed on the basis of density function theory (DFT). Although fully characterized, the complexes $Ph_2EP(O)C(I^iPr_2Me_2)$ turned out to be metastable with respect to the formation of the tetraphenyldipnictines Ph_2EEPh_2 and the salt $[(I^iPr_2Me_2)PC(O)(I^iPr_2Me_2)][PCO]$, as slow decomposition was observed even at −37 °C in the solid state (Scheme 1). The formation of the tetraphenyldipnictines Ph_2EEPh_2 might have been facilitated by the secondary pnictogen-pnictogen interactions evident in the crystal structures of $Ph_2EP(O)C(I^iPr_2Me_2)$.

In this work, we addressed the stability issues Benkő and Gilliard et al.[4] were facing in their work, using bulky *m*-terphenyl substituents providing sufficient kinetic stabilization not only to the NHC-supported complexes (2,6-$Mes_2C_6H_3$)$_2$EP(O)C(IMe_4) but also the unsupported complexes (2,6-$Mes_2C_6H_3$)$_2$EPCO, which were fully characterized (E = Sb, Bi). This strategy proved useful for the preparation of the analogous group 13 compounds (2,6-$Mes_2C_6H_3$)$_2$EPCO (E = Ga, In).[5] The experimental work was augmented by DFT calculations, which provided PCO dissociation energies as well as relative energies of different PCO coordination. Electronic bond characteristics of the PCO fragment within its different chemical environments,

[a] D. Duvinage,[+] M. Janssen,[+] Dr. E. Lork, Prof. Dr. J. Beckmann
Institut für Anorganische Chemie und Kristallographie,
Universität Bremen, Leobener Straße 7,
28359 Bremen, Germany
E-mail: j.beckmann@uni-bremen.de
[b] Prof. Dr. H. Grützmacher
Laboratory of Inorganic Chemistry,
ETH Zürich, Vladimir-Prelog-Weg 1–5/10,
8093 Zürich, Switzerland
[c] Dr. S. Mebs
Institut für Experimentalphysik,
Freie Universität Berlin, Arnimallee 14,
14195 Berlin, Germany
E-mail: stefan.mebs@fu-berlin.de
[+] These authors contributed equally.

Supporting information for this article is available on the WWW under https://doi.org/10.1002/zaac.202200133

© 2022 The Authors. Zeitschrift für anorganische und allgemeine Chemie published by Wiley-VCH GmbH. This is an open access article under the terms of the Creative Commons Attribution License, which permits use, distribution and reproduction in any medium, provided the original work is properly cited.

Journal of Inorganic and General Chemistry
ZAAC
Zeitschrift für anorganische und allgemeine Chemie
RESEARCH ARTICLE

15213749, 2022, 19, Downloaded from https://onlinelibrary.wiley.com/doi/10.1002/zaac.202200133 by Staats- und Universitätsbibliothek, Wiley Online Library on [18/06/2023]. See the Terms and Conditions (https://onlinelibrary.wiley.com/terms-and-conditions) on Wiley Online Library for rules of use; OA articles are governed by the applicable Creative Commons License

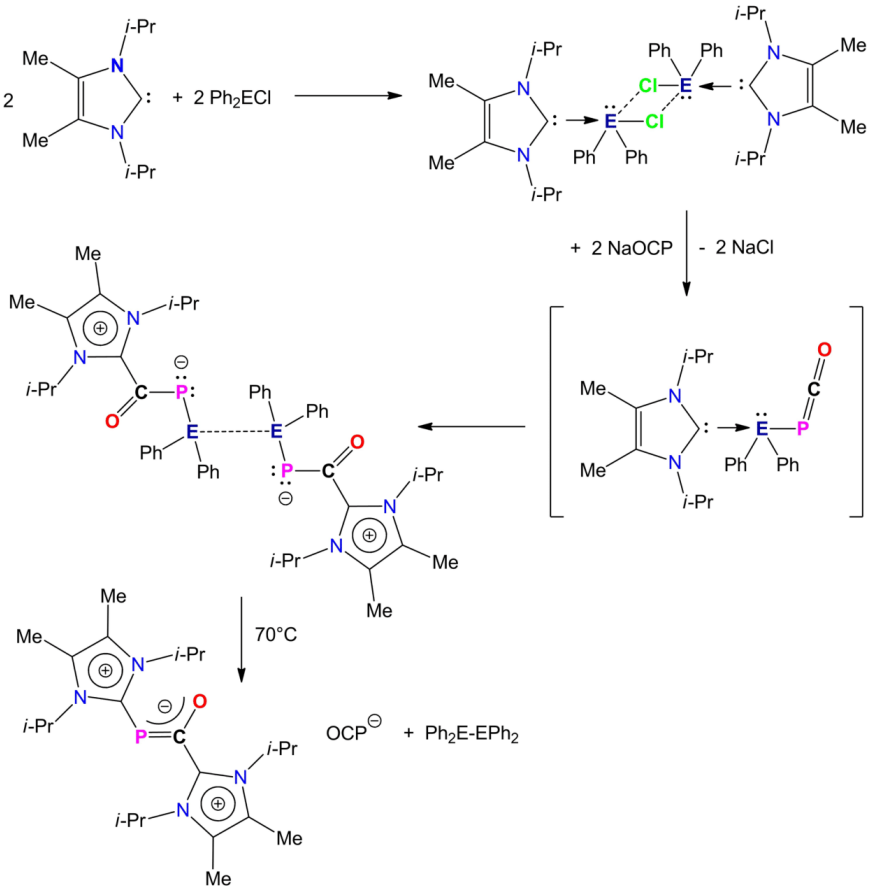

Scheme 1. Reaction of NHC-substituted heavier diphenylpnictogene chlorides with sodium phosphaethynolate according to Benkő and Gilliard et al.[4]

including the deconvolution of covalent and non-covalent bonding aspects, was provided by subsequent real-space bonding indicator (RSBI) analysis of the electron and electron pair densities.

Results and Discussion

Synthesis and Characterization

The reaction of the bis(*m*-terphenyl)element halides, (2,6-$Mes_2C_6H_3)_2SbCl$[6] and (2,6-$Mes_2C_6H_3)_2BiCl$[7] with [Na(1,4-dioxane)$_{2.5}$][PCO][3] afforded the bis(*m*-terphenyl)element phosphaethynolates, (2,6-$Mes_2C_6H_3)_2EPCO$ (**1**, E = Sb; **2**, E = Bi) as yellow and orange solids in yields of 80 and 86% (Scheme 2). The ^{31}P NMR spectra (C_6D_6) of **1** and **2** exhibit signals at −314.9 and −324.0 ppm are midway to those of the group 13 analogues (2,6-$Mes_2C_6H_3)_2GaPCO$ (−283.3 ppm) and (2,6-$Mes_2C_6H_3)_2InPCO$ (−336.2 ppm). The molecular structures of **1** and **2** are shown in Figure 1. For both compounds, the phosphaketene coordination mode applies. The Sb–P and Bi–P bond lengths of **1** (2.5479(8) Å) and **2** (2.655(3) Å) are in good agreement with sum of covalence radii (2.51 and 2.62 Å).[8] The M–P–C angles are almost rectangular and the P–C–O angle is nearly straight (M = Sb, Bi). The P–C bond lengths of **1** (1.655(4) Å) and **2** (1.67(2) Å) are larger than in the group 13

 © 2022 The Authors. Zeitschrift für anorganische und allgemeine Chemie published by Wiley-VCH GmbH

Journal of Inorganic and General Chemistry
ZAAC
Zeitschrift für anorganische und allgemeine Chemie

RESEARCH ARTICLE

15213749, 2022, 9, Downloaded from https://onlinelibrary.wiley.com/doi/10.1002/zaac.202200133 by Staats- und Universitätsbibliothek, Wiley Online Library on [18/06/2023]. See the Terms and Conditions (https://onlinelibrary.wiley.com/terms-and-conditions) on Wiley Online Library for rules of use; OA articles are governed by the applicable Creative Commons License

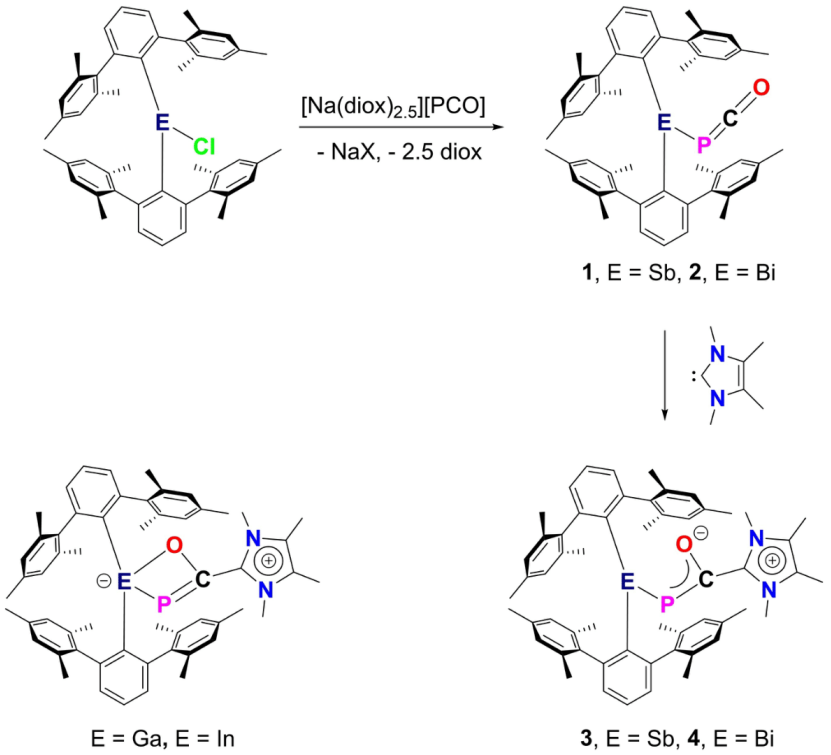

Scheme 2. Synthesis of **1**–**4**.

analogues (2,6-$Mes_2C_6H_3)_2$GaPCO (1.567(5) Å) and (2,6-$Mes_2C_6H_3)_2$InPCO (1.636(2) Å).[5] The C–O bond lengths of **1** (1.178(4) Å) and **2** (1.08(2) Å) as well as (2,6-$Mes_2C_6H_3)_2$GaPCO (1.224(5) Å) and (2,6-$Mes_2C_6H_3)_2$InPCO (1.174(2) Å) show a rather large variance, which is most likely an artifact of the crystal structure determination as (2,6-$Mes_2C_6H_3)_2EX_n$ structures often showing large vibrational displacement or disorder for the groups X. The asymmetric PCO stretching vibration of **1** (1920 cm^{-1}) and **2** (1901 cm^{-1}) are a more reliable parameter to evaluate the C–O bond, similar as in metal carbonyls.[9] Both parameters are slightly larger than in (2,6-$Mes_2C_6H_3)_2$GaPCO (1898 cm^{-1}) and (2,6-$Mes_2C_6H_3)_2$InPCO (1880 cm^{-1}). Judged by these values, the C–O bond strength most likely decreases for a series of (2,6-$Mes_2C_6H_3)_2$EPCO compounds in the order E = In > Ga > Bi > Sb. Additionally, for the evaluation of the C–P bond strength, the ^{13}C–^{31}P coupling constant in ^{13}C NMR spectroscopy, can be used. By the comparison of these, **1** ($^1J(^{13}C–^{31}P)$ = 113.9 Hz) and **2** ($^1J(^{13}C–^{31}P)$ = 114.8 Hz) show a much larger coupling constant than the group 13 homologs (2,6-$Mes_2C_6H_3)_2$GaPCO ($^1J(^{13}C–^{31}P)$ = 99.8 Hz) and (2,6-$Mes_2C_6H_3)_2$InPCO ($^1J(^{13}C–^{31}P)$ = 96.1 Hz), which proves that with decreasing C–O bond strength, the C–P bond strength increases in the order E = In < Ga < Sb ≤ Bi.

The reaction of **1** and **2** with 1,3,4,5-tetramethylimidazol-2-ylidene, IMe_4,[10] afforded the complexes (2,6-$Mes_2C_6H_3)_2$EP(O)C-(IMe_4) (**3**, E = Sb; **4**, E = Bi) as orange solids in 69 and 74% yield (Scheme 2). Interestingly, **4** is photo-sensitive in solution and even in the solid state when exposed to ambient light. During the course of days at room temperature, **4** decomposes into dibismuthene (2,6-$Mes_2C_6H_3Bi)_2$ and unaccounted decomposition products,[11] which suggest that migration of *m*-terphenyl substituents take place. In contrast, **3** is quite stable in solution and the solid state. The ^{31}P NMR spectra (C_6D_6) of **3** and **4** show signals at δ = 65.6 and 72.3 ppm, which are consistent with those of $Ph_2E(I^iPr_2Me_2)PCO$ (58.2 ppm for E = Sb and 82.2 ppm for E = Bi; $I^iPr_2Me_2$ = 1,3-diisopropyl-4,5-dimethylimidazol-2-ylidene),[4] but in marked difference to the ^{31}P NMR chemical shifts observed for (2,6-$Mes_2C_6H_3)_2$EP(O)C(IMe_4) (245.5 ppm for E = Ga and 219.7 ppm for E = In).[5] The different ^{31}P NMR chemical shifts are attributed to the bidentate coordination of

 © 2022 The Authors. Zeitschrift für anorganische und allgemeine Chemie published by Wiley-VCH GmbH

Journal of Inorganic and General Chemistry
ZAAC
Zeitschrift für anorganische und allgemeine Chemie

RESEARCH ARTICLE

15213749, 2022, 9, Downloaded from https://onlinelibrary.wiley.com/doi/10.1002/zaac.202200133 by Staats- und Universitätsbibliothek, Wiley Online Library on [18/06/2023]. See the Terms and Conditions (https://onlinelibrary.wiley.com/terms-and-conditions) on Wiley Online Library for rules of use; OA articles are governed by the applicable Creative Commons License

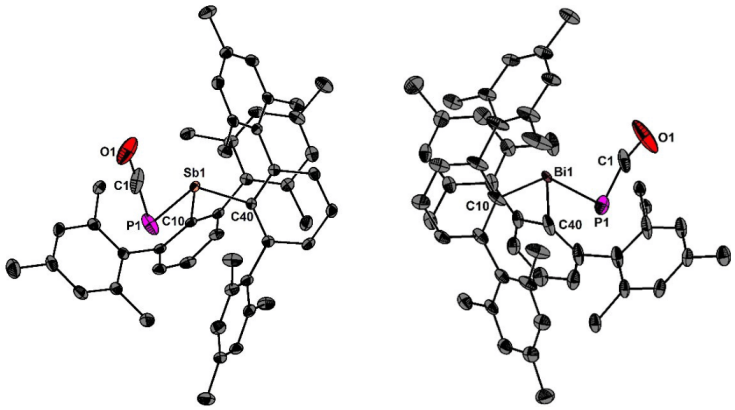

Figure 1. Molecular structures of **1** and **2** showing 50% probability ellipsoids and the essential numbering scheme. Selected bond parameters for **1** [Å, °]: Sb1-P1 2.5479(8), Sb1-C10 2.198(2), Sb1-C40 2.191(2), P1-C1 1.655(4), C1-O1 1.178(4), P1-Sb1-C10 101.68(6), P1-Sb1-C40 97.77(6), C10-Sb1-C40 103.94(8), C1-P1-Sb1 86.20(12), O1-C1-P1 176.7(3). Selected bond parameters for **2** [Å, °]: Bi1-P1 2.655(3), Bi1-C10 2.252(6), Bi1-C40 2.397(7), P1-C1 1.67(2), C1-O1 1.08(2), P1-Bi1-C10 91.6(2), P1-Bi1-C40 101.6(2), C10-Bi1-C40 103.7(2), C1-P1-Bi1 85.1(4), O1-C1-P1 166.1(1).

the PCO linkage (e.g. via P and O) in the group 13 compounds and the monodentate coordination of the PCO linkage (e.g. only via P) in the group 15 compounds (Scheme 2). The molecular structures of **3** and **4** are shown in Figure 2. The spatial arrangement of the Sb and Bi is tetrahedral taking into account the C_2P donor set and the electron lone pair. Repulsion of the latter presumably prevents a bidentate coordination mode. This observation is reminiscent to the bond situation in the zwitterionic diaryltelluronium acetimidate (8-$Me_2NC_{10}H_6)_2TeN(O)CH_3$, in which the lone pair at Te prevents

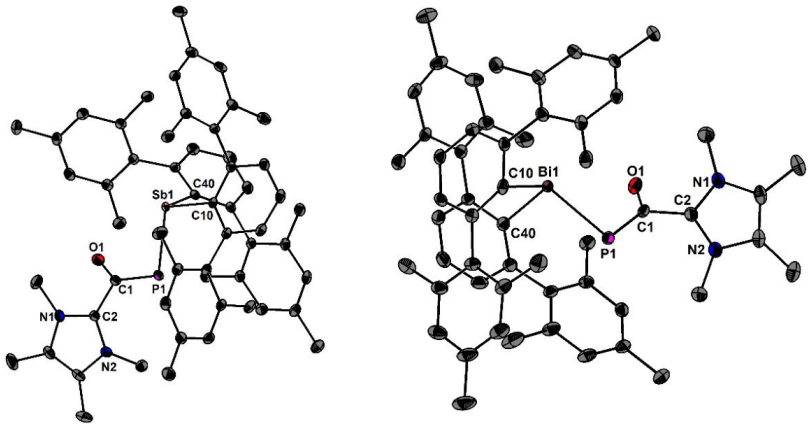

Figure 2. Molecular structures of **3** and **4** showing 50% probability ellipsoids and the essential numbering scheme. Selected bond parameters of **3** [Å, °]: Sb1-P1 2.4833(5), Sb1-C40 2.213(2), Sb1-C10 2.201(2), P1-C1 1.759(2), C1-O1 1.249(2), C1-C2 1.516(3), P1-Sb1-C10 105.17(5), P1-Sb1-C40 94.37(5), C10-Sb1-C40 100.13(7), O1-C1-P1 132.89(15). Selected bond parameters of **4** [Å, °]: Bi1-P1 2.605(2), Bi1-C10 2.329(4), Bi1-C40 2.361(4), P1-C1 1.753(6), C1-O1 1.263(7), C1-C2 1.518(7), P1-Bi1-C10 99.7(1), P1-Bi1-C40 108.7(1), C10-Bi1-C40 99.8(1), O1-C1-P1 129.4(4).

 © 2022 The Authors. Zeitschrift für anorganische und allgemeine Chemie published by Wiley-VCH GmbH

Journal of Inorganic and General Chemistry
ZAAC
Zeitschrift für anorganische und allgemeine Chemie

RESEARCH ARTICLE

15213749, 2022, 9, Downloaded from https://onlinelibrary.wiley.com/doi/10.1002/zaac.202200133 by Staats- und Universitätsbibliothek, Wiley Online Library on [18/06/2023]. See the Terms and Conditions (https://onlinelibrary.wiley.com/terms-and-conditions) on Wiley Online Library for rules of use; OA articles are governed by the applicable Creative Commons License

the coordination of the oxygen atom.[12] The Sb–P and Bi–P bond lengths of **3** (2.4833(5) Å) and **4** (2.605(2) Å) are slighter shorter than those of **1** and **2**. The C–C-bond lengths accounting for the coordination of the NHCs to the PCO moieties of **3** (1.516(3) Å) and **4** (1.518(7) Å) are consistent with values observed for $Ph_2E(I^iPr_2Me_2)PCO$ (1.529(7) Å for E = Sb and 1.515(1) Å for E = Bi; $I^iPr_2Me_2$ = 1,3-diisopropyl-4,5-dimethylimidazol-2-ylidene).[4] In contrast to **3** and **4**, the C–C bond lengths between the NHC moiety and the OCP unit in $(2,6\text{-}Mes_2C_6H_3)_2EP(O)C(IMe_4)$ (1.489(6) Å for E = Ga and 1.462(8) for E = In)[5] are shorter suggesting that this interaction is stronger in group 13 than in group 15 element compounds. No reaction of **3** or **4** with sulfur, selenium or tellurium was observed, which is another difference to the group 13 species.

Computational analysis

Efforts were made to obtain relaxed gas-phase geometries of the entire series of group 15 bis(*m*-terphenyl)element phosphaethynolates in the phosphaketene coordination mode $(2,6\text{-}Mes_2C_6H_3)_2EPCO$ as well as in the oxyphosphaalkyne coordination mode $(2,6\text{-}Mes_2C_6H_3)_2EOCP$ (E = N-Bi) by using density functional theory (DFT) calculations at the B3PW91/6-311 + G(2df,p) level of theory. For E = N–As, the phosphaketene coordination is energetically favored by 105–244 kJ mol^{-1} (Table S**1**) over oxyphosphaalkyne coordination. All attempts to optimize the oxyphosphaalkyne coordination mode for E = Sb, Bi lead to conversion into the phosphaketene coordination mode. The same trend was observed for the related series of compounds involving group 13 elements (B–Tl), although the energetic differences were considerably smaller.[5] Using the experimentally obtained structure of **3**, relaxed gas-phase geometries and energies were calculated for the whole series of $(2,6\text{-}Mes_2C_6H_3)_2EP(O)(IMe_4)$ (E=N–Bi). In all cases, except P, the monodentate coordination mode was confirmed. Only for E=P, the bidentate coordination mode reminiscent of the group 13 elements was found.[5] The electronic characteristics of the P–C and C–O bonds of the PCO ligand, and the E–P bonds (E = Sb, Bi) of 1–**4** were determined by a suitable set of real-space bonding indicator (RSBI) parameters for the gas-phase structures. RSBI comprise several complementary tools, such as the Atoms-In-Molecules (AIM)[13] bond topology, noncovalent interactions index (NCI)[14] derived intramolecular contact patches, as well as bonding and lone-pair basins using the electron localizability indicator (ELI-D).[15] Bond polarities are estimated by the Raub-Jansen Index (RJI),[16] which superimposes ELI-D (bonding) basins with the contributing adjacent AIM atoms, thus quantifying the electron density (ED, $\rho(\mathbf{r})$) distribution along a bond. Iso-surfaces of NCI and ELI-D show spatial complementary, suggesting at least partial spatial separation of covalent and non-covalent bonding aspects.[17–19] The combined use of AIM, NCI, and ELI-D provides a comprehensive picture of chemical bonds in real-space. For **1** and **3**, the topological and integrated AIM and ELI-D parameters are collected in Table 1 and the AIM topology as well as suitable NCI and ELI-D isosurfaces are displayed in Figures 3 and 4 (for **2** and **4**, see Figures S17 and S18). For all bonds, d is the geometric contact distance, $\rho(\mathbf{r})_{bcp}$ is the electron density at the bcp, $\nabla^2\rho(\mathbf{r})_{bcp}$ is the corresponding Laplacian, ε is the bond ellipticity, $G/\rho(\mathbf{r})_{bcp}$ and $H/\rho(\mathbf{r})_{bcp}$ are the kinetic and total energy density over $\rho(\mathbf{r})_{bcp}$ ratios, N_{ELI} and V_{ELI} are electron populations and volumes of related ELI-D basins, γ_{ELI} is the ELI-D value at the attractor position, RJI is the Raub-Jansen Index. The E–P bond formation is visible in the AIM topology, and in addition numerous weak secondary interactions are found between the P atom and the organic ligands (Figures 3a, 4a S17a and S18a). For the C–O bond, strong covalent as well as strong ionic bond contributions are present. In terms of topological ED analysis at the bond critical point (bcp), this results in a strongly negative ratio of the total energy density and the ED ($H/\rho(\mathbf{r})_{bcp}$; covalent bonding aspects) and strongly positive ratio of the kinetic energy density and the ED ($G/\rho(\mathbf{r})_{bcp}$; ionic bonding aspects). Consequently, the Laplacian of the ED ($\nabla^2\rho(\mathbf{r})_{bcp}$) is close to zero

Table 1. Topological and integrated AIM and ELI-D properties of relevant interactions.

	contact or basin	d [Å]	$\rho(\mathbf{r})_{bcp}$ [eÅ^{-3}]	$\nabla^2\rho(\mathbf{r})_{bcp}$ [eÅ^{-5}]	ε	$G/\rho(\mathbf{r})_{bcp}$ [a.u.]	$H/(\mathbf{r})_{bcp}$ [a.u.]	N_{ELI} [e]	V_{ELI} [Å^3]	γ_{ELI}	RJI
$[PCO]^-$	C–O	1.195	2.90	−1.3	0.00	1.80	−1.83	2.18	2.3	1.49	80.8
1	C–O	1.160	3.14	5.9	0.01	2.01	−1.88	2.61	4.1	1.53	81.8
2	C–O	1.163	3.12	5.3	0.01	2.00	−1.88	2.57	3.9	1.53	81.7
3	C–O	1.245	2.64	−10.8	0.09	1.48	−1.76	1.93	2.1	1.55	76.2
4	C–O	1.246	2.63	−11.1	0.10	1.47	−1.76	1.93	2.1	1.55	76.1
3	C–C	1.495	1.76	−16.0	0.09	0.28	−0.92	2.52	6.1	1.97	66.3
4	C–C	1.495	1.76	−15.9	0.09	0.28	−0.92	2.51	6.0	1.97	66.3
$[PCO]^-$	P–C	1.619	1.22	13.7	0.00	1.67	−0.88	2.47	8.4	1.53	95.5
1	P–C	1.661	1.15	10.6	0.36	1.53	−0.88	3.17	10.7	1.67	93.1
2	P–C	1.657	1.16	11.0	0.33	1.54	−0.88	3.22	11.3	1.66	93.1
3	P–C	1.757	1.14	0.6	0.37	1.01	−0.97	2.59	6.7	1.79	86.0
4	P–C	1.755	1.14	0.8	0.36	1.02	−1.07	2.59	6.7	1.79	86.2
1	Sb–P	2.554	0.49	−0.2	0.02	0.35	−0.37	1.48	5.3	1.54	58.9
2	Bi–P	2.654	0.44	0.6	0.02	0.40	−0.31	1.10	4.0	1.52	61.9
3	Sb–P	2.493	0.57	−0.7	0.06	0.32	−0.41	1.82	6.8	1.56	55.3
4	Bi–P	2.594	0.51	0.1	0.07	0.37	−0.35	1.59	6.3	1.52	58.5

 © 2022 The Authors. Zeitschrift für anorganische und allgemeine Chemie published by Wiley-VCH GmbH

Journal of Inorganic and General Chemistry
ZAAC
Zeitschrift für anorganische und allgemeine Chemie
RESEARCH ARTICLE

15213749, 2022, 9, Downloaded from https://onlinelibrary.wiley.com/doi/10.1002/zaac.202200133 by Staats- und Universitätsbibliothek, Wiley Online Library on [18/06/2023]. See the Terms and Conditions (https://onlinelibrary.wiley.com/terms-and-conditions) on Wiley Online Library for rules of use; OA articles are governed by the applicable Creative Commons License

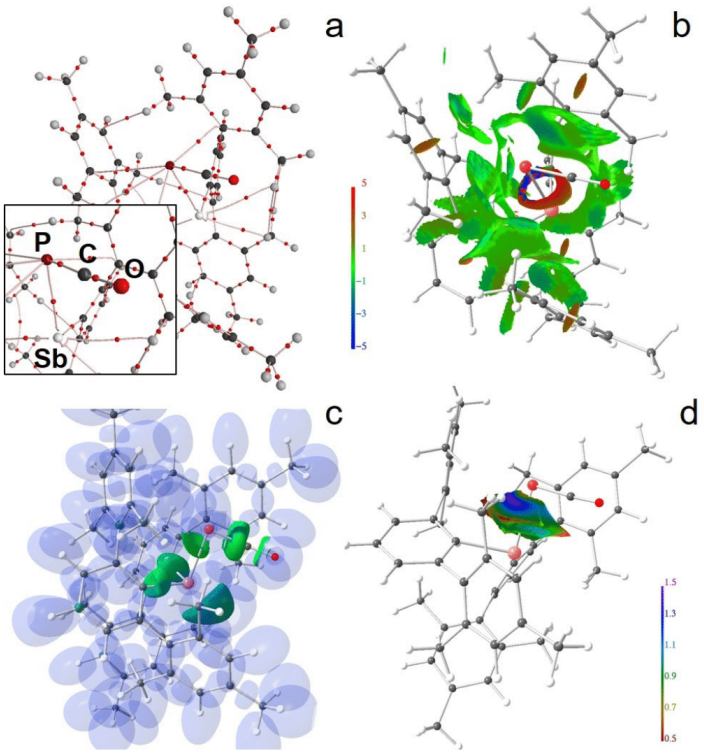

Figure 3. RSBI analysis of **1** (a) AIM bond paths motif, (b) NCI *iso*-surface at s(**r**) = 0.5, (c) ELI-D localization domain representation at *iso*-value of 1.3, (d) ELI-D distribution mapped on the Sb–P ELI-D basin.

in the $[PCO]^-$ ion (in CO it is positive ($\nabla^2\rho(\mathbf{r})_{bcp} = 11$ eÅ^{-5}) because $G/\rho(\mathbf{r})_{bcp} = 2.17$ a.u. dominates over $H/\rho(\mathbf{r})_{bcp} = -1.94$ a.u.). The double-bond character of the C–O bond in PCO is reflected in a very large ED ($\rho(\mathbf{r})_{bcp} = 2.9$ eÅ^{-3}), compared to 3.4 eÅ^{-3} in free CO. With 81% the RJI bond polarity is between that obtained for covalent bonds (<70%) and ionic/dative bonds (>90%), i.e. about 80% of the ED within the C–O ELI-D bonding basin is located within the AIM basin of the C atom. Ionic bond contributions prevail in the P–C bond, which gives rise to a positive Laplacian ($|G/\rho(\mathbf{r})_{bcp}| > |H/\rho(\mathbf{r})_{bcp}|$; $\nabla^2\rho(\mathbf{r})_{bcp} = 14$ eÅ^{-5}) and a RJI of about 96%. The electronic characteristics of both bonds are only slightly affected by coordination to the (2,6-$Mes_2C_6H_4$)$_2$E moiety: The C–O bond becomes a little shorter/stronger and the P–C bond becomes a little longer and weaker. In contrast, subsequent attachment of IMe_4 causes bending of the P–C–O axis and considerable bond elongation by about 0.09 Å (C–O) and 0.10 Å (P–C). Consequently, one finds decreased accumulations of the ED at the bcp in case of the C–O bond and inside the ELI-D bonding basin in both cases. For both bonds, the bond character changes towards higher relevance for covalent bonding aspects: $|H/\rho(\mathbf{r})_{bcp}| > |G/\rho(\mathbf{r})_{bcp}|$, RJ < 80% for C–O, and $|H/\rho(\mathbf{r})_{bcp}| \approx |G/\rho(\mathbf{r})_{bcp}|$, RJI < 90% for P–C, i.e. the changes exclusively go to the expense of ionic bonding aspects. The longer and weaker E–P bonds (E = Sb, Bi) become about 0.06 Å shorter *via* NHC coordination, however, with similar trends (diminished ionic bond contributions) in the electronic bond characteristics. Notably, in the group 13 series, they tend to become 0.02–0.04 Å longer.[5] In the NCI framework, thin ring-shaped basins enclose the E–P bond axes (E = Sb, Bi), pointing towards minor non-covalent bond contributions (Figures 3a, 4a S17a and S18a). In addition, numerous (extended) flat and greenish coloured basins are visible, uncovering a multitude of weak Van-der-Waals type interactions, some of which even give rise to the formation of a bcp in AIM topology, together transcending the Lewis picture of chemical bonding. The localization domain representation of the ELI-D shows that the E–P bonding basins stem from formerly non-bonding lone-pair basins of the P atom in **1** and **2**; at this *iso*-value ($\gamma = 1.3$) they are still topologically connected to the remaining lone-pair basins (Figures 3c, 4c S17c and

 © 2022 The Authors. Zeitschrift für anorganische und allgemeine Chemie published by Wiley-VCH GmbH

Journal of Inorganic and General Chemistry
ZAAC
Zeitschrift für anorganische und allgemeine Chemie

RESEARCH ARTICLE

15213749, 2022, 9, Downloaded from https://onlinelibrary.wiley.com/doi/10.1002/zaac.202200133 by Staats- und Universitätsbibliothek, Wiley Online Library on [18/06/2023]. See the Terms and Conditions (https://onlinelibrary.wiley.com/terms-and-conditions) on Wiley Online Library for rules of use; OA articles are governed by the applicable Creative Commons License

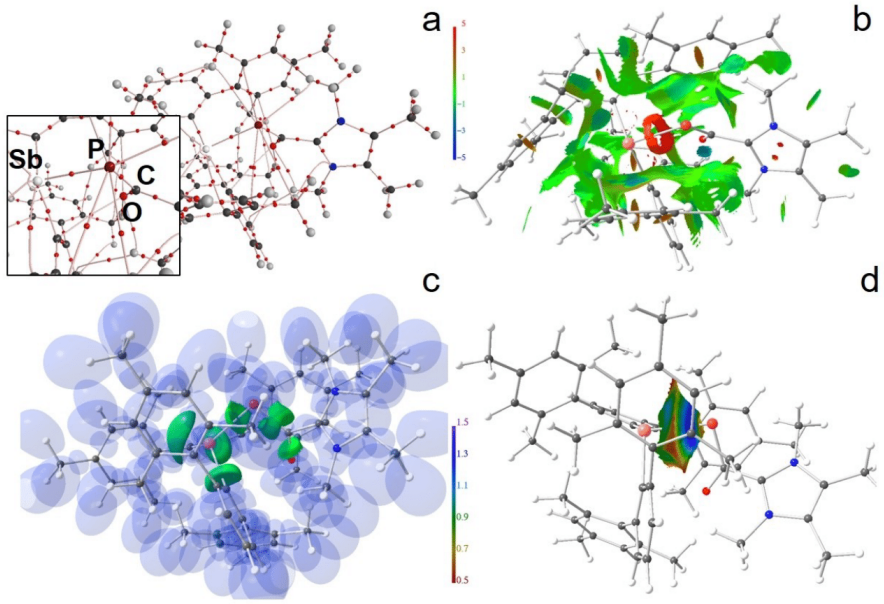

Figure 4. RSBI analysis of **3** (a) AIM bond paths motif, (b) NCI *iso*-surface at s(**r**) = 0.5, (c) ELI-D localization domain representation at *iso*-value of 1.3, (d) ELI-D distribution mapped on the Sb–P ELI-D basin.

S18c). The spatial requirements of the full E–P bonding basins is visible in Figures 3d, 4d S17d and S18d. Especially in **2**, the basin shape is almost flat in direction of the Bi atom, and only a shallow increase of electron localizability is visible, confirming the bond to be rather coordinative than dative, although these two terms are often used synonymously. AIM atomic and fragmental charges (Q_{AIM}) disclose effects of charge redistributions upon formation of **1**–**4**, whereby free CO and $[PCO]^-$ ion serve as reference (Table 2). Within the AIM framework, the strongly electronegative O and N atoms typically show strongly negative charges and vary only little in different chemical environments. It is thus not of surprise that Q_{AIM} for the O atoms vary only between −1.15 and −1.26 e in all compounds. Bearing this in mind, and comparing free CO with the free $[PCO]^-$ ion, the negative charge in the latter results in a situation in which the P and C atoms are *not* very positively charged, although being close to the O atom. Charge separation between the $(2,6\text{-}Mes_2C_6H_3)_2E]^+$ cation and PCO is less pronounced for Sb and Bi (about 0.3 e) than for Ga and In (about 0.5 e).[5] The hypothetical formation of **3** and **4** from $(2,6\text{-}Mes_2C_6H_3)_2E]^+$ and $[PCO]^-$ is accompanied by a charge transfer of about 0.7 e from the $[PCO]^-$ anion to the $(2,6\text{-}Mes_2C_6H_3)_2E]^+$ cation (E = Sb, Bi), which stem from the P atom (about 0.3 e), the C atom (about (0.3 e), and the O atom (about 0.1 e). This effect is partially inverted by addition of the IMe_4, which loses about 0.55 e in the process, bringing the atomic charges of the PCO moiety again closer to those found in the free $[PCO]^-$ ion.

Table 2. Atomic and fragmental AIM charges (in e).

	CO	$[PCO]^-$	**1**	**2**	**3**	**4**
E			1.04	1.00	0.94	0.91
R[a]			−0.36	−0.33	−0.39	−0.37
R′[a]			−0.37	−0.34	−0.40	−0.38
ERR′			0.31	0.33	0.15	0.16
P		0.19	0.46	0.48	0.20	0.21
C	1.20	0.07	0.39	0.36	0.33	0.32
O	−1.20	−1.26	−1.15	−1.16	−1.20	−1.20
PCO		−1.00	−0.30	−0.32	−0.67	−0.67
IMe_4					0.55	0.54
Σ	0.00	0.00	0.00	0.01	0.03	0.03

Conclusions

The kinetically stabilized diarylantimony and diarylbismuth phosphaethynolates $(2,6\text{-}Mes_2C_6H_3)_2EPCO$ (1, E = Sb; 2, E = Bi) were prepared and fully characterized. The stability of **1** and **2** is in marked contrast to the lighter congers Ph_2EPCO (E = Sb, Bi) that could not be isolated. The reaction of **1** and **2** with the small N-heterocyclic carbene (NHC), namely 1,3,4,5-tetramethylimidazol-2-ylidene (IMe_4) provided the complexes (2,6-

 © 2022 The Authors. Zeitschrift für anorganische und allgemeine Chemie published by Wiley-VCH GmbH

Journal of Inorganic and General Chemistry
ZAAC
Zeitschrift für anorganische und allgemeine Chemie

RESEARCH ARTICLE

15213749, 2022, 9, Downloaded from https://onlinelibrary.wiley.com/doi/10.1002/zaac.202200133 by Staats- und Universitätsbibliothek, Wiley Online Library on [18/06/2023]. See the Terms and Conditions (https://onlinelibrary.wiley.com/terms-and-conditions) on Wiley Online Library for rules of use; OA articles are governed by the applicable Creative Commons License

$Mes_2C_6H_3)_2EP(O)C(IMe_4)$ (**3**, E = Sb; **4**, E = Bi) that also show a higher thermal stability than $Ph_2E(I^iPr_2Me_2)PCO$ (E = Sb, Bi; $I^iPr_2Me_2$ = 1,3-diisopropyl-4,5-dimethylimidazol-2-ylidene).[4] In **3** and **4**, the coordination of the P(O)C(IMe_4) moiety occurs in a monodentate fashion (e.g. via P), whereas in the group 13 counterparts, $(2,6\text{-}Mes_2C_6H_3)_2EP(O)C(IMe_4)$ (E = Ga, In), the coordination is bidentate.[5] DFT quantified the energetic difference between different PCO coordination modes and found a significant preference for phosphaketene coordination; this preference is substantially larger than for the related group 13 compounds. Subsequent RSBI analysis indicated that – just like in CO – covalent and non-covalent (ionic) bonding aspects are equally relevant for the C–O bond in PCO^-, whereas ionic contributions prevail in the P–C bonds. Adduct formation with the IMe_4 moiety mainly goes to the expense of ionic bonding aspects in both bond types.

Experimental Section

General Information

All reactions and manipulations were performed under inert atmosphere (argon) using anhydrous solvents stored over 4 Å molecular sieves. Detailed general informations and synthetic aspects as well as NMR figures, UV-Vis figures and Computational and crystallographic details can be found in the supporting information. The NMR numbering scheme is different from the crystallographic numbering scheme. For details see the NMR figures in the supporting information.

Synthesis and characterization of $(2,6\text{-}Mes_2C_6H_3)_2SbPCO$ (1). $(2,6\text{-}Mes_2C_6H_3)_2SbCl$ (50.0 mg, 57.4 µmol, 1.00 eq.) and $Na(1,4\text{-dioxane})_{2.5}OCP$ (17.3 mg, 57.4 µmol, 1.00 eq.) were suspended in toluene (6 mL) and stirred for 18 hours, additionally the suspension is filtered and the solvent of the remaining solution is removed under vacuum to yield the target compound $(2,6\text{-}Mes_2C_6H_3)_2SbPCO$ as yellow solid (40.3 mg, 50.3 µmol, 83 %). Crystals suitable for X-Ray structure determination were grown from a hot toluene solution.

^{1}H NMR (600 MHz, C_6D_6): δ(ppm) = 6.99 (t, $^3J(^1H–^1H)$ = 7.51 Hz, 1H, H4), 6.76 (s, 2H, H9 or H11), 6.74 (s, 2H, H9 or H11), 6.72 (d, $^3J(^1H–^1H)$ = 7.52 Hz, 2H, H3 and H5), 2.18 (s, 6H, H14), 1.92 (s, 6H, H13), 1.82 (s, 6H, H15). **$^{13}C\{^1H\}$ NMR (151 MHz, C_6D_6)**: δ(ppm) = 193.58 (d, $^1J(^{13}C–^{31}P)$ = 113.88 Hz, C16), 150.48 (s, C2 and C6), 140.78 (s, C7), 140.66 (d, $^2J(^{13}C–^{31}P)$ = 7.57 Hz, C1), 137.73 (s, C12), 137.46 (s, C10), 137.31 (s, C8), 131.27 (s, C3 and C5), 129.32 (s, C9 and C11), 129.13 (s, C4), 22.64 (s, C13), 22.53 (s, C15), 21.04 (s, C14). **$^{31}P\{^1H\}$ NMR (243 MHz, C_6D_6)**: δ(ppm) = −314.94 (s). **HRMS ESI (m/z)**: No signal found in positive nor negative mode. **IR (ATR, neat)**: $\tilde{\nu}$ = 2915 (m), 1920 (s), 1610 (w), 1552 (w), 1435 (m), 1378 (w), 1180 (w), 1068 (w), 1034 (w), 909 (w), 847 (s), 802 (m), 760 (w), 736 (w), 695 (w), 657 (w) cm^{-1}. UV-Vis (Toluene, 10 µM) λ(abs) = 286, 344 nm. Melting point = 198 °C (decomp.).

Synthesis and characterization of $(2,6\text{-}Mes_2C_6H_3)_2BiPCO$ (2). $(2,6\text{-}Mes_2C_6H_3)_2BiCl$ (50.0 mg, 57.4 µmol, 1.00 eq.) and $Na(1,4\text{-dioxane})_{2.5}OCP$ (17.3 mg, 57.4 µmol, 1.00 eq.) were suspended in toluene (6 mL) and stirred for 18 hours, additionally the suspension is filtered and the solvent of the remaining solution is removed under vacuum to yield the target compound $(2,6\text{-}Mes_2C_6H_3)_2BiPCO$ as orange solid (40.3 mg, 50.3 µmol, 83 %). Crystals suitable for X-Ray structure determination were grown from a hot toluene solution.

^{1}H-NMR (600 MHz, C_6D_6): δ(ppm) = 7.04 (t, $^3J(^1H–^1H)$ = 7.39 Hz, 1H, H4), 6.94 (d, $^3J(^1H–^1H)$ = 7.43 Hz, 2H, H3 and H5), 6.81 (s, 4H, H9 and H11), 2.22 (s, 6H, H14), 1.98 (s, 6H, H13), 1.90 (s, 6H, H15). **$^{13}C\{^1H\}$ NMR (151 MHz, C_6D_6)**: δ(ppm) = 193.60 (d, $^1J(^{13}–)$ = 114.78 Hz, C16), 173.45 (s, C1), 150.71 (s, C2 and C6), 141.60 (s, C7), 137.30 (s, C12), 137.26 (s, C8), 136.75 (s, C10), 132.71 (s, C3 and C5), 129.32 (s, C9 and C11), 129.02 (s, C4), 22.45 (s, C13), 22.41 (s, C15), 21.20 (s, C14). **$^{31}P\{^1H\}$ NMR (243 MHz, C_6D_6)**: δ(ppm) = −324.04. **HRMS ESI (m/z)**: $[M+Cu]^+$ calculated. for $C_{49}H_{59}BiCuOP$*, 957.26938; found, 957.26769, $[M\text{-}CO+Cu]^+$ calculated for $C_{48}H_{50}BiCuP$, 929.27446; found, 929.27291, $[M\text{-}PCO]^+$ calculated. for $C_{48}H_{50}Bi$, 835.37110; found, 835.36947. **IR (ATR, neat)**: $\tilde{\nu}$ = 2915 (w), 1901 (s), 1610 (w), 1557 (w), 1435 (m), 1377 (w), 1179 (w), 1032 (w), 995 (w), 847 (s), 800 (m), 733 (m), 657 (w) cm^{-1}. UV-Vis (toluene, 10 µM) λ(abs) = 280, 352 nm. Melting point = 127 °C (decomp.).

* Measurement was repeated at different days. The Cu source is most likely the instrument.

Synthesis of $(2,6\text{-}Mes_2C_6H_3)_2SbP(O)C(IMe_4)$ (3). 1 (50.0 mg, 61.9 µmol, 1.00 eq.) and 1,3,4,5-tetramethylimidazol-2-ylidene (7.69 mg, 61.9 µmol, 1.00 eq.) were dissolved in THF (6 mL) and stirred for 24 hours. After filtration the solvent is removed under vacuum to yield the target compound $(Mes_2C_6H_3)_2SbP(O)C(IMe_4)$ (3) as yellow solid (40.0 mg, 42.9 µmol, 69 %). Crystals suitable for X-Ray structure determination were grown from a hot benzene solution.

^{1}H NMR (600 MHz, THF-d8): δ(ppm) = 7.11 (t, $^3J(^1H–^1H)$ = 7.46 Hz, 1H, H4), 6.59 (s (br), 4H, H9 and H11), 6.56 (d, $^3J(^1H–^1H)$ = 7.43 Hz, 2H, H3 and H5), 3.52 (s, 3H, H20 and H23), 2.22 (s (br), 6H, H14), 2.17 (s, 3H, H21 and H22), 1.76 (m, 12H). **$^{13}C\{^1H\}$ NMR (151 MHz, THF-d8)**: δ(ppm) = 198.53 (d, $^1J(^{13}C–^{31}P)$ = 81.55 Hz, C16), 152.34 (s, C2 and C6), 149.24 (d, $^2J(^{13}C–^{31}P)$ = 53.71 Hz, C17), 143.77 (s, (br), C7), 142.91 (d, $^2J(^{13}C–^{31}P)$ = 5.26 Hz, C1), 138.05 (s (br), C8 and C12), 136.07 (s (br), C10), 128.94 (s (br), C3 and C5), 128.02 (s, C9 and C11), 124.32 (s, C18 and C19), 33.35 (s, C20 or C23), 33.31 (s, C20 or C23), 23.52 (s (br), C13 and C15), 21.27 (s, C14), 8.33 (s, C21 and C22). **$^{31}P\{^1H\}$ NMR (243 MHz, THF-d8)**: δ(ppm) = 65.55. **HRMS ESI (m/z)**: $[M\text{-}PCO\text{-}NHC]^+$ calculated for $C_{48}H_{50}Sb$, 747.29452; found, 747.29452. **IR (ATR, neat)**: $\tilde{\nu}$ = 2915 (m), 2853 (m), 1771 (w), 1651 (w), 1610 (w), 1568 (w), 1505 (w), 1478 (m), 1435 (s), 1374 (s), 1261 (w), 1231 (w), 1177 (w), 1075 (w), 1032 (m), 928 (w), 847 (s), 801 (s), 735 (s), 680 (s) cm^{-1}. UV-Vis (toluene, 10 µM) λ(abs) = 288, 406 nm. Melting point = 126 °C (decomp.).

Synthesis of $(2,6\text{-}Mes_2C_6H_3)_2BiP(O)C(IMe_4)$ (4). 2 (50.0 mg, 55.9 µmol, 1.00 eq.) and 1,3,4,5-tetramethylimidazol-2-ylidene (6.94 mg, 55.9 µmol, 1.00 eq.) were dissolved in THF (6 mL) and stirred for 24 hours. After filtration the solvent is removed under vacuum to yield the target compound $(Mes_2C_6H_3)_2BiP(O)C(IMe_4)$ (4) as red solid (42.3 mg, 44.5 µmol, 74 %). Crystals suitable for X-Ray structure determination were grown from a hot benzene solution.

^{1}H NMR (600 MHz, C_6D_6): δ(ppm) = 7.19 (t, $^3J(^1H–^1H)$ = 7.44 Hz, 1H, H4), 6.98 (d, $^3J(^1H–^1H)$ = 7.44 Hz, 2H, H3 and H5), 6.84 (s, 2H, H9 or H11), 6.83 (s, 2H, H9 or H11), 3.16 (s, 3H, H20 and H23), 2.24 (s, 6H, H14), 2.12 (m, 12H, H13 and H15), 1.07 (s, 3H, H21 and H22). **$^{13}C\{^1H\}$ NMR (151 MHz, C_6D_6)**: δ(ppm) = 197.23 (d, $^1J(^{13}C–^{31}P)$ = 86.01 Hz, C16), 158.95 (s, C1), 152.37 (s, C2 and C6), 150.82 (d, $^2J(^{13}C–^{31}P)$ = 48.94 Hz, C17), 144.36 (s, C7), 137.74 (s, C8 or C12), 137.54 (s, C8 or C12), 135.47 (s, C10), 130.93 (s, C3 and C5), 128.74 (s, C9 and C11), 127.29 (s, C4), 122.31 (s, C18 and C19), 32.95 (s, C20 or C23), 32.91 (s, C20 or C23), 23.19 (s, C13 and C15), 21.26 (s, C14), 7.53 (s, C20 and C21). **$^{31}P\{^1H\}$ NMR (243 MHz, C_6D_6)**: δ(ppm) = 67.90. **HRMS ESI (m/z)**: $[M\text{-}PCO\text{-}NHC]^+$ calculated for $C_{48}H_{50}Bi$, 835.37110; found,

 © 2022 The Authors. Zeitschrift für anorganische und allgemeine Chemie published by Wiley-VCH GmbH

Journal of Inorganic and General Chemistry
ZAAC
Zeitschrift für anorganische und allgemeine Chemie

RESEARCH ARTICLE

15213749, 2022, 9, Downloaded from https://onlinelibrary.wiley.com/doi/10.1002/zaac.202200133 by Staats- und Universitätsbibliothek, Wiley Online Library on [18/06/2023]. See the Terms and Conditions (https://onlinelibrary.wiley.com/terms-and-conditions) on Wiley Online Library for rules of use; OA articles are governed by the applicable Creative Commons License

835.36947. **IR (ATR, neat)**: $\tilde{\nu}$ = 2914 (m), 1645 (w), 1563 (w), 1436 (s), 1371 (m), 1231 (w), 1176 (w), 1087 (w), 1031 (w), 1009 (w), 931 (w), 843 (s), 794 (s), 776 (w), 730 (s), 716 (w), 677 (m) cm^{-1}. UV-Vis (Toluene, 10 μM) λ(abs) = 305, 506 nm. melting point > 100 °C (decomp.).

Accession Codes

CCDC nos. 2127081–2127084 contain the supplementary crystallographic data for this paper. These data can be obtained free of charge from The Director, CCDC, 12 Union Road, Cambridge CB2 1EZ, UK (Fax: +44-1223-336033; e-mail: deposit@ccdc.cam.ac.uk or http://www.ccdc.cam.ac.uk).

Acknowledgment

The Deutsche Forschungsgemeinschaft (DFG) is gratefully acknowledged for financial support. Open Access funding enabled and organized by Projekt DEAL.

Conflict of Interest

The authors declare no conflict of interest.

Data Availability Statement

The data that support the findings of this study are available from the corresponding author upon reasonable request.

Keywords: Antimony · Bismuth · Phosphaethynolate · Terphenyl · N-heterocyclic carbene

[1] J. M. Goicoechea, H. Grützmacher, *Angew. Chem. Int. Ed.* **2018**, *57*, 16968–16994; *Angew. Chem.* **2018**, *130*, 17214–17240.
[2] L. Weber, *Eur. J. Inorg. Chem.* **2018**, *20–21*, 2175–2227.
[3] R. E. Schreiber, J. M. Goicoecha, *Angew. Chem. Int. Ed.* **2021**, *60*, 3759–3767; *Angew. Chem.* **2021**, *133*, 3803–3811.
[4] J. E. Walley, E. Kertész, G. Wang, D. A. Dickie, Z. Benkő, R. J. Gillard, *Inorg. Chem.* **2021**, *60*, 4733–4743.
[5] D. Duvinage, M. Janssen, E. Lork, H. Grützmacher, S. Mebs, J. Beckmann, *Dalton Trans.* **2022**, *51*, 7622–7629.
[6] M. Olaru, D. Duvinage, E. Lork, S. Mebs, J. Beckmann, *Angew. Chem. Int. Ed.* **2018**, *57*, 10080–10084; *Angew. Chem.* **2018**, *130*, 10237–10241.
[7] N. J. Hardman, B. Twamley, P. P. Power, *Angew. Chem. Int. Ed.* **2000**, *39*, 2771–2773; *Angew. Chem.* **2000**, *112*, 2884–2886.
[8] B. Cordero, V. Gómez, A. E. Platero-Prats, M. Revés, J. Echeverría, E. Cremades, F. Barragán, S. Alvarez, *Dalton Trans.* **2008**, 2832–2838.
[9] D. Heift, Z. Benkő, H. Grützmacher, *Dalton Trans.* **2014**, *43*, 5920–5928.
[10] A. J. Arduengo III, H. V. R. Dias, R. L. Harlow, M. Kline, *J. Am. Chem. Soc.* **1992**, *114*, 5530–5534.
[11] a) B. Twamley, C. D. Sofield, M. M. Olmstead, P. P. Power, *J. Am. Chem. Soc.* **1999**, *121*, 3357–3367; b) N. J. Hardman, B. Twamley, P. P. Power, *Angew. Chem. Int. Ed.* **2000**, *15*, 2771–2773.
[12] O. Mallow, J. Bolsinger, P. Finke, M. Hesse, Y.-S. Chen, A. Duthie, S. Grabowsky, P. Luger, S. Mebs, J. Beckmann, *J. Am. Chem. Soc.* **2014**, *136*, 10870–10873.
[13] R. W. F. Bader, *Atoms in Molecules: A Quantum Theory*, Cambridge University Press: Oxford U. K., **1991**.
[14] E. R. Johnson, S. Keinan, P. Mori-Sanchez, J. Contreras-García, A. J. Cohen, W. Yang, *J. Am. Chem. Soc.* **2010**, *132*, 6498–6506.
[15] M. Kohout, *Int. J. Quantum Chem.* **2004**, *97*, 651–658.
[16] S. Raub, G. Jansen, *Theor. Chem. Acc.* **2001**, *106*, 223–232.
[17] N. Gillet, R. Chaudret, J. Contreras-García, W. Yang, B. Silvi, J.-P. Piquemal, *J. Chem. Theory Comput.* **2012**, *8*, 3993–3997.
[18] P. de Silva, C. Corminboeuf, *J. Chem. Theory Comput.* **2014**, *10*, 3745–3756.
[19] S. Mebs, *Chem. Phys. Lett.* **2016**, *651*, 172–177.

Manuscript received: April 1, 2022
Revised manuscript received: June 7, 2022
Accepted manuscript online: June 13, 2022

 © 2022 The Authors. Zeitschrift für anorganische und allgemeine Chemie published by Wiley-VCH GmbH

2.9 Synthesis and Single-Electron Oxidation of Bulky Bis(*m*-terphenyl)chalcogenides: The Quest for Kinetically Stabilized Radical Cations

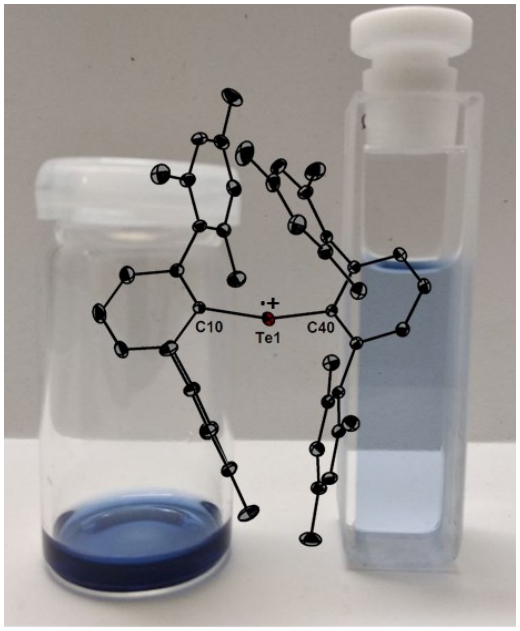

2.9.1 Synopsis

The stabilization of chalcogen centred radicals is of tremendous interest, not only in fundamental research but also as a possible explanation for Alzheimer's disease.[151] The bis(*m*-terphenyl)chalcogenides Ter_2E (E = S, Se, Te) were synthesized previously in our workgroup from chalcogen tetrafluorides, which was not reliable.[152] Due to this, a reproducible synthesis was developed starting from the chalcogen tetrafluorides, which were reacted with three equivalents *m*-terphenyllithium. The third equivalent of organolithium is used as a reduction agent, reducing the chalcogen (IV) to the chalcogenide (II). Also, alternative synthesis methods were examined to avoid the use of chalcogen tetrafluorides, especially sulfur tetrafluoride. For this, the NHC-SF_2 adduct was formed and reacted with *m*-terphenyllithium. For selenium tetrafluoride no substitute was found. For tellurium, the stepwise reaction was performed to study formed intermediates and also to find an alternative synthesis avoiding tellurium tetrafluoride. Tellurium tetrafluoride forms *m*-terphenyltellurium trifluoride $TerTeF_3$ with one equivalent of organolithium, which can also be obtained by the oxidation of bis(*m*-terphenyl)ditelluride with xenon difluoride. The reaction with another equivalent of organolithium results in the formation of the bis(*m*-terphenyl)tellurium

difluoride Ter_2TeF_2, which reacts with another equivalent *m*-terphenyllithium to the bis(*m*-terphenyl)telluride. The three bis(*m*-terphenyl)chalcogenides Ter_2E (E = S, Se, Te) were isolated and fully characterized by NMR spectroscopy, mass spectrometry and single crystal X-ray diffraction analysis. Their oxidation was studied by electrochemical and chemical oxidation. The oxidation potentials and the electrochemical oxidation were studied by cyclic voltammetry indicating a reversible single electron oxidation of bis(*m*-terphenyl)telluride and irreversible single electron oxidation of the selenide and an irreversible two-electron oxidation for the sulfide. Therefore, the chemical oxidation with xenon difluoride and potassium tetrakis(pentafluorophenyl)borate was attempted for all three chalcogenides, resulting in deep brown solutions in case of the sulfide and selenide. NMR spectroscopy indicated the formation of multiple unidentified species. The telluride formed an ink blue solution, from which single crystals were obtained. By single crystal X-ray analysis, the molecular structure of the bis(*m*-terphenyl)tellurenyl radical cation was obtained. The radical cation shows sharp signals in NMR spectroscopy, except for a not observed ^{13}C signal of the *ipso* carbon and the absence of a signal in ^{125}Te NMR spectroscopy, indicating that the radical is located at the tellurium center. For additional characterization, EPR spectroscopy and spectroelectrochemical UV-Vis spectroscopy was used. The radical cation provided no EPR signal at room temperature, suggesting an extremely fast relaxation. Because of this, the EPR spectrum was measured at 40 K in glassy DCM. The electronic structures of the parent Ter_2E compounds, the radical cations $Ter_2E^{\cdot+}$ and the dicationic species Ter_2E^{2+} were studied by means of DFT calculations.

2.9.2 Scientific contribution

I developed and optimized all reactions and performed the characterization of all compounds. I did the crystallographic part and co-wrote the manuscript. F. Mostaghimi synthesized the bis(*m*-terphenyl)chalcogenides from the chalcogen tetrafluorides. Under my supervision, M. Damrath developed the synthesis of the *m*-terphenylelement chlorides (E = S, Se) and J. Spils attempted the reduction of bis(*m*-terphenyl)sulfoxide. P. Komorr synthesized bis(*m*-terphenyl)sulfide *via* the NHC-SF_2 adduct. D. S. Odintsov, M. Fedin and L. Shuldrin conducted the electrochemical measurements and L. Shundrin co-wrote the manuscript. S. Mebs

executed the computational calculations and co-wrote the manuscript. J. Beckmann was principal investigator and co-wrote the manuscript.

Percentage of my contribution of the total workload:

Experimental concept and design: ca. 90%, experimental work and acquisition of experimental data: ca. 60%, data analysis and interpretation: ca. 70%, preparation of figures and tables: ca. 70%, drafting of the manuscript: ca. 40%.

The article was published in the journal “Chemistry – A European Journal“ in 2023 as an Open Access article:

Daniel Duvinage, Farzin Mostaghimi, Mattis Damrath, Julian Spils, Pascal Komorr, Danila S. Odintsov, Matvey Fedin, Leonid A. Shundrin, Stefan Mebs, Jens Beckmann, *Chem. Eur. J.* **2023**, e202203498.

DOI: 10.1002/chem.202203498

The Supporting Information includes experimental procedures, NMR and IR spectra, X-ray crystallographic data and structure refinement and computational data and is available free of charge on the journal′s website:

https://chemistry-europe.onlinelibrary.wiley.com/action/downloadSupplement?doi=10.1002%2Fchem.202203498&file=chem202203498-sup-0001-misc_information.pdf

Check for updates

Chemistry–A European Journal

Research Article
doi.org/10.1002/chem.202203498

Chemistry Europe
European Chemical Societies Publishing

www.chemeurj.org

Synthesis and Single-Electron Oxidation of Bulky Bis(*m*-terphenyl)chalcogenides: The Quest for Kinetically Stabilized Radical Cations

Daniel Duvinage,[a] Farzin Mostaghimi,[a] Mattis Damrath,[a] Julian Spils,[a] Pascal Komorr,[a] Danila S. Odintsov,[b] Matvey Fedin,[c] Leonid A. Shundrin,*[b] Stefan Mebs,*[d] and Jens Beckmann*[a]

In memory of Professor Robert West.

Abstract: Sterically encumbered bis(*m*-terphenyl)chalcogenides, (2,6-$Mes_2C_6H_3)_2E$ (E = S, Se, Te) were obtained by the reaction of the chalcogen tetrafluorides, EF_4, with three equivalents of *m*-terphenyl lithium, 2,6-$Mes_2C_6H_3Li$. The single-electron oxidation of (2,6-$Mes_2C_6H_3)_2Te$ using XeF_2/$K[B(C_6F_5)_4]$ afforded the radical cation $[(2,6\text{-}Mes_2C_6H_3)_2Te][B(C_6F_5)_4]$ that was isolated and fully characterized. The electrochemical oxidation of the lighter homologs (2,6-$Mes_2C_6H_3)_2E$ (E = S, Se) was irreversible and impaired by rapid decomposition.

Introduction

Main group element centered radicals have received tremendous interest ever since Gomberg's seminal discovery of the trityl radical.[1,2] Amongst those, sulfur-based radicals play a pivotal role.[3–6] Diorgano sulfide radical cations, $[R_2S]^{\bullet+}$ (R = alkyl, aryl), generated from their neutral parents, R_2S, by chemical one-electron oxidation, photolysis in the presence of a sensitizer or gamma radiolysis are only short-lived.[7] In the absence of other fragmentation pathways, radical cations, $[R_2S]^{\bullet+}$, undergo complexation with their neutral parents, R_2S, giving rise to dinuclear radical cations, $[R_2SSR_2]^{\bullet+}$, comprising two-center three-electron (2c3e) bonds, which have been studied by quantum chemical calculations.[8–12] Besides fundamental interest, these species are small molecule models relevant for the pathogenesis of Alzheimer's disease, which involves methionine radical cation moieties interacting with the protein environment.[13–15] The life span of these dinuclear radical cations, $[R_2SSR_2]^{\bullet+}$, rarely exceeds milliseconds. The first notable exception involves the 1,5-dithiooctane radical cation **I**, which persists for several days due to the transannular S–S-bond (Figure 1).[16] More recently, the 1,8-bis(phenylsulfanyl)naphthalene radical cation **II** and its selenium analog were isolated and fully characterized by X-ray crystallography and EPR spectroscopy (Figure 1).[17,18] Besides the two-center three-electron (2c3e) bond stabilization, evidence was found that radical cations, $[R_2S]^{\bullet+}$, may also favorably interact with adjacent aromatic rings.[19,20] A series of *m*-terphenyl thio, seleno- and telluroethers, showed systematically lowered oxidation potentials, which were attributed to through-space chalcogen···π interactions in the related short-lived radical cations. For a related series of bis(*m*-terphenyl)dichalcogenide

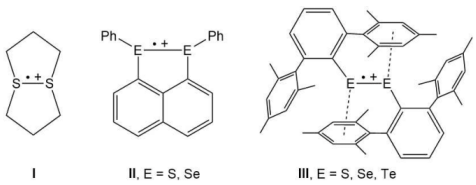

I **II**, E = S, Se **III**, E = S, Se, Te

Figure 1. Examples of dinuclear chalcogen radical cations.

[a] D. Duvinage, Dr. F. Mostaghimi, M. Damrath, J. Spils, P. Komorr, Prof. Dr. J. Beckmann
Institut für Anorganische Chemie und Kristallographie
Universität Bremen
Leobener Strasse 7, 28359 Bremen (Germany)
E-mail: j.beckmann@uni-bremen.de

[b] Dr. D. S. Odintsov, Prof. Dr. L. A. Shundrin
N. N. Vorozhtsov Institute of Organic Chemistry
Siberian Branch of Russian Academy of Sciences
Acad. Lavrentiev Avenue 9, 630090 Novosibirsk (Russia)
E-mail: shundrin@nioch.nsc.ru

[c] Prof. Dr. M. Fedin
Laboratory of Magnetic Resonance
International Tomography Center Siberian Branch of Russian Academy of Sciences
Institutskaya 3a, 630090 Novosibirsk (Russia)

[d] Dr. S. Mebs
Institut für Experimentalphysik
Freie Universität Berlin
Arnimallee 14, 14195 Berlin (Germany)
E-mail: stefan.mebs@fu-berlin.de

Supporting information for this article is available on the WWW under https://doi.org/10.1002/chem.202203498

© 2022 The Authors. Chemistry - A European Journal published by Wiley-VCH GmbH. This is an open access article under the terms of the Creative Commons Attribution License, which permits use, distribution and reproduction in any medium, provided the original work is properly cited.

© 2022 The Authors. Chemistry - A European Journal published by Wiley-VCH GmbH

Chemistry–A European Journal | Research Article doi.org/10.1002/chem.202203498 | Chemistry Europe European Chemical Societies Publishing

radical cations **III** such chalcogen···π interactions were indeed structurally confirmed.[21] This observation raises the question whether the oxidation of extremely bulky bis(*m*-terphenyl)chalcogenides may similarly provide a route for the preparation for stable diorgano chalcogenide radical cations that resist electron stabilization via two-center three-electron (2c3e) bonds and formally contain 7 valence electrons.

Results and Discussion

The synthesis of the bis(*m*-terphenyl) chalcogenides, (2,6-$Mes_2C_6H_3)_2E$ (**1 a**, E = S; **1 b**, E = Se; **1 c**, E = Te) turned out to be surprisingly difficult. After numerous failed attempts trying to adopt established routes for sterically less encumbered diaryl chalcogenides,[22] the preparation was eventually achieved by the reaction of the chalcogen tetrafluorides EF_4 (E = S, Se, Te) with three equivalents of the *m*-terphenyl lithium reagent, 2,6-

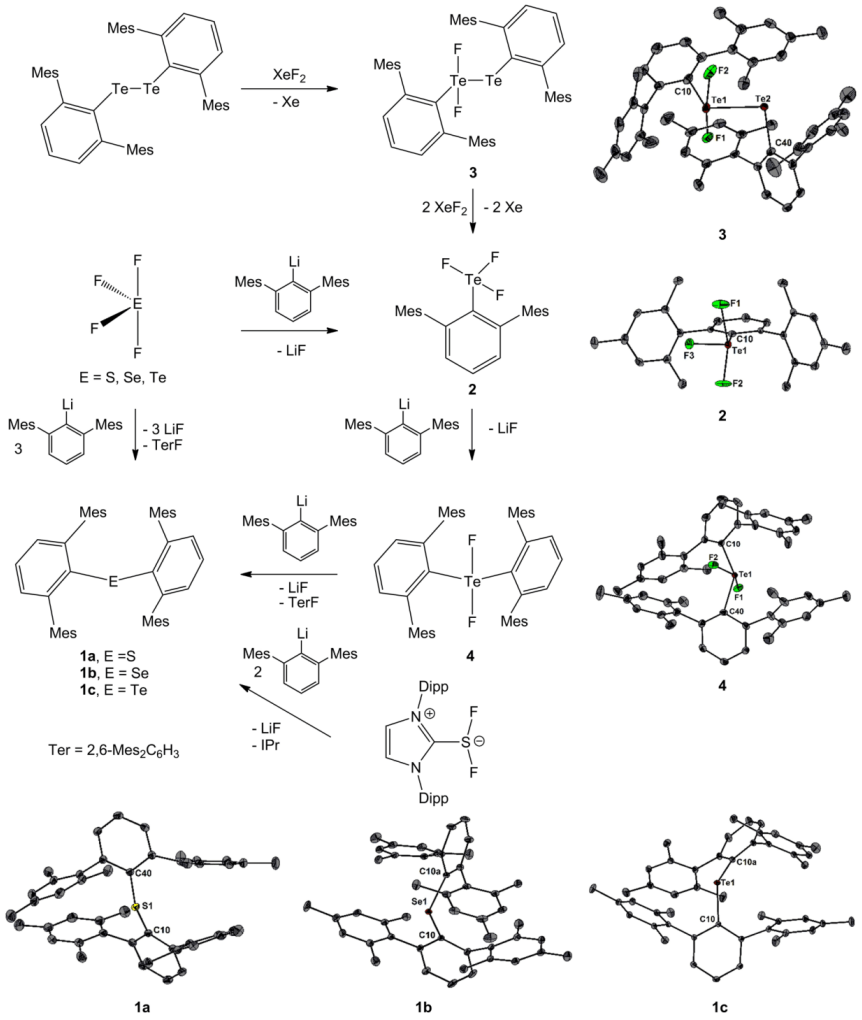

Figure 2. Synthesis of **1 a**–**c** and **2**–**4**. Molecular structures of **1 a**–**c** and **2**–**4**. Thermal ellipsoids set at 50% probability. Hydrogen atoms were omitted for clarity.

© 2022 The Authors. Chemistry - A European Journal published by Wiley-VCH GmbH

15213765, 2023, 11, Downloaded from https://chemistry-europe.onlinelibrary.wiley.com/doi/10.1002/chem.202203498 by Staats- und Universitätsbibliothek, Wiley Online Library on [18/06/2023]. See the Terms and Conditions (https://onlinelibrary.wiley.com/terms-and-conditions) on Wiley Online Library for rules of use; OA articles are governed by the applicable Creative Commons License

Chemistry–A European Journal | Research Article doi.org/10.1002/chem.202203498 | Chemistry Europe European Chemical Societies Publishing

15213765, 2023, 11, Downloaded from https://chemistry-europe.onlinelibrary.wiley.com/doi/10.1002/chem.202203498 by Staats- und Universitätsbibliothek, Wiley Online Library on [18/06/2023]. See the Terms and Conditions (https://onlinelibrary.wiley.com/terms-and-conditions) on Wiley Online Library for rules of use; OA articles are governed by the applicable Creative Commons License

$Mes_2C_6H_3Li$, which fulfils two functions. The first two equivalents substitute two fluorine atoms by *m*-terphenyl groups at the chalcogen atom in the oxidation state IV. The last equivalent reduces the chalcogen to the oxidation state II. In this way, **1a**, **1b** were obtained as colorless and **1c** as yellow crystals in 42, 64 and 52% yield (Figure 2). Compounds **1a** and **1c** are indefinitely stable even when exposed to the air, whereas **1b** slowly decomposes in the presence of moisture.[23] The two heavier bis-(*m*-terphenyl) chalcogenides were characterized by heteronuclear NMR spectroscopy. The ^{77}Se NMR spectrum of **1b** shows a signal at $\delta = 981.0$ that is less shielded than those of Ph_2Se ($\delta = 422$)[24] and Mes_2Se ($\delta = 225$).[25] The ^{125}Te NMR spectrum of **1c** exhibits a signal at $\delta = 572.0$ that lies midway between those of Ph_2Te ($\delta = 707$) and Mes_2Te ($\delta = 275$).[26]

The molecular structures of **1a**, **1b** and **1c** show the large steric encumbrance of the bulky *m*-terphenyl substituents,[27] which, however, has only a small effect on the average E–C bond lengths (E = S, Se, Te) that are only slightly elongated compared to Mes_2S (1.787(1) vs. 1.785(1) Å),[28] Mes_2Se (1.944(4) vs. 1.931(1) Å)[29] and Mes_2Te (2.150(1) vs. 2.140(3) Å).[30] The effect is more pronounced for the C–E–C angles of **1a**–**c**, which are considerably larger than those of Mes_2S (114.5(1) vs. 106.4(1)°),[28] Mes_2Se (116.1(2) vs. 102.0(1)°)[29] and Mes_2Te (116.2(2) vs. 101.0(1)°).[30]

We also studied the stepwise reaction of TeF_4 with 2,6-$Mes_2C_6H_3Li$ to shed light on the intermediates leading to the formation of **1c**. At an equimolar ratio this reaction afforded the mono-substituted *m*-terphenyl tellurium trifluoride 2,6-$Mes_2C_6H_3TeF_3$ (**3**) in 61% yield. In an effort to avoid TeF_4, the same product may also be obtained by fluorination of (2,6-$Mes_2C_6H_3$)TeTe(2,6-$Mes_2C_6H_3$) with XeF_2, which proceeds via the initial formation of mixed valent *m*-terphenyl tellurenyl fluoride (2,6-$Mes_2C_6H_3$)F_2TeTe(2,6-$Mes_2C_6H_3$) (**2**)[31,32] and eventually gives **3** in 42% yield.[33] The reaction of 2,6-$Mes_2C_6H_3TeF_3$ (**3**) with 2,6-$Mes_2C_6H_3Li$ allows the introduction of a second *m*-terphenyl substituent at tellurium, following the formation of the bis-(*m*-terphenyl) tellurium difluoride (2,6-$Mes_2C_6H_3)_2TeF_2$ (**4**) in 53% yield.[34] Interestingly, the C–Te–C bond angle of **4** (140.7(1)°)[27] is dramatically larger than those of **1c** (116.2(2)°) and Mes_2TeF_2 (110.1(1)°),[35] which supposedly gives rise to a weaker repulsion between the two *m*-terphenyl substituents. The reaction of **4** with one equivalent of 2,6-$Mes_2C_6H_3Li$ indeed proceeded with reduction[36] of the tellurium giving rise to the telluride **1c**, which confirms the mechanism proposed for the reaction of TeF_4 with three equivalents of 2,6-$Mes_2C_6H_3Li$ (see above). The major drawback of this method of preparation is the handling of highly corrosive and gaseous SF_4, which is not only needed as starting material for **1a**, but also for the preparation of liquid SeF_4[37] and solid TeF_4[38] (from SeO_2 and TeO_2), the starting materials of **1b** and **1c**. Sulfur tetrafluoride, SF_4, often contains thionyl fluoride, $S(O)F_2$, as an impurity, which forms as a side product during the synthesis of SF_4, or by hydrolysis caused by traces of water. Due to their similar boiling points, SF_4 and $S(O)F_2$, cannot be separated by distillation. The reaction of three equivalents of 2,6-$Mes_2C_6H_3Li$ with mixtures of SF_4 and $S(O)F_2$ gave rise to inseparable mixtures of **1a** and the sulfoxide, (2,6-$Mes_2C_6H_3)_2SO$.[39,40] Consequently, high purity of SF_4 was instrumental for the synthesis of **1a** via this route. Therefore, we turned our attention to the reaction of the donor acceptor complex $IPrSF_2$ (IPr = 1,3-bis(2,6-diisopropylphenyl)imidazol-2-ylidene)[41] with two equivalents of the *m*-terphenyl lithium reagent, 2,6-$Mes_2C_6H_3Li$. Indeed, this reaction provides an alternative method for the preparation of **1a**, which was isolated after column chromatography in 23% yield.[22,42]

The electrochemical oxidation (ECO) of the bis(*m*-terphenyl) chalcogenides, studied by cyclic voltammetry in CH_2Cl_2, was irreversible for **1a** and **1b** at their half-wave potentials of $E_{1/2} =$ 1.59 and 1.22 V, respectively (Figure 3).[43] In contrast, the first ECO step of telluride **1c** is a reversible one-electron and diffusion-controlled process ($E_{1/2} = 1.08$ V) associated with the formation of the corresponding long-lived radical cation $[\mathbf{1c}]^{\bullet+}$. The transition of the electron transfer kinetics to an irreversible process was observed for this ECO stage at increased potential sweep rates, starting from 400 mV s^{-1} (see the Supporting Information). The second ECO step of **1c** is irreversible ($E_{peak} =$ 1.65 V) and is at least a two-electron process.[43] The ECO revealed a two-electron ECO process for **1a** and a one-electron process for **1b**, both in correlation with irreversible electron transfer kinetics (see the Supporting Information). The oxidation potentials suggest that the ionization potentials decrease in the order **1a** > **1b** > **1c** (see DFT calculations below).

After examination of the redox properties, we studied the (single-electron) oxidation of the bis-(*m*-terphenyl) chalcogenides **1a**–**1c** using XeF_2 in the presence of $K[B(C_6F_5)_4]$.[44] While the reaction with **1a** and 1**b** gave ill-defined dark mixtures even at low temperatures, the reaction of **1c** provided a persistently blue solution, from which the radical cation salt [(2,6-$Mes_2C_6H_3)_2Te]^{\bullet+}[B(C_6F_5)_4]^-$, $[\mathbf{1c}]^{\bullet+}[B(C_6F_5)_4]^-$, was isolated as blue crystals in 96% yield (Figure 4). In the solid-state, it is indefinitely stable under inert conditions. When exposed to the air, it is even stable for up to a week without signs of degradation. In solutions of chlorinated solvents such as CH_2Cl_2, it is stable for up to 3 months if the solvent is properly dried and degassed. In wet solvents a degradation is visible by loss of color over the course of an hour. The molecular structure of

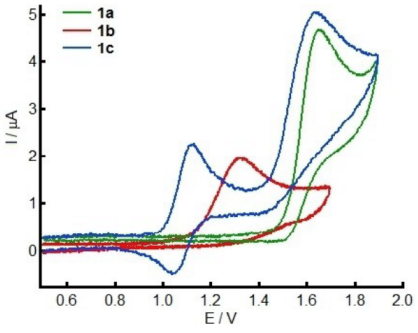

Figure 3. Normalized cyclic voltammograms of **1a**–**1c** in CH_2Cl_2. (Normalization to equal concentration of 1 mM, potential sweep rate was 0.1 V s^{-1}).

© 2022 The Authors. Chemistry - A European Journal published by Wiley-VCH GmbH

Chemistry–A European Journal | Research Article doi.org/10.1002/chem.202203498 | Chemistry Europe European Chemical Societies Publishing

15213765, 2023, 11, Downloaded from https://chemistry-europe.onlinelibrary.wiley.com/doi/10.1002/chem.202203498 by Staats- und Universitätsbibliothek, Wiley Online Library on [18/06/2023]. See the Terms and Conditions (https://onlinelibrary.wiley.com/terms-and-conditions) on Wiley Online Library for rules of use; OA articles are governed by the applicable Creative Commons License

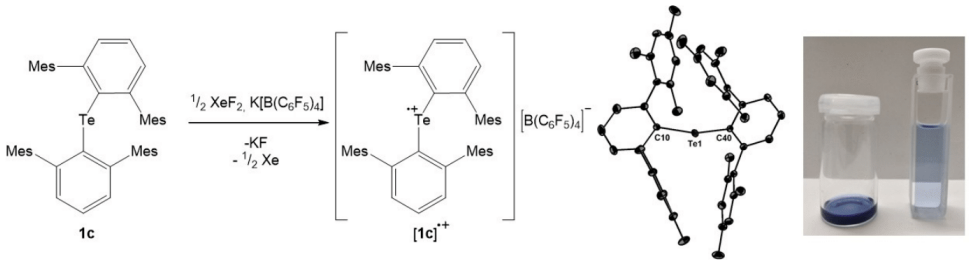

Figure 4. From left to right: Synthesis of the radical cation [**1 c**]$^{\bullet+}$ by oxidation of **1 c** with XeF_2 and $K[B(C_6F_5)_4]$. Molecular structure of [**1 c**]$^{\bullet+}$. Thermal ellipsoids set at 50 % probability. Hydrogen atoms and the $[B(C_6F_5)_4]^-$ anion are omitted for clarity. Selected bond lengths and angles of [**1 c**]$^{\bullet+}$: Te1-C10 2.165(1) Å, Te1-C40 2.179(1) Å, C10-Te1-C40 114.9(1)°. A solution of [**1 c**]$^{\bullet+}$ (CH_2Cl_2 (50 μM) (left), CH_2Cl_2 (10 μM) (right)).

[**1 c**]$^{\bullet+}[B(C_6F_5)_4]^-$ shows clear ion separation.[27] This is in marked contrast to Roesky's bis(trimethylsilyl)amide tellurium radical cation $[\{(Me_3Si)_2N\}_2Te]^{\bullet+}[AsF_6]^-$, which is not only electronically stabilized by conjugation with the lone pairs at the N atoms, but is also affected by ion pairing.[45] In [**1 c**]$^{\bullet+}[B(C_6F_5)_4]^-$, the individual Te–C bond lengths (2.166(1) and 2.179(1) Å) are significantly different and surprisingly, the average value (2.173(1) Å) is somewhat larger than in the neutral parent **1 c** (2.150(1) Å). Even more surprising, the C–Te–C (114.9(1)°) slightly decreases compared to the neutral parent **1 c** (116.2(2)°), which is counterintuitive with respect to the loss of one electron. We note that the Te–N bond lengths of $[\{(Me_3Si)_2N\}_2Te]^{\bullet+}[AsF_6]^-$ are slightly shorter than in the neutral telluride $\{(Me_3Si)_2N\}_2Te$, which was attributed to the conjugation with the lone pairs at the N atoms.[45]

The radical cation [**1 c**]$^{\bullet+}$ was characterized by electron paramagnetic resonance (EPR) spectroscopy. Due to the extremely fast relaxation time, the EPR spectrum of [**1 c**]$^{\bullet+}$ was not observed in a liquid CH_2Cl_2 solution at room temperature and was measured in frozen glassy CH_2Cl_2 at 40 K using CW and spin echo detection modes (see the Supporting Information for details). The EPR spectrum at the X-band is characterized by a *g*-tensor with principal components of 1.9593, 2.0455, 2.2125 (Figure 5).

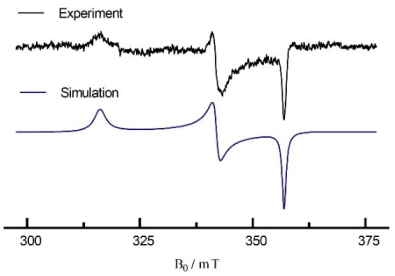

Figure 5. CW EPR spectrum of radical cation [1c]$^{\bullet+}$ in glassy CH_2Cl_2 at 40 K (upper spectrum) and its simulation (lower spectrum).

Compared to related bis(*m*-terphenyl)ditelluride radical cation $[(2,6\text{-}Mes_2C_6H_3Te)_2]^{\bullet+}$,[21] the *g*-tensor of [**1 c**]$^{\bullet+}$ has a smaller g_z component, while the values of g_x, g_y are comparable in magnitude. Unlike $[(2,6\text{-}Mes_2C_6H_3Te)_2]^{\bullet+}$, no hyperfine structure was observed for [**1 c**]$^{\bullet+}$ under the experimental conditions used (see the Supporting Information).

The radical cation [**1 c**]$^{\bullet+}$ was also characterized by NMR spectroscopy (see the Supporting Information for details). In the ^{1}H NMR spectrum, an increase of sterical restraint of the flanking mesityl substituents is observed, as the *meta* hydrogen atoms and *ortho* methyl groups of the mesityl substituents become magnetically inequivalent. This is caused by a steric restriction in rotation and leads to three signals with equal integral in the aliphatic region, as well as two signals with equal integral in the aromatic region for the *meta* hydrogen atoms of the mesityl ring. In the ^{13}C NMR spectrum the steric restraint is also visible in six mesityl assigned aromatic signals and three aliphatic signals, which were assigned to the methyl groups, even though the *ortho* methyl groups only differ slightly by their chemical shifts ($\Delta\delta = 0.04$ ppm). The signal of the *ipso* carbon is not visible in the ^{13}C NMR spectrum which might be attributed to spin density situated at the tellurium. This is consistent with the disappearance of the ^{125}Te NMR shift in an area of (−4000)–(+16000) ppm and the fact that the remaining signals in ^{1}H and ^{13}C NMR spectra are displayed as narrow, sharp signals without any broadening effects.

The radical cation [**1 c**]$^{\bullet+}$ was also characterized by UV-VIS-NIR spectroscopy using a 3D spectroelectrochemical technique (the Supporting Information). The differential spectroelectrochemical surface of the ECO of **1 c** obtained in CH_2Cl_2 with a triangular potential sweep in the range $0 < E < 1.5$ V ($0 < t <$ 700 s), showed a high reversibility of optical absorption consistent with the formation of radical cation [**1 c**]$^{\bullet+}$ (Figure 6a).

The optical absorption spectrum (Figure 6b) of [**1 c**]$^{\bullet+}$ is characterized by intense absorption bands in the near IR ($\lambda_1 =$ 951 nm), visible ($\lambda_2 = 693$ nm, $\lambda_3 = 613$ nm) and near UV area ($\lambda_4 = 339$ nm, $\lambda_5 = 284$ nm), resulting in an intense blue color of the corresponding solution (Figure 4).

© 2022 The Authors. Chemistry - A European Journal published by Wiley-VCH GmbH

Chemistry–A European Journal | Research Article doi.org/10.1002/chem.202203498 | Chemistry Europe European Chemical Societies Publishing

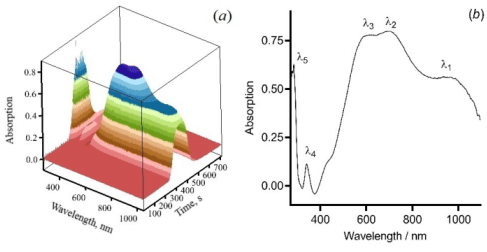

Figure 6. (a) 3D UV-VIS-NIR spectroelectrochemical surface of **1 c** oxidation in CH_2Cl_2, (b) maximum intensity optical absorption spectrum obtained at E = 1.4 V, t = 360 s.

The electronic structures of the neutral parents **1 a–c**, the radical cations $[\mathbf{1\,a–c}]^{\bullet+}$ as well as the dications $[\mathbf{1\,a–c}]^{2+}$ were determined by means of density functional theory (DFT) calculations and subsequent real-space bonding indicator (RSBI) analysis. RSBI included the Atoms-In-Molecules (AIM)[46] theory, the electron localizability indicator (ELI-D)[47] toolkit, as well as the noncovalent interactions (NCI)[48] index, providing topological, surface, and integrated bonding descriptors in real space. For the radical cations, the picture is complemented by inspection of the frontier orbitals and UV-VIS calculations employing time-dependent DFT (TD-DFT). All structures were fully optimized in the gas-phase. First and second vertical and adiabatic ionization energies (IE_v, IE_a) have been extracted, which follow the expected decrease along the series, for example IE_a = 649.6 kJ mol^{-1} (**1 a**), IE_a = 631.3 kJ mol^{-1} (**1 b**), IE_a = 592.2 kJ mol^{-1} (**1 c**) (Table S8). Notably, the geometric parameters of neutral parents **1 a–c**, the radical cations $[\mathbf{1\,a–c}]^{\bullet+}$ as well as the dications $[\mathbf{1\,a–c}]^{2+}$ do not follow clear trends in DFT, as they apparently are affected by weak intramolecular secondary interactions (Table S10). The primary E–C contact distance decreases with increased charge for Se (1.922→1.912→1.909 Å) and Te (2.125→2.121→2.115 Å), but is larger for $[\mathbf{1\,a}]^{2+}$ than for $[\mathbf{1\,a}]^{\bullet+}$ (1.768→1.755→1.761 Å). Similarly, the largest C–E–C angle is found for the radical cations $[\mathbf{1\,b}]^{\bullet+}$ and $[\mathbf{1\,c}]^{\bullet+}$, but for the neutral [**1 a**]. It is not surprising that the experimental structural findings for $[\mathbf{1\,c}]^{\bullet+}$ are not well reflected in DFT, as the geometric parameters are likely also sensitive against the effect on weak inter-molecular secondary interactions. In contrast to the X-ray structure, $[\mathbf{1\,c}]^{\bullet+}$ almost obeys C_2-symmetry (unrestrained optimization) in DFT, the Te–C bond distance has decreased compared to **1 c**, and the C–Te–C angle was widened from 101.5 to 119.2°. The AIM bond topology, NCI contact patches, spin-density (SD) distribution, and electron localizability distribution mapped on the ELI-D lone-pair (LP) basin of the Te atom in $[\mathbf{1\,c}]^{\bullet+}$ are displayed in Figure 7.[49]

The AIM topology discloses four secondary Te···H as well as two Te···C_π contacts (Figure 7a), characterized by bond critical points (bcps, red dots) in the electron density (ED, $\rho(\mathbf{r})$). The spatial extension of these contacts is visible in the NCI, largely covering the coordination space around the central atom

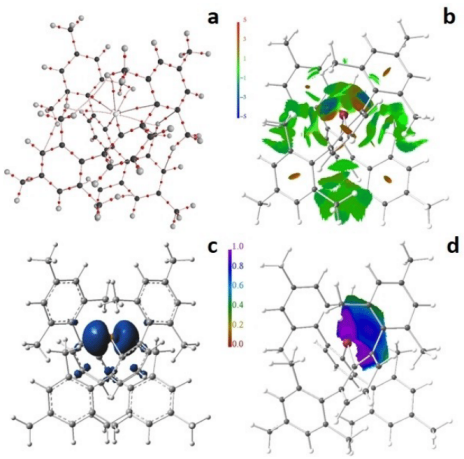

Figure 7. RSBI analysis of $[\mathbf{1\,c}]^{\bullet+}$. (a) AIM bond paths motif, (b) NCI *iso*-surface at $s(\mathbf{r}) = 0.5$, (c) spin-density (SD) distribution at $\phi = 0.005$ a.u., (d) ELI-D distribution mapped on the lone-pair basin of the Te atom.

(Figure 7b), highlighting their role for kinetic stabilization of the radical. The rather localized blueish areas in the NCI and the disc-shaped area of increased localizability in the ELI-D (Figure 7d) reflect the attractive interaction between the chalcogen atom and the π-electron density of the mesityl side groups. Similar results were obtained for the bis-(*m*-terphenyl) element cations $[(2,6\text{-}Mes_2C_6H_3)_2E]^+$ of group 13[50] and 15[51] formally possessing 4 and 6 valence electrons.

The quantitative AIM bond parameters (Tables S11 and S12) characterize the primary E–C (E = S, Se, Te) bonds to be of polarized-covalent nature with medium charge accumulations at the E–C bpcs ($\rho(r) = 0.8–1.4$ eÅ^{-3}) and a (slightly) negative Laplacian of the ED ($\nabla^2\rho(\mathbf{r}) = -8$ to about 0 eÅ^{-5}). The total energy density over ED ratio ($H/\rho(\mathbf{r})$) is considerably negative, reflecting covalency, and moreover being larger in absolute numbers than the kinetic energy density over ED ratio ($G/\rho(\mathbf{r})$), suggesting (slight) dominance of covalent over ionic bonding aspects (Table S11). Bond ellipticities (ε) of about 0.1 indicate minor distortions from cylindrical ED accumulation at the bcp, thus bending or 'smearing'. To the contrast, all secondary intramolecular interactions are of the Van-der-Waals type, with low ED values at the bcps of 0.06–0.21 eÅ^{-3}, (slightly) positive Laplacians, and clearly dominating $G/\rho(\mathbf{r})$ ratios. $H/\rho(\mathbf{r})$ in most cases is even slightly positive, indicating the total absence of covalent bond contributions. Ellipticities of up to 2.8 are caused by electron smearing along the considerably bent Te···H and Te···C_π bond paths. Whereas oxidation goes along with increased AIM charges for one-electron oxidation, it rather goes to the expense of substituent charge in the second oxidation (Table S10). In the ELI-D picture, one electron oxidation causes the transfer of electron population ($N_{(ELI)}$) from the LP(E) basins

© 2022 The Authors. Chemistry - A European Journal published by Wiley-VCH GmbH

15213765, 2023, 11, Downloaded from https://chemistry-europe.onlinelibrary.wiley.com/doi/10.1002/chem.202203498 by Staats- und Universitätsbibliothek, Wiley Online Library on [18/06/2023]. See the Terms and Conditions (https://onlinelibrary.wiley.com/terms-and-conditions) on Wiley Online Library for rules of use; OA articles are governed by the applicable Creative Commons License

Chemistry–A European Journal | Research Article doi.org/10.1002/chem.202203498 | Chemistry Europe European Chemical Societies Publishing

towards the E–C bonding basins, resulting in almost inverted $N_{(ELI)}$ values between neutral and cationic counterparts. Electron loss is accompanied by decrease of ELI-D basin volume and decreased localizability (γ) and *vice versa* (Table S10). As an exception, the Te–C basins also show reduced localizability after oxidation. In accordance with the AIM charges of the chalcogen atoms, little changes are observed for the chalcogen-related ELI-D basins after the second oxidation.

The p_z-shaped SD around the Te atom shows a very low level of delocalization and polarization, suggesting that the terphenyl substituents are electronically innocent (Figure 7c and Figure S53c). A slightly larger level of delocalization of spin density into the ligand system is obtained for the $[\{(Me_3Si)_2N\}_2Te]^{\bullet+}$ radical cation in an otherwise similar overall SD distribution (Figure S53d). The ELI-D localization domain representation of $[\{(Me_3Si)_2N\}_2Te]^{\bullet+}$ unravels two LP-basins, which are still fused at an *iso*-value of 1.4, mirroring the p_z(Te)-shaped SD, thereby not supporting the proposed 'rehybridization'[45] of the non-bonding electrons. Similar ELI-D figures are obtained for the three radical cations $[(2,6\text{-}Mes_2C_6H_3)_2E]^+$ $[\mathbf{1a}\text{–}\mathbf{c}]^{\bullet+}$. In case of E = S the two LP(E)-basins are topologically fused for all three oxidation states (Figure S54g-i). In contrast, they are separated for the neutral **1 b** and **1 c**, but fuse after extraction of one electron (Figures S55g–h and S56 g–h). In case of E = Te, this goes to the extreme for the dication $[\mathbf{1c}]^{2+}$ as the formerly two LP(Te) basins fully fuse to form a single ELI-D basin (Figure S56i). This suggests that the local electronic environment around the Te atom shows stronger effects against one or two electron oxidation than the lighter analogues.

Inspection of the frontier orbital energies uncovers comparable HOMO-LUMO gaps of 0.17–0.18 a.u. for the neutral compounds **1 a**–**c** (Table S9). One electron oxidation drops the energies of the α-HOMOs, α-LUMOs, and β-HOMOs by about 0.11–0.15 a.u. (ΔE), but the energies of the β-LUMOs by about 0.25 a.u., decreasing the gap between β-HOMO and β-LUMO to about 0.04 a.u. for $[\mathbf{1a}]^{\bullet+}$, 0.05 a.u. for $[\mathbf{1b}]^{\bullet+}$, 0.06 a.u. for $[\mathbf{1c}]^{\bullet+}$, shifting the transitions into the UV/vis area. In the radical cations, the β-HOMOs are dominated by contributions from the *m*-terphenyl π-electron densities, whereas the β-LUMOs are dominated by p_z(E) contributions. Notably, the α-HOMOs are dominated by contributions of the substituents in $[\mathbf{1a}]^{\bullet+}$ and $[\mathbf{1b}]^{\bullet+}$, and only $[\mathbf{1c}]^{\bullet+}$ shows p_z(Te)-like contributions, which is in contrast to the picture obtained for the $[\{(Me_3Si)_2N\}_2Te]^{\bullet+}$ radical cation in which both α-HOMO and β-LUMO are dominated by p_z(Te)-like contributions (Figure S9). For $[\mathbf{1a}]^{\bullet+}$ and $[\mathbf{1b}]^{\bullet+}$, p_z(Te) character is contributing to the HOMO-1 orbitals. UV/vis transitions were computed for $[\mathbf{1a}\text{–}\mathbf{c}]^{\bullet+}$ employing TD-DFT, (Figure S57 and Tables S13-S15). Considerable oscillator strengths are obtained for $[\mathbf{1c}]^{\bullet+}$ at 620 and 770 nm, matching very well with the experimental data (Figure 6). All donor orbitals are associated with the substituents and of π-character, whereas the acceptor orbital is p_z(Te)-like in $[\mathbf{1c}]^{\bullet+}$, pointing to a substituent-to-chalcogen transition. Comparable transitions are obtained for $[\mathbf{1a}]^{\bullet+}$ and $[\mathbf{1b}]^{\bullet+}$, but significantly red-shifted as the first relevant transitions occur at close to 1000 nm. Single-reference techniques are known to be problematic for open-shell systems,[52] so the UV-VIS calculations are at best semi-quantitative.

Conclusion

The one-electron oxidation of the extremely bulky bis(*m*-terphenyl) telluride, $(2,6\text{-}Mes_2C_6H_3)_2Te$ (**1 c**) was the key to the preparation of the first kinetically stabilized radical cation $(2,6\text{-}Mes_2C_6H_3)_2Te][B(C_6F_5)_4]$ ($[\mathbf{1c}][B(C_6F_5)_4]$). A related species was recently postulated as intermediate in a catalytic Te(II)/Te(III) cycle.[53] The spin density of $[\mathbf{1c}]^{\bullet+}$ is almost exclusively situated at the Te atom, unlike in Roesky's $[\{(Me_3Si)_2N\}_2Te]^{\bullet+}$ radical cation, which is electronically stabilized and comprises spin density also at the N atoms.[45] The oxidation of the lighter analogues $(2,6\text{-}Mes_2C_6H_3)_2E$ (**1 a**, E = S; **1 b**, E = Se) provided only ill-defined decomposition products.

Experimental Section

Synthesis and characterization of $(2,6\text{-}Mes_2C_6H_3)_2S$ (1 a)

Method A: 2,6-$Mes_2C_6H_3Li$ (1.60 g, 5.00 mmol, 1.00 equiv) was placed in a Schlenk tube, to this Et_2O (60 mL) was added and the solution was cooled to −78 °C. To this sulfur tetrafluoride (8.00 g, 7.36 mmol, 14.8 equiv) was condensed and the reaction was slowly warmed to room temperature. After 18 h, the solvent was removed under reduced pressure. To the remaining residue 2,6-$Mes_2C_6H_3Li$ (1.60 g, 5.00 mmol, 1.00 equiv) was added and the solids were cooled to −78 °C. Et_2O (50 mL) was added and the reaction mixture was again slowly warmed up to room temperature over the course of 18 h. The solvent was removed under reduced pressure and the remaining solid was dissolved in CH_2Cl_2 (50 mL) and worked up aqueous (3 × 50 mL). After removal of CH_2Cl_2 the crude product was separated by column chromatography (cyclohexane: toluene 4 : 1, R_f = 0.6). After removal of the solvent under reduced pressure **1 a** was obtained as a colorless solid (1.38 g, 42 %).

Method B: 2,6-$Mes_2C_6H_3Li$ (256 mg, 0.76 mmol, 1.00 equiv) and $IPrSF_2$ (183 mg, 0.359 mmol, 0.50 equiv) were placed in a Schlenk tube and cooled to −78 °C. To this toluene (8 mL) was slowly added and the reaction was stirred for 30 minutes at −78 °C. The cooling bath was removed and the reaction mixture was stirred for additional 20 h. The solvent was removed under reduced pressure. The residue was washed with ethanol (3 × 10 mL) and *n*-hexane (3 × 10 mL). The residual off white solid was separated by column chromatography (cyclohexane: toluene 4 : 1, R_f = 0.6). After removal of the solvent under reduced pressure **1 a** was obtained as a colorless solid (54.4 mg, 23 %).

Crystals suitable for X-Ray diffraction measurements were grown by cooling down a hot solution of **1 a** a minimum amount of heptane.

^{1}H NMR (600 MHz, $CDCl_3$): δ = 7.02 (t, $^3J(^1H\text{-}^1H)$ = 7.6 Hz, 2H, H4), 6.74 (d, $^3J(^1H\text{-}^1H)$ = 7.6 Hz, 4H, H3 and H5), 6.73 (s, 8H, H9 and H11), 2.36 (s, 12H, H14), 1.64 (s, 24H, H13 and H15) ppm. **$^{13}C\{^1H\}$ NMR (151 MHz, $CDCl_3$)**: δ = 145.4 (s, C2 and C6), 138.8 (s, C7), 136.8 (s, C8 and C12), 136.2 (s, C10), 134.9 (s, C1), 131.6 (s, C3 and C5), 128.3 (s, C9 and C11), 126.5 (s, C4), 21.4 (s, C13 and C15), 21.3 (s, C14) ppm. **HRMS ESI (m/z)**: $[M+H]^+$ calculated. for $C_{48}H_{51}S$, 659.37060; found, 659.36925; $[M+Na]^+$ calculated for $C_{48}H_{50}SNa$, 681.35254; found, 681.35110; $[M+K]^+$ calculated for $C_{48}H_{50}SK$ 697.32648; found

© 2022 The Authors. Chemistry - A European Journal published by Wiley-VCH GmbH

15213765, 2023, 11, Downloaded from https://chemistry-europe.onlinelibrary.wiley.com/doi/10.1002/chem.202203498 by Staats- und Universitätsbibliothek, Wiley Online Library on [18/06/2023]. See the Terms and Conditions (https://onlinelibrary.wiley.com/terms-and-conditions) on Wiley Online Library for rules of use; OA articles are governed by the applicable Creative Commons License

Chemistry–A European Journal | Research Article doi.org/10.1002/chem.202203498 | Chemistry Europe European Chemical Societies Publishing

15213765, 2023, 11, Downloaded from https://chemistry-europe.onlinelibrary.wiley.com/doi/10.1002/chem.202203498 by Staats- und Universitätsbibliothek, Wiley Online Library on [18/06/2023]. See the Terms and Conditions (https://onlinelibrary.wiley.com/terms-and-conditions) on Wiley Online Library for rules of use; OA articles are governed by the applicable Creative Commons License

697.32489. $[M\text{-}C_{24}H_{25}]^+$ calculated for $C_{24}H_{25}S$, 345.16175; found 345.16676.

Synthesis and characterization of (2,6-$Mes_2C_6H_3$)$_2$Se (1 b): 2,6-$Mes_2C_6H_3Li$ (572 mg, 1.79 mmol, 1.00 equiv) was charged in a Schlenk tube and dissolved in Et_2O (20 mL) and cooled to −78 °C. To this SeF_4 (0.10 mL, 1.79 mmol, 1.00 equiv) was added dropwise. The solution was slowly warmed to room temperature and the solvent was removed under reduced pressure. To the residue 2,6-$Mes_2C_6H_3Li$ (1.14 g, 3.58 mmol, 2.00 equiv) was added and the Schlenk tube was cooled to −78 °C. To this Et_2O (40 mL) was added and the suspension was stirred for one hour at −78 °C and then slowly warmed up to room temperature. The solvent was removed under reduced pressure and the residue dissolved in CH_2Cl_2 (50 mL) and worked up aqueous (3×50 mL). The organic phase was separated and dried over sodium sulphate. After removal of the solvent the crude product was separated by column chromatography (cyclohexane: ethyl acetate 9:1, R_f = 0.2). After removal of the solvent the residual yellow oil was triturated with *n*-pentane until the product crystallized. After decantation and drying under reduced pressure **1 b** was obtained as a colorless solid (241 mg, 64 %).

Crystals suitable for X-Ray diffraction measurements were grown by diffusion of *n*-hexane into a CH_2Cl_2 solution of **1 b**.

^{1}H NMR (600 MHz, $CDCl_3$): δ = 7.30 (t, $^3J(^1H\text{-}^1H)$ = 7.5 Hz, 1H, H4), 6.82 ((d, $^3J(^1H\text{-}^1H)$ = 7.5 Hz, 2H, H3 and H5), 6.76 (s, 4H,H9 and H11), 2.34 (s, 6H, H14), 1.75 (s, 6H, H13), 1.72 (s, 6H, H15) ppm.**$^{13}C\{^1H\}$ NMR (151 MHz, CD_2Cl_2)**: δ = 144.3 (s, C2 and C6), 143.6 (s, C1), 137.71 (s, C7), 137.3 (s, C12), 136.9 (s, C10), 136.5 (s, C8), 133.2 (s, C3 and C5), 129.9 (s, C4), 128.6 (s, C9), 128.5 (s, C11), 22.3 (s, C13), 22.1 (s, C15), 21.1 (s, C14) ppm. **^{77}Se NMR (CD_2Cl_2, 115 MHz)**: δ = 981.0 ppm. **HRMS ESI (m/z)**: $[M+OH]^+$ calculated. for $C_{48}H_{51}OSe$, 723.30996; found, 723.30921.

Synthesis and characterization of (2,6-$Mes_2C_6H_3)_2Te$ (1c): TeF_4 (204 mg, 1.0 mmol, 1.00 equiv) was placed in a Schlenk tube, Et_2O (5 mL) was added and cooled to −78 °C. To this a solution of 2,6-$Mes_2C_6H_3Li$ (320 mg, 1.0 mmol, 1.00 equiv) in Et_2O (10 mL) was added dropwise and the suspension was stirred for one hour. After this, additional 2,6-$Mes_2C_6H_3Li$ (640 mg, 2.0 mmol, 2.00 equiv) was added and the reaction was slowly warmed up to room temperature and stirred for 18 h. The solvent was removed under reduced pressure and the residue was dissolved in CH_2Cl_2 (10 mL). The suspension was filtered through a PTFE syringe filter and the solvent of the filtrate was removed under reduced pressure. The remaining solid was washed with MeCN (3×5 mL) and dried under reduced pressure to obtain 1c as a yellow solid (367 mg, 52 %).

Crystals suitable for X-Ray diffraction measurements were grown by evaporation from a solution of **1 c** in CH_2Cl_2/hexane.

^{1}H NMR (600 MHz, $CDCl_3$): δ = 7.14 (t, $^3J(^1H\text{-}^1H)$ = 7.5 Hz, 1H, H4), 6.80 (s, 4H, H9 and H11), 6.76 (d, $^3J(^1H\text{-}^1H)$ = 7.5 Hz, 2H, H3 and H5), 2.36 (s, 6H, H14), 1.70 (s, 12H, H13 and H15) ppm.**$^{13}C\{^1H\}$ NMR (151 MHz, $CDCl_3$)**: δ = 148.8 (s, C2 and C6), 142.1 (s, C7), 136.3 (s, C10), 136.1 (s, C8 and C12), 129.2 (s, C3 and C5), 128.1 (s, C9 and C11), 128.0 (s, C4), 119.9 (s, C1), 21.5 (s, C13 and C15), 21.4 (s, C14) ppm. **^{125}Te NMR ($CDCl_3$, 189 MHz)**: δ = 572.0 ppm. **HRMS ESI (m/z)**: $[M+Na]^+$ calculated. for $C_{48}H_{50}TeNa$, 779.28727; found, 779.28612.

Synthesis and characterization of 2,6-$Mes_2C_6H_3TeF_3$ (2)

Method A: (2,6-$Mes_2C_6H_3)_2Te_2$ (220 mg, 0.25 mmol, 1.00 equiv) was dissolved in CH_2Cl_2 (4 mL) and cooled to −78 °C. To this XeF_2 (127 mg, 0.75 mmol, 3.00 equiv) was added. The reaction mixture was slowly warmed to room temperature and stirred for 18 h. The solvent was removed under reduced pressure and the residue extracted with MeCN (3×5 mL). The solvent was removed under reduced pressure and the residue was dissolved in hot *n*-heptane (20 mL), upon cooling the title compound crystallized out. The supernatant was removed via syringe and the residual crystalline solid dried under reduced pressure to obtain **2** as a colorless crystalline solid (102 mg, 42 %).

Method B: 2,6-$Mes_2C_6H_3Li$ (360 mg, 1.00 mmol, 1.00 equiv) was placed in a Schlenk tube, dissolved in Et_2O (10 mL) and cooled to −78 °C. To this, TeF_4 (204 mg, 1.00 mmol, 1.00 equiv) was added and the suspension was slowly warmed up to room temperature and stirred for 18 h. After this, the solvent was removed under reduced pressure and the residual solid was dissolved in CH_2Cl_2 (5 mL) and the suspension was filtered through a PTFE syringe filter. The solvent of the filtrate was removed under reduced pressure and the remaining solid was dissolved in hot *n*-heptane (20 mL) and upon cooling the title compound crystallized out. The residual solvent was decanted off, and the residual solid was dried under reduced pressure to obtain **2** as a colorless crystalline solid (303 mg, 61 %).

Crystals suitable for X-Ray diffraction measurements were grown by slow cooling of a hot saturated *n*-heptane solution of **2**.

^{1}H NMR (600 MHz, CD_2Cl_2): δ = 7.71 (t, $^3J(^1H\text{-}^1H)$ = 7.6 Hz, 1H, H4), 7.33 (t, $^3J(^1H\text{-}^1H)$ = 8.2 Hz, 2H, H3 and H5), 7.07 (s, 2H, H9 and H11), 6.92 (s, 2H, H19 and H21), 2.37 (s, 3H, H15), 2.32 (s, 3H, H25), 2.12 (s, 6H, H13 and H15), 2.06 (s, 6H, H23 and H25) ppm. **$^{13}C\{^1H\}$ NMR (151 MHz, CD_2Cl_2)**: δ = 150.5 (s, C1), 144.3 (s, C2), 142.9 (s, C6), 142.2 (s, C10), 140.1 (s, C8 and C12), 138.0 (s, C20), 137.4 (s, C18 and C22), 134.8 (s, C17), 133.6 (s, C7), 133.1 (s, C3), 133.1 (s, C4), 129.8 (s, C9 and C11), 129.7 (s, C5), 128.0 (s, C19 and C21), 21.6 (s, C14), 21.4 (s, C24), 21.0 (s, C13, C15, C23 and C25) ppm. **^{19}F NMR (565 MHz, CD_2Cl_2)**: δ = −59.2 (d ($^2J(^{19}F\text{-}^{19}F)$ = 31.1 Hz), −125.3 (t ($^2J(^{19}F\text{-}^{19}F)$ = 31.1 Hz) ppm. **^{125}Te NMR (189 MHz, CD_2Cl_2)**: δ = 1635.7 (dt, $^1J(^{125}Te\text{-}^{19}F)$ = 2285.97, 313.84 Hz) ppm. **HRMS ESI (m/z)**: $[M+Na]^+$ calculated. For $C_{24}H_{25}F_3NaTe$ 523.08683; found, 523.08594.

Synthesis and characterization of (2,6-$Mes_2C_6H_3)_2Te_2F_2$ (3): (2,6-$Mes_2C_6H_3)_2Te_2$ (212 mg, 0.5 mmol, 1.00 equiv) was placed in a Schlenk tube, to this CH_2Cl_2 (4 mL) was added and the solution was cooled to −78 °C. To this XeF_2 (320 mg, 1.0 mmol, 2.00 equiv) was added and the reaction was warmed to −40 °C and stirred for 2 h. The solvent was removed under reduced pressure to obtain a deep red solid. Monitoring by means of ^{19}F and ^{125}Te NMR spectroscopy showed 3 as a major species but also decomposition at room temperature in solution. Attempts to measure ^{1}H and ^{13}C spectra lead only to impure spectra due to decomposition in solution.

Crystals suitable for X-Ray diffraction measurements were grown by diffusion of hexane into a solution of **3** in CH_2Cl_2 at −30 °C.

^{19}F NMR (565 MHz, CD_2Cl_2): δ = −95.0 ppm. **^{125}Te NMR (189 MHz, CD_2Cl_2)**: δ = 1519.2 (td, $J(^{125}Te\text{-}^{19}F)$ = 1130.5 Hz), 1210.8 (t, $J(^{125}Te\text{-}^{19}F)$ = 72.5 Hz) ppm.

Synthesis and characterization of (2,6-$Mes_2C_6H_3)_2TeF_2$ (4)

Method A: TeF_4 (101 mg, 0.50 mmol, 1.00 equiv) and 2,6-$Mes_2C_6H_3Li$ (160 mg, 0.50 mmol, 1.00 equiv) were placed in a Schlenk tube and cooled to −78 °C. To this Et_2O (5 mL) was added and the reaction mixture was stirred for 1 h at −78 °C. After stirring for an hour 2,6-$Mes_2C_6H_3Li$ (160 mg, 0.50 mmol, 1.00 equiv) was added and the reaction mixture was slowly warmed to room temperature and stirred for 18 h. After this, the solvent was removed under reduced pressure and the residue was dissolved in CH_2Cl_2 (4 mL). The suspension was filtered via a PTFE syringe filter and the solvent of

© 2022 The Authors. Chemistry - A European Journal published by Wiley-VCH GmbH

Chemistry–A European Journal | Research Article doi.org/10.1002/chem.202203498 | Chemistry Europe European Chemical Societies Publishing

15213765, 2023, 11, Downloaded from https://chemistry-europe.onlinelibrary.wiley.com/doi/10.1002/chem.202203498 by Staats- und Universitätsbibliothek, Wiley Online Library on [18/06/2023]. See the Terms and Conditions (https://onlinelibrary.wiley.com/terms-and-conditions) on Wiley Online Library for rules of use; OA articles are governed by the applicable Creative Commons License

the filtrate was removed under reduced pressure. The remaining solid was washed with MeCN (3×5 mL) and *n*-hexane (3×5 mL) and the solid was dried under reduced pressure to obtain **4** as a colorless solid (241 mg, 64%).

Method B: 2,6-$Mes_2C_6H_3TeF_3$ (249 mg, 0.50 mmol, 1.00 equiv) and 2,6-$Mes_2C_6H_3Li$ (160 mg, 0.50 mmol, 1.00 equiv) were placed in a Schlenk tube and cooled with an ice bath. To this, n-hexane (5 mL) is added and the reaction mixture is stirred for 72 h at room temperature. The solvent was removed under reduced pressure and the residue was dissolved in CH_2Cl_2 (4 mL). The reaction mixture was filtered via a PTFE syringe filter and the solvent was removed under reduced pressure. The residual solid was washed with MeCN (3×5 mL) and n-hexane (3×5 mL) and dried extensively to obtain **4** as a colorless solid (210 mg, 53%).

Crystals suitable for X-Ray diffraction measurements were grown from a hot solution of **4** in heptane.

^{1}H NMR (600 MHz, $CDCl_3$): $\delta = 7.30$ (t, $^3J(^1H\text{-}^1H) = 7.16$ Hz, 2H, H4), 6.83 (d, $^3J(^1H\text{-}^1H) = 7.0$ Hz, 4H, H3 and H5), 6.80 (s, 2H, H9 and H11), 2.42 (s, 6H, H14), 1.65 (s, 12H, H13 and H15) ppm.**$^{13}C\{^1H\}$ NMR (151 MHz, $CDCl_3$)**: $\delta = 151.9$ (s, C1), 144.6 (s, C2 and C6), 138.3 (s, C7), 137.8 (s, C8 and C12), 136.7 (s, C10), 131.1 (s, C3 and C5), 130.4 (s, C10), 128.1 (s, C9 and C11), 21.4 (s, C14), 20.7 (s, C13 and C15) ppm. **^{19}F NMR ($CDCl_3$, 565 MHz)**: $\delta = -103.1$ ppm. **^{125}Te NMR ($CDCl_3$, 189 MHz)**: $\delta = 1289.2$ (t, $^1J(^{125}Te\text{-}^{19}F) = 313.6$ Hz) ppm. **HRMS ESI (m/z)**: $[M-F]^+$ calculated. for $C_{48}H_{50}FTe$, 775.29533; found, 775.29481; $[M+Na]^+$ calculated. For $C_{48}H_{50}F_2NaTe$ 817.28350; found, 817.28274; $[M+K]^+$ calculated. For $C_{48}H_{50}F_2KTe$ 833.25744; found, 833.25652.

Synthesis and characterization of $[(2,6\text{-}Mes_2C_6H_3)_2Te][B(C_6F_5)_4]$ ($[\mathbf{1c}]^{\bullet+}[B(C_6F_5)_4]^-$): 1c (49.0 mg, 65 µmol, 1.00 equiv) and $K[B(C_6F_5)_4]$ (45.5 mg, 65 µmol, 1.00 equiv) were placed in a Schlenk tube, to this CH_2Cl_2 (4.00 mL) was added and the suspension was cooled to −78 °C. To this XeF_2 (5.50 mg, 32.5 µmol, 0.50 equiv) was added. The solution was slowly warmed up to room temperature and stirred for additional 48 h. The deep blue solution was filtered and layered with *n*-hexane (20 mL). The crystallized compound was washed with *n*-hexane (2×5 mL) and dried under reduced pressure to obtain 1c as deep blue crystalline solid (89.2 mg, 96%).

Crystals suitable for X-Ray diffraction measurements were grown by diffusion from a solution of **1 c** in CH_2Cl_2 with *n*-hexane.

^{1}H NMR (600 MHz, CD_2Cl_2): $\delta = 7.73$ (t, $^3J(^1H\text{-}^1H) = 7.5$ Hz, 1H, H4), 7.2 (d, $2^3J(^1H\text{-}^1H) = 7.5$ Hz, 2H, H3 and H5), 6.97 (s, 2H, H9 or H11), 6.95 (s, 2H, H9 or H11), 4.70 (s, br, 7 H, CH_2Cl_2 coordinated), 2.37 (s, 6H, H14), 1.86 (s, 6H, H15), 1.65 (s, 6H, H13) ppm.**$^{13}C\{^1H\}$ NMR (151 MHz, CD_2Cl_2)**: $\delta = 148.7$ (d, $^1J(^{13}C\text{-}^{19}F) = 235.4$ Hz, br, C_6F_5), 147.6 (s, C2 and C6), 141.8 (s, C7), 138.8 (d, $^1J(^{13}C\text{-}^{19}F) = 245.2$ Hz, br, C_6F_5), 139.0 (s, C8), 137.9 (s, C12), 136.9 (d, $^1J(^{13}C\text{-}^{19}F) = 235.4$ Hz, br, C_6F_5), 136.1 (s, br, C4), 134.7 (s, C3 and C5), 134.1 (s, C10), 130.3 (s, C9), 129.8 (s, C11), 22.1 (s, C15), 22.0 (s, C13), 21.7 (s, C14) ppm. **$^{11}B\{^1H\}$ NMR (CD_2Cl_2, 193 MHz)**: $\delta = -16.5$ ($B(C_6F_5)_4$) ppm. **^{19}F NMR (CD_2Cl_2, 565 MHz)**: $\delta = -132.9$ (s, br, 2F, *o*-C_6F_5), −163.6 (t, $^3J(^{19}F\text{-}^{19}F) = 20.4$ Hz, 1F, *p*-C_6F_5), −167.4 (t, $^3J(^{19}F\text{-}^{19}F) = 17.8$ Hz, 2F, *m*-C_6F_5) ppm. **^{125}Te NMR (CD_2Cl_2, 189 MHz)**: $\delta =$ no visible signal from (−4000)–(+16000) ppm. **HRMS ESI (m/z)**: $[M+OH]^+$ calculated. for $C_{48}H_{51}OTe$, 773.29967; found, 773.29850. **UV-Vis (CH_2Cl_2, 10 µM)** λ(abs) = 350, 613, 707, 951 nm.

Acknowledgements

The Deutsche Forschungsgemeinschaft (Project BE 3716/6-2) and Russian Science Foundation (Project 22-13-00108) are gratefully acknowledged for financial support. Open Access funding enabled and organized by Projekt DEAL.

Conflict of Interest

The authors declare no conflict of interest.

Data Availability Statement

The data that support the findings of this study are available from the corresponding author upon reasonable request.

Keywords: chalcogenes · *m*-terphenyl · radical cations · tellurium

[1] P. P. Power, *Chem. Rev.* **2003**, *103*, 789–810.
[2] Z. Feng, S. Tang, Y. Su, X. Wang, *Chem. Soc. Rev.* **2022**, *51*, 5930–5973.
[3] R. S. Glass, Sulfur Radical Cations, *Top. Curr. Chem.* **1999**, *205*, 1–87.
[4] T. Nishinaga, K. Komatsu, *Org. Biomol. Chem.* **2005**, *3*, 551–569.
[5] L. V. Shuvaev, J. Passmore, *Coord. Chem. Rev.* **2013**, *237*, 1067–1091.
[6] R. S. Glass, Sulfur Radicals and Their Applications, *Top. Curr. Chem.* **2018**, *376*, 22.
[7] O. Lanzalunga, A. Lapi, *J. Sulfur Chem.* **2012**, *33*, 101–129.
[8] Y. Deng, A. J. Illies, M. A. James, M. L. McKee, P. Peschke, *J. Am. Chem. Soc.* **1995**, *117*, 420–428.
[9] F. M. Bickelhaupt, A. Diefenbach, S. P. de Visser, L. J. de Koning, N. M. M. Nibbering, *J. Phys. Chem. A* **1998**, *102*, 9549–9553.
[10] C. H. Hendon, D. R. Carbery, A. Walsh, *Chem. Sci.* **2014**, *5*, 1390–1395.
[11] D. Wang, A. Fuji, *Chem. Sci.* **2017**, *10*, 7260–7268.
[12] D. Wang, K. Hattori, A. Fujii, *Chem. Sci.* **2019**, *10*, 7260.
[13] C. Schönreich, D. Pogocki, G. L. Hug, K. Bobrowski, *J. Am. Chem. Soc.* **2003**, *125*, 13700–13713.
[14] D. A. Butterfield, D. Boyd-Kimball, *Biochim. Biophys. Acta* **2005**, 149–156.
[15] T. Quiñones-Ruiz, M. F. Rosario-Alomar, K. Ruiz-Esteves, M. Shanmuga-sundaram, V. Grigoryants, C. Scholes, J. López-Garriga, I. K. Lednev, *J. Am. Chem. Soc.* **2017**, *139*, 9755–9758.
[16] W. K. Musker, T. L. Wolford, *J. Am. Chem. Soc.* **1976**, *98*, 3055–3056.
[17] S. Zhang, X. Wang, Y. Sui, X. Wang, *J. Am. Chem. Soc.* **2014**, *136*, 14666–14669.
[18] S. Zhang, X. Wang, Y. Sui, Y. Qiu, Z. Zhang, X. Wing, *Nat. Commun.* **2014**, *5*, 4127.
[19] M. Ammam, U. I. Zakai, G. S. Wilson, R. S. Glass, *Pure Appl. Chem.* **2010**, *82*, 555–563.
[20] N. P.-A. Monney, T. Bally, T. Yamamoto, R. S. Glass, *J. Phys. Chem. A* **2015**, *119*, 12990–12998.
[21] O. Mallow, M. A. Khanfar, M. Malischewski, P. Finke, M. Hesse, E. Lork, T. Augenstein, F. Breher, J. R. Harmer, N. V. Vasileva, A. Zibarev, A. S. Bogomyakov, K. Seppelt, J. Beckmann, *Chem. Sci.* **2015**, *6*, 497–504.
[22] In one failed attempt, the dechalcogenation of $(2,6\text{-}Mes_2C_6H_3E)_2$ (E = S, Se, Te) using copper powder was tried. In another failed attempt we prepared 2,6-$Mes_2C_6H_3SCl$ and 2,6-$Mes_2C_6H_3SeCl$, which were fully characterized (see the Supporting Information). However, no reaction of the latter with 2,6-$Mes_2C_6H_3Li$ was observed.
[23] From the decomposition products, a small crop of colorless crystals of 2,6-$Mes_2C_6H_3Se(O)OH$ was isolated which, was characterized by an X-Ray diffraction experiment (see the Supporting Information).
[24] J. Oddershede, L. Henriksen, S. Larsen, *Org. Biomol. Chem.* **2003**, *1*, 1053–1060.
[25] T. M. Klapötke, B. Krumm, M. Scherr, *Inorg. Chem.* **2008**, *47*, 4712–4722.
[26] Y. Okada, M. Oba, A. Arai, K. Tanaka, K. Nishiyama, W. Ando, *Inorg. Chem.* **2010**, *49*, 383–385.
[27] Deposition Number(s) 2215859 (**1 a**), 2215860 (**1 b**), 2215861 (**1 c**), 2215862 [**1 c**][$B(C_6F_5)_4$], 2215863 (**2**), 2215864 (**3**) and 2215865 (**4**) contain(s) the supplementary crystallographic data for this paper. These data are provided free of charge by the joint Cambridge Crystallographic Data Centre and Fachinformationszentrum Karlsruhe Access Structures service.

© 2022 The Authors. Chemistry - A European Journal published by Wiley-VCH GmbH

Chemistry–A European Journal | Research Article doi.org/10.1002/chem.202203498 | Chemistry Europe European Chemical Societies Publishing

15213765, 2023, 11, Downloaded from https://chemistry-europe.onlinelibrary.wiley.com/doi/10.1002/chem.202203498 by Staats- und Universitätsbibliothek, Wiley Online Library on [18/06/2023]. See the Terms and Conditions (https://onlinelibrary.wiley.com/terms-and-conditions) on Wiley Online Library for rules of use; OA articles are governed by the applicable Creative Commons License

[28] S. Grilli, L. Lunazzi, A. Mattanti, *J. Org. Chem.* **2001**, *66*, 4444–4446.
[29] J. Kahr, C. Moser, S. Spirk, F Belaj, R. Pietschnig, *Phosphorus Sulfur Silicon Relat. Elem.* **2014**, *189*, 1467–1474.
[30] T. M. Klapötke, B. Krumm, P. Mayer, K. Polborn, I. Schwab, *Z. Anorg. Allg. Chem.* **2005**, *631*, 2677–2682.
[31] a) J. Beckmann, M. Hesse, H. Poleschner, K. Seppelt, *Angew. Chem. Int. Ed. Engl.* **2007**, *46*, 8277–8280.
[32] H. Poleschner, S. Ellrodt, M. Malischewski, J. Nakatsuji, C. Rohner, K. Seppelt, *Angew. Chem. Int. Ed. Engl.* **2012**, *51*, 419–422.
[33] Unfortunately, 2,6-$Mes_2C_6H_3SF_3$ and 2,6-$Mes_2C_6H_3SeF_3$ could not be obtained by either of these ways.
[34] The characterization of **2**–**4** benefits from the indicative NMR nuclei. The mixed valent *m*-terphenyl tellurenyl fluoride (2,6-$Mes_2C_6H_3$)F_2TeTe(2,6-$Mes_2C_6H_3$) (**2**) has ^{125}Te chemical shifts (CD_2Cl_2) at $\delta = 1519.17$ and 1210.78 ppm, which split up as a triplet of doublets with a coupling constant of $^1J(^{125}\text{Te-}^{19}\text{F}) = 1130.48$ Hz and $^1J(^{125}\text{Te-}^{125}\text{Te}) = 12.14$ Hz and a triplet with a coupling constant of $^2J(^{125}\text{Te-}^{19}\text{F}) = 74.46$ Hz. The ^{19}F NMR spectrum (CD_2Cl_2) of **2** shows a singlet at $\delta = -95.01$ ppm. The ^{125}Te NMR spectrum (CD_2Cl_2) of 2,6-$Mes_2C_6H_3TeF_3$ (**3**) shows a doublet of triplet at $\delta = 1635.7$ ppm and coupling constants of $^1J(^{125}\text{Te-}^{19}\text{F}) = 2286$ and 314 Hz. The ^{19}F NMR spectrum (CD_2Cl_2) of **3** shows two signals in an integral ratio of 2 : 1, a doublet at $\delta = -59.23$ ppm and a triplet at $\delta = -125.25$ ppm both providing a coupling constant of $^3J(^{19}\text{F-}^{19}\text{F}) = 31.1$ Hz. The ^{125}Te NMR spectrum (CD_2Cl_2) of **4** shows a triplet at $\delta = 1289.22$ ppm with a $^1J(^{125}\text{Te-}^{19}\text{F})$ coupling of 313.6 Hz. The ^{19}F NMR spectrum ($CDCl_3$) shows a singlet at $\delta = -103.13$ ppm.
[35] T. M. Klapötke, B. Krumm, P. Mayer, K. Polborn, I. Schwab, *Z. Anorg. Allg. Chem.* **2005**, *631*, 2677–2682.
[36] Surprisingly, no reaction occurred between **4** and other more conventional reducing agents, such as $LiAlH_4$, $NaBH_4$, Na_2S, BH_3-THF, magnesium and zinc. Sodium and potassium led to decomposition.
[37] K. Seppelt, D. Lentz, G. Klöter, *Inorg. Synth.* **1986**, *24*, 27–31.
[38] D. Lentz, H. Pritzkow, K. Seppelt, *Inorg. Chem.* **1978**, *17*, 1926–1931.
[39] In separate experiments, the reaction of one or two equivalents of 2,6-$Mes_2C_6H_3Li$ with pure $S(O)F_2$ exclusively provided 2,6-$Mes_2C_6H_3S(O)F$ and (2,6-$Mes_2C_6H_3)_2SO$, respectively, which were isolated as colorless crystals and fully characterized (see the Supporting Information). All attempts to reduce the sulfoxide (2,6-$Mes_2C_6H_3)_2SO$ with reducing agents, such $LiAlH_4$, $NaBH_4$, $BH_3 \cdot SMe_2$ or Na_2S, gave no reaction, whereas harsher conditions involving alkaline metals lead to decomposition.
[40] In order to synthesize (2,6-$Mes_2C_6H_3)_2SO$ in a rational way also 2,6-$Mes_2C_6H_3S(O)Cl$ and 2,6-$Mes_2C_6H_3S(O)OMe$ were synthesized and fully characterized (see the Supporting Information). Following reactions with 2,6-$Mes_2C_6H_3Li$ showed no reaction at all.
[41] P. Komorr, M. Olaru, E. Hupf, S. Mebs, J. Beckmann, *Chem. Eur. J.* **2022**, *28*, e202201023.
[42] Unfortunately, the analogous reaction with the more labile selenium complex $IPrSeF_2$ and 2,6-$Mes_2C_6H_3Li$ did not work in the same way.
[43] Half-wave potentials were quoted with reference to a saturated calomel electrode (SCE). For detailed information on CV studies, determination of $E_{1/2}$ potentials and the number of electrons transferred, see the Supporting Information.
[44] For single-electron oxidations with XeF_2 in the presence of fluoride acceptors, see: H. Poleschner, K. Seppelt, *Angew. Chem. Int. Ed. Engl.* **2013**, *52*, 12838–12842.
[45] M. Björgvinsson, T. Heinze, H. W. Roesky, F. Pauer, D. Stalke, G. M. Sheldrick, *Angew. Chem. Int. Ed. Engl.* **1991**, *30*, 1677–1678.
[46] R. W. F. Bader, *Atoms in Molecules. A Quantum Theory*; Cambridge University Press: Oxford U. K., **1991**.
[47] M. Kohout, *Int. J. Quantum Chem.* **2004**, *97*, 651–658.
[48] E. R. Johnson, S. Keinan, P. Mori-Sanchez, J. Contreras-García, A. J. Cohen, W. Yang, *J. Am. Chem. Soc.* **2010**, *132*, 6498–6506.
[49] The results for the S and Se analogues are given in the Supporting Information (see Figures S53–S55).
[50] D. Duvinage, L. A. Malaspina, S. Grabowksy, S. Mebs, J. Beckmann, *Eur. J. Inorg. Chem.* **2022**, e202200482.
[51] M. Olaru, D. Duvinage, E. Lork, S. Mebs, J. Beckmann, *Angew. Chem. Int. Ed. Engl.* **2018**, *57*, 10080–10084.
[52] Z. Li, W. Liu, *J. Chem. Theory Comput.* **2016**, *12*, 238–260.
[53] C. Cremer, M. Goswami, C. K. Rank, B. de Bruin, F. W. Patureau, *Angew. Chem. Int. Ed. Engl.* **2021**, *60*, 6451–6456.

Manuscript received: November 10, 2022
Accepted manuscript online: November 23, 2022
Version of record online: January 10, 2023

© 2022 The Authors. Chemistry - A European Journal published by Wiley-VCH GmbH

3 Summary

In the works that are covered by the present dissertation, a wide range of different novel bis(*m*-terphenyl)element compounds of the p-block elements were synthesized and characterized. The main focus was initially on the synthesis of the group 15 pnictogenium ions Ter_2E^+ (E = P, As, Sb, Bi), since bis(*m*-terphenyl)bismuth chloride and hydride are already known from the literature and provide access to the synthesis of a low valent bismuthenium ion. Subsequently, the bis(*m*-terphenyl)antimony chloride and hydride were synthesized and by selective abstraction, the bis(*m*-terphenyl)pnictogenium ion Ter_2E^+ (E = Sb, Bi) were obtained. By this, a novel compound class of group 15 six valence electron (6 VE) cations was generated (**scheme 18**).

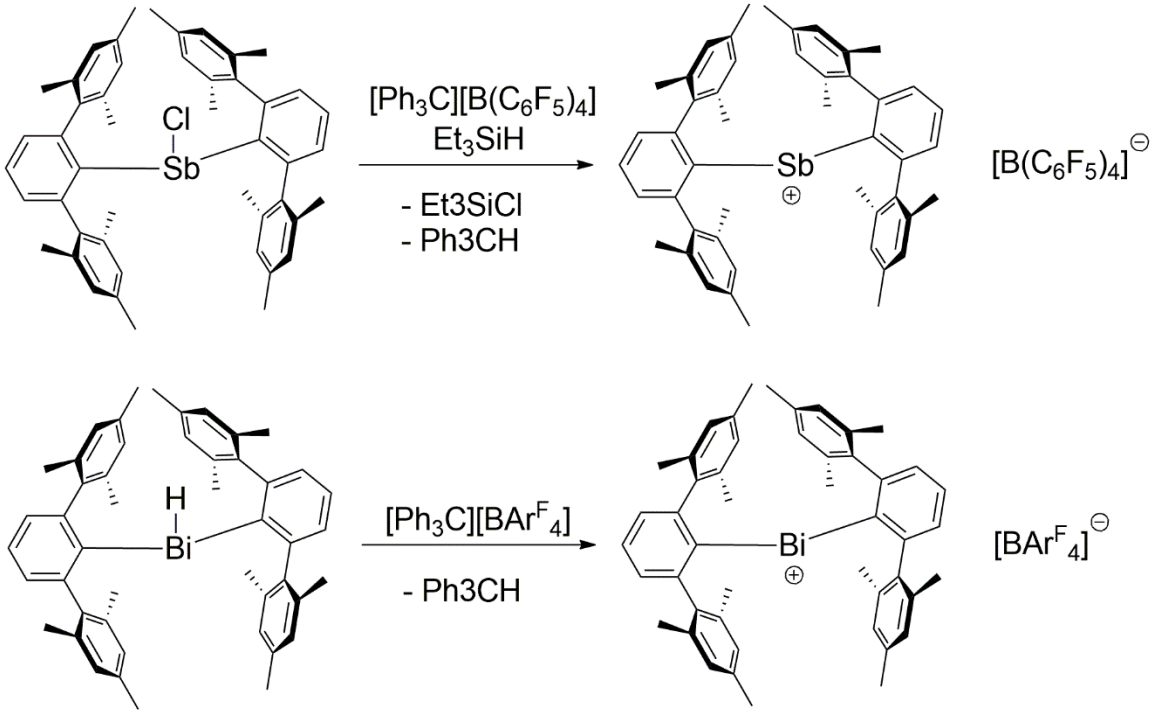

Scheme 18. Formation of the first kinetically stabilized stibenium R_2Sb^+ and bismuthenium R_2Bi^+ ions (R = Ter).

Subsequently, the lighter bis(*m*-terphenyl)pnictogen fluorides Ter_2EF (E = P, As) were synthesized. By fluoride abstraction, the bis(*m*-terphenyl)pnictogenium ions were formed, but due to the high Lewis acidity, only as a transient species. The phosphenium and arsenium ion attacked the flanking group forming an arsolium and phospholium ion by a 1,2-methyl shift (**Scheme 19**).

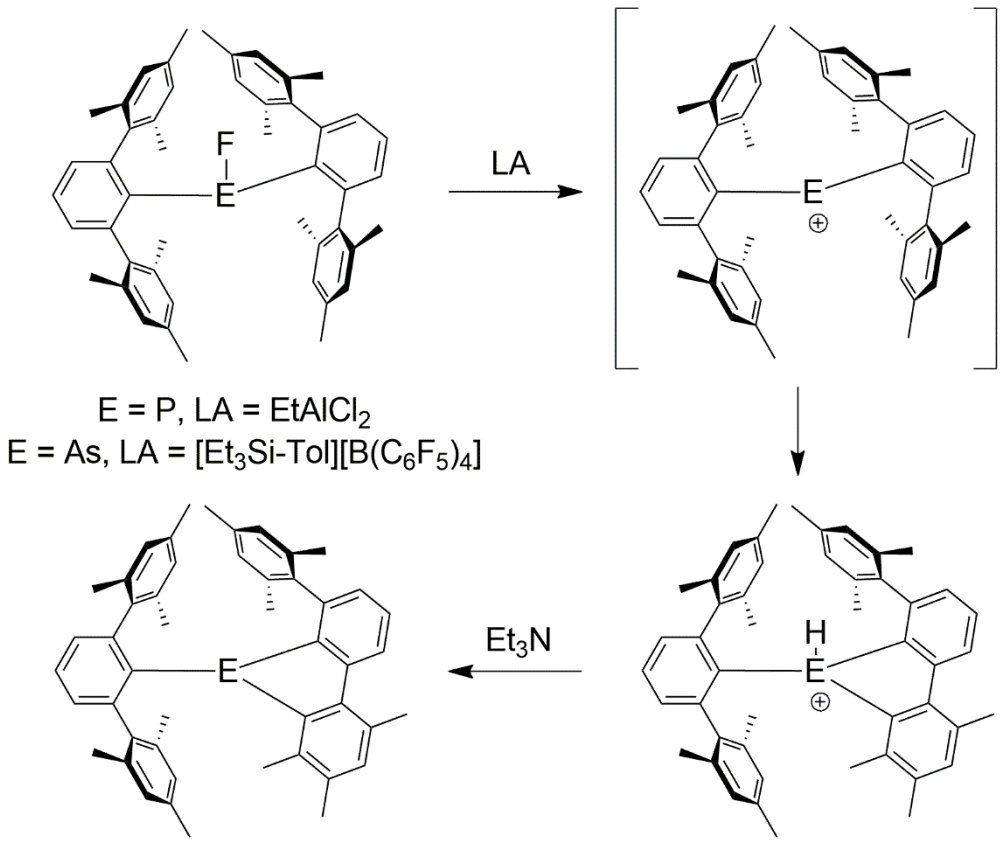

Scheme 19. Intramolecular 1,2-methyl shift by the transient pnictogenium Ions Ter_2E^+ (E = P, As). Anions are omitted for clarity.

Due to the high reactivity and the methyl group migration, the permethylated 2,6-bis(pentamethylphenyl)phenyl *m*-terphenyl system was used for phosphorus and arsenic to inhibit the 1,2-methyl group migration. The synthesis of the aryl pnictogen fluorides proceeded similar to the mesityl-substituted terphenyl system followed by the abstraction of the fluoride. Again, a ring closure and a methyl group rearrangement was observable during the abstraction, leading to the dearomatization of a mesityl group forming an isolable arenium ion (**scheme 20**).

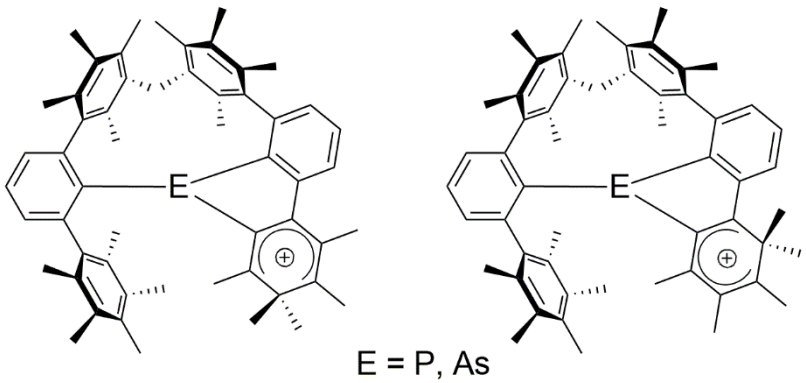

Scheme 20. The two isomers of the formed arenium ion by the intramolecular reaction of the transient pnictogenium ion with one of the flanking groups. Anions are omitted for clarity.

With the idea of forming a kinetically stabilized bis(*m*-terphenyl)carbene and a bis(*m*-terphenyl)carbenium ion, the carboxylic acid fluoride TerC(O)F was synthesized. However, since this did not react with *m*-terphenyllithium, attempts were made to form a stable acylium ion by fluoride abstraction. Here, the formed acylium ion reacted directly in an intramolecular Friedel-Crafts reaction with one of the mesityl rings resulting in a methyl group rearrangement to form a stable 9-hydroxyfluorenium ion (**Scheme 21**). The formed fluorenium ion exhibits a 5-membered ring with four π electrons, which exhibits antiaromaticity according to Hückel's rule.

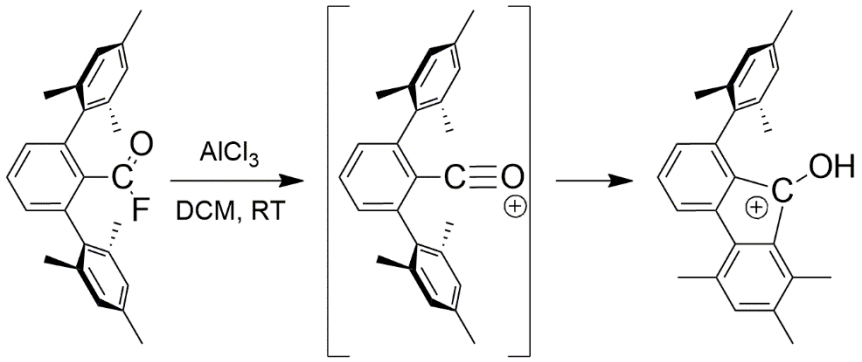

Scheme 21. The formed acylium ion reacts directly intramolecularly forming a hydroxyfluorenium ion, which exhibits antiaromaticity. Anions are omitted for clarity.

Since bis(*m*-terphenyl) element compounds of the group 13 (E = Al, Ga, In, Tl) and stable four VE cations (E = Al, Ga, Tl) have already been prepared, the completion of the series for indium and boron was targeted. A useful starting point was the reported bis(*m*-terphenyl)indium bromide, from which the bromide was successfully abstracted using potassium tetrakis(pentafluorophenyl)borate. This enabled the synthesis and characterization of the first stable indinium ion Ter_2In^+ (**scheme 22**).

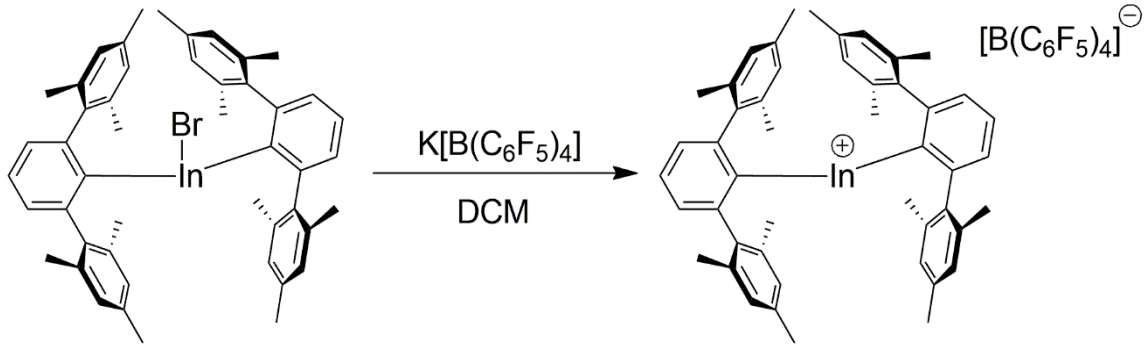

Scheme 22. Formation of the first kinetically stabilized indinium ion R_2In^+ by the selective abstraction of a bromide from bis(*m*-terphenyl)indium bromide with potassium tetrakis(pentafluorophenyl)borate.

Similar to the strategy of the lighter group 15 elements, the bis(*m*-terphenyl)boron fluoride and hydride were synthesized. Both compounds were used as starting materials for the formation of the borinium ion Ter_2B^+, but in all cases either no reaction happened or ill-defined mixtures were formed, which was indicated by NMR spectroscopy revealing the degradation of the *m*-terphenyl substituent and the weakly coordinating anion. This degradation can be explained by the high Lewis acidity of the borinium ion.

In addition, the previously prepared as well as reported bis(*m*-terphenyl)element halides Ter_2EX (E = B, Al, Ga, In, P, As, Sb, Bi; X= F, Cl, Br) were reacted with sodium phosphaethynolate, from which the heavier group 13 and group 15 elements formed stable bis(*m*-terphenyl)element phosphaethynolate salts Ter_2EPCO (E = Ga, In, Sb, Bi) (**Scheme 23**).

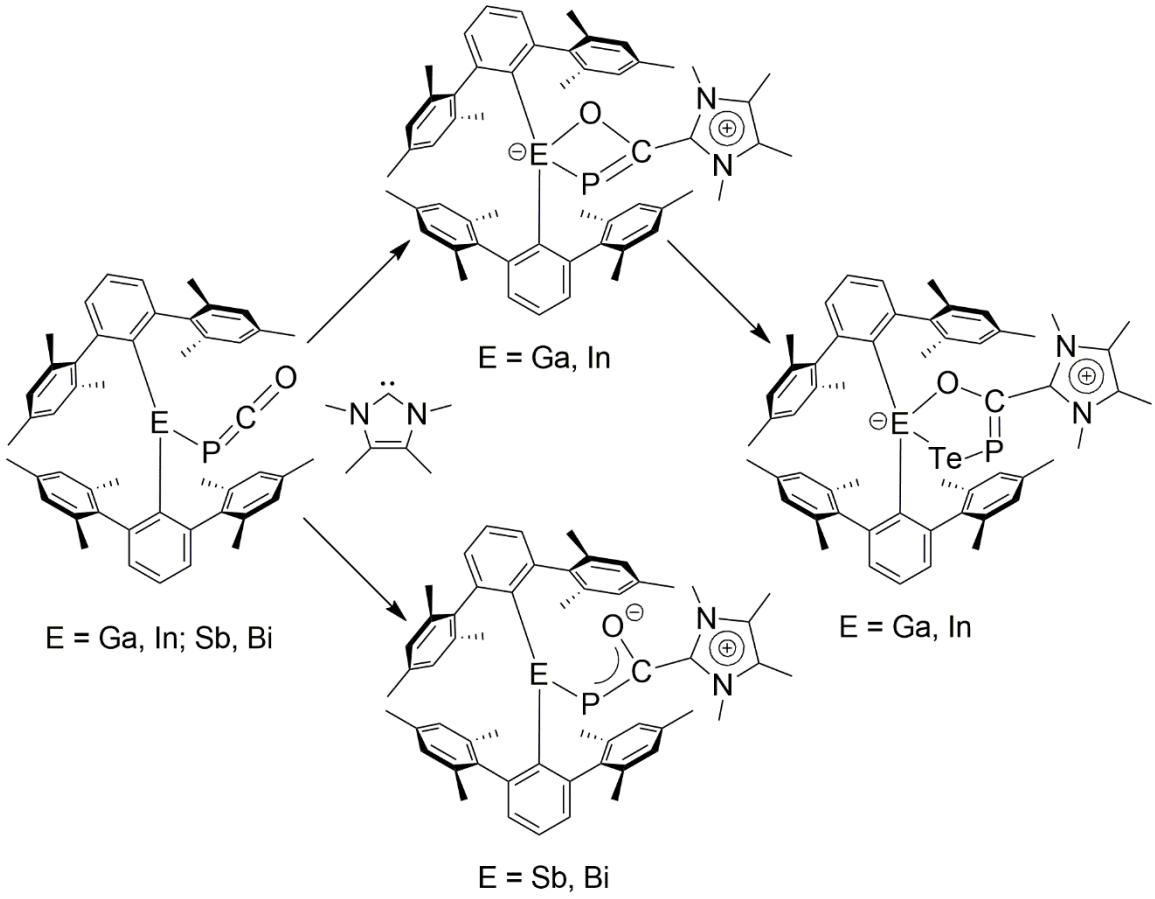

Scheme 23. Reaction of Bis(*m*-terphenyl) main group phosphaethynolates Ter_2EPCO (E = Ga, In; Sb, Bi) with an NHC giving different coordination and different reactivities towards oxidation by tellurium.

In the attempt to scavenge a transient phosphinidene by an NHC, the element phosphaethynolate compounds were reacted with an NHC. This led to the

coordination of the NHC to the PCO carbon atom. In group 13, coordination of the NHC to PCO shows, due to electron vacancy on the central atom, bidentate coordination of the PCO to form a four-membered E-O-C-P ring. The addition of tellurium led to the insertion of tellurium in the E-P bond to form a five-membered ETePCO ring (**Scheme 23**).

With respect to group 15 elements, upon coordination of the NHC, no coordination of the oxygen atom is evident, and the addition of tellurium resulted in no reaction. The comparison between group 13 and group 15 provided information regarding the coordination of phosphaethynolate as a bidentate ligand and the formation of unique heterocycles.

As the last project of this thesis, the synthesis of bis(*m*-terphenyl) group 16 compounds was addressed, in which preliminary results were made as a part of a previous dissertation in the Beckmann group.[152]
The bis(*m*-terphenyl)chalcogenides Ter_2E (E = S, Se, Te) were prepared *via* the chalcogen tetrafluorides The access to the bis(*m*-terphenyl)chalcogenides enabled the study of the oxidation by electrochemical and chemical methods. The oxidation potential was determined using cyclic voltammetry and by oxidation with xenon difluoride and potassium tetrakis(pentafluorophenyl)borate, the bis(*m*-terphenyl)chalcogenides were oxidized. In contrast to the lighter chalcogenides, which only produced ill-defined mixtures, the telluride formed an ink-blue solution, from which the radical cation tetrakis(pentafluorophenyl)borate $Ter_2Te^{\cdot+}[B(C_6F_5)_4]^-$ was obtained (**Scheme 24**).

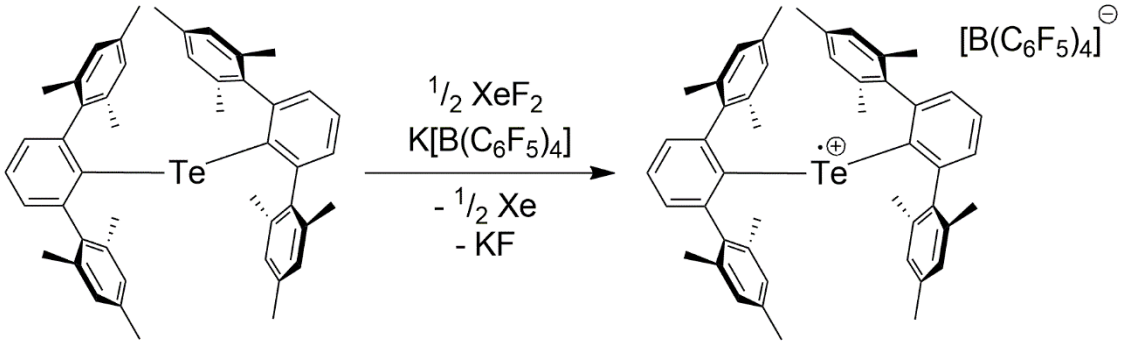

Scheme 24. Oxidation of the bis(*m*-terphenyl)telluride Ter_2Te to the first kinetically stabilized tellurenyl radical cation $Ter_2Te^{\cdot+}[B(C_6F_5)_4]^-$.

It is noteworthy that the latter compound is, the first purely kinetical stabilized tellurenyl radical cation that does not form an ion pair. This could open the research field of kinetically stabilized 7 valence electron chalcogenide species.

In conclusion, novel low valent compound classes were synthesized and characterized in the works that are covered by this thesis, namely the first bismuthenium R_2Bi^+ and stibenium ion R_2Sb^+ providing six valence electron species, the first indinium ion R_2In^+ as a four valence electron species and a tellurenyl radical cation $R_2Te^{\cdot+}$ as a seven valence electron species.

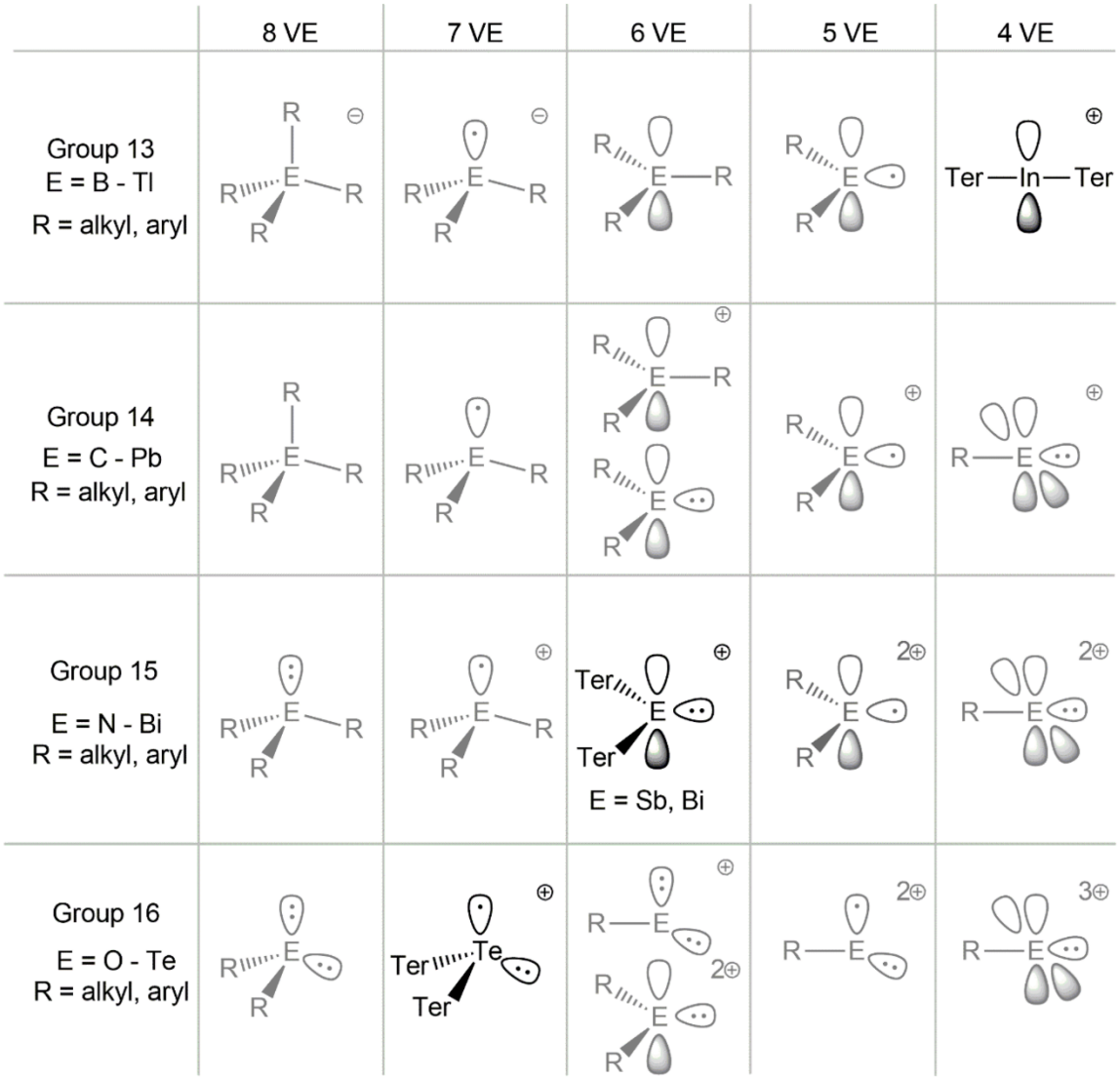

Figure 21. Overview of the low valent bis(*m*-terphenyl)element cations that were synthesized and characterized in this thesis.

Furthermore, the use of aluminium salts as Lewis acid for the abstraction of fluoride on sterically highly demanding systems was established and, in the case of the lighter congeners of group 13 and 15, the limitations of the mesityl substituted *m*-terphenyl system was shown. Additionally, an isolable antiaromatic fluorenium ion was synthesized and novel main group phosphaethynolates were studied regarding the coordination of an N-heterocyclic carbene and oxidation by tellurium forming unique heterocycles.

4 Zusammenfassung

Im Rahmen der vorliegenden Dissertation wurde eine große Bandbreite verschiedener neuartiger Bis(*m*-terphenyl)-Elementverbindungen der p-Block-Elemente synthetisiert und charakterisiert. Das Hauptaugenmerk lag zunächst auf der Synthese der Pniktogeniumionen der Gruppe 15 Ter_2E^+ (E = P, As, Sb, Bi), da Bis(*m*-terphenyl)bismuthchlorid und -hydrid bereits aus der Literatur bekannt sind und daher einen guten Zugang bieten zur Synthese eines niedervalenten Bismutheniumions. Anschließend wurden Bis(*m*-terphenyl)antimonchlorid und -hydrid synthetisiert und durch selektive Abstraktion die Bis(*m*-terphenyl)-pniktogenium-Ionen Ter_2E^+ (E = Sb, Bi) erhalten. Dadurch wurde eine neuartige Verbindungsklasse von Gruppe 15 Kationen mit sechs Valenzelektronen dargestellt (**Scheme 25**).

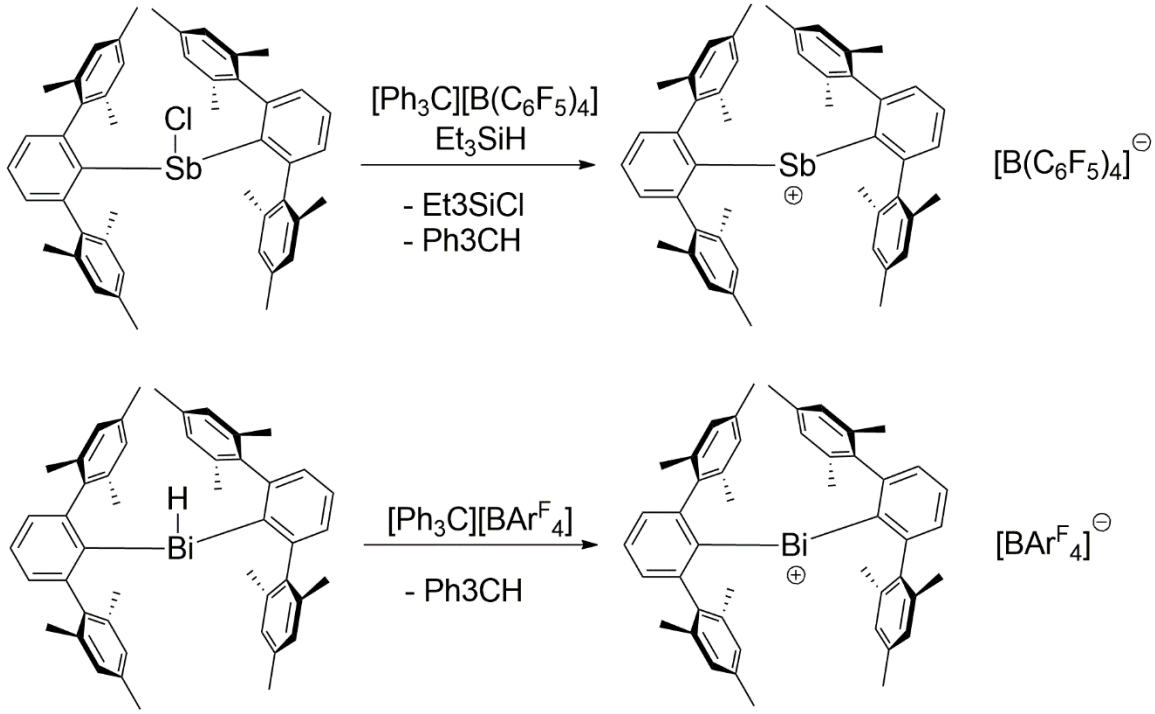

Scheme 25. Synthese des ersten Stibenium- und Bismutheniumions.

Anschließend wurden die leichteren Bis(*m*-terphenyl)pniktogenfluoride Ter_2EF (E = P, As) synthetisiert. Durch Fluoridabstraktion wurden die kurzlebigen Bis(*m*-terphenyl)pniktogeniumionen gebildet, welche aufgrund der hohen Lewis-

Acidität die flankierende Mesitylgruppe angriffen. Hierbei bildeten sich durch eine 1,2-Methylverschiebung ein Arsolium- und Phospholium-Ion (**Scheme 26**).

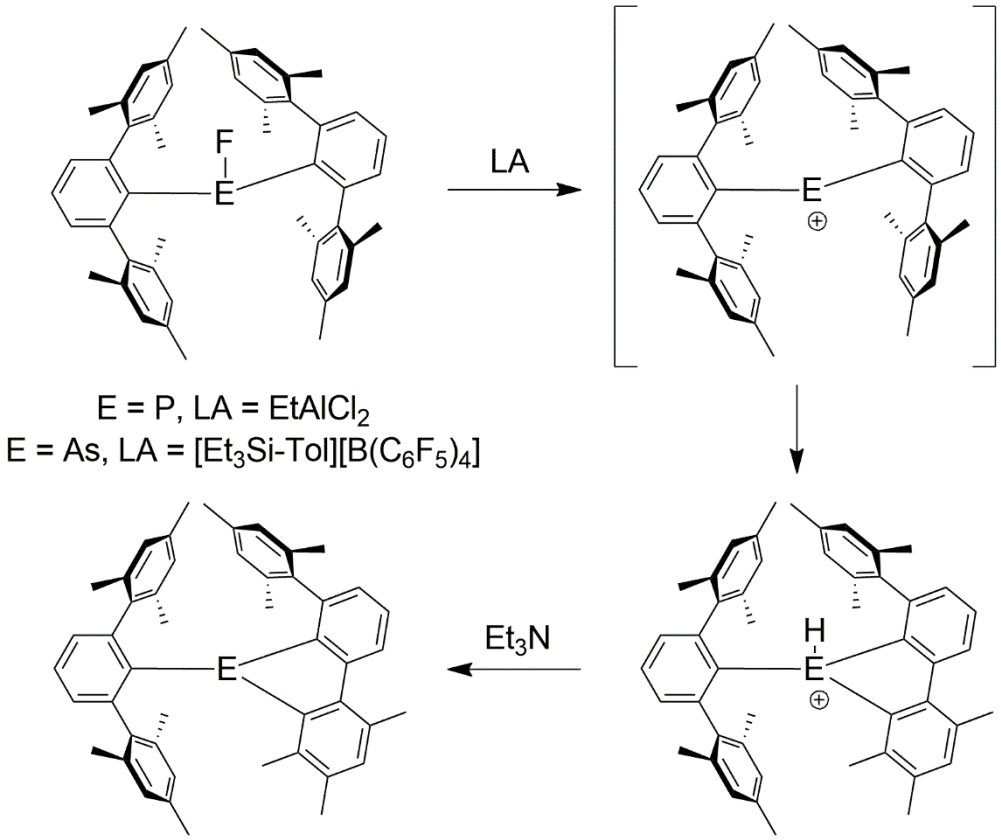

Scheme 26. Intramolekulare 1,2-Methylverschiebung durch die transienten Pniktogeniumionen Ter_2E^+ (E = P, As). Die Anionen sind zur Übersichtlichkeit nicht abgebildet.

Aufgrund der hohen Reaktivität, welche zu einem Ringschluss führte, wurde darauffolgend für Phosphor und Arsen auf das Pentamethylphenyl substituierte *m*-Terphenylsystem ausgewichen um die 1,2-Methylgruppen-Wanderung zu verhindern. Zudem war angedacht, dass durch die Substitution aller Positionen am Aromaten mit Methylgruppen, der induktive Effekt das erhaltene Pniktogenium-Ion stabilisiert. Die Synthese der Arylpniktogenfluoride verlief analog zum Mesityl-substituierten *m*-Terphenylsystem. Bei der Abstraktion des Fluorids konnte jedoch ebenfalls ein Ringschluss sowie eine Methylgruppenumlagerung beobachtet werden. Dies lässt darauf schließen, dass eine Dearomatisierung stattgefunden hat, wodurch in beiden Fällen ein isolierbares Arenium-Ion erhalten werden konnte (**Scheme 27**).

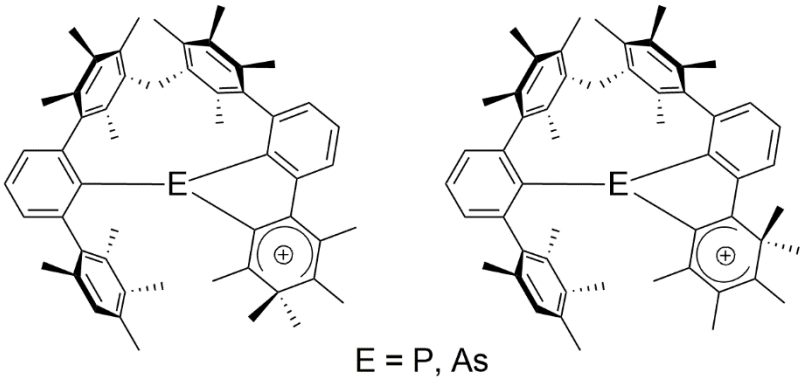

Scheme 27. Die durch die intramolekulare Reaktion der kurzlebigen Pniktogeniumionen mit dem Liganden gebildeten Isomere des Areniumions. Die Anionen sind zur Übersichtlichkeit nicht abgebildet.

Im Zusammenhang mit der Idee, ein Bis(*m*-terphenyl)carben und ein Bis(*m*-terphenyl)carbenium-Ion zu bilden, wurde das Carbonsäurefluorid TerC(O)F synthetisiert. Da dieses keine Reaktivität gegenüber *m*-Terphenyllithium zeigte, wurde versucht, unter Fluoridabstraktion ein stabiles Acylium-Ion zu bilden, da diese eine essentielle Rolle in Friedel-Crafts-Reaktionen spielen. Hierbei reagierte das gebildete Acylium-Ion direkt in einer intramolekularen Friedel-Crafts-Reaktion mit einem der Mesitylringe, wodurch ebenfalls eine Methylgruppen-Wanderung unter Bildung eines stabilen 9-Hydroxyfluorenium-Ions stattfand (**Scheme 28**). Das gebildete Fluorenium-Ion weist einen fünf-gliedrigen Ring mit vier π-Elektronen auf, welcher gemäß der Hückel-Regel Antiaromatizität aufweist.

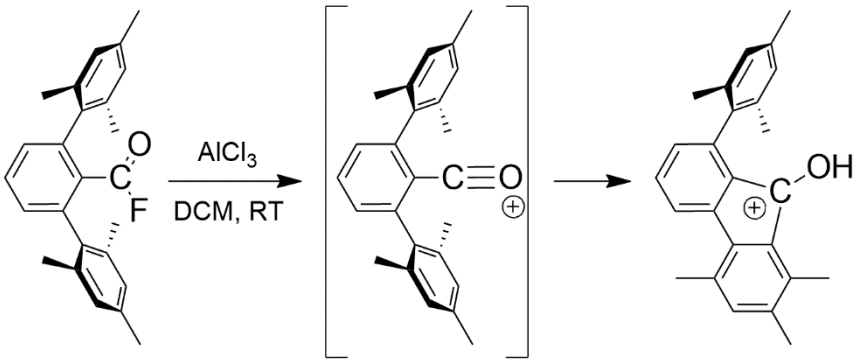

Scheme 28. Bildung des Hydroxyfluoreniumions durch eine intramolekulare Friedel-Crafts-Reaktion. Die Anionen sind zur Übersichtlichkeit nicht abgebildet.

Des Weiteren wurde die Gruppe 13 betrachtet, da bereits Bis(*m*-terphenyl)elementverbindungen (E = Al, Ga, In, Tl) sowie stabile 4 VE-Spezies (E = Al, Ga, Tl) hergestellt wurden. Das bereits bekannte

Bis(*m*-terphenyl)indiumbromid wurde genutzt um unter Abstraktion des Bromids das erste stabile Indinium-Ion Ter_2In^+ zu bilden und zu isolieren (**Scheme 29**).

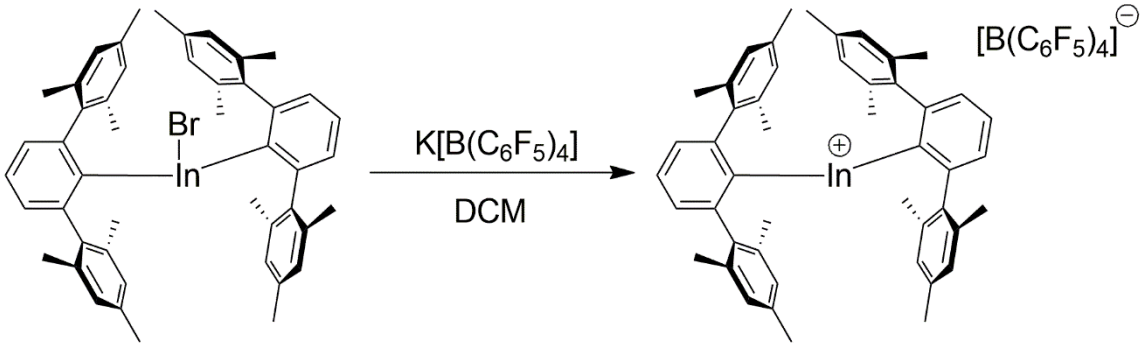

Scheme 29. Synthese des ersten kinetisch stabilisierten Indiniumions R_2In^+ (R = Ter).

Analog zu der Strategie der leichteren Gruppe 15 Elemente, wurde das Bis(*m*-terphenyl)borfluorid und -hydrid synthetisiert. Beide Verbindungen wurden als Edukt zur Bildung des Borinium-Ions Ter_2B^+ genutzt, wobei in allen Fällen entweder keine Reaktion zu beobachten war oder ein undefinierbares Gemisch erhalten wurde. Per NMR-Spektroskopie konnte die Zersetzung des *m*-Terphenyl-Substituenten sowie des schwach koordinierenden Anions beobachtet werden. Diese Zersetzung lässt sich durch die hohe Lewis-Acidität des Borinium-Ions erklären.

Zusätzlich wurden die bereits hergestellten Bis(*m*-terphenyl)elementhalogenide Ter_2EX (E = Ga, In, Sb, Bi; X = Cl, Br) mit Natriumphosphaethynolat umgesetzt, wovon die schweren Elemente der Gruppe 13 und 15 stabile Phosphaethynolatverbindungen des Typs Ter_2EPCO (E = Ga, In; Sb, Bi) bildeten. Um kurzlebige Phosphinidene zu stabilisieren, wurden die Phosphaethynolat-Verbindungen mit einem N-Heterozyklischen Carben umgesetzt. Hierbei koordinierte das NHC an den Kohlenstoff der PCO-Einheit. Bei den Elementen der Gruppe 13 wurde hierbei, durch die Elektronenlücke am Element, die PCO-Einheit unter Ausbildung eines E-O-C-P Rings bidentat. Durch die Zugabe von Tellur konnte eine Insertion in die E-P Bindung beobachtet werden, wodurch sich ein E-Te-P-C-O Ring gebildet hat (**Scheme 30**).

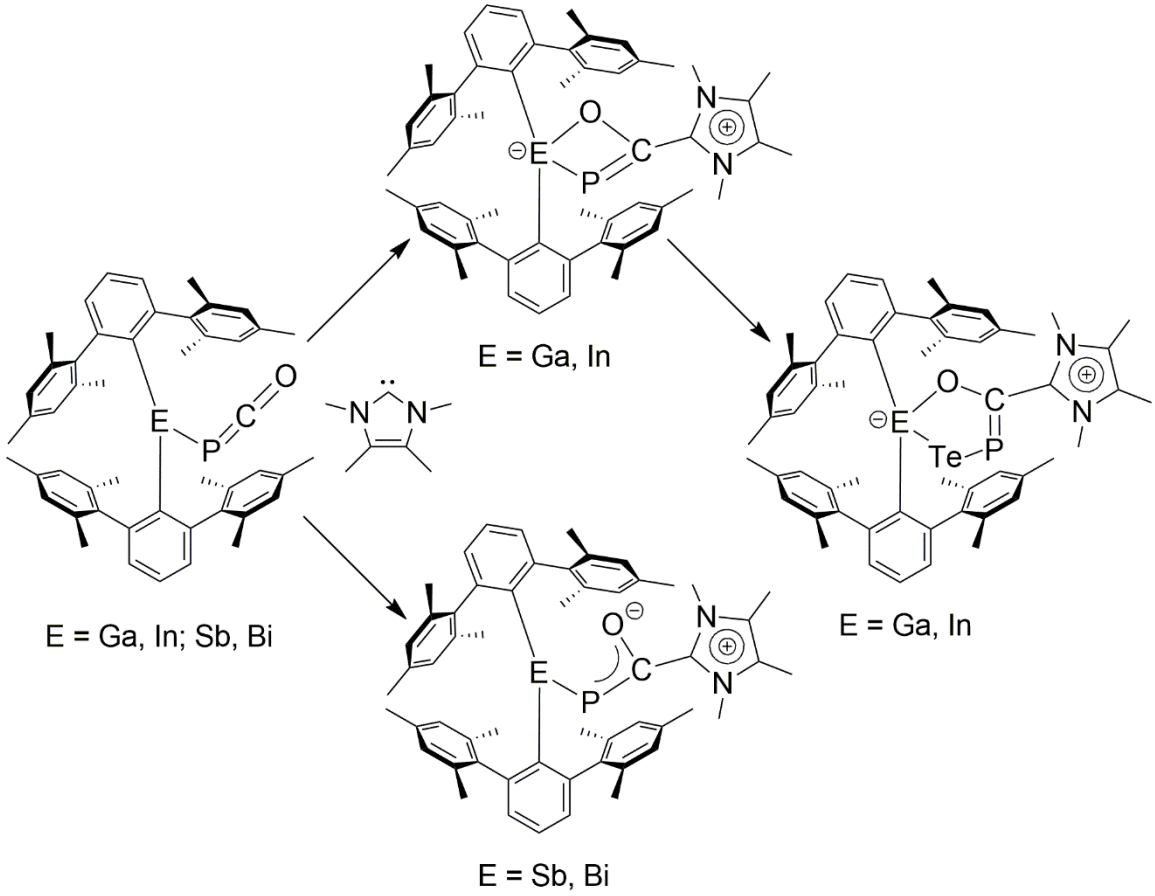

Scheme 30. Reaktion der gebildeten Phosphaethynolate Ter_2EPCO (E = Ga, In; Sb, Bi) mit einem NHC und darauffolgender Oxidation durch Tellur.

Bei den Elementen der Gruppe 15 wurde durch Koordination des N-heterozyklischen Carbens keine Koordination des Sauerstoffatoms beobachtet. Zusätzlich zeigte die Umsetzung mit Tellur keine Insertion. Der Vergleich zwischen den Elementen der Gruppe 13 und 15 konnte Informationen bezüglich des Koordinationsmusters der Phosphaethynolat-Einheit als bidentater Ligand sowie der Bildung einzigartiger Heterozyklen zeigen.

Abschließend wurden die Elemente der Gruppe 16 untersucht, zu welchen bereits in einer vorrangegangenen Dissertation in der AG Beckmann vorläufige Ergebnisse erhalten wurden.[152] Die Bis(*m*-terphenyl)chalkogenide Ter_2E (E = S, Se, Te) wurden über die Chalkogentetrafluoride synthetisiert. Der Zugang zu den Bis(*m*-terphenyl)chalkogeniden ermöglichte die Studie der Ein-Elektronen-Oxidation mittels elektrochemischer und chemischer Methoden. Hierzu wurde mithilfe der Cyclovoltammetrie das Oxidationspotential bestimmt und mittels Xenondifluorid und Kaliumtetrakis(pentafluorphenyl)borat chemisch oxidiert. Im

Gegensatz zu den leichten Chalkogeniden, welche nur undefinierte Mischungen bei der Oxidation produzierten, konnte im Fall des Tellurids eine tief-blaue Lösung erhalten werden, aus welcher das Bis(*m*-terphenyl)tellurenyl Radikalkation $Ter_2Te^{\cdot+}$ als Tetrakis(pentafluorphenyl)borat Salz erhalten werden konnte (**Schema 31**). Somit konnte das erste vollständig kinetisch stabilisierte Tellurenyl-Radikalkation, welches kein Ionenpaar bildet, erhalten werden, wodurch sich eine Tür zur Chemie der kinetisch stabilisierten sieben Valenzelektronen (7 VE) Chalkogenide geöffnet hat.

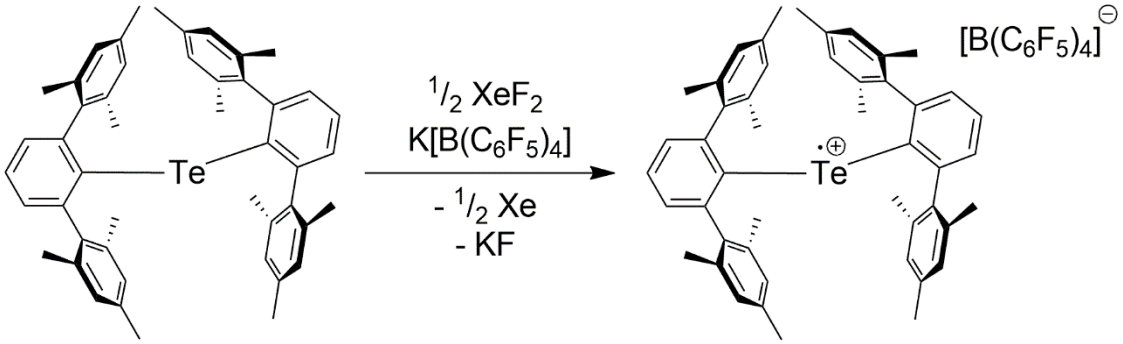

Scheme 31. Bildung des ersten kinetisch stabilisierten Tellurenylradikalkations $Ter_2Te^{\cdot+}$.

In dieser Arbeit konnte eine Vielzahl neuer Verbindungen und Verbindungsklassen synthetisiert und charakterisiert werden. Hierbei konnte das erste Bismuthenium-R_2Bi^+ und Stibenium-Ion R_2Sb^+, als sechs Valenzelektronen (6 VE) Spezies isoliert werden. Des Weiteren wurde das erste Indinium-Ion R_2In^+, als vier Valenzelektronen (4 VE) Spezies sowie ein Tellurenyl-Radikalkation $R_2Te^{\cdot+}$, als sieben Valenzelektronen (7 VE) Spezies dargestellt.

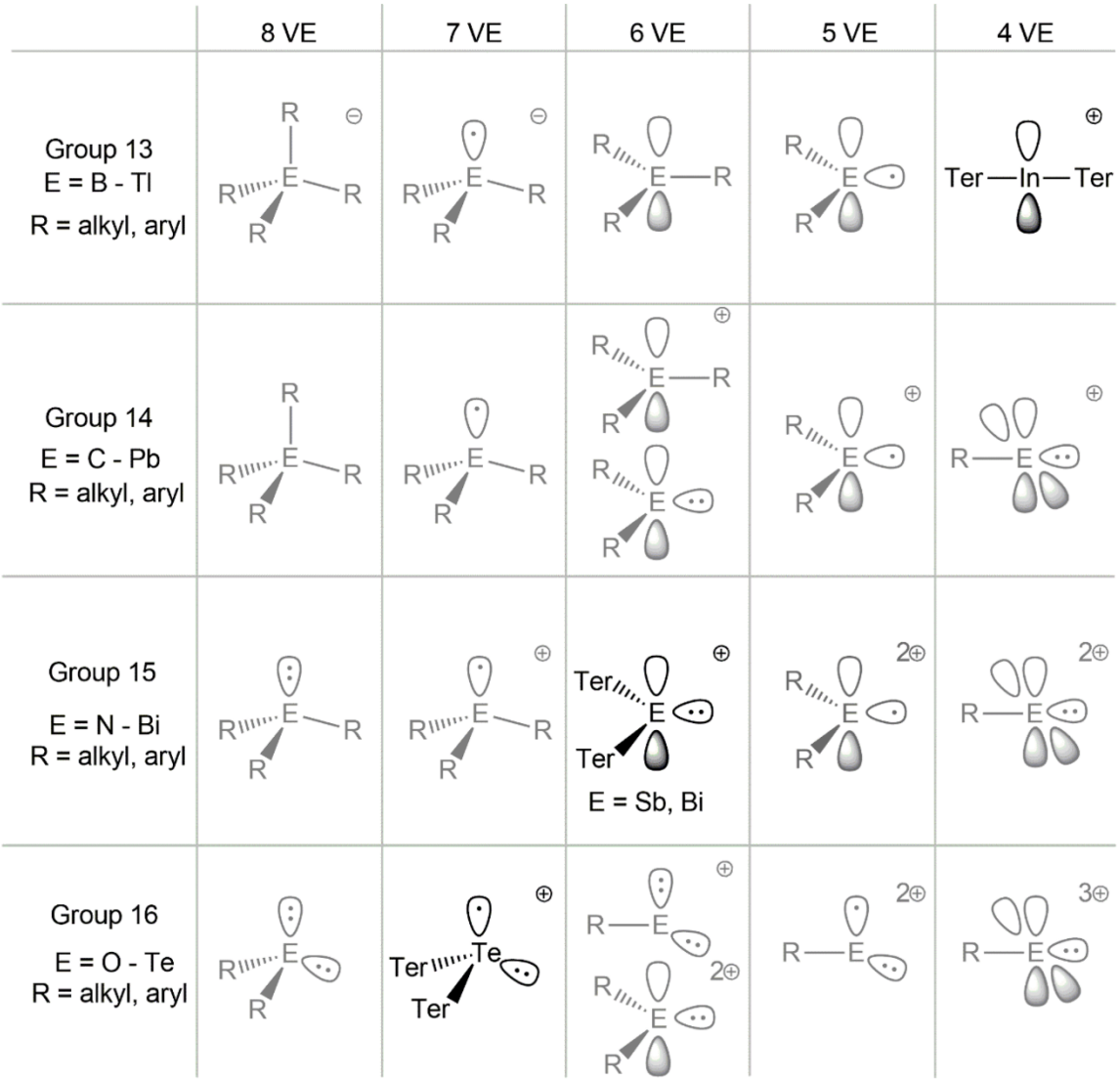

Figure 22. Überblick der dargestellten kationischen niedervalenten Bis(*m*-terphenyl)-Hauptgruppenelement-Verbindungen.

Zusätzlich konnten die Aluminiumsalze $EtAlCl_2$ und $AlCl_3$ als Fluorid-Abstrahierungsreagenzien für sterisch hoch anspruchsvolle Systeme etabliert werden. Für die leichteren Elemente der Gruppe 13 und 15 konnten zudem die Grenzen des Mesityl- und Pentamethylphenyl- substituierten *m*-Terphenylsystems gezeigt werden. Desweiteren konnte ein antiaromatisches Fluorenium-Ion isoliert werden und neue Elementphosphaethynolate bezüglich ihrer Koordination mittels eines N-heterzyklischen Carbens sowie der Oxidation mit Tellur, unter der Bildung einzigartiger Heterozyklen, studiert werden.

5 References

[1] G. N. Lewis, *J. Am. Chem. Soc.* **1916**, *38*, 762-785.

[2] L. C. Bateman, M. G. Church, E. D. Hughes, C. K. Ingold, N. A. Taher, *J. Chem. Soc.* **1940**, 979-1011.

[3] T. A. Engesser, M. R. Lichtenthaler, M. Schleep, I. Krossing, *Chem. Soc. Rev.* **2016**, *45*, 789-899.

[4] Y. Shoji, N. Tanaka, K. Mikami, M. Uchiyama, T. Fukushima, *Nat. Chem.* **2014**, *6*, 498-503.

[5] J. B. Lambert, Y. Zhao, *Angew. Chem. Int. Ed.* **1997**, *36*, 400-401.

[6] A. Baeyer, V. Villiger, *Ber. Dtsch. Chem. Ges.* **1902**, *35*, 1189-1201.

[7] P. Šimon, F. de Proft, R. Jambor, A. Růžička, L. Dostál, *Angew. Chem. Int. Ed.* **2010**, *49*, 5468-5471.

[8] R. Kannan, S. Kumar, A. P. Andrews, E. D. Jemmis, A. Venugopal, *Inorg. Chem.* **2017**, *56*, 9391-9395.

[9] D. Franz, S. Inoue, *Chem. Eur. J.* **2019**, *25*, 2898-2926.

[10] H.-C. Tseng, C.-T. Shen, K. Matsumoto, D.-N. Shih, Y.-H. Liu, S.-M. Peng, S. Yamaguchi, Y.-F. Lin, C.-W. Chiu, *Organometallics* **2019**, *38*, 4516-4521.

[11] R. Oshimizu, N. Ando, S. Yamaguchi, *Angew. Chem. Int. Ed.* **2022**, *61*, e202209394.

[12] G. C. Welch, R. R. S. Juan, J. D. Masuda, D. W. Stephan, *Science* **2006**, *314*, 1124-1126.

[13] J. D. Young, M. A. Khan, R. J. Wehmschulte, *Organometallics* **2004**, *23*, 1965-1967.

[14] H. Schmidbaur, *Angew. Chem. Int. Ed.* **1985**, *24*, 893-904.

[15] H. Schmidbaur, A. Schier, *Organometallics* **2008**, *27*, 2361-2395.

[16] W. J. Grigsby, P. P. Power, *J. Am. Chem. Soc.* **1996**, *118*, 7981-7988.

[17] J. B. Lambert, S. Zhang, C. L. Stern, J. C. Huffman, *Science* **1993**, *260*, 1917-1918.

[18] J. B. Lambert, L. Kania, W. Schilf, J. A. McConnell, *Organometallics* **1991**, *10*, 2578-2584.

[19] L. Pauling, G. A. Olah, G. Rasul, X.-y. Li, H. A. Buchholz, G. Sandford, G. K. S. Prakash, J. B. Lambert, S. Zhang, C. A. Reed, Z. Xie, *Science* **1994**, *263*, 983-986.

[20] G. A. Olah, G. Rasul, G. K. Surya Prakash, *J. Organomet. Chem.* **1996**, *521*, 271-277.

[21] C. A. Reed, Z. Xie, R. Bau, A. Benesi, *Science* **1993**, *262*, 402-404.

[22] Z. Xie, D. J. Liston, T. Jelínek, V. Mitro, R. Bau, C. A. Reed, *J. Chem. Soc., Chem. Commun.* **1993**, 384-386.

[23] Z. Xie, R. Bau, A. Benesi, C. A. Reed, *Organometallics* **1995**, *14*, 3933-3941.

[24] Z. Xie, J. Manning, R. W. Reed, R. Mathur, P. D. W. Boyd, A. Benesi, C. A. Reed, *J. Am. Chem. Soc.* **1996**, *118*, 2922-2928.

[25] K.-C. Kim, C. A. Reed, D. W. Elliott, L. J. Mueller, F. Tham, L. Lin, J. B. Lambert, *Science* **2002**, *297*, 825-827.

[26] R. West, M. J. Fink, J. Michl, *Science* **1981**, *214*, 1343-1344.

[27] J. D. Masuda, A. J. Hoskin, T. W. Graham, C. Beddie, M. C. Fermin, N. Etkin, D. W. Stephan, *Chem. Eur. J.* **2006**, *12*, 8696-8707.

[28] A. J. Roering, J. J. Davidson, S. N. MacMillan, J. M. Tanski, R. Waterman, *Dalton Trans.* **2008**, 4488-4498.

[29] R. Waterman, T. D. Tilley, *Angew. Chem. Int. Ed.* **2006**, *45*, 2926-2929.

[30] W. Ando, Y. Hamada, A. Sekiguchi, *J. Chem. Soc., Chem. Commun.* **1983**, 952-954.

[31] K. L. Hurni, K. M. Baines, *Can. J. Chem.* **2007**, *85*, 668-674.

[32] M. Yoshifuji, I. Shima, N. Inamoto, K. Hirotsu, T. Higuchi, *J. Am. Chem. Soc.* **1981**, *103*, 4587-4589.

[33] Y. Masaaki, S. Takahiro, I. Naoki, *Chem. Lett.* **1988**, *17*, 1735-1738.

[34] E. Y. Misochko, A. V. Akimov, D. V. Korchagin, Y. S. Ganushevich, E. A. Melnikov, V. A. Miluykov, *Phys. Chem. Chem. Phys.* **2020**, *22*, 27626-27631.

[35] E. Urnéžius, J. D. Protasiewicz, *Main Group Chem.* **1996**, *1*, 369-372.

[36] B. Twamley, C. D. Sofield, M. M. Olmstead, P. P. Power, *J. Am. Chem. Soc.* **1999**, *121*, 3357-3367.

[37] T. Nguyen, A. D. Sutton, M. Brynda, J. C. Fettinger, G. J. Long, P. P. Power, *Science* **2005**, *310*, 844-847.

[38] M. Stender, A. D. Phillips, R. J. Wright, P. P. Power, *Angew. Chem. Int. Ed.* **2002**, *41*, 1785-1787.

[39] A. D. Phillips, R. J. Wright, M. M. Olmstead, P. P. Power, *J. Am. Chem. Soc.* **2002**, *124*, 5930-5931.

[40] L. Pu, B. Twamley, P. P. Power, *J. Am. Chem. Soc.* **2000**, *122*, 3524-3525.

[41] Z. Zhu, X. Wang, Y. Peng, H. Lei, J. C. Fettinger, E. Rivard, P. P. Power, *Angew. Chem. Int. Ed.* **2009**, *48*, 2031-2034.

[42] R. S. Simons, L. Pu, M. M. Olmstead, P. P. Power, *Organometallics* **1997**, *16*, 1920-1925.

[43] Y. Peng, J.-D. Guo, B. D. Ellis, Z. Zhu, J. C. Fettinger, S. Nagase, P. P. Power, *J. Am. Chem. Soc.* **2009**, *131*, 16272-16282.

[44] Y. Peng, B. D. Ellis, X. Wang, P. P. Power, *J. Am. Chem. Soc.* **2008**, *130*, 12268-12269.

[45] C. J. F. Du, H. Hart, K. K. D. Ng, *J. Org. Chem.* **1986**, *51*, 3162-3165.

[46] B. Schiemenz, P. P. Power, *Organometallics* **1996**, *15*, 958-964.

[47] K. V. Bukhryakov, R. R. Schrock, A. H. Hoveyda, P. Müller, J. Becker, *Org. Lett.* **2017**, *19*, 2607-2609.

[48] C. Stanciu, A. F. Richards, J. C. Fettinger, M. Brynda, P. P. Power, *J. Organomet. Chem.* **2006**, *691*, 2540-2545.

[49] S. Duttwyler, Q. Q. Do, A. Linden, K. K. Baldridge, J. S. Siegel, *Angew. Chem. Int. Ed.* **2008**, *47*, 1719-1722.

[50] P. Romanato, S. Duttwyler, A. Linden, K. K. Baldridge, J. S. Siegel, *J. Am. Chem. Soc.* **2010**, *132*, 7828-7829.

[51] P. Romanato, S. Duttwyler, A. Linden, K. K. Baldridge, J. S. Siegel, *J. Am. Chem. Soc.* **2011**, *133*, 11844-11846.

[52] J. D. Queen, A. Lehmann, J. C. Fettinger, H. M. Tuononen, P. P. Power, *J. Am. Chem. Soc.* **2020**, *142*, 20554-20559.

[53] J. D. Queen, S. Irvankoski, J. C. Fettinger, H. M. Tuononen, P. P. Power, *J. Am. Chem. Soc.* **2021**, *143*, 6351-6356.

[54] T. P. Hamilton, A. W. Shaikh, *Inorg. Chem.* **1997**, *36*, 754-755.

[55] A. Y. Timoshkin, H. F. Schaefer III, *J. Phys. Chem. A* **2008**, *112*, 13180-13196.

[56] S.-L. Zhang, M.-C. Yang, M.-D. Su, *RSC Adv.* **2019**, *9*, 12195-12208.

[57] J. F. Norris, *Am. Chem. J.* **1901**, *117*, 117-122.

[58] F. Kehrmann, F. Wentzel, *Ber. Dtsch. Chem. Ges.* **1901**, *34*, 3815-3819.

[59] T. Nishiuchi, H. Sotome, R. Fukuuchi, K. Kamada, H. Miyasaka, T. Kubo, *Aggregate* **2021**, *2*, e126.

[60] H. J. Dauben, L. R. Honnen, K. M. Harmon, *J. Org. Chem.* **1960**, *25*, 1442-1445.

[61] D. A. Straus, C. Zhang, T. D. Tilley, *J. Organomet. Chem.* **1989**, *369*, C13-C17.

[62] S. R. Bahr, P. Boudjouk, *J. Org. Chem.* **1992**, *57*, 5545-5547.

[63] G. A. Olah, E. B. Baker, J. C. Evans, W. S. Tolgyesi, J. S. McIntyre, I. J. Bastien, *J. Am. Chem. Soc.* **1964**, *86*, 1360-1373.

[64] G. A. Olah, J. Lukas, *J. Am. Chem. Soc.* **1967**, *89*, 4739-4744.

[65] G. A. Olah, G. Klopman, R. H. Schlosberg, *J. Am. Chem. Soc.* **1969**, *91*, 3261-3268.

[66] The Nobel Prize in Chemistry 1994. NobelPrize.org. Nobel Prize Outreach AB 2024. Thu. 18 Jan 2024. https://www.nobelprize.org/prizes/chemistry/1994/summary/

[67] S. M. Ivanova, B. G. Nolan, Y. Kobayashi, S. M. Miller, O. P. Anderson, S. H. Strauss, *Chem. Eur. J.* **2001**, *7*, 503-510.

[68] K. Shelly, D. C. Finster, Y. J. Lee, W. R. Scheidt, C. A. Reed, *J. Am. Chem. Soc.* **1985**, *107*, 5955-5959.

[69] I. M. Riddlestone, A. Kraft, J. Schaefer, I. Krossing, *Angew. Chem. Int. Ed.* **2018**, *57*, 13982-14024.

[70] I. Krossing, I. Raabe, *Angew. Chem. Int. Ed.* **2004**, *43*, 2066-2090.

[71] K. Shelly, C. A. Reed, Y. J. Lee, W. R. Scheidt, *J. Am. Chem. Soc.* **1986**, *108*, 3117-3118.

[72] K.-C. Kim, C. A. Reed, G. S. Long, A. Sen, *J. Am. Chem. Soc.* **2002**, *124*, 7662-7663.

[73] R. J. Wehmschulte, J. M. Steele, M. A. Khan, *Organometallics* **2003**, *22*, 4678-4684.

[74] M. M. Schwab, D. Himmel, S. Kacprzak, D. Kratzert, V. Radtke, P. Weis, K. Ray, E.-W. Scheidt, W. Scherer, B. de Bruin, S. Weber, I. Krossing, *Angew. Chem. Int. Ed.* **2015**, *54*, 14706-14709.

[75] O. Mallow, M. A. Khanfar, M. Malischewski, P. Finke, M. Hesse, E. Lork, T. Augenstein, F. Breher, J. R. Harmer, N. V. Vasilieva, A. Zibarev, A. S. Bogomyakov, K. Seppelt, J. Beckmann, *Chem. Sci.* **2015**, *6*, 497-504.

[76] M. Schmitt, M. Mayländer, J. Goost, S. Richert, I. Krossing, *Angew. Chem. Int. Ed.* **2021**, *60*, 14800-14805.

[77] H. Poleschner, K. Seppelt, *Angew. Chem. Int. Ed.* **2013**, *52*, 12838-12842.

[78] Y. Marcus, G. Hefter, *Chem. Rev.* **2006**, *106*, 4585-4621.

[79] R. G. Pearson, *J. Am. Chem. Soc.* **1963**, *85*, 3533-3539.

[80] C. A. Reed, T. Mashiko, S. P. Bentley, M. E. Kastner, W. R. Scheidt, K. Spartalian, G. Lang, *J. Am. Chem. Soc.* **1979**, *101*, 2948-2958.

[81] R. F. Jordan, W. E. Dasher, S. F. Echols, *J. Am. Chem. Soc.* **1986**, *108*, 1718-1719.

[82] K. Shelly, T. Bartczak, W. R. Scheidt, C. A. Reed, *Inorg. Chem.* **1985**, *24*, 4325-4330.

[83] R. V. Honeychuck, W. H. Hersh, *Inorg. Chem.* **1989**, *28*, 2869-2886.

[84] M. Björgvinsson, T. Heinze, H. W. Roesky, F. Pauer, D. Stalke , G. M. Sheldrick, *Angew. Chem. Int. Ed.* **1991**, *30*, 1677-1678.

[85] D. O'Hagan, *Chem. Soc. Rev.* **2008**, *37*, 308-319.

[86] A. G. Massey, A. J. Park, *J. Organomet. Chem.* **1964**, *2*, 245-250.

[87] N. Hiroshi, T. Naoko, Y. Masaji, S. Takaaki, K. Hiroshi, *Bull. Chem. Soc. Jpn.* **1984**, *57*, 2600-2604.

[88] I. Krossing, *Chem. Eur. J.* **2001**, *7*, 490-502.

[89] A. Martens, P. Weis, M. C. Krummer, M. Kreuzer, A. Meierhöfer, S. C. Meier, J. Bohnenberger, H. Scherer, I. Riddlestone, I. Krossing, *Chem. Sci.* **2018**, *9*, 7058-7068.

[90] M.-C. Chen, J. A. S. Roberts, A. M. Seyam, L. Li, C. Zuccaccia, N. G. Stahl, T. J. Marks, *Organometallics* **2006**, *25*, 2833-2850.

[91] S. J. Lancaster, D. A. Walker, M. Thornton-Pett, M. Bochmann, *Chem. Commun.* **1999**, 1533-1534.

[92] T. Jelínek, J. Plešek, S. Heřmánek, B. Štíbr, *Collect. Czech. Chem. Commun.* **1986**, *51*, 819-829.

[93] S. V. Ivanov, J. J. Rockwell, O. G. Polyakov, C. M. Gaudinski, O. P. Anderson, K. A. Solntsev, S. H. Strauss, *J. Am. Chem. Soc.* **1998**, *120*, 4224-4225.

[94] B. T. King, J. Michl, *J. Am. Chem. Soc.* **2000**, *122*, 10255-10256.

[95] M. D. Noirot, O. P. Anderson, S. H. Strauss, *Inorg. Chem.* **1987**, *26*, 2216-2223.

[96] A. Wiesner, T. W. Gries, S. Steinhauer, H. Beckers, S. Riedel, *Angew. Chem. Int. Ed.* **2017**, *56*, 8263-8266.

[97] H. P. A. Mercier, J. C. P. Sanders, G. J. Schrobilgen, *J. Am. Chem. Soc.* **1994**, *116*, 2921-2937.

[98] U. Mayer, V. Gutmann, W. Gerger, *Monatsh. Chem.* **1975**, *106*, 1235-1257.

[99] M. A. Beckett, G. C. Strickland, J. R. Holland, K. Sukumar Varma, *Polymer* **1996**, *37*, 4629-4631.

[100] P. Erdmann, L. Greb, *Angew. Chem. Int. Ed.* **2022**, *61*, e202114550.

[101] J. Ramler, C. Lichtenberg, *Chem. Eur. J.* **2020**, *26*, 10250-10258.

[102] R. F. Childs, D. L. Mulholland, A. Nixon, *Can. J. Chem.* **1982**, *60*, 801-808.

[103] G. Hilt, A. Nödling, *Eur. J. Org. Chem.* **2011**, *2011*, 7071-7075.

[104] S. Künzler, S. Rathjen, A. Merk, M. Schmidtmann, T. Müller, *Chem. Eur. J.* **2019**, *25*, 15123-15130.

[105] T. Krahl, E. Kemnitz, *J. Fluor. Chem.* **2006**, *127*, 663-678.

[106] N. A. Shcherbina, A. V. Pomogaeva, A. S. Lisovenko, I. V. Kazakov, N. Y. Gugin, O. V. Khoroshilova, Y. V. Kondrat'ev, A. Y. Timoshkin, *Z. Anorg. Allg. Chem.* **2020**, *646*, 873-881.

[107] L. O. Müller, D. Himmel, J. Stauffer, G. Steinfeld, J. Slattery, G. Santiso-Quiñones, V. Brecht, I. Krossing, *Angew. Chem. Int. Ed.* **2008**, *47*, 7659-7663.

[108] G. A. Olah, P. Schilling, I. M. Gross, *J. Am. Chem. Soc.* **1974**, *96*, 876-883.

[109] J. F. Kögel, D. A. Sorokin, A. Khvorost, M. Scott, K. Harms, D. Himmel, I. Krossing, J. Sundermeyer, *Chem. Sci.* **2018**, *9*, 245-253.

[110] P. Erdmann, L. Greb, *ChemPhysChem* **2021**, *22*, 935-943.

[111] A. P. Altshuller, *J. Am. Chem. Soc.* **1955**, *77*, 6187-6188.

[112] J. C. Haartz, D. H. McDaniel, *J. Am. Chem. Soc.* **1973**, *95*, 8562-8565.

[113] K. O. Christe, D. A. Dixon, D. McLemore, W. W. Wilson, J. A. Sheehy, J. A. Boatz, *J. Fluor. Chem.* **2000**, *101*, 151-153.

[114] F. Sladky, H. Kropshofer, O. Leitzke, *J. Chem. Soc., Chem. Commun.* **1973**, 134-135.

[115] D. Lentz, K. Seppelt, *Z. Anorg. Allg. Chem.* **1983**, *502*, 83-88.

[116] M. J. Collins, G. J. Schrobilgen, *Inorg. Chem.* **1985**, *24*, 2608-2614.

[117] P. Erdmann, J. Leitner, J. Schwarz, L. Greb, *ChemPhysChem* **2020**, *21*, 987-994.

[118] J. M. Slattery, S. Hussein, *Dalton Trans.* **2012**, *41*, 1808-1815.

[119] L. Greb, *Chem. Eur. J.* **2018**, *24*, 17881-17896.

[120] R. H. Crabtree, *The Organometallic Chemistry of the Transition Metals*, Wiley, New York, **2005**.

[121] F. A. W. Cotton, G. , *Advanced Inorganic Chemistry*, Wiley, New York, **1988**.

[122] A. F. E. W. Holleman, *Lehrbuch der Anorganischen Chemie, Vol. 102*, Walter de Gruyter, Berlin, **2007**.

[123] E. Riedel, *Anorganische Chemie*, Walter de Gruyter, Berlin, **2004**.

[124] P. P. Power, *Nature* **2010**, *463*, 171-177.

[125] P. P. Power, *Chem. Rev.* **1999**, *99*, 3463-3504.

[126] Y. Mizuhata, T. Sasamori, N. Tokitoh, *Chem. Rev.* **2009**, *109*, 3479-3511.

[127] G. Linti, H. Schnöckel, *Coord. Chem. Rev.* **2000**, *206-207*, 285-319.

[128] D. W. Stephan, *Dalton Trans.* **2009**, 3129-3136.

[129] P. P. Power, *Chem. Rev.* **2003**, *103*, 789-810.

[130] L. V. Ya., N. Masaaki, S. Akira, *Chem. Lett.* **2008**, *37*, 128-133.

[131] F. Breher, *Coord. Chem. Rev.* **2007**, *251*, 1007-1043.

[132] G. H. Spikes, J. C. Fettinger, P. P. Power, *J. Am. Chem. Soc.* **2005**, *127*, 12232-12233.

[133] G. D. Frey, V. Lavallo, B. Donnadieu, W. W. Schoeller, G. Bertrand, *Science* **2007**, *316*, 439-441.

[134] H. Braunschweig, I. Krummenacher, M.-A. Légaré, A. Matler, K. Radacki, Q. Ye, *J. Am. Chem. Soc.* **2017**, *139*, 1802-1805.

[135] K. L. Bamford, Z.-W. Qu, D. W. Stephan, *J. Am. Chem. Soc.* **2019**, *141*, 6180-6184.

[136] A. Saednya, H. Hart, *Synthesis* **1996**, *1996*, 1455-1458.

[137] J. Beckmann, M. Hesse, H. Poleschner, K. Seppelt, *Angew. Chem. Int. Ed.* **2007**, *46*, 8277-8280.

[138] J. Beckmann, J. Bolsinger, P. Finke, M. Hesse, *Angew. Chem. Int. Ed.* **2010**, *49*, 8030-8032.

[139] A. Schröder, E. Lork, J. Beckmann, *Organometallics* **2014**, *33*, 6263-6266.

[140] S. U. Ahmad, J. Beckmann, *Organometallics* **2009**, *28*, 6893-6901.

[141] X.-W. Li, G. H. Robinson, W. T. Pennington, *Main Group Chem.* **1996**, *1*, 301-307.

[142] N. J. Hardman, B. Twamley, P. P. Power, *Angew. Chem. Int. Ed.* **2000**, *39*, 2771-2773.

[143] M. Olaru, A. Schröder, L. Albers, D. Duvinage, S. Mebs, J. Beckmann, *Chem. Eur. J.* **2019**, *25*, 9861-9865.

[144] M. Bolte, I. Ruderfer, T. Muller, *Acta Cryst. E* **2005**, *61*, m1581-m1582.

[145] M. Kuprat, M. Lehmann, A. Schulz, A. Villinger, *Organometallics* **2010**, *29*, 1421-1427.

[146] E. S. Akturk, S. J. Scappaticci, R. N. Seals, M. P. Marshak, *Inorg. Chem.* **2017**, *56*, 11466-11469.

[147] B. Chevrier, J. M. Le Carpentier, R. Weiss, *J. Am. Chem. Soc.* **1972**, *94*, 5718-5723.

[148] M. G. Davlieva, S. V. Lindeman, I. S. Neretin, J. K. Kochi, *New J. Chem.* **2004**, *28*, 1568-1574.

[149] S. Patel, B. Rathod, S. Regu, S. Chak, A. Shard, *ChemistrySelect* **2020**, *5*, 10673-10691.

[150] J. D. Young, M. A. Khan, D. R. Powell, R. J. Wehmschulte, *Eur. J. Inorg. Chem.* **2007**, *2007*, 1671-1681.

[151] C. Schöneich, D. Pogocki, G. L. Hug, K. Bobrowski, *J. Am. Chem. Soc.* **2003**, *125*, 13700-13713.

[152] F. Mostaghimi (2021), Radical Cations of the Heavier Chalcogenides (doctoral dissertation, Universität Bremen), Staats- und Universitätsbibliothek Bremen, https://doi.org/10.26092/elib/1076

6 Supporting Information

6.1 Heavy Carbene Analogues: Donor-Free Bismuthenium and Stibenium Ion

Angewandte Chemie
Eine Zeitschrift der Gesellschaft Deutscher Chemiker

Supporting Information

Heavy Carbene Analogues: Donor-Free Bismuthenium and Stibenium Ions

Marian Olaru, Daniel Duvinage, Enno Lork, Stefan Mebs, and Jens Beckmann**

anie_201803160_sm_miscellaneous_information.pdf

Table of Contents

Experimental procedures

General information

All reactions and manipulations were performed under inert argon atmosphere using anhydrous solvents. Unless otherwise stated, reagents used in this work including $SbCl_3$ and $BiCl_3$ (anhydrous, 99%) were obtained commercially and were used as received. Commercial $LiAlH_4$ was purified by extraction with anhydrous Et_2O (thus removing insoluble gray material). 2,6-$Mes_2C_6H_3Li$ (Mes = 2,4,6-$Me_3C_6H_2$),[1] (2,6-$Mes_2C_6H_3)_2BiCl$,[2] and $Na[BAr^F{}_4]$[3,4] [Ar^F = 3,5-$(F_3C)_2C_6H_3$] were prepared following the published procedures; $[Ph_3C][BAr^F{}_4]$[5] was prepared following the procedure describing the synthesis of the related $[Ph_3C][B(C_6F_5)_4]$.[6,7] (2,6-$Mes_2C_6H_3)_2BiH$[2] was prepared according to the published protocol with some modifications (*vide infra*). Anhydrous dichloromethane, hexane, tetrahydrofuran and toluene were collected from an SPS800 mBraun solvent purification system and stored over 4 Å molecular sieves. 1,2-Difluorobenzene was degassed and dried under argon over 4 Å molecular sieves. Et_2O was dried by refluxing it over Na/benzophenone under argon atmosphere. Deuterated solvents were degassed and dried over 4 Å molecular sieves under argon.

Unless otherwise noted, NMR spectra were recorded at room temperature on a Bruker Avance 360 spectrometer. ^1H, $^{13}C\{^1H\}$, $^{11}B\{^1H\}$, and $^{19}F\{^1H\}$ NMR spectra are reported on the δ scale (ppm) and are referenced against $SiMe_4$, $BF_3{\cdot}Et_2O$ (15% in $CDCl_3$), and $CFCl_3$ respectively. ^1H and $^{13}C\{^1H\}$ chemical shifts are reported relative to the residual peak of the solvent ($CHCl_3$ 7.26 ppm for $CDCl_3$; C_6D_5H 7.16 ppm for C_6D_6; $CDHCl_2$ 5.32 ppm for CD_2Cl_2; C_4D_7HO 3.58 ppm for THF-*d8*) in the ^1H NMR spectra, and to the peak of the deuterated solvent ($CDCl_3$ 77.16 ppm; C_6D_6 128.06; CD_2Cl_2 53.84 ppm; THF-*d8* 36.57 ppm) in the $^{13}C\{^1H\}$ NMR spectra[8]. The assignment of the ^1H and $^{13}C\{^1H\}$ resonance signals was made in accordance with the COSY, HSQC and HMBC spectra.

The ESI HRMS spectra were measured on a Bruker Impact II spectrometer. Acetonitrile or dichloromethane/acetonitrile solutions ($c = 1{\cdot}10^{-5}$ mol·L^{-1}) were injected directly into the spectrometer at a flow rate of 3 µL·min^{-1}. Nitrogen was used both as a drying gas and for nebulization with flow rates of approximately 5 L·min^{-1} and a pressure of 5 psi. Pressure in the mass analyzer region was usually about $1{\cdot}10^{-5}$ mbar. Spectra were collected for 1 min and averaged. The nozzle-skimmer voltage was adjusted individually for each measurement.

IR spectra were recorded with a Thermo Scientific Nicolet iS10 instrument.

The UV-Vis spectra were recorded on a Varian Cary 50 Scan UV-Visible Spectrophotometer.

Elemental analyses (C, H) were carried out using an Elementar Vario Macro instrument.

Synthesis and characterization of (2,6-$Mes_2C_6H_3)_2BiH$[2]

To a pre-cooled (−90 °C) suspension of (2,6-$Mes_2C_6H_3)_2BiCl$ (2.120 g, 2.4 mmol) in Et_2O (15 mL), $LiAlH_4$ (0.100 g, 2.6 mmol) was added as a solid. The reaction mixture was allowed to warm up slowly to −20 °C. Between −30 °C and −20 °C the characteristic dark yellow color of (2,6-$Mes_2C_6H_3)_2BiCl$ faded slowly; a beige suspension was obtained. After stirring the reaction mixture at −20 °C for 0.5 h, the solvent was evaporated to dryness at reduced pressure while maintaining the temperature around −20 °C. Toluene (60 mL) was added subsequently at room temperature and the suspension was filtered. The dark red to violet solution was reduced to dryness by evaporating the solvent at reduced pressure; a beige solid with some purple contaminant was obtained. Toluene (5 mL) and hexane (40 mL) were added, the contents were warmed to 60 °C and the solid was separated by decantation. Subsequently the solid was dried at reduced pressure. The title product was obtained as a beige solid (1.020 g, 51%). An additional crop of product (0.210 g; overall yield 1.230 g, 61%) in the form of large parallelepipedic crystals was obtained after placing the dark red to violet toluene/hexane solution in the fridge (4 °C) for 5 days. The product is only slightly soluble in benzene or THF. The compound is stable at room temperature as a solid for at least several months. In solution (C_6D_6 or THF-*d8*) it decomposed (slowly at room temperature, faster at 60 °C) to the purple dibismuthene [(2,6-$Mes_2C_6H_3)Bi]_2$ as previously noted[2]. **^1H NMR (360 MHz, C_6D_6)**: δ = 19.61 (s, br, 1H, Bi*H*), 7.02 (t, $^3J(^1H{-}^1H)$ = 7 Hz, 2H, *p*-C_6H_3), 6.85 (d, $^3J(^1H{-}^1H)$ = 7 Hz, 4H, *m*-C_6H_3), 6.83, 6.82 (singlets, br, 8H, *m*-Mes), 2.25 (s, 12H, *p*-CH_3), 1.89 (s, 12H, *o*-CH_3), 1.86 (s, 12H, *o*-CH_3). **$^{13}C\{^1H\}$ NMR (91 MHz, C_6D_6)**: δ = 153.61 (s, *i*-C_6H_3), 150.94 (s, br, *o*-C_6H_3), 144.38 (s, *i*-Mes), 136.42 (s, *p*-Mes), 136.11 (s, *o*-Mes), 135.79 (s, *o*-Mes), 128.97 (s, *m*-C_6H_3), 128.85 (s, *m*-Mes), 128.81 (s, *m*-Mes), 128.40 (s, *p*-C_6H_3), 21.93 (s, *o*-CH_3), 21.36 (s, *p*-CH_3). **^1H NMR (360 MHz, THF-*d8*)**: δ = 19.39 (s, br, 1H, Bi*H*), 7.17 (t, $^3J(^1H{-}^1H)$ = 7 Hz, 2H, *p*-C_6H_3), 6.87–6.69 (m, 12H, *m*-C_6H_3, *m*-Mes), 2.30 (s, *p*-CH_3), 1.69 (s, *o*-CH_3), 1.66 (s, *o*-CH_3). **$^{13}C\{^1H\}$ NMR (91 MHz, THF-*d8*)**: δ = 154.32 (s, br, *i*-C_6H_3), 151.55 (s, *o*-C_6H_3), 144.93 (s, *i*-Mes), 137.04 (s, *p*-Mes), 136.60 (s, *o*-Mes), 136.26 (s, *o*-Mes), 129.47 (s, *m*-C_6H_3), 129.25 (s, *m*-Mes), 128.81 (s, *p*-C_6H_3), 22.13 (s, *o*-CH_3), 22.08 (s, *o*-CH_3), 21.52 (s, *p*-CH_3). **IR (ATR, cm^{-1})**: $\tilde{\nu}$ = 1763 (m, BiH). **Analysis (calculated, found for $C_{48}H_{51}Bi$):** C (68.89, 68.59), H (6.14, 6.48).

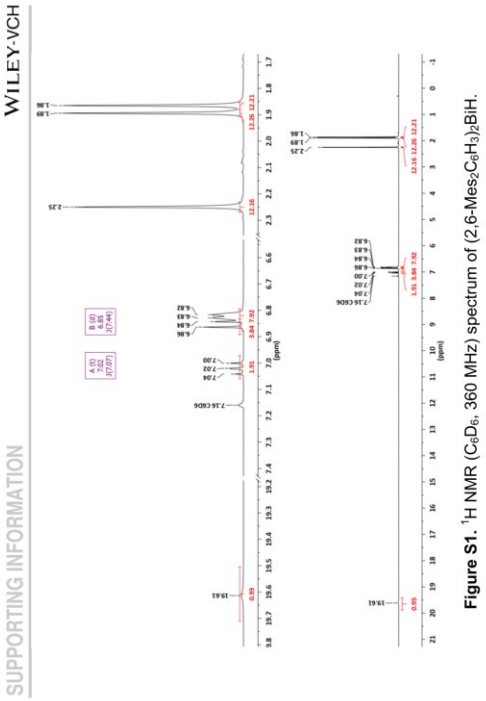

Figure S1. ^{1}H NMR (C_6D_6, 360 MHz) spectrum of (2,6-$Mes_2C_6H_3$)$_2$BiH.

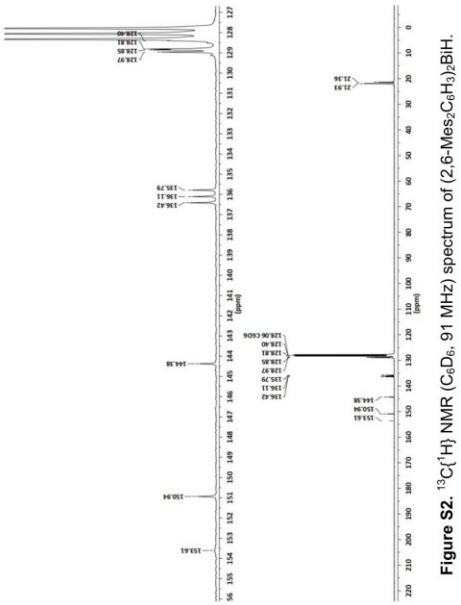

Figure S2. $^{13}C\{^{1}H\}$ NMR (C_6D_6, 91 MHz) spectrum of (2,6-$Mes_2C_6H_3$)$_2$BiH.

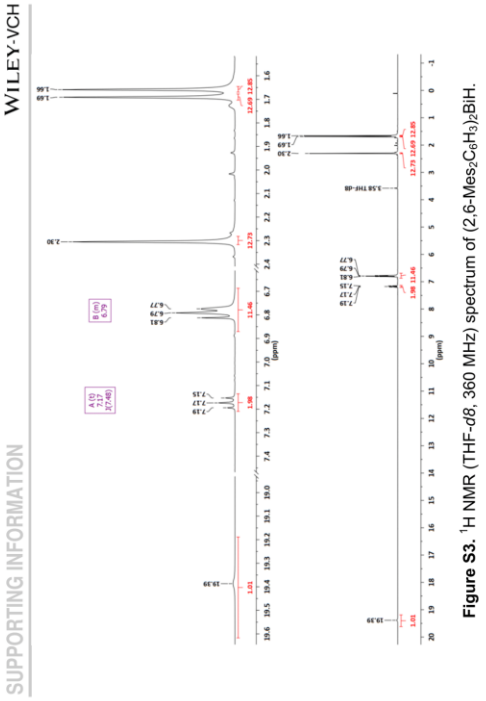

Figure S3. ^{1}H NMR (THF-*d8*, 360 MHz) spectrum of (2,6-$Mes_2C_6H_3$)$_2$BiH.

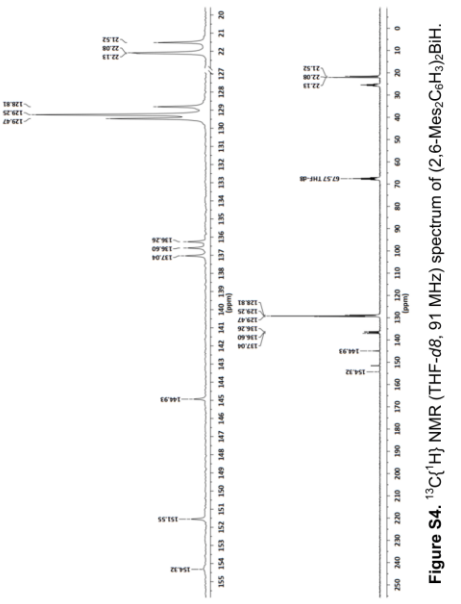

Figure S4. $^{13}C\{^{1}H\}$ NMR (THF-*d8*, 91 MHz) spectrum of (2,6-$Mes_2C_6H_3$)$_2$BiH.

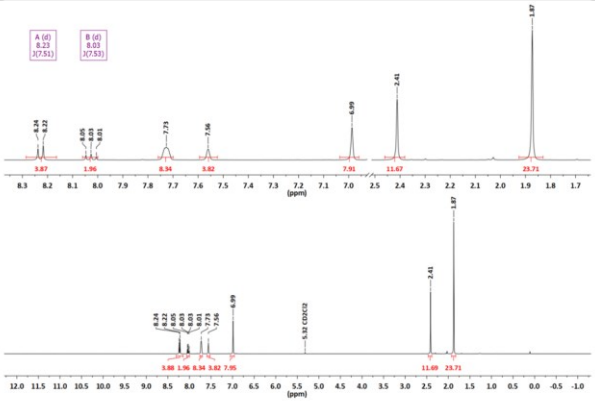

Figure S5. ^{1}H NMR (CD_2Cl_2, 360 MHz) spectrum of **1**.

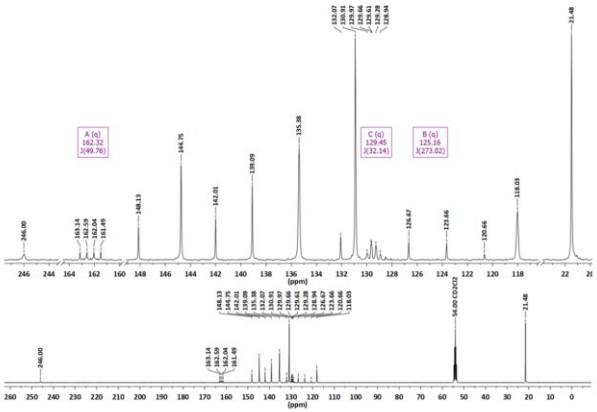

Figure S6. $^{13}C\{^{1}H\}$ NMR (CD_2Cl_2, 91 MHz) spectrum of **1**.

Synthesis and characterization of [(2,6-$Mes_2C_6H_3$)$_2$Bi][BAr^F_4] (1)

To a solid mixture of (2,6-$Mes_2C_6H_3$)$_2$BiH (0.125 g, 0.15 mmol) and [Ph_3C][BAr^F_4] (0.165 g, 0.15 mmol) was added 1,2-difluorobenzene (3 mL) at room temperature. The reaction mixture was stirred for 5 h; a dark green-brown solution was obtained. All volatiles were removed at reduced pressure and the solid residue was washed with hexane (3×25 mL), then dried at reduced pressure. The title product was obtained as a black solid (0.220 g, 87%). **Mp.** 178–180 °C. **^{1}H NMR (360 MHz, CD_2Cl_2)**: δ = 8.23 (d, $^{3}J(^{1}H–^{1}H)$ = 8 Hz, 4H, *m*-C_6H_3), 8.03 (t, $^{3}J(^{1}H–^{1}H)$ = 8 Hz, 2H, *p*-C_6H_3), 7.73 (s, br, 8H, *o*-Ar^F), 7.56 (s, 4H, *p*-Ar^F), 6.99 (s, 8H, *m*-Mes), 2.41 (s, 12H, *p*-CH_3), 1.87 (s, 24H, *o*-CH_3). **$^{13}C\{^{1}H\}$ NMR (91 MHz, CD_2Cl_2)**: δ = 246.00 (s, *i*-C_6H_3), 162.32 (q, $^{1}J(^{11}B–^{13}C)$ = 50 Hz, *i*-Ar^F), 148.13 (s, *o*-C_6H_3), 144.75 (s, *m*-C_6H_3), 142.01 (s, *p*-Mes), 139.09 (s, *o*-Mes), 135.38 (s, *o*-Ar^F), 132.07 (s, *i*-Mes), 130.91 (s, *m*-Mes, *p*-C_6H_3), 129.45 (q, $^{2}J(^{19}F–^{13}C)$ = 32 Hz, *m*-Ar^F), 125.16 (q, $^{1}J(^{19}F–^{13}C)$ = 273 Hz, CF_3), 118.03 (s, br, *p*-Ar^F), 21.48 (s, *o*-CH_3, *p*-CH_3). **^{19}F NMR (339 MHz, CD_2Cl_2)**: δ = −64.08 (s). **^{11}B NMR (116 MHz, CD_2Cl_2)**: δ = −5.72 (s). **HRMS ESI (m/z):** $[M]^+$ calculated. for $C_{48}H_{50}Bi$, 835.37110; found, 835.37086. UV-Vis (nm): 400 (ε = 10813 $M^{-1}\cdot cm^{-1}$), 551 (ε = 3283 $M^{-1}\cdot cm^{-1}$). **Analysis (calculated, found for $C_{80}H_{62}BBiF_{24}$):** C (56.55, 56.55), H (3.68, 3.41).

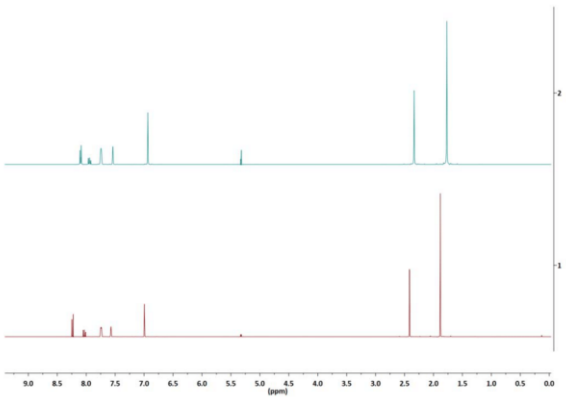

Figure S9. Variable temperature ^{1}H NMR (CD_2Cl_2, 360 MHz) spectra of **1**. (1) ^{1}H NMR spectrum at −70 °C. (2) ^{1}H NMR spectrum at room temperature (20 °C).

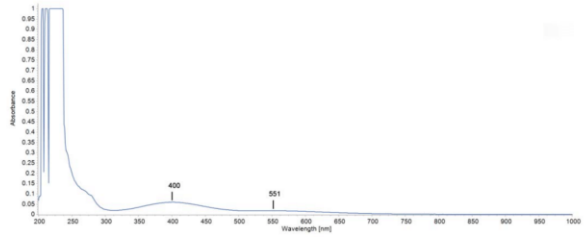

Figure S10. UV-VIS (CH_2Cl_2) spectrum of **1**.

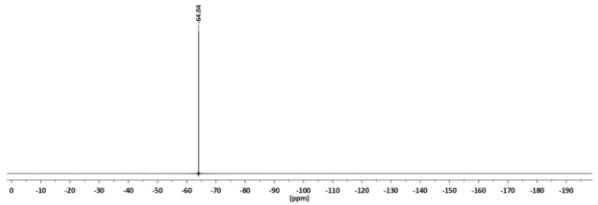

Figure S7. $^{19}F\{^{1}H\}$ NMR (CD_2Cl_2, 339 MHz) spectrum of **1**.

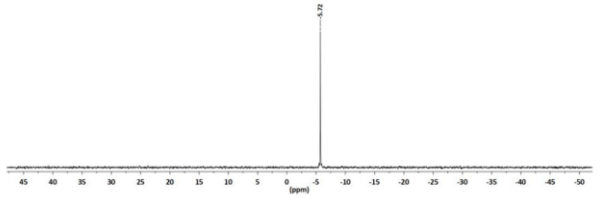

Figure S8. $^{11}B\{^{1}H\}$ NMR (CD_2Cl_2, 116 MHz) spectrum of **1**.

Synthesis and characterization of (2,6-$Mes_2C_6H_3$)$_2$SbCl

To a solution of $SbCl_3$ (0.713 g, 3.13 mmol) in Et_2O (10 mL) was added dropwise a solution of 2,6-$Mes_2C_6H_3Li$ (1.000 g, 3.13 mmol) in Et_2O (10 mL) at room temperature. The reaction mixture was stirred for 2 hours at room temperature and afterwards cooled down to 0 °C. Subsequently a solution of 2,6-$Mes_2C_6H_3Li$ (1.000 g, 3.13 mmol) in Et_2O (10 mL) was added dropwise over the course of 0.5 h and the reaction mixture was stirred for an additional hour at 0 °C and 1 h at room temperature. The solvent was removed under reduced pressure and CH_2Cl_2 (20 mL) was added. The suspension was filtered and the solvent of the filtrate was removed at reduced pressure. The remaining solid was washed with 3×10 mL hexane and dried at 80 °C ($2\cdot10^{-2}$ mbar). The title compound was obtained as a white solid (1.70 g, 70 %). **Mp.** 133–135°C. **^{1}H NMR (360 MHz, CD_2Cl_2)**: δ = 7.27 (t, $^3J(^1H–^1H)$ = 8 Hz, 2H, *p*-C_6H_3), 6.78 (d, $^3J(^1H–^1H)$ = 8 Hz, 4H, *m*-C_6H_3), 6.76 (s, br, 8H, *m*-Mes), 2.30 (s, 12H, *p*-CH_3), 1.78 (s, 12H, *o*-CH_3), 1.68 (s, 12H, *o*-CH_3). **$^{13}C\{^1H\}$ NMR (91 MHz, CD_2Cl_2)**: δ = 149.68 (s, *i*-C_6H_3), 148.95 (s, *o*-C_6H_3), 139.44 (s, *i*-Mes), 137.88 (s, *o*-Mes), 137.52 (s, *p*-Mes), 137.17 (s, *o*-Mes), 131.71 (s, *m*-C_6H_3), 129.75 (s, *p*-C_6H_3), 128.92 (s, *m*-Mes), 128.73 (s, *m*-Mes), 22.53 (s, *o*-CH_3), 21.38 (s, *p*-CH_3). **HRMS ESI (m/z):** $[M+Na]^+$ calculated. for $C_{48}H_{50}SbClNa$, 805.25314; found, 805.25244. **Analysis (calculated, found for $C_{48}H_{50}SbCl$):** C (73.52, 73.17), H (6.43, 6.56).

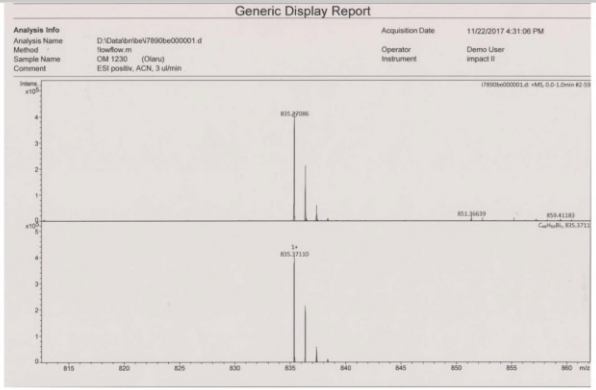

Figure S11. Measured (top) and calculated (bottom) isotopic pattern of $[M]^+$ of **1**.

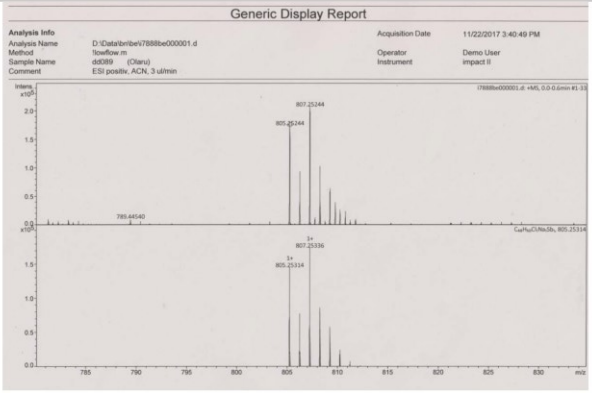

Figure S14. Measured (top) and calculated (bottom) isotopic pattern of $[M+Na]^+$ of (2,6-$Mes_2C_6H_3)_2SbCl$.

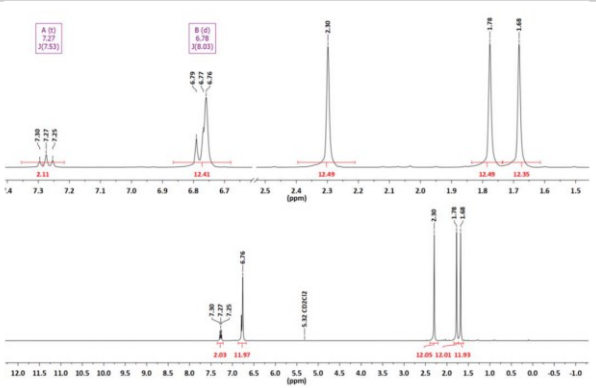

Figure S12. ^1H NMR (CD_2Cl_2, 360 MHz) spectrum of (2,6-$Mes_2C_6H_3)_2SbCl$.

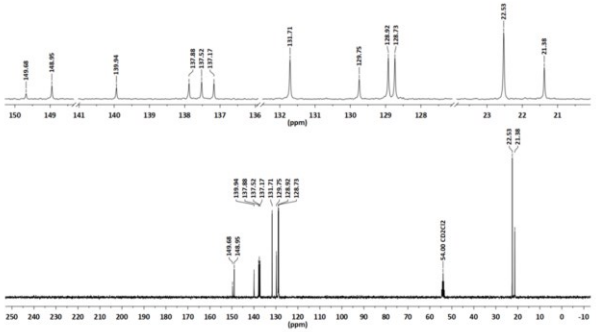

Figure S13. $^{13}C\{^1H\}$ NMR (CD_2Cl_2, 91 MHz) spectrum of (2,6-$Mes_2C_6H_3)_2SbCl$.

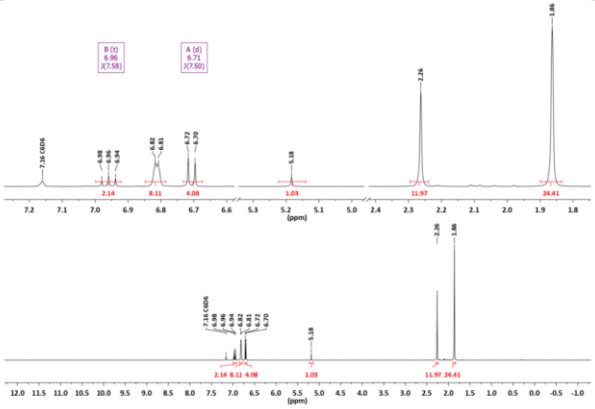

Figure S15. ^{1}H NMR (C_6D_6, 360 MHz) spectrum of (2,6-$Mes_2C_6H_3$)$_2$SbH.

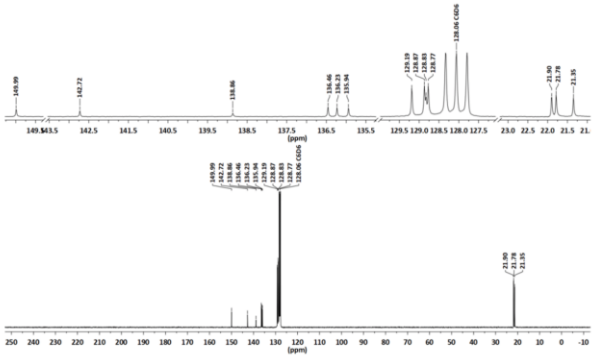

Figure S16. $^{13}C\{^{1}H\}$ NMR (C_6D_6, 91 MHz) spectrum of (2,6-$Mes_2C_6H_3$)$_2$SbH.

Synthesis and characterization of (2,6-$Mes_2C_6H_3$)$_2$SbH

A mixture of (2,6-$Mes_2C_6H_3$)$_2$SbCl (1.000 g, 1.28 mmol) and $LiAlH_4$ (0.048 mg, 1.28 mmol) in Et_2O (15 mL) was stirred at room temperature for 20 h. A light grey suspension was obtained. All volatiles were evaporated at reduced pressure and toluene (80 mL) was added. The suspension was filtered and the filtrate evaporated to dryness at reduced pressure. The resulting solid was washed with 2×20 mL Et_2O/hexane (15 mL/5 mL) and 1×15 mL Et_2O, then dried at reduced pressure. The title product was obtained as a white solid (0.670 g, 70%). **Mp.** 198–200 °C (dec.). **^{1}H NMR (360 MHz, C_6D_6)**: δ = 6.96 (t, $^{3}J(^{1}H–^{1}H)$ = 8 Hz, 2H, *p*-C_6H_3), 6.82 and 6.81 (s, br, 8H, *m*-Mes), 6.71 (d, $^{3}J(^{1}H–^{1}H)$ = 8 Hz, 4H, *m*-C_6H_3), 5.18 (s, 1H, SbH), 2.26 (s, 12H, *p*-CH_3), 1.86 (s, 24H, *o*-CH_3). **$^{13}C\{^{1}H\}$ NMR (91 MHz, C6D6)**: δ = 149.99 (s, *i*-C_6H_3), 142.72 (s, *i*-Mes), 138.86 (s, *o*-C_6H_3), 136.46 (s, *p*-Mes), 136.23 (s, *o*-Mes), 135.94 (s, *o*-Mes), 129.19 (s, *m*-C_6H_3), 128.87 (s, *m*-Mes), 128.83 (s, *p*-C_6H_3), 127.77 (s, *m*-Mes), 21.90 (s, *p*-CH_3), 21.78 (s, *p*-CH_3), 21.35 (s, *o*-CH_3). **IR (ATR, cm^{-1})**: $\tilde{\nu}$ = 1935 (m, SbH). **HRMS ESI (m/z):** $[M+Na]^+$ calculated. for $C_{48}H_{51}SbNa$, 771.29211; found, 771.29250. **Analysis (calculated, found for $C_{48}H_{51}Sb$):** C (76.90, 76.51), H (6.86, 7.21).

Synthesis and characterization of [(2,6-$Mes_2C_6H_3$)$_2$Sb][$B(C_6F_5)_4$] (2)

To a mixture of (2,6-$Mes_2C_6H_3$)$_2$SbCl (0.235 g, 0.30 mmol) and [Ph_3C][$B(C_6F_5)_4$] (0.277 g, 0.30 mmol) in 1,2-difluorobenzene (3 mL) was added at room temperature a solution of Et_3SiH (0.035 mg, 0.30 mmol) in 1,2-difluorobenzene (1.2 mL). The reaction mixture was stirred 14 h at room temperature. A dark red-brown solution was obtained. The product was triturated with hexane (45 mL), the solid separated by decantation and subsequently washed with 3×15 mL hexane then dried at 70 °C ($1\cdot10^{-3}$ mbar). The title product was obtained as a dark green-brown solid (0.352 g, 82%). Mp. 173–175 °C. **^{1}H NMR (360 MHz, CD_2Cl_2)**: δ = 7.66 (t, $^3J(^1H–^1H)$ = 8 Hz, 2H, *p*-C_6H_3), 7.18 (d, $^3J(^1H–^1H)$ = 8 Hz, 4H, *m*-C_6H_3), 7.03 (s, 8H, *m*-Mes), 2.36 (s, 12H, *p*-CH_3), 1.81 (s, 24H, *o*-CH_3). **$^{13}C\{^1H\}$ NMR (91 MHz, CD_2Cl_2)**: δ = 156.36 (s, *i*-C_6H_3), 148.70 (doublet of multiplet, br, $^1J(^{19}F-^{13}C)$ = 241 Hz, C_6F_5), 147.57 (s, *o*-C_6H_3), 141.81 (s, *p*-Mes), 138.86 (doublet of multiplet, br, $^1J(^{19}F-^{13}C)$ = 245 Hz, C_6F_5), 137.43 (s, *o*-Mes), 136.94 (doublet of multiplet, br, $^1J(^{19}F-^{13}C)$ = 249 Hz, C_6F_5), 136.00 (s, *i*-Mes), 133.82 (s, *p*-C_6H_3), 133.77 (s, *m*-C_6H_3), 132.35 (s, *m*-Mes), 22.10 (s, *o*-CH_3), 21.47 (s, *p*-CH_3); the resonance signal corresponding to *i*-C_6F_5 was not observed. **$^{19}F\{^1H\}$ NMR (339 MHz, CD_2Cl_2)**: δ = −134.76 (br, 8F, *o*-C_6F_5), −164.46 (br, 4F, *p*-C6F5), −168.45 (br, 8F, *m*-C_6F_5). **$^{11}B\{^1H\}$ NMR (116 MHz, CD_2Cl_2)**: δ = −15.78 (s). **HRMS ESI (m/z):** $[M]^+$ calculated. for $C_{48}H_{50}Sb$, 747.29452; found, 747.29407. UV-Vis (nm): 380 (ε = 7783 $M^{-1}\cdot cm^{-1}$), 560 (ε = 3057 $M^{-1}\cdot cm^{-1}$). **Analysis (calculated, found for $C_{72}H_{50}BF_{20}Sb$):** C (60.57, 58.88), H (3.53, 3.13); incomplete combustion of the perfluorinated anion is assumed to have affected the carbon value.[9]

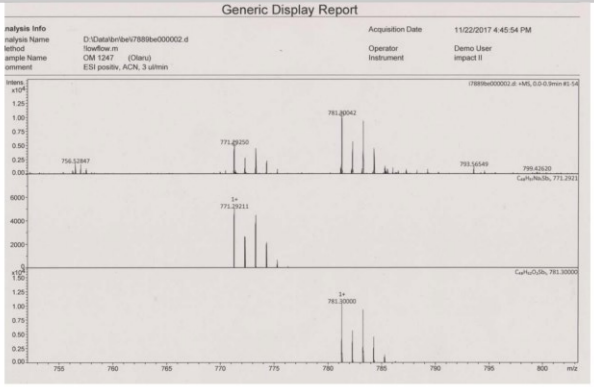

Figure S17. Measured (top) and calculated (middle) isotopic pattern of $[M]^+$ of (2,6-$Mes_2C_6H_3$)$_2$SbH (partial decomposition of (2,6-$Mes_2C_6H_3$)$_2$SbH took place during the measurement giving $[(2,6\text{-}Mes_2C_6H_3)_2Sb(OH)_2]^+$ at m/z = 781.30042; the calculated isotopic pattern of $[(2,6\text{-}Mes_2C_6H_3)_2Sb(OH)_2]^+$ is shown at the bottom).

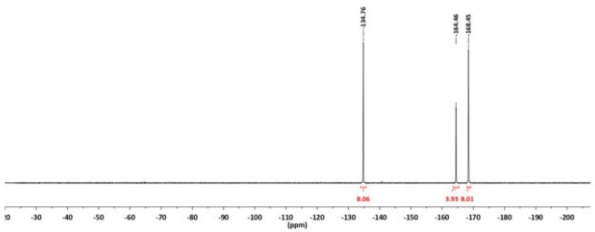

Figure S20. $^{19}F\{^{1}H\}$ NMR (CD_2Cl_2, 339 MHz) spectrum of **2**.

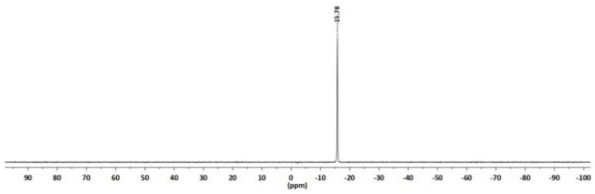

Figure S21. $^{11}B\{^{1}H\}$ NMR (CD_2Cl_2, 116 MHz) spectrum of **2**.

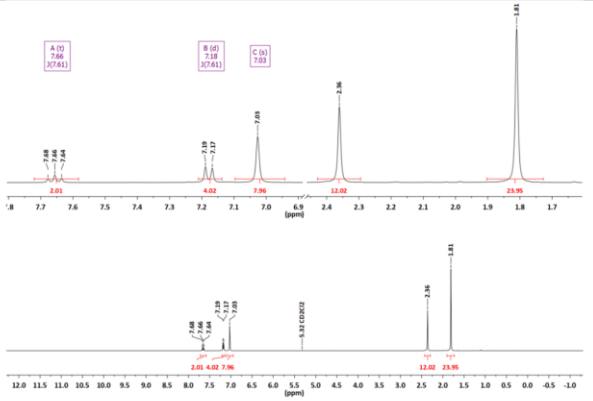

Figure S18. ^{1}H NMR (CD_2Cl_2, 360 MHz) spectrum of **2**.

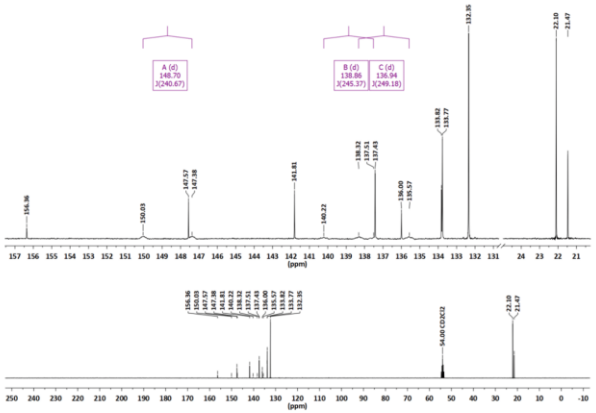

Figure S19. $^{13}C\{^{1}H\}$ NMR (CD_2Cl_2, 91 MHz) spectrum of **2**.

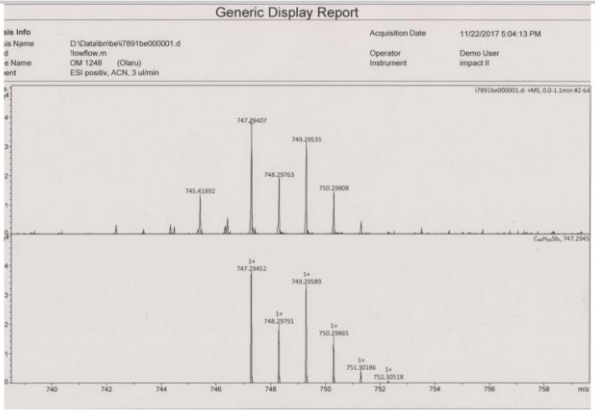

Figure S24. Measured (top) and calculated (bottom) isotopic pattern of $[M]^+$ of **2**.

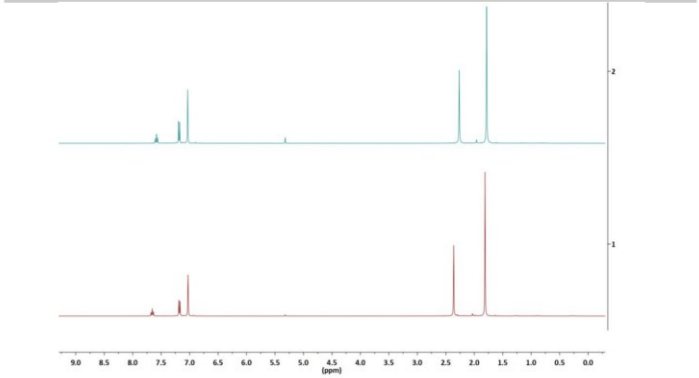

Figure S22. Variable temperature ^{1}H NMR (CD_2Cl_2, 360 MHz) spectra of **2**. (1) ^{1}H NMR spectrum at −70 °C; (2) ^{1}H NMR spectrum at room temperature (20 °C).

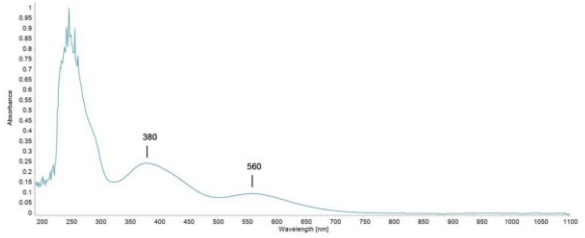

Figure S23. UV-VIS (CH_2Cl_2) spectrum of **2**.

Table S1. Crystal data and structure refinement of **1**·0.5hexane and **2**·hexane·0.5(1,2-difluorobenzene).

	1·0.5hexane	**2**·hexane·0.5(1,2-difluorobenzene)
Formula	$C_{83}H_{69}BBiF_{24}$	$C_{81}H_{66}BF_{21}Sb$
Formula weight, g mol^{-1}	1742.17	1570.90
Crystal system	Triclinic	Triclinic
Crystal size, mm	0.08 × 0.08 × 0.05	0.08 × 0.04 × 0.04
Space group	$P\bar{1}$	$P\bar{1}$
a, Å	12.9690(2)	18.5736(8)
b, Å	16.5674(3)	20.1998(8)
c, Å	18.6768(4)	20.5585(8)
α, °	72.400(1)	63.982(1)
β, °	82.531(1)	86.922(1)
γ, °	86.136(1)	86.397(1)
V, Å^3	3791.0(1)	6914.9(5)
Z	2	4
ρ_{calcd}, Mg m^{-3}	1.526	1.509
μ (Mo *Kα*), mm^{-1}	2.429	0.502
F(000)	1742	3188
θ range, deg	1.00 to 32.08	1.00 to 30.07
Index ranges	–18 ≤ h ≤ 18	–19 ≤ h ≤ 22
	–23 ≤ k ≤ 23	–24 ≤ k ≤ 24
	–26 ≤ l ≤ 26	–24 ≤ l ≤ 24
No. of reflns collected	90563	179954
Completeness to θ_{max}	99.5%	99.9%
No. indep. Reflns	22173	25729
No. obsd reflns with ($I>2\sigma(I)$)	19117	19889
No. refined params	1022	1901
GooF (F^2)	1.024	1.059
R_1 (F) ($I > 2\sigma(I)$)	0.0324	0.0467
wR_2 (F^2) (all data)	0.0727	0.1262
Largest diff peak/hole, e Å^{-3}	1.484 / –0.948	2.001 / –1.301
CCDC number	1823886	1823887

X-Ray diffraction studies

Intensity data of **1**·0.5hexane, **2**·hexane·0.5(1,2-difluorobenzene), (2,6-$Mes_2C_6H_3)_2$SbCl and (2,6-$Mes_2C_6H_3)_2$SbH was collected on a Bruker Venture D8 diffractometer at 100 K with graphite-monochromated Mo-Kα (0.7107 Å) radiation. All structures were solved by direct methods and refined based on F^2 by use of the SHELX program package as implemented in WinGX.[10,11] The absolute structure of (2,6-$Mes_2C_6H_3)_2$SbH was inferred by refinement of the Flack parameter 0.06(1).[12] Disorder was resolved for (2,6-$Mes_2C_6H_3)_2$SbCl by refining Sb1 and Cl1 over two sites with an occupancy ratio of 0.9 : 0.1. All non-hydrogen atoms were refined using anisotropic displacement parameters. Hydrogen atoms attached to carbon atoms were included in geometrically calculated positions using a riding model. Crystal and refinement data are collected in Tables S1 and S2. Figures were created using DIAMOND.[13] Crystallographic data for the structural analyses have been deposited with the Cambridge Crystallographic Data Centre. Copies of this information may be obtained free of charge from The Director, CCDC, 12 Union Road, Cambridge CB2 1EZ, UK (Fax: +44-1223-336033; e-mail: deposit@ccdc.cam.ac.uk or http://www.ccdc.cam.ac.uk).

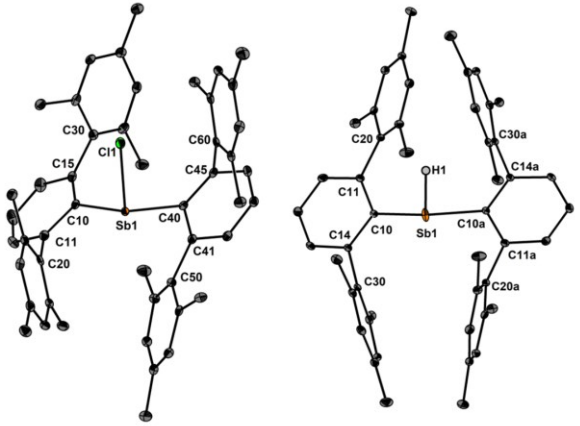

Figure S25. Molecular structures of (2,6-$Mes_2C_6H_3)_2SbCl$ (left) and (2,6-$Mes_2C_6H_3)_2SbH$ (right). Thermal ellipsoids are set at 30% probability.

Table S2. Crystal data and structure refinement of R_2SbCl and R_2SbH (R = 2,6-$Mes_2C_6H_3$).

	R_2SbCl	R_2SbH
Formula	$C_{48}H_{50}ClSb$	$C_{48}H_{51}Sb$
Formula weight, g mol^{-1}	784.08	749.64
Crystal system	Monoclinic	Orthorhombic
Crystal size, mm	0.07 × 0.06 × 0.06	0.05 × 0.05 × 0.05
Space group	$P2_1/c$	Fdd2
a, Å	10.594(5)	20.862(4)
b, Å	16.112(5)	43.896(9)
c, Å	22.732(5)	8.194(2)
α, °	90.00	90.00
β, °	94.525(5)	90.00
γ, °	90.00	90.00
V, $Å^3$	3868(2)	7504(3)
Z	4	8
ρ_{calcd}, Mg m^{-3}	1.346	1.327
μ (Mo *Kα*), mm^{-1}	0.815	0.768
F(000)	1624	3120
θ range, deg	2.31 to 25.53	2.69 to 32.61
Index ranges	$-12 \le h \le 12$	$-20 \le h \le 31$
	$-19 \le k \le 19$	$-38 \le k \le 66$
	$-27 \le l \le 23$	$-12 \le l \le 12$
No. of reflns collected	21157	18118
Completeness to θ_{max}	99.6%	99.3%
No. indep. Reflns	7222	6627
No. obsd reflns with ($I>2\sigma(I)$)	5559	6086
No. refined params	481	232
GooF (F^2)	1.108	1.091
R_1 (F) ($I > 2\sigma(I)$)	0.0432	0.0287
wR_2 (F^2) (all data)	0.1092	0.0606
Largest diff peak/hole, e $Å^{-3}$	0.585 / –1.486	0.507 / –1.041
CCDC number	1823888	1823889

Computational data

Starting from the solid-state molecular geometries of **1** and **2** structural optimizations were conducted for all R_2E (R = 2,6-$Mes_2C_6H_3$; E = Si, Ge, Sn, Pb) and $[R_2E]^+$ (E = P, As, Sb, Bi) compounds by density functional theory (DFT) at the B3PW91/6-311+G(2df,p)[14,15] level of theory using Gaussian09.[16] The starting geometries of the smaller compounds Ph_2E (E = Si, Ge, Sn, Pb) and $[Ph_2E]^+$ (E = P, As, Sb, Bi) were modeled at the computer with GaussView 5. For the Sn, Pb, Sb, and Bi atoms fully relativistic effective core potentials (Sn, Sb: ECP28MDF; Pb, Bi: ECP60MDF) and corresponding cc-pVTZ basis sets[17,18] were utilized. Normal mode (or frequency) analysis proved all single state calculations of $[Ph_2E]^+$ structures to be local minima. However, despite tremendous computational effort, this was not the case for the big compounds (R = 2,6-$Mes_2C_6H_3$) and for the triplet state calculations of the small compounds. All negative frequencies are considerably below 50 cm^{-1} (resembling low-energy phononic-like modes) hence the electronic effect can be neglected. The wavefunction files were employed for a topological analysis of the electron density according to the Atoms-In-Molecules (AIM)[19] space-partitioning scheme using AIM2000,[20] whereas DGRID[21] was used to generate and analyze the Electron-Localizability-Indicator (ELI-D)[22,23] related real-space bonding descriptors applying a grid step size of 0.05 a.u.. For ELI-D figures, additional grids of 0.15 a.u. step size were computed. NCI[24] grids were generated with NCIplot.[25] Molecular orbitals (MO) were extracted from the formatted checkpoint files with the cubegen subroutine of Gaussian09. Natural bond orbitals (NBO)[26,27] were calculated with NBO 5.9.[28] Bond paths are displayed with AIM2000, ELI-D and NCI figures are displayed with MolIso,[29] MO and NBO images are generated with GaussView 5.

Table S3. Selected bond parameters [Å, °] of **1**·0.5hexane.

C10–Bi1	2.274(3)	C10–C15–C30	127.4(2)
C40–Bi1	2.277(2)	Bi1–C40–C41	103.7(2)
C10–Bi1–C40	116.7(1)	Bi1–C40–C45	133.9(2)
Bi1–C10–C11	102.5(2)	C40–C41–C50	119.5(2)
Bi1–C10–C15	134.7(2)	C40–C45–C60	126.8(2)
C10–C11–C20	118.7(2)		

Table S4. Selected bond parameters [Å, °] of **2**·hexane·0.5(1,2-difluorobenzene).

C10–Sb1	2.176(3)	C70–Sb2	2.165(3)
C40–Sb1	2.182(3)	C100–Sb2	2.157(4)
C10–Sb1–C40	121.4(1)	C70–Sb2–C100	122.8(1)
Sb1–C10–C11	101.9(2)	Sb2–C70–C75	133.9(2)
Sb1–C10–C15	135.3(3)	Sb2–C70–C71	106.5(2)
C10–C11–C20	117.8(3)	C70–C71–C80	121.0(3)
C10–C15–C30	125.0(3)	C70–C75–C90	126.4(3)
Sb1–C40–C41	103.6(2)	Sb2–C100–C101	134.4(3)
Sb1–C40–C45	133.8(3)	Sb2–C100–C105	99.8(2)
C40–C41–C50	119.1(3)	C100–C105–C120	116.4(3)
C40–C45–C60	125.7(3)	C100–C101–C110	124.8(3)

Table S5. Selected bond parameters [Å, °] of (2,6-$Mes_2C_6H_3)_2$SbCl.

C10–Sb1	2.203(3)	Sb1–C10–C15	131.3(3)
C40–Sb1	2.191(4)	C10–C11–C20	122.3(3)
Cl1–Sb1	2.382(2)	C10–C15–C30	128.1(3)
C10–Sb1–C40	103.4(1)	Sb1–C40–C41	115.2(3)
C10–Sb1–Cl1	98.1(1)	Sb1–C40–C45	125.0(2)
C40–Sb1–Cl1	100.8(1)	C40–C41–C50	128.0(3)
Sb1–C10–C11	109.8(2)	C40–C45–C60	126.9(3)

Table S6. Selected bond parameters [Å, °] of (2,6-$Mes_2C_6H_3)_2$SbH.

C10–Sb1	2.187(2)	Sb1–C10–C14	117.1(1)
C10–Sb1–C10a	117.5(1)	C10–C11–C20	127.0(1)
Sb1–C10–C11	123.0(1)	C10–C14–C30	124.7(1)

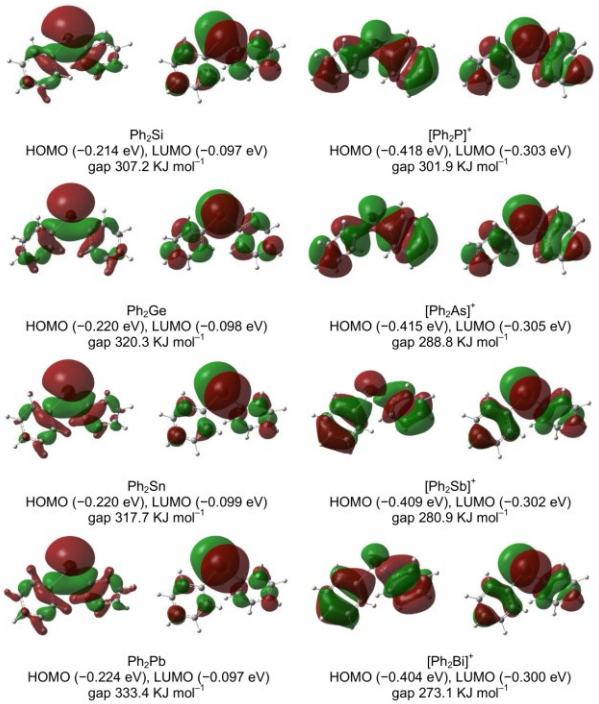

Figure S27. Molecular orbitals (HOMO, LUMO) of Ph_2E (E = Si, Ge, Sn, Pb) and $[Ph_2E]^+$ (E = P, As, Sb, Bi).

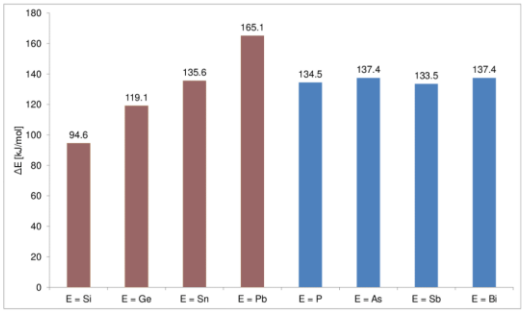

Figure S26. Energy difference between the singlet and triplet ground states of Ph_2E (E = Si, Ge, Sn, Pb) and $[Ph_2E]^+$ (E = P, As, Sb, Bi).

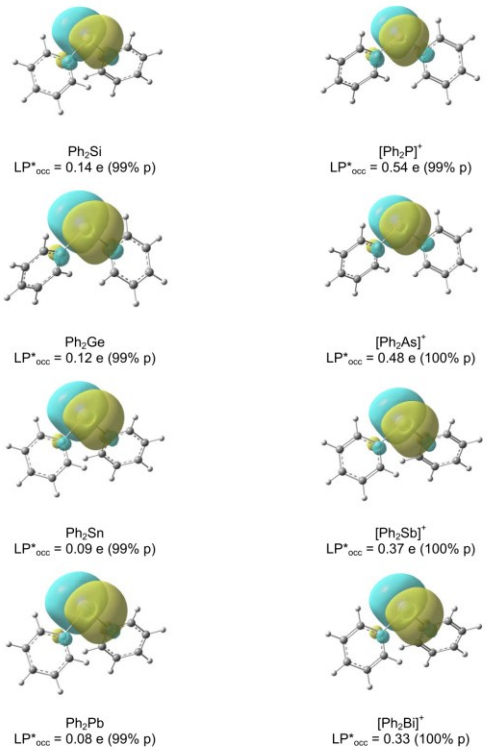

Figure S29. Natural Bond Orbitals (NBO) of the antibonding LPs of Ph_2E (E = Si, Ge, Sn, Pb) and $[Ph_2E]^+$ (P, As, Sb, Bi).

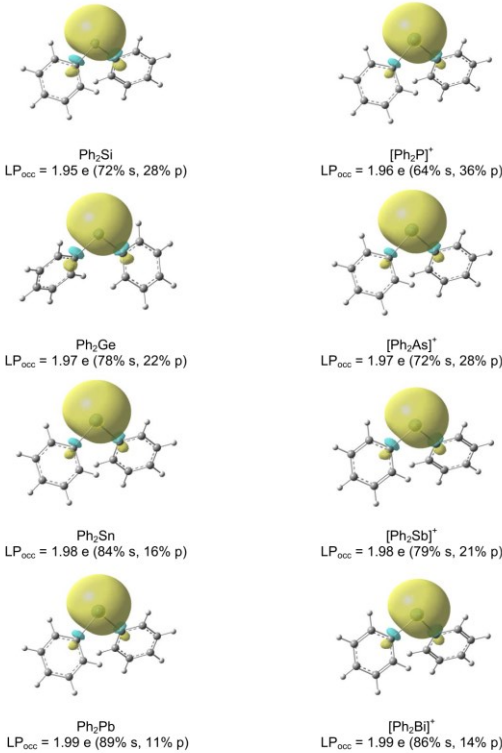

Figure S28. Natural Bond Orbitals (NBO) of LPs of Ph_2E (E = Si, Ge, Sn, Pb) and $[Ph_2E]^+$ (E = P, As, Sb, Bi).

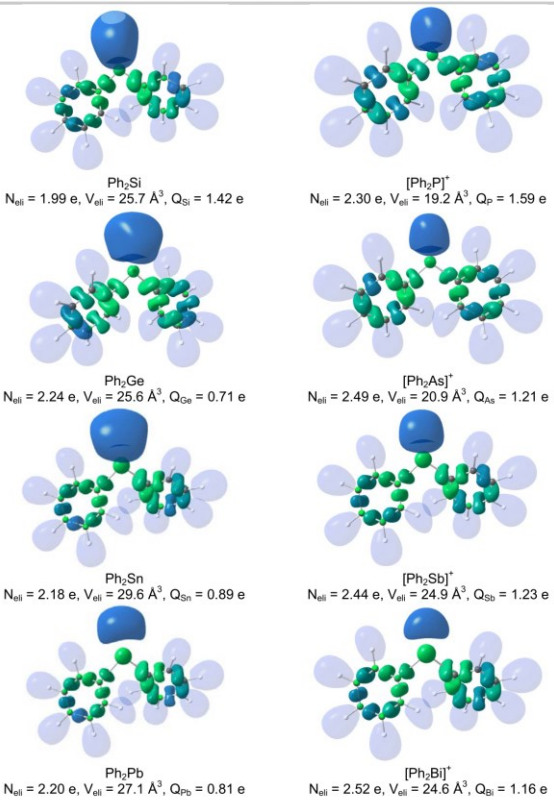

Figure S30. Electron localization indicator (ELI-D) of Ph_2E (E = Si, Ge, Sn, Pb) and $[Ph_2E]^+$ (E = P, As, Sb, Bi).

Table S7. Wiberg bond indices of primary E–C bonds in Ph_2E (E = Si, Ge, Sn, Pb) and $[Ph_2E]^+$ (E = P, As, Sb, Bi).

	bond	WBI		bond	WBI
Ph_2Si	Si–C	2 × 0.755	$[Ph_2P]^+$	P-C	2 × 1.147
Ph_2Ge	Ge–C	2 × 0.765	$[Ph_2As]^+$	As–C	2 × 1.094
Ph_2Sn	Sn–C	2 × 0.694	$[Ph_2Sb]^+$	Sb–C	2 × 0.978
Ph_2Pb	Pb–C	2 × 0.691	$[Ph_2Bi]^+$	Bi–C	2 × 0.954

Table S8. AIM and ELI-D properties of primary E–C bonds of Ph_2E (E = Si, Ge, Sn, Pb) and $[Ph_2E]^+$ (E = P, As, Sb, Bi).

	bond	d [Å]	d_s/d [%]	$\rho(r)_{bcp}$ [eÅ^{-3}]	$\nabla^2\rho(r)_{bcp}$ [eÅ^{-5}]	ε	$G/\rho(r)_{bcp}$ [he^{-1}]	$H/\rho(r)_{bcp}$ [he^{-1}]
Ph_2Si	Si–C	1.886	0.39	0.81	3.8	0.07	1.01	–0.68
Ph_2Ge	Ge–C	1.978	0.47	0.84	1.0	0.06	0.69	–0.60
Ph_2Sn	Sn–C	2.187	0.50	0.67	2.9	0.06	0.71	–0.41
R_2Pb	Pb–C	2.277	0.53	0.63	2.7	0.06	0.66	–0.37
$[Ph_2P]^+$	P–C	1.752	0.39	1.23	–3.7	0.13	0.84	–1.04
$[Ph_2As]^+$	As–C	1.875	0.48	1.10	–2.4	0.12	0.58	–0.73
$[Ph_2Sb]^+$	Sb–C	2.081	0.51	0.85	1.6	0.12	0.65	–0.52
$[Ph_2Bi]^+$	Bi–C	2.178	0.53	0.78	1.8	0.11	0.62	–0.45

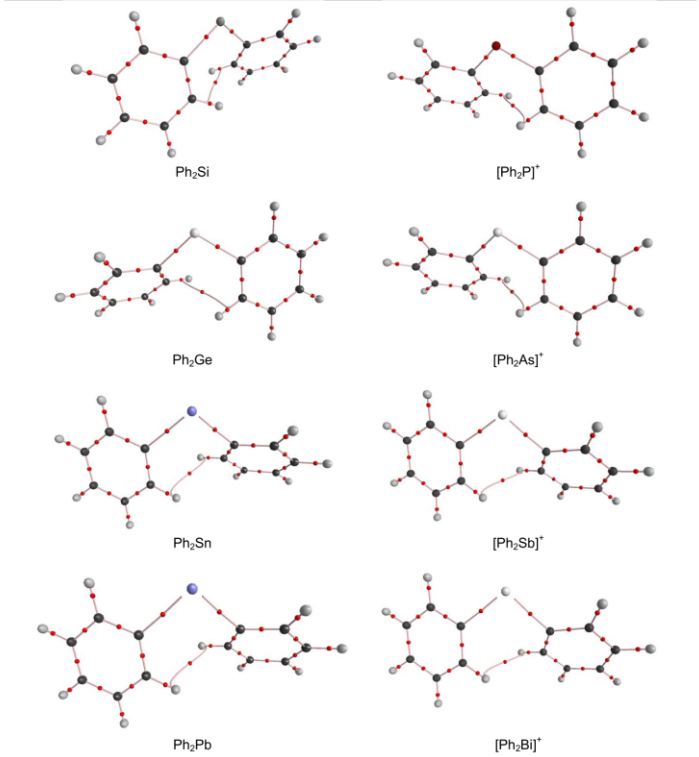

Figure S31. Atoms in Molecules (AIM) topology of Ph_2E (E = Si, Ge, Sn, Pb) and $[Ph_2E]^+$ (E = P, As, Sb, Bi).

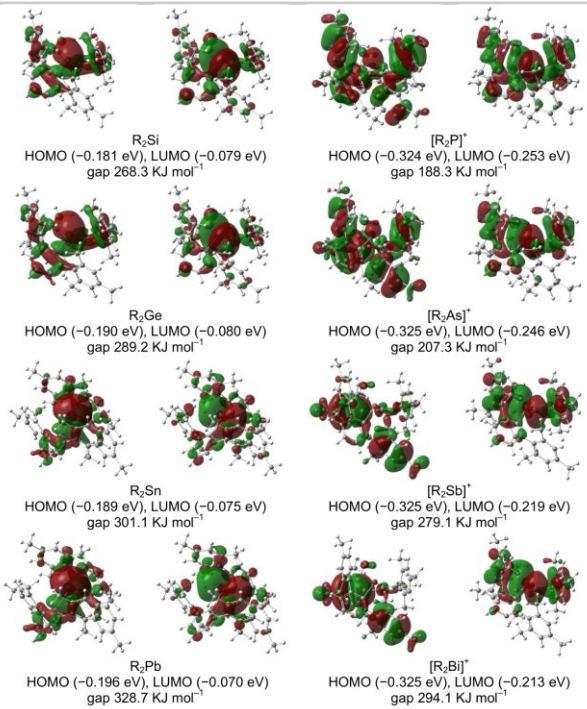

Figure S33. Molecular orbitals (HOMO, LUMO) of R_2E (R = 2,6-$Mes_2C_6H_3$; E = Si, Ge, Sn, Pb) and $[R_2E]^+$ (E = P, As, Sb, Bi).

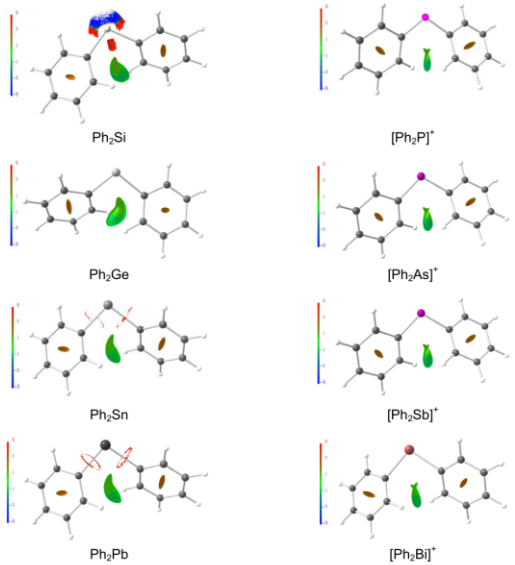

Figure S32. Non-covalent interaction (NCI) index of Ph_2E (E = Si, Ge, Sn, Pb) and $[Ph_2E]^+$ (E= P, As, Sb, Bi).

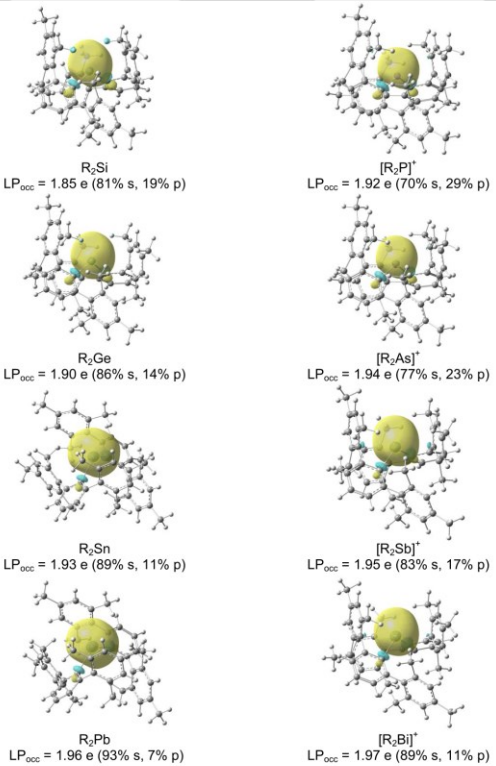

Figure S35. Natural Bond Orbitals (NBO) of LPs of R_2E (R = 2,6-$Mes_2C_6H_3$; E = Si, Ge, Sn, Pb) and $[R_2E]^+$ (E = P, As, Sb, Bi).

Figure S34. Molecular orbitals reflecting the LP of $[R_2Sb]^+$ and $[R_2Bi]^+$ (R = 2,6-$Mes_2C_6H_3$).

Table S9. Wiberg bond indices of primary E-C bonds in R_2E (R = 2,6-$Mes_2C_6H_3$; E = Si, Ge, Sn, Pb) and $[R_2E]^+$ (E = P, As, Sb, Bi).

	bond	WBI		bond	WBI
R_2Si	Si–C	2 × 0.578	$[R_2P]^+$	P–C	2 × 0.921
R_2Ge	Ge–C	2 × 0.566	$[R_2As]^+$	As–C	2 × 0.868
R_2Sn	Sn–C	2 × 0.518	$[R_2Sb]^+$	Sb–C	2 × 0.786
R_2Pb	Pb–C	2 × 0.531	$[R_2Bi]^+$	Bi–C	2 × 0.780

Table S10. Wiberg bond indices of intramolecuar E···C and E···H contacts in R_2E (R = 2,6-$Mes_2C_6H_3$; E = Si, Ge, Sn, Pb) and $[R_2E]^+$ (E = P, As, Sb, Bi).

	bond	WBI		Bond	WBI
R_2Si	Si···C	2 × 0.041	$[R_2P]^+$	P···C	2 × 0.111
	Si···H	2 × 0.022		P···H	2 × 0.012
		2 × 0.021			2 × 0.012
R_2Ge	Ge···C	2 × 0.040	$[R_2As]^+$	As···C	2 × 0.143
	Ge···H	2 × 0.020		As···H	2 × 0.014
		2 × 0.019			2 × 0.010
R_2Sn	Sn···C	2 × 0.037	$[R_2Sb]^+$	Sb···C	2 × 0.169
	Sn···H	2 × 0.017		Sb···H	2 × 0.010
		2 × 0.015			2 × 0.005
R_2Pb	Pb···C	2 × 0.039	$[R_2Bi]^+$	Bi···C	2 × 0.151
	Pb···H	2 × 0.012		Bi···H	2 × 0.007
		2 × 0.011			2 × 0.004

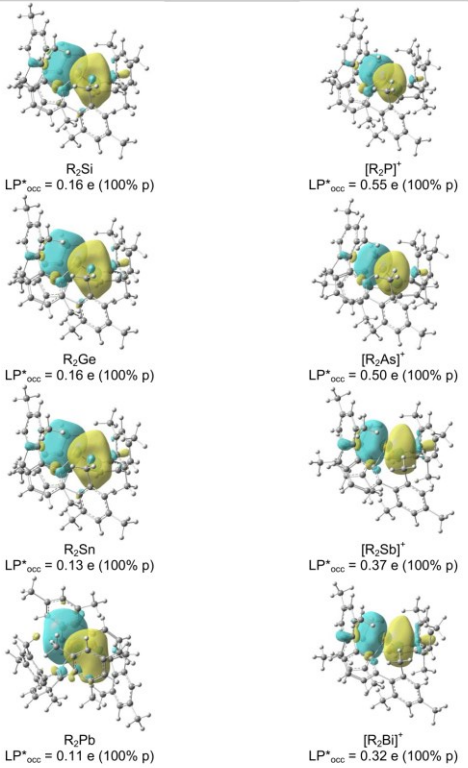

Figure S36. Natural Bond Orbitals (NBO) of the antibonding LPs of R_2E (R = 2,6-$Mes_2C_6H_3$; E = Si, Ge, Sn, Pb) and $[R_2E]^+$ (E = P, As, Sb, Bi).

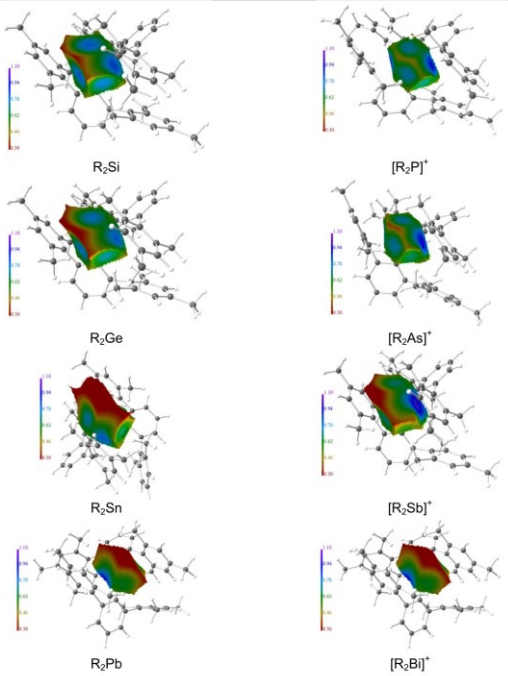

Figure S38. ELI-D distribution mapped on the lone pair basins of R_2E (R = 2,6-$Mes_2C_6H_3$; E = Si, Ge, Sn, Pb) and $[R_2E]^+$ (E = P, As, Sb, Bi).

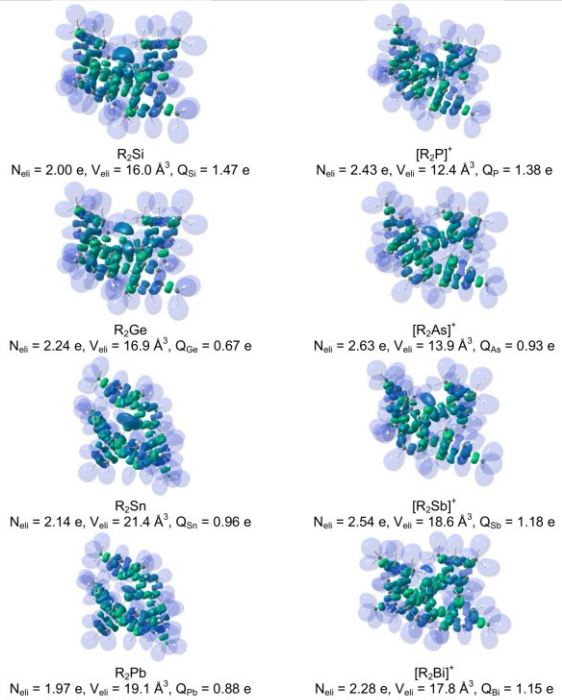

Figure S37. Electron localization indicator (ELI-D) of R_2E (R = 2,6-$Mes_2C_6H_3$; E = Si, Ge, Sn, Pb) and $[R_2E]^+$ (E = P, As, Sb, Bi).

Table S11. AIM and ELI-D properties of primary E–C bonds of R_2E (R = 2,6-$Mes_2C_6H_3$; E = Si, Ge, Sn, Pb) and $[R_2E]^+$ (E = P, As, Sb, Bi).

	bond	d [Å]	d_1/d [%]	$\rho(r)_{bcp}$ [eÅ^{-3}]	$\nabla^2\rho(r)_{bcp}$ [eÅ^{-5}]	ε	$G/\rho(r)_{bcp}$ [he^{-1}]	$H/\rho(r)_{bcp}$ [he^{-1}]
R_2Si	Si–C	1.912	0.39	0.78	2.7	0.13	0.92	–0.68
R_2Ge	Ge–C	2.024	0.47	0.78	0.3	0.10	0.61	–0.58
R_2Sn	Sn–C	2.242	0.50	0.61	2.4	0.09	0.65	–0.38
R_2Pb	Pb–C	2.347	0.52	0.56	2.3	0.08	0.62	–0.33
$[R_2P]^+$	P–C	1.799	0.40	1.17	–6.8	0.14	0.61	–1.02
$[R_2As]^+$	As–C	1.943	0.49	0.99	–2.8	0.11	0.46	–0.66
$[R_2Sb]^+$	Sb–C	2.176	0.51	0.73	0.7	0.10	0.54	–0.47
$[R_2Bi]^+$	Bi–C	2.284	0.53	0.65	1.4	0.10	0.54	–0.39

Table S12. AIM and ELI-D properties of intramolecular (secondary) E···X contacts of R_2E (R = 2,6-$Mes_2C_6H_3$; E = Si, Ge, Sn, Pb; X = H) and $[R_2E]^+$ (E = P, As, Sb, Bi; X = C, H).

	contact	d [Å]	d_1/d [%]	$\rho(r)_{bcp}$ [eÅ^{-3}]	$\nabla^2\rho(r)_{bcp}$ [eÅ^{-5}]	ε	$G/\rho(r)_{bcp}$ [he^{-1}]	$H/\rho(r)_{bcp}$ [he^{-1}]
R_2Si	Si···H	2.682	0.63	0.10	0.7	0.18	0.48	0.03
		2.734	0.61	0.07	0.5	0.28	0.47	0.01
R_2Ge	Ge···H	2.736	0.63	0.09	0.7	0.20	0.52	0.05
		2.802	0.61	0.06	0.5	0.29	0.51	0.05
R_2Sn	Sn···H	2.907	0.63	0.07	0.6	0.22	0.51	0.05
		3.013	0.61	0.05	0.4	0.33	0.50	0.07
R_2Pb	Pb···H	3.001	0.63	0.06	0.6	0.44	0.58	0.09
		3.157	0.61	0.04	0.4	0.62	0.57	0.11
$[R_2P]^+$	P···H	2.672	0.61	0.10	1.0	0.54	0.62	0.08
		2.750	0.61	0.07	0.6	0.41	0.57	0.06
$[R_2As]^+$	As···C	2.803	0.52	0.17	1.2	1.46	0.53	–0.04
	As···H	2.703	0.62	0.10	1.0	0.57	0.62	0.08
		2.849	0.61	0.06	0.6	0.43	0.56	0.08
$[R_2Sb]^+$	Sb···C	2.737	0.52	0.22	1.1	0.31	0.48	–0.13
	Sb···H	2.972	0.62	0.07	0.7	3.43	0.62	0.10
$[R_2Bi]^+$	Bi···C	2.765	0.53	0.22	1.4	0.20	0.56	–0.10

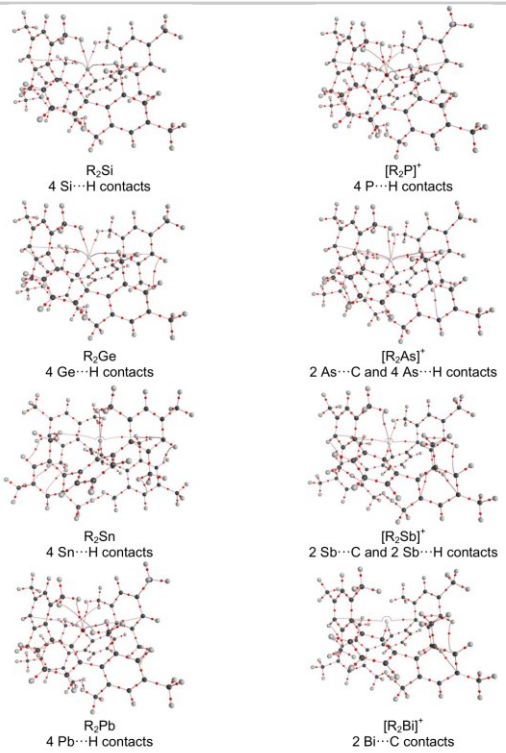

Figure S39. Atoms in Molecules (AIM) topology of R_2E (R = 2,6-$Mes_2C_6H_3$; E = Si, Ge, Sn, Pb) and $[R_2E]^+$ (E = P, As, Sb, Bi).

References

1. K. Ruhlandt-Senge, J. J. Ellison, R. J. Wehmschulte, F. Pauer, P. P. Power, *J. Am. Chem. Soc.* **1993**, 115, 11353–11357.
2. N. J. Hardman, B. Twamley, P. P. Power, *Angew. Chem. Int. Ed.* **2000**, *39*, 2771–2773.
3. N. A. Yakelis, R. G. Bergman, *Organometallics* **2005**, *24*, 3579–3581.
4. M. Brookhart, B. Grant, A. F. Volpe Jr., *Organometallics* **1992**, *11*, 3920–3922.
5. S. R. Bahr, P. Boudjouk, *J. Org. Chem.* **1992**, *57*, 5545–5547.
6. M. Lehmann, A. Schulz, A. Villinger, *Angew. Chem., Int. Ed.* **2009**, *48*, 7444–7447.
7. V. J. Scott, R. Çelenligil-Çetin, O. V. Ozerov, *J. Am. Chem. Soc.* **2005**, *127*, 2852–2853.
8. G. R. Fulmer, A. J. M. Miller, N. H. Sherden, H. E. Gottlieb, A. Nudelman, B. M. Stoltz, J. E. Bercaw, K. I. Goldberg, *Organometallics* **2010**, *29*, 2176–2179.
9. A. Marcó, R. Compañó, R. Rubio, I. Casals, *Microchim. Acta* **2003**, *142*, 13–19.
10. G. M. Sheldrick, *Acta Cryst.* **2008**, *A64*, 112–122.
11. L. Farrugia, *J. Appl. Cryst.* **1999**, *32*, 837–838.
12. H. D. Flack, *Acta Cryst.* **1983**, *A39*, 876–881.
13. K. Brandenburg, Diamond, version 4.0.4, Crystal Impact GbR: Bonn, Germany, **2012**.
14. J. P Perdew, J. A. Chevary, S. H. Vosko, K. A. Jackson, M. R. Pederson, D. J. Singh, C. Fiolhais, *Phys. Rev.* B **1992**, *46*, 6671–6687.
15. A. D. Becke, *J. Chem. Phys.* **1993**, *98*, 5648–5652.
16. M. J. Frisch, G. W. Trucks, H. B. Schlegel, G. E. Scuseria, M. A. Robb, J. R. Cheeseman, G. Scalmani, V. Barone, B. Mennucci, G. A. Petersson, H. Nakatsuji, M. Caricato, X. Li, H. P. Hratchian, A. F. Izmaylov, J. Bloino, G. Zheng, J. L. Sonnenberg, M. Hada, M. Ehara, K. Toyota, R. Fukuda, J. Hasegawa, M. Ishida, T. Nakajima, Y. Honda, O. Kitao, H. Nakai, T. Vreven, J. A. Montgomery, Jr., J. E. Peralta, F. Ogliaro, M. Bearpark, J. J. Heyd, E. Brothers, K. N. Kudin, V. N. Staroverov, R. Kobayashi, J. Normand, K. Raghavachari, A. Rendell, J. C. Burant, S. S. Iyengar, J. Tomasi, M. Cossi, N. Rega, J. M. Millam, M. Klene, J. E. Knox, J. B. Cross, V. Bakken, C. Adamo, J. Jaramillo, R. Gomperts, R. E. Stratmann, O. Yazyev, A. J. Austin, R. Cammi, C. Pomelli, J. W. Ochterski, R. L. Martin, K. Morokuma, V. G. Zakrzewski, G. A. Voth, P. Salvador, J. J. Dannenberg, S. Dapprich, A. D. Daniels, Ö. Farkas, J. B. Foresman, J. V. Ortiz, J. Cioslowski, D. J. Fox, Gaussian 09, Revision B.01, Gaussian Inc., Wallingford CT, **2010**.
17. B. Metz, H. Stoll, M. Dolg, *J. Chem. Phys.* **2000**, *113*, 2563–2569.
18. K. A. Peterson, *J. Chem. Phys.* **2003**, *119*, 11099–11123.
19. R. F. W. Bader, *Atoms in Molecules: A Quantum Theory*, Oxford University Press, Oxford UK, **1990**.
20. F. Biegler-König, J. Schönbohm, D. Bayles, *J. Comput. Chem.* **2001**, *22*, 545–559.
21. M. Kohout, DGRID-4.6 Radebeul, **2015**.
22. M. Kohout, *Int. J. Quantum Chem.* **2004**, *97*, 651–658.
23. M. Kohout, F. R. Wagner, Y. Grin, *Theor. Chem. Acc.* **2008**, *119*, 413–420.
24. E. R. Johnson, S. Keinan, P. Mori-Sanchez, J. Contreras-García, A. J. Cohen, W. Yang, *J. Am. Chem. Soc.* **2010**, *132*, 6498–6506.
25. J. Contreras-García, E. Johnson, S. Keinan, R. Chaudret, J.-P. Piquemal, D. Beratan, W. Yang, *J. Chem. Theor. Comp.* **2011**, *7*, 625–632.
26. J. P. Foster, F. Weinhold, *J. Am. Chem. Soc.* **1980**, *102*, 7211–7218.
27. A. E. Reed, L. A. Curtiss, F. Weinhold, *Chem. Rev.* **1988**, *88*, 899–926.
28 E. D. Glendening, J. K. Badenhoop, A. E. Reed, J. E. Carpenter, J. A. Bohmann, C. M. Morales, F. Weinhold, NBO 5.9, Theoretical Chemistry Institute, University of Wisconsin, Madison, WI, 2009; http://www.chem.wisc.edu/~nbo5
29. C. B. Hübschle, P. Luger, *J. Appl. Crystallogr.* **2006**, *39*, 901–904.

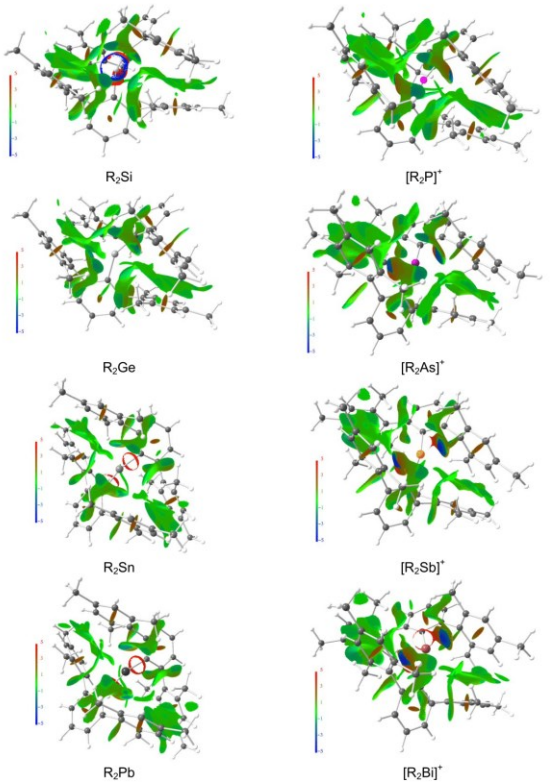

Figure S40. Non-covalent interaction (NCI) index of R_2E (R = 2,6-$Mes_2C_6H_3$; E = Si, Ge, Sn, Pb) and $[R_2E]^+$ (E = P, As, Sb, Bi).

6.2 Transient Phosphenium and Arsenium Ions versus Stable Stibenium and Bismuthenium Ions

CHEMISTRY
A European Journal

Supporting Information

Transient Phosphenium and Arsenium Ions versus Stable Stibenium and Bismuthenium Ions

Marian Olaru,[a] Daniel Duvinage,[a] Enno Lork,[a] Stefan Mebs,*[b] and Jens Beckmann*[a]

chem_201902520_sm_miscellaneous_information.pdf

Table of Contents

Experimental procedures

General information

Unless otherwise stated, all reactions and manipulations were performed under inert atmosphere (argon) using anhydrous solvents. Reagents used in this work including PCl_3 and $AsCl_3$ were obtained commercially and were used as received. CsF was dried at 140 °C under reduced pressure. The reagents 2,6-$Mes_2C_6H_3Li$ (Mes = 2,4,6-$Me_3C_6H_2$),[S1] $Na[BAr^F{}_4]$,[S2] $Li[B(C_6F_5)_4]$[S3] [Ar^F = 3,5-$(F_3C)_2C_6H_3$], $[Ph_3C][B(C_6F_5)_4]$[S4,S5] and $[Et_3Si(toluene)][B(C_6F_5)_4]$[S6] were prepared following the published procedures. The synthesis of (2,6-$Mes_2C_6H_3)_2PF$ was reported recently.[9] Anhydrous dichloromethane, hexane, tetrahydrofuran and toluene were collected from an SPS800 mBraun solvent purification system and stored over 4 Å molecular sieves. 1,2-Difluorobenzene was degassed and dried under argon over 4 Å molecular sieves. Et_2O was dried by refluxing it over Na/benzophenone under argon atmosphere. Deuterated solvents were degassed and dried over 4 Å molecular sieves under argon.

Unless otherwise noted, NMR spectra were recorded at room temperature on a Bruker Avance 360 and Avance 600 MHz spectrometers. ^1H, $^{13}C\{^1H\}$, $^{11}B\{^1H\}$, ^{31}P and ^{19}F NMR spectra are reported on the δ scale (ppm) and are referenced against $SiMe_4$, $BF_3{\cdot}Et_2O$ (15% in $CDCl_3$), H_3PO_4 (85% in water) and $CFCl_3$, respectively. ^1H and $^{13}C\{^1H\}$ chemical shifts are reported relative to the residual peak of the solvent ($CDHCl_2$ 5.32 ppm for CD_2Cl_2) in the ^1H NMR spectra, and to the peak of the deuterated solvent (CD_2Cl_2 53.84 ppm) in the $^{13}C\{^1H\}$ NMR spectra.[8] The assignment of the ^1H and $^{13}C\{^1H\}$ resonance signals was made in accordance with the COSY, HSQC and HMBC spectra. The labelling schemes are attached to the ^1H and ^{13}C spectra; in the case of **3a**, **3b**, and [**2a**]$^+$ the NMR and the crystal structure labelling schemes are identical.

The ESI HRMS spectra were measured on a Bruker Impact II spectrometer. Acetonitrile or dichloromethane/acetonitrile solutions (c =$1{\cdot}10^{-5}$ mol$\cdot$L^{-1}) were injected directly into the spectrometer at a flow rate of 3 µL$\cdot$min^{-1}. Nitrogen was used both as a drying gas and for nebulization with flow rates of approximately 5 L$\cdot$min^{-1} and a pressure of 5 psi. Pressure in the mass analyzer region was usually about $1{\cdot}10^{-5}$ mbar. Spectra were collected for 1 min and averaged. The nozzle-skimmer voltage was adjusted individually for each measurement.

Synthesis and characterization of (2,6-$Mes_2C_6H_3)_2AsF$

A solution of 2,6-$Mes_2C_6H_3Li$ (4.00 g, 12.5 mmol) in Et_2O (50 mL) was added over a solution of $AsCl_3$ (2.50 g, 13.9 mmol) in Et_2O (50 mL) at room temperature over the course of 20 minutes. The reaction mixture was stirred for 2 hours at room temperature and the solvent was removed under reduced pressure. To the crude mixture CsF (6.30 g, 41.3 mmol) and THF (60 mL) were added. The reaction mixture was stirred for 18 h and the solvent was removed under vacuum. To the residue additional 2,6-$Mes_2C_6H_3Li$ (4.00 g, 12.5 mmol) and hexane (40 mL) were added. The mixture was stirred for 18 hours and the reaction was monitored by ^{19}F NMR. The solvent was removed under reduced pressure and the crude product was extracted with CH_2Cl_2 (60 mL). The solvent was removed under vacuum and the remaining beige solid was washed with acetonitrile (3×50 mL) and cold (0 °C) acetone (1×10 mL) and dried at 80 °C ($5{\cdot}10^{-2}$ mbar) to yield (2,6-$Mes_2C_6H_3)_2AsF$ as a white solid (5.10 g, 56%).

^1H NMR (360 MHz, CD_2Cl_2): δ = 7.25 (t, $^3J(^1H{-}^1H)$ = 8 Hz, 2H, H4), 6.73 (m, 6H, H3, H7, H9), 2.30 (s, 12H, H13), 1.70 (s, 12H, H12), 1.66 (s, 12H, H11). **$^{13}C\{^1H\}$ NMR (91 MHz, CD_2Cl_2)**: δ = 146.54 (s, C2), 146.05 (d, $^2J(^{13}C{-}^{19}F)$ = 12 Hz, C1), 139.68 (s, C5), 137.43 (s, C10), 136.94 (s, C8), 136.68 (s, C6), 131.95 (s, C3), 129.73 (s, C4), 128.78 (s, C9), 128.64 (s, C7), 22.28 (s, C12), 22.21 (s, C11), 21.28 (s, C13). **$^{19}F\{^1H\}$ NMR (360 MHz, CD_2Cl_2)**: δ = −209.66 (s). **HRMS ESI (m/z):** [M+Na]$^+$ calculated. for $C_{48}H_{50}AsFNa$, 743.30047; found, 743.30012.

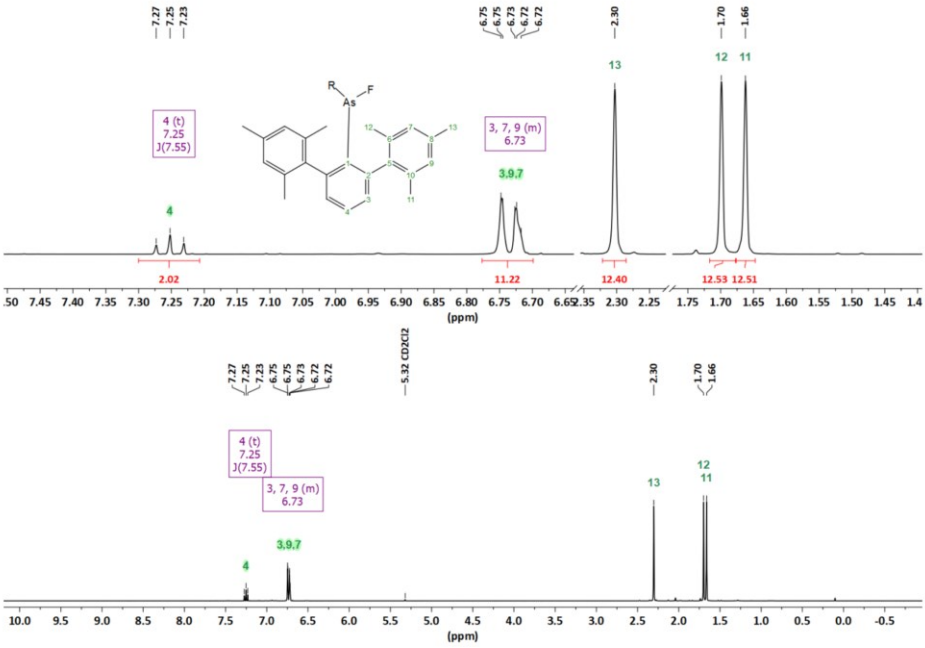

Figure S1. ^{1}H NMR (CD_2Cl_2, 360 MHz) spectrum of (2,6-$Mes_2C_6H_3$)$_2$AsF

4

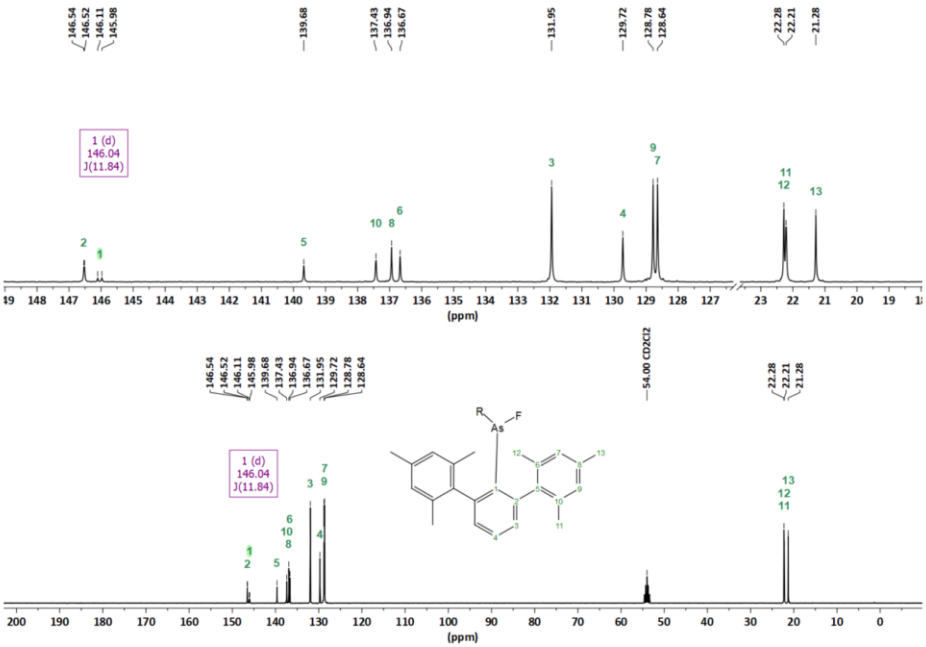

Figure S2. $^{13}C\{^{1}H\}$ NMR (CD_2Cl_2, 91 MHz) spectrum of (2,6-$Mes_2C_6H_3$)$_2$AsF.

5

Figure S3. $^{19}F\{^{1}H\}$ NMR (CD_2Cl_2, 188 MHz) spectrum of $(2,6\text{-}Mes_2C_6H_3)_2AsF$.

Synthesis and characterization of 3a

To a suspension of $(2,6\text{-}Mes_2C_6H_3)_2PF$ (330 mg, 0.49 mmol) in hexane (10 mL) a solution of $EtAlCl_2$ in heptane (0.9 M, 2.6 mL, 2.34 mmol) was added at room temperature. The reaction mixture was stirred at room temperature for 30 minutes. The solution was separated and the residue washed with 10 mL of hexane. Hexane (5 mL), toluene (5 mL) and Et_3N (0.3 mL, 2.15 mmol) were added and after 15 minutes the mixture was filtered through a pad (2 cm) of aluminium oxide. The reaction flask and the pad were washed with a 1:1 mixture of hexane (20 mL) and toluene (20 mL). All volatiles were removed by rotary evaporation. The colourless oil was triturated with a small amount of MeOH and the solid dried under reduced pressure. A mixture of $(2,6\text{-}Mes_2C_6H_3)_2PF$ (variable amount) and the title product is obtained (220 mg). The separation of $(2,6\text{-}Mes_2C_6H_3)_2PF$ is rather difficult and can be done by careful crystallization of $(2,6\text{-}Mes_2C_6H_3)_2PF$ (over several days at −40 °C) from a solution of the mixture in the minimum volume (6-7 mL) of boiling heptane. Alternatively, the mixture can be reacted again with $EtAlCl_2$ in order to completely consume $(2,6\text{-}Mes_2C_6H_3)_2PF$. For example: to a mixture of $(2,6\text{-}Mes_2C_6H_3)_2PF$ and **3a** (140 mg, 1:10 molar ratio) in hexane[a] (7 mL) was added a solution of $EtAlCl_2$ (0.9 M, 1 mL, 0.90 mmol). The suspension was stirred for 30 minutes then Et_3N (0.3 mL, 2.15 mmol) and toluene (7 mL) were added and the mixture was filtered through a pad (2 cm) of aluminium oxide. The reaction flask and the pad were washed with a 1:1 mixture of hexane (20 mL) and toluene (20 mL). All volatiles were removed by rotary evaporation. The colourless oil was triturated with a small amount of MeOH and the solid dried under reduced pressure to obtain **3a** (130 mg, 94%) as a white solid.

3a:

^{1}H NMR (600 MHz, CD_2Cl_2): δ =7.68 (d, $^{3}J(^{1}H–^{1}H)$ = 8 Hz, 1H, H12), 7.38 (t, $^{3}J(^{1}H–^{1}H)$ = 8 Hz, 1H, H13)m, 7.31 (t, $^{3}J(^{1}H–^{1}H)$ = 8 Hz, 1H, H43), 6.91 (dd, $^{3}J(^{1}H–^{1}H)$ = 8 Hz, $^{4}J(^{1}H–^{1}H)$ = 4 Hz,

[a] If the reaction is performed in CH_2Cl_2 a mixture of 5-(chloromethyl)-5-*m*-terphenyl-6-mesityl-1,3,4-trimethyl-benzo[b]phospholium salt [**4**][$AlCl_4$] (major species) and [**2a**][A] (minor species, A = $EtAlCl_3$ or $AlCl_4$). [**4**][$AlCl_4$] can be isolated by recrystallization of the crude mixture of products from $CHCl_3$ and Et_2O. Although for [**4**]$^{+}$ we expected [$EtAlCl_3$]$^{-}$ as an counter ion, neither the NMR of the isolated product nor the structure determined (by single crystal X-ray diffraction) after recrystallization of the sample indicated any [$EtAlCl_3$]$^{-}$, most likely due to redistribution reactions.

1H, H44), 6.84 (s, 1H, H6), 6.80 (s, 1H, H24), 6.78 (s, 2H, H32, H34), 6.72 (s, 1H, H62), 6.64 (m, 2H, H14, H42), 6.41 (s, 1H, H54), 6.04 (s, 1H, H52), 2.39 (s, 3H, H28), 2.33 (s, 3H, H37), 2.31 (s, 3H, H67), 2.20 (s, 3H, H57), 2.18 (s, 3H, H27), 2.06 (s, 3H, H26), 1.82 (s, 3H, H68), 1.76 (s, 3H, H36), 1.50 (s, 3H, H38), 1.38 (s, 3H, H58), 1.26 (s, 3H, H66), 1.17 (s, 3H, H56). **^{13}C{^{1}H} NMR (151 MHz, CD_2Cl_2)**: δ = 152.77 (d, $^{2}J(^{13}C–^{31}P)$ = 42 Hz, C45), 150.57 (s, C11), 149.29 (d, $^{2}J(^{13}C–^{31}P)$ = 7 Hz, C41), 145.67 (d, $^{2}J(^{13}C–^{31}P)$ = 22 Hz, C15), 142.01 (s, C21), 240.88 (s, C20, C30), 140.76 (d, $^{1}J(^{13}C–^{31}P)$ = 6 Hz, C10), 140.44 (d, $^{3}J(^{13}C–^{31}P)$ = 8 Hz, C60), 137.80 (s, C65), 137.50 (d, $^{3}J(^{13}C–^{31}P)$ = 10 Hz, C50), 137.46 (s, C33), 137.30 (d, C35, C61), 137.01 (s, C51), 136.86 (s, C63), 136.74 (s, C55), 136.67 (s, C31), 136.36 (d, $^{2}J(^{13}C–^{31}P)$ = 21 Hz, C22), 135.67 (s, C53), 134.70 (s, C23), 134.66 (s, C24), 132.93 (d, $^{1}J(^{13}C–^{31}P)$ = 35 Hz, C40), 131.82 (s, C25), 131.60 (s, C42), 130.46 (d, $^{3}J(^{13}C–^{31}P)$ = 9 Hz, C44), 130.19 (s, C43), 129.62 (s, C13), 129.51 (s, C32), 129.02 (d, $^{3}J(^{13}C–^{31}P)$ = 5 Hz, C14), 128.94 (s, C34), 128.22 (s, C54), 128.20 (s, C64), 127.75 (s, C62), 127.63 (s, C52), 124.21 (s, C12), 23.39 (s, C28), 22.21 (s, C68), 21.29 (s, C37, C57, C67), 21.18 (s, C58), 20.89 (d, $^{5}J(^{13}C–^{31}P)$ = 8 Hz, C38), 20.59 (d, $^{3}J(^{13}C–^{31}P)$ = 16 Hz, C26), 20.17 (d, $^{5}J(^{13}C–^{31}P)$ = 6 Hz, C66), 19.80 (d, $^{2}J(^{13}C–^{31}P)$ = 11 Hz, C27). **^{31}P NMR (CD_2Cl_2, 243 MHz)**: δ = −25.21. **HRMS ESI (m/z):** $[M+Na]^+$ calculated. for $C_{48}H_{49}PNa$, 679.34604; found, 679.34641.

[**4**][$AlCl_4$]:

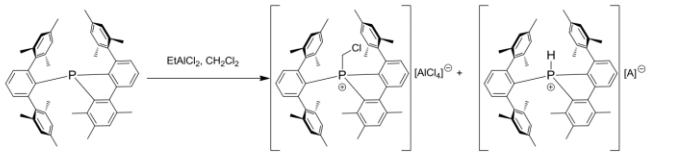

^{1}H NMR (600 MHz, CD_2Cl_2): δ = 7.89–7.84 (m, 3H, H12, H143, H13), 7.35–7.33 (m, 1H, H42), 7.20 (s, 1H, H24), 7.19–7.17 (m, 1H, H44), 7.01 (s, 1H, H52), 6.98 (s, 1H, H32), 6.93–6.91 (m, 1H, H14), 6.89 (s, 1H, H54), 6.82 (s, 1H, H34), 6.60 (s, 1H, H64), 6.12 (s, 1H, H62), 3.78 (dd, $^{2}J(^{1}H–^{31}P)$ = 14 Hz, $^{2}J(^{1}H–^{1}H)$ = 6 Hz, 1H, H1), 3.11 (dd, $^{2}J(^{1}H–^{31}P)$ = 14 Hz, $^{2}J(^{1}H–^{1}H)$ = 5 Hz, 1H, H1), 2.46 (s, 3H, H28), 2.34 (two singlets partially overlapped, 6H, H37, H57), 2.30 (s, 6H, H26, H27), 2.19 (s, 3H, H67), 1.81 (s, 3H, H56), 1.69 (3H, H36), 1.47 (s, 3H, H38), 1.39 (two singlets partially overlapped, 6H, H66, H68), 1.26 (3H, H58). **^{13}C{^{1}H} NMR (151 MHz, CD_2Cl_2)**: δ = 151.24 (d, $^{2}J(^{13}C–^{31}P)$ = 11 Hz, C41), 150.88 (d, $^{2}J(^{13}C–^{31}P)$ = 20 Hz, C11), 150.63 (d, $^{2}J(^{13}C–^{31}P)$ = 11 Hz, C45), 148.35 (d, $^{2}J(^{13}C–^{31}P)$ = 10 Hz, C15), 141.64 (d, $^{4}J(^{13}C–^{31}P)$ = 2 Hz, C24), 141.03 (s, C53), 140.76 (d, $^{2}J(^{13}C–^{31}P)$ = 18 Hz, C22), 140.29 (s, C33),

139.28 (d, $^{3}J(^{13}C–^{31}P)$ = 12 Hz, C23), 139.19 (s, C63), 138.84 (s, C31), 138.28 (s, C51), 137.43 (d, $^{3}J(^{13}C–^{31}P)$ = 7 Hz, C20), 137.88 (s, C61), 137.52 (s, C65), 137.43 (d, $^{4}J(^{13}C–^{31}P)$ = 2 Hz, C13), 137.22 (s, C35), 136.38 (d, $^{4}J(^{13}C–^{31}P)$ = 3 Hz, C43), 136.36 (s, C55), 135.74 (d, $^{3}J(^{13}C–^{31}P)$ = 3 Hz, C50), 135.14 (d, $^{3}J(^{13}C–^{31}P)$ = 11 Hz, C25), 135.02 (d, $^{3}J(^{13}C–^{31}P)$ = 3 Hz, C30), 134.41 (d, $^{3}J(^{13}C–^{31}P)$ = 12 Hz, C44), 134.25 (d, $^{3}J(^{13}C–^{31}P)$ = 4 Hz, C60), 134.18 (d, $^{3}J(^{13}C–^{31}P)$ = 12 Hz, C42), 134.00 (d, $^{3}J(^{13}C–^{31}P)$ = 12 Hz, C14), 130.89 (s, C34), 130.00 (s, C52), 129.80 (s, C32), 129.59 (s, C54), 129.10 (s, C64), 128.50 (s, C62), 126.38 (d, $^{3}J(^{13}C–^{31}P)$ = 10 Hz, C12), 121.24 (d, $^{1}J(^{13}C–^{31}P)$ = 92 Hz, C21), 118.82 (d, $^{1}J(^{13}C–^{31}P)$ = 92 Hz, C10), 115.71 (d, $^{1}J(^{13}C–^{31}P)$ = 75 Hz, C40), 32.72 (d, $^{1}J(^{13}C–^{31}P)$ = 46 Hz, C1), 23.33 (s, C28), 22.52 (s, C68), 22.10 (s, C38), 21.96 (s, C56), 21.30 (s, C57), 21.17 (s, C37), 21.13 (s, C66, C67), 20.93 (s, C36), 20.80 (d, $^{3}J(^{13}C–^{31}P)$ = 6 Hz, C26), 19.84 (s, C58), 19.64 (d, $^{4}J(^{13}C–^{31}P)$ = 2 Hz, C27). **^{31}P{1H} NMR (243 MHz, CD_2Cl_2)**: δ = 31.95 (s). **HRMS ESI (m/z):** $[M]^+$ calculated. for $C_{49}H_{51}PCl$, 705.34114; found, 705.34092.

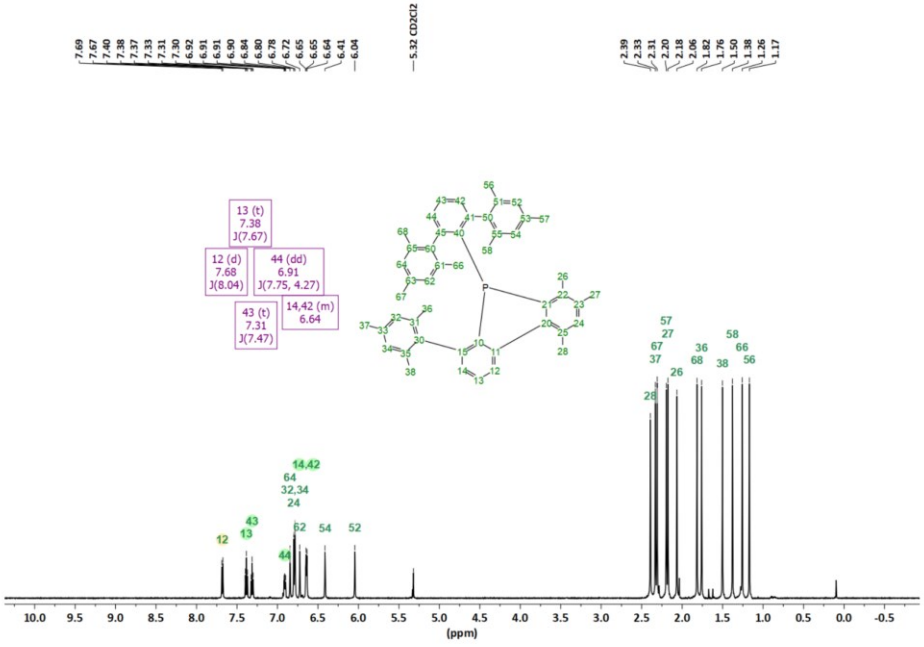

Figure S4. ^{1}H NMR (CD_2Cl_2, 600 MHz) spectrum of **3a**.

10

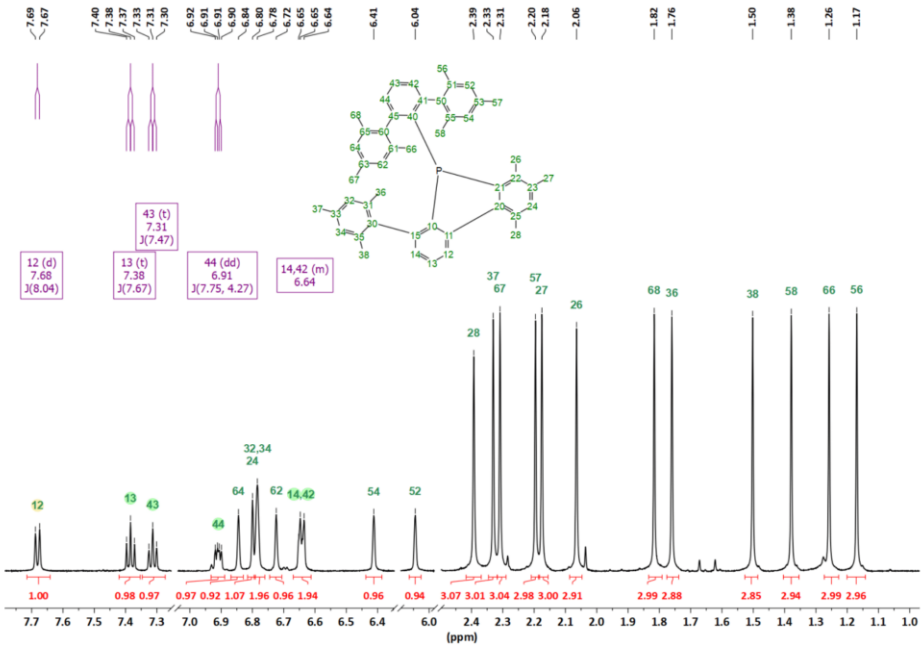

Figure S5. ^{1}H NMR (CD_2Cl_2, 600 MHz) spectrum (detail) of **3a**.

11

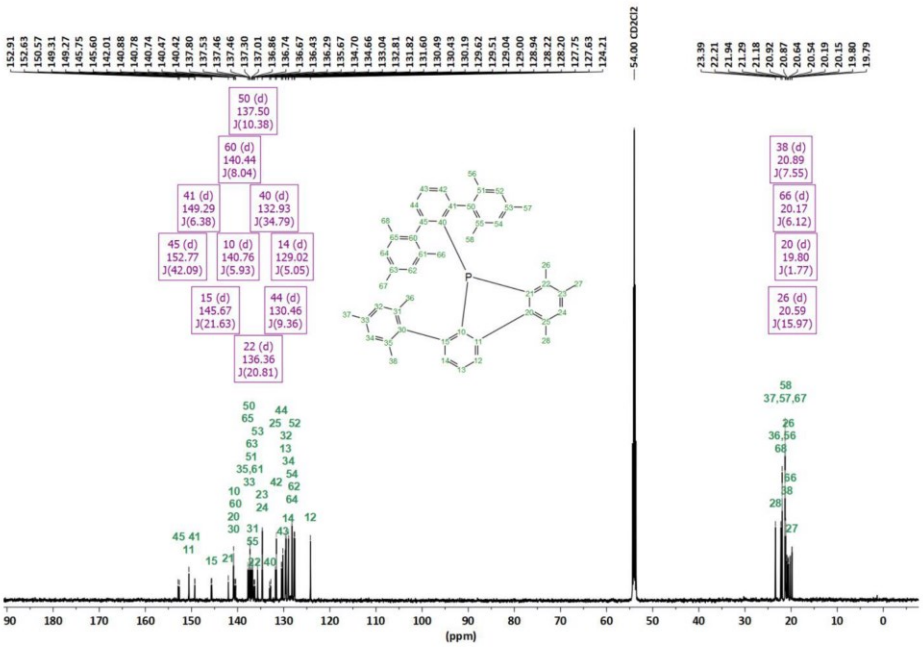

Figure S6. ^{13}C NMR (CD_2Cl_2, 151 MHz) spectrum of **3a**.

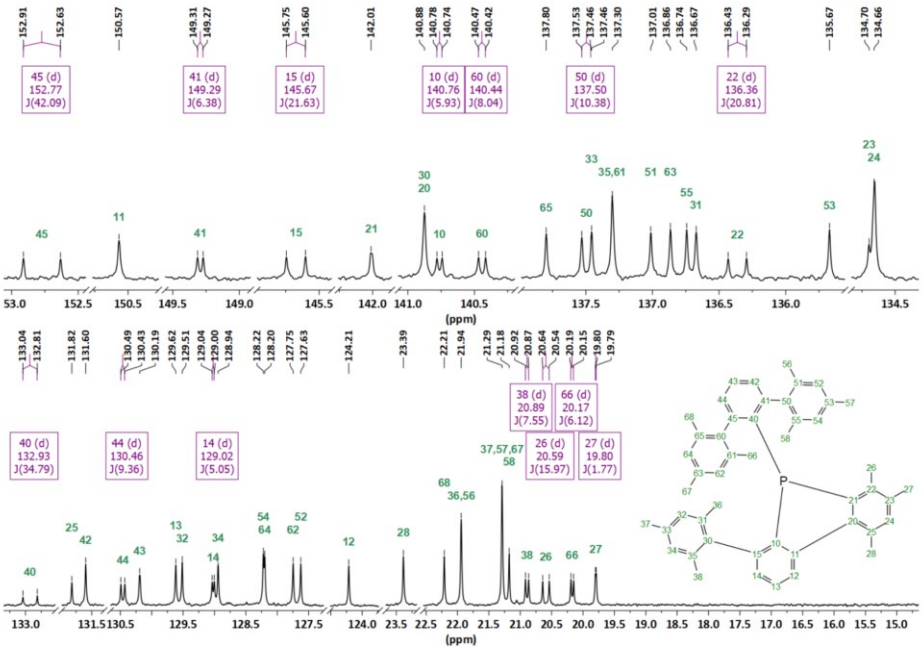

Figure S7. ^{13}C NMR (CD_2Cl_2, 151 MHz) spectrum (detail) of **3a**.

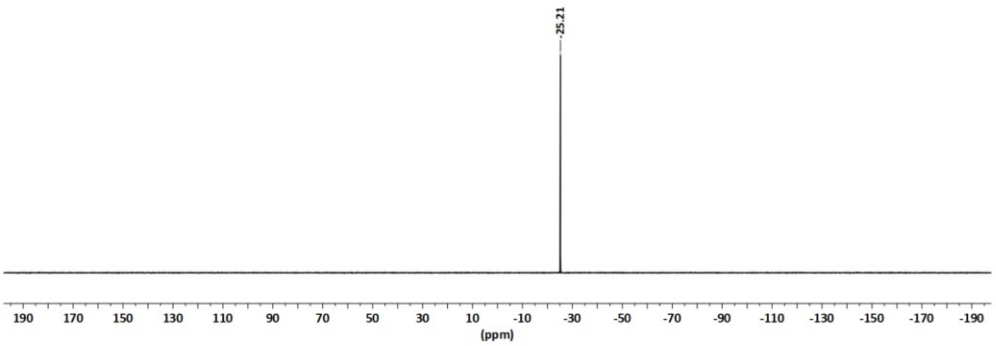

Figure S8. $^{31}P\{1H\}$ NMR (CD_2Cl_2, 243 MHz) spectrum of **3a**.

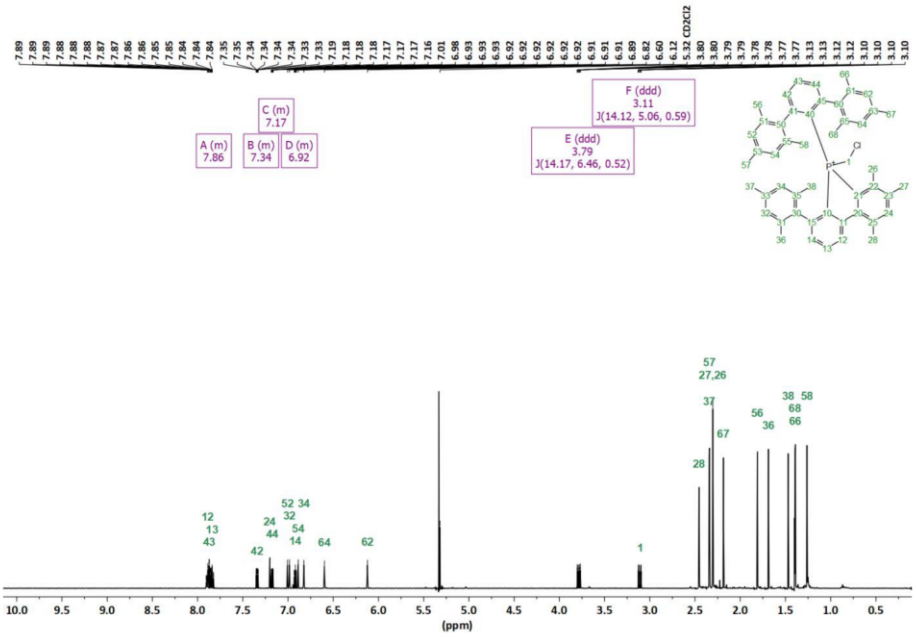

Figure S9. ^{1}H NMR (CD_2Cl_2, 600 MHz) spectrum of [**4**][$AlCl_4$].

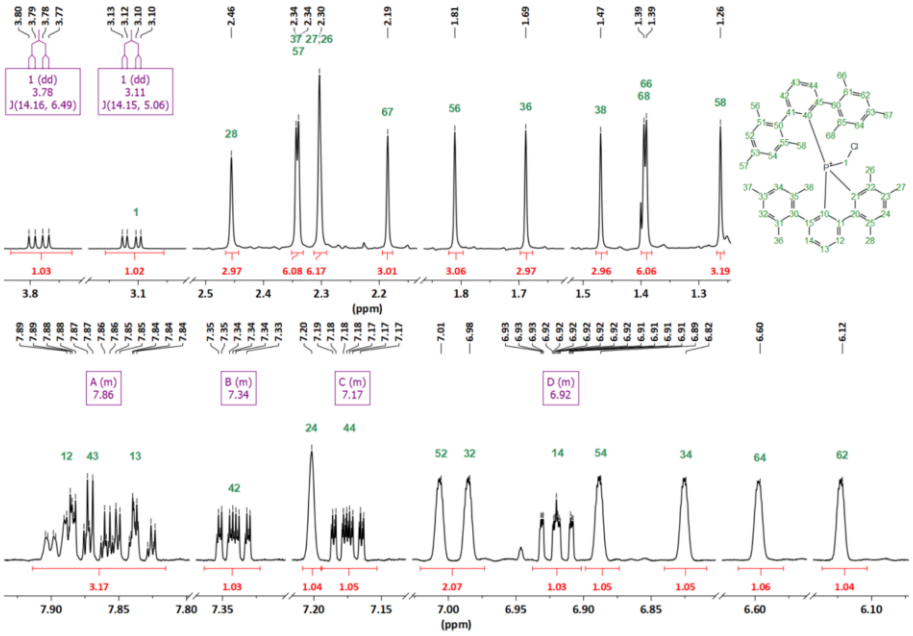

Figure S10. ^{1}H NMR (CD_2Cl_2, 600 MHz) spectrum (detail) of [**4**][$AlCl_4$].

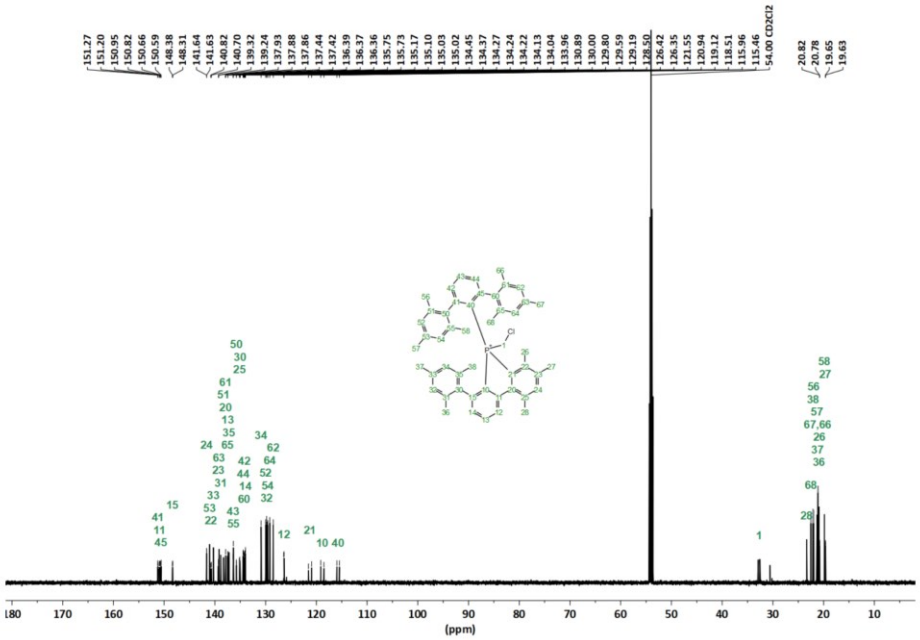

Figure S11. ^{13}C NMR (CD_2Cl_2, 151 MHz) spectrum of [**4**][$AlCl_4$].

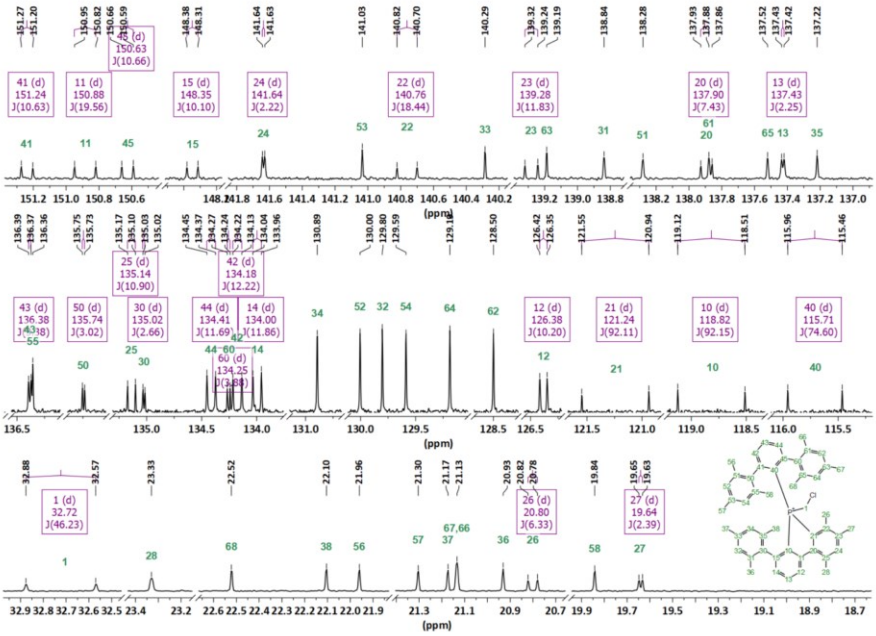

Figure S12. ^{13}C NMR (CD_2Cl_2, 151 MHz) spectrum of [**4**][$AlCl_4$].

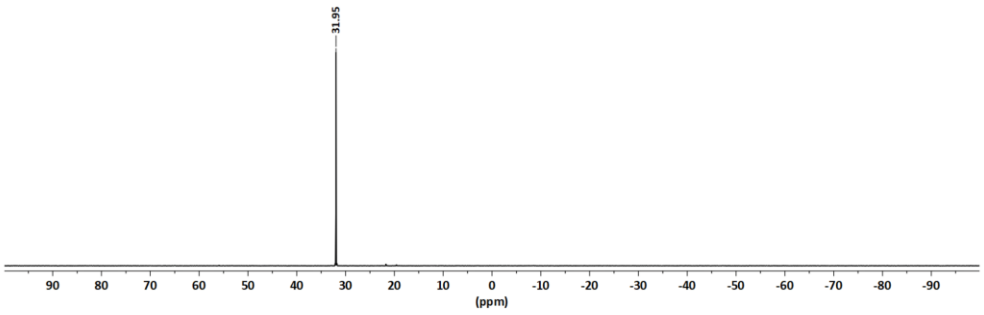

Figure S13. $^{31}P\{1H\}$ NMR (CD_2Cl_2, 243 MHz) spectrum of [**4**][$AlCl_4$].

Synthesis and characterization of 3b

A 50 mL Schlenk tube fitted with a J. Young valve was charged under argon atmosphere with (2,6-$Mes_2C_6H_3$)$_2$AsF (100 mg, 0.14 mmol) and [Et_3Si(toluene)][$B(C_6F_5)_4$] (150 mg, 0.16 mmol). 1,2-difluorobenzene (4 mL) was added over the solid mixture at room temperature. The initially dark red solution turned dark yellow after a few seconds. After 1 h, triethylamine (0.1 mL, 0.72 mmol) was added and the resulting light yellow solution was stirred for 1 h. All volatiles were removed under reduced pressure. Hexane (10 mL), was added and the suspension was filtered through a PTFE syringe filter. The solvent was allowed to slowly evaporate (in a glovebox) to give **3b** as a colourless crystalline solid (50 mg, 54 %).

^{1}H NMR (600 MHz, CD_2Cl_2): δ = 7.74 (d, ^3J(^{1}H–^{1}H) = 8 Hz, 1H, H12), 7.41 (d, ^3J(^{1}H–^{1}H) = 7 Hz, 1H, H13), 7.32 (t, ^3J(^{1}H–^{1}H) = 8 Hz, 1H, H13), 7.32 (t, ^3J(^{1}H–^{1}H) = 8 Hz, 1H, H43), 6.94 (dd, ^3J(^{1}H–^{1}H) = 8 Hz, ^4J(^{1}H–^{1}H) = 1 Hz, 1H, H44), 6.92 (s, 1H, H62), 6.86 (s, 1H, H34), 6.84 (s, 1H, H32), 6.84 (s, 1H, H24), 673 (d, ^3J(^{1}H–^{1}H) = 7 Hz, 1H, H14), 6.73 (s, 1H, H64), 6.65 (dd, ^3J(^{1}H–^{1}H) = 8 Hz, ^4J(^{1}H–^{1}H) = 1 Hz, 1H, H42), 6.44 (s, 1H, H54), 6.10 (s, 1H, H52), 2.46 (s, 3H, H28), 2.46 (s, 3H, H37), 2.37 (s, 3H, H67), 2.25 (s, 3H, H57), 2.23 (s, 3H, H27), 2.22 (s, 3H, H26), 1.97 (s, 3H, H66), 1.95 (s, 3H, H38), 1.62 (s, 3H, H36), 1.43 (s, 3H, H58), 1.29 (s, 3H, H68), 1.27 (s, 3H, H56). **^{13}C{^{1}H} NMR (151 MHz, CD_2Cl_2):** δ = 152.24 (s, C15), 151.07 (s, C41), 148.87 (s, C45), 146.29 (s, C21), 145.91 (s, C11), 144.24 (s, C10), 142.64 (s, C20), 141.03 (s, C30), 140.80 (s, C60), 137.68 (s, C50), 137.44 (s, C33), 137.25 (s, C31), 137.09 (s, C61), 137.07 (s, C40), 136.80 (s, C51, C63), 136.68 (s, C23), 136.59 (s, C55), 136.56 (s, C35), 135.48 (s, C53), 135.12 (s, C24), 134.49 (s, C22), 132.60 (s, C25), 131.49 (s, C42), 129.88 (s, C44), 129.70 (s, C34), 129.62 (s, C43), 129.47 (s, C13), 128.97 (s, C32), 128.69 (s, C14) 128.20 (s, C62), 128.19 (s, C54), 125.16 (s, C12), 24.12 (s, C28), 22.48 (s, C26), 22.08 (s, C38), 21.97 (s, C66), 21.89 (s, C56), 21.48 (s, 57), 21.41 (s, C37, C67), 21.26 (s, C36), 21.20 (s, C58), 20.56 (s, C68), 20.00 (s, C27). **HRMS ESI (m/z):** [M+Na]$^+$ calculated. for $C_{48}H_{49}AsNa$, 723.29424; found, 723.29385.

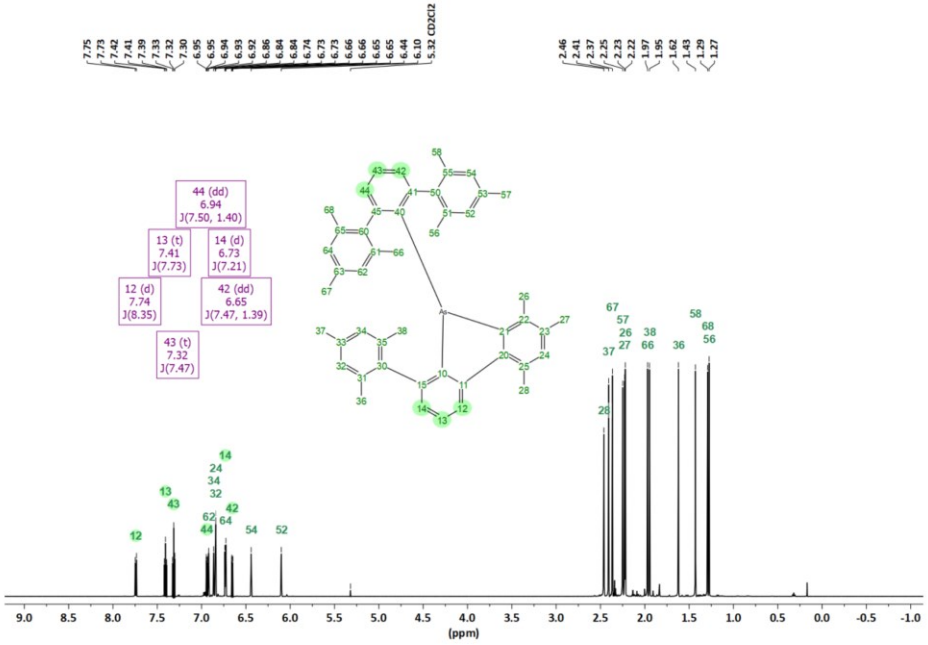

Figure S14. ^{1}H NMR (CD_2Cl_2, 600 MHz) spectrum of **3b**.

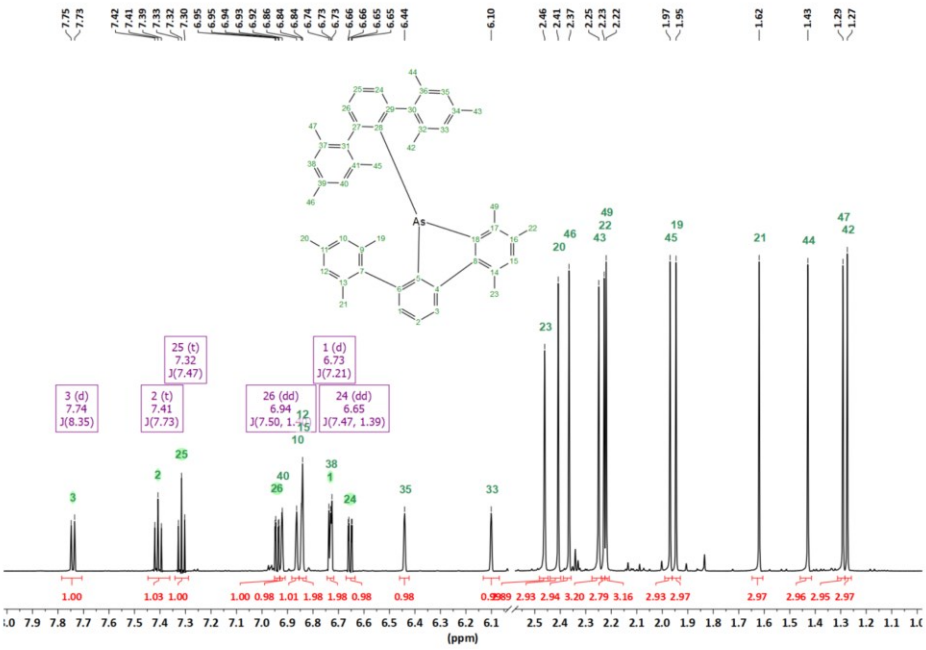

Figure S15. ^{1}H NMR (CD_2Cl_2, 600 MHz) spectrum (detail) of **3b**.

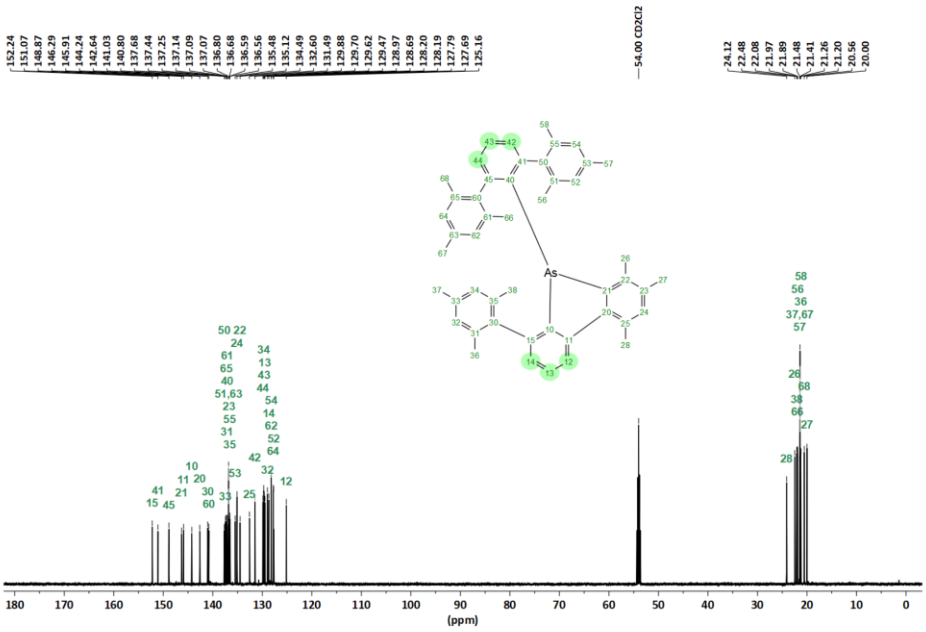

Figure S16. ^{13}C NMR (CD_2Cl_2, 151 MHz) spectrum of **3b**.

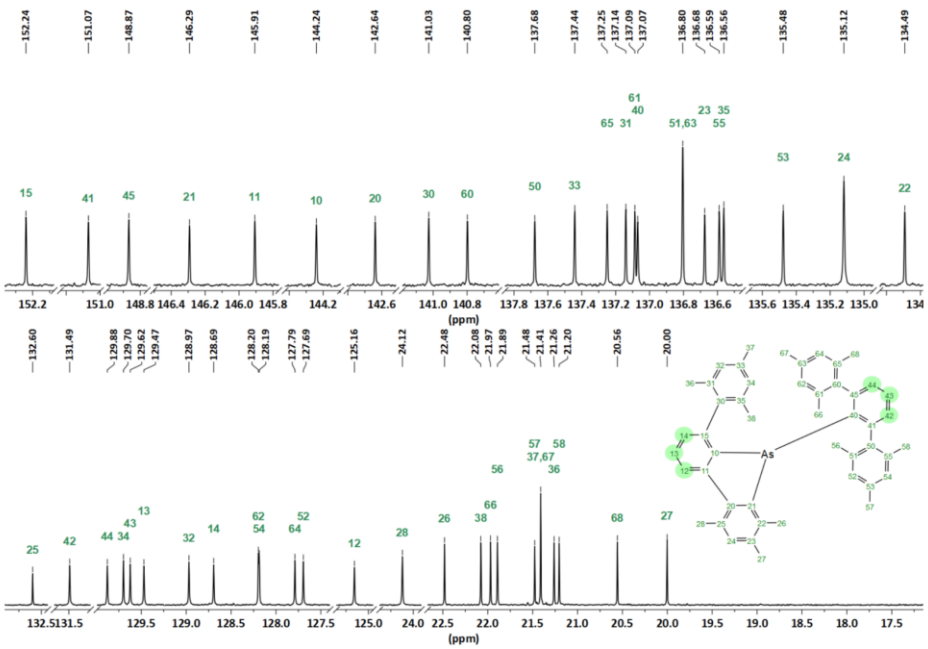

Figure S17. ^{13}C NMR (CD_2Cl_2, 151 MHz) spectrum (detail) of **3b**.

Synthesis and characterization of [2a][BAr$^F_4$]

A 50 mL Schlenk tube fitted with a J. Young valve was charged under argon atmosphere with **3a** (50 mg, 0.076 mmol) and $NaBAr^F_4$ (67 mg, 0.076 mmol) and CH_2Cl_2 (3 mL). To the resulting solution, HCl in Et_2O (1.7 M, 0.1 mL, 0.17 mmol) was added. After 5 minutes of stirring, all volatiles were evaporated at reduced pressure. CH_2Cl_2 was added and the turbid solution was filtered through a PTFE syringe filter. The solvent was evaporated under reduced pressure. The remaining solid was washed with 2×4 mL hexane and dried at 80 °C ($2{\cdot}10^{-2}$ mbar). Compound **[2a][BAr$^F_4$]** (110 mg, 96%) was obtained as a white powder.

^{1}H NMR (600 MHz, CD_2Cl_2): δ = 7.82 (td, $^3J(^1H–^1H)$ = 8 Hz, $^5J(^1H–^{31}P)$ = 2 Hz, 1H, H43), 7.75 (m, 10 H, *o*-H-Ar^F, H12, H13), 7.57 (s, 4H, *p*-H-Ar^F), 7.42 (d, $^1J(^1H–^{31}P)$ = 500 Hz, 1H, PH), 7.33 (ddd, $^3J(^1H–^1H)$ = 7 Hz, $^4J(^1H–^1H)$ = 6 Hz, $^4J(^1H–^1H)$ = 1 Hz, 1H, H43), 7.22 (s, 1H, H24), 7.17 (m, 1H, H42), 7.01 (s, 1H, H62), 7.00 (m, 2H, H32, H14), 6.82 (s, 1H, H34), 6.66 (s, 1H, H64, 6.54 (s, 1H, H54), 6.31 (s, 1H, H52), 2.42 (s, 6H, H28, H37), 2.32 (s, 3H, H67), 2.26 (s, 3H, H57), 2.23 (s, 3H, H27), 2.16 (s, 3H, H26), 2.04 (s, 3H, H66), 2.03 (s, 3H, H36), 1.56 (s, 3H, 58), 1.49 (s, 3H, H38), 1.33 (s, 3H, H56). **$^{13}C\{^1H\}$ NMR (151 MHz, CD_2Cl_2):** δ = 162.4 (m, *i*-C-Ar^F), 151.67 (d, $^2J(^{13}C–^{31}P)$ = 13 Hz, C45), 150.02 (d, $^2J(^{13}C–^{31}P)$ = 11 Hz, C41), 149.93 (d, $^2J(^{13}C–^{31}P)$ = 21 Hz, C11), 147.84 (d, $^2J(^{13}C–^{31}P)$ = 10 Hz, C15), 142.16 (d, $^4J(^{13}C–^{31}P)$ = 2 Hz, C24), 141.05 (d, $^2J(^{13}C–^{31}P)$ = 20 Hz, C20), 140.40 (s, C33), 139.94 (s, C63), 139.51 (d, $^3J(^{13}C–^{31}P)$ = 10 Hz, C23), 139.51 (d, $^2J(^{13}C–^{31}P)$ = 12 Hz, C22), 139.19 (s, C53), 137.42 (s, C51), 137.20 (s, C55), 136.99 (s, C65), 136.92 (d, $^4J(^{13}C–^{31}P)$ = 2 Hz, C13), 136.79 (s, C61), 136.63 (s, C31), 136.51 (d, $^4J(^{13}C–^{31}P)$ = 3 Hz), 136.23 (d, $^3J(^{13}C–^{31}P)$ = 3 Hz C30), 136.22 (s, C35), 135.55 (d, $^3J(^{13}C–^{31}P)$ = 11 Hz, C25), 135.40 (s, br, *o*-C-Ar^F), 134.05 (d, $^3J(^{13}C–^{31}P)$ = 7 Hz, C60), 133.77 (d, $^3J(^{13}C–^{31}P)$ = 12 Hz, C42), 133.73 (d, $^3J(^{13}C–^{31}P)$ = 5 Hz, C50), 133.57 (d, $^3J(^{13}C–^{31}P)$ = 12 Hz, C14), 133.17 (d, $^3J(^{13}C–^{31}P)$ = 10 Hz, C44), 130.96 (s, C32), 130.25 (s, C34), 129.76 (s, C62), 129.49 (qq, $^2J(^{13}C–^{19}F)$ = 31 Hz, $^4J(^{13}C–^{19}F)$ = 3 Hz, *m*-C-Ar^F), 129.40 (s, C64), 129.38 (s, C54), 129.19 (s, C52), 126.13 (d, $^3J(^{13}C–^{31}P)$ = 11 Hz, C12), 125.19 (q, $^1J(^{13}C–^{19}F)$ = 273 Hz, CF$_3$-Ar^F), 119.21 (d, $^1J(^{13}C–^{31}P)$ = 89.38 Hz, C21), 118.80 (d, $^1J(^{13}C–^{31}P)$ = 91 Hz, C10), 118.06 (septet, $^3J(^{13}C–^{19}F)$ = 4 Hz, *p*-C-Ar^F), 114.35 (d, $^1J(^{13}C–^{31}P)$ = 91 Hz, C40), 22.82 (s, br, C28), 22.16 (s, C66), 22.10 (s, C36), 21.59 (s, C58), 21.57(d, $^3J(^{13}C–^{31}P)$ = 7 Hz, C26), 21.48 (s, C56), 21.46 (s, C37), 21.40 (s, C57), 21.30 (s, C67), 20.56 (s, C68), 20.54 (d, $^5J(^{13}C–^{31}P)$ = 2 Hz, C38), 19.56 (d, $^4J(^{13}C–^{31}P)$ = 2 Hz, C27). **^{31}P NMR (243 MHz, CD_2Cl_2):** δ = −14.95 (d, $^1J(^{31}P-^1H)$ = 501 Hz). **^{19}F NMR (339 MHz, CD_2Cl_2):** δ = −62.81 (s). **HRMS ESI (m/z):** $[M+H]^+$ calculated. for $C_{48}H_{50}P$, 657.36418; found, 657.36446.

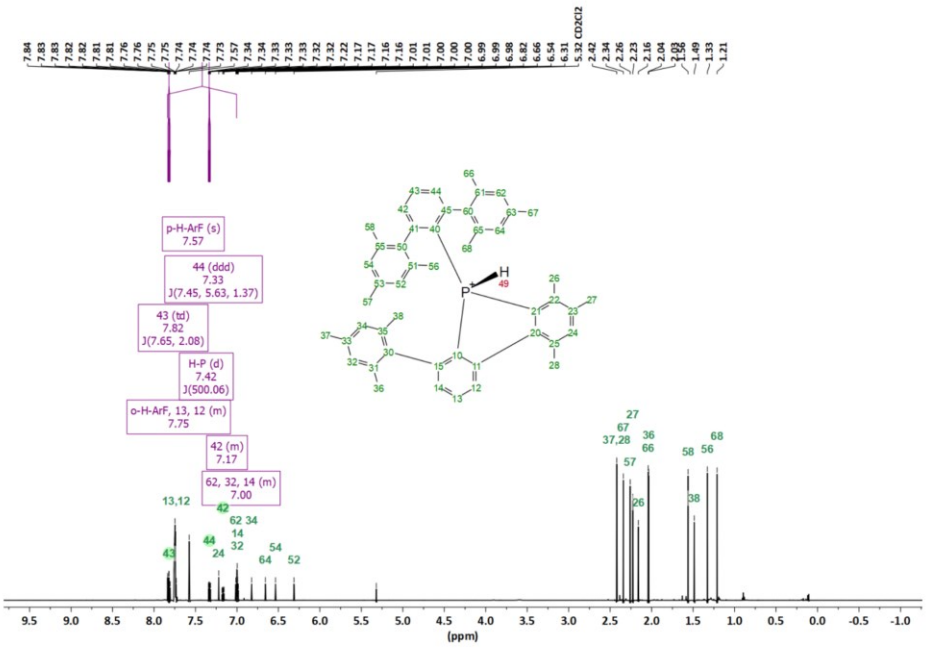

Figure S18. ^{1}H NMR (CD_2Cl_2, 600 MHz) spectrum of [**2a**][BAr^F_4].

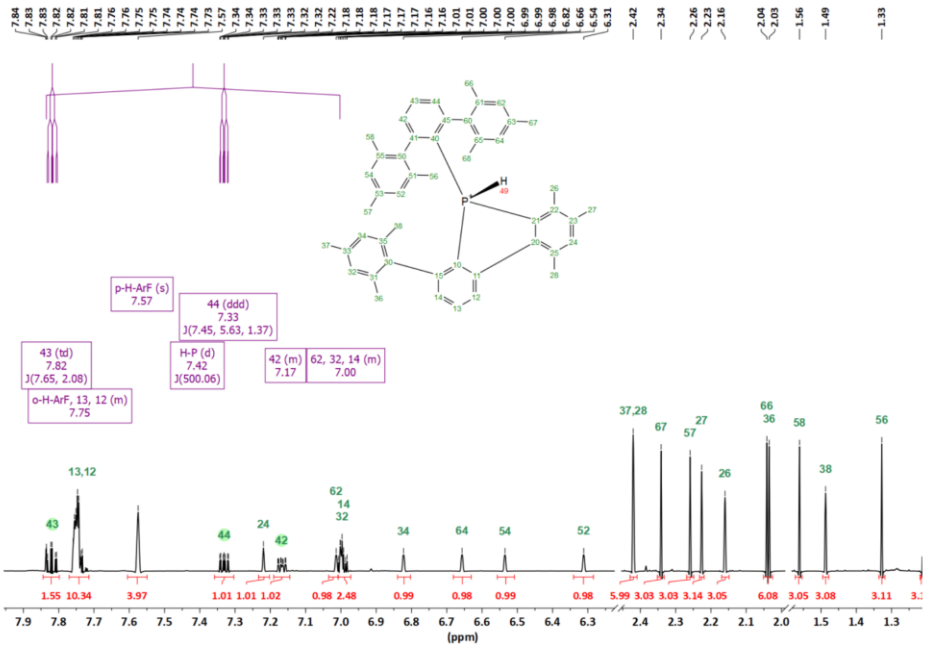

Figure S19. ^{1}H NMR (CD_2Cl_2, 600 MHz) spectrum (detail) of [**2a**][BAr^F_4].

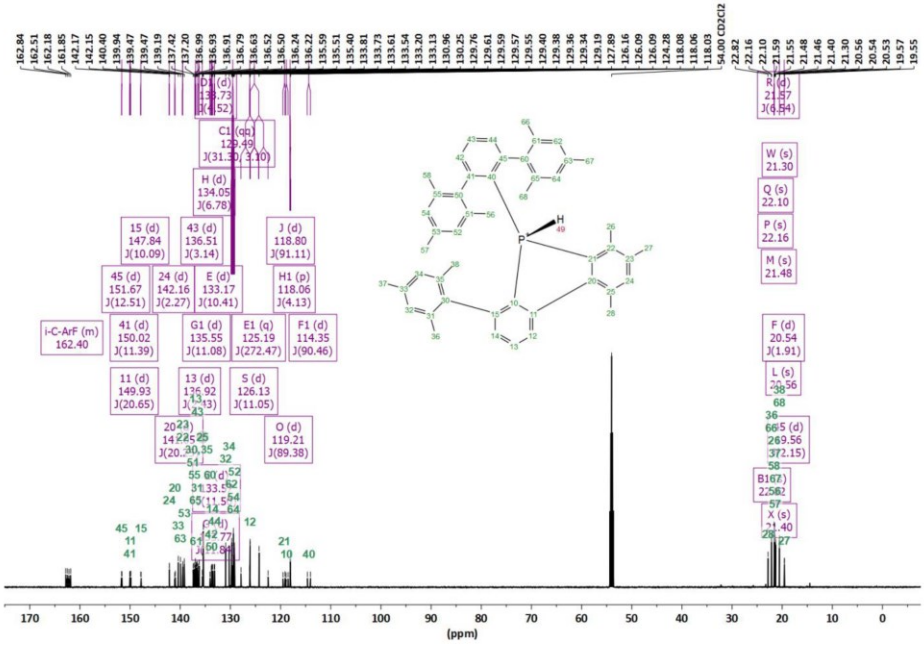

Figure S20. ^{13}C NMR (CD_2Cl_2, 151 MHz) spectrum of [**2a**][BAr^F_4].

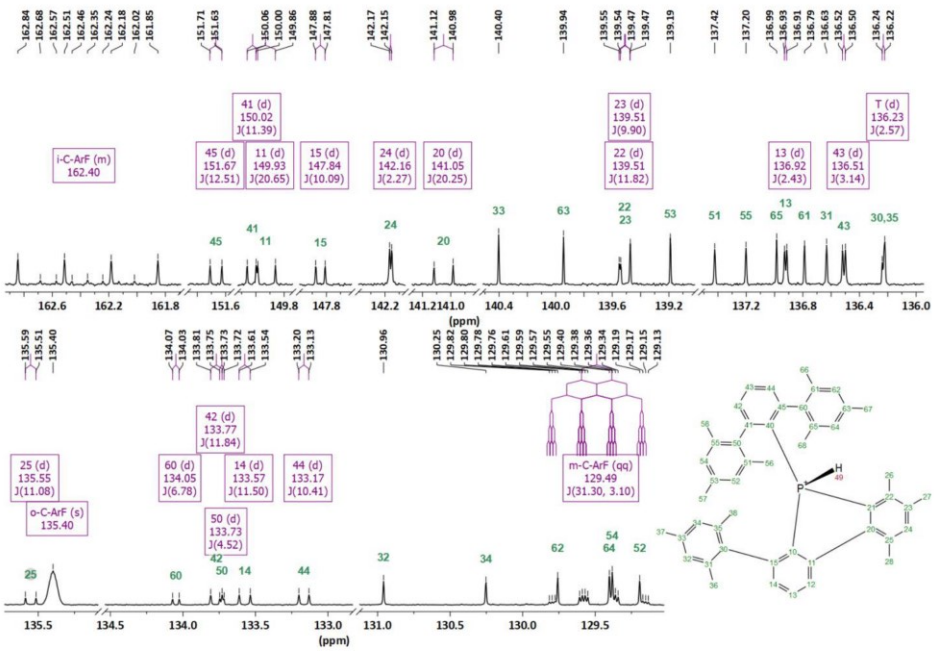

Figure S21. ^{13}C NMR (CD_2Cl_2, 151 MHz) spectrum (detail) of [**2a**][BAr^F_4].

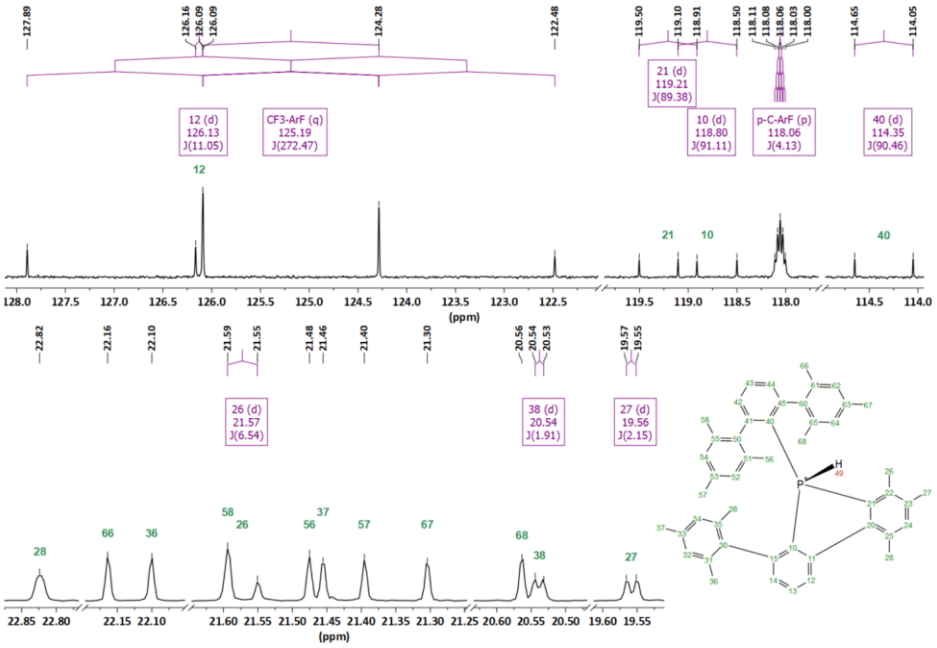

Figure S22. ^{13}C NMR (CD_2Cl_2, 151 MHz) spectrum (detail) of [**2a**][BAr^F_4].

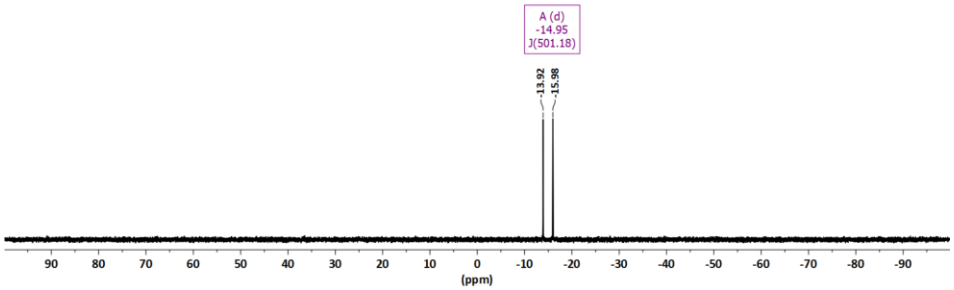

Figure S23. $^{31}P\{^1H\}$ NMR (CD_2Cl_2, 243 MHz) spectrum of [**2a**][BAr^F_4].

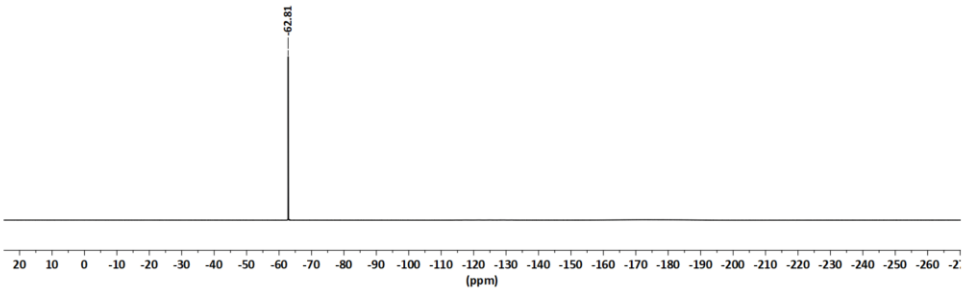

Figure S24. $^{19}F\{^1H\}$ NMR (CD_2Cl_2, 565 MHz) spectrum of [**2a**][BAr^F_4].

Table S1. Crystal data and structure refinement of (2,6-$Mes_2C_6H_3)_2AsF$, [**2a**][BAr^F_4] and **3a**.

	(2,6-$Mes_2C_6H_3)_2AsF$	[**2a**][BAr^F_4]	**3a**
Formula	$C_{48}H_{50}AsF$	$C_{80}H_{62}BF_{24}P$	$C_{48}H_{49}P$
Formula weight, g mol^{-1}	720.80	1521.07	656.84
Crystal system	Triclinic	Triclinic	Triclinic
Crystal size, mm	0.07×0.05×0.05	0.2×0.2×0.2	0.06×0.06×0.05
Space group	$P\bar{1}$	$P\bar{1}$	$P\bar{1}$
a, Å	10.957(5)	17.8152(7)	11.2904(5)
b, Å	11.542(5)	21.7642(8)	12.9577(6)
c, Å	16.417(5)	21.8095(8)	15.0899(7)
α, º	74.469(5)	68.0540(10)	72.905(2)
β, º	70.535(5)	76.9950(10)	84.767(2)
γ, º	78.956(5)	77.8320(10)	73.838(2)
V, Å^3	1874.0(13)	7566.9(5)	2026.57(16)
Z	2	4	2
ρ_{calcd}, g cm^{-3}	1.277	1.335	1.076
μ (Mo *Kα*), mm^{-1}	0.945	0.138	0.098
F(000)	760	3112	704
θ range, deg	4.74 to 61.2	4.654 to 56.752	4.62 to 51
Index ranges	−15 ≤ h ≤ 15	−23 ≤ h ≤ 23	−13 ≤ h ≤ 12
	−16 ≤ k ≤ 16	−29 ≤ k ≤ 29	−15 ≤ k ≤ 15
	−23 ≤ l ≤ 23	−29 ≤ l ≤ 29	−18 ≤ l ≤ 18
No. of reflns collected	248957	176027	40455
Completeness to θ_{max}	0.998	0.981	0.999
No. indep. Reflns	11512	37158	7558
No. obsd reflns with ($I>2\sigma(I)$)	10571	30061	6814
No. refined params	481	2053	454
GooF (F^2)	1.064	1.049	1.070
R_1 (F) ($I > 2\sigma(I)$)	0.0258	0.0705	0.0412
wR_2 (F^2) (all data)	0.0686	0.1702	0.1139
Largest diff peak/hole, e Å^{-3}	0.41/−0.48	0.98/−0.78	0.30/−0.32
CCDC number	1918428	1918429	1918430

X-Ray diffraction studies

Intensity data of (2,6-$Mes_2C_6H_3)_2AsF$, [**2a**][BAr^F_4], **3a**, **3b** and [**4**][$AlCl_4$] was collected on a Bruker Venture D8 diffractometer at 100 K with graphite-monochromated Mo-Kα (0.7107 Å) radiation. All structures were solved by direct methods and refined based on F^2 by use of the SHELX program package[S7] as implemented in WinGX and OLEX.[S8] All non-hydrogen atoms were refined using anisotropic displacement parameters. Hydrogen atoms attached to carbon atoms were included in geometrically calculated positions using a riding model. Diffuse electron density due to heavily disordered solvent molecules was account for **3a** using the SQUEEZE routine.[S9] Crystal and refinement data are collected in Tables S1 and S2. Figures were created using DIAMOND.[S10] Crystallographic data for the structural analyses have been deposited with the Cambridge Crystallographic Data Centre. Copies of this information may be obtained free of charge from The Director, CCDC, 12 Union Road, Cambridge CB2 1EZ, UK (Fax: +44-1223-336033; e-mail: deposit@ccdc.cam.ac.uk or http://www.ccdc.cam.ac.uk).

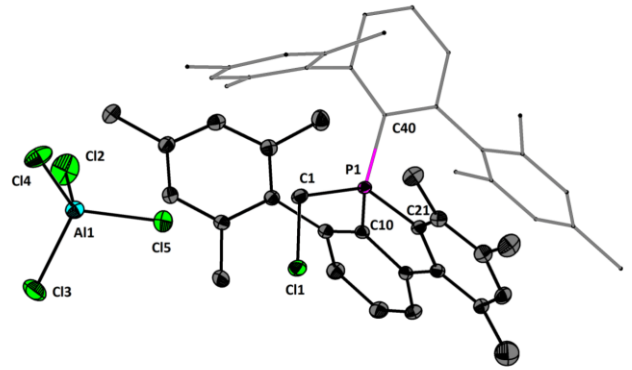

Figure S24. Molecular structures of [**4**][$AlCl_4$] showing 50% probability ellipsoids and the essential atom numbering scheme. Selected bond parameters [Å, °] of [**4**]$^+$: P1-C1 1.837(1), P1-C10 1.799(1), P1-C21 1.786(1), P1-C40 1.826(1), C10-P1-C40 113.14(5), C21-P1-C10 94.75(5), C21-P1-C40 114.04(5).

Table S2. Crystal data and structure refinement of **3b** and [**4**][AlCl$_4$]

	3b	[**4**][AlCl$_4$]
Formula	$C_{48}H_{49}As$	$C_{49}H_{51}AlCl_5P$
Formula weight, g mol^{-1}	700.79	875.10
Crystal system	Triclinic	Triclinic
Crystal size, mm	0.3×0.2×0.2	0.08×0.06×0.05
Space group	$P\bar{1}$	$P\bar{1}$
a, Å	8.3779(3)	10.4702(4)
b, Å	13.7181(5)	14.6934(5)
c, Å	16.0602(5)	15.5911(5)
α, º	90.9720(10)	96.2860(10)
β, º	95.7560(10)	104.9190(10)
γ, º	101.3350(10)	105.3360(10)
V, Å^3	1799.38(11)	2194.23(13)
Z	2	2
ρ_{calcd}, g cm^{-3}	1799.38(11)	1.325
μ (Mo $K\alpha$), mm^{-1}	0.978	0.421
F(000)	740	916
θ range, deg	4.98 to 61.2	2.19 to 31.60
Index ranges	−11 ≤ h ≤ 11	−15 ≤ h ≤ 15
	−19 ≤ k ≤ 19	−21 ≤ k ≤ 21
	−22 ≤ l ≤ 22	−22 ≤ l ≤ 22
No. of reflns collected	43216	58416
Completeness to θ_{max}	0.996	0.997
No. indep. Reflns	10997	14694
No. obsd reflns with ($I>2\sigma(I)$)	9865	12524
No. refined params	454	517
GooF (F^2)	1.039	1.060
R_1 (F) ($I > 2\sigma(I)$)	0.0284	0.0377
wR_2 (F^2) (all data)	0.0697	0.1118
Largest diff peak/hole, e Å^{-3}	0.43/−0.31	0.88 / −0.73
CCDC number	1918431	1918432

Computational data

The structures of all starting materials, transition states, intermediates, and products were optimized in the gas-phase by density functional theory (DFT) at the B3PW91/6-311+G*[S11,S12] level of theory using Gaussian09.[S13] For the heavier atoms fully relativistic effective core potentials (Sb: ECP28MDF; Bi: ECP60MDF) and corresponding cc-pVTZ basis sets[S14,S15] were utilized. The starting geometries were modelled at the computer with GaussView 5. Transition states were calculated with the QST2 routine in Gaussian, using the optimized onset and end structures as starting point. Dispersion effects were accounted for using the empirical Grimme correction (GD3BJ).[S16]

References

S1. K. Ruhlandt-Senge, J. J. Ellison, R. J. Wehmschulte, F. Pauer, P. P. Power, *J. Am. Chem. Soc.* **1993**, *115*, 11353-11357.

S2. (a) N. A. Yakelis, R. G. Bergman, *Organometallics* **2005**, *24*, 3579–3581; (b) M. Brookhart, B. Grant, A. F. Volpe Jr., *Organometallics* **1992**, *11*, 3920-3922.

S3. M. Kuprat, M. Lehmann, A. Schulz and A. Villinger, *Organometallics*, **2010**, *29*, 1421-1427.

S4. M. Lehmann, A. Schulz, A. Villinger, *Angew. Chem., Int. Ed.* **2009**, *48*, 7444-7447.

S5. V. J. Scott, R. Çelenligil-Çetin, O. V. Ozerov, *J. Am. Chem. Soc.* **2005**, *127*, 2852-2853.

S6. J. B. Lambert, S. Zhang, C. L. Stern, J. C. Huffman, *Science* **1993**, *260*, 1917-1918.

S7. G. M. Sheldrick, *Acta Cryst.* **2008**, *A64*, 112-122.

S8. (a) L. Farrugia, *J. Appl. Cryst.* **1999**, *32*, 837-838. (b) O. V. Dolomanov, L. J. Bourhis, R. J. Gildea, J. A. K. Howard, H. Puschmann, *J. Appl. Cryst.* **2009**, *42*, 339-341.

S9. A. Spek *J. Appl. Cryst.* **2003**, *36*, 7-13.

S10. K. Brandenburg, Diamond, version 4.0.4, Crystal Impact GbR: Bonn, Germany, **2012**.

S11. J. P Perdew, J. A. Chevary, S. H. Vosko, K. A. Jackson, M. R. Pederson, D. J. Singh, C. Fiolhais, *Phys. Rev.* B **1992**, *46*, 6671-6687.

S12. A. D. Becke, *J. Chem. Phys.* **1993**, *98*, 5648-5652.

S13. M. J. Frisch, G. W. Trucks, H. B. Schlegel, G. E. Scuseria, M. A. Robb, J. R. Cheeseman, G. Scalmani, V. Barone, B. Mennucci, G. A. Petersson, H. Nakatsuji, M. Caricato, X. Li, H. P. Hratchian, A. F. Izmaylov, J. Bloino, G. Zheng, J. L. Sonnenberg, M. Hada, M. Ehara, K. Toyota, R. Fukuda, J. Hasegawa, M. Ishida, T. Nakajima, Y. Honda, O. Kitao, H. Nakai, T. Vreven, J. A. Montgomery, Jr., J. E. Peralta, F. Ogliaro, M. Bearpark, J. J. Heyd, E. Brothers, K. N. Kudin, V. N. Staroverov, R. Kobayashi, J. Normand, K. Raghavachari, A. Rendell, J. C. Burant, S. S. Iyengar, J. Tomasi, M. Cossi, N. Rega, J. M. Millam, M. Klene, J. E. Knox, J. B. Cross, V. Bakken, C. Adamo, J. Jaramillo, R. Gomperts, R. E. Stratmann, O. Yazyev, A. J. Austin, R. Cammi, C. Pomelli, J. W. Ochterski, R. L. Martin, K. Morokuma, V. G. Zakrzewski, G. A. Voth, P. Salvador, J. J. Dannenberg, S. Dapprich, A. D. Daniels, Ö. Farkas, J. B. Foresman, J. V. Ortiz, J. Cioslowski, D. J. Fox, Gaussian 09, Revision B.01, Gaussian Inc., Wallingford CT, **2010**.

S14. B. Metz, H. Stoll, M. Dolg, *J. Chem. Phys.* **2000**, *113*, 2563–2569.

S15. K. A. Peterson, *J. Chem. Phys.* **2003**, *119*, 11099–11123.

S16. S. Grimme, J. Antony, S. Ehrlich and H. Krieg, *J. Chem. Phys.*, **2010**, *132*,154104.

6.3 Intramolecular Reaction of Transient Phosphenium and Arsenium Ions Giving Rise to Isolable 9-Phospha- and 9-Arsena-Fluorenium Ions

Supporting Information

Intramolecular Reaction of Transient Phosphenium and Arsenium Ions Giving Rise to Isolable 9-Phospha- and 9-Arsena-Fluorenium Ions

*Marian Olaru, Daniel Duvinage, Yannik Naß, Lorraine A. Malaspina, Stefan Mebs, and Jens Beckmann**

anie_202006728_sm_miscellaneous_information.pdf

Table of Contents

Synthesis and characterization of 1a

To a suspension of 2,6-(Me_5C_6)$_2$$C_6H_3$Li (3.01 g, 8.00 mmol) in hexane (10 mL) cooled to −80 °C was added a PCl_3 (1.17 g, 8.52 mmol). The reaction mixture was stirred for 20 min at −80 °C then brought to room temperature for 30 minutes after which all volatiles were removed under reduced pressure. CH_2Cl_2 was added and the suspension was filtered under argon to remove LiCl. All volatiles were removed under reduced pressure to obtain 3.44 g of crude 2,6-(Me_5C_6)$_2$$C_6H_3PCl_2$ that was used without further purification in the next step.* To the crude 2,6-(Me_5C_6)$_2$$C_6H_3PCl_2$, CsF (3.32 g, 21.85 mmol) and THF (15 mL) were added. The reaction mixture was stirred for 72 h at 88 °C. All volatiles were removed under reduced pressure and CH_2Cl_2 (80 mL) was added. The suspension was filtered under argon over a pad of dry Celite, and the solvent was evaporated to dryness to obtain 2.40 g of crude 2,6-(Me_5C_6)$_2$$C_6H_3PF_2$ that was used without further purification in the next step.† To the crude 2,6-(Me_5C_6)$_2$$C_6H_3PF_2$ (2.1 g), additional 2,6-(Me_5C_6)$_2$$C_6H_3$Li (2.01 g, 5.34 mmol) and hexane (50 mL) were added. The mixture was stirred for 18 hours at 65 °C until the 2,6-(Me_5C_6)$_2$$C_6H_3PF_2$ was completely consumed. The solvent was removed under reduced pressure and the crude product was purified by column chromatography (silicagel, hexane:CH_2Cl_2 1:0.4 v/v) to obtain **1a** as a white solid (0.63 g, 17%‡). **Mp** 244–246 °C (decomp.). **^{1}H NMR (600 MHz, CD_2Cl_2)**: δ = 7.13 (t, ^3J(^{1}H–^{1}H) = 8 Hz, 2H, H4), 6.59 (dd, ^3J(^{1}H–^{1}H) = 8 Hz, 2H, ^4J(^{1}H–^{31}P) = 2 Hz, 4H, H3, H5), 2.27 (s, 6H, H15), 2.08 (s, 6H, H14 or H16), 2.056 (s, 6H, H14 or H16), 1.60 (s, 6H, H13 or H17), 1.56 (s, 6H, H13 or H17) ppm. **^{13}C{^{1}H} NMR (151 MHz, CD_2Cl_2)**: δ = 147.92 (dd, ^2J(^{13}C–^{31}P) = 20 Hz, ^3J(^{13}C–^{19}F) = 4 Hz, C6, C2), 140.88 (d, ^2J(^{13}C–^{31}P) = 3 Hz, C7), 139.89 (dd, ^1J(^{13}C–^{31}P) = 52 Hz, ^2J(^{13}C–^{19}F) = 12 Hz, C1), 133.39 (s, C10), 132.71 (s, br, C8 or C12), 132.54 (d, ^3J(^{13}C–^{31}P) = 2 Hz, C3, C5), 132.02 (s, C9 or C11), 131.96 (s, br, C8 or C12), 131.84 (s, C8 or C11), 128.92 (s, C4), 19.87 (d, ^2J(^{13}C–^{31}P) = 7 Hz, C13 or 17), 19.68 (s, C13 or C17), 17.10 (s, C15), 16.91 (s, C14 or C16), 16.80 (s, C14 or C16) ppm. **^{31}P{^{1}H} NMR (146 MHz, CD_2Cl_2)**: δ = 193.75 (d, ^1J(^{31}P–^{19}F) = 851 Hz) ppm. **^{19}F NMR (565 MHz, CD_2Cl_2)**: δ = −200.33 (d, ^1J(^{31}P–^{19}F) = 849 Hz). **HRMS ESI (m/z)**: [M+Na]$^+$ calculated. for $C_{56}H_{66}PFNa$, 811.47784; found, 811.47769.

*^{31}P{^{1}H} (THF-*d8*) = 162.5 ppm (s).
† ^{31}P{^{1}H} (C_6D_6) = 214.0 ppm (t, ^1J(^{19}F–^{31}P) = 1164 Hz; ^{19}F (C_6D_6) = −92.92 ppm (d, ^1J(^{19}F–^{31}P) = 1164 Hz).
‡ Several attempts to optimize the reaction for a better yield were unsuccessful.

Experimental procedures

General information

Unless otherwise stated, reactions and manipulations were performed under inert atmosphere (argon) using anhydrous solvents. Reagents used in this work including PCl_3 $AsCl_3$, ZnF_2, $AlCl_3$ and $EtAlCl_2$ (0.9 M in Heptane) were obtained commercially and were used as received. CsF was dried at 140 °C under reduced pressure. The reagents 2,6-(Me_5C_6)$_2$$C_6H_3$I and 2,6-($Me_5C_6$)$_2$$C_6H_3$Li were prepared following the published procedures.[S1] Anhydrous dichloromethane, hexane, tetrahydrofuran and toluene were collected from an SPS800 mBraun solvent purification system and stored over 4 Å molecular sieves. 1,2-Difluorobenzene was degassed and dried under argon over 4 Å molecular sieves. Et_2O was dried by refluxing it over Na/benzophenone under argon atmosphere. Deuterated solvents were degassed and dried over 4 Å molecular sieves under argon.

Unless otherwise noted, NMR spectra were recorded at room temperature on a Bruker Avance 360 and Avance 600 MHz spectrometers. ^{1}H, ^{13}C{^{1}H}, ^{11}B{^{1}H}, ^{31}P{1H} and ^{19}F NMR spectra are reported on the δ scale (ppm) and are referenced against $SiMe_4$, $BF_3{\cdot}Et_2O$ (15% in $CDCl_3$), H_3PO_4 (85% in water) and $CFCl_3$, respectively. ^{1}H and ^{13}C{^{1}H} chemical shifts are reported relative to the residual peak of the solvent ($CDHCl_2$ 5.32 ppm for CD_2Cl_2) in the ^{1}H NMR spectra, and to the peak of the deuterated solvent (CD_2Cl_2 53.84 ppm) in the ^{13}C{^{1}H} NMR spectra.[S2] The assignment of the ^{1}H and ^{13}C{^{1}H} resonance signals was made in accordance with the COSY, HSQC and HMBC spectra. The labelling schemes are attached to the ^{1}H and ^{13}C{^{1}H} spectra. With the exception of **1a** and **1b**, for all other compounds, the NMR and the crystal structure labelling schemes are identical.

The ESI HRMS spectra were measured on a Bruker Impact II spectrometer. Acetonitrile or dichloromethane/acetonitrile solutions (c =1·10^{-5} mol·L^{-1}) were injected directly into the spectrometer at a flow rate of 3 µL·min^{-1}. Nitrogen was used both as a drying gas and for nebulization with flow rates of approximately 5 L·min^{-1} and a pressure of 5 psi. Pressure in the mass analyzer region was usually about 1·10^{-5} mbar. Spectra were collected for 1 min and averaged. The nozzle-skimmer voltage was adjusted individually for each measurement.

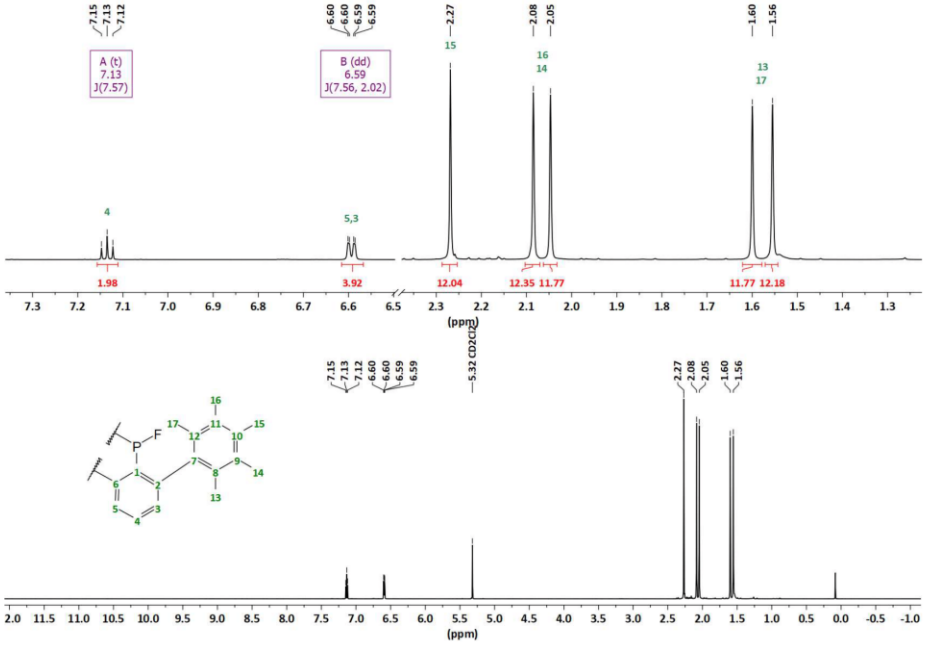

Figure S1. ^{1}H NMR (CD_2Cl_2, 600 MHz) spectrum of **1a**.

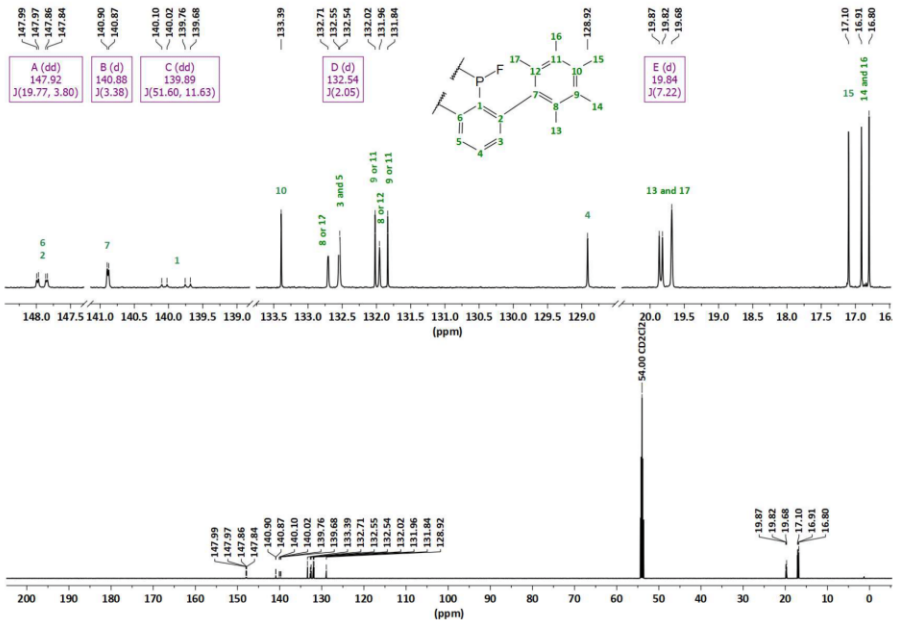

Figure S2. $^{13}C\{^{1}H\}$ NMR (CD_2Cl_2, 151 MHz) spectrum of **1a**.

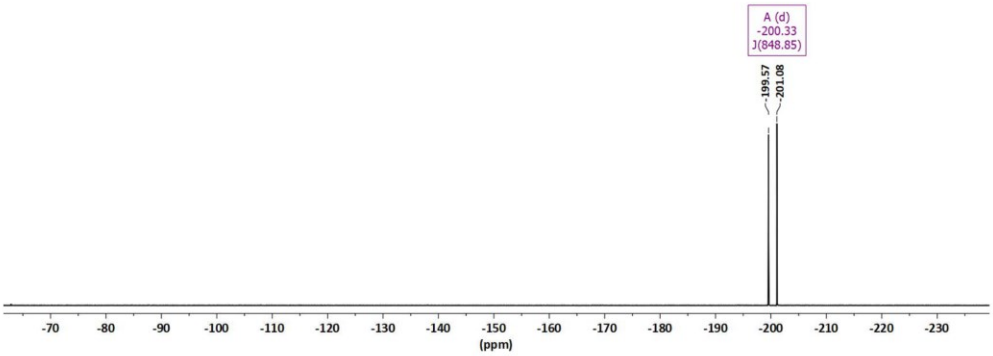

Figure S3. ^{19}F NMR (CD_2Cl_2, 565 MHz) spectrum of **1a**.

6

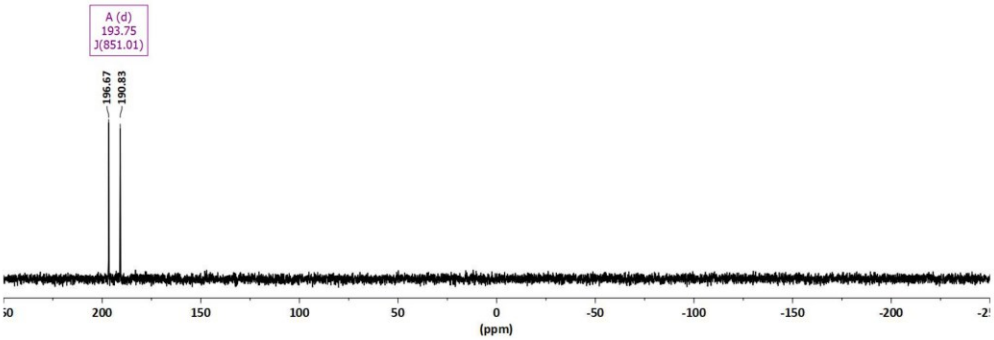

Figure S4. $^{31}P\{^1H\}$ NMR (CD_2Cl_2, 146 MHz) spectrum of **1a**.

7

Synthesis and characterization of 1b

A solution of 2,6-$(Me_5C_6)_2C_6H_3Li$ (4.20 g, 11.15 mmol) in Et_2O (50 mL) was added to a solution of $AsCl_3$ (2.10 g, 11.58 mmol) in Et_2O (20 mL) at 0°C over the course of 20 minutes. The reaction mixture was brought to room temperature and stirred for additional 16 hours. The solvent was removed under reduced pressure. To the crude mixture ZnF_2 (5.50 g, 53.19 mmol) and MeCN (120 mL) were added. The reaction mixture was stirred for 120 h at 80 °C. After reaction control by ^{19}F NMR spectroscopy the solvent was removed under vacuum and to the residue CH_2Cl_2 (120 mL) was added. The suspension was filtered through a pad of Celite and the solvent of the solution was removed under reduced pressure. The remaining solid was washed with cold MeCN (3×20 mL) and with cold hexane (3×10 mL). To the crude 2,6-$(Me_5C_6)_2C_6H_3AsF_2$ thus obtained, 2,6-$(Me_5C_6)_2C_6H_3Li$ (4.20 g, 11.16 mmol) was added and the solids were suspended in hexane. The reaction mixture was stirred for 24 h at room temperature and controlled by ^{19}F NMR spectroscopy. Afterwards the solvent was removed under reduced pressure and to the residual solid CH_2Cl_2 (300 mL) was added. The suspension was worked up aqueous by washing the organic phase with distilled H_2O (3×100 mL). The organic phase was dried over sodium sulphate and the solvent was removed under vacuum to afford a beige solid. This was washed with cold MeCN (3×40 mL) and cold hexane (3×40 mL) to obtain the title compound **1b** as colourless solid (4.29 g, 46%). Crystals suitable for X-ray diffraction were obtained by dissolving **1b** in CH_2Cl_2 and slow diffusion of hexane. **Mp**: 250–255 °C (decomp.). **^{1}H NMR (600 MHz, CD_2Cl_2)**: δ = 7.15 (2H, t, $^3J(^1H–^1H)$ = 7.5 Hz, H4), 6.60 (4H, d, $^2J(^1H–^1H)$ = 7.5 Hz, H3 and H5), 2.28 (12H, s, H15), 2.11 (12H, s, H14 or H16), 2.06 (12H, s, H14 or 16), 1.62 (12H, s, H13 or H17), 1.60 (12H, s, H13 or H17) ppm. **$^{13}C\{^1H\}$ NMR (151 MHz, CD_2Cl_2)**: δ = 148.33 (4C, s, C2 and C6), 145.74. (2C, d, $^3J(^{13}C–^{19}F)$ = 11.8 Hz, C1), 140.59 (4C, s, C7), 133.77 (4C, s, C10), 132.89 (4C, s, C8 or C12), 132.40 (4C, s, C9 or C11), 132.20 (4C, s, C3), 132.03 (4C, s, C9 or C11), 131.96 (4C, s, C8 or C12), 128.96 (2C, s, C4), 19.83 (4C, s, C13 or C17), 19.72 (4C, s, C13 or C17), 17.14 (4C, s, C15), 16.99 (4C, s, C14 or C16), 16.83 (4C, s, C14 or C16) ppm. **^{19}F NMR (565 MHz, CD_2Cl_2)**: δ = –216 (1F, s, As–F) ppm. **HRMS ESI (m/z)**: $[M+Na]^+$ calculated for $C_{56}H_{66}AsFNa$ 855.42567; found 855.42504.

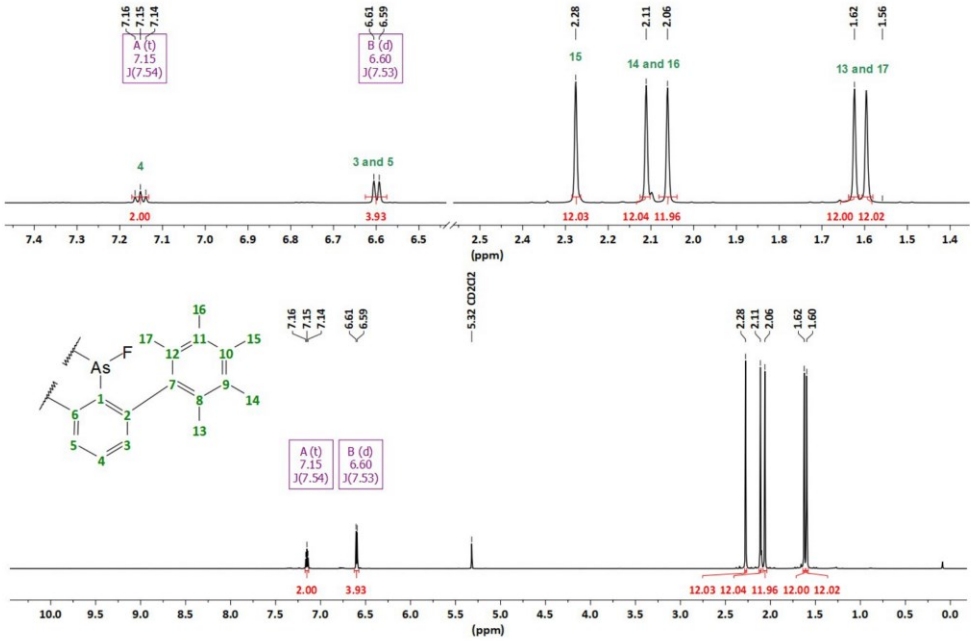

Figure S5. ^{1}H NMR (CD_2Cl_2, 600 MHz) spectrum of **1b**.

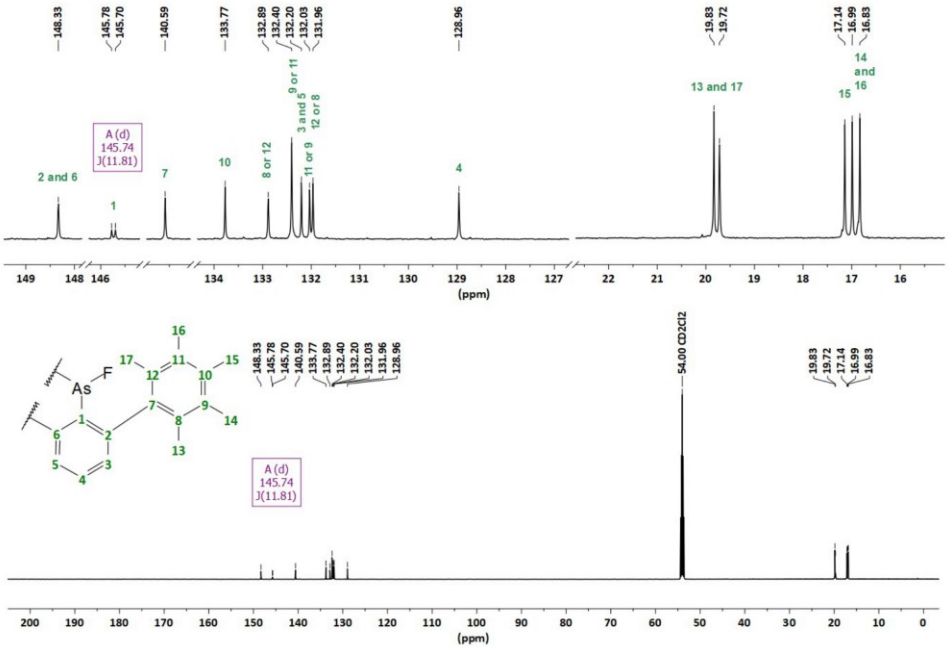

Figure S6. $^{13}C\{^{1}H\}$ NMR (CD_2Cl_2, 151 MHz) spectrum of **1b**.

10

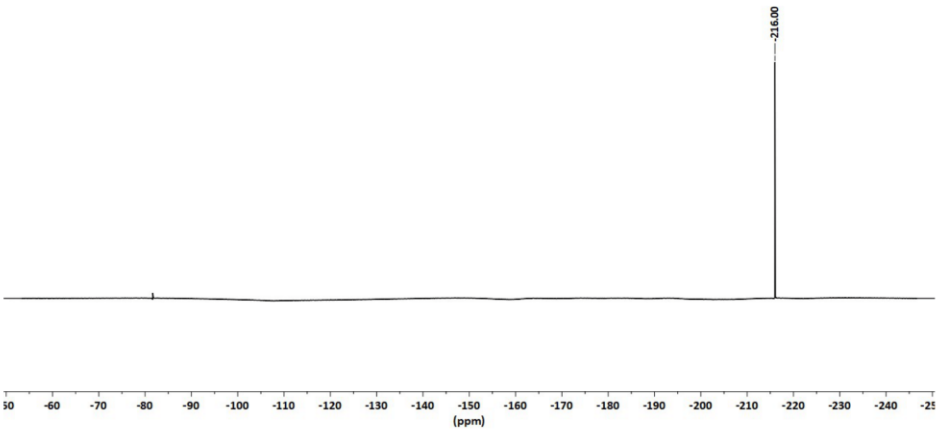

Figure S7. ^{19}F NMR (CD_2Cl_2, 565 MHz) spectrum of **1b**.

11

Synthesis and characterization of [5a][AlCl4] (and [7a][AlCl4])

To a suspension of **1a** (100 mg, 0.13 mmol) in pentane (3 mL) and CH_2Cl_2 (3 mL) a solution of $EtAlCl_2$ in heptane (0.9 M, 0.7 mL, 0.63 mmol) was added at room temperature. The reaction mixture was stirred at room temperature for 10 minutes. Pentane (20 mL) was layered and the Schlenk tube was placed in a refrigerator at 4 °C for 4–6 h. The crystals were separated from the solution and then dried under reduced pressure to obtain a dark red-brown crystalline solid (110 mg, virtually quantitative yield). The NMR spectra indicated a mixture of two products, [**5a**][$AlCl_4$] (major) and [**7a**][$AlCl_4$] (minor) always in the same molar ratio (*ca.* 1:0.35). From all crystallization experiments only [**5a**][$AlCl_4$] produced crystals suitable for single-crystal X-ray structure determination. The identity of [**7a**][$AlCl_4$] was inferred from NMR spectra.

Major isomer [**5a**]$^+$:

^{1}H NMR (600 MHz, CD_2Cl_2): δ =8.13 (d, $^3J(^1H–^1H)$ = 8 Hz, $^5J(^1H–^{31}P)$ = 1 Hz, 1H, H12), 7.68 (dd, $^3J(^1H–^1H)$ = 8, 7.3 Hz, 1H, H13), 7.44 (td, $^3J(^1H–^1H)$ = 8 Hz, $^5J(^1H–^{31}P)$ = 1 Hz, 1H, H63), 7.39 (ddd, $^3J(^1H–^1H)$ = 8 Hz, $^4J(^1H–^1H)$ = 4 Hz, $^5J(^1H–^{31}P)$ = 1 Hz, 1H, H14), 7.03 (ddd, $^3J(^1H–^1H)$ = 8 Hz, $^4J(^1H–^1H)$ = 5 Hz, $^5J(^1H–^{31}P)$ = 2 Hz, 1H, H64), 6.68 (dd, $^3J(^1H–^1H)$ = 8 Hz, $^5J(^1H–^{31}P)$ = 2 Hz, 1H, H62), 2.52 (d, $^6J(^1H–^{31}P)$ = 3 Hz, 3H, H29), 2.43 (d, $^3J(^1H–^{31}P)$ = 2 Hz, 3H, H26), 2.34 (s, 3H, H48), 2.28 (s, 3H, H78), 2.28 (s, 3H, H30), 2.27 (s, 3H, H97), 2.20 (s, 6H, H98, H47), 2.17 (s, 3H, H49), 2.09 (s, 3H, H79), 2.00 (s, 6H, H46, H99), 1.78 (s, 3H, H77),1.70 (s, br, 6H, H28, H96), 1.54 (s, 3H, H80), 1.25 (s, 3H, H27), 1.20 (s, 3H, H50), 1.16 (s, 3H, H76), 0.91 (s, 3H, H100) ppm. **^{13}C{^{1}H} NMR (151 MHz, CD_2Cl_2)**: δ = 192.43 (d, $^2J(^{13}C–^{31}P)$ = 16 Hz, C22), 188.97 (d, $^4J(^{13}C–^{31}P)$ = 3 Hz, C24), 157.17 (s, C20), 155.58 (d, $^1J(^{13}C–^{31}P)$ = 12 Hz, C10), 154.80 (s, $^2J(^{13}C–^{31}P)$ = 46 Hz, C65), 150.48 (d, $^2J(^{13}C–^{31}P)$ = 22 Hz, C11), 150.00 (d, $^2J(^{13}C–^{31}P)$ = 7 Hz, C61), 146.12 (d, $^2J(^{13}C–^{31}P)$ = 4 Hz, C15), 143.39 (s, $^1J(^{13}C–^{31}P)$ = 11 Hz, C21), 142.42 (d, $^3J(^{13}C–^{31}P)$ = 6 Hz, C14), 139.48 (d, $^3J(^{13}C–^{31}P)$ = 10 Hz, C90), 138.92 (d, $^3J(^{13}C–^{31}P)$ = 2 Hz, C40), 137.75 (s, C70), 136.51 (s, C43), 135.46 (s, C73), 135.01 (s, C93), 134.94 (s, C74), 134.02 (s, C42), 133.81 (d, $^3J(^{13}C–^{31}P)$ = 3 Hz, C25), 133.46 (s, C44), 133.42 (s, C12), 133.24 (s, C72), 132.88 (s, C75), 132.73 (s, C71), 132.58 (s, C92), 132.56 (s, C62, C95), 132.19 (s, C94), 132.13 (s, C91), 132.13 (s, C63), 132.04 (s, C45), 131.90 (s, C41), 131.70 (d, $^3J(^{13}C–^{31}P)$ = 9 Hz, C64), 131.13 (s, C13), 127.01 (d, $^1J(^{13}C–^{31}P)$ = 34 Hz, C60), 54.24 (d, $^3J(^{13}C–^{31}P)$ = 3 Hz, C23), 30.90 (s, C27), 25.31 (d, $^3J(^{13}C–^{31}P)$ = 22 Hz, C26), 24.35 (s, C28), 22.11 (s, br, C29), 21.18 (s, C80), 20.06 (s, C96), 19.95 (s, C46), 19.52 (s, C76), 19.15 (s, C30). 17.98 (d, $^4J(^{13}C–^{31}P)$ = 8 Hz, C50), 17.44 (s, C78) 17.37 (d, $^5J(^{13}C–^{31}P)$ = 5 Hz, C100), 17.25 (s, C48), 17.11 (s, C49), 17.08 (s, C97),

16.92 (s, C77), 16.87 (s, C47, C98), 16.83 (s, C79), 16.29 (s, C99) ppm. **^{31}P{^{1}H} NMR (CD_2Cl_2, 243 MHz)**: δ = −26.93 (s) ppm.

Minor isomer [**7b**]$^+$:

^{1}H NMR (600 MHz, CD_2Cl_2): δ = 7.96 (d, $^3J(^1H–^1H)$ = 8 Hz, $^5J(^1H–^{31}P)$ = 1 Hz, 1H, H12), 7.74 (dd, $^3J(^1H–^1H)$ = 8, 7.4 Hz, 1H, H13), 7.46 (td, $^3J(^1H–^1H)$ = 8 Hz, $^5J(^1H–^{31}P)$ = 1 Hz, H, H63), 7.31 (ddd, $^3J(^1H–^1H)$ = 7 Hz, $^4J(^1H–^1H)$ = 4 Hz, $^5J(^1H–^{31}P)$ = 1 Hz, 1H, H14), 7.09 (ddd, $^3J(^1H–^1H)$ = 8 Hz, $^4J(^1H–^1H)$ = 6 Hz, $^5J(^1H–^{31}P)$ = 2 Hz, 1H, H64), 6.62 (dd, $^3J(^1H–^1H)$ = 8 Hz, $^5J(^1H–^{31}P)$ = 2 Hz, 1H, H62), 2.74 (d, $^3J(^1H–^{31}P)$ = 1 Hz, 3H, H26), 2.51 (s, br, 3H, H28), 2.34 (s, 3H, H34), 2.29 (s, 3H, H27), 2.26 (s, 3H, H98), 2.21 (s, 3H, H47), 2.20 (s, 3H, H97), 2.15 (s, 3H, H49), 2.10 (s, 3H, H78), 2.01 (s, 3H, H46), 2.00 (s, 3H, H99), 1.93 (s, 3H, H79), 1.84 (s, 3H, H77), 1.79 (s, 3H, H96), 1.49 (s, 3H, H30), 1.43 (s, 3H, H80), 1.29 (s, 3H, H76), 1.26 (s, 3H, H29), 1.15 (s, 3H, H50), 0.94 (s, 3H, H100) ppm. **^{13}C{^{1}H} NMR (151 MHz, CD_2Cl_2)**: δ = 191.61 (d, $^2J(^{13}C–^{31}P)$ = 7 Hz, C20), 189.39 (s, C24), 183.70 (d, $^2J(^{13}C–^{31}P)$ = 18 Hz, C22), 154.90 (d, $^2J(^{13}C–^{31}P)$ = 45 Hz, C65), 151.15 (d, $^2J(^{13}C–^{31}P)$ = 6 Hz, C61), 150.47 (d, $^1J(^{13}C–^{31}P)$ = 4 Hz, C10), 150.37 (s, $^2J(^{13}C–^{31}P)$ = 15 Hz, C11), 145.92 (d, $^1J(^{13}C–^{31}P)$ = 10 Hz, C21), 145.75 (s, $^2J(^{13}C–^{31}P)$ = 3 Hz, C15), 139.94 (d, $^3J(^{13}C–^{31}P)$ = 7 Hz, C14), 139.46 (d, $^3J(^{13}C–^{31}P)$ = 9 Hz, C90), 139.27 (s, C40), 137.43 (s, C70), 136.46 (s, C43), 135.82 (d, $^3J(^{13}C–^{31}P)$ = 5 Hz, C23), 135.46 (s, C73), 135.15 (s, C93), 133.95 (s, C42), 133.50 (s, C44), 133.15 (s, C74), 132.86 (s, C71) 132.70 (d, $^4J(^{13}C–^{31}P)$ = 2 Hz, C95), 132.67 (s, C92), 132.50 (d, $^3J(^{13}C–^{31}P)$ = 2 Hz, C62), 132.35 (s, C75), 132.33 (s, C94), 132.30 (d, $^4J(^{13}C–^{31}P)$ = 2 Hz, C63), 132.20 (s, C45), 131.99 (d, $^3J(^{13}C–^{31}P)$ = 10 Hz, C64), 131.94 (s, C91, C41), 131.53 (s, C72), 131.00 (s, C13), 129.39 (s, C12), 125.45 (d, $^1J(^{13}C–^{31}P)$ = 25 Hz, C60), 52.41 (d, $^3J(^{13}C–^{31}P)$ = 2 Hz, C25) 35.11 (d, $^4J(^{13}C–^{31}P)$ = 3 Hz, C29), 28.69 (d,$^3J(^{13}C–^{31}P)$ = 17 Hz, C26), 25.17 (d, $^4J(^{13}C–^{31}P)$ = 2 Hz, C30), 21.75 (s, C28), 20.61 (s, C80), 20.26 (s, C96), 19.84 (s, C46), 19.65 (s, C76), 17.71 (d, $^5J(^{13}C–^{31}P)$ = 7 Hz, C50), 17.48 (d, $^5J(^{13}C–^{31}P)$ = 4 Hz, C100), 17.25 (s, C48), 17.14 (s, C78), 17.08 (s, C49, C98), 16.87 (s, C97), 16.84 (s, br, C47, C77), 16.52 (s, C79), 16.31 (s, C99), 15.83 (d, $^4J(^{13}C–^{31}P)$ = 2 Hz, C27) ppm. **^{31}P{^{1}H} NMR (243 MHz, CD_2Cl_2)**: δ = −22.15 (s) ppm.

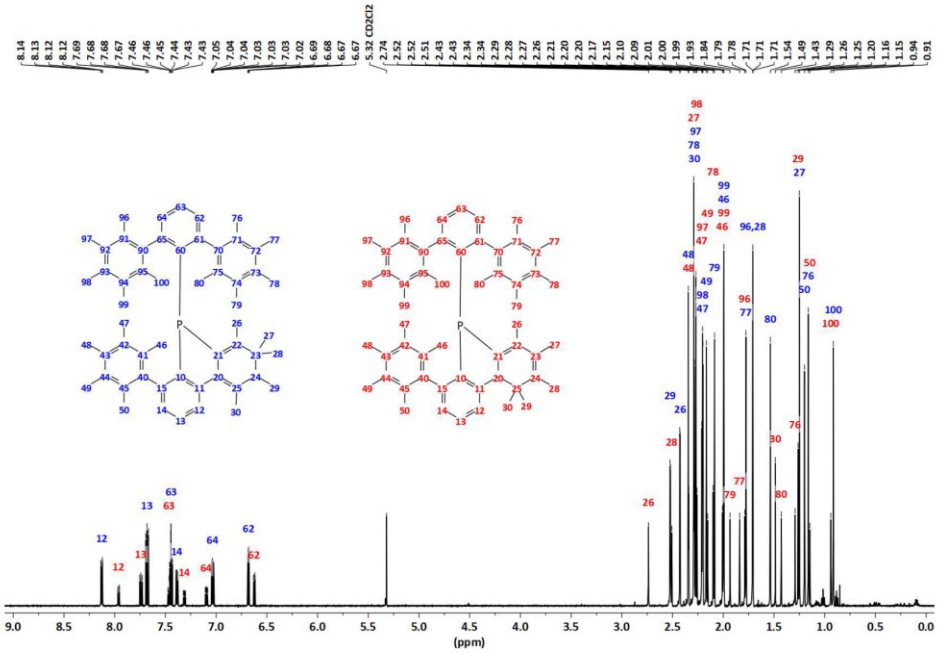

Figure S8. ^{1}H NMR (CD_2Cl_2, 600 MHz) spectrum (full) of [**5a**]$^{+}$ and [**7a**]$^{+}$.

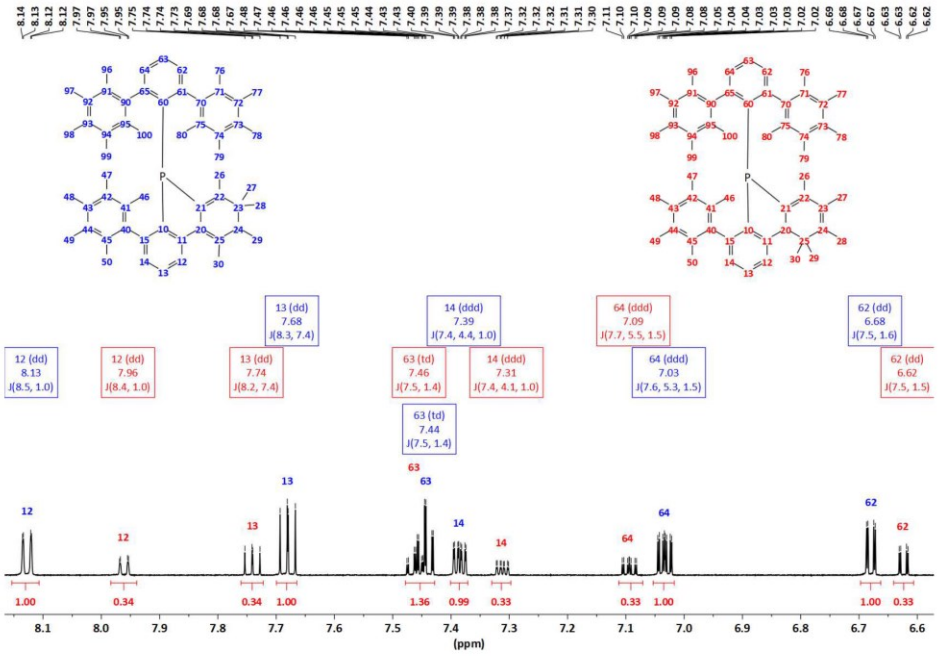

Figure S9. ^{1}H NMR (CD_2Cl_2, 600 MHz) spectrum (detail) of [**5a**]$^{+}$ and [**7a**]$^{+}$.

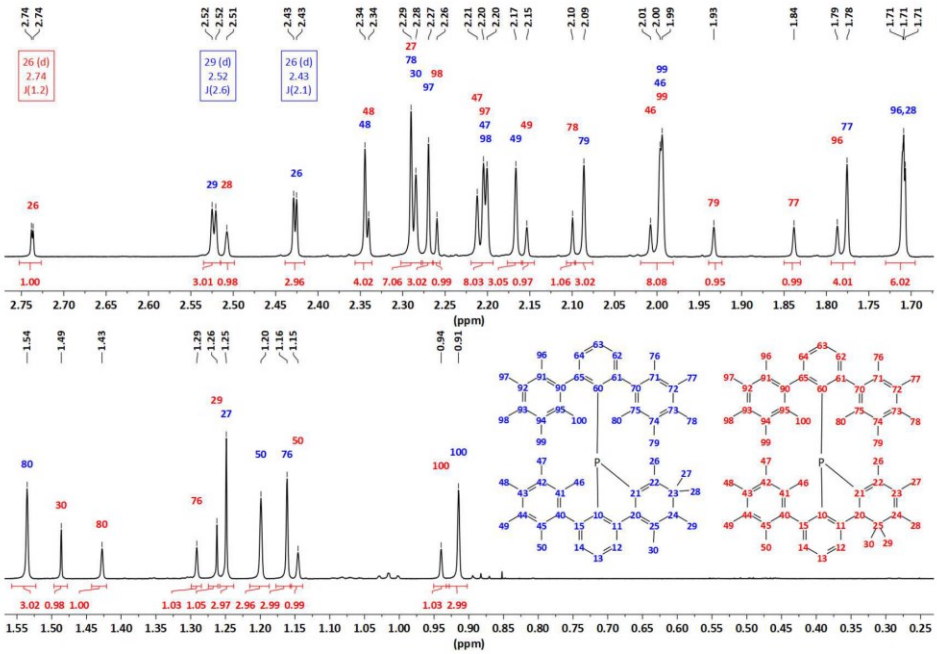

Figure S10. ^{1}H NMR (CD_2Cl_2, 600 MHz) spectrum (detail) of [**5a**]$^{+}$ and [**7a**]$^{+}$.

16

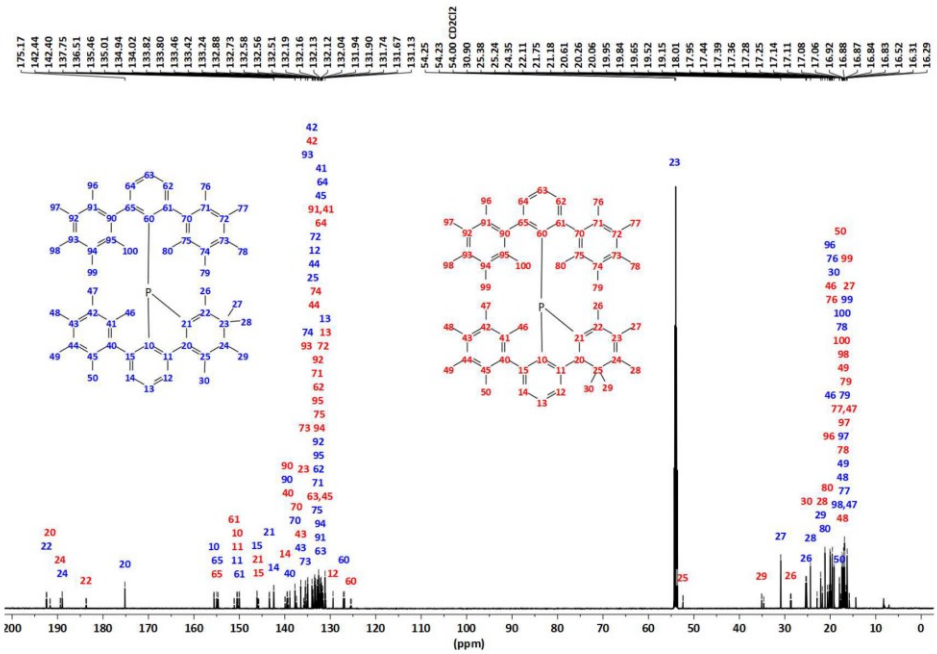

Figure S11. ^{13}C NMR (CD_2Cl_2, 151 MHz) spectrum (full) of [**5a**]$^{+}$ and [**7a**]$^{+}$.

17

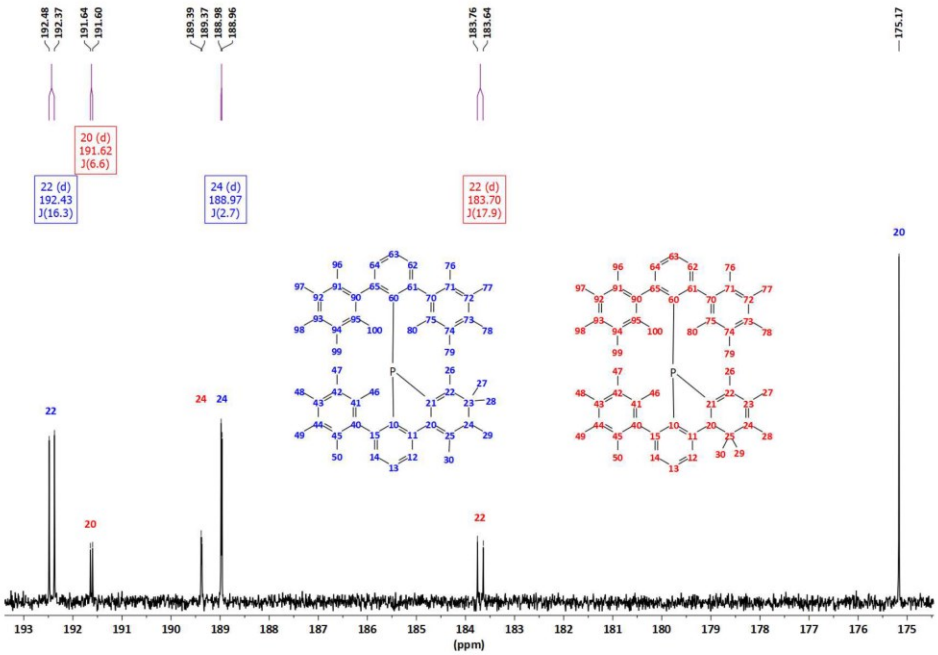

Figure S12. ^{13}C NMR (CD_2Cl_2, 151 MHz) spectrum (detail) of **[5a]**$^+$ and **[7a]**$^+$.

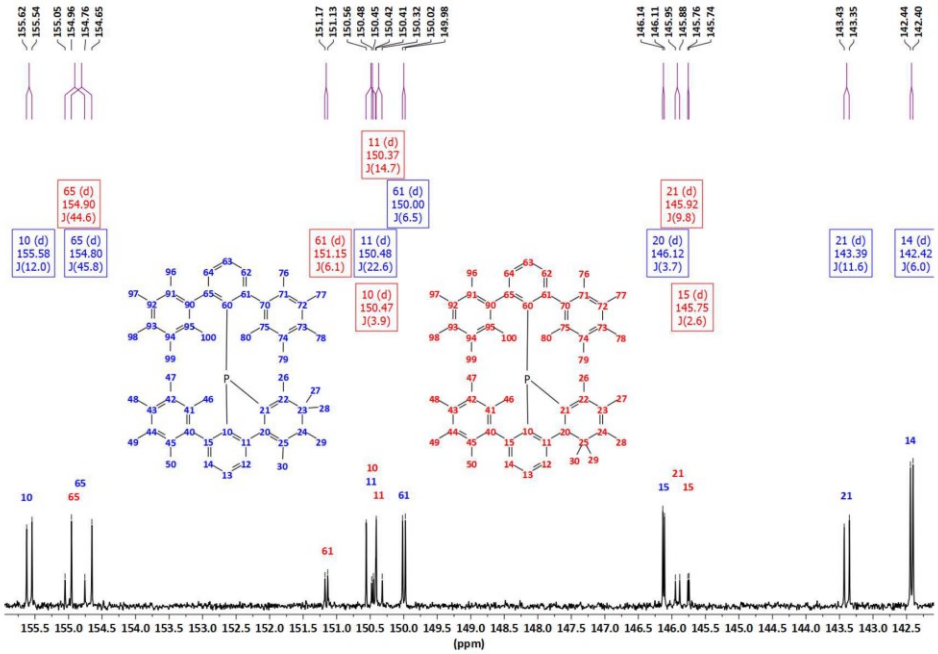

Figure S13. ^{13}C NMR (CD_2Cl_2, 151 MHz) spectrum (detail) of **[5a]**$^+$ and **[7a]**$^+$.

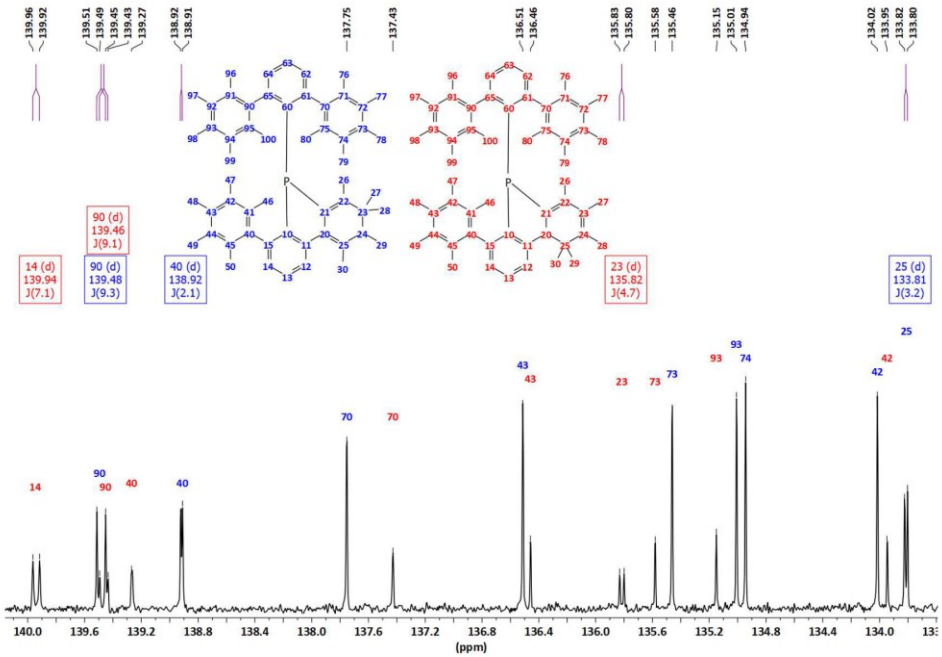

Figure S14. ^{13}C NMR (CD_2Cl_2, 151 MHz) spectrum (detail) of [**5a**]$^+$ and [**7a**]$^+$.

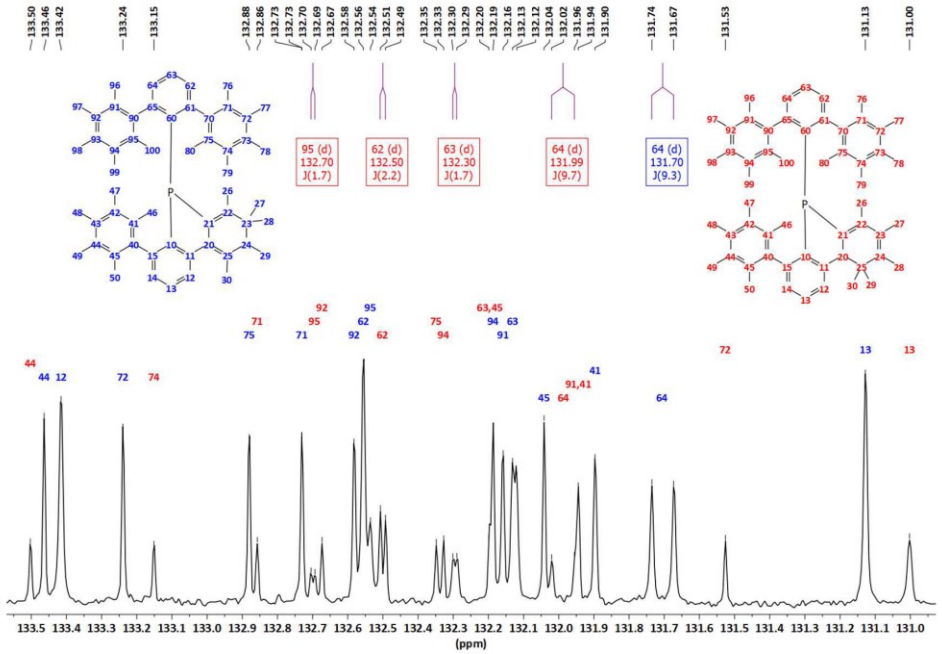

Figure S15. ^{13}C NMR (CD_2Cl_2, 151 MHz) spectrum (detail) of [**5a**]$^+$ and [**7a**]$^+$.

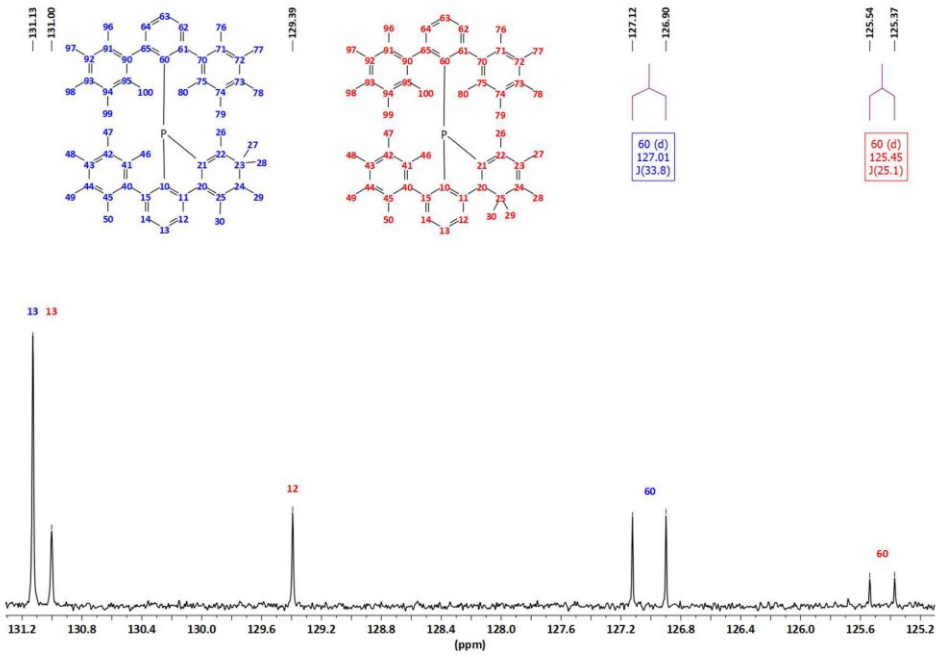

Figure S16. ^{13}C NMR (CD_2Cl_2, 151 MHz) spectrum (detail) of [**5a**]$^+$ and [**7a**]$^+$.

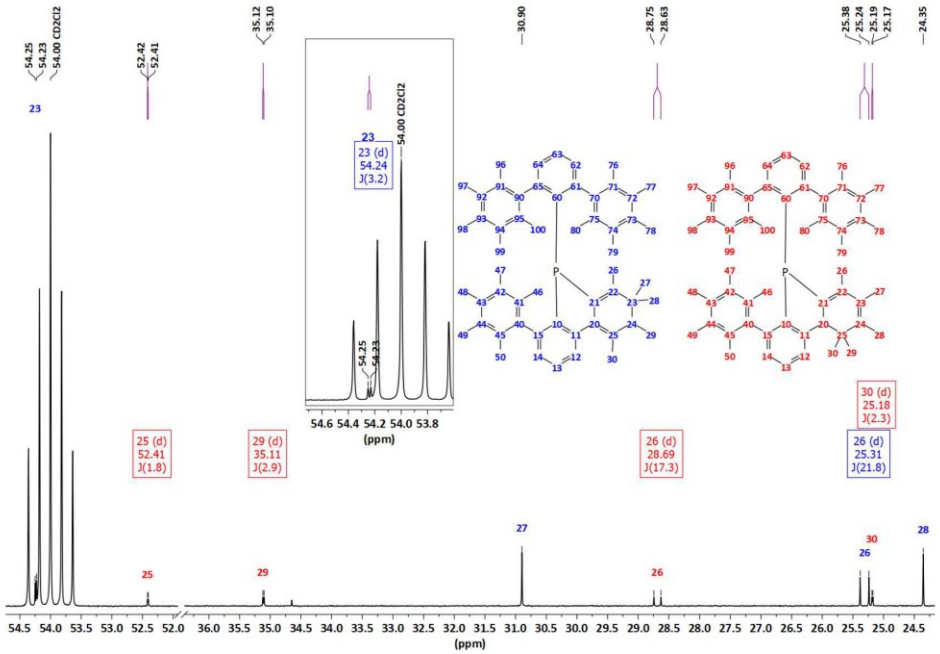

Figure S17. ^{13}C NMR (CD_2Cl_2, 151 MHz) spectrum (detail) of [**5a**]$^+$ and [**7a**]$^+$.

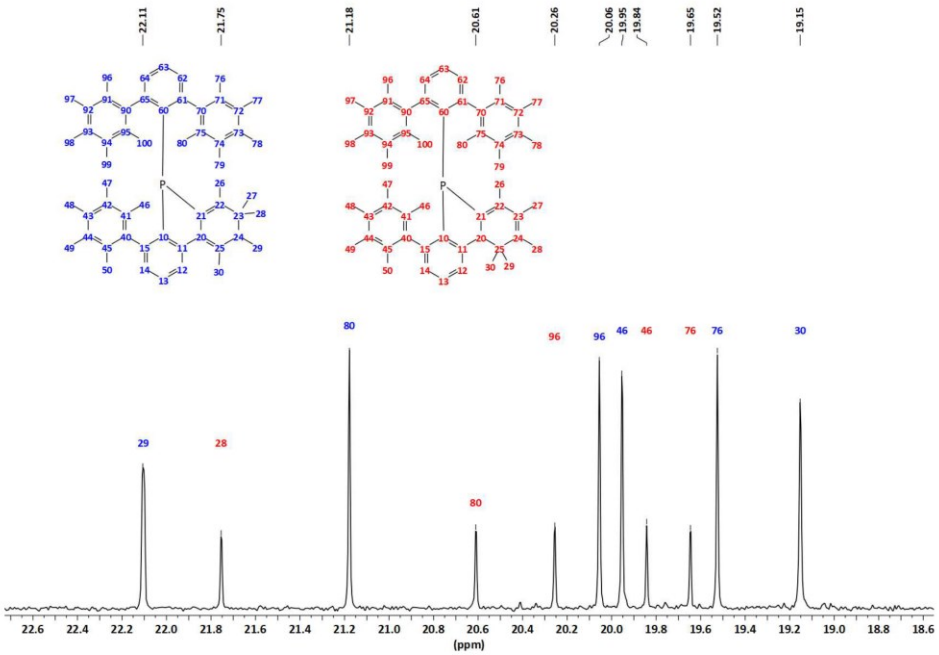

Figure S18. ^{13}C NMR (CD_2Cl_2, 151 MHz) spectrum (detail) of [**5a**]$^+$ and [**7a**]$^+$.

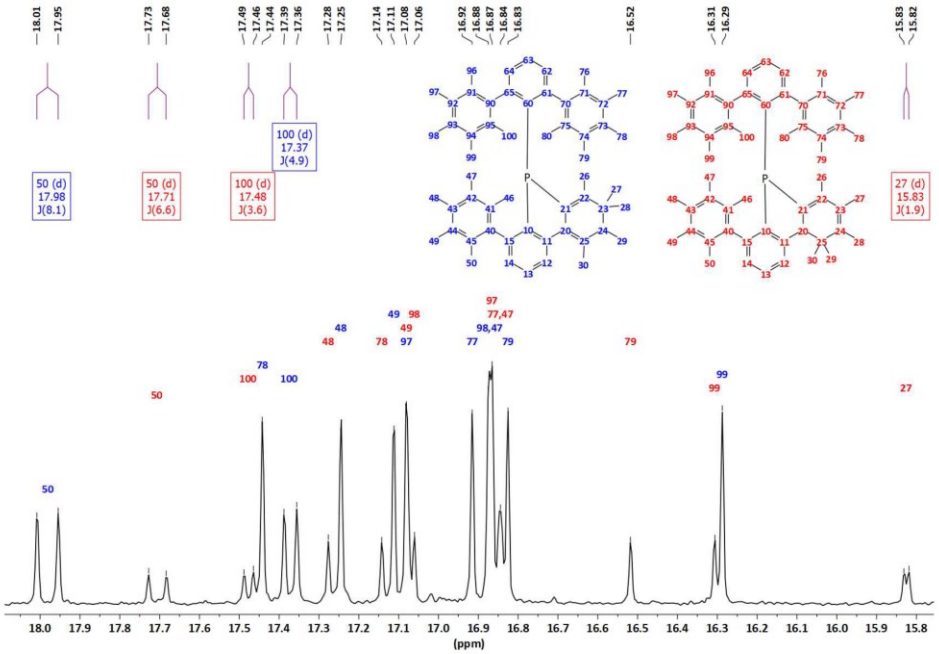

Figure S19. ^{13}C NMR (CD_2Cl_2, 151 MHz) spectrum (detail) of [**5a**]$^+$ and [**7a**]$^+$.

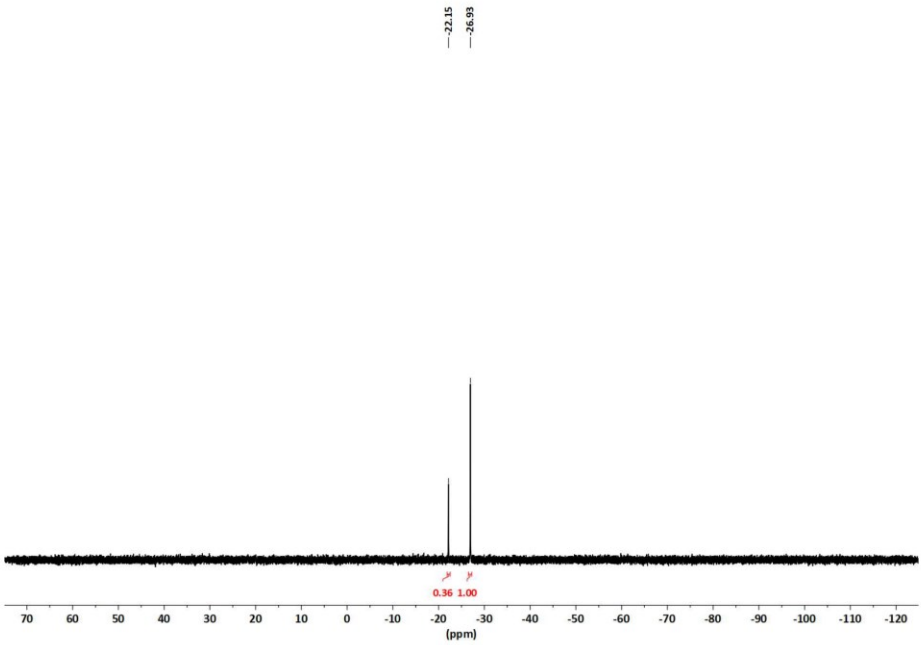

Figure S20. $^{31}P\{1H\}$ NMR (CD_2Cl_2, 243 MHz) spectrum of [**5a**]$^+$ and [**7a**]$^+$.

26

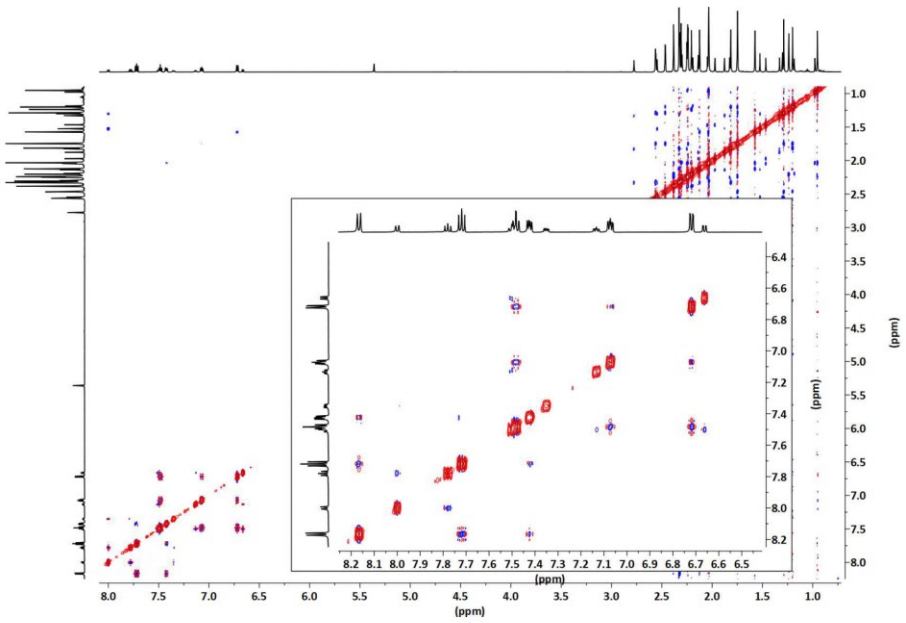

Figure S21. NOESY (CD_2Cl_2, 600 MHz) spectrum showing no exchange between [**5a**]$^+$ and [**7a**]$^+$.(mixing time = 0.2 s).

27

Synthesis and characterization of [5b][AlCl$_4$] (and [7b][AlCl$_4$])

1b (50 mg, 0.06 mmol) and $AlCl_3$ (8 mg, 0.06 mmol) were placed in a Schlenk tube and dry CH_2Cl_2 (4 mL) was added. Upon addition of the solvent the reaction turns immediately deep red. The solution was stirred for 1h at room temperature and after that it was filtered through a syringe filter to remove any insoluble materials that might form. The solution was layered with hexane (20 mL) and after diffusion the solvent was removed. The remaining crystalline solid was dried under vacuum to yield a deep red crystalline solid (58 mg, quantitative yield). NMR analysis indicated that always a mixture of [5b][AlCl$_4$] and [7b][AlCl$_4$] in a molar ratio of *ca.* 0.70:0.30 was obtained. From all crystallization experiments only [5b][AlCl$_4$] produced crystals suitable for single-crystal X-ray structure determination. The identity of [7b][AlCl$_4$] was inferred from NMR spectra.

Major isomer [5b]$^+$:

^{1}H NMR (600 MHz, CD_2Cl_2): δ = 8.20 (d, $^3J(^1H–^1H)$ = 8.30 Hz, 1H, H12), 7.68 (t, $^3J(^1H–^1H)$ = 7.65 Hz, 1H, H13), 7.40 (d, $^3J(^1H–^1H)$ = 8 Hz, 1H, H14), 7.38 (t, $^3J(^1H–^1H)$ = 7.50 Hz, 1H, H63), 7.00 (d, $^3J(^1H–^1H)$ = 7.50 Hz, $^4J(^1H–^1H)$ = 1.30 Hz, 1H, H64), 6.59 (d, $^3J(^1H–^1H)$ = 7.50 Hz, $^4J(^1H–^1H)$ = 1.30 Hz, 1H, H62), 2.53 (s, 3H, H26), 2.48 (s, 3H, H29), 2.36 (s, 3H, H48), 2.29 (s, 3H, H30), 2.28 (s, 3H, H78), 2.27 (s 3H, H98), 2.23 (s, 3H, H49), 2.21 (s, 3H, H97), 2.16 (s, 3H, H47), 2.08 (s, 3H, H46), 2.06 (s, 3H, H79), 1.98 (s, 3H, H99), 1.81 (s, 3H, H77) 1.79 (s, 3H, H96) 1.71 (s, 3H, H27), 1.50 (s, 3H, H80), 1.29 (s, 3H, H28), 1.28 (s, 3H, H50) 1.21 (s, 3H, H76), 0.97 (s, 3H, H100) ppm. **^{13}C NMR (151 MHz, CD_2Cl_2)**: δ = 192.08 (s, C22), 190.71 (s, C24), 179.49 (s, C20), 160.21 (s, C10), 152.75 (s, C65), 150.90 (s, C11), 149.58 (s, C61), 147.62 (s, C15), 146.76 (s, C21), 141.68 (s, C14), 139.74 (s, C90), 139.07 (s, C40), 137.94 (s, C70), 136.52 (s, C43), 135.37 (s, C73), 135.06 (s, C93), 134.80 (s, C25), 134.68 (s, C12), 134.36 (s, C74), 134.18 (s, C45), 133.63 (s, C41), 132.94 (s, C75), 132.84 (s, C71), 132.77 (s, C91), 132.57 (s, C95), 132.54 (s, C60), 132.35 (s, C72), 132.31 (s, C94), 132.22 (s, C62), 132.14 (s, C42), 131.83 (s, C44), 131.71 (s, C92), 131.38 (s, C13 and C63), 131.12 (s, C64), 54.27 (s, C23), 30.95 (s, C28), 27.05 (s, C29), 24.46 (s, C27), 22.46 (s, C26), 21.15 (s, C80), 20.00 (s, C50), 19.88 (s, C30), 19.85 (s, C96), 19.48 (s, C76), 18.42 (s, C46), 17.50 (s, C78), 17.30 (s, C48), 17.24 (s, C100), 17.19 (s, C98), 17.13 (s, C47), 16.95 (s, C49), 16.91 (s, C77), 16.85 (s, C97), 16.73 (s, C79), 16.32 (s, C99) ppm.

Minor isomer [7b]$^+$:

^{1}H NMR (600 MHz, CD_2Cl_2): *δ* = 7.96 (d, $^3J(^1H–^1H)$ = 7.80 Hz, H12), 7.73 (t, $^3J(^1H–^1H)$ = 7.80 Hz, H13), 7.37 (m, H63), 7.33 (d, $^3J(^1H–^1H)$ = 7.80 Hz, H14), 7.04 (dd, $^3J(^1H–^1H)$ = 7.50 Hz, $^4J(^1H–^1H)$ = 1.30 Hz, H64), 6.54 ($^3J(^1H–^1H)$ = 7.50 Hz, $^4J(^1H–^1H)$ = 1.30 Hz, H62), 2.78 (s, 3H,

H26), 2.53 (s, 3H, H28), 2.36 (s, 3H, H48), 2.31 (s, 3H, H27), 2.28 (s, 3H, H78), 2.27 (s, 3H, H98), 2.23 (s, 3H, H49), 2.22 (s, 3H, H97), 2.15 (s, 3H, H47), 2.11 (s, 3H, H50), 2.10 (s, 3H, H99), 1.92 (s, 3H, H79), 1.85 (s, 6H, H77 and H96), 1.50 (s, 3H, H30), 1.41 (s, 3H, H80), 1.32 (s, 3H, H29), 1.32 (s, 3H, H76), 1.24 (s, 3H, H46), 0.95 (s, 3H, H100) ppm. **^{13}C{^{1}H} NMR (151 MHz, CD_2Cl_2)**: *δ* = 196.62 (s, C20), 190.75 (s, C24), 183.96 (s, C22), 154.97 (s, C10), 152.94 (s, C65), 150.71 (s, C11), 150.31 (s, C21), 150.24 (s, C61), 147.62 (s, C15), 139.85 (s, C90), 139.42 (s, C40), 139.39 (s, C14), 137.80 (s, C70), 136.46 (s, C43), 135.56 (s, C23), 135.42 (s, C73), 135.14 (s, C93), 134.15 (s, C45), 133.63 (s, C41), 132.84 (s, C95 and C72), 132.77 (s, C75), 132.57 (s, C94), 132.47 (s, C74), 132.39 (s, C62), 132.16 (s, C71), 132.14 (s, C91), 131.92 (s, C42), 131.89 (s, C44), 131.71 (s, C60), 131.46 (s, C64), 131.42 (s, C92), 131.38 (s, C63) 130.87 (s. C13), 130.87 (s, C12), 53.59 (s, C25), 35.91 (s, C29), 30.56 (s, C26), 25.36 (s, C30), 22.11 (s, C28), 20.78 (s, C80), 20.00 (s, C50 and C96), 19.62 (s, C76), 18.24 (s, C46), 17.31 (s, C78), 17.26 (s, C48), 17.19 (s, C98), 17.16 (s, C100), 17.13 (s, C47), 17.09 (s, C99), 16.95 (s, C49), 16.85 (s, C97), 16.73 (s, C77), 16.41 (s, C79), 15.93 (s, C27) ppm.

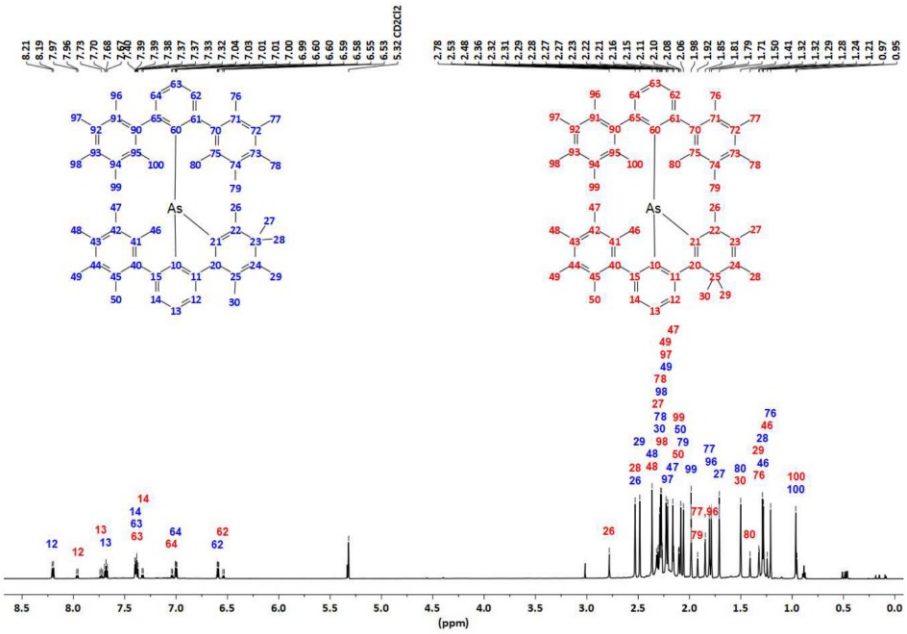

Figure S22. ^{1}H NMR (CD_2Cl_2, 600 MHz) spectrum of **[5b]**$^+$ and **[7b]**$^+$.

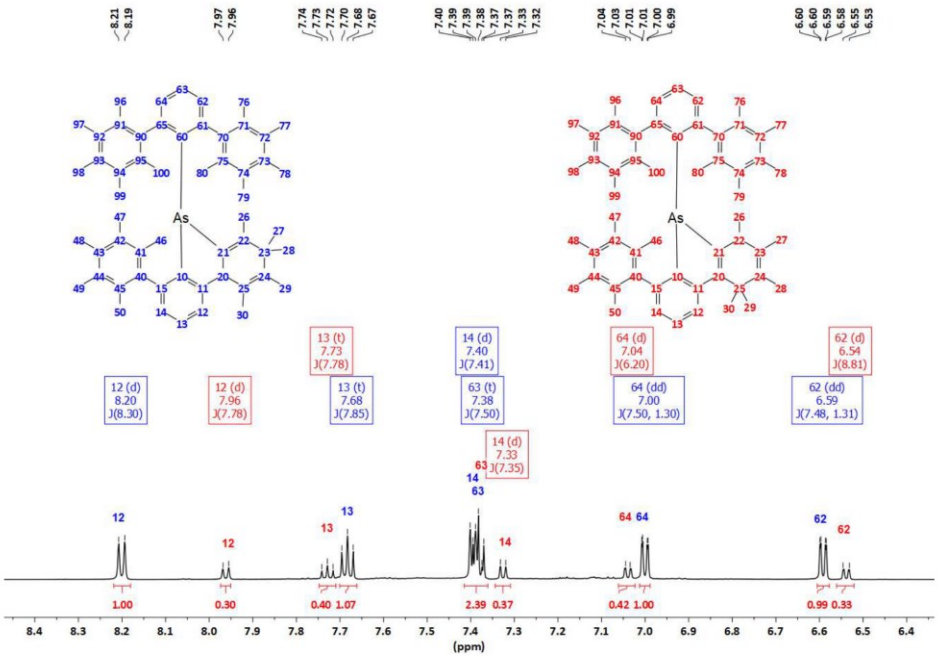

Figure S23. ^{1}H NMR (CD_2Cl_2, 600 MHz) spectrum (detail) of **[5b]**$^+$ and **[7b]**$^+$.

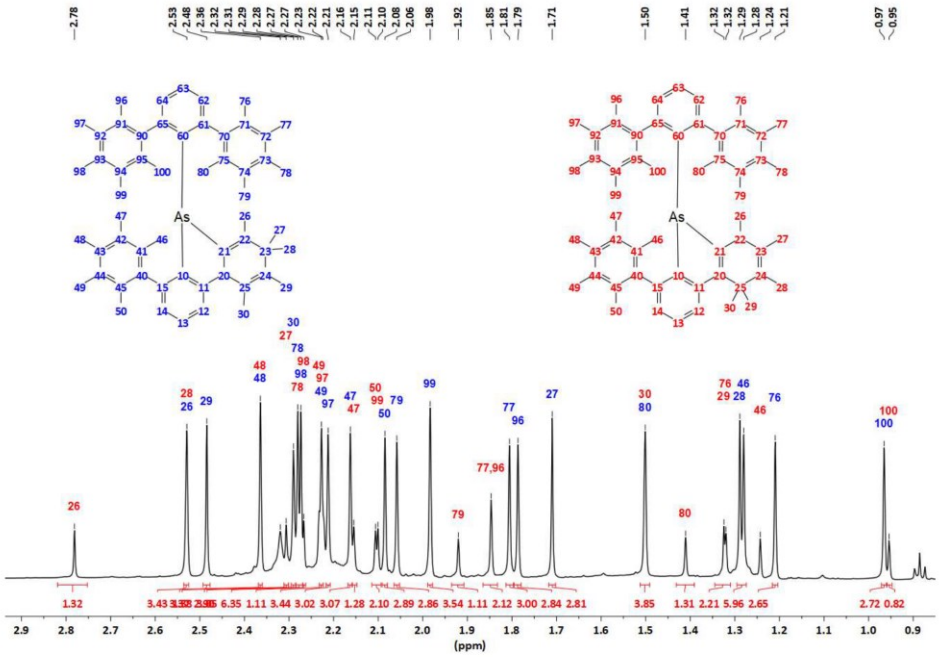

Figure S24. ^{1}H NMR (CD_2Cl_2, 600 MHz) spectrum (detail) of [**5b**]$^{+}$ and [**7b**]$^{+}$.

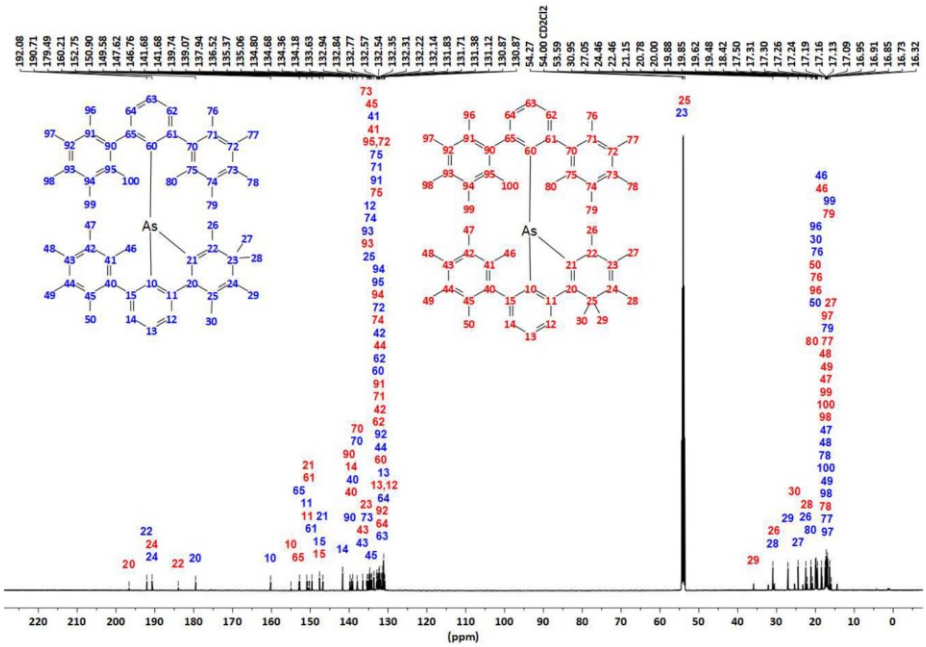

Figure S25. ^{13}C NMR (CD_2Cl_2, 151 MHz) spectrum of [**5b**]$^{+}$ and [**7b**]$^{+}$.

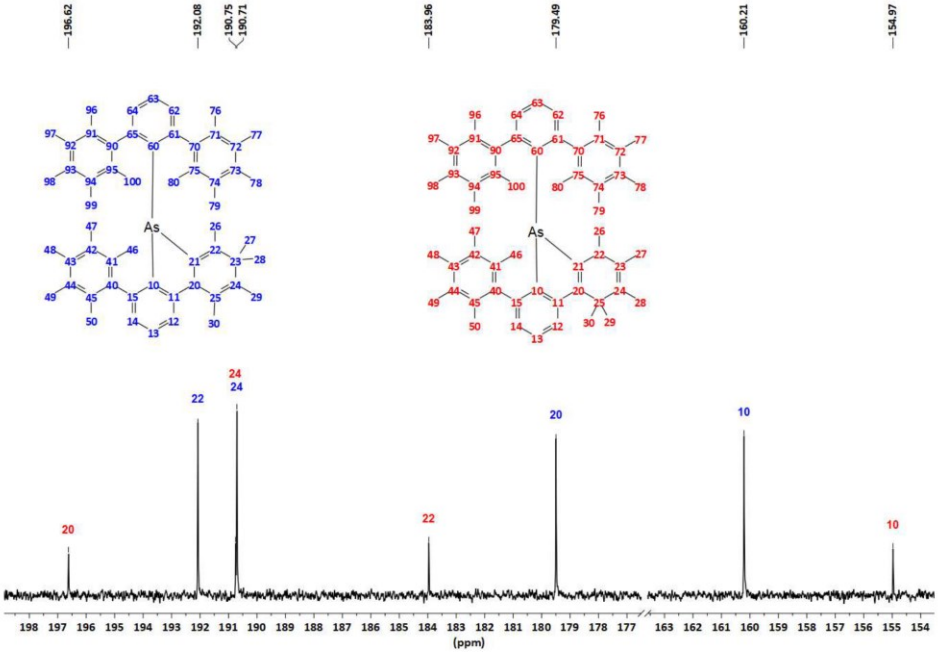

Figure S26. ^{13}C NMR (CD_2Cl_2, 151 MHz) spectrum (detail) of [**5b**]$^+$ and [**7b**]$^+$.

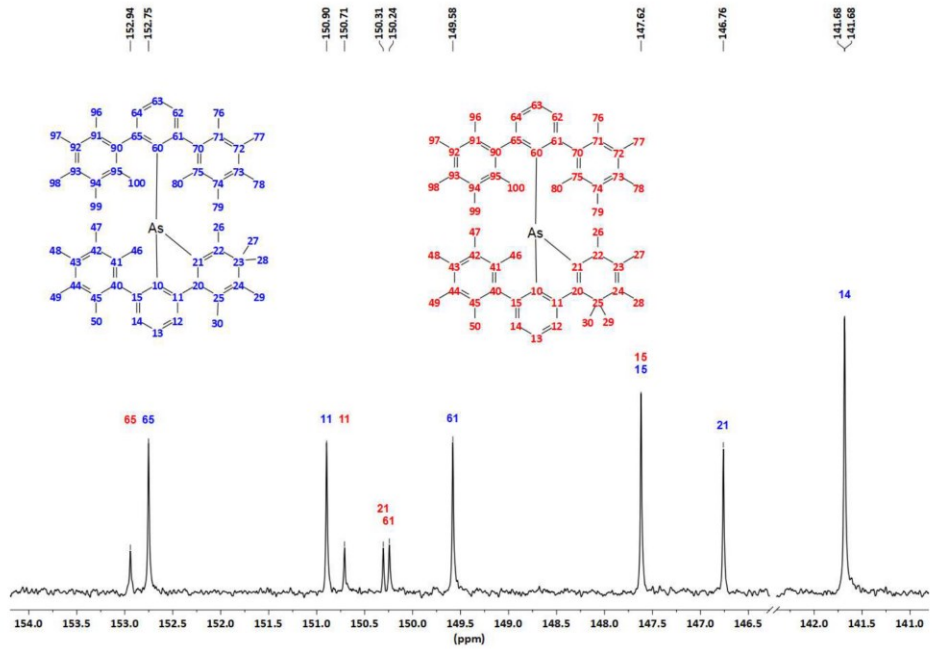

Figure S27. ^{13}C NMR (CD_2Cl_2, 151 MHz) spectrum (detail) of [**5b**]$^+$ and [**7b**]$^+$.

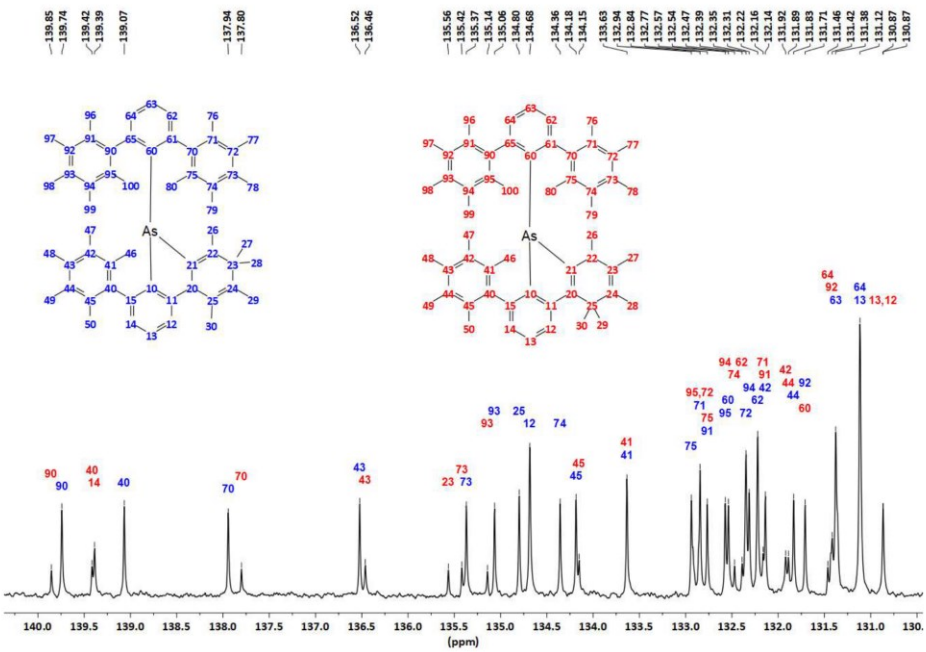

Figure S28. ^{13}C NMR (CD_2Cl_2, 151 MHz) spectrum (detail) of [**5b**]$^+$ and [**7b**]$^+$.

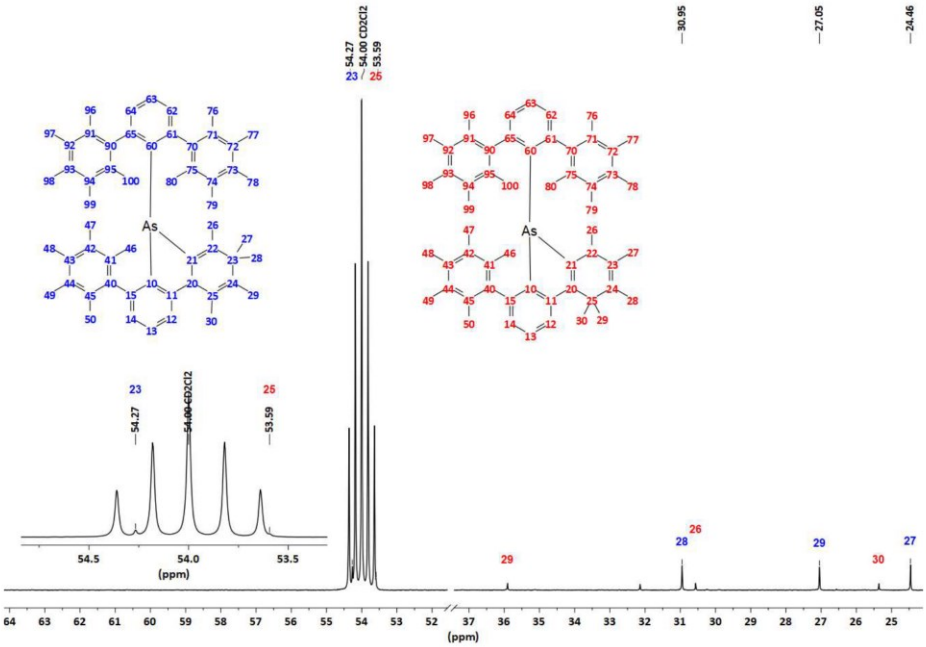

Figure S29. ^{13}C NMR (CD_2Cl_2, 151 MHz) spectrum (detail) of [**5b**]$^+$ and [**7b**]$^+$.

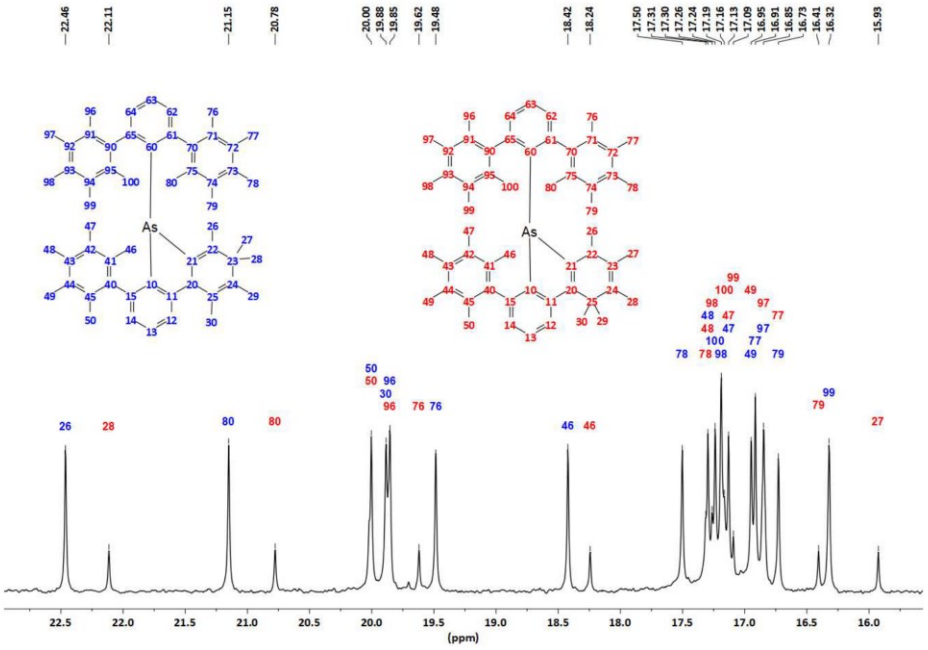

Figure S30. ^{13}C NMR (CD_2Cl_2, 151 MHz) spectrum (detail) of [**5b**]$^+$ and [**7b**]$^+$.

Synthesis and characterization of [8a][AlCl$_4$]

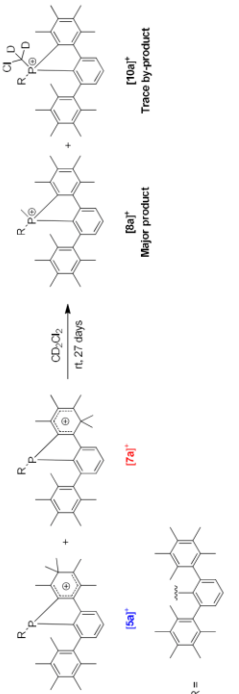

A J. Young NMR tube charged with a mixture of [**5a**][AlCl$_4$] and [**7a**][AlCl$_4$] (29 mg), in CD_2Cl_2 (0.6 mL) was allowed to stand under argon at room temperature in ambient light for *ca.* 1 month during which time the reaction was monitored by NMR spectroscopy.[§] Compound [**8a**][AlCl$_4$] was the major product that was observed. A minor byproduct ([**10a**]$^+$) formed as well. Crystals suitable for single crystal X-ray diffraction (20 mg) were grown by diffusing hexane into the CD_2Cl_2 solution. Neither multiple re-crystallizations nor other attempts (including chromatography) were successful at obtaining [**8a**][AlCl$_4$] as a pure compound. **^{1}H NMR (600 MHz, CD_2Cl_2)**: δ = 7.89 (dd, $^3J(^1H–^1H)$ = 8 Hz, $^4J(^1H–^{31}P)$ = 3 Hz, 1H, H12), 7.76 (m, 1H, H13), 7.74 (dd, $^3J(^1H–^1H)$ = 8 Hz, $^5J(^1H–^{31}P)$ = 2 Hz, 1H, H63), 7.28 (ddd, $^3J(^1H–^1H)$ = 8 Hz, $^4J(^1H–^1H)$ = 5 Hz, $^4J(^1H–^{31}P)$ = 2 Hz, 1H, H64), 7.03 (ddd, $^3J(^1H–^1H)$ = 8 Hz, $^4J(^1H–^1H)$ = 5 Hz, $^4J(^1H–^{31}P)$ = 2 Hz, 1H, H62), 6.84 (ddd, $^3J(^1H–^1H)$ = 8 Hz, $^4J(^1H–^1H)$ = 5 Hz, $^4J(^1H–^{31}P)$ = 1 Hz, 1H, H14), 2.36 (s, 3H, H48), 2.34 (s, 6H, H29, H28), 2.32 (s, 3H, H26), 2.28 (s, 3H, H98), 2.25 (s, 3H, H27), 2.22 (s, 3H, H99), 2.19 (s, 3H, H47), 2.18 (s, 6H, H49, H78), 2.05 (s, 3H, H77), 2.00 (s, 3H, H97), 1.77 (s, 3H, H100), 1.74 (s, 3H, H46), 1.66 (s, 3H, H79), 1.39 (s, 3H, H76), 1.34 (s, 3H, H50), 1.27 (d, $^4J(^1H–^{31}P)$ = 13 Hz, 3H, H1), 1.26 (s, 3H, H80), 1.11 (s, 3H, H96) ppm. **$^{13}C\{^1H\}$ NMR (151 MHz, CD_2Cl_2)**: δ = 152.57 (d, $^2J(^{13}C–^{31}P)$ = 11 Hz, C61), 152.41 (d, $^2J(^{13}C–^{31}P)$ = 11 Hz, C65), 149.82 (d, $^2J(^{13}C–^{31}P)$ = 10 Hz, C15), 149.41 (d, $^2J(^{13}C–^{31}P)$ = 20 Hz, C11), 144.80 (d, $^4J(^{13}C–^{31}P)$ = 3 Hz, C24), 138.82 (d, $^2J(^{13}C–^{31}P)$ = 18 Hz, C20), 137.51 (d, $^3J(^{13}C–^{31}P)$ = 11 Hz, C23), 137.14 (s, C43), 136.90 (s, C93), 136.89 (d, $^3J(^{13}C–^{31}P)$ = 3 Hz, C40), 136.31 (d, $^3J(^{13}C–^{31}P)$ = 2 Hz, C90), 136.28 (s, C22), 136.25 (s, C73), 135.78 (d, $^4J(^{13}C–^{31}P)$ = 2 Hz, C13), 135.51 (d, $^3J(^{13}C–^{31}P)$ = 4 Hz, C70), 135.04 (s, C42), 134.92 (d, $^4J(^{13}C–^{31}P)$ = 3 Hz, C63), 134.24 (s, C94), 134.21 (d, $^3J(^{13}C–^{31}P)$ = 10 Hz, C64), 134.18 (d, $^3J(^{13}C–^{31}P)$ = 10 Hz, C25), 134.14 (d, $^3J(^{13}C–^{31}P)$ = 9 Hz, C62), 133.86 (s, C44), 133.30 (s,

[§] A control reaction was ran in parallel in complete darkness. The progression of this reaction was significantly slower, and formation of the P-methylated product appeared to be inhibited.

C74), 133.22 (s, C71), 133.17 (s, C45, C92), 133.09 (d, $^{3}J(^{13}C–^{31}P)$ = 11 Hz, C14), 132.79 (s, C95), 132.68 (s, C75), 132.52 (s, C41), 132.18 (s, C72), 131.81 (s, C91), 125.47 (d, $^{3}J(^{13}C–^{31}P)$ = 10 Hz, C12), 123.05 (d, $^{1}J(^{13}C–^{31}P)$ = 83 Hz, C21), 122.45 (d, $^{1}J(^{13}C–^{31}P)$ = 85 Hz, C10), 116.34 (d, $^{1}J(^{13}C–^{31}P)$ = 82 Hz, C60), 22.51 (d, $^{3}J(^{13}C–^{31}P)$ = 7 Hz, C26), 20.14 (s, C100), 19.76 (d, C46, C76), 19.61 (s, C80), 19.26 (s, C29), 19.23 (s, C50), 18.25 (s, C28), 17.93 (s, C96), 17.40 (s, C78), 17.16 (s, C48), 17.13 (s, C98), 16.98 (s, C77), 16.95 (s, C27, C47), 16.86 (s, C49), 16.80 (s, C99), 16.30 (s, C79), 16.80 (s, C97), 10.30 (d, $^{1}J(^{13}C–^{31}P)$ = 49 Hz, C1) ppm. **$^{31}P\{^{1}H\}$ NMR (243 MHz, CD_2Cl_2)**: δ = 21.68 ppm. **HRMS ESI (m/z)**: $[M]^+$ calculated for $C_{56}H_{66}P$, 769.48967; found, 769.48911; $[M–CH_3+CD_2Cl]^+$ calculated. for $C_{56}H_{66}D_2PCl$, 805.46325; found, 805.46278.

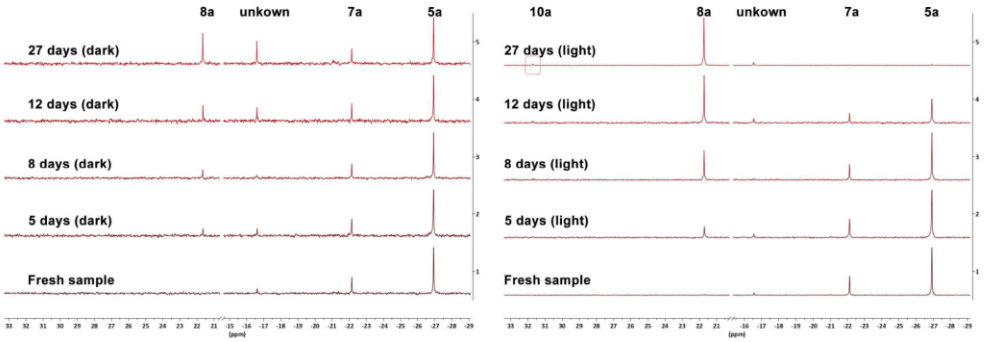

Figure S31. ^{31}P NMR (CD_2Cl_2, 600 MHz) spectra showing the conversion progress of a mixture of [**5a**]$^+$ and [**7a**]$^+$ into [**8a**]$^+$.

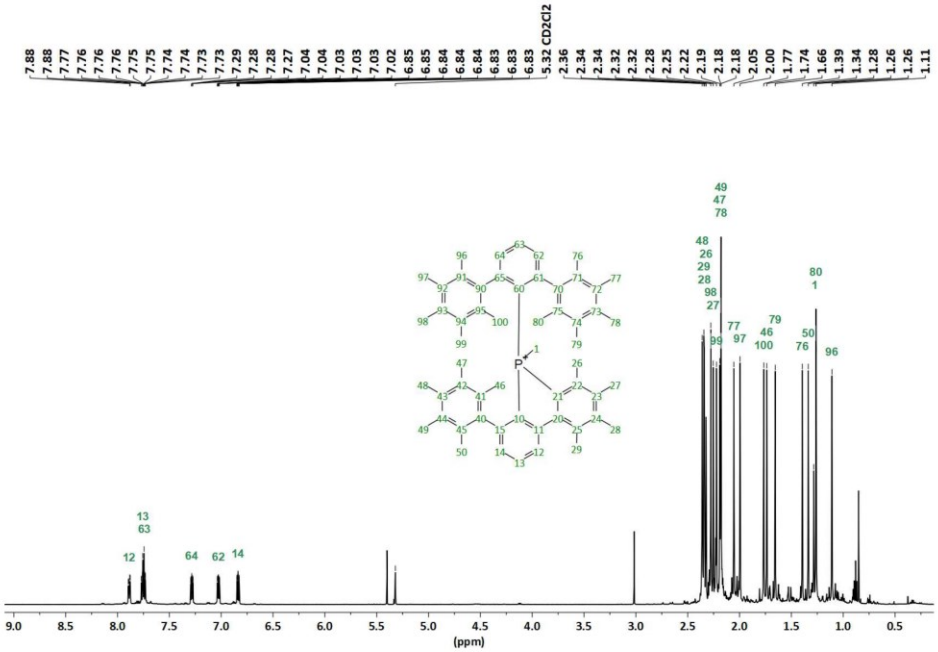

Figure S32. ^{1}H NMR (CD_2Cl_2, 600 MHz) spectrum (full) of [**8a**]$^{+}$.

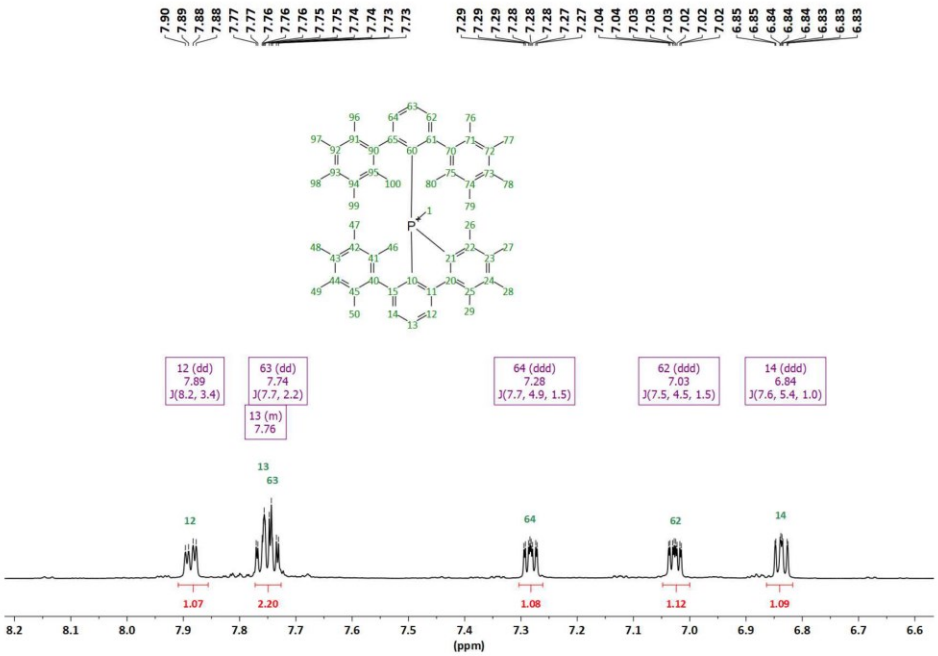

Figure S33. ^{1}H NMR (CD_2Cl_2, 600 MHz) spectrum (detail) of [**8a**]$^{+}$.

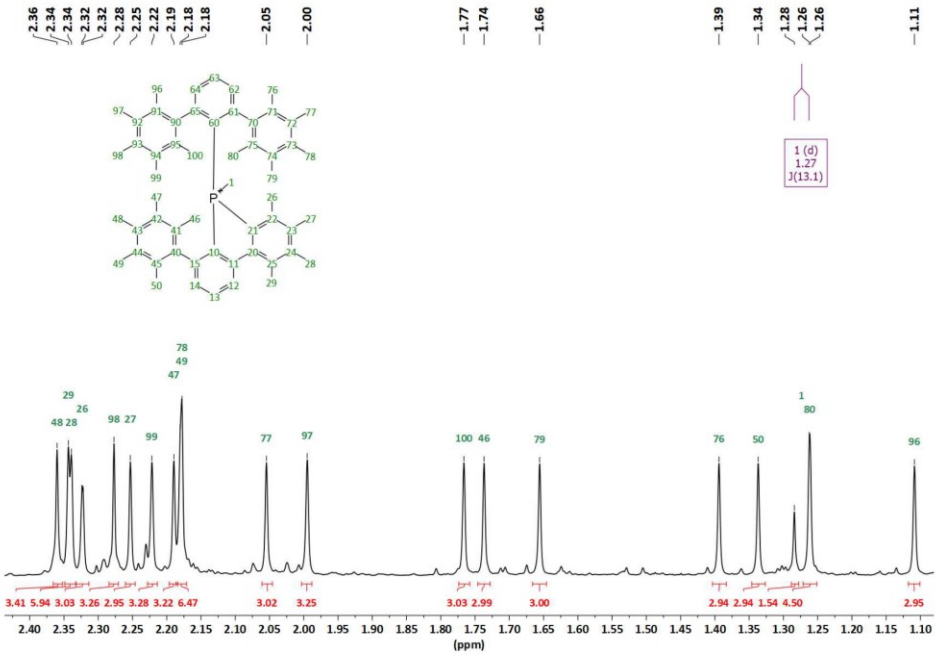

Figure S34. ^{1}H NMR (CD_2Cl_2, 600 MHz) spectrum (detail) of [**8a**]$^{+}$.

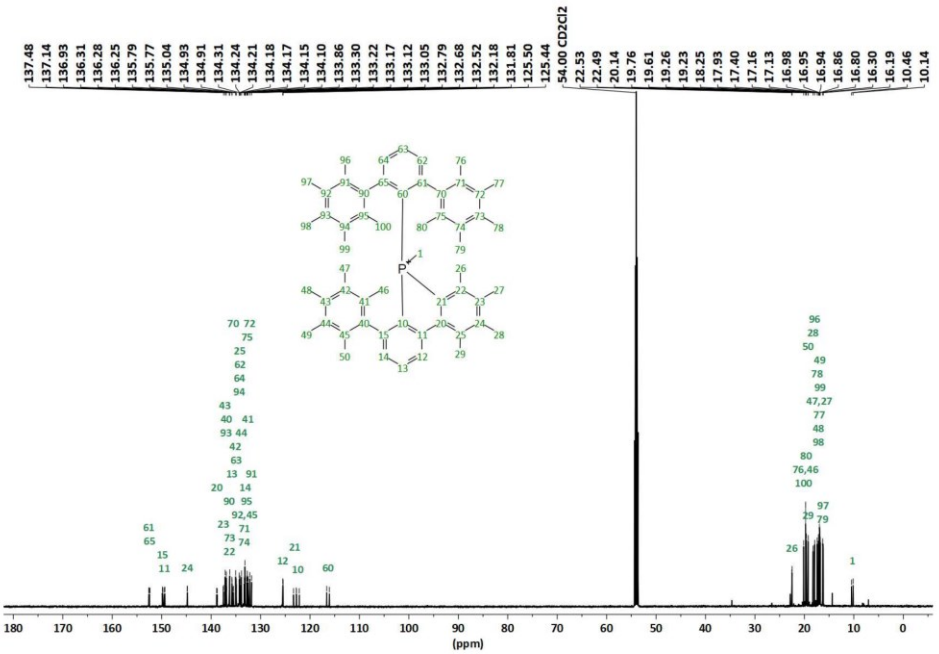

Figure S35. $^{13}C\{^{1}H\}$ NMR (CD_2Cl_2, 151 MHz) spectrum (full) of [**8a**]$^{+}$.

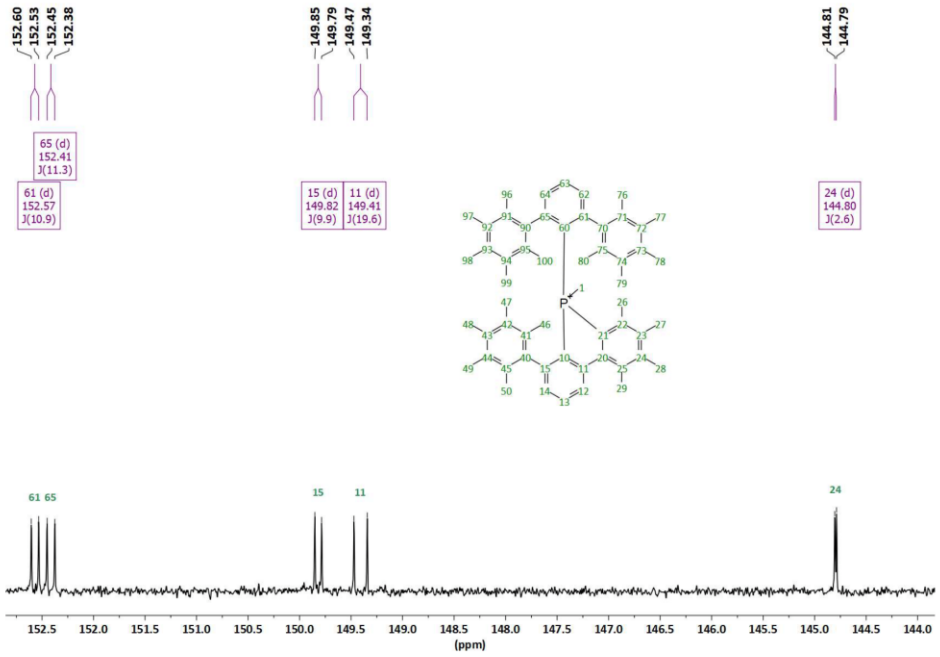

Figure S36. $^{13}C\{^{1}H\}$ NMR (CD_2Cl_2, 151 MHz) spectrum (detail) of [**8a**]$^+$.

46

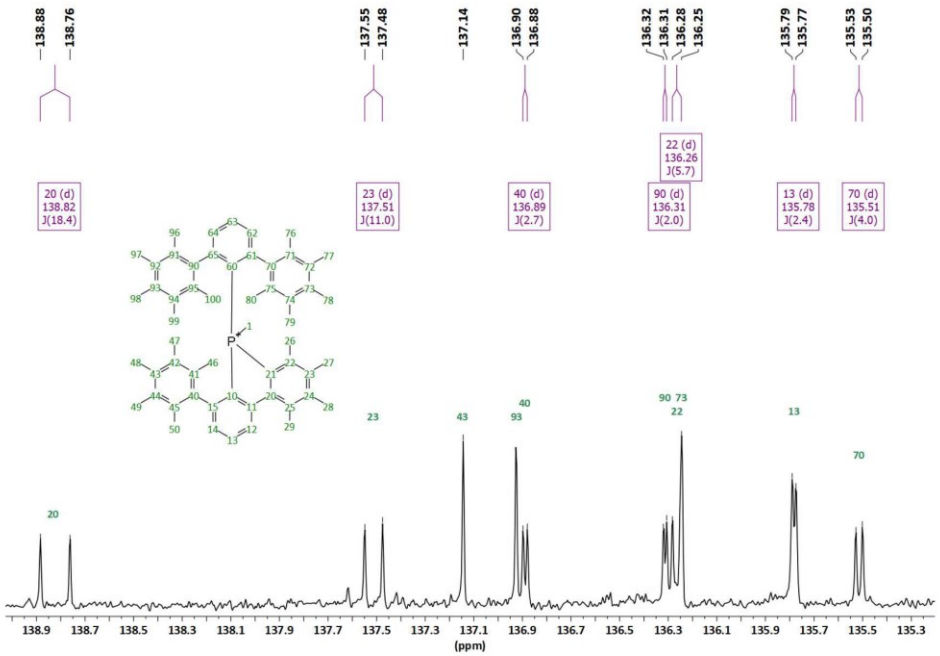

Figure S37. $^{13}C\{^{1}H\}$ NMR (CD_2Cl_2, 151 MHz) spectrum (detail) of [**8a**]$^+$.

47

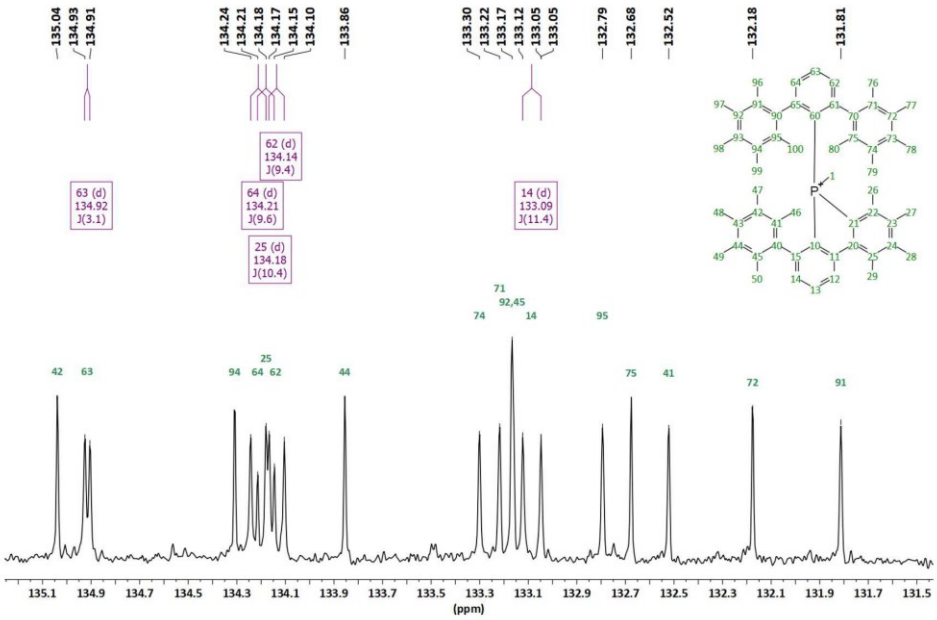

Figure S38. $^{13}C\{^{1}H\}$ NMR (CD_2Cl_2, 151 MHz) spectrum (detail) of **[8a]**$^{+}$.

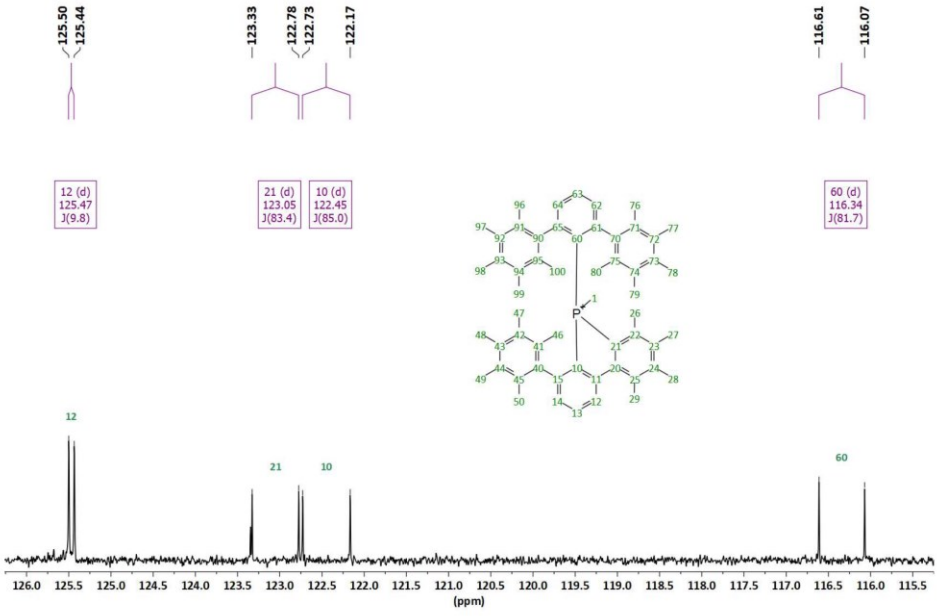

Figure S39. $^{13}C\{^{1}H\}$ NMR (CD_2Cl_2, 151 MHz) spectrum (detail) of **[8a]**$^{+}$.

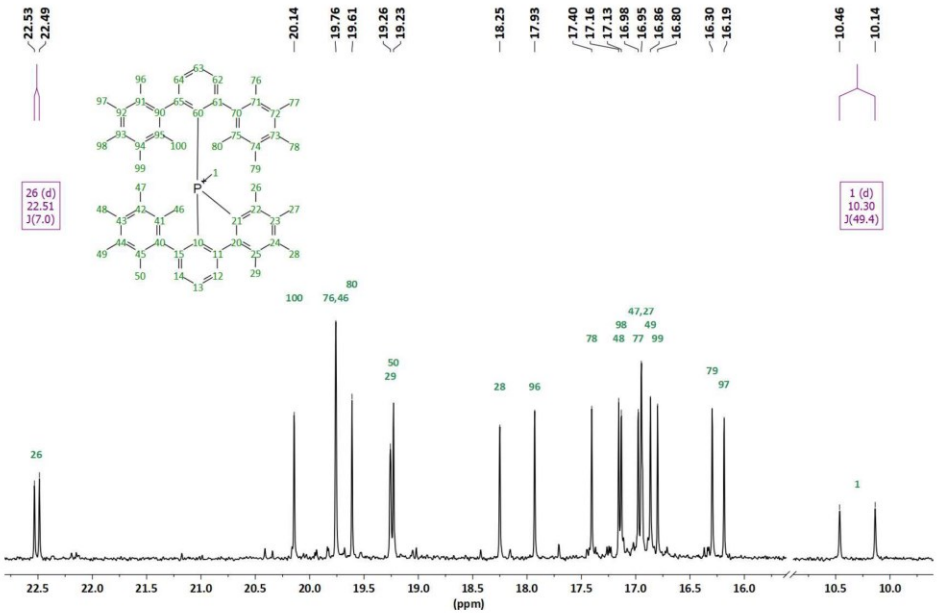

Figure S40. $^{13}C\{^{1}H\}$ NMR (CD_2Cl_2, 151 MHz) spectrum (detail) of [**8a**]$^+$.

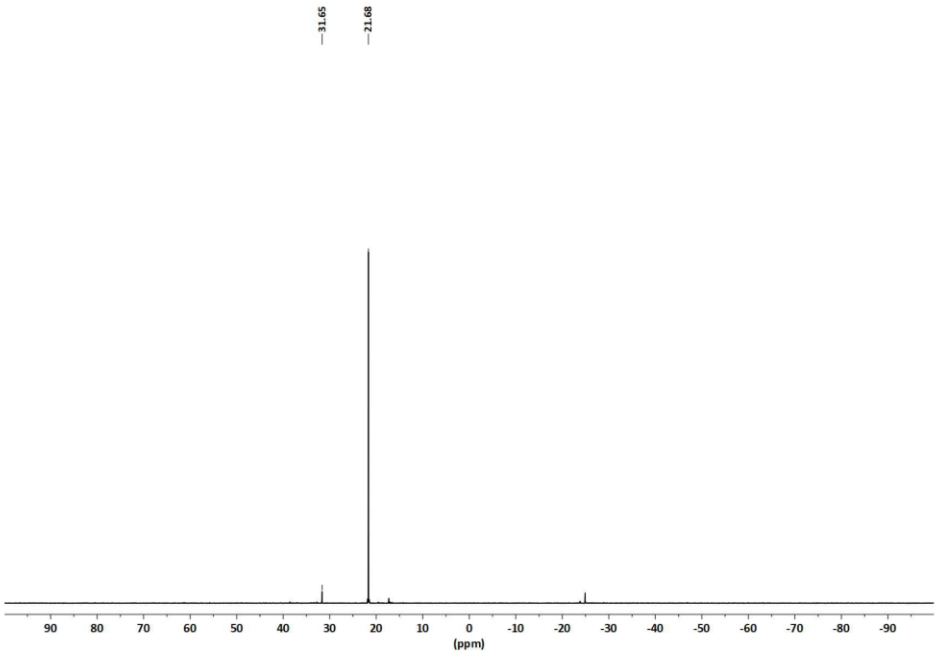

Figure S41. $^{31}P\{^{1}H\}$ NMR (CD_2Cl_2, 243 MHz) spectrum of [**8a**]$^+$. A minor by-product ([**10a**]$^+$) is visible at δ = 31.65 ppm.

Synthesis and characterization of 9a

A J. Young NMR tube was charged with a mixture of [5a][AlCl4] and [7a][AlCl4] (24 mg) and THF-*d8* (0.5 mL). The solution discoloured to pale red (at higher dilutions it became pale yellow). After NMR spectra were recorded, the solution was diluted with THF (2 mL) and hexane (10 mL) and filtered through a short plug of aluminium oxide. Crystals suitable (16 mg) for single crystal X-ray diffraction were grown by slow evaporation of a solution of **9a** in CH_2Cl_2 and hexane. Neither multiple re-crystallizations nor other attempts (including chromatography) were successful in obtaining **9a** as a pure compound. **^{1}H NMR (600 MHz, THF-*d8*)**: δ = 7.35 (d, $^3J(^1H–^1H)$ = 8 Hz, $^5J(^1H–^{31}P)$ = 1 Hz, 1H, H12), 7.25 (td, $^3J(^1H–^1H)$ = 7 Hz, $^5J(^1H–^{31}P)$ = 1 Hz, 1H, H63), 7.23 (t, $^3J(^1H–^1H)$ = 8 Hz, 1H, H13), 6.88 (ddd, $^3J(^1H–^1H)$ = 8 Hz, $^4J(^1H–^1H)$ = 5 Hz, $^5J(^1H–^{31}P)$ = 2 Hz, 1H, H64), 6.57 (ddd, $^3J(^1H–^1H)$ = 7 Hz, $^4J(^1H–^1H)$ = 5 Hz, $^5J(^1H–^{31}P)$ = 1 Hz, 1H, H14), 6.49 (dd, $^2J(^1H–^1H)$ = 20 Hz, $^4J(^1H–^{31}P)$ = 3 Hz, 1H, H62), 4.79 ($^3J(^1H–^1H)$ = 8 Hz, $^5J(^1H–^{31}P)$ = 2 Hz, 2H, H26), 2.31 (s, 3H, H48), 2.21 (s, 3H, H98), 2.17 (s, 3H, H99), 2.16 (s, 3H, H49), 2.14 (s, 3H, H47), 2.11 (s, 3H, H78), 2.00 (s, 6H, H50, H97), 1.95 (s, 3H, H77), 1.92 (s, 3H, H79), 1.85 (s, 3H, H27), 1.79 (s, 3H, H28), 1.70 (s, 3H, H100), 1.45 (s, 6H, H76, H80), 1.19 (s, 3H, H46), 1.07 (s, 3H, H30), 1.05 (s, 3H, H29), 0.93 (s, 3H, H96) ppm. **^{13}C{^{1}H} NMR (151 MHz, THF-*d8*)**: δ = 155.23 (d, $^2J(^{13}C–^{31}P)$ = 44 Hz, C65), 152.46 (d, $^2J(^{13}C–^{31}P)$ = 7 Hz, C61), 150.92 (d, $^2J(^{13}C–^{31}P)$ = 3 Hz, C20), 149.44 (d, $^2J(^{13}C–^{31}P)$ = 13 Hz, C11), 148.57 (d, $^2J(^{13}C–^{31}P)$ = 21 Hz, C15), 142.91 (d, $^1J(^{13}C–^{31}P)$ = 5 Hz, C10), 142.58 (s, br, C40), 141.78 (d, $^3J(^{13}C–^{31}P)$ = 7 Hz, C90), 141.69 (d, $^2J(^{13}C–^{31}P)$ = 15 Hz, C22), 140.50 (s, C24), 140.30 (d, $^1J(^{13}C–^{31}P)$ = 5 Hz, C21), 139.81 (s, C70), 134.77 (s, C43), 134.54 (s, C71), 173.06 (s, C73), 133.88 (s, C93), 133.58 (s, C41), 133.03 (s, C42), 132.96 (s, br, C44, C95), 132.83 (s, C45), 132.26 (s, C75), 132.04 (s, C74), 132.01 (d, $^1J(^{13}C–^{31}P)$ = 29 Hz, C60), 131.92 (s, C94), 131.81 (s, C62),131.43 (s, C92), 131.40 (s, C91), 131.28 (s, C72), 130.62 (d, $^1J(^{13}C–^{31}P)$ = 9 Hz, C64), 130.22 (d, $^4J(^{13}C–^{31}P)$ = 1 Hz, C63) 129.54 (d, $^3J(^{13}C–^{31}P)$ = 6 Hz, C14), 128.47 (s, C13), 124.59 (d, $^3J(^{13}C–^{31}P)$ = 4 Hz, C23), 123.18 (s, C12), 110.10 (d, $^3J(^{13}C–^{31}P)$ = 18 Hz, C26), 41.12 (s, C25), 28.16 (s, br, C30), 24.76 (d, $^4J(^{13}C–^{31}P)$ = 2 Hz, C29), 20.73 (s, C80), 20.25 (s, C100), 19.87 (s, C50), 19.59 (s, C76), 17.69 (d,$^5J(^{13}C–^{31}P)$ = 4 Hz, C46), 17.61 (d,$^5J(^{13}C–^{31}P)$ = 7 Hz, C96), 17.12 (s, C48), 17.09 (s, C47), 17.08 (s, C78), 16.95 (s, C98), 16.84 (s, C49), 16.76 (s, C99), 16.74 (s, C77), 16.44 (s, C79), 16.42 (s, C97), 15.75 (s, C28), 14.98 (d, $^4J(^{13}C–^{31}P)$ = 3 Hz, C27) ppm. **^{31}P{1H} NMR (243 MHz, THF-*d8*)**: δ = −24.23 (s) ppm. **HRMS ESI (*m/z*)**: $[M–H]^+$ calculated. for $C_{66}H_{64}P$,767.47402; found, 767.47264.

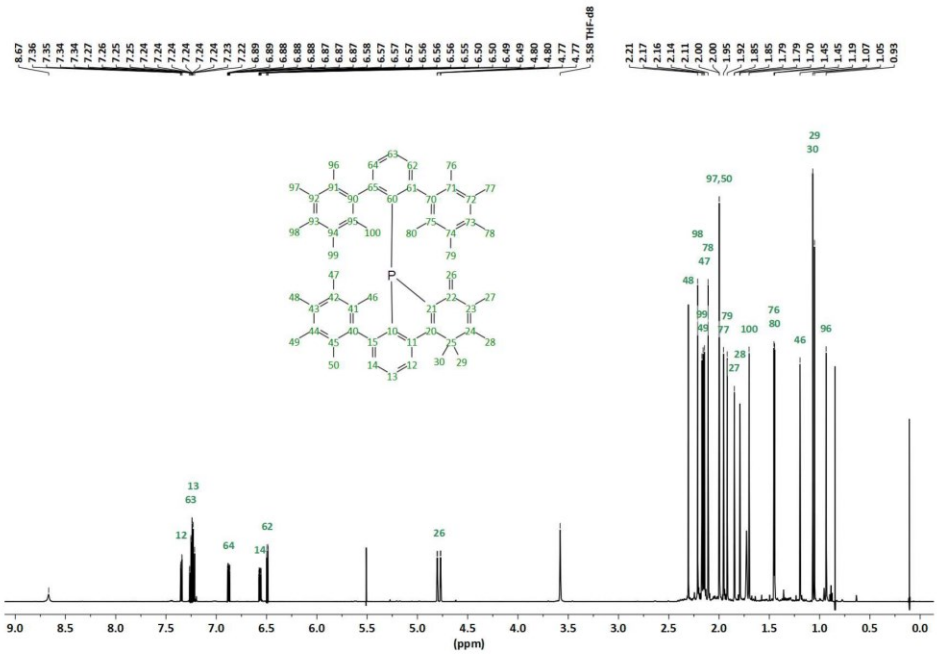

Figure S42. ^{1}H NMR (CD_2Cl_2, 600 MHz) spectrum (full) of **9a**.

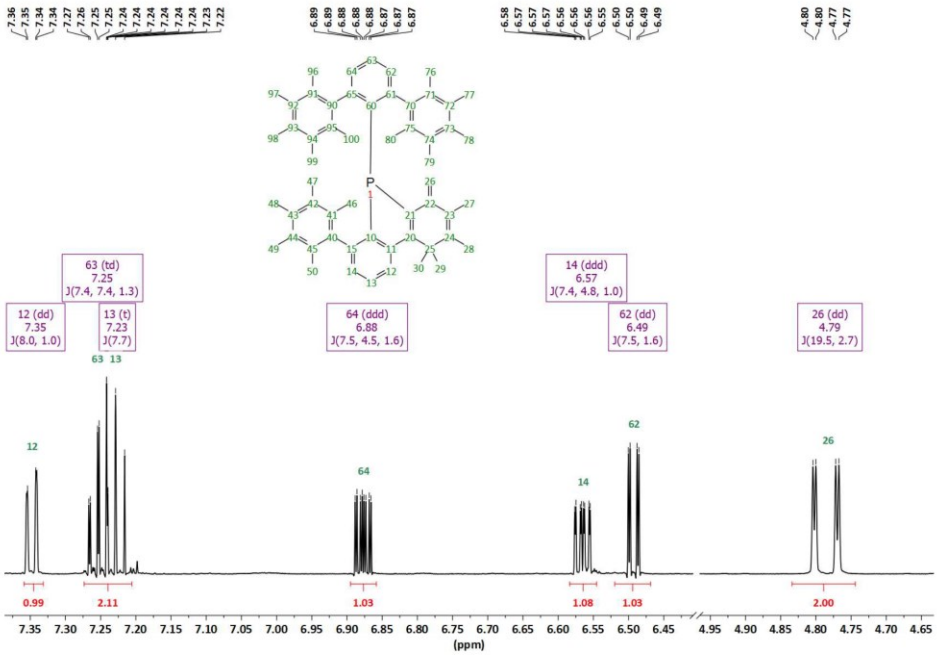

Figure S43. ^{1}H NMR (CD_2Cl_2, 600 MHz) spectrum (detail) of **9a**.

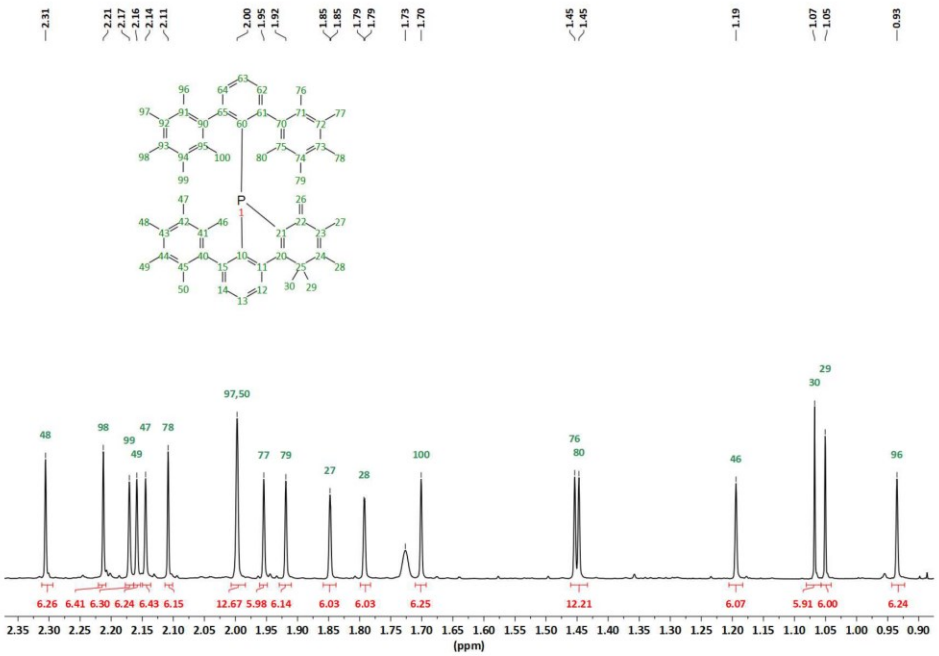

Figure S44. ^{1}H NMR (CD_2Cl_2, 600 MHz) spectrum (detail) of **9a**.

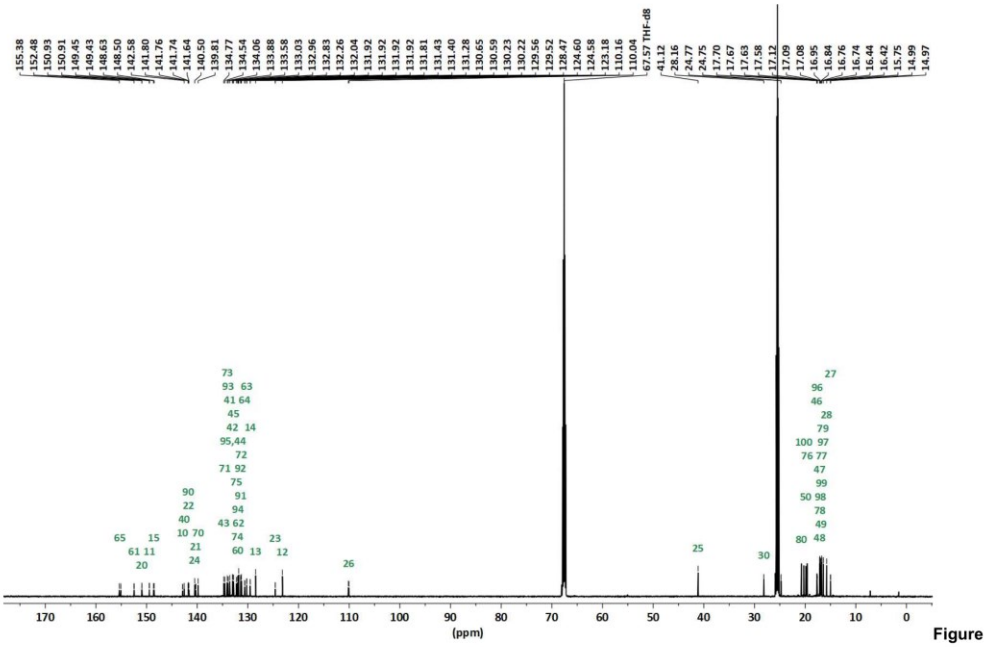

Figure S45. $^{13}C\{^{1}H\}$ NMR (CD_2Cl_2, 151 MHz) spectrum (full) of **9a**.

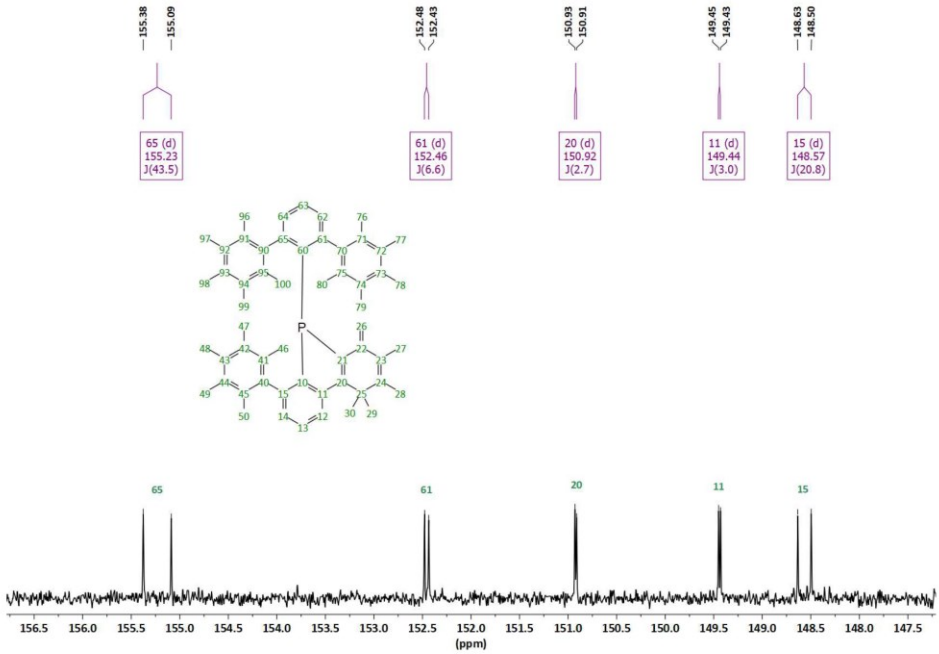

Figure S46. $^{13}C\{^{1}H\}$ NMR (CD_2Cl_2, 151 MHz) spectrum (detail) of **9a**.

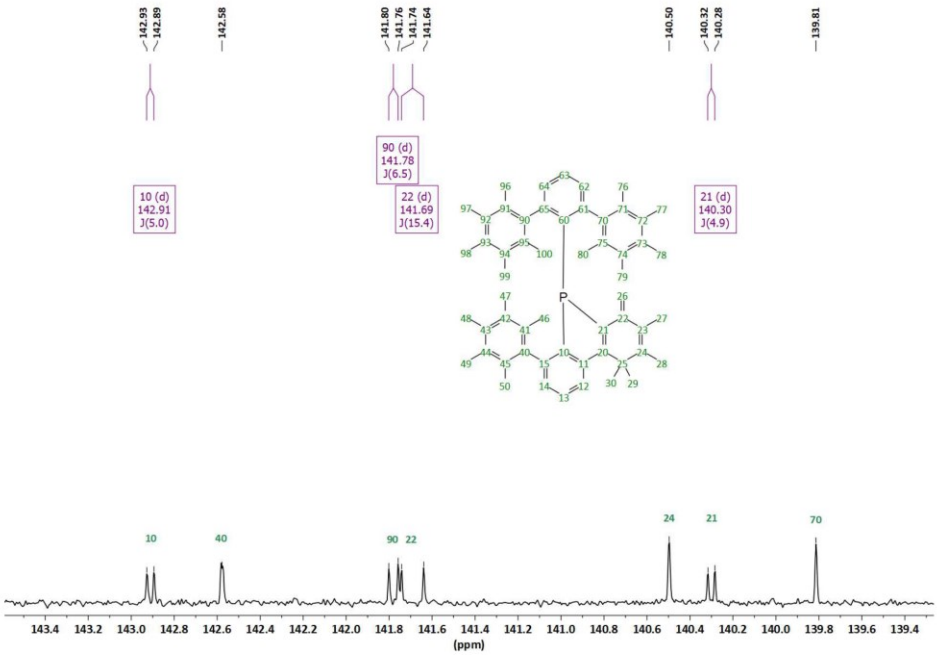

Figure S47. $^{13}C\{^{1}H\}$ NMR (CD_2Cl_2, 151 MHz) spectrum (detail) of **9a**.

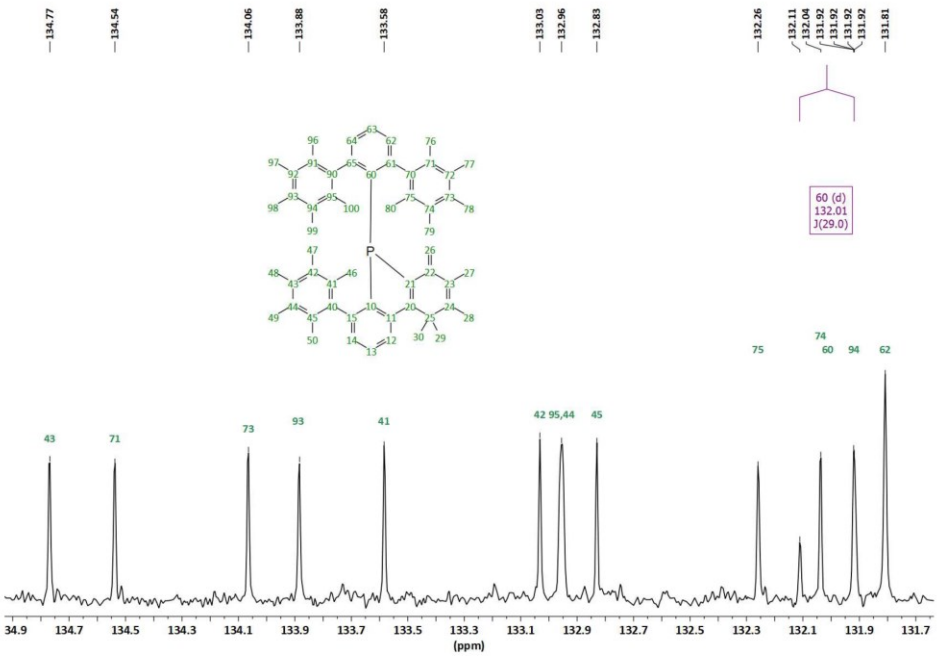

Figure S48. $^{13}C\{^{1}H\}$ NMR (CD_2Cl_2, 151 MHz) spectrum (detail) of **9a**.

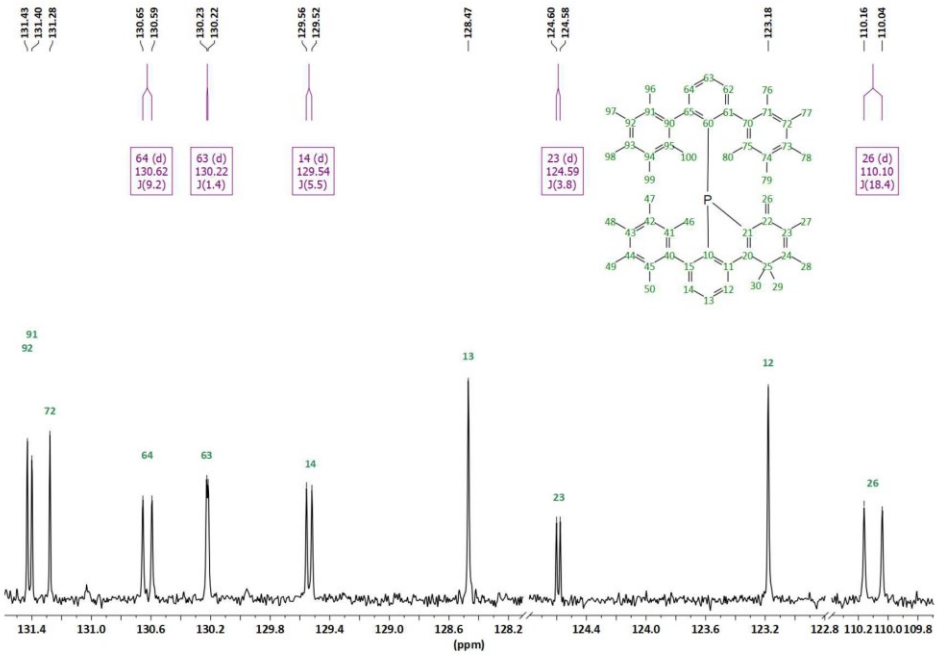

Figure S49. $^{13}C\{^{1}H\}$ NMR (CD_2Cl_2, 151 MHz) spectrum (detail) of **9a**.

60

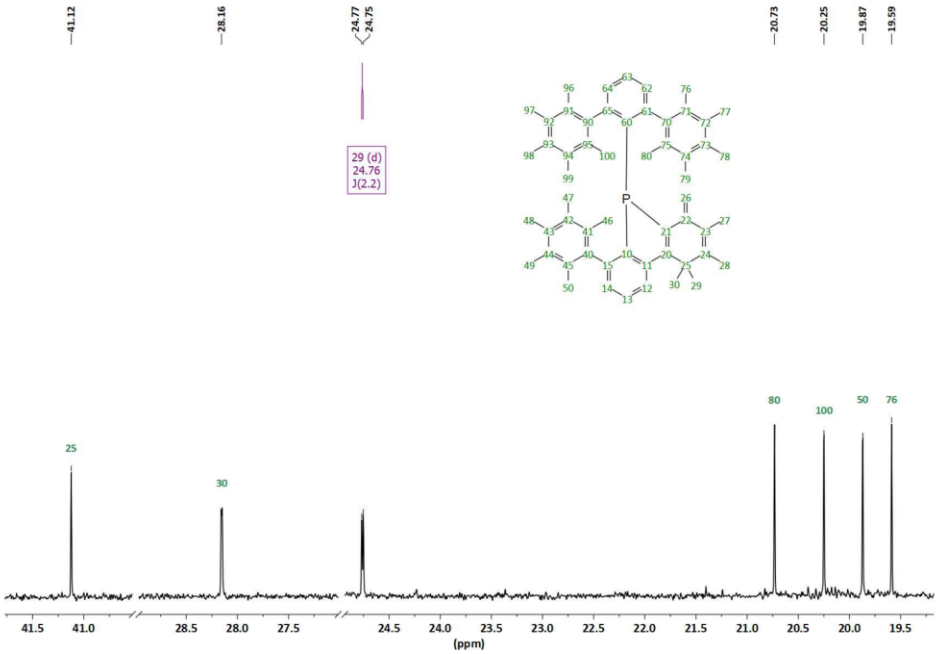

Figure S50. $^{13}C\{^{1}H\}$ NMR (CD_2Cl_2, 151 MHz) spectrum (detail) of **9a**.

61

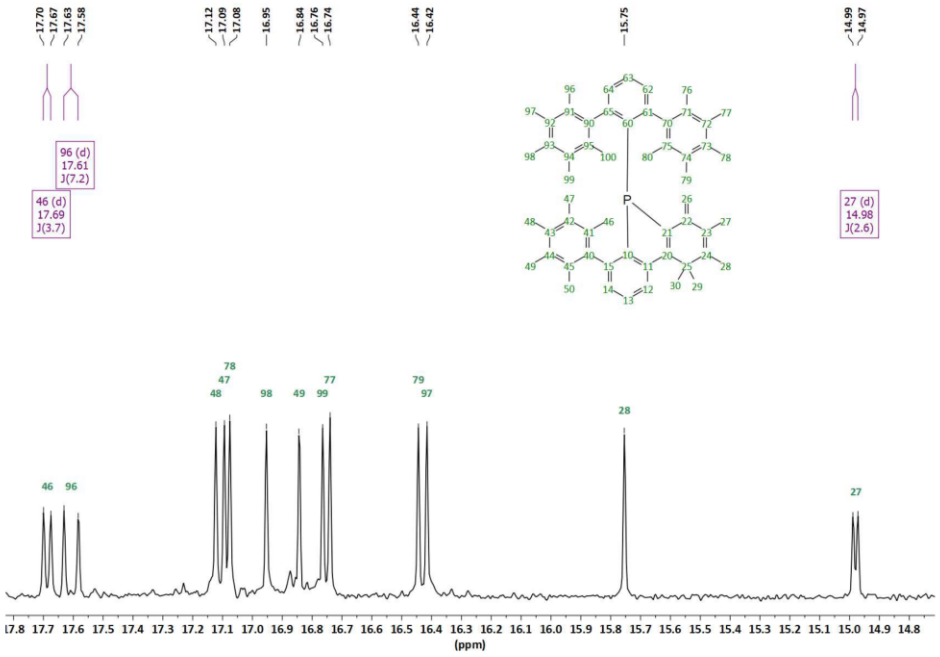

Figure S51. $^{13}C\{^{1}H\}$ NMR (CD_2Cl_2, 151 MHz) spectrum (detail) of **9a**.

62

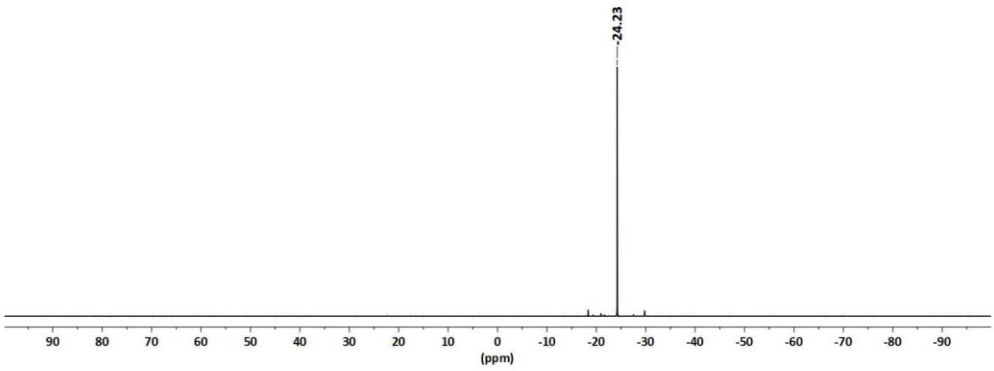

Figure S52. $^{31}P\{^{1}H\}$ NMR (CD_2Cl_2, 243 MHz) spectrum of **9a**.

63

Synthesis and characterization of 9b

A mixture of [5b][AlCl4] and [7b][AlCl4] (50 mg, 0.05 mmol) was added to a Schlenk tube and to this dry THF (4 mL) was added. The mixture was stirred for 1h at room temperature and then layered with hexane (40 mL). After diffusion the remaining solution was filtered and washed with water (3×40 mL). The solution was slowly evaporated to yield **9b** as pale orange crystalline solid (27 mg, 65%). Crystals suitable for X-ray diffraction measurement were grown by evaporation of a heptane solution. **Mp** 285–290 °C (decomp.). **^{1}H-NMR (600 MHz, THF-*d8*)**: δ = 7.29 (d, $^3J(^1H–^1H)$ = 7.60 Hz, 1H, H12), 7.24 (t, $^3J(^1H–^1H)$ = 7.60 Hz, 1H, H13), 7.23 (t, $^3J(^1H–^1H)$ = 7.50 Hz, 1H, H63), 6.85 (dd, $^3J(^1H–^1H)$ = 7.50 Hz, $^4J(^1H–^1H)$ = 1.50 Hz, 1H, H64), 6.63 (d, $^3J(^1H–^1H)$ = 7.60 Hz, 1H, H14), 6.46 (dd, $^3J(^1H–^1H)$ = 7.50 Hz, $^4J(^1H–^1H)$ = 1.50 Hz, 1H, H62), 4.84(s, 1H, H26), 4.61 (s, 1H, H26), 2.33 (s, 3H, H48), 2.27 (s, 3H, H98), 2.21 (s, 3H, H78), 2.18 (s, 3H, H47), 2.15 (s, 3H, H49), 2.11 (s, 3H, H77), 2.05 (s, 3H, H46), 2.00 (s, 3H, H99), 1.95 (s, 3H, H79), 1.91 (s, 3H, H97), 1.83 (s, 3H, H27), 1.79 (s, 3H, H28), 1.76 (s, 3H, H96), 1.46 (s, 3H, H80), 1.42 (s, 3H, H76), 1.31 (s, 3H, H50), 1.12 (s, 3H, H29), 1.03 (s, 3H, H30), 0.92 (s, 3H, H100) ppm. **^{13}C{^{1}H}-NMR (151 MHz, THF-*d8*)**: δ = 152.56 (s, C65), 152.47 (s, C20), 151.29 (s, C61), 150.83 (s, C11), 148.05 (s, C15), 145.64 (s, C10), 143.95 (s, C21), 142.41 (s, C22), 142.01 (s, C40), 141.73 (s, C90), 141.42 (s, C24), 139.41 (s, C70), 136.08 (s, C60), 134.70 (s, C43), 134.16 (s, C74), 133.92 (s, C93 and C73), 133.11 (s, C44), 132.96 (s, C41), 132.77 (s, C45), 132.63 (s, C95), 132.28 (s, C91), 132.19 (s, C92), 131.84 (s, C42), 131.66 (s, C72), 131.58 (s, C64), 131.28 (s, C94), 131.22 (s, C71), 131.14 (s, C75), 129.66 (s, C62), 129.21 (s, C63), 128.88 (s, C14), 128.08 (s, C13), 123.97 (s, C12), 123.30 (s, C23), 109.84 (s, C26), 41.23 (s, C25), 28.10 (s, C29), 24.86 (s, C30), 20.63 (s, C76), 19.72 (s, C96), 19.64 (s, C46), 19.28 (s, C80), 17.90 (s, C50), 17.11 ((s, C48 and C100), 17.09 (s, C49), 17.04 (s, C77), 17.02 (s, C98), 16.83 (s, C78), 16.80 (s, C47), 16.57 (s, C79), 16.33 (s, C99), 16.24 (s, C97), 15.99 (s, C28), 14.70 (s, C27) ppm. **HRMS ESI (m/z):** $[M+H]^+$ calculated for $C_{56}H_{66}As$ 813.43750; found 813.43640.

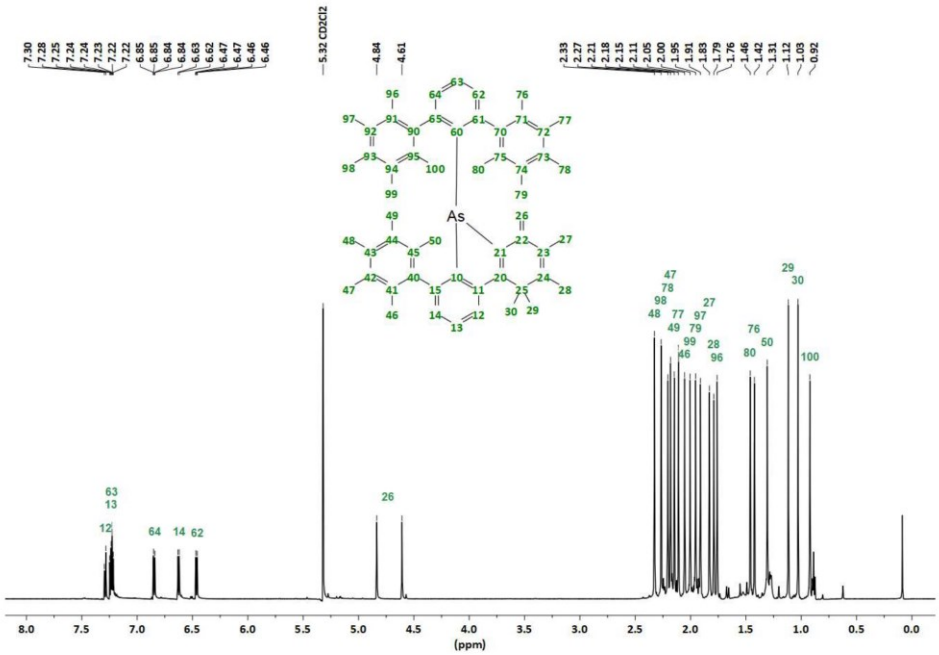

Figure S53. ^{1}H NMR (CD_2Cl_2, 600 MHz) spectrum (full) of **9b**.

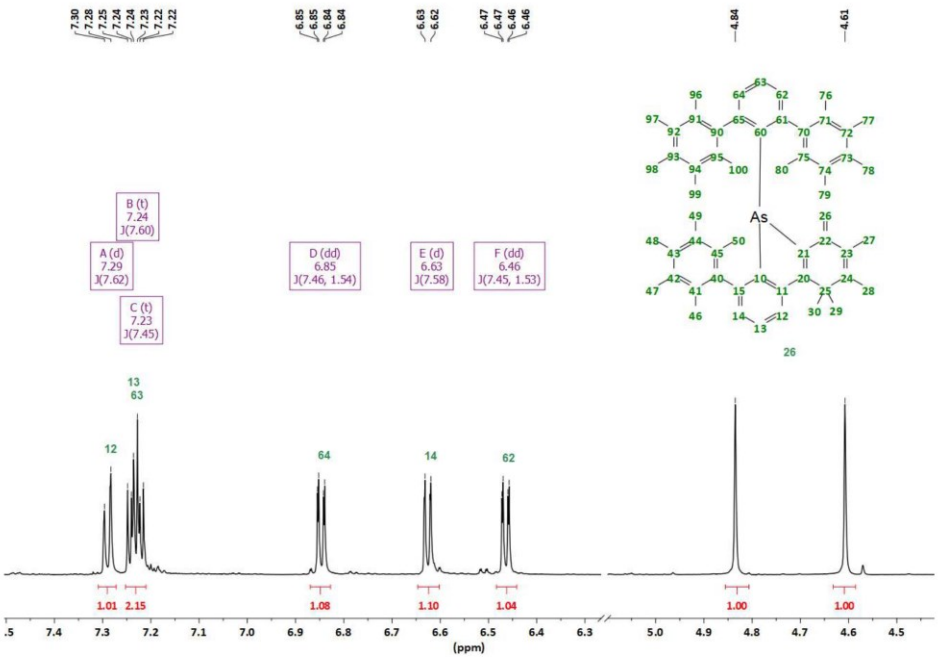

Figure S54. ^{1}H NMR (CD_2Cl_2, 600 MHz) spectrum (detail) of **9b**.

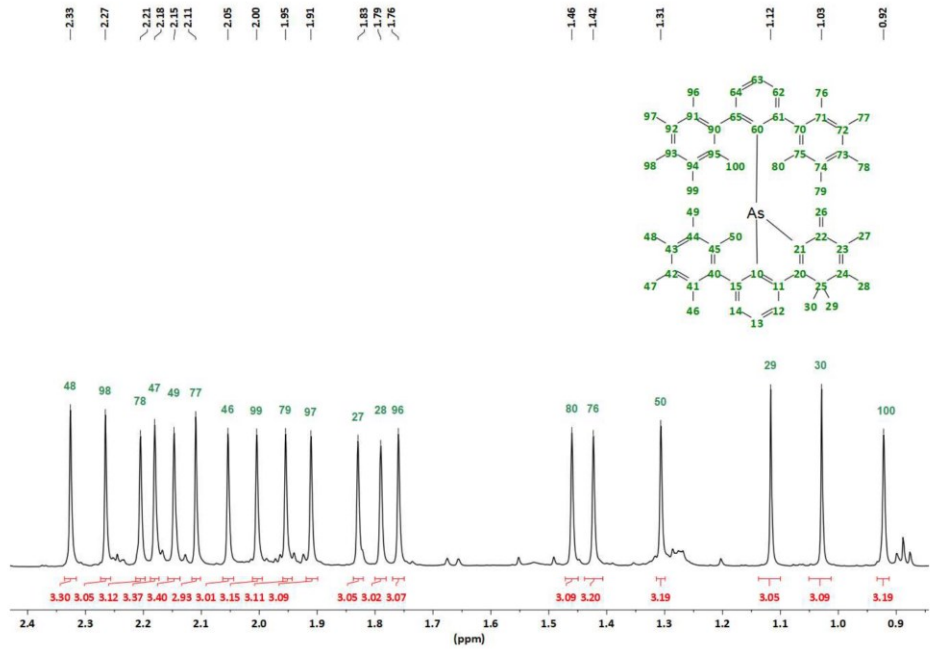

Figure S55. ^{1}H NMR (CD_2Cl_2, 600 MHz) spectrum (detail) of **9b**.

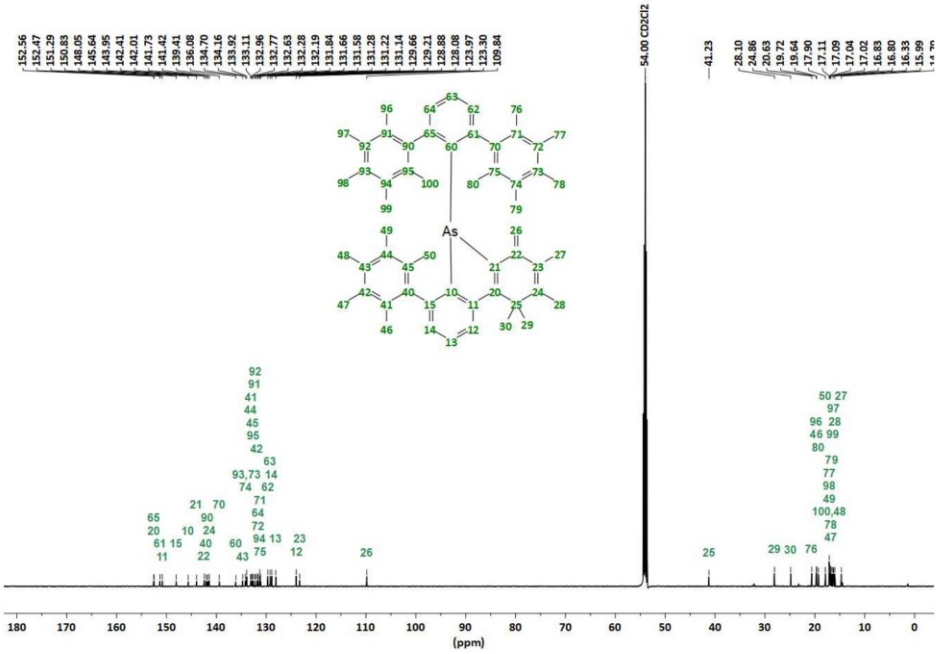

Figure S56. $^{13}C\{^{1}H\}$ NMR (CD_2Cl_2, 151 MHz) spectrum (full) of **9b**.

68

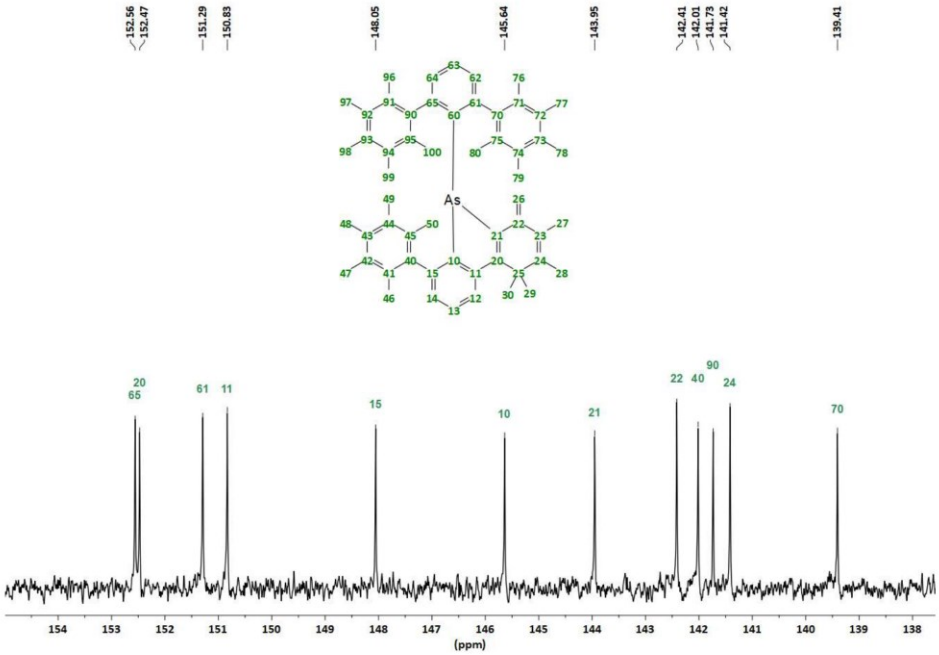

Figure S57. $^{13}C\{^{1}H\}$ NMR (CD_2Cl_2, 151 MHz) spectrum (detail) of **9b**.

69

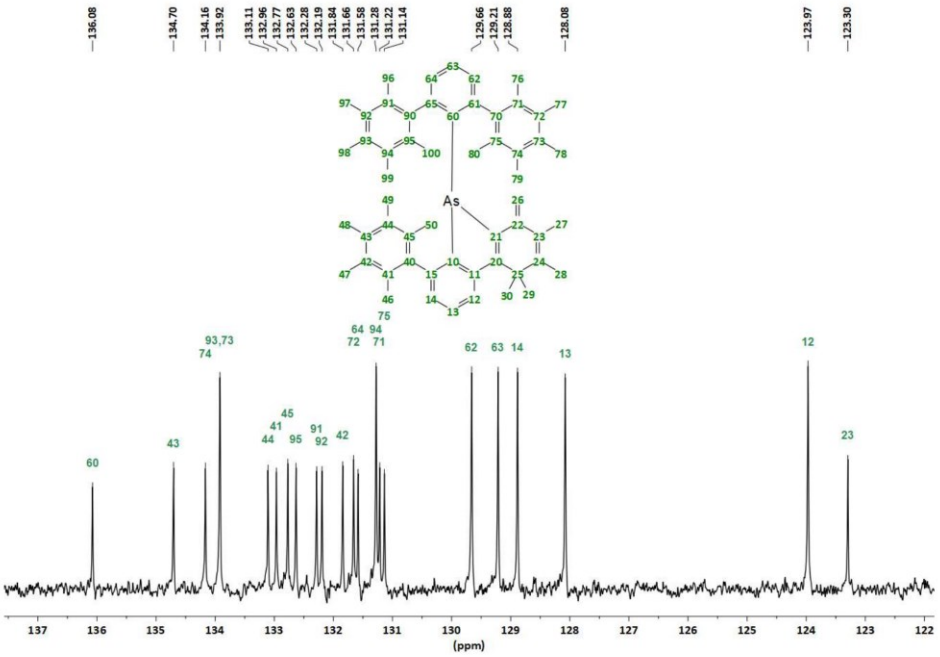

Figure S58. $^{13}C\{^{1}H\}$ NMR (CD_2Cl_2, 151 MHz) spectrum (detail) of **9b**.

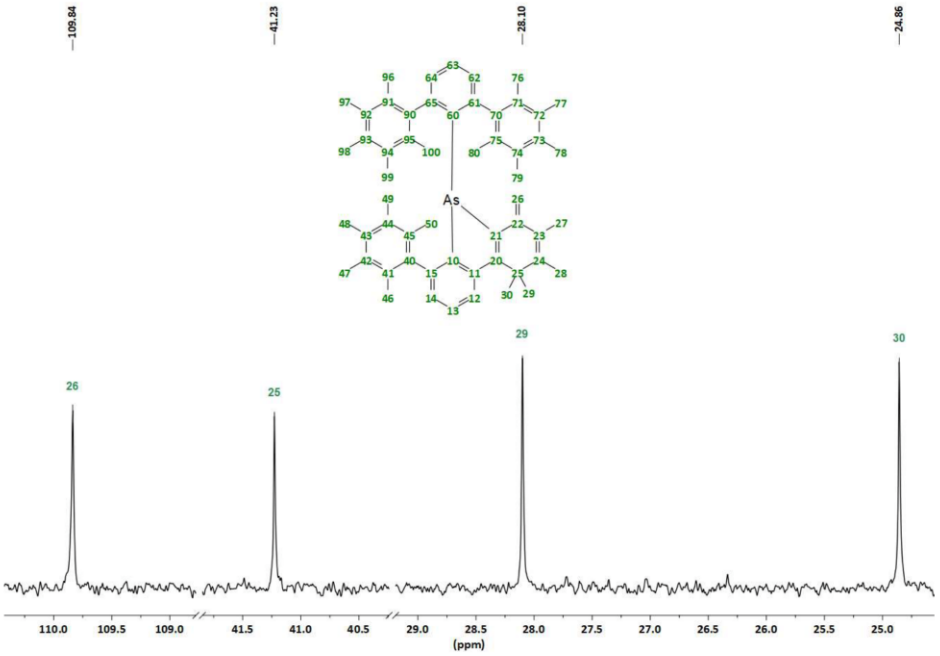

Figure S59. $^{13}C\{^{1}H\}$ NMR (CD_2Cl_2, 151 MHz) spectrum (detail) of **9b**.

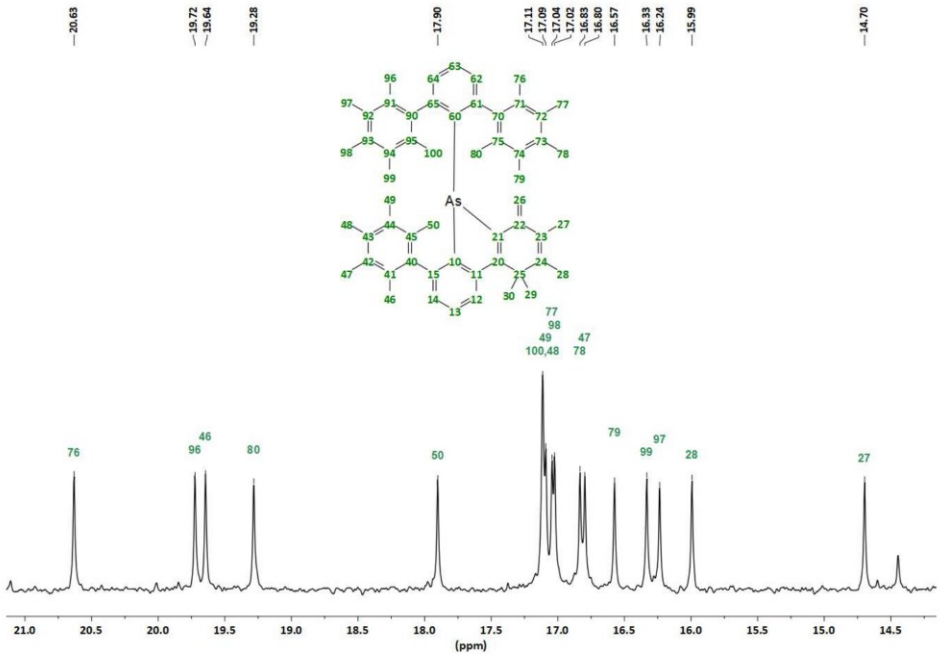

Figure S60. $^{13}C\{^{1}H\}$ NMR (CD_2Cl_2, 151 MHz) spectrum (detail) of **9b**.

X-Ray diffraction studies

Intensity data of **1a**, **1b**, **[5a]**[0.75·$AlCl_4$+0.25·$EtAlCl_3$], **[5b]**[$AlCl_4$], **[8a]**[$AlCl_4$]·CH_2Cl_2, **9a** and **9b** was collected on a Bruker Venture D8 diffractometer at 100 K with graphite-monochromated Mo-Kα (0.7107 Å) radiation. All structures were solved by direct methods and refined based on F^2 by use of the SHELX program package as implemented in WinGX.[S3,S4] All non-hydrogen atoms were refined using anisotropic displacement parameters. Hydrogen atoms attached to carbon atoms were located form the difference Fourier map and refined freely for **1a**. For **[5a]**[0.75·$AlCl_4$+0.25·$EtAlCl_3$], **[8a]**[$AlCl_4$]·CH_2Cl_2, **9a**, and **9b** H atoms were treated as a mixture of freely refined and geometrically constrained positions within the ridding model.

The diffraction pattern measured during data collection for crystals of **1b** revelled a non-merohedral twin with a two-fold twin law. Unfortunately, the crystal quality and scattering power were not enough to obtain sufficient resolution to provide a high quality structure. Despite the fact that the twin law solve most problems during the structure refinement, there are still many reflection overlaps that were not properly de-convoluted by the twin law solely, but most importantly the derived weak intensities for the highest resolution shells (0.93–0.75A) prevent a better model to be presented, as it can be seen from the large derived K factors of 13.326. Crystal and refinement data are collected in Tables S1 and S2. Figures were created using DIAMOND.[S5] Crystallographic data for the structural analyses have been deposited with the Cambridge Crystallographic Data Centre. Copies of this information may be obtained free of charge from The Director, CCDC, 12 Union Road, Cambridge CB2 1EZ, UK (Fax: +44-1223-336033; e-mail: deposit@ccdc.cam.ac.uk or http://www.ccdc.cam.ac.uk).

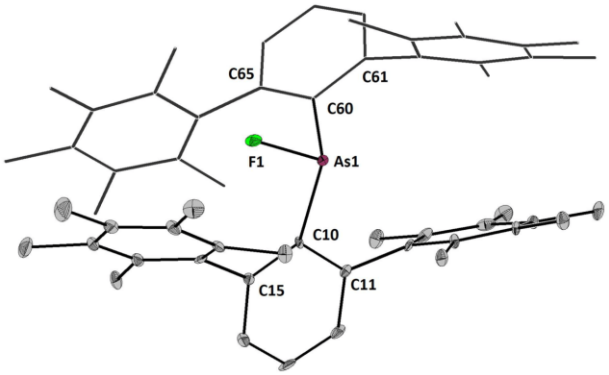

Figure S62. Preliminary molecular structure of **1b** showing 30% probability ellipsoids and the essential atom numbering scheme.

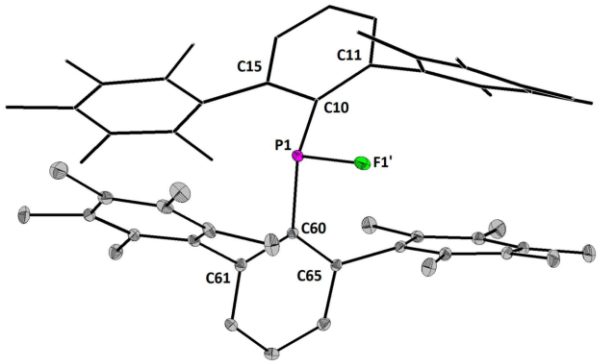

Figure S61. Molecular structure of **1a** showing 30% probability ellipsoids and the essential atom numbering scheme. Selected bond parameters [Å, °] of **1a**: C10–P1 1.853(3), C60–P1–1.848(2), F1'–P1–1.602(3), F1'–P1–C60 96.7(1), F1'–P1–C10 100.1(1), C60–P1–C10 111.5(1), C15–C10–P1 114.7(1), C11–C10–P1 125.2(2), C61–C60–P1 113.1(1), C65–C60–P1 128.0(2).

Table S1. Crystal data and structure refinement of **1a**, **1b**, [**5a**][0.75·$AlCl_4$+0.25·$EtAlCl_3$].

	1a	**1b**	[**5a**][0.75·$AlCl_4$+0.25·$EtAlCl_3$]
Formula	$C_{56}H_{66}FP$	$C_{56}H_{66}AsF$	$C_{56}H_{66}P·C_{0.52}H_{1.29}AlCl_{3.74}$
Formula weight, g mol^{-1}	789.05	833	937.19
Crystal system	Triclinic	Orthorhombic	Triclinic
Crystal size, mm	0.2×0.2×0.2	0.6×0.4×0.2	0.08×0.07×0.07
Space group	$P\bar{1}$	Pbca	$P\bar{1}$
a, Å	12.4535(6)	15.901(1)	11.1666(4)
b, Å	12.5560(6)	16.105(1)	11.6683(4)
c, Å	16.3309(8)	34.642(2)	19.2087(7)
α, °	68.0885(15)	90	92.0876(13)
β, °	71.6618(16)	90	99.9649(13)
γ, °	76.814(16)	90	91.0749(14)
V, Å^3	2230.99(19)	8871.7 (10)	2462.61(15)
Z	2	8	2
ρ_{calcd}, g cm^{-3}	1.175	1.247	1.264
μ (Mo *Kα*), mm^{-1}	0.103	0.81	0.314
F(000)	852	3552	996
θ range, deg	2.3–29.7	2.5–28.3	2.5–29.6
Index ranges	−17 ≤ h ≤ 17 −17 ≤ k ≤ 17 −22 ≤ l ≤ 22	−21 ≤ h ≤ 21 −21 ≤ k ≤ 21 −46 ≤ l ≤ 46	−13 ≤ h ≤ 13 −13 ≤ k ≤ 13 −22 ≤ l ≤ 22
No. of reflns collected	51821	131233	42596
Completeness to θ_{max}	0.997	0.973	0.999
No. indep. Reflns	12661	11523	8669
No. obsd reflns with ($I>2\sigma(I)$)	10005	10667	7281
No. refined params	582	564	668
GooF (F^2)	1.123	1.22	1.05
R_1 (F) ($I > 2\sigma(I)$)	0.071	0.152	0.0417
wR_2 (F^2) (all data)	0.177	0.348	0.0417
Largest diff peak/hole, e Å^{-3}	0.5/−0.35	5.28/−2.43	0.7/−0.62
CCDC number	1993654	not deposited	1993655

Table S2. Crystal data and structure refinement of [**5b**][$AlCl_4$], [**8a**][$AlCl_4$]·CH_2Cl_2, **9a** and **9b**.

	[**5b**][$AlCl_4$]	[**8a**][$AlCl_4$]·CH_2Cl_2	**9a**	**9b**
Formula	$C_{56}H_{66}As·AlCl_4$	$C_{56}H_{65.68}Cl_{0.05}P·AlCl_4·CH_2Cl_2$	$C_{56}H_{65}P$	$C_{56}H_{65}As$
Formula weight, g mol^{-1}	982.78	1025.22	769.05	813.01
Crystal system	Triclinic	Triclinic	Monoclinic	Triclinic
Crystal size, mm	0.36×0.31×0.17	0.25×0.25×0.25	0.07×0.07×0.05	0.29×0.28×0.18
Space group	$P\bar{1}$	$P\bar{1}$	$P2_1/c$	$P\bar{1}$
a, Å	11.1651(4)	12.1874(3)	15.1170(6)	12.0629(6)
b, Å	11.7015(5)	15.1040(4)	19.9711(7)	12.2645(7)
c, Å	19.3134(7)	15.5399(4)	14.8307(6)	16.1347(7)
α, °	92.154(1)	77.572(1)	90	69.928(2)
β, °	100.440(1)	70.442(1)	105.4962(14)	88.099(2)
γ, °	91.535(1)	85.716(1)	90	86.440(2)
V, Å^3	2478.29 (17)	2632.34(12)	4314.7(3)	2237.6(2)
Z	2	2	4	2
ρ_{calcd}, g cm^{-3}	1.317	1.293	1.184	1.207
μ (Mo *Kα*), mm^{-1}	0.956	0.413	0.101	0.80
F(000)	1032	1081	1664	870
θ range, deg	2.5–33.2	2.6–40.2	2.5–28.3	2.2–33.1
Index ranges	−17≤ h ≤ 17 −18 ≤ k ≤ 17 −24 ≤ l ≤ 24	−19 ≤ h ≤ 19 −23 ≤ k ≤ 23 −24 ≤ l ≤ 24	−20 ≤ h ≤ 20 −26 ≤ k ≤ 26 −19 ≤ l ≤ 19	−18 ≤ h ≤ 18 −18 ≤ k ≤ 18 −24 ≤ l ≤ 24
No. of reflns collected	85724	211012	94259	76408
Completeness to θ_{max}	0.998	0.999	0.999	0.995
No. indep. Reflns	19004	22020	10802	17063
No. obsd reflns with ($I>2\sigma(I)$)	16307	18729	8556	13656
No. refined params	625	690	584	565
GooF (F^2)	1.03	1.04	1.08	1.06
R_1 (F) ($I > 2\sigma(I)$)	0.033	0.040	0.0377	0.048
wR_2 (F^2) (all data)	0.088	0.121	0.067	0.118
Largest diff peak/hole, e Å^{-3}	0.52/−0.41	1.30/−1.08	1.18/−0.36	0.85/−0.47
CCDC number	1993656	1993657	1993658	1993659

Computational data

The structures of all cations were optimized in the gas-phase by density functional theory (DFT) at the B3PW91/6-311+G*[S6,S7] level of theory using Gaussian09.[S8] The starting geometries were modelled at the computer with GaussView 5. Dispersion effects were accounted for using the empirical Grimme correction (GD3BJ).[S9]

References

S1. S. Hino, M. M. Olmstead, J. C. Fettinger, P. P. Power, *J. Organomet. Chem.*, **2005**, *690*, 1638–1644.

S2. G. R. Fulmer, A. J. M. Miller, N. H. Sherden, H. E. Gottlieb, A. Nudelman, B. M. Stoltz, J. E. Bercaw, K. I. Goldberg, *Organometallics* **2010**, *29*, 2176–2179.

S3. G. M. Sheldrick, *Acta Cryst*. **2008**, *A64*, 112-122.

S4. L. Farrugia, *J. Appl. Cryst*. **1999**, *32*, 837-838.

S5. K. Brandenburg, Diamond, version 4.0.4, Crystal Impact GbR: Bonn, Germany, **2012**.

S6. J. P Perdew, J. A. Chevary, S. H. Vosko, K. A. Jackson, M. R. Pederson, D. J. Singh, C. Fiolhais, *Phys. Rev*. B **1992**, *46*, 6671-6687.

S7. A. D. Becke, *J. Chem. Phys*. **1993**, *98*, 5648-5652.

S8. M. J. Frisch, G. W. Trucks, H. B. Schlegel, G. E. Scuseria, M. A. Robb, J. R. Cheeseman, G. Scalmani, V. Barone, B. Mennucci, G. A. Petersson, H. Nakatsuji, M. Caricato, X. Li, H. P. Hratchian, A. F. Izmaylov, J. Bloino, G. Zheng, J. L. Sonnenberg, M. Hada, M. Ehara, K. Toyota, R. Fukuda, J. Hasegawa, M. Ishida, T. Nakajima, Y. Honda, O. Kitao, H. Nakai, T. Vreven, J. A. Montgomery, Jr., J. E. Peralta, F. Ogliaro, M. Bearpark, J. J. Heyd, E. Brothers, K. N. Kudin, V. N. Staroverov, R. Kobayashi, J. Normand, K. Raghavachari, A. Rendell, J. C. Burant, S. S. Iyengar, J. Tomasi, M. Cossi, N. Rega, J. M. Millam, M. Klene, J. E. Knox, J. B. Cross, V. Bakken, C. Adamo, J. Jaramillo, R. Gomperts, R. E. Stratmann, O. Yazyev, A. J. Austin, R. Cammi, C. Pomelli, J. W. Ochterski, R. L. Martin, K. Morokuma, V. G. Zakrzewski, G. A. Voth, P. Salvador, J. J. Dannenberg, S. Dapprich, A. D. Daniels, Ö. Farkas, J. B. Foresman, J. V. Ortiz, J. Cioslowski, D. J. Fox, Gaussian 09, Revision B.01, Gaussian Inc., Wallingford CT, **2010**.

S9. S. Grimme, J. Antony, S. Ehrlich and H. Krieg, *J. Chem. Phys.*, **2010**, *132*,154104.

6.4 Isolation of an Antiaromatic 9-Hydroxy Fluorenyl Cation

Chemistry–A European Journal

Supporting Information

Isolation of an Antiaromatic 9-Hydroxy Fluorenyl Cation

Daniel Duvinage, Stefan Mebs,* and Jens Beckmann*

Table of Contents

Experimental procedures

General information

Unless otherwise stated, all reactions and manipulations were performed under inert atmosphere (argon) using anhydrous solvents. Reagents used in this work including CO_2, $SOCl_2$, pyridine, $AlCl_3$ and CsF were obtained commercially and were used as received. The reagent 2,6-$Mes_2C_6H_3Li$ (Mes = 2,4,6-$Me_3C_6H_2$) was prepared following the published procedure.[S1] Anhydrous dichloromethane, hexane, tetrahydrofurane and toluene were collected from an SPS800 mBraun solvent purification system and stored over 4 Å molecular sieves. Et_2O was dried by refluxing it over Na/benzophenone under argon atmosphere. Deuterated solvents were degassed and dried over 4 Å molecular sieves under argon.

Unless otherwise noted, NMR spectra were recorded at room temperature on a Bruker Avance 600 MHz spectrometer. ^1H, $^{13}C\{^1H\}$ and ^{19}F NMR spectra are reported on the δ scale (ppm) and are referenced against $SiMe_4$ respectively. ^1H and $^{13}C\{^1H\}$ chemical shifts are reported relative to the residual peak of the solvent ($CDHCl_2$ 5.32 ppm for CD_2Cl_2) in the ^1H NMR spectra, and to the peak of the deuterated solvent (CD_2Cl_2 53.84 ppm) in the $^{13}C\{^1H\}$ NMR spectra.[8] The assignment of the ^1H and $^{13}C\{^1H\}$ resonance signals was made in accordance with the COSY, HSQC and HMBC spectra. The labelling schemes are attached to the ^1H and ^{13}C spectra.

The ESI HRMS spectra were measured on a Bruker Impact II spectrometer. Acetonitrile or dichloromethane/acetonitrile solutions ($c = 1\cdot10^{-5}$ mol·L^{-1}) were injected directly into the spectrometer at a flow rate of 3 µL·min^{-1}. Nitrogen was used both as a drying gas and for nebulization with flow rates of approximately 5 L·min^{-1} and a pressure of 5 psi. Pressure in the mass analyser region was usually about $1\cdot10^{-5}$ mbar. Spectra were collected for 1 min and averaged. The nozzle-skimmer voltage was adjusted individually for each measurement.

The UV-Vis spectra were recorded on a Varian Cary 50 Scan UV-Visible Spectrophotometer.

The Fluorescence spectra were recorded on a Jasco Spectrofluorometer FP-8300. The spectral correction was done with an integrated calibrated WI lamp.

Synthesis of $Mes_2C_6H_3C(O)OH$ according to a modified literature procedure.[S2] CO_2 was bubbled through a solution of 2,6-$Mes_2C_6H_3Li$ (3.20 g, 10.0 mmol, 1.00 eq.) in Et_2O (50 mL) at 0 °C. After 1 hour to the suspension was added aqueous HCl (50.0 mL, 3 M) and the reaction was worked up aqueous. The organic phase was separated and the solvent was removed under reduced pressure. The remaining colorless solid is washed with *n*-hexane (3 x 10 mL) and dried under reduced pressure to yield the title compound as colorless solid (3.19 g, 89 %). The analytical data are in accordance with the literature.[S2]

Synthesis and characterization of $Mes_2C_6H_3C(O)Cl$. $Mes_2C_6H_3C(O)Cl$ was prepared according to the literature.[S3] To a stirred suspension of $Mes_2C_6H_3C(O)OH$ (1.79 g, 5.00 mmol, 1.00 eq.) in CH_2Cl_2 (20 mL) thionyl chloride (1.10 mL, 15.0 mmol, 3.00 eq.) was added and after this pyridine (0.10 mL, 1.20 mmol, 0.24 eq.) was added dropwise which starts an evolution of SO_2 and HCl. The solution is stirred for an additional 18 h after which the solvent is removed in vacuum to remove excess thionyl chloride and the residue is dissolved in CH_2Cl_2 (20 mL). The solution is washed with water (3 x 50 mL) and dried over sodium sulphate. The volatiles are removed under reduced pressure to yield the target compound as colorless crystalline solid (1.76 g, 94%). The analytical data are in accordance with the literature.[S3]

Synthesis and characterization of 1. 2,6-$Mes_2C_6H_3C(O)Cl$ (0.50 g, 1.32 mmol, 1.00 eq.) is suspended with CsF (0.50 g, 3.2 mmol, 2.20 eq.) in MeCN (10 mL) and warmed to 80 °C for 48 hours. Afterwards the reaction diluted with CH_2Cl_2 (40 mL) and washed with distilled water (3 x 20 mL). The solvent is removed under reduced pressure and the colorless residue is washed with *n*-hexane (3 x 10 mL) to afford $Mes_2C_6H_3C(O)F$ as colorless solid (0.38 g, 80 %; Mp. 255°C).

^1H NMR (600 MHz, $CDCl_3$): δ = 7.65 (t, $^3J(^1H\text{-}^1H)$ = 7.66 Hz, 1H, H4), 7.22 (d, $^3J(^1H\text{-}^1H)$ = 7.66 Hz, 2H, H3 and H5), 6.94 (s, 4H, H9 and H11), 2.33 (s, 6H, H14), 2.04 (s, 12H, H13 and H15) ppm. **$^{13}C\{^1H\}$ NMR (151 MHz, $CDCl_3$)**: δ = 157.70 (d, $^1J(^{13}C\text{-}^{19}F)$ = 357.18 Hz, C16), 140.80 (s, C2 and C6), 137.75 (s, C10), 136.11 (s, C8 and C12) 135.68 (s, C7), 131.96 (s, C4), 129.25 (d, $^2J(^{13}C\text{-}^{19}F)$ = 53.70 Hz, C1), 128.98 (s, C3 and C5), 128.26 (s, C9 and C11), 21.26 (s, C14), 20.43 (s, C13 and C15) ppm. **$^{19}F\{^1H\}$ NMR ($CDCl_3$, 565 MHz)**: δ = 52.17 ppm. **HRMS ESI (m/z):** $[M+Na]^+$ calculated. for $C_{25}H_{25}FNaO$, 383.17816; found, 383.17823.

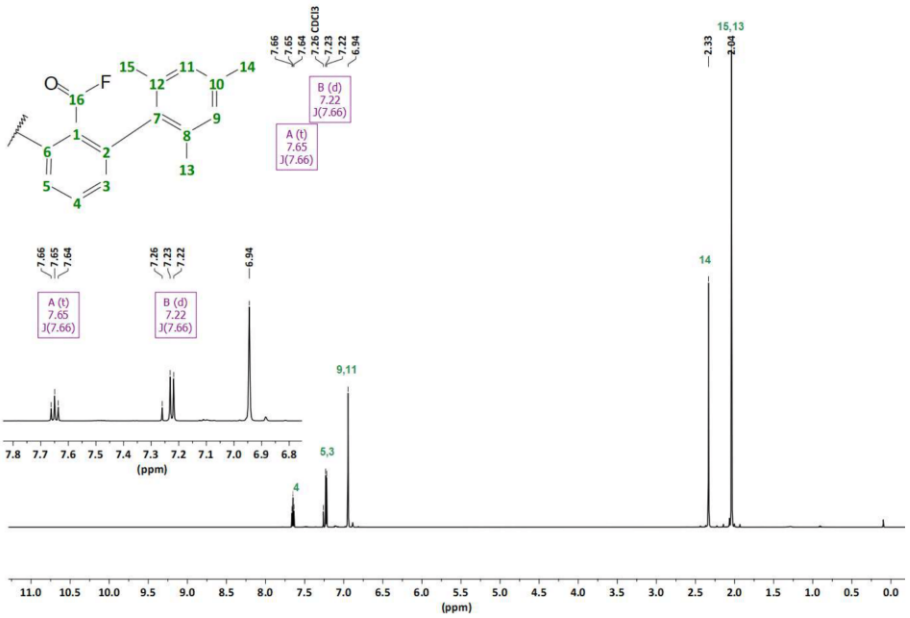

Figure S1. ^{1}H NMR ($CDCl_3$, 600 MHz) spectrum of 2,6-$Mes_2C_6H_3C(O)F$.

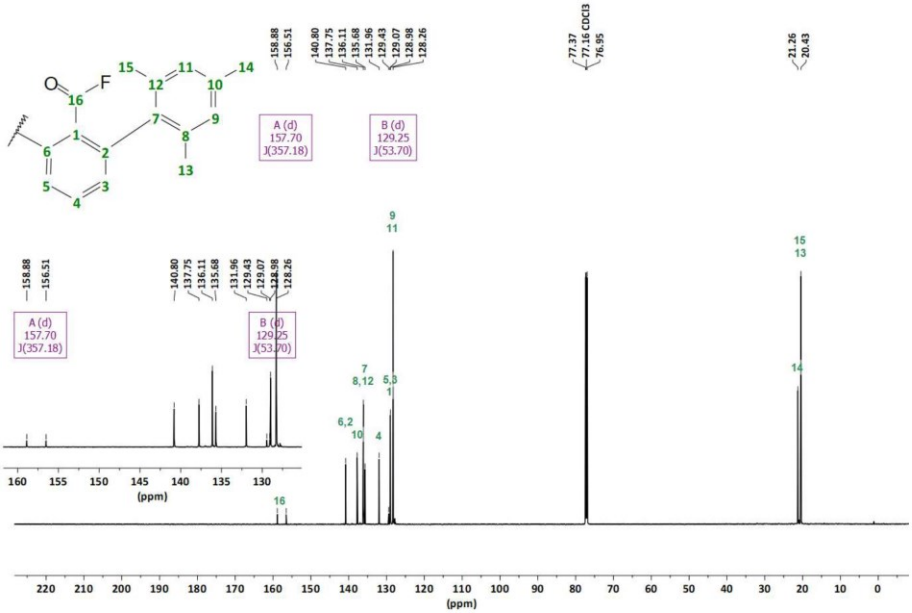

Figure S2. $^{13}C\{^{1}H\}$ NMR ($CDCl_3$, 151 MHz) spectrum of 2,6-$Mes_2C_6H_3C(O)F$.

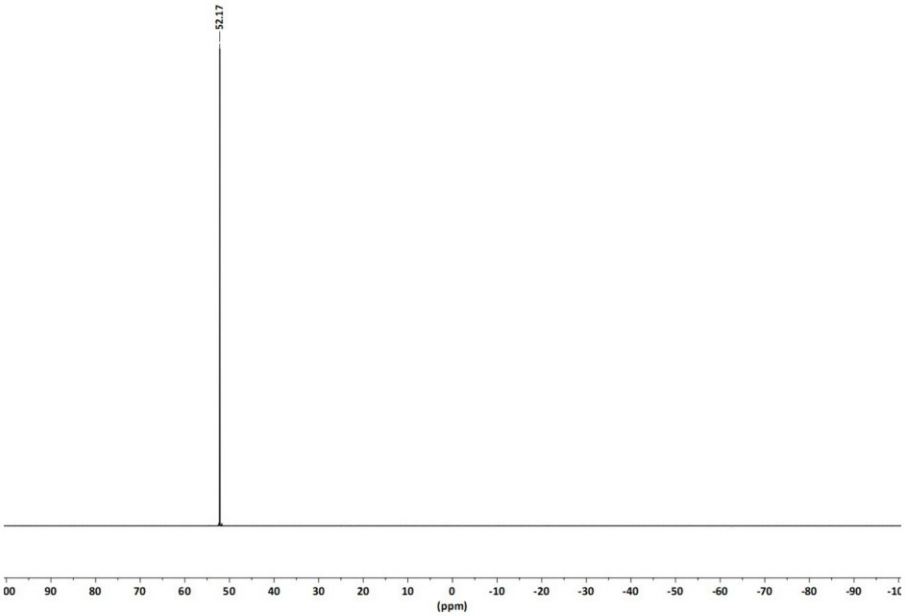

Figure S3. $^{19}F\{^{1}H\}$ NMR ($CDCl_3$, 565 MHz) spectrum of 2,6-$Mes_2C_6H_3C(O)F$

Synthesis and characterization of 2. 1 (72.0 mg, 0.20 mmol, 1.00 eq.) and $AlCl_3$ (26.6 mg, 0.20 mmol, 1.00 eq.) are placed in a Schlenk tube. To this, CH_2Cl_2 (4 mL) is added. During the addition the solution darkens to a dark yellow. After stirring for 2 hours at 20 °C the solution is layered with *n*-hexane (20 mL). After complete diffusion the solvent is removed by decantation and the remaining solid is washed with *n*-hexane (3 x 10 mL) and dried under reduced pressure to yield **2** as deep-brown crystalline solid (99.3 mg, 91 %).

^{1}H NMR (600 MHz, CD_2Cl_2): δ = 9.71 (s, br, 1H, H26), 7.65 (t, $^{3}J(^{1}H\text{-}^{1}H)$ = 7.66 Hz, 1H, H4), 7.42 (d, $^{3}J(^{1}H\text{-}^{1}H)$ = 7.52 Hz, 1H, H5), 7.17 (s, 2H, H19 and H21), 7.14 (s, 1H, H11), 6.92 (d, $^{3}J(^{1}H\text{-}^{1}H)$ = 7.77 Hz, 1H, H3), 2.43 (s. 3H, H14), 2.40 (s, 3H, H24), 2.36 (s, 3H, H13), 2.19 (s, 3H, H15), 2.11 (s, 6H, H23 and H25) ppm. **$^{13}C\{^{1}H\}$ NMR (151 MHz, CD_2Cl_2)**: δ = 200.61 (s, C16), 147.16 (s, C8), 146.98 (s. C2), 146.74 (s, C11), 145.68 (s, C6), 142.18 (s, C4), 141.78 (s, C7), 141.54 (s, C9), 140.93 (s, C20), 135.88 (s, C18 and C22), 135.22 (s, C12), 131.62 (s, C3), 130.34 (s. C19 and C21), 129.37 (s, C17), 128.99 (s C10), 128.17 (s, C1), 124.76 (s, C5), 20.97 (s, C24), 20.02 (s. C23 and C25), 19.27 (s, C14), 18.73 (s. C15), 15.44 (s. C13) ppm. **HRMS ESI (m/z):** $[M]^+$ calculated. for $C_{25}H_{26}O$ 341.18999; found, 341.18981. **UV-Vis:** (50µM, **CH_2Cl_2**) = 421 nm.

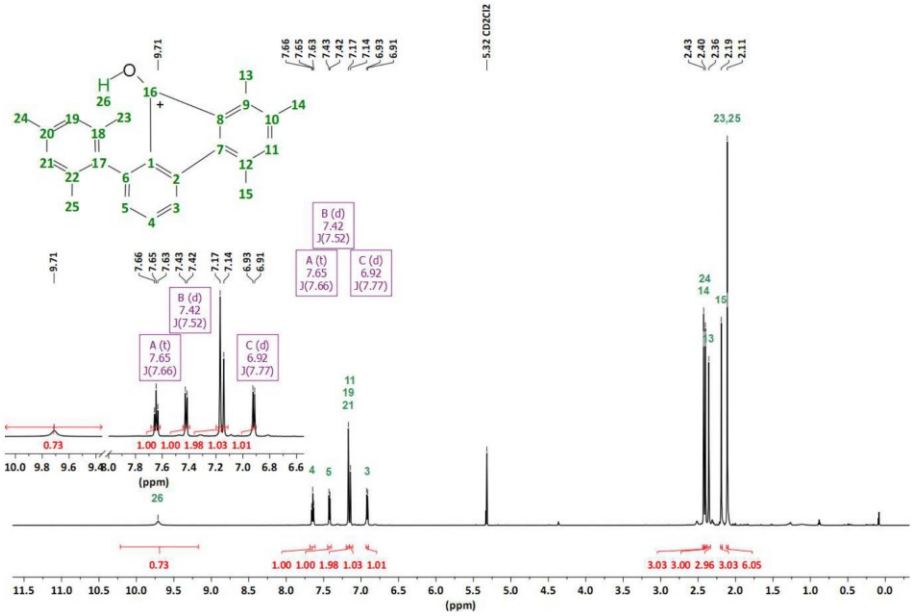

Figure S4. ^{1}H NMR (CD_2Cl_2, 600 MHz) spectrum of **1**.

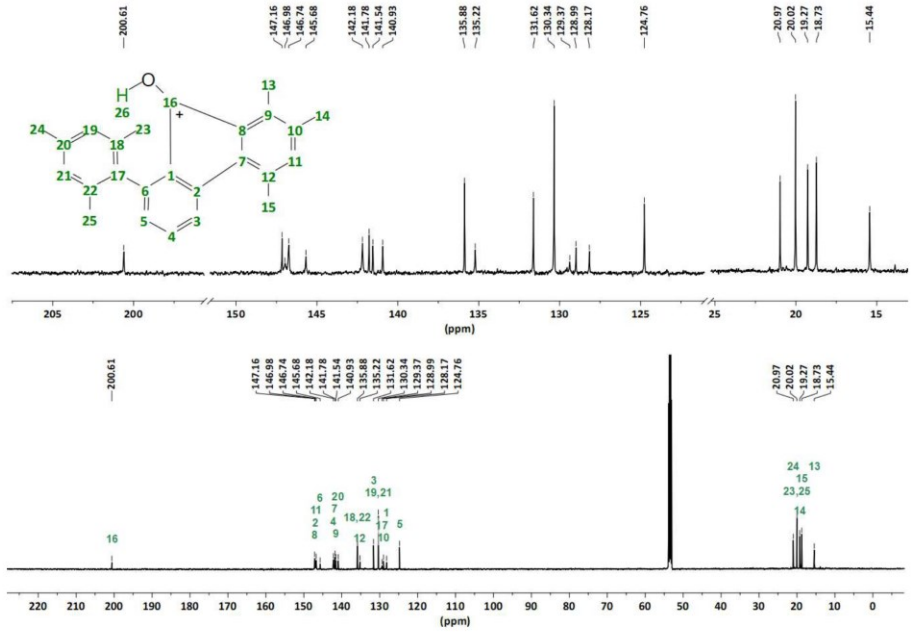

Figure S5. $^{13}C\{^{1}H\}$ NMR (CD_2Cl_2, 151 MHz) spectrum of **1**.

Figure S6. UV-Vis spectrum of **1** (50μM, DCM).

Synthesis and characterization of 3. A solution of **2** (51.0 mg, 0.10 mmol, 1.00 eq.) in CH_2Cl_2 (5 mL) is treated with sodium hydroxide solution (2.5 M) (0.5 mL) and stirred for 10 minutes. Afterwards the solution is filtered through a pad of Na_2SO_4. The solvent is removed in vacuum and the bright yellow oil is dissolved in *n*-hexane. The solution is flushed through a pad of silica and the product is eluted with CH_2Cl_2. After removal of the solvent in vacuum, **3** was obtained as yellow solid (34.0 mg, quant.; Mp. 176°C).

^{1}H NMR (600 MHz, CDCl$_3$): δ = 7.63 (d, ^{3}J(^{1}H-^{1}H) = 7.55 Hz, 1H, H5), 7.51 (t, ^{3}J(^{1}H-^{1}H) = 7.60 Hz, 1H, H4), 7.04 (s, H11), 7.00 (s, 2H, H19 and H21), 6.97 (d, ^{3}J(^{1}H-^{1}H) = 7.60 Hz, 1H, H3), 2.59 (s, 3H, H15), 2.49 (s, 3H, H13), 2.39 (s, 3H, H24), 2.26 (s, 3H, H14), 2.00 (s, 6H, H23 and H25) ppm. 2.34 (s, 6H, H14), 2.03 (s, 12H, H13 and H15) ppm.**^{13}C{^{1}H} NMR (151 MHz, CDCl$_3$):** δ = 195.29 (s, C16), 145.43 (s, C2), 140.26 (s, C6), 139.98 (s, C7), 139.09 (s, C9), 137.93 (s, C11), 136.77 (s, C10), 136.13 (s C12), 135.54 (s, C20), 135.13 (s, C18 and C22), 134.07 (s, C4), 131.52 (s, C1), 131.31 (s, C8), 130.48 (s, C3), 128.17 (s, C17, C19 and C21), 121.82 (s, C5), 21.36 (s, C24), 20.52 (s, C23 and C25), 20.37 (s, C15), 19.22 (s, C14), 13.17 (s, C13) ppm. **HRMS ESI (m/z):** $[M+Na]^+$ calculated. for $C_{25}H_{24}NaO$, 363.17194; found, 363.17170. **UV-Vis:** (50 µM, DCM) = 333, 346, 421 nm. **Fluorescence:** (50 µMol, 1:100 MeCN/H_2O) λ_{exc} = 320 nm, λ_{em} = 512 nm.

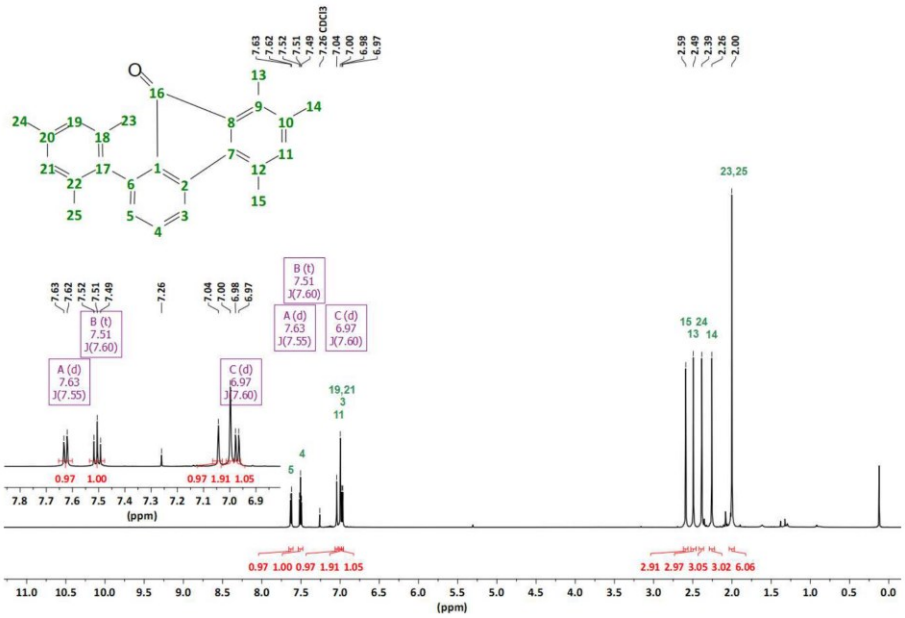

Figure S7. ^{1}H NMR ($CDCl_3$, 600 MHz) spectrum of **2**.

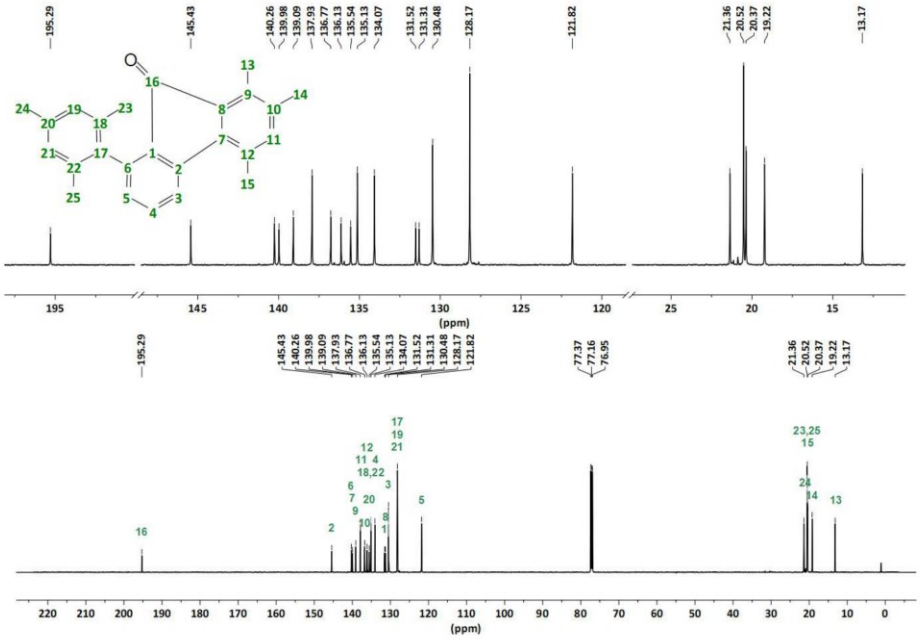

Figure S8. $^{13}C\{^{1}H\}$ NMR ($CDCl_3$, 151 MHz) spectrum of **2**.

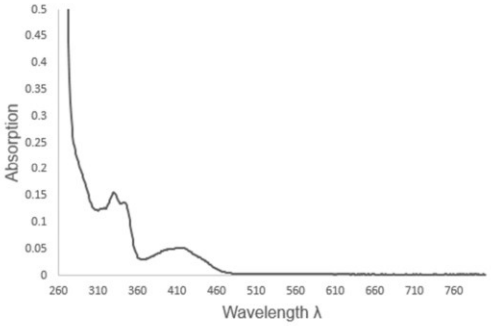

Figure S9. UV-Vis spectrum of **2** (50 µM, CH_2Cl_2).

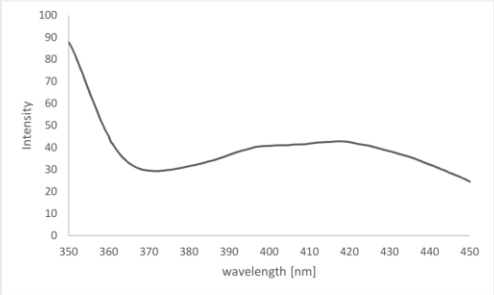

Figure S10. Excitation spectrum of **3** (50µM, 1:100 MeCN/H_2O)

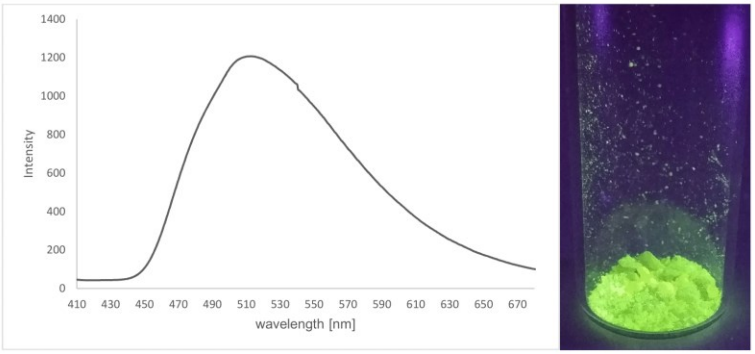

Figure S11. Emission spectrum of **3** (λ_{exi} = 320 nm, 50 µM, 1:100 MeCN/H_2O)

X-Ray diffraction studies

Single crystals of **1** and **3** were grown by slowly cooling hot solutions in toluene and *n*-heptane, respectively. Single crystals of **2** were obtained by diffusion of *n*-hexane into a CH_2Cl_2 solution. Intensity data of **1** - **3** was collected on a Bruker Venture D8 diffractometer at 100 K with graphite-monochromated Mo-Kα (0.7107 Å) radiation. All structures were solved by direct methods and refined based on F^2 by use of the SHELX program package as implemented in OLEX.[S4] All non-hydrogen atoms were refined using anisotropic displacement parameters. Hydrogen atoms attached to carbon atoms were included in geometrically calculated positions using a riding model. Crystal and refinement data are collected in Tables S1. Figures were created using DIAMOND.[S5] Crystallographic data for the structural analyses have been deposited with the Cambridge Crystallographic Data Centre. Copies of this information may be obtained free of charge from The Director, CCDC, 12 Union Road, Cambridge CB2 1EZ, UK (Fax: +44-1223-336033; e-mail: deposit@ccdc.cam.ac.uk or http://www.ccdc.cam.ac.uk).

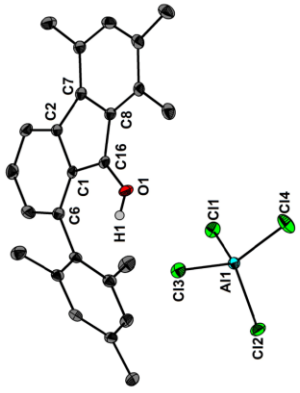

Figure S12. Molecular structure of **2** showing 50% probability ellipsoids. The closest cation anion contacts are Cl1–O1 3.234(2) Å and Cl3–O1 3.214(2) Å.

Computational data

The structures of all starting materials, transition states, intermediates, and products were optimized in the gas-phase by density functional theory (DFT) at the B3PW91/6-311+G(2df,p)[S6,S7] level of theory using Gaussian09.[S8] The starting geometries were modelled at the computer with GaussView 5. Transition states were calculated with the QST3 routine in Gaussian, using the optimized onset and end structures as starting point. Dispersion effects were accounted for using the empirical Grimme correction (GD3BJ).[S9] The wavefunction files were used for a topological analysis of the electron density according to the Atoms-In-Molecules space-partitioning scheme[16] using AIM2000,[S10] whereas NCI[17] grids were computed with NCIplot (0.1 a.u. grids).[S11] Bond paths are displayed with AIM2000, NCI figures are displayed with MolIso[S12] AIM provides a bond paths motif, which resembles and exceeds the Lewis picture of chemical bonding, disclosing all types and strengths of interactions. Analyses of the reduced density gradient, $s(\mathbf{r}) = [1/2(3\pi^2)^{1/3}]|\nabla\rho|/\rho^{4/3}$, according to the NCI method is used to visualize non-covalent bonding aspects. An estimation of different non-covalent contact types according to steric/repulsive ($\lambda_2 > 0$), van der Waals-like ($\lambda_2 \approx 0$), and attractive ($\lambda_2 < 0$) is facilitated by mapping the ED times the sign of the second eigenvalue of the Hessian ($\mathrm{sign}(\lambda_2)\rho$) on the *iso*-surfaces of $s(\mathbf{r})$.

Table S1. Crystal data and structure refinement of **1** - **3**.

	1	**2**	**3**
Formula	$C_{25}H_{25}FO$	$C_{25}H_{25}AlCl_4O$	$C_{25}H_{24}O$
Formula weight, g mol^{-1}	360.45	510.23	340.44
Crystal system	Orthorhombic	Monoclinic	Orthorhombic
Crystal size, mm	0.29×0.28×0.17	0.14×0.13×0.11	0.25×0.23×0.17
Space group	Pbca	C2/c	$Pca2_1$
a, Å	17.4412(9)	33.2496(18)	17.6380(6)
b, Å	7.8647(4)	8.3292(5)	6.8510(2)
c, Å	28.8522(17)	18.2357(10)	31.0807(9)
α, °	90	90	90
β, °	90	104.693(2)	90
γ, °	90	90	90
V, Å^3	3957.7(4)	4885.1(5)	3755.7(2)
Z	8	8	8
ρ_{calcd}, g cm^{-3}	1.210	1.387	1.204
μ (Mo $K\alpha$), mm^{-1}	0.078	0.537	0.071
F(000)	1536	2112	1456
θ range, deg	2.72 to 28.28	4.654 to 56.752	4.62 to 51
Index ranges	−23 ≤ h ≤ 22 −10 ≤ k ≤ 10 −28 ≤ l ≤ 36	−43 ≤ h ≤ 43 −10 ≤ k ≤ 10 −22 ≤ l ≤ 23	−25 ≤ h ≤ 25 −9 ≤ k ≤ 9 −44 ≤ l ≤ 40
No. of reflns collected	53770	46417	61464
Completeness to θ_{max}	99.9%	99.9%	99.9%
No. indep. Reflns	4909	5634	11306
No. obsd reflns with ($I>2\sigma(I)$)	4290	4531	10082
No. refined params	250	290	481
GooF (F^2)	1.053	1.033	1.050
R_1 (F) ($I > 2\sigma(I)$)	0.0484	0.0400	0.0476
wR_2 (F^2) (all data)	0.1323	0.0892	0.1188
Largest diff peak/hole, e Å^{-3}	0.357 /−0.332	0.98/−0.78	0.30/−0.32
CCDC number	2063417	2063418	2063419

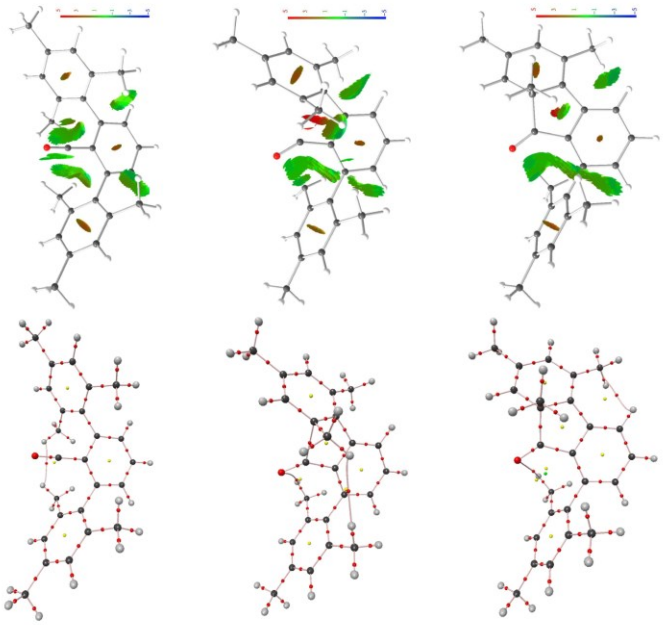

Figure S13. AIM molecular graphs and NCI *iso*-surfaces of models **A**, **B**[#], and **C**.

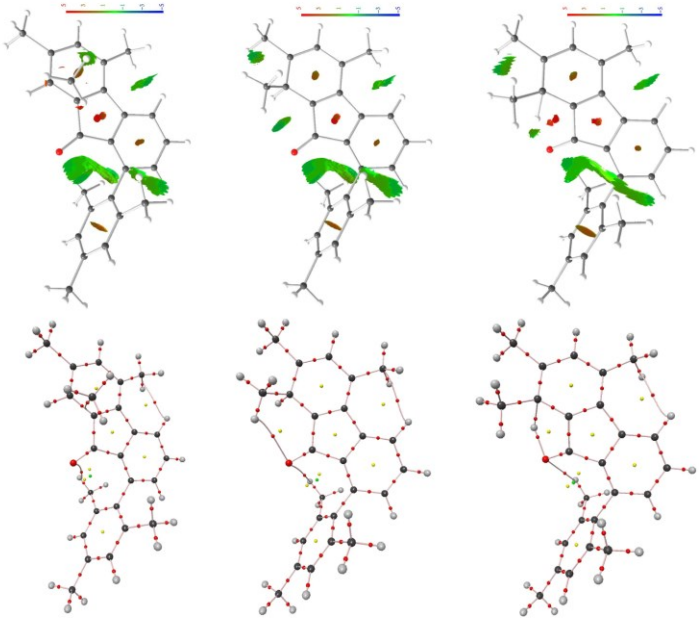

Figure S14. AIM molecular graphs and NCI *iso*-surfaces of models **D**[#], **E**, and **F**[#].

Table S2. Calculated NICS(0) and NICS(1)-values

no.	1	3	A	B	C	D	E	F	G	H
51		-4.89								9.83
52		-7.02	-6.75	-4.49	-0.79	-3.33	1.33	-2.27	1.75	5.04
53	-7.36	-7.02	-8.65	-7.76	-4.60	-6.05	-3.95	-5.60	-1.61	5.03
54	-9.09	11.58	-8.47	-7.00	-4.33	-6.62	-3.75	-4.23	-1.61	24.36
55	-8.96	4.05	-5.60	-1.73	3.43	9.34	12.19	10.73	15.57	15.48
56	-7.83	4.05	-7.03	-3.81	-2.50	1.31	3.50	3.37	9.60	15.71
57	-8.80	-4.54	-7.10	-1.52	-0.79	2.59	3.76	6.36	9.60	9.89
58	-8.95	-6.70	-6.76	-7.46	-5.86	-4.43	-3.63	-2.62	0.72	5.09
59	-7.31	-6.70	-8.65	-9.32	-8.63	-6.95	-5.95	-5.18	-2.38	5.11
60	-8.97	-7.37	-8.47	-8.41	-7.77	-6.80	-5.89	-4.76	-2.38	-5.42
61	-8.93	-8.70		-7.29	-7.01	-7.18	-6.46	-7.49	-6.95	-7.47
62		-9.01		-8.98	-8.67	-8.72	-8.13	-9.17	-8.67	-7.63
63				-8.81	-8.62	-8.70	-8.13	-8.97	-8.68	

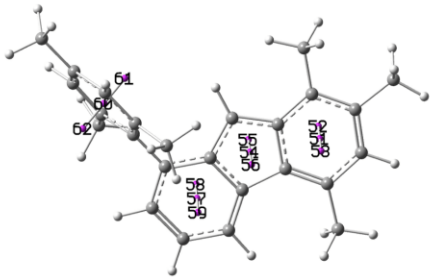

Figure S17. NICS(0) and NICS(1) points of the non-substituted reference fluorenyl cation **H**.

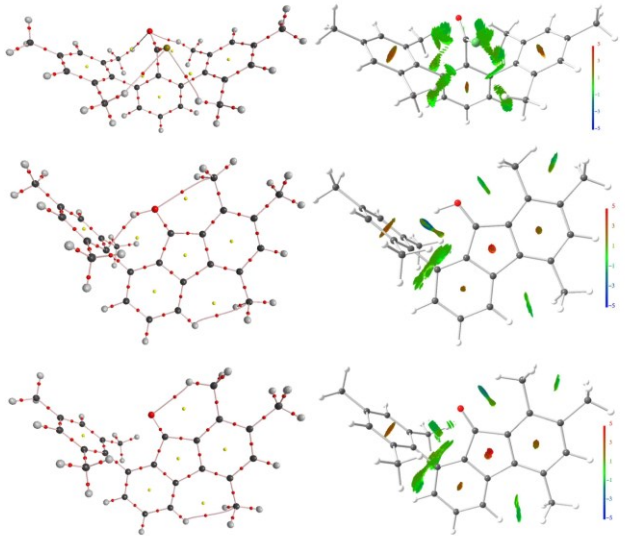

Figure S15. AIM molecular graphs and NCI *iso*-surfaces of models **1**–**3**.

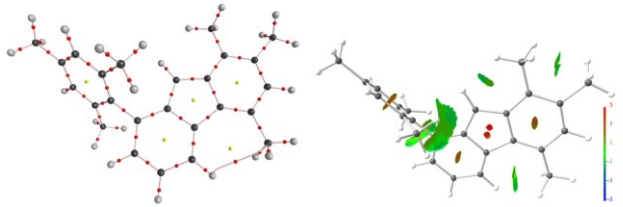

Figure S16. AIM molecular graph and NCI *iso*-surface of the non-substituted reference fluorenyl cation **H**.

Figure S18. NICS(0) and NICS(1) points of models **A**, **B**#, and **C**.

Figure S19. NICS(0) and NICS(1) points of models **D**#, **E**, and **F**#.

Additional References

S1. K. Ruhlandt-Senge, J. J. Ellison, R. J. Wehmschulte, F. Pauer, P. P. Power, *J. Am. Chem. Soc.* **1993**, *115*, 11353-11357.

S2. J. R. Hagadorn, L. Que, W. B. Tolman, *J. Am. Chem. Soc.* **1998**, *120*, 13531–13532]

S3. E. S. Akturk, S. J. Scappaticci, R. N. Seals, M. P. Marshak, *Inorg. Chem.* **2017**, *56*, 11466−11469.

S4. O. V. Dolomanov, L. J. Bourhis, R. J. Gildea, J. A. K. Howard, H. Puschmann, *J. Appl. Cryst.* **2009**, *42*, 339-341.

S5. K. Brandenburg, Diamond, version 4.0.4, Crystal Impact GbR: Bonn, Germany, **2012**.

S6. J. P Perdew, J. A. Chevary, S. H. Vosko, K. A. Jackson, M. R. Pederson, D. J. Singh, C. Fiolhais, *Phys. Rev.* B **1992**, *46*, 6671-6687.

S7. A. D. Becke, *J. Chem. Phys.* **1993**, *98*, 5648-5652.

S8. M. J. Frisch, G. W. Trucks, H. B. Schlegel, G. E. Scuseria, M. A. Robb, J. R. Cheeseman, G. Scalmani, V. Barone, B. Mennucci, G. A. Petersson, H. Nakatsuji, M. Caricato, X. Li, H. P. Hratchian, A. F. Izmaylov, J. Bloino, G. Zheng, J. L. Sonnenberg, M. Hada, M. Ehara, K. Toyota, R. Fukuda, J. Hasegawa, M. Ishida, T. Nakajima, Y. Honda, O. Kitao, H. Nakai, T. Vreven, J. A. Montgomery, Jr., J. E. Peralta, F. Ogliaro, M. Bearpark, J. J. Heyd, E. Brothers, K. N. Kudin, V. N. Staroverov, R. Kobayashi, J. Normand, K. Raghavachari, A. Rendell, J. C. Burant, S. S. Iyengar, J. Tomasi, M. Cossi, N. Rega, J. M. Millam, M. Klene, J. E. Knox, J. B. Cross, V. Bakken, C. Adamo, J. Jaramillo, R. Gomperts, R. E. Stratmann, O. Yazyev, A. J. Austin, R. Cammi, C. Pomelli, J. W. Ochterski, R. L. Martin, K. Morokuma, V. G. Zakrzewski, G. A. Voth, P. Salvador, J. J. Dannenberg, S. Dapprich, A. D. Daniels, Ö. Farkas, J. B. Foresman, J. V. Ortiz, J. Cioslowski, D. J. Fox, Gaussian 09, Revision B.01, Gaussian Inc., Wallingford CT, 2010.

S9. S. Grimme, J. Antony, S. Ehrlich and H. Krieg, *J. Chem. Phys.*, **2010**, *132*, 154104.

S10. F. Biegler-König, J. Schönbohm, D. Bayles *J. Comput. Chem.* **2001**, *22*, 545–559.

S11. J. Contreras-García, E. Johnson, S. Keinan, R. Chaudret, J.-P. Piquemal, D. Beratan, W. Yang, *J. Chem. Theor. Comp.* **2011**, *7*, 625–632.

S12. C. B. Hübschle, P Luger *J. Appl. Crystallogr.* **2006**, *39*, 901–904.

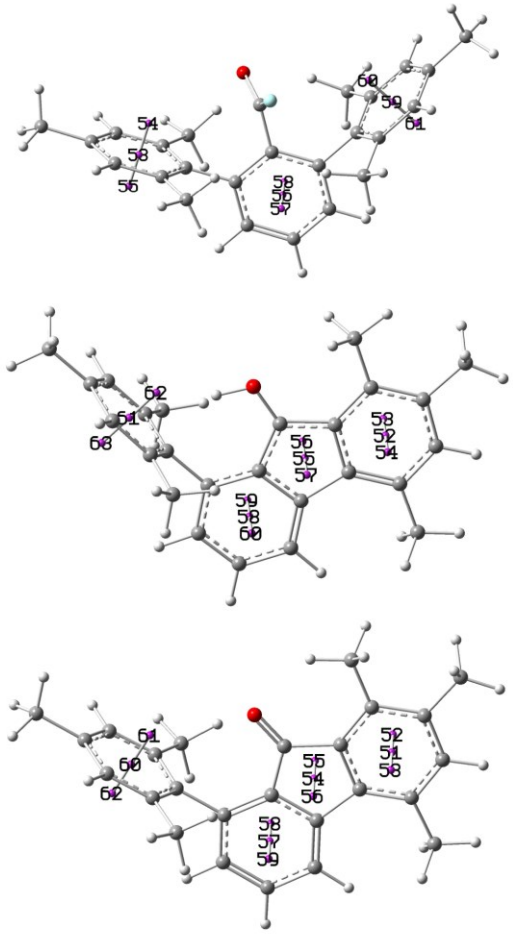

Figure S20. NICS(0) and NICS(1) points of models **1**, **2**, and **3**.

6.5 Divalent Bis(*m*-terphenyl)element Cations [(2,6-$Mes_2C_6H_3)_2E]^+$ of Group 13 Revisited and Extended (E = B, Al, Ga, In, Tl)

European Journal of Inorganic Chemistry

Supporting Information

Lewis Superacidic Divalent Bis(*m*-terphenyl)element Cations $[(2,6\text{-}Mes_2C_6H_3)_2E]^+$ of Group 13 Revisited and Extended (E=B, Al, Ga, In, Tl)

Daniel Duvinage, Lorraine A. Malaspina, Simon Grabowsky,* Stefan Mebs,* and Jens Beckmann*

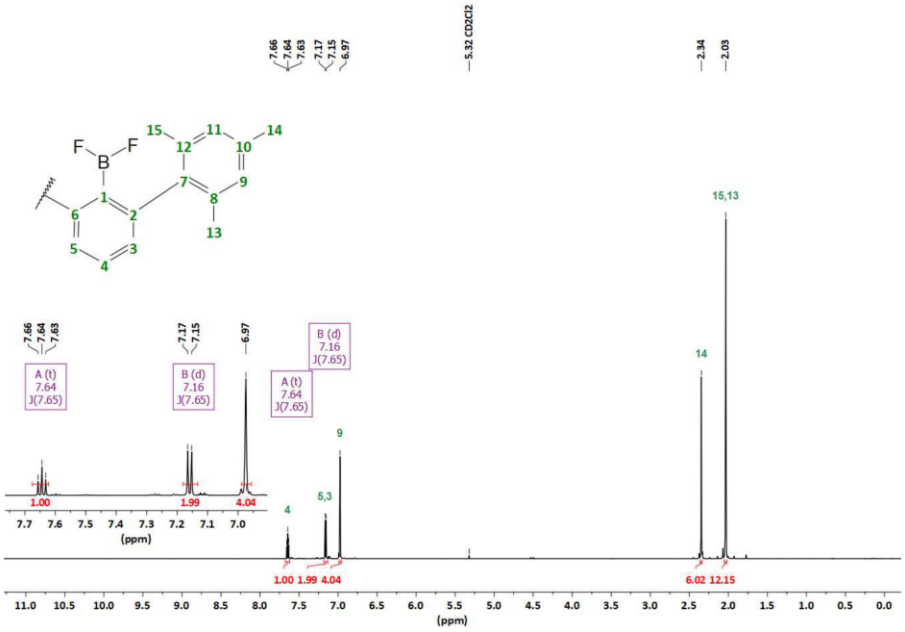

Figure S1. ^1H NMR (CD_2Cl_2, 600 MHz) spectrum of 2,6-$Mes_2C_6H_3BF_2$ (**10**)

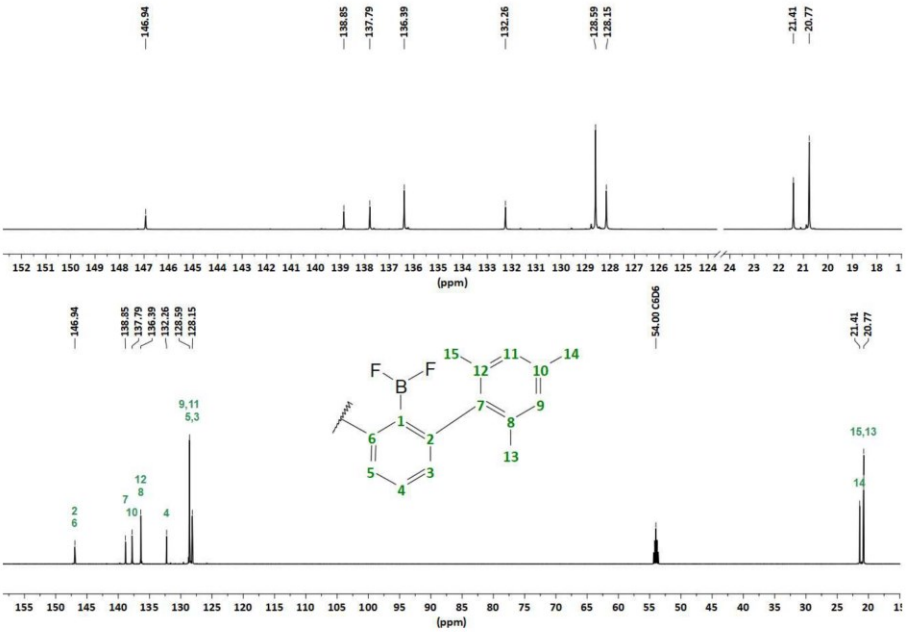

Figure S2. $^{13}C\{^{1}H\}$ NMR (CD_2Cl_2, 151 MHz) spectrum of 2,6-$Mes_2C_6H_3BF_2$ (**10**)

2

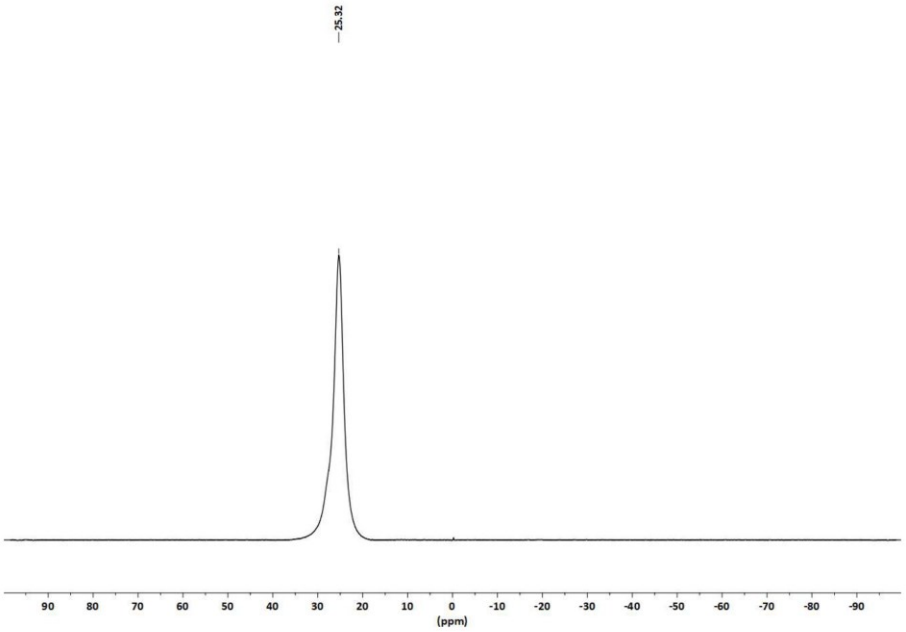

Figure S3. $^{11}B\{^{1}H\}$ NMR (CD_2Cl_2, 193 MHz) spectrum of 2,6-$Mes_2C_6H_3BF_2$ (**10**)

3

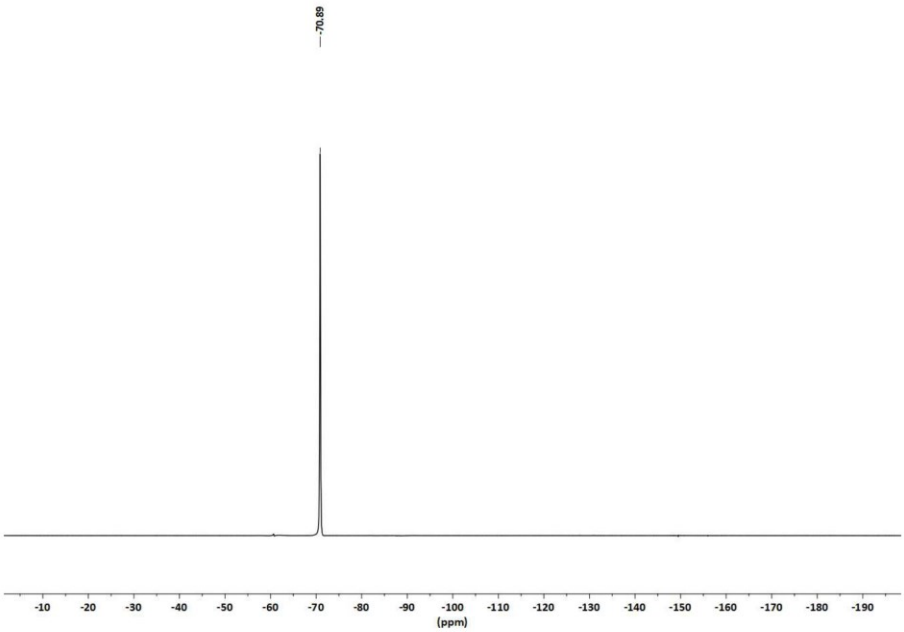

Figure S4. $^{19}F\{^{1}H\}$ NMR (CD_2Cl_2, 565 MHz) spectrum of 2,6-$Mes_2C_6H_3BF_2$ (**10**)

4

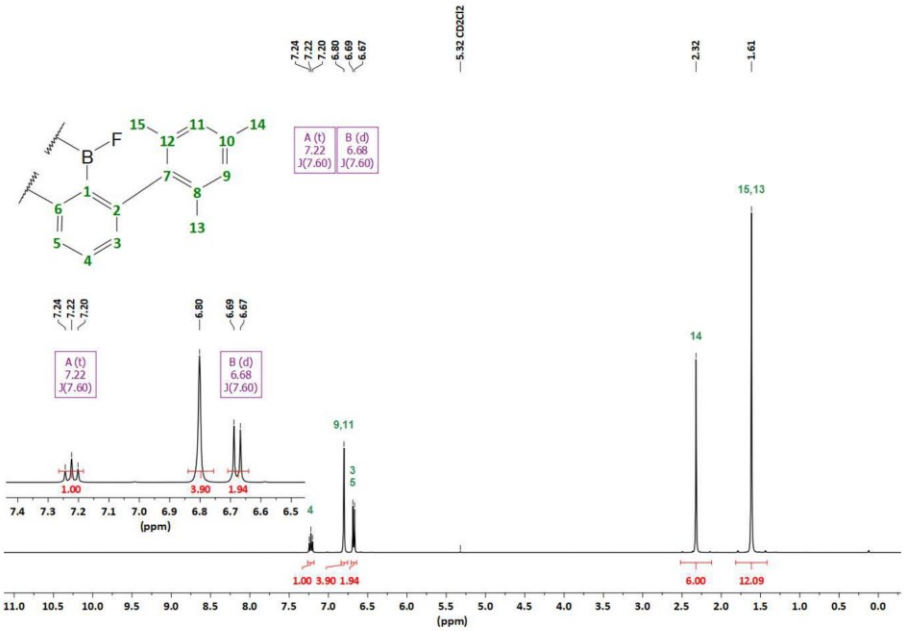

Figure S5. ^{1}H NMR (CD_2Cl_2, 600 MHz) spectrum of (2,6-$Mes_2C_6H_3)_2BF$ (**11**).

5

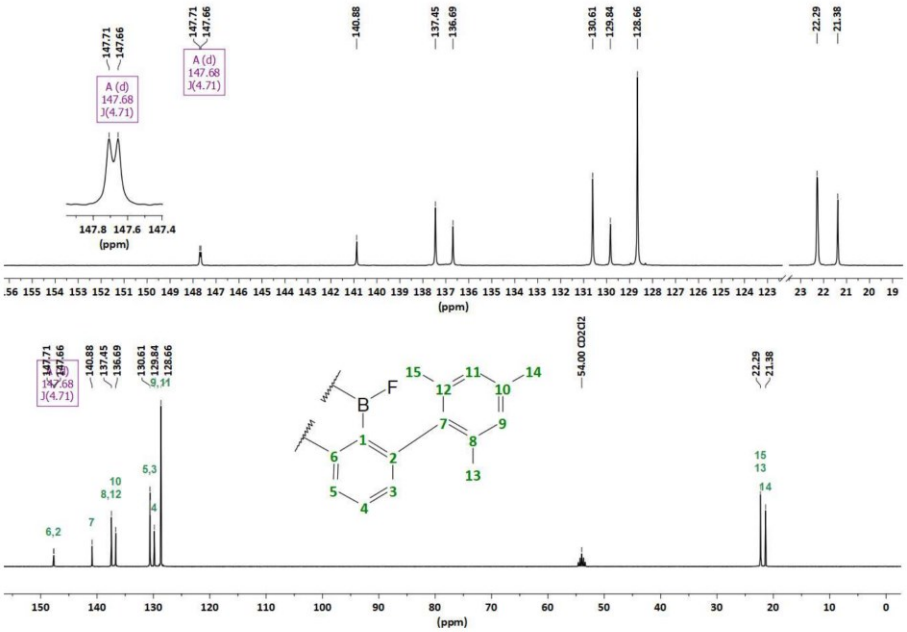

Figure S6. ^{13}C NMR (CD_2Cl_2, 151 MHz) spectrum of (2,6-$Mes_2C_6H_3$)$_2$BF (**11**).

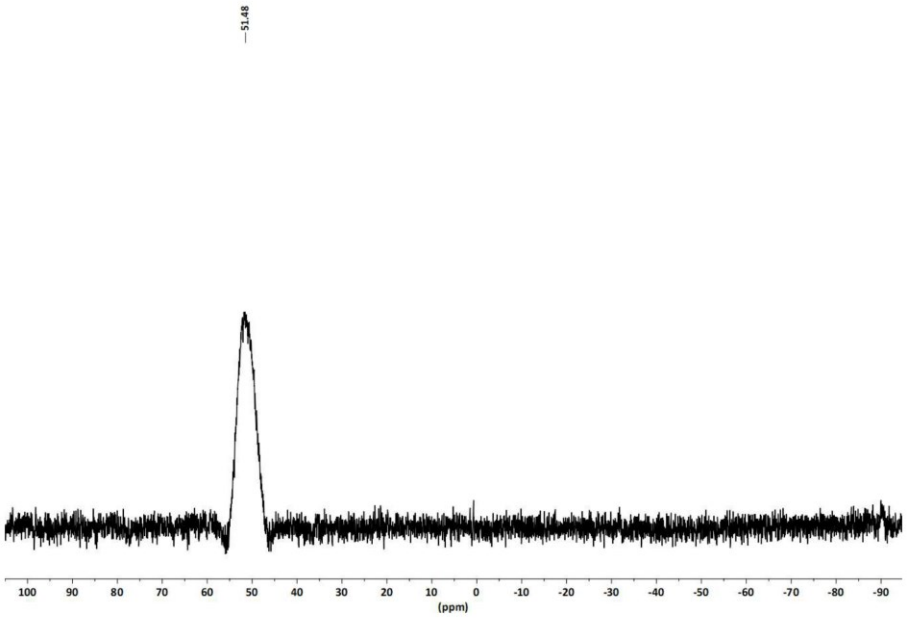

Figure S7. ^{11}B NMR (CD_2Cl_2, 193 MHz) spectrum of (2,6-$Mes_2C_6H_3$)$_2$BF (**11**).

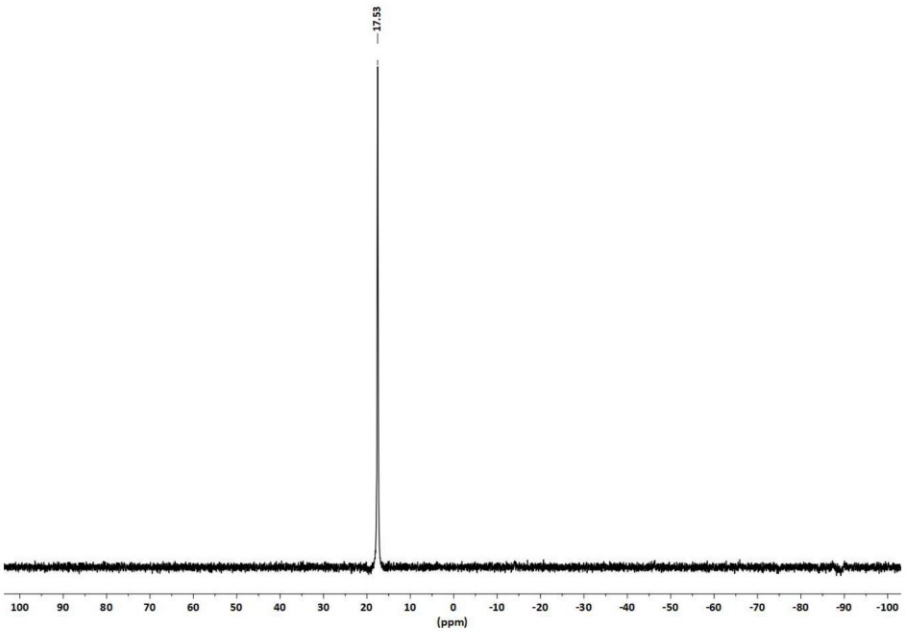

Figure S8. $^{19}F\{^{1}H\}$ NMR (CD_2Cl_2, 565 MHz) spectrum of (2,6-$Mes_2C_6H_3$)$_2$BF (**11**).

8

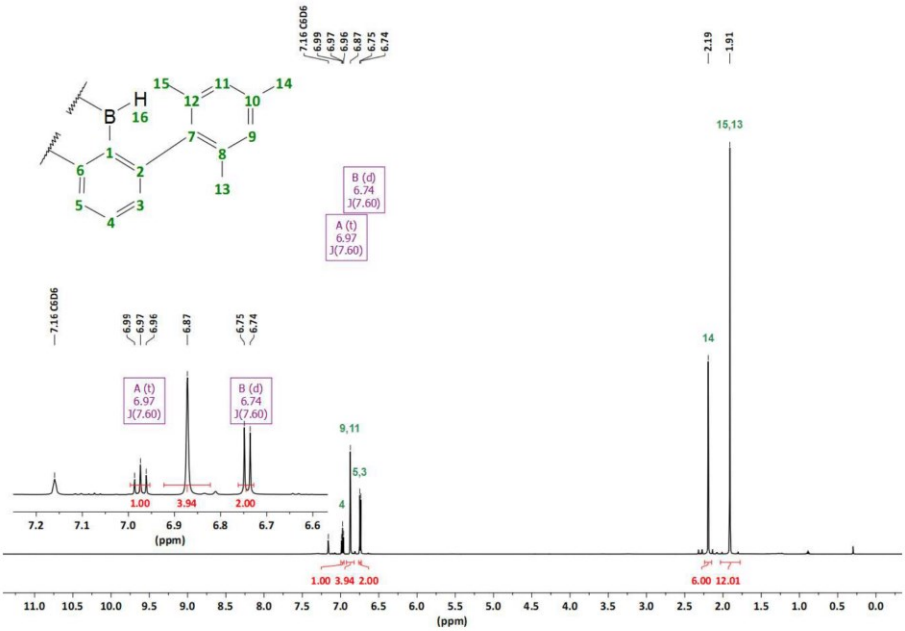

Figure S9. ^{1}H NMR (C_6D_6, 600 MHz) spectrum of (2,6-$Mes_2C_6H_3$)$_2$BH (**12**).

9

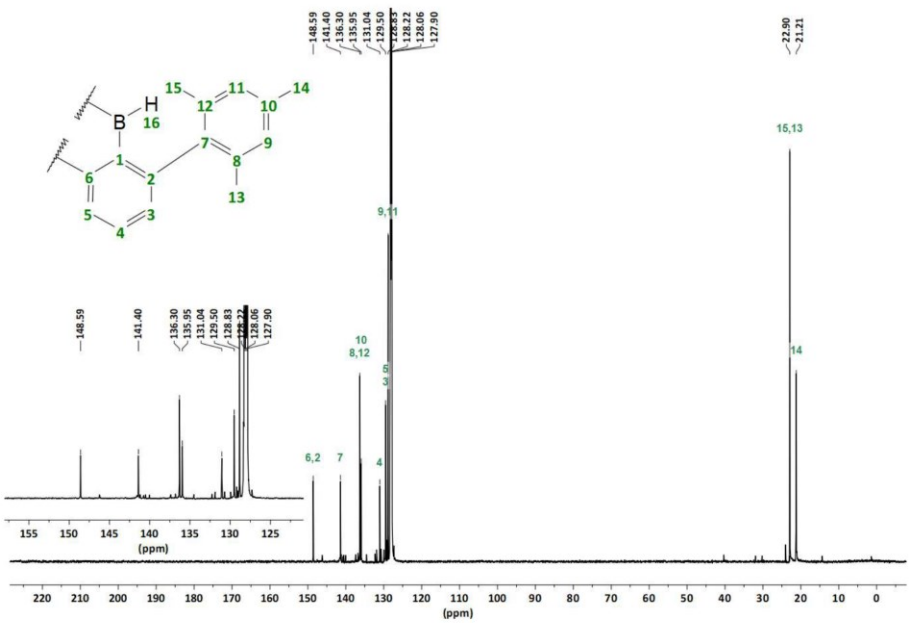

Figure S10. ^{13}C NMR (C_6D_6, 151 MHz) spectrum of (2,6-$Mes_2C_6H_3$)$_2$BH (**12**).

10

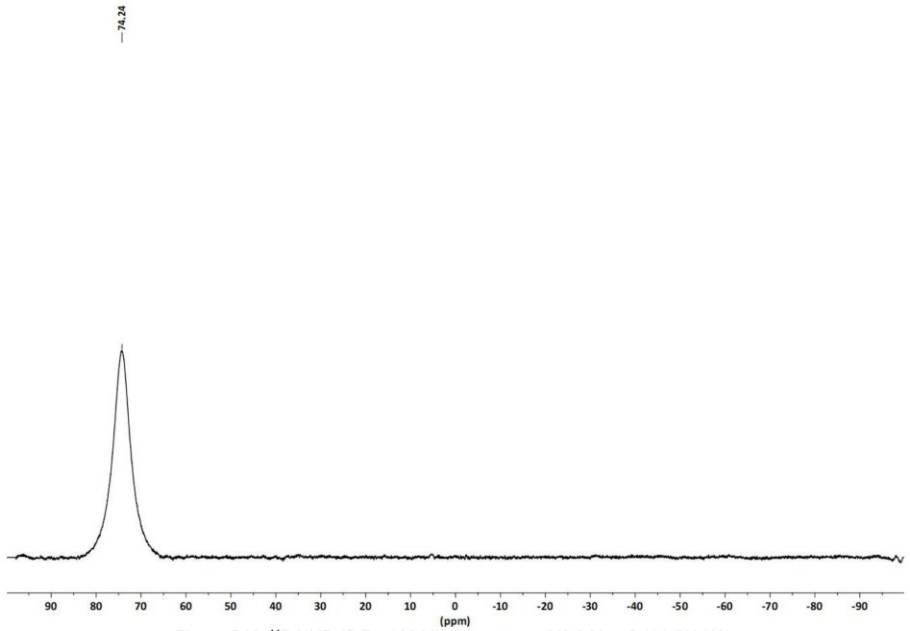

Figure S11. ^{11}B NMR (C_6D_6, 193 MHz) spectrum of (2,6-$Mes_2C_6H_3$)$_2$BH (**12**).

11

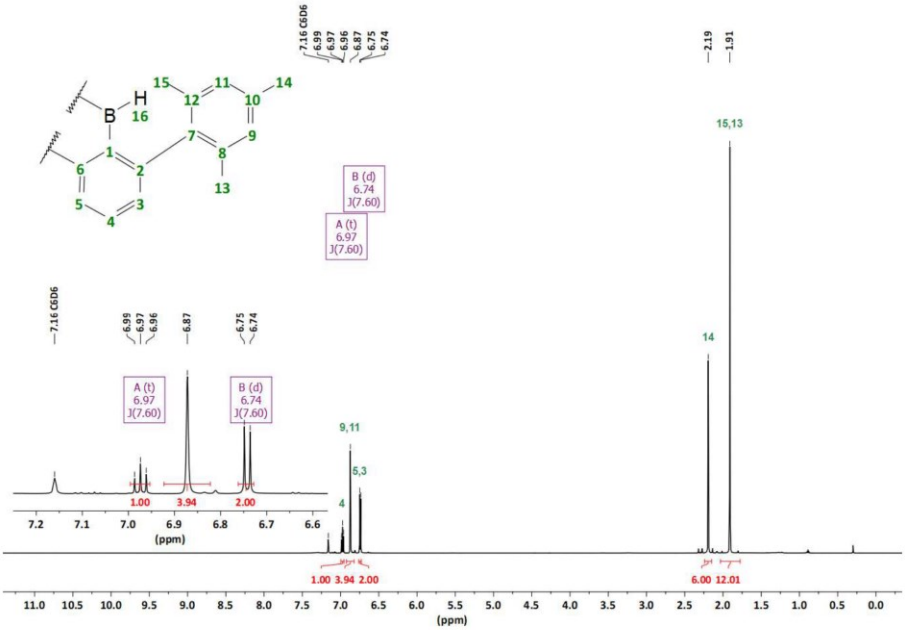

Figure S12. ^{1}H NMR (C_6D_6, 600 MHz) spectrum of (2,6-$Mes_2C_6H_3$)$_2$BH (**12**).

12

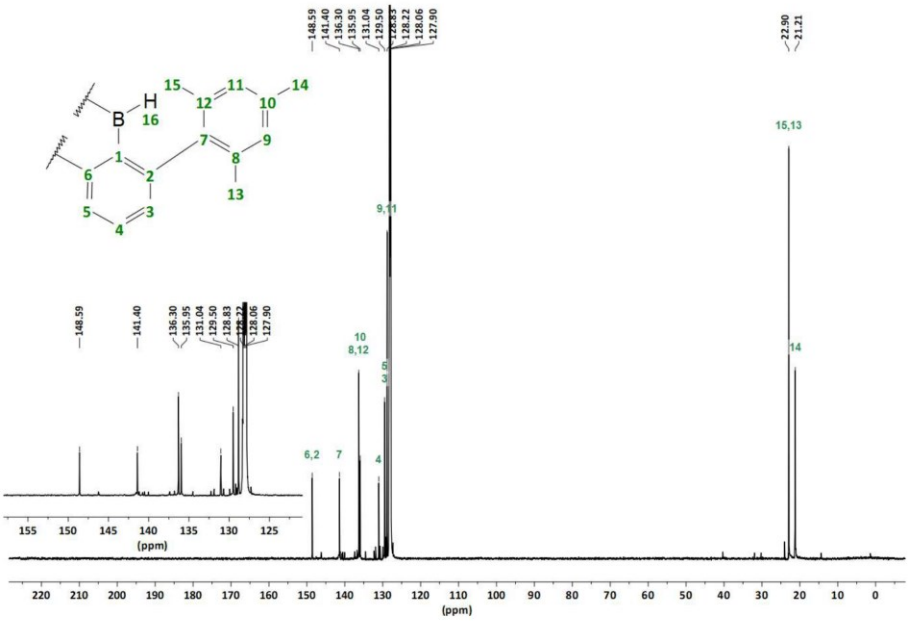

Figure S13. ^{13}C NMR (C_6D_6, 151 MHz) spectrum of (2,6-$Mes_2C_6H_3$)$_2$BH (**12**).

13

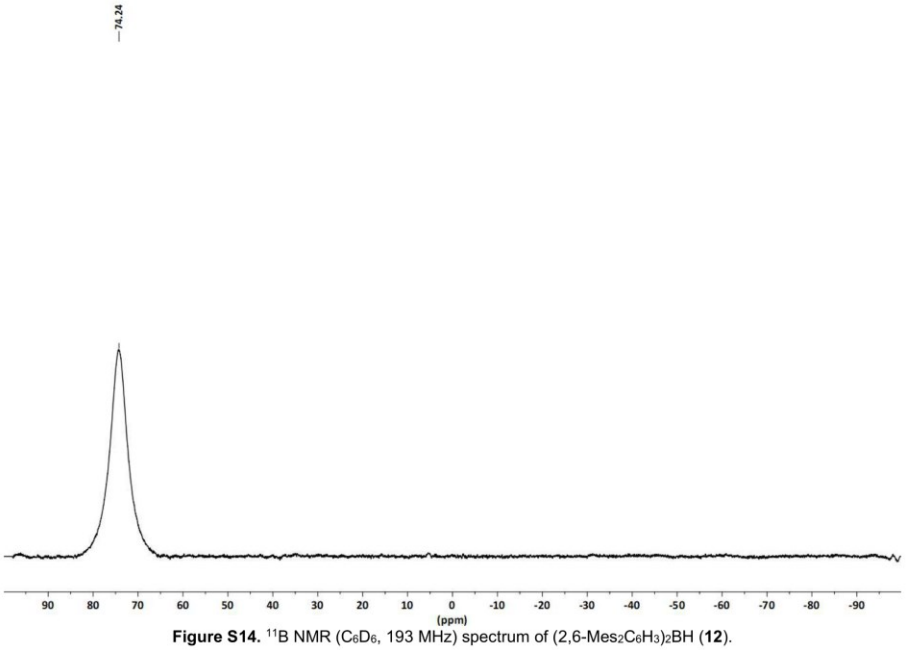

Figure S14. ^{11}B NMR (C_6D_6, 193 MHz) spectrum of (2,6-$Mes_2C_6H_3$)$_2$BH (**12**).

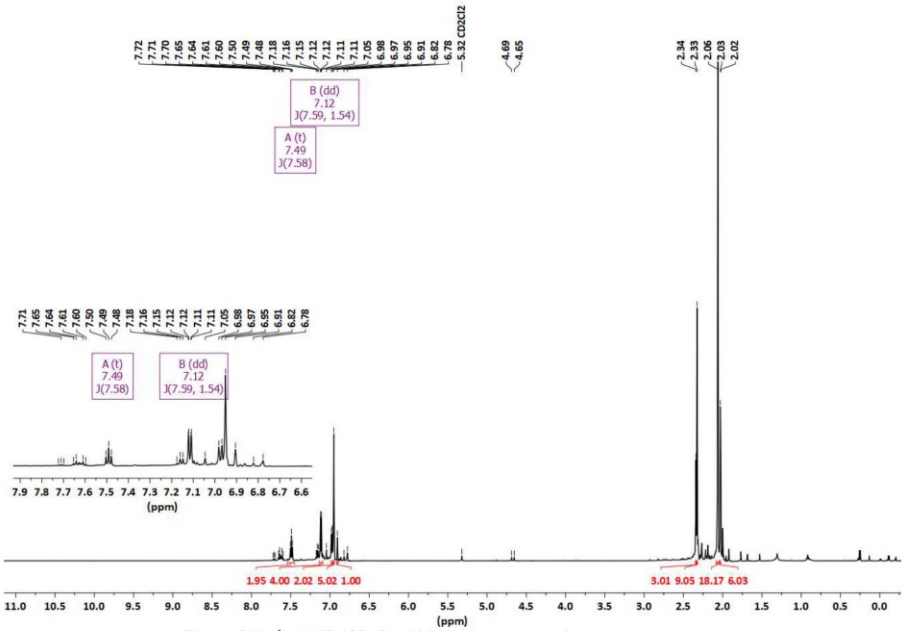

Figure S15. ^{1}H NMR (CD_2Cl_2, 600 MHz) spectrum of the reaction mixture.

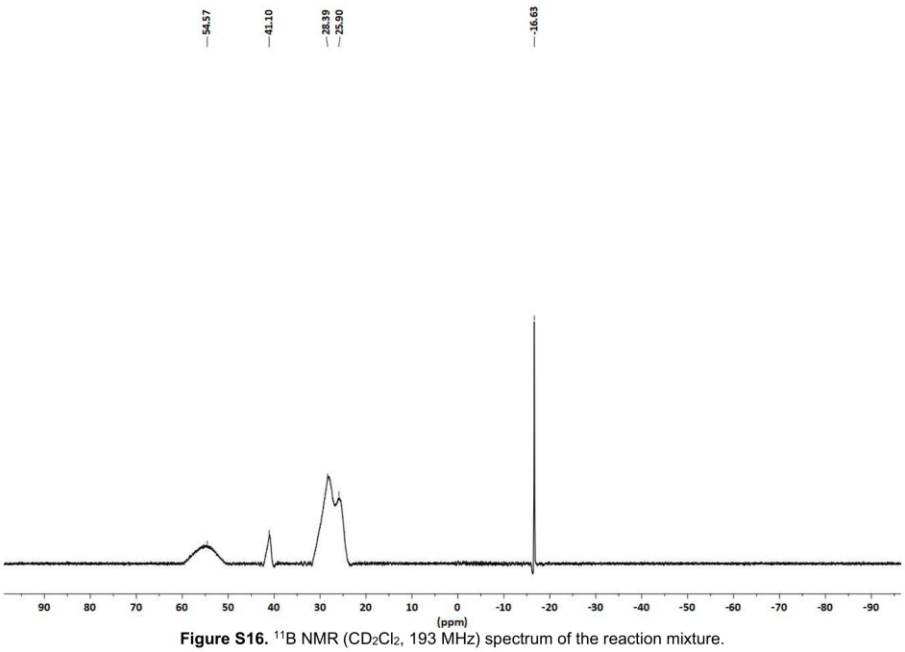

Figure S16. ^{11}B NMR (CD_2Cl_2, 193 MHz) spectrum of the reaction mixture.

16

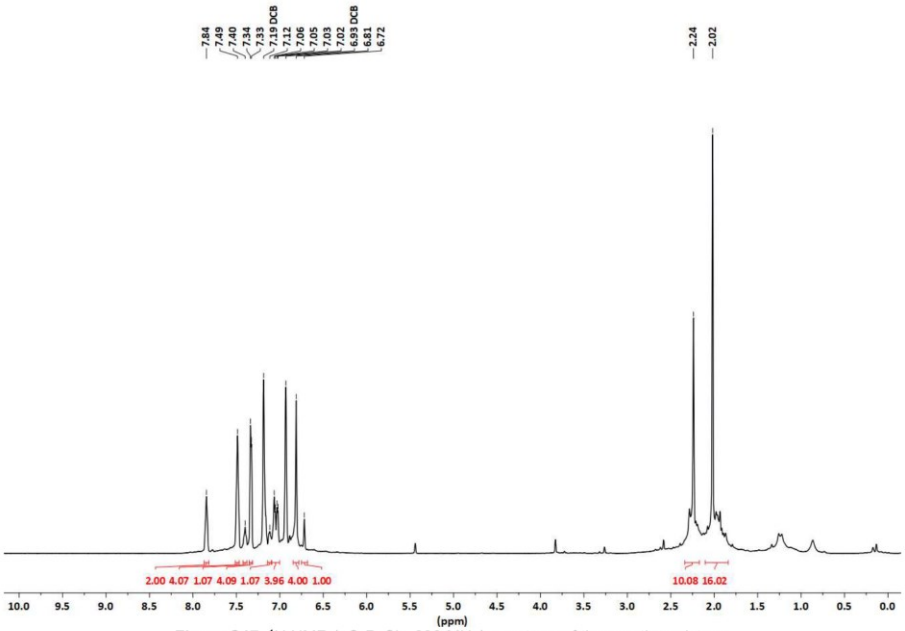

Figure S17. ^1H NMR ($oC_6D_4Cl_2$, 600 MHz) spectrum of the reaction mixture.

17

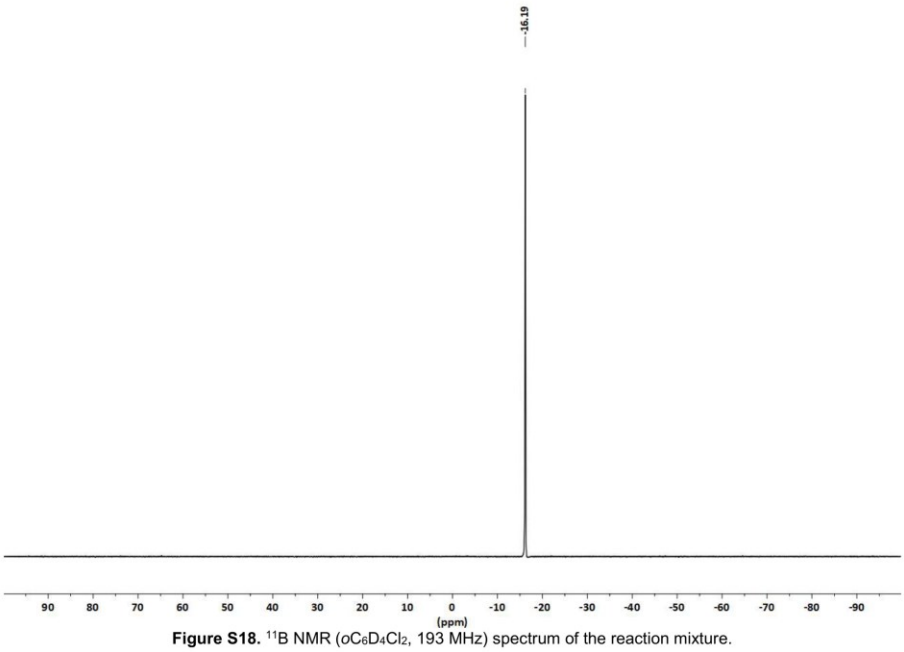

Figure S18. ^{11}B NMR ($oC_6D_4Cl_2$, 193 MHz) spectrum of the reaction mixture.

18

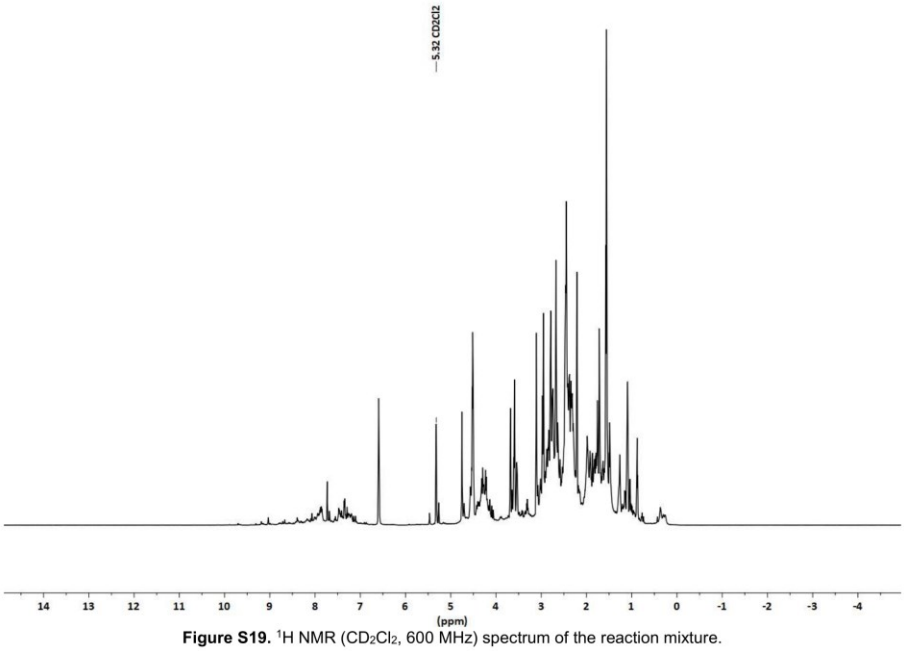

Figure S19. ^{1}H NMR (CD_2Cl_2, 600 MHz) spectrum of the reaction mixture.

19

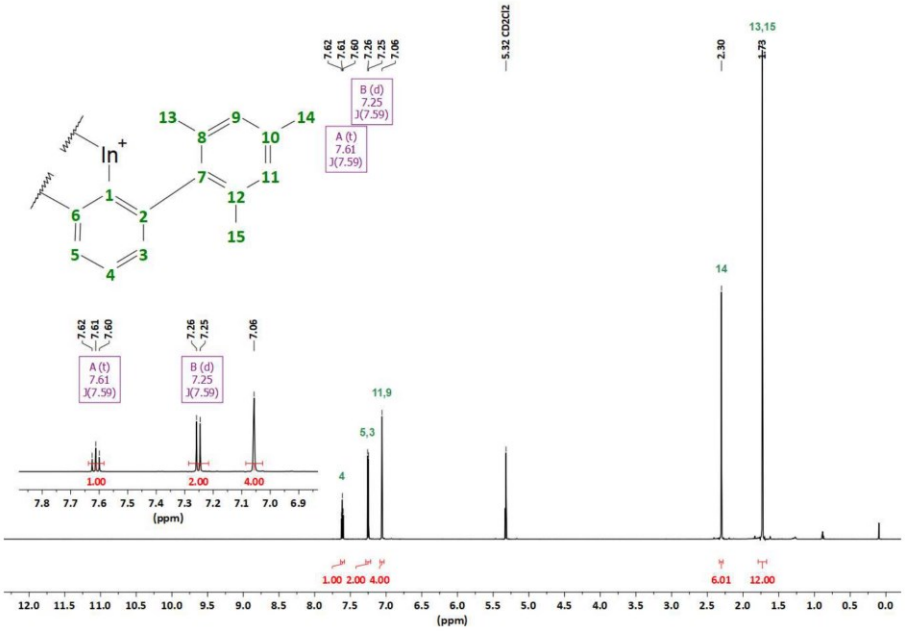

Figure S20. ^{1}H NMR (CD_2Cl_2, 600 MHz) spectrum of [2,6-$Mes_2C_6H_3$)$_2$In][$B(C_6F_5)_4$] (**4**).

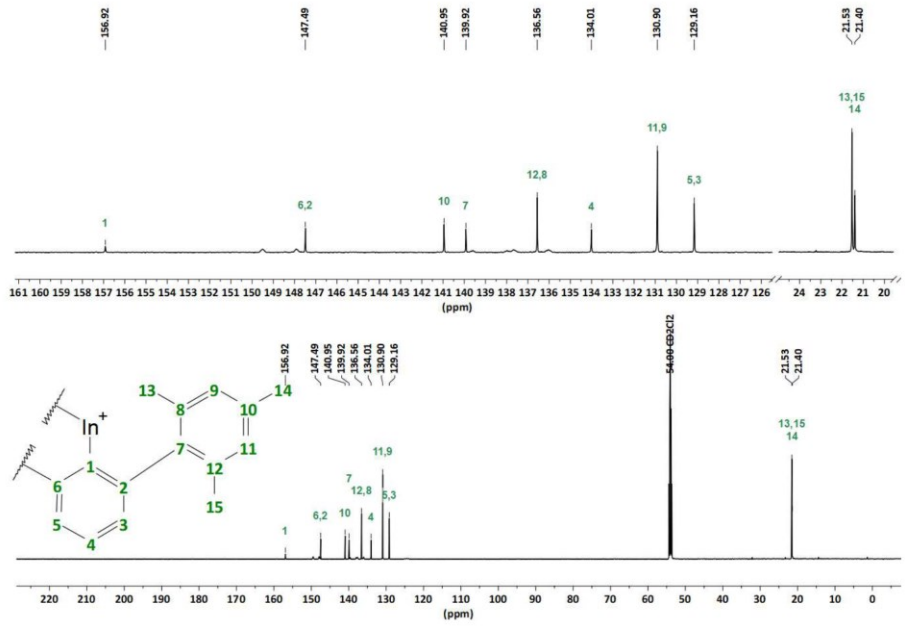

Figure S21. $^{13}C\{^{1}H\}$ NMR (CD_2Cl_2, 151 MHz) spectrum of [2,6-$Mes_2C_6H_3$)$_2$In][$B(C_6F_5)_4$] (**4**).

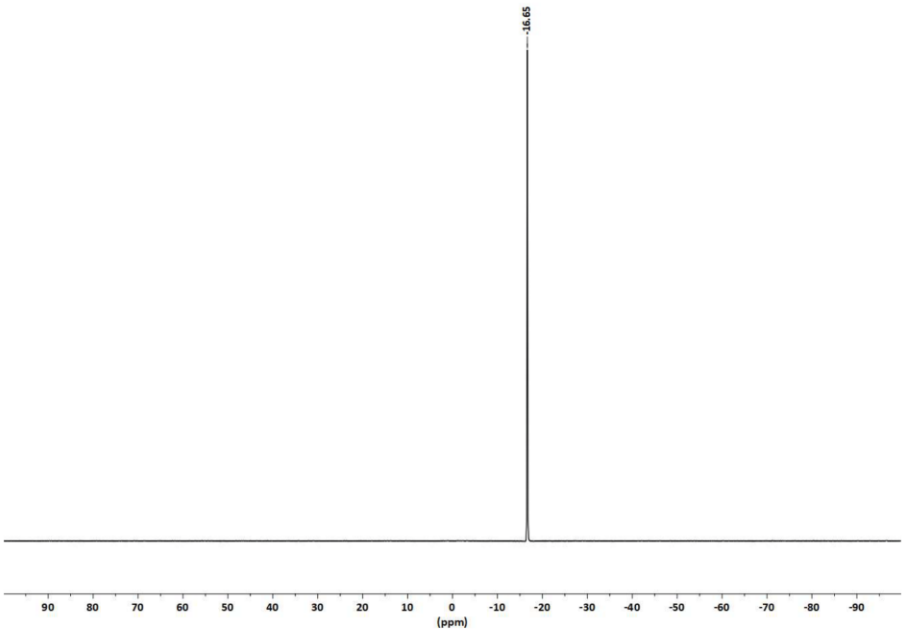

Figure S22. $^{11}B\{^{1}H\}$ NMR (CD_2Cl_2, 151 MHz) spectrum of $[2,6\text{-}Mes_2C_6H_3)_2In][B(C_6F_5)_4]$ (**4**).

22

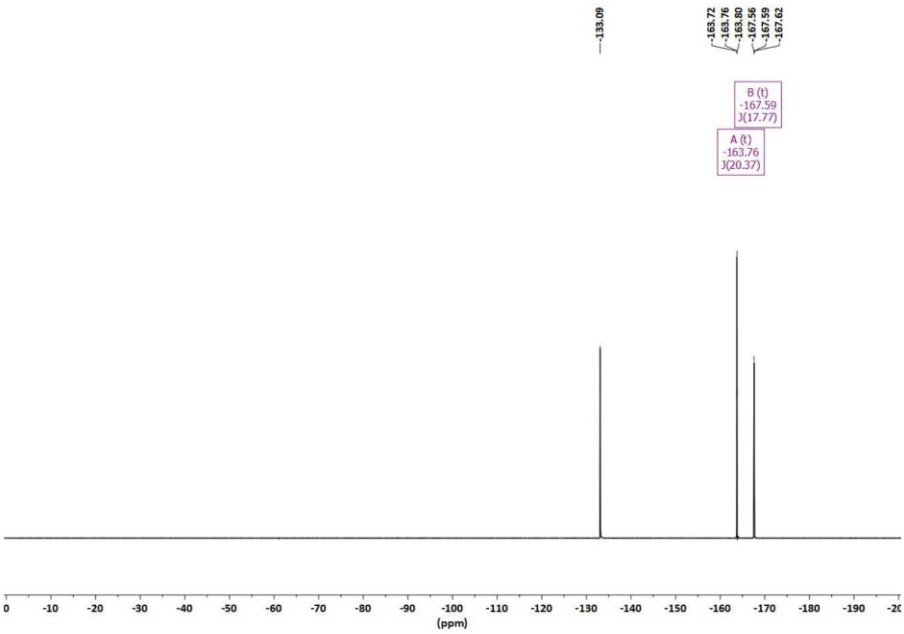

Figure S23. ^{19}F NMR (CD_2Cl_2, 565 MHz) spectrum of $[2,6\text{-}Mes_2C_6H_3)_2In][B(C_6F_5)_4]$ (**4**).

23

Figure S24. UV-Vis spectrum (CH_2Cl_2, 100μM) of [2,6-$Mes_2C_6H_3$)$_2$In][$B(C_6F_5)_4$] (**4**).

Table S1. Crystal data and structure refinement of **4**, **10**, **11**, **12** and **13**.

	4	**10**	**11**
Formula	$C_{72}H_{50}BF_{20}In$	$C_{24}H_{25}BF_2$	$C_{48}H_{50}BF$
Formula weight, g mol^{-1}	1420.75	362.25	656.69
Crystal system	Orthorhombic	Orthorhombic	Monoclinic
Crystal size, mm	0.58 × 0.22 × 0.22	0.33 × 0.28 × 0.21	0.18 × 0.19 × 0.19
Space group	Pbca	Pbca	$P2_1/c$
a, Å	17.7067(7)	17.4465(5)	9.6429(3)
b, Å	21.7449(8)	7.9412(3)	22.4678(8)
c, Å	31.2692(11)	29.0883(10)	17.3375(8)
α, °	90	90	90
β, °	90	90	92.546(2)
γ, °	90	90	90
V, Å^3	12039.6(8)	4030.1(2)	3752.5(2)
Z	8	8	4
ρ_{calcd}, Mg m^{-3}	1.568	1.194	1.162
μ(Mo *Kα*), mm^{-1}	0.500	0.080	0.068
F(000)	5728.0	1536	1408
θ range, deg	2.28 to 32.82	2.38 to 33.28	2.52 to 28.24
Index ranges	$-23 \le h \le 23$	$-26 \le h \le 24$	$-12 \le h \le 12$
	$-28 \le k \le 27$	$-12 \le k \le 12$	$-29 \le k \le 29$
	$-41 \le l \le 41$	$-39 \le l \le 44$	$-23 \le l \le 23$
No. of reflns collected	180708	75090	60635
Completeness to θ_{max}	99.9%	99.9%	99.9%
No. indep. Reflns	14937	7703	9333
No. obsd reflns with($I > 2\sigma(I)$)	12000	5672	7751
No. refined params	859	250	463
GooF (F^2)	1.041	1.031	1.024
R_1 (F) ($I > 2\sigma(I)$)	0.0348	0.0559	0.0504
wR_2 (F^2) (all data)	0.0900	0.1634	0.1297
Largest diff peak/hole, e Å^{-3}	1.52 / −0.59	0.51 / −0.40	0.35 / −0.26
CCDC number	2177924	2177925	2177926

Table S3. Topological and integrated AIM and ELI-D properties of the individual E–C contacts in R_2E^+ and R_2EF (E = B, Al, Ga, In, Tl; R = 2,6-$Mes_2C_6H_3$).

	contact or basin	d [Å]	$\rho(\mathbf{r})_{bcp}$ [eÅ^{-3}]	$\nabla^2\rho(\mathbf{r})_{bcp}$ [eÅ^{-5}]	ε	$G/\rho(\mathbf{r})_{bcp}$ [a.u.]	$H/\rho(\mathbf{r})_{bcp}$ [a.u.]	N_{ELI} [e]	V_{ELI} [Å^3]	γ_{ELI}	RJI
$[R_2B]^+$	B-C1	1.476	1.52	-10.2	0.14	0.71	-1.18	2.78	10.4	1.99	81.5
$[R_2B]^+$	B-C50	1.476	1.52	-10.2	0.14	0.71	-1.18	2.78	10.4	1.99	81.5
R_2BF	B-C1	1.574	1.29	-8.9	0.09	0.63	-1.11	2.36	6.9	2.19	84.2
R_2BF	B-C50	1.574	1.29	-8.8	0.09	0.63	-1.11	2.36	6.9	2.19	84.2
$[R_2Al]^+$	Al-C50	1.939	0.61	6.4	0.08	1.13	-0.39	2.49	12.4	1.98	89.7
$[R_2Al]^+$	Al-C1	1.938	0.63	6.4	0.07	1.12	-0.40	2.42	9.9	1.98	89.6
R_2AlF	Al-C50	1.963	0.59	6.2	0.05	1.11	-0.38	2.44	12.8	2.06	88.4
R_2AlF	Al-C1	1.965	0.59	6.1	0.09	1.11	-0.38	2.46	13.2	2.04	88.2
$[R_2Ga]^+$	Ga-C1	1.925	0.87	2.5	0.07	0.73	-0.52	2.61	10.7	1.68	63.0
$[R_2Ga]^+$	Ga-C50	1.934	0.85	2.5	0.07	0.73	-0.52	2.66	13.1	1.69	63.5
R_2GaF	Ga-C1	1.961	0.81	3.0	0.06	0.76	-0.50	2.55	12.7	1.75	69.3
R_2GaF	Ga-C50	1.962	0.81	3.0	0.06	0.76	-0.50	2.51	11.8	1.76	69.1
$[R_2In]^+$	In-C1	2.094	0.77	2.9	0.08	0.69	-0.43	2.16	10.4	1.64	72.7
$[R_2In]^+$	In-C50	2.096	0.77	2.8	0.08	0.69	-0.43	2.17	10.6	1.64	72.5
R_2InF	In-C1	2.137	0.71	3.3	0.07	0.73	-0.40	2.20	10.4	1.71	75.5
R_2InF	In-C50	2.137	0.71	3.3	0.07	0.73	-0.40	2.20	10.4	1.71	75.5
$[R_2Tl]^+$	Tl-C1	2.110	0.85	1.6	0.08	0.59	-0.46	1.84	7.0	1.56	72.7
$[R_2Tl]^+$	Tl-C50	2.110	0.85	1.6	0.08	0.59	-0.46	1.84	7.0	1.56	72.9
R_2TlF	Tl-C1	2.141	0.80	2.1	0.05	0.62	-0.43	1.84	6.4	1.62	75.3
R_2TlF	Tl-C50	2.143	0.80	2.1	0.06	0.62	-0.43	1.89	7.4	1.61	75.2

For all bonds, d is the geometric contact distance, $\rho(\mathbf{r})_{bcp}$ is the electron density at the bcp, $\nabla^2\rho(\mathbf{r})_{bcp}$ is the corresponding Laplacian, ε is the bond ellipticity, $G/\rho(\mathbf{r})_{bcp}$ and $H/\rho(\mathbf{r})_{bcp}$ are the kinetic and total energy density over $\rho(\mathbf{r})_{bcp}$ ratios, N_{ELI} and V_{ELI} are electron populations and volumes of related ELI-D basins, γ_{ELI} is the ELI-D value at the attractor position, RJI is the Raub-Jansen Index.

Table S1. cont.

	12	**13**
Formula	$C_{48}H_{51}B$	$C_{24}H_{25}BCl_2$
Formula weight, g mol^{-1}	638.69	395.15
Crystal system	Monoclinic	Monoclinic
Crystal size, mm	0.28 × 0.27 × 0.23	0.46 × 0.23 × 0.21
Space group	I2/a	C2/c
a, Å	16.426 (2)	15.3940(4)
b, Å	13.398(2)	9.0375(4)
c, Å	17.098 (2)	16.1523(7)
α, °	90	90
β, °	93.948 (11)	111.125(2)
γ, °	90	90
V, Å^3	3753.9(9)	2096.14(14)
Z	4	4
ρ_{calcd}, Mg m^{-3}	1.130	1.252
μ (Mo *Kα*), mm^{-1}	0.063	0.316
F(000)	1376.0	832
θ range, deg	2.49 to 33.23	2.66 to 33.24
Index ranges	–35 ≤ h ≤ 35	–23 ≤ h ≤ 23
	–20 ≤ k ≤ 20	–13 ≤ k ≤ 13
	–25 ≤ l ≤ 25	–24 ≤ l ≤ 24
No. of reflns collected	113861	34828
Completeness to θ_{max}	99.9%	99.9%
No. indep. Reflns	7232	4017
No. obsd reflns with($I>2\sigma(I)$)	6043	3620
No. refined params	452	127
GooF (F^2)	2.060	1.066
R_1 (F) ($I > 2\sigma(I)$)	0.023	0.0359
wR_2 (F^2) (all data)	N/A	0.1117
Largest diff peak/hole, e Å^{-3}	0.13 / –0.16	0.52 / –0.58
CCDC number	2177927	2177928

Table S4. AIM atomic and fragmental charges of R_2EF and R_2E^+ (E = B, Al, Ga, In, Tl; R = 2,6-$Mes_2C_6H_3$).

Q_{AIM}	R_2BF	$[R_2B]^+$	R_2AlF	$[R_2Al]^+$	R_2GaF	$[R_2Ga]^+$	R_2InF	$[R_2In]^+$	R_2TlF	$[R_2Tl]^+$
Ter1	-0.63	-0.46	-0.73	-0.61	-0.37	-0.17	-0.32	-0.12	-0.16	-0.01
Ter2	-0.63	-0.46	-0.73	-0.61	-0.38	-0.15	-0.32	-0.12	-0.16	-0.01
F	-0.86		-0.90		-0.79		-0.79		-0.77	
E	2.12	1.92	2.36	2.22	1.53	1.35	1.41	1.25	1.09	1.02
Σ	-0.01	1.00	0.00	1.00	-0.01	1.02	-0.01	1.00	0.00	0.99

Table S5. Topological and integrated AIM and ELI-D properties of the E-F contacts in R_2EF (E = B, Al, Ga, In, Tl; R = 2,6-$Mes_2C_6H_3$).

	contact	d [Å]	$\rho(\mathbf{r})_{bcp}$ [eÅ^{-3}]	$\nabla^2\rho(\mathbf{r})_{bcp}$ [eÅ^{-5}]	ε	$G/\rho(\mathbf{r})_{bcp}$ [a.u.]	$H/\rho(\mathbf{r})_{bcp}$ [a.u.]	basin	N_{ELI} [e]	V_{ELI} [Å^3]	γ_{ELI}
R_2BF	B-F	1.334	1.35	28.5	0.18	2.25	-0.77	F-B	1.33	1.6	1.52
								LP(F)	3.22	6.1	1.62
								LP(F)	3.22	6.1	1.62
									7.8	*13.8*	*1.59*
R_2AlF	Al-F	1.672	0.71	22.0	0.03	2.17	0.02	F-Al	0.70	0.5	1.50
								LP(F)	3.58	8.4	1.57
								LP(F)	3.55	8.8	1.57
									7.8	*17.7*	*1.55*
R_2GaF	Ga-F	1.798	0.78	18.0	0.01	1.76	-0.15	LP(F)	3.84	8.0	1.58
								LP(F)	3.96	9.2	1.58
									7.8	*17.2*	*1.58*
R_2InF	In-F	2.016	0.62	13.0	0.01	1.57	-0.11	LP(F)	3.86	9.2	1.57
								LP(F)	3.86	9.2	1.57
									7.7	*18.4*	*1.57*
R_2TlF	Tl-F	2.152	0.54	9.7	0.01	1.34	-0.10	LP(F)	3.68	7.5	1.57
								LP(F)	3.99	9.8	1.57
									7.7	*17.3*	*1.57*

For all bonds, d is the geometric contact distance, $\rho(\mathbf{r})_{bcp}$ is the electron density at the bcp, $\nabla^2\rho(\mathbf{r})_{bcp}$ is the corresponding Laplacian, ε is the bond ellipticity, $G/\rho(\mathbf{r})_{bcp}$ and $H/\rho(\mathbf{r})_{bcp}$ are the kinetic and total energy density over $\rho(\mathbf{r})_{bcp}$ ratios, N_{ELI} and V_{ELI} are electron populations and volumes of related ELI-D basins, γ_{ELI} is the ELI-D value at the attractor position.

Comment

The E─F bonds basically show the same trends observed for the E─C bonds. A considerable difference between the B─F and B─C bonds is the fact, that ionic bond contributions are much higher in the B─F bonds leading to a strongly positive Laplacian of the ED in contrast to the negative values obtained for the B─C bonds. R_2BF and R_2AlF behave different than their higher counterparts in that a tiny E─F bonding basin is formed as a consequence of non-negligible covalent bond contributions. This is also reflected by the ELI-D value at the attractor position of those E─F basins (γ_{ELI}), which are slightly smaller than the corresponding values of the F atoms lone-pair (LP) basins, indicating more pronounced electron sharing. The electron population of these small E─F bonding basins basically stem from the formerly non-bonding lone-pairs of the F atoms, also reflected in RJI values of 92.4% for B─F and 95.5% for Al─F. Summing up all ELI-D valence basins related to the F atoms (including E─F and LP) results in almost identical overall electron populations of 7.7-7.8 e for all five R_2EF compounds.

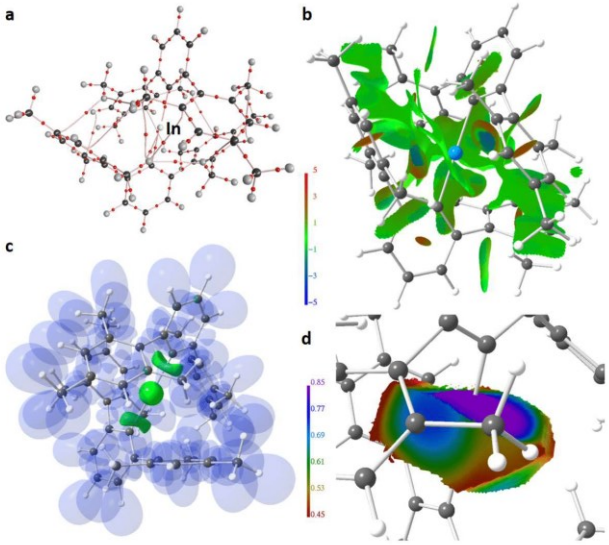

Figure S26. RSBI analysis of **4**: (a) AIM bond paths motif, (b) and (f) NCI *iso*-surface at s(**r**) = 0.5, (c) and (g) ELI-D localization domain representation at *iso*-value of 1.3, (d) and (h) ELI-D distribution mapped on the In atom ELI-D core basin.

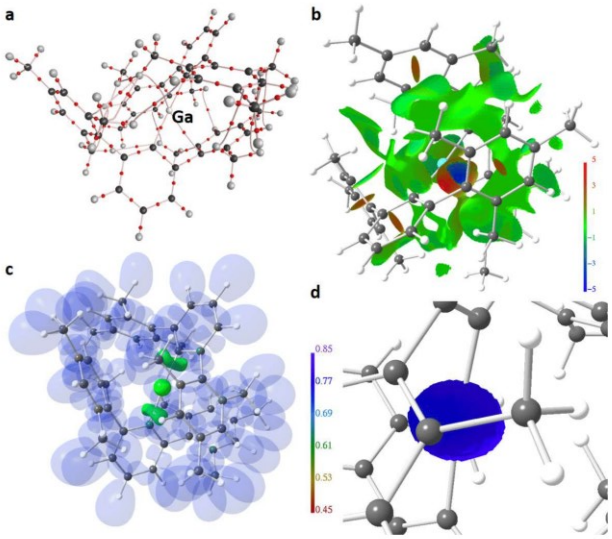

Figure S25. RSBI analysis of **3**: (a) AIM bond paths motif, (b) and (f) NCI *iso*-surface at s(**r**) = 0.5, (c) and (g) ELI-D localization domain representation at *iso*-value of 1.3, (d) and (h) ELI-D distribution mapped on the Ga atom ELI-D core basin.

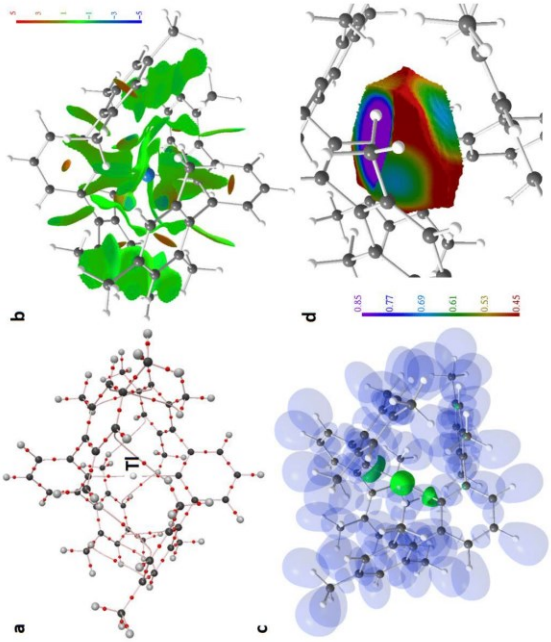

Figure S27. RSBI analysis of **5**: (a) AIM bond paths motif, (b) and (f) NCI *iso*-surface at $s(\mathbf{r}) = 0.5$, (c) and (g) ELI-D localization domain representation at *iso*-value of 1.3, (d) and (h) ELI-D distribution mapped on the Tl atom ELI-D core basin.

32

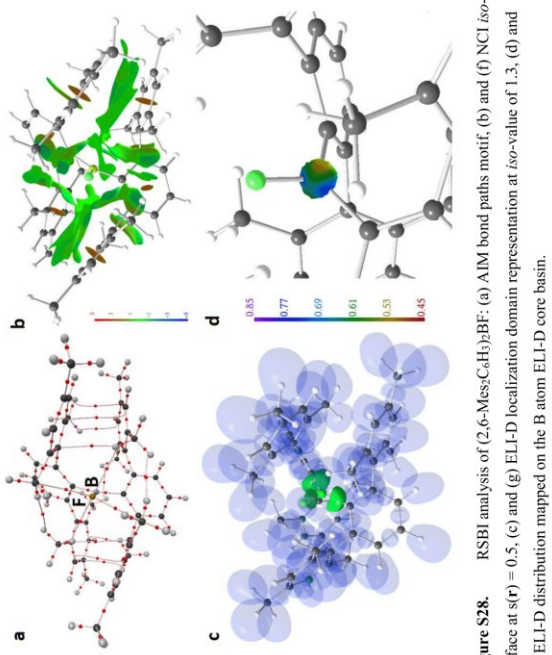

Figure S28. RSBI analysis of $(2,6\text{-Mes}_2C_6H_3)_2BF$: (a) AIM bond paths motif, (b) and (f) NCI *iso*-surface at $s(\mathbf{r}) = 0.5$, (c) and (g) ELI-D localization domain representation at *iso*-value of 1.3, (d) and (h) ELI-D distribution mapped on the B atom ELI-D core basin.

33

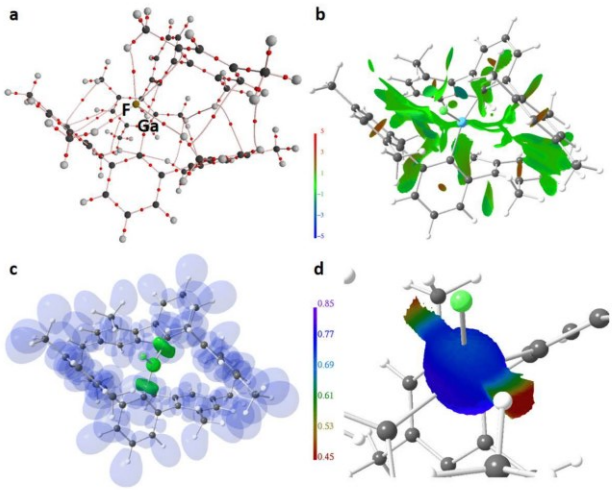

Figure S30. RSBI analysis of (2,6-$Mes_2C_6H_3$)$_2$GaF: (a) AIM bond paths motif, (b) and (f) NCI *iso*-surface at s(**r**) = 0.5, (c) and (g) ELI-D localization domain representation at *iso*-value of 1.3, (d) and (h) ELI-D distribution mapped on the Ga atom ELI-D core basin.

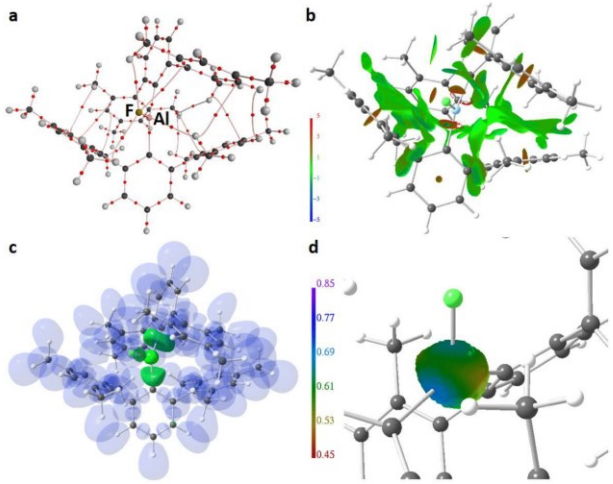

Figure S29. RSBI analysis of (2,6-$Mes_2C_6H_3$)$_2$AlF: (a) AIM bond paths motif, (b) and (f) NCI *iso*-surface at s(**r**) = 0.5, (c) and (g) ELI-D localization domain representation at *iso*-value of 1.3, (d) and (h) ELI-D distribution mapped on the Al atom ELI-D core basin.

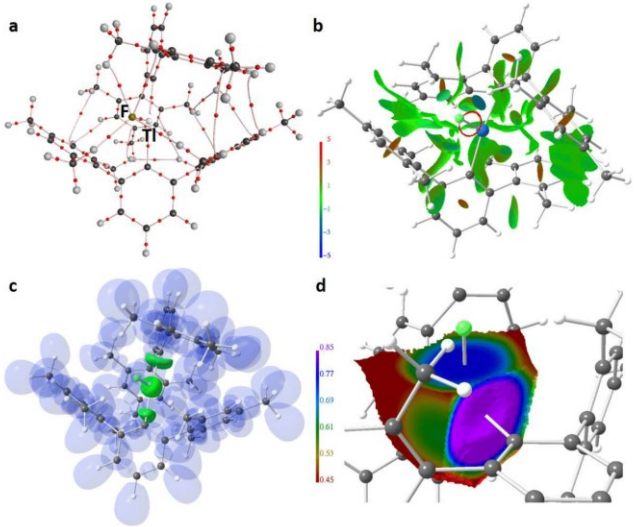

Figure S31. RSBI analysis of (2,6-$Mes_2C_6H_3$)$_2$InF: (a) AIM bond paths motif, (b) and (f) NCI *iso*-surface at s(**r**) = 0.5, (c) and (g) ELI-D localization domain representation at *iso*-value of 1.3, (d) and (h) ELI-D distribution mapped on the In atom ELI-D core basin.

Figure S32. RSBI analysis of (2,6-$Mes_2C_6H_3$)$_2$TlF: (a) AIM bond paths motif, (b) and (f) NCI *iso*-surface at s(**r**) = 0.5, (c) and (g) ELI-D localization domain representation at *iso*-value of 1.3, (d) and (h) ELI-D distribution mapped on the Tl atom ELI-D core basin.

Table S6. Molecular energies and FIA values of small reference compounds

B3PW91/6-311+G(2df,p)

	energy	diff.	sum of fragments	diff.	diff.	-209.0
	a.u.	a.u.	a.u.	a.u.	kJ mol^{-1}	kJ mol^{-1}
COF_2	-313.0122					
$[COF_3]^-$	-412.9391	-99.9269				
$[Me_2P]^+$	-420.8271		-833.7662			
Me_2PF	-520.9357	-100.1085	-833.9479	-0.1817	-477.0	-686.0
$[Ph_2P]^+$	-804.3589		-1217.2980			
Ph_2PF	-904.5095	-100.1505	-1217.5217	-0.2237	-587.3	-796.3
$[Et_3Si]^+$	-526.9232		-939.8623			
Et_3SiF	-627.0782	-100.1550	-940.0904	-0.2281	-598.9	-807.9
$EtAlCl_2$	-1242.1298		-1655.0689			
$[EtAlCl_2F]^-$	-1342.1435	-100.0137	-1655.1558	-0.0869	-228.1	-437.1
$(EtAlCl_2)_2$	-2484.3021		-3310.1804			
2 $[EtAlCl_2F]^-$	-2684.2871	-99.9925	-3310.3116	-0.0656	-172.2	-381.2
$[Mes_3Si]^+$	-1337.9466		-1750.8857			
Mes_3SiF	-1438.0902	-100.1436	-1751.1024	-0.2167	-568.9	-777.9
$[Et_3Si(Tol)]^+$	-798.4566		-1211.3957			
Tol+ Et_3SiF	-898.6212	-100.1646	-1211.6334	-0.2377	-624.2	-833.2
$[Et_3Si\text{-}H\text{-}SiEt_3]^+$	-1054.6959		-1467.6350			
Et_3SiH + Et_3SiF	-1154.8425	-100.1466	-1467.8547	-0.2198	-577.0	-786.0
$AlCl_3$	-1623.1461		-2036.0852			
$[AlCl_3F]^-$	-1723.1768	-100.0307	-2036.1891	-0.1039	-272.7	-481.7
SbF_5	-739.6481		-1152.5872			
$[SbF_6]^-$	-839.6785	-100.0304	-1152.6907	-0.1035	-271.7	-480.7

Table S7. Molecular energies and FIA values of small reference compounds

BP86/6-311+G(2df,p)

	energy	diff.	sum of fragments	diff.	diff.	-209.0
	a.u.	a.u.	a.u.	a.u.	kJ mol^{-1}	kJ mol^{-1}
COF_2	-313.1385					
$[COF_3]^-$	-413.1069	-99.9684				
$[Me_2P]^+$	-420.8766		-833.9835			
Me_2PF	-521.0673	-100.1908	-834.2059	-0.2224	-583.9	-792.9
$[Ph_2P]^+$	-804.5985		-1217.7054			
Ph_2PF	-904.7829	-100.1844	-1217.9215	-0.2161	-567.3	-776.3
$[Et_3Si]^+$	-527.0459		-940.1528			
Et_3SiF	-627.2390	-100.1930	-940.3775	-0.2247	-589.9	-798.9
$EtAlCl_2$	-1242.3683		-1655.4752			
$[EtAlCl_2F]^-$	-1342.4188	-100.0505	-1655.5573	-0.0821	-215.6	-424.6
$(EtAlCl_2)_2$	-2484.7757		-3310.9894			
2 $[EtAlCl_2F]^-$	-2584.7871	-100.0115	-3311.1146	-0.0626	-164.4	-373.4
$[Mes_3Si]^+$	-1338.3689		-1751.4758			
Mes_3SiF	-1438.5471	-100.1781	-1751.6856	-0.2098	-550.7	-759.7
$[Et_3Si(Tol)]^+$	-798.6775		-1211.7844			
Tol + Et_3SiF	-898.8773	-100.1998	-1212.0158	-0.2314	-607.5	-816.5
$[Et_3Si\text{-}H\text{-}SiEt_3]^+$	-1054.9461		-1468.0530			
Et_3SiH + Et_3SiF	-1155.1271	-100.1810	-1468.2657	-0.2127	-558.3	-767.3
$AlCl_3$	-1623.4422		-2036.5491			
$[AlCl_3F]^-$	-1723.5104	-100.0682	-2036.6489	-0.0998	-262.1	-471.1
SbF_5	-739.8500		-1152.9568			
$[SbF_6]^-$	-839.9153	-100.0653	-1153.0538	-0.0969	-254.5	-463.5

Table S8. Molecular energies and FIA values of small reference compounds

MP2 single-point optimized @B3PW91/6-311+G(2df,p)

	energy	diff.	sum of fragments	diff.	diff.	-209.0
	a.u.	a.u.	a.u.	a.u.	kJ mol^{-1}	kJ mol^{-1}
COF_2	-312.5216					
$[COF_3]^-$	-412.3249	-99.8033				
$[Me_2P]^+$	-420.1145		-832.4394			
Me_2PF	-520.1455	-100.0310	-832.6671	-0.2277	-597.9	-806.9
$[Ph_2P]^+$	-802.8403		-1215.1652			
Ph_2PF	-902.8770	-100.0367	-1215.3986	-0.2334	-612.8	-821.8
$[Et_3Si]^+$	-525.8403		-938.1652			
Et_3SiF	-625.9205	-100.0802	-938.4420	-0.2769	-726.9	-935.9
$EtAlCl_2$	-1240.5571		-1652.8820			
$[EtAlCl_2F]^-$	-1340.4590	-99.9020	-1652.9806	-0.0987	-259.0	-468.0
$(EtAlCl_2)_2$	-2481.1711		-3305.8209			
$2\ [EtAlCl_2F]^-$	-2581.0161	-99.8450	-3305.9612	-0.0702	-184.2	-393.2
$[Mes_3Si]^+$		out-of-memory				
Mes_3SiF		out-of-memory				
$[Et_3Si(Tol)]^+$	-796.8142		-1209.1391			
$Tol + Et_3SiF$	-896.8428	-100.0286	-1209.3644	-0.2253	-591.4	-611.4
$[Et_3Si\text{-}H\text{-}SiEt_3]^+$	-1052.6052		-1464.9301			
$Et_3SiH + Et_3SiF$	-1152.6277	-100.0225	-1465.1493	-0.2192	-575.5	-595.5
$AlCl_3$	-1621.3062		-2033.6311			
$[AlCl_3F]^-$	-1721.2237	-99.9175	-2033.7453	-0.1142	-299.9	-508.9
SbF_5	-738.1546		-1150.4795			
$[SbF_6]^-$	-838.0737	-99.9191	-1150.5953	-0.1158	-303.9	-512.9

Table S9. Molecular energies and FIA values

B3PW91/6-311+G(2df,p)

	energy	diff.	sum of fragments	diff.	diff.	-209.0
	a.u.	a.u.	a.u.	a.u.	kJ mol^{-1}	kJ mol^{-1}
COF_2	-313.0122					
$[COF_3]^-$	-412.9391	-99.9269				
$[R_2B]^+$	-1884.0135		-2296.9526			
R_2BF	-1984.1368	-100.1233	-2297.1491	-0.1965	-515.8	-724.8
$[R_2Al]^+$	-2101.6276		-2514.5667			
R_2AlF	-2201.7416	-100.1139	-2514.7538	-0.1871	-491.2	-700.2
$[R_2Ga]^+$	-3784.0489		-4196.9880			
R_2GaF	-3884.1347	-100.0858	-4197.1469	-0.1590	-417.4	-626.4
$[R_2In]^+$	-2049.4587		-2462.3978			
R_2InF	-2149.5258	-100.0672	-2462.5381	-0.1403	-368.4	-577.4
$[R_2Tl]^+$	-2031.8282		-2444.7673			
R_2TlF	-2131.8736	-100.0454	-2444.8859	-0.1186	-311.3	-520.3
$[R_2P]^+$	-2200.4646		-2613.4037			
R_2PF	-2300.5791	-100.1145	-2613.5914	-0.1876	-492.7	-701.7
$[R_2As]^+$	-4095.0029		-4507.9420			
R_2AsF	-4195.1004	-100.0976	-4508.1127	-0.1707	-448.2	-657.2
$[R_2Sb]^+$	-2099.5401		-2512.4792			
R_2SbF	-2199.6287	-100.0886	-2512.6410	-0.1618	-424.7	-633.7
$[R_2Bi]^+$	-2073.9285		-2486.8676			
R_2BiF	-2174.0053	-100.0768	-2487.0175	-0.1500	-393.8	-602.8

R = 2,6-$Mes_2C_6H_3$

6.6 Heavier Bis(*m*-terphenyl)element Phosphaethynolates of Group 13

Electronic Supplementary Material (ESI) for Dalton Transactions.
This journal is © The Royal Society of Chemistry 2022

Supporting Information

Heavier Bis(*m*-terphenyl)element phosphaethynolates of Group 13

Daniel Duvinage,[a] Marvin Janssen,[a] Enno Lork,[a] Hansjörg Grützmacher,[b] Stefan Mebs,*[c] Jens Beckmann*[a]

[a] *Institut für Anorganische Chemie und Kristallographie, Universität Bremen, Leobener Straße 7, 28359 Bremen, Germany*

[b] *Department of Chemistry and Applied Biosciences, ETH Zürich, Vladimir-Prelog Weg 1, Hönggerberg, 8093 Zürich, Switzerland.*

[c] *Institut für Experimentalphysik, Freie Universität Berlin, Arnimallee 14, 14195 Berlin, Germany*

* Correspondence to Jens Beckmann (E-mail: j.beckmann@uni-bremen.de) and Stefan Mebs (E-mail: stefan.mebs@fu-berlin.de)

Table of Contents

Synthesis of (2,6-$Mes_2C_6H_3)_2GaPCO$ (1)

(2,6-$Mes_2C_6H_3)_2GaCl$ (50.0 mg, 68.3 µmol, 1.00 eq.) and [Na(1,4-dioxane)$_{2.5}$][PCO] (17.3 mg, 68.3 µmol, 1.00 eq.) were suspended in toluene (6 mL) and stirred for 18 hours. The suspension has been filtered and the solvent of the remaining solution has been removed under reduced pressure to yield **1** as yellow solid (43 mg, 56.9 µmol, 82%).

^{1}H-NMR (601 MHz, C_6D_6): δ (ppm) = 7.02 (t, $^3J(^1H\text{-}^1H)$ = 7.58 Hz, 1H, H4), 6.84 (s, 4H, H9 and H11), 6.68 (d,$^3J(^1H\text{-}^1H)$ = 7.60 Hz, 2H, H3 and H5), 2.25 (s, 6H, H14), 1.89 (s,12H, H13 and H15). **^{13}C{^{1}H}-NMR** (151 MHz, C_6D_6): δ (ppm) = 186.50 (d,$^1J(^{31}P\text{-}^{13}C)$ = 99.82 Hz, C16), 150.72 (d,$^2J(^{31}P\text{-}^{13}C)$ = 10.53 Hz, C1), 148.18 (s, C2 and C6), 141.46 (s, C7), 137.51 (s, C8 and C12), 137.11 (s, C10), 130.18 (s, C4), 129.51 (s, C3, C5, C9 and C11), 21.96 (s, C13 or C15), 21.94 (s, C13 or C15), 21.28 (s, C14).). **^{31}P{^{1}H}-NMR** (243 MHz, C_6D_6): δ (ppm) = –283.29 (s). **HRMS ESI (**m/z): $[M\text{-}PCO]^+$ calculated. for $C_{48}H_{50}Ga$, 695.31628; found, 695.31476. **IR** (ATR, neat): $\tilde{\nu}$= 2950 (w), 2914 (m), 1898 (s), 1610 (m), 1559 (w), 1482 (w), 1440 (s), 1374 (m), 1261 (w), 1176 (w), 1112 (w), 1081 (w), 1031 (m), 844 (s), 804 (s), 771 (w), 739 (s), 706 (w) cm^{-1}.

Experimental procedures

General information

Unless otherwise stated, all reactions and manipulations were performed under inert atmosphere (argon) using anhydrous solvents. The starting materials (2,6-$Mes_2C_6H_3)_2GaCl$,[S1] (2,6-$Mes_2C_6H_3)_2InBr$,[S2] [Na(1,4-dioxane)$_{2.5}$][PCO][S3] and 1,2,3,4-tetramethylimidazol-2-ylidene, IMe_4,[S4] were prepared following the published procedures. Anhydrous dichloromethane, hexane, tetrahydrofuran and toluene were collected from an SPS800 mBraun solvent purification system and stored over 4 Å molecular sieves. Dimethoxyethane was dried over CaH_2 and distilled over 4 Å molecular sieves for storage. Deuterated solvents were degassed and dried over 4 Å molecular sieves under argon.

NMR spectra were recorded at room temperature on a Bruker Avance 600 MHz spectrometer. ^{1}H, ^{13}C{^{1}H}, ^{31}P{^{1}H} and ^{125}Te NMR spectra are reported on the δ scale (ppm) and are referenced against $SiMe_4$, H_3PO_4 (85% in water) and Me_2Te (90% in C_6D_6). ^{1}H and ^{13}C{^{1}H} chemical shifts are calibrated to the residual peak of the solvent ($CDHCl_2$ 5.32 ppm for CD_2Cl_2; C_6D_5H 7.16 ppm for C_6D_6 and C_4HD_7O: 1.71 ppm for THF-d_8) in the ^{1}H NMR spectra, and to the peak of the deuterated solvent (CD_2Cl_2 53.84 ppm, C_6D_6 128.06 ppm and THF-d_8: 67.21 ppm) in the ^{13}C{^{1}H} NMR spectra. The assignment of the ^{1}H and ^{13}C{^{1}H} resonance signals was made in accordance with the COSY, HSQC and HMBC spectra. The ESI HRMS spectra were measured on a Bruker Impact II spectrometer. Acetonitrile or toluene/acetonitrile solutions ($c = 1 \cdot 10^{-5}$ mol·L^{-1}) were injected directly into the spectrometer at a flow rate of 3 µL·min^{-1}. Nitrogen was used both as a drying gas and for nebulization with flow rates of approximately 5 L·min^{-1} and a pressure of 5 psi. Pressure in the mass analyzer region was usually about $1 \cdot 10^{-5}$ mbar. Spectra were collected for 1 min and averaged. The nozzle-skimmer voltage was adjusted individually for each measurement. IR spectra were recorded on a *Nicolet* Thermo iS10 scientific spectrometer with a diamond ATR unit. The absorption bands are reported in cm^{-1} with indicated relative intensities: s (strong, 0 – 33 % T); m (medium, 34 – 66 % T), w (weak, 67 – 100 % T), and br (broad).

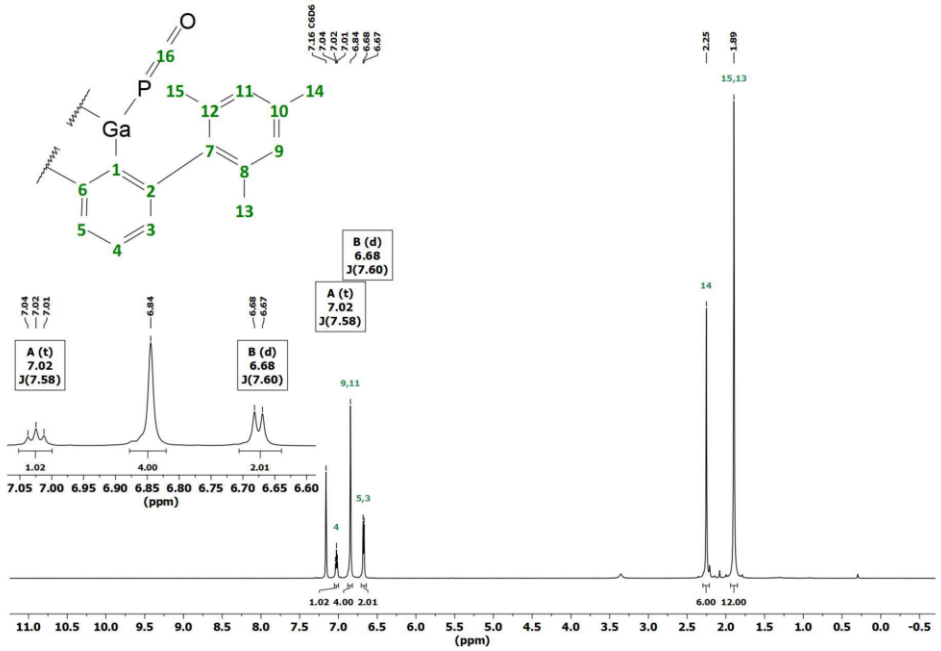

Figure S1. ^{1}H NMR (C_6D_6, 600 MHz) spectrum of (2,6-$Mes_2C_6H_3$)$_2$GaPCO (**1**).

5

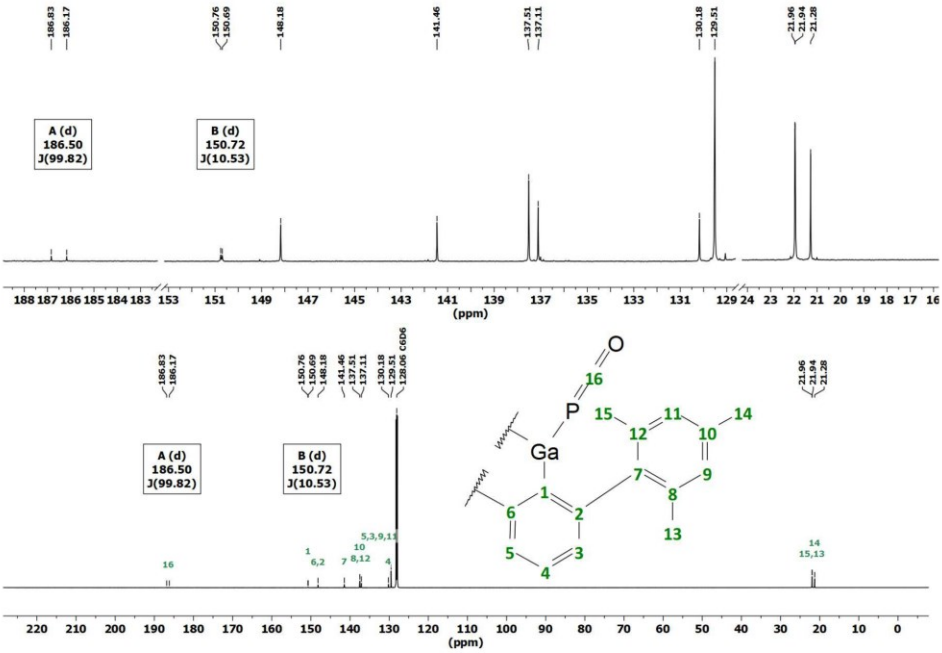

Figure S2. ^{13}C{^{1}H} NMR (C_6D_6, 151 MHz) spectrum of (2,6-$Mes_2C_6H_3$)$_2$GaPCO (**1**).

6

Figure S3. ^{31}P NMR (C_6D_6, 243 MHz) spectrum of (2,6-$Mes_2C_6H_3$)$_2$GaPCO (**1**)

Synthesis and characterization of (2,6-$Mes_2C_6H_3$)$_2$InPCO (2)

(2,6-$Mes_2C_6H_3$)$_2$InBr (50.0 mg, 57.4 µmol, 1.00 eq.) and [Na(1,4-dioxane)$_{2.5}$][PCO] (17.3 mg, 57.4 µmol, 1.00 eq.) were suspended in toluene (6 mL) and stirred for 18 hours. The suspension is filtered and the solvent of the remaining solution has been removed under vacuum to yield **2** as yellow solid (40.3 mg, 50.3 µmol, 83%).

^{1}H-NMR (600 MHz, C_6D_6): δ (ppm) = 7.08 (t, ^3J/^{1}H-^{1}H) = 7.54 Hz, 1H, H4), 6.87 (s, 4H, H9 and H11), 6.77 (d, ^3J/^{1}H-^{1}H) = 7.53 Hz, 2H, H3 and H5), 2.24 (s, 6H, H14), 1.91 (s, 12H, H13 and H15). **^{13}C{^{1}H}-NMR** (151 MHz, C_6D_6): δ (ppm) = 182.65 (d, ^1J(^{31}P-^{13}C) = 96.12 Hz, C16), 158.96 (d, ^1J(^{31}P-^{13}C) = 9.35 Hz, C1), 148.74 (s, C2 and C6), 141.88 (s, C7), 137.38 (s, C10), 137.24 (s, C8 and C12), 129.65 (s, C4), 129.60 (s, C9 and C11), 128.95 (s, C3 and C5), 21.65 (s, C13 and C15), 21.28 (s, C14). **^{31}P{^{1}H} NMR** (C_6D_6, 243 MHz): δ (ppm) = –336.19 (s). **HRMS ESI** (m/z): $[M\text{-}PCO]^+$ calculated. for $C_{48}H_{50}In$, 741.29458; found, 741.29441. **IR** (ATR, neat): $\tilde{\nu}$= 2914 (m), 1880 (s), 1610 (w), 1564 (w), 1482 (w), 1441 (m), 1374 (w), 1261 (w), 1221 (w), 1175 (w), 1083 (w), 1030 (w), 1012 (w), 879 (w), 846 (s), 801 (s), 774 (w), 746 (w), 735 (s), 699 (w) cm^{-1}.

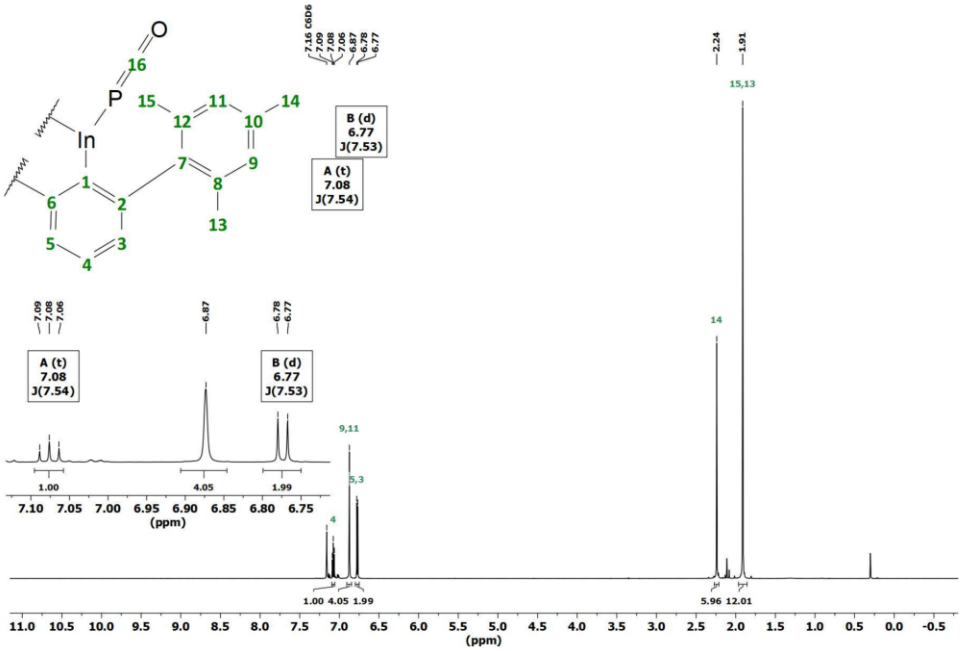

Figure S4. ^{1}H NMR (C_6D_6, 600 MHz) spectrum of (2,6-$Mes_2C_6H_3$)$_2$InPCO (**2**).

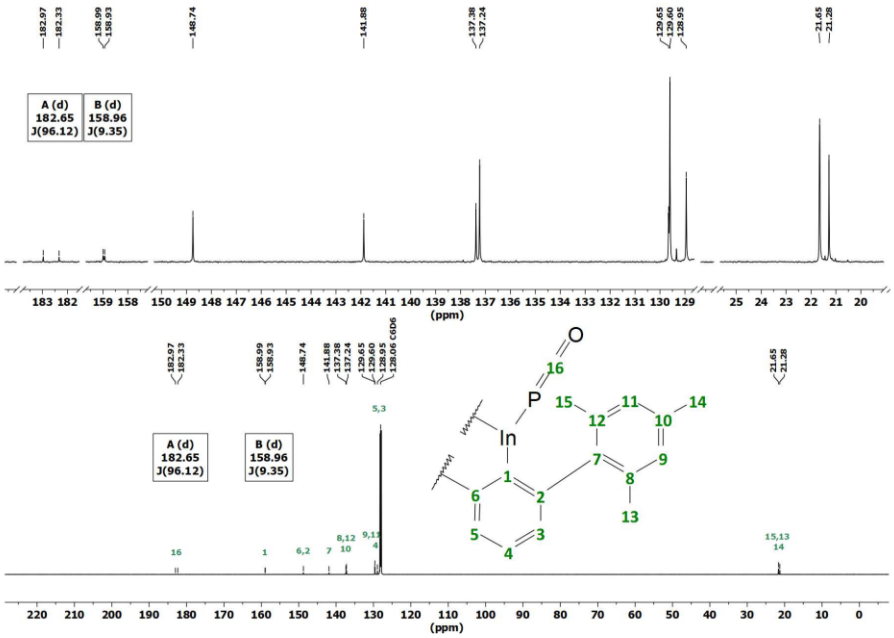

Figure S5. $^{13}C\{^{1}H\}$ NMR (C_6D_6, 151 MHz) spectrum of (2,6-$Mes_2C_6H_3$)$_2$InPCO (**2**).

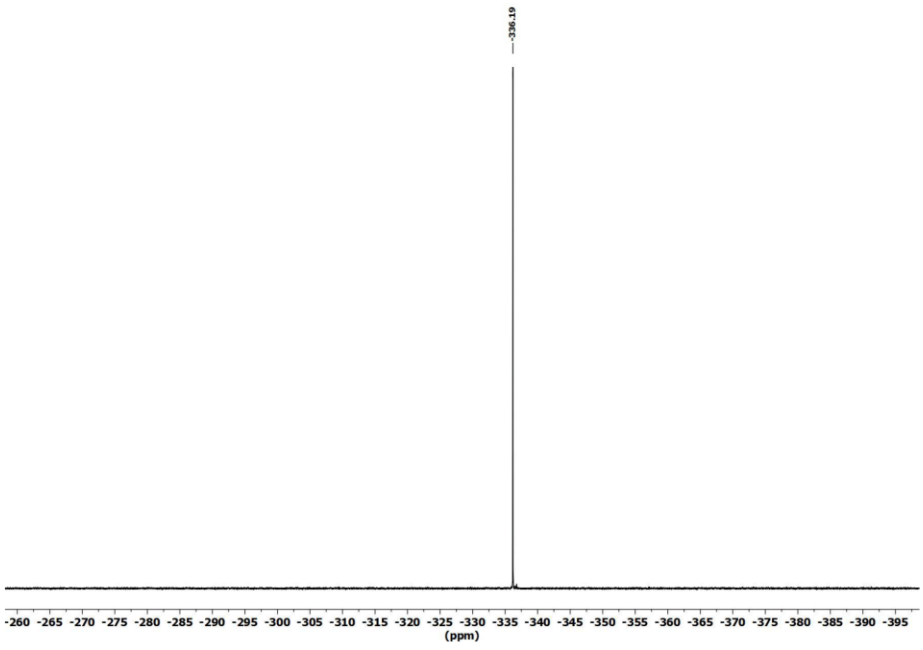

Figure S6. ^{31}P NMR (C_6D_6, 243 MHz) spectrum of (2,6-$Mes_2C_6H_3$)$_2$InPCO (**2**).

Synthesis and characterization of (Mes$_2$C$_6$H$_3$)$_2$GaP(O)C(IMe$_4$) (3)

1 (50.0 mg, 66.2 µmol, 1.00 eq.) and 1,3,4,5-tetramethylimidazol-2-ylidene (8.35 mg, 66.2 µmol, 1.00 eq.) were dissolved in toluene (6 mL) and stirred for 4 hours. Afterwards the solution has been filtered through a PTFE syringe filter and the solvent has been removed under vacuum to yield **3** as yellow solid (45.0 mg, 48.6 µmol, 73%).

^{1}H-NMR (600 MHz, CD_2Cl_2): δ (ppm) = 7.06 (t, ^3J/^{1}H-^{1}H) = 7.50 Hz, 1H, H4), 6.64 (s (br), 2H, H9 or H11), 6.61 (s (br), 2H, H9 or H11), 6.51 (d, ^3J/^{1}H-^{1}H) = 7.46 Hz, 2H, H3 and H5), 3.65 (s, 3H, H20 and H23), 2.19 (s, 6H, H14), 2.15 (s, 3H, H21 and H22), 1.69 (s (br), 6H, H13 or H15), 1.67 (s (br), 6H, H13 or H15). **^{13}C{^{1}H}-NMR** (151 MHz, CD_2Cl_2): δ (ppm) = 196.20 (d, ^1J(^{31}P-^{13}C) = 73.74 Hz, C16), 153.40 (d, ^2J(^{31}P-^{13}C) = 4.14 Hz, C1), 149.63 (s, C2 and C6), 144.48 (s, C7), 141.96 (d, ^2J(^{31}P-^{13}C) = 17.41 Hz, C17), 137.53 (s, C8 or C12), 137.38 (s, C8 or C12), 135.22 (s, C10), 128.65 (s, C3 and C5), 128.32 (s, C9 or C11), 127.90 (s, C9 or C11), 126.55 (s, C4), 124.36 (s, C18 and C19), 34.93 (s, C20 or C23), 34.85 (s, C20 or C23), 22.77 (s, C13 or C15), 22.67 (s, C13 or C15), 21.25 (s, C14), 9.27 (s, C21 and C22). **^{31}P{^{1}H}-NMR** (243 MHz, CD_2Cl_2): δ (ppm) = 245.41 (s). **HRMS ESI** (m/z): [M-PCO-NHC]$^+$ calculated. for $C_{48}H_{50}Ga$, 695.31628; found, 695.31588. **IR** (ATR, neat): $\tilde{\nu}$= 2949 (w), 2912 (m), 2842 (w), 1647 (w), 1609 (w), 1558 (w), 1480 (m), 1433 (s), 1372 (m), 1238 (w), 1215 (s), 1178 (w), 1116 (w), 1073 (w), 1030 (m), 1015 (m), 845 (s), 802 (s), 765 (w), 736 (s), 710 (w), 697 (m), 666 (w) cm^{-1}.

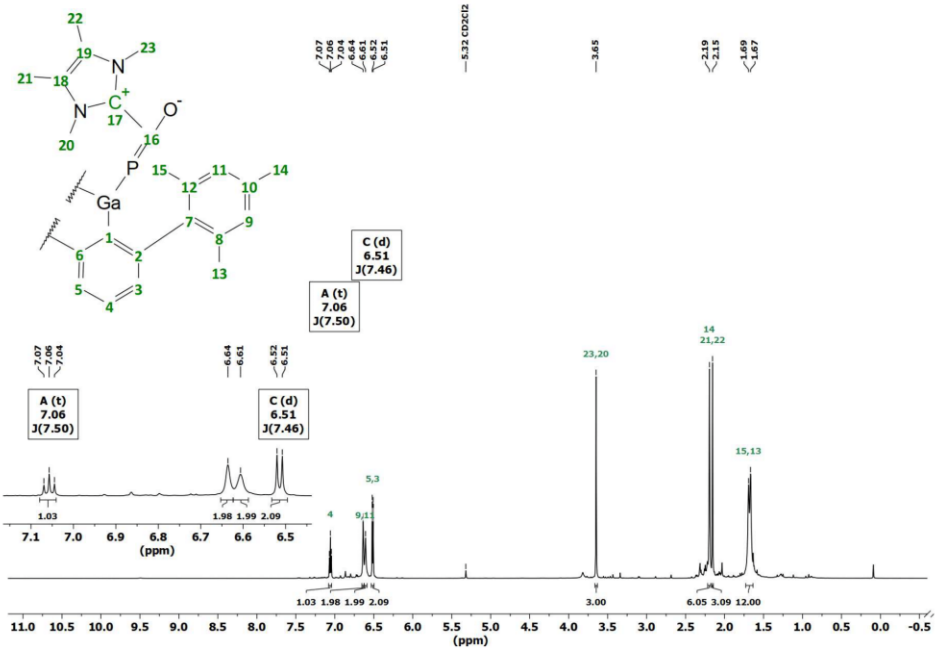

Figure S7. ^{1}H NMR (CD_2Cl_2, 600 MHz) spectrum of (2,6-$Mes_2C_6H_3$)$_2$GaP(O)C(IMe$_4$) (**3**).

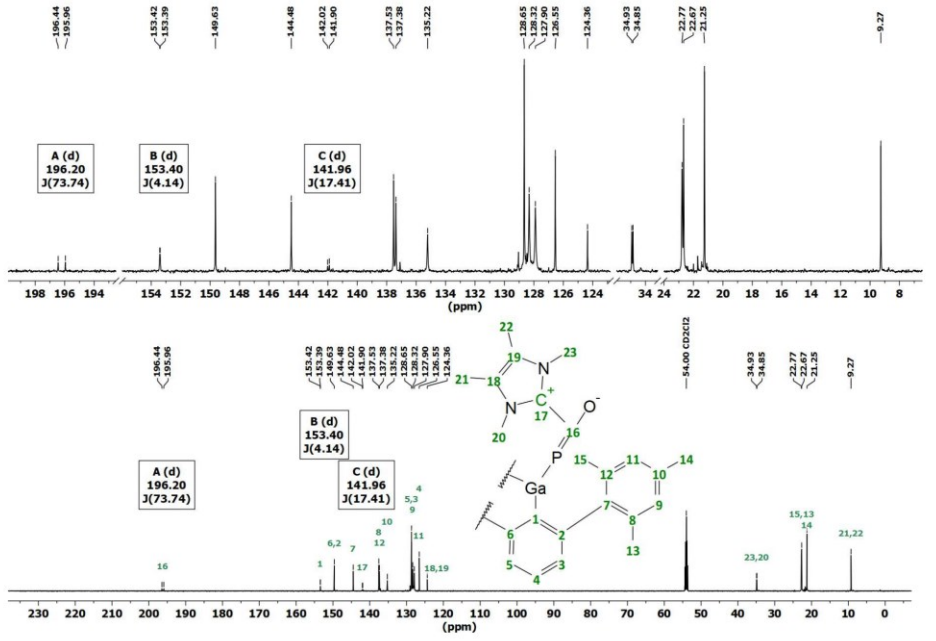

Figure S8. ^{13}C{^{1}H} NMR (CD_2Cl_2, 151 MHz) spectrum of (2,6-$Mes_2C_6H_3$)$_2$GaP(O)C(IMe$_4$) (**3**).

Figure S9. ^{31}P NMR (CD_2Cl_2, 243 MHz) spectrum of (2,6-$Mes_2C_6H_3$)$_2$GaP(O)C(IMe$_4$) (**3**).

Synthesis and characterization of (Mes$_2$C$_6$H$_3$)$_2$InP(O)C(IMe$_4$) (4)

2 (50.0 mg, 62.4 µmol, 1.00 eq.) and 1,3,4,5-tetramethylimidazol-2-ylidene (7.75 mg, 62.4 µmol, 1.00 eq.) were dissolved in toluene (6 mL) and stirred for 4 hours. The solution has been filtered with a PTFE syringe filter and the remaining solvent has been removed under reduced pressure to yield **4** as yellow solid (41.2 mg, 44.5 µmol, 71%).

^{1}H-NMR (600MHz, THF-d$_8$): δ(ppm) = 7.01 (t,^{3}J(^{1}H-^{1}H) = 7.48 Hz, 1H, H4), 6.66 (s (br), 2H, H9 or H11), 6.62 (s (br), 2H, H9 or H11), 6,55 (d,^{3}J(^{1}H-^{1}H) = 7.49 Hz, 2H, H3 and H5), 3.70 (s,3H, H20 and H23), 2.19 (s, 3H, H21 and H22), 2.17 (s, 6H, H14), 1.75 (s, 6H, H13 or H15), 1.72 (s, 6H, H13 or H15). **^{13}C{^{1}H}-NMR** (151 MHz, THF-d$_8$): δ(ppm) = 198.68 (d,^{1}J(^{31}P-^{13}C) = 79.69 Hz, C16), 161.98 (s, C1), 150.56 (s, C2 and C6), 145.55 (d,^{2}J(^{31}P-^{13}C) = 24.36 Hz, C17), 145.05 (s,C7), 137.32 (s, C8 or C12), 137.28 (s, C8 or C12), 135.41 (s, C10), 129.16 (s, C9), 128.60 (s, C11), 128.19 (s, C3 and C5), 127.06 (s, C4), 124.58 (s, C18 and C19), 34.93 (s,C20 or C23), 34.85 (s, C20 or C23), 22.83 (s, C13 or C15), 21.47 (s, C14), 8.62 (s, C21 and C22). **^{31}P{^{1}H}-NMR** (243MHz,THF-d$_8$): δ(ppm) = 219.65 (s).

HRMS ESI (m/z): [M-PCO-NHC]$^+$ calculated. for $C_{48}H_{50}In$, 741.29458; found, 741.29282, [M-PCO]$^+$ calculated. for $C_{53}H_{62}InN_2$, 865.39463; found, 865.39352. **IR** (ATR, neat): $\tilde{\nu}$= 2913 (s), 2853 (m), 1770 (w) 1648 (w), 1610 (w), 1558 (w), 1481 (m), 1436 (s), 1372 (m), 1249 (s), 1222 (m), 1177 (w), 1078 (w), 1030 (m), 1008 (m), 952 (w), 845 (s), 800 (s), 768 (w), 734 (s), 712 (m), 697 (m) cm^{-1}.

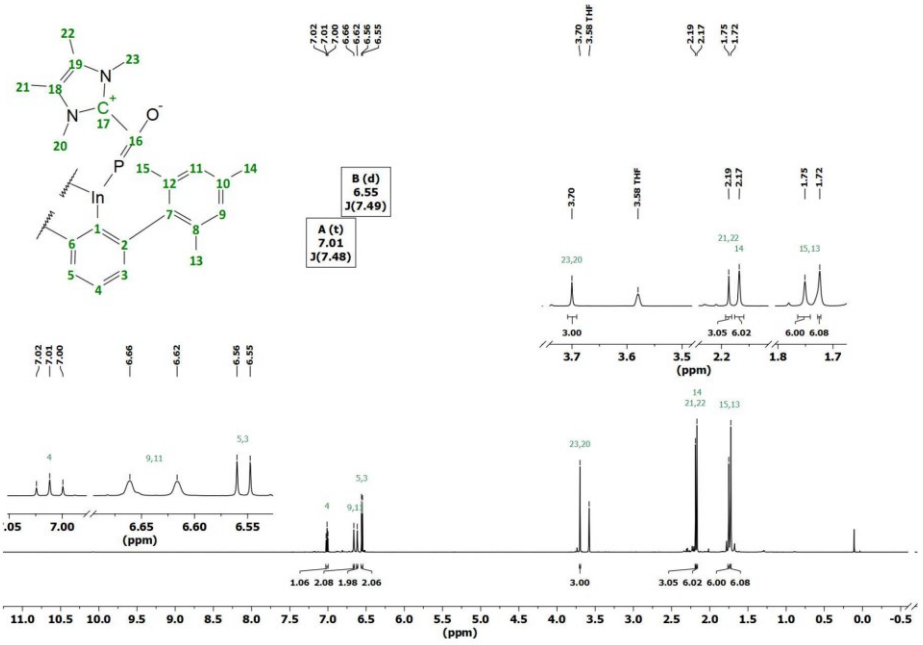

Figure S10. ^{1}H NMR (C_6D_6, 600 MHz) spectrum of (2,6-$Mes_2C_6H_3$)$_2$InP(O)C(IMe$_4$) (**4**).

17

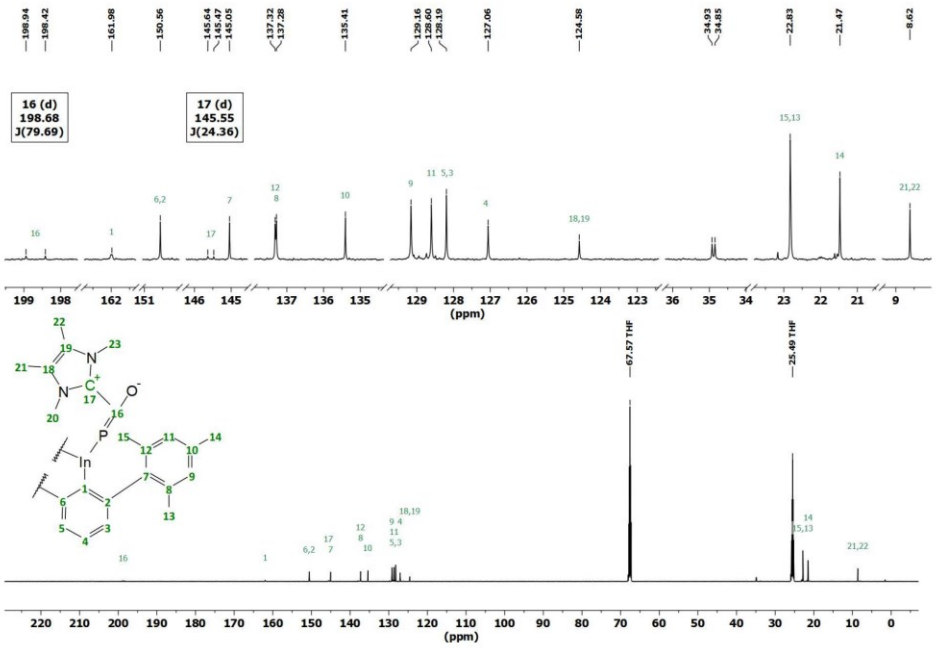

Figure S11. $^{13}C\{^{1}H\}$ NMR (C_6D_6, 151 MHz) spectrum of (2,6-$Mes_2C_6H_3$)$_2$InP(O)C(IMe$_4$) (**4**).

18

Figure S12. ^{31}P NMR (C_6D_6, 243 MHz) spectrum of (2,6-$Mes_2C_6H_3$)$_2$InP(O)C(IMe$_4$) (**4**).

Synthesis and characterization of (2,6-$Mes_2C_6H_3$)$_2$GaTeP(O)C(IMe$_4$) (5)

To a solution of **3** (50.0 mg, 56.8 µmol, 1.00 eq.) in toluene was added an excess of tellurium powder (70.0 mg, 549 µmol, 9.65 Eq.) at room temperature. The resulting suspension was stirred for 18 h. The suspension has been filtered and the solvent of the remaining solution has been removed under reduced pressure to yield **5** as red solid (45.7 mg, 45.3 µmol, 80%).

^{1}H-NMR (600 MHz, THF-d_8): δ (ppm) = 7.10 (t, $^3J(^1H\text{-}^1H)$ = 7.48 Hz, 1H, *p*-C_6H_3), 7.04 (t, $^3J(^1H\text{-}^1H)$ = 7.47 Hz, 1H, *p*-C_6H_3), 6.69 (s (br), 1H, *m*-Mes), 6.68 (s (br), 2H, *m*-Mes), 6.63 (dd, $^3J(^1H\text{-}^1H)$ = 7.54 Hz, $^4J(^1H\text{-}^1H)$ = 1.48 Hz, 1H, *m*-C_6H_3), 6.60 (s (br), 1H, *m*-Mes), 6.57 (s (br), 1H, *m*-Mes), 6.47 (m, 3H, *m*-C_6H_3), 6.36 (s (br), 1H, *m*-Mes), 6.28 (s (br), 1H, *m*-Mes), 6.24 (s (br), 1H, *m*-Mes), 3.49 (s, 3H), 3.48 (s, 3H), 2.27 (s, 3H), 2.26 (s, 3H), 2.18 (s, 6H), 2.14 (s, 3H), 1.84 (s, 3H), 1.81 (s, 3H), 1.79 (s, 3H), 1.78 (s, 3H), 1.75 (s, 3H),1.73 (s, 3H), 1.62 (s, 3H), 1.44 (s, 3H), 1.26 (s, 3H). **^{13}C{^{1}H}-NMR** (151 MHz, THF-d_8): δ(ppm) = 181.75 (d, $^1J(^{31}P\text{-}^{13}C)$ = 79.29 Hz, **O**C**P**), 155.02 (s), 152.15 (s), 151.66 (s), 150.53 (s), 150.42 (s), 149.03 (s), 146.72 (d, $^2J(^{31}P\text{-}^{13}C)$ = 40.24 Hz), 145.76 (s), 144.10 (s), 144.07 (s), 139.91 (s), 139.82 (s), 138.33 (s), 138.29 (s), 137.97 (s), 137.46 (s), 137.15 (s), 136.82 (s), 136.53 (s), 136.06 (s), 135.45 (s), 133.53 (s), 131.19 (s, *m*-C_{Ph}), 130.75 (s, *m*-C_{Mes}), 130.39 (s, *m*-C_{Ph}), 130.27 (s, *m*-C_{Mes}), 129.72 (s), 129.60 (s, *m*-C_{Ph}), 129.40 (s, *m*-C_{Mes}), 129.27 (s, *m*-C_{Mes}), 129.10 (s, *m*-C_{Ph}), 128.96 (s), 128.74 (s, *m*-C_{Mes}), 128.59 (s, *m*-C_{Mes}), 127.61 (s, *p*-C_{Ph}), 127.29 (s, *m*-C_{Ph}), 126.73 (s, *m*-C_{Mes}), 126.48 (s, *m*-C_{Mes}), 125.91 (s), 36.24 (s), 36.14 (s), 24.18 (s), 24.15 (s), 24.06 (s), 23.41 (s), 23.28 (s), 23.23 (s), 22.96 (s), 22.30 (s), 21.26 (s), 21.16 (s), 21.12 (s), 20.93 (s), 8.79 (s). **^{31}P{^{1}H}-NMR** (243MHz, THF-d_8): δ(ppm) = 171.86 ($^1J(^{125}Te\text{-}^{31}P)$ = 840.09 Hz. **^{125}Te{^{1}H}-NMR** (189MHz, THF-d_8): δ(ppm) = –414.42 (d, $^1J(^{125}Te\text{-}^{31}P)$ = 840.09 Hz). **HRMS ESI** (m/z): $[M]^+$ calculated. for $C_{56}H_{66}GaN_2OPTe$, 1008.29097; found, 1008.29103. **IR** (ATR, neat): $\tilde{\nu}$= 2951 (w), 2915 (m), 2840 (w), 1651 (m), 1609 (w), 1548 (w), 1478 (m), 1432 (s), 1374 (m), 1272 (m), 1221 (w), 1177 (w), 1159 (w), 1113 (w), 1083 (w), 1030 (w), 847 (s), 801 (s), 731 (s), 695 (m) cm^{-1}.

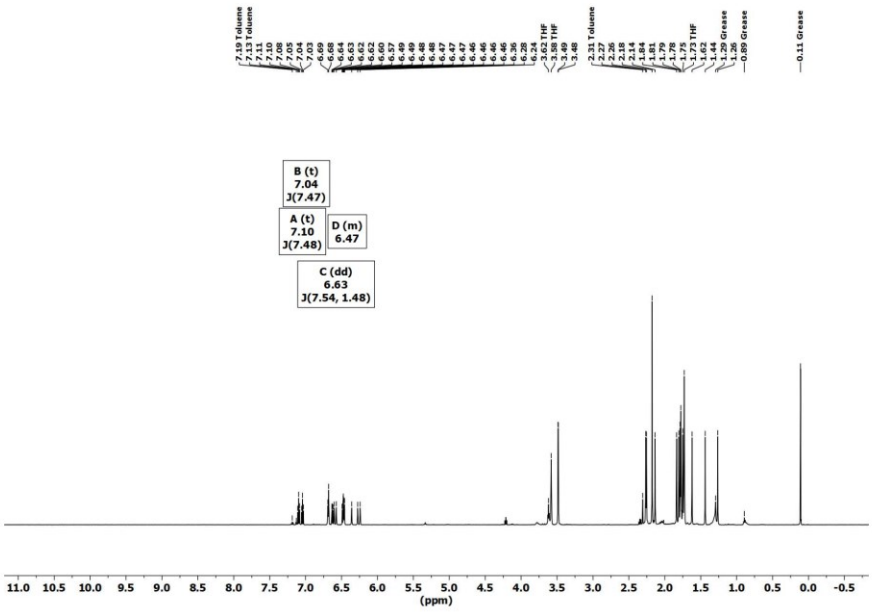

Figure S13. ^{1}H NMR (THF-d_8, 600 MHz) spectrum of (2,6-$Mes_2C_6H_3$)$_2$GaTeP(O)C(IMe$_4$) (**5**).

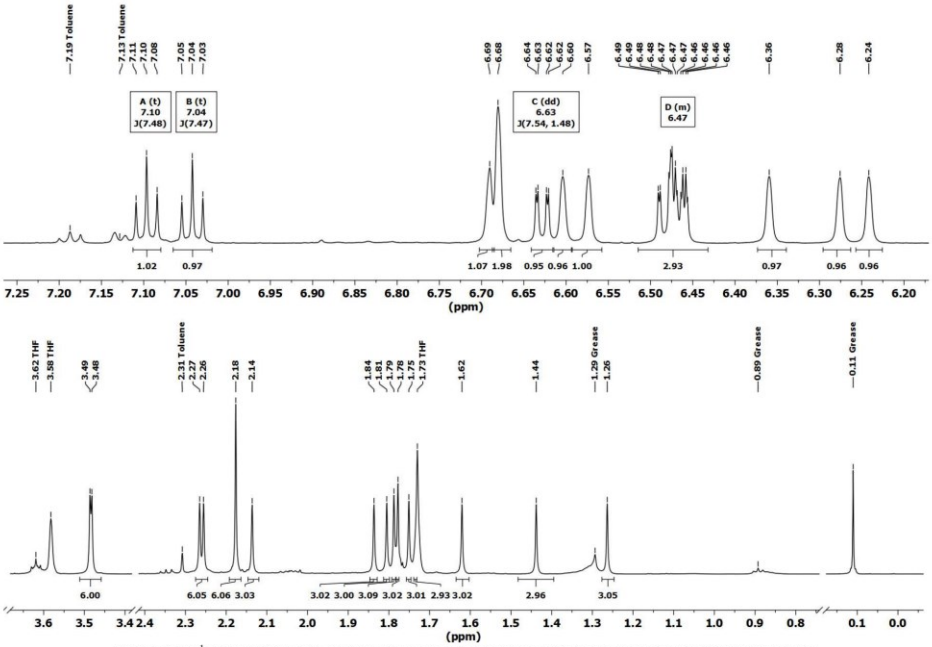

Figure S14. ^{1}H NMR (THF-d8, 600 MHz) zoomed in spectrum of (2,6-$Mes_2C_6H_3$)$_2$GaTeP(O)C(IMe$_4$) (**5**).

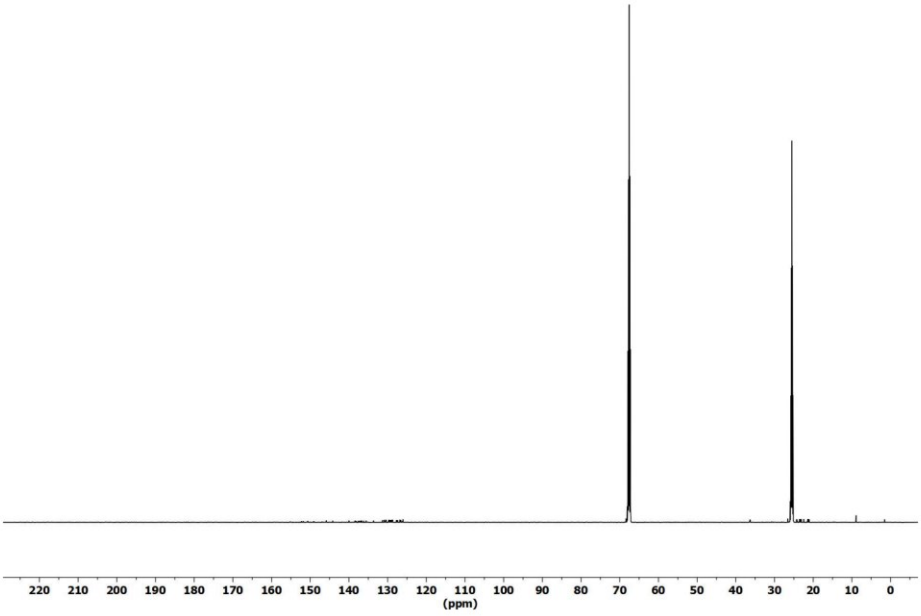

Figure S15. $^{13}C\{^{1}H\}$ NMR (THF-d_8, 151 MHz) spectrum of (2,6-$Mes_2C_6H_3$)$_2$GaTeP(O)C(IMe_4) (**5**).

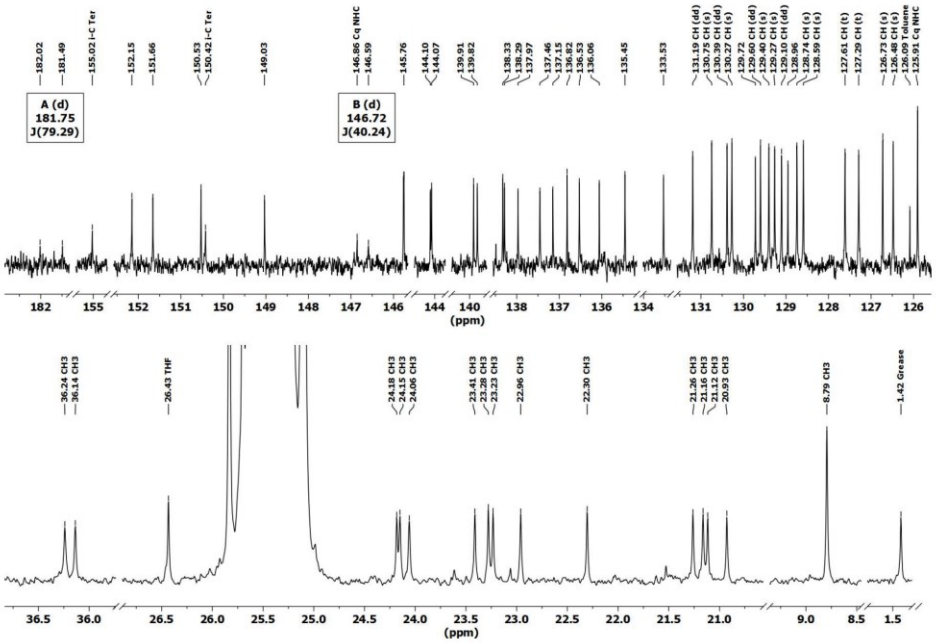

Figure S16. $^{13}C\{^{1}H\}$ NMR (THF-d_8, 151 MHz) zoomed in spectrum of (2,6-$Mes_2C_6H_3$)$_2$GaTeP(O)C(IMe_4) (**5**).

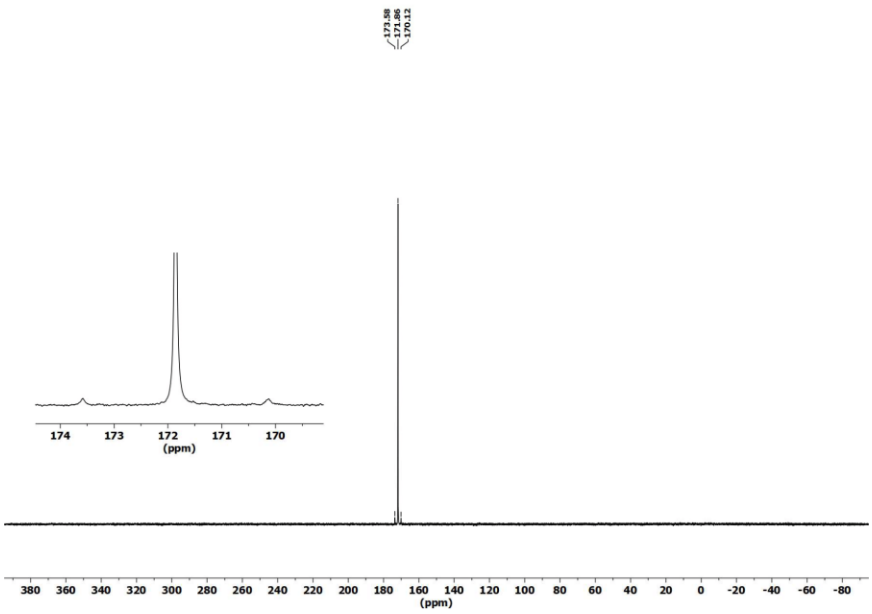

Figure S17. ^{31}P NMR (THF-d_8, 243 MHz) spectrum of (2,6-$Mes_2C_6H_3$)$_2$GaTeP(O)C(IMe$_4$) (**5**).

25

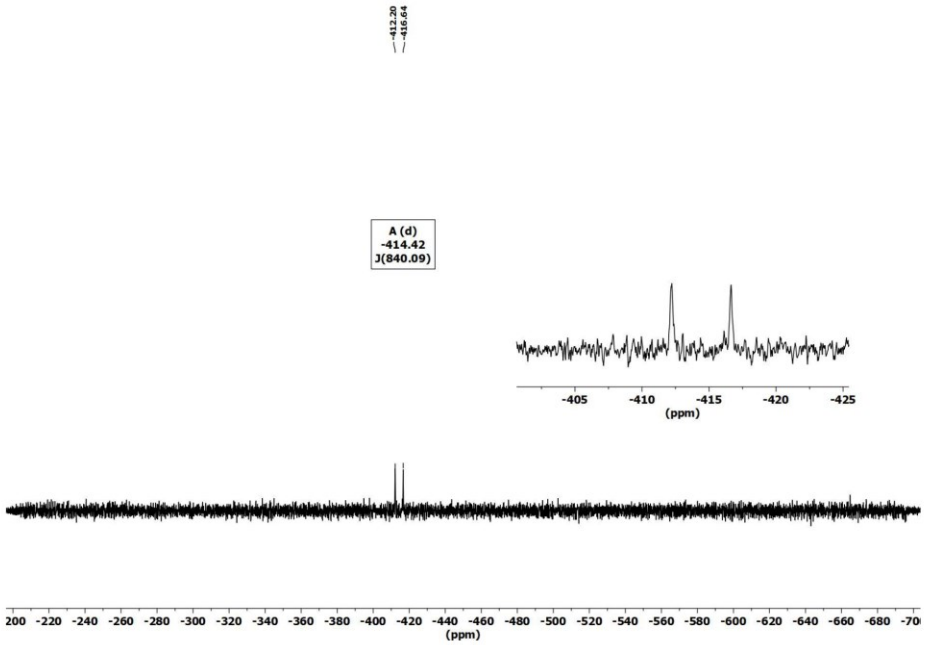

Figure S18. ^{125}Te NMR (THF-d_8, 189 MHz) spectrum of (2,6-$Mes_2C_6H_3$)$_2$GaTeP(O)C(IMe$_4$) (**5**)

26

Synthesis and characterization of (2,6-Mes$_2$C$_6$H$_3$)$_2$InTeP(O)C(IMe$_4$) (6)

To a solution of **4** (50.0 mg, 56.1 µmol, 1.00 eq.) in toluene was added an excess of tellurium powder (70.0 mg, 549 µmol, 10.0 Eq.) at room temperature. The resulting suspension was stirred for 18 h. The suspension has been filtered and the solvent of the remaining solution has been removed under reduced pressure to yield **6** as orange solid (46.3 mg, 44.0 µmol, 81%).

^{1}H-NMR (600 MHz, THF-d_8) δ (ppm) = 7.06 (t, ^3J(^{1}H-^{1}H) = 7.49 Hz, 2H, *p*-C$_6$H$_3$), 7.01 (s (br), 1H, *m*-Mes), 6.97 (s (br), 1H, *m*-Mes), 6.80 (s (br), 1H, *m*-Mes), 6.77 (s (br), 1H, *m*-Mes) 6.66 (dd, ^3J(^{1}H-^{1}H) = 2.83 Hz, ^4J(^{1}H-^{1}H) = 1.42 Hz, 1H, *m*-C$_6$H$_3$), 6.65 (dd, ^3J(^{1}H-^{1}H) = 2.72 Hz, ^4J(^{1}H-^{1}H) = 1.43 Hz, 1H, *m*-C$_6$H$_3$), 6.64 (s (br), 1H, *m*-Mes), 6.63 (s (br), 1H, *m*-Mes), 6.59 (s (br), 1H, *m*-Mes), 6.56 (dd, ^3J(^{1}H-^{1}H) = 7.58 Hz, ^4J(^{1}H-^{1}H) = 1.43 Hz, 1H, *m*-C$_6$H$_3$), 6.54 (s (br), 1H, *m*-Mes), 6.53 (dd, ^3J(^{1}H-^{1}H) = 7.52 Hz, ^4J(^{1}H-^{1}H) = 1.42 Hz, 1H, *m*-C$_6$H$_3$), 3.23 (s, 6H), 2.35 (s, 3H), 2.28 (s, 3H), 2.25 (s, 3H), 2.16 (s, 9H), 2.07 (s, 3H), 2x 2.01 (s, 6H), 1.93 (s, 3H), 1.78 (s, 3H), 1.70 (s, 3H), 0.96 (s, 3H), 0.90 (s, 3H). **^{13}C{^{1}H}-NMR** (151 MHz, THF-d$_8$): δ(ppm) = 198.68 (d, ^1J(^{31}P-^{13}C) = 73.63 Hz, O**C**P), 166.21 (s), 160.23 (s), 151.37 (s), 149.78 (s), 148.97 (s), 148.60 (s) , 148.30 (s), 145.01 (s), 144.73 (s), 143.95 (s), 143.09 (s), 139.47 (s), 139.40 (s), 138.08 (s), 138.05 (s), 137.82 (s), 137.29 (s), 137.05 (s), 136.88 (s), 136.48 (s), 136.42 (s), 135.74 (s), 134.62 (s), 131.29 (s, *m*-C$_{Mes}$), 130.11 (s, *m*-C$_{Mes}$), 129.88 (s, *m*-C$_{Mes}$), 129.37 (s, *m*-C$_{Ph}$), 129.26 (s, *m*-C$_{Ph}$), 128.99 (s, *m*-C$_{Mes}$), 128.76 (s *m*-C$_{Mes}$), 128.64 (s, *m*-C$_{Mes}$), 128.50 (s, *m*-C$_{Mes}$), 128.28 (s, *m*-C$_{Ph}$), 128.05 (s, *m*-C$_{Ph}$), 127.57 (s, *p*-C$_{Ph}$), 127.51 (s, *p*-C$_{Ph}$), 127.29 (s), 125.62 (s), 33.85 (s), 33.81 (s), 24.35 (s), 24.04 (s), 23.57 (s), 23.14 (s), 22.96 (s), 22.59 (s, *m*-C$_{Mes}$), 22.54 (s), 21.74 (s), 21.61 (s), 21.54 (s), 21.01 (s), 8.29 (s). **^{31}P{^{1}H}-NMR** (243MHz,THF-d$_8$): δ(ppm) = 122.26 (^1J(^{125}Te-^{31}P) = 684.13 Hz). **^{125}Te{^{1}H}-NMR** (189MHz,THF-d$_8$): δ(ppm) = –544.38 (d, ^1J(^{125}Te-^{31}P) = 682.56 Hz). **HRMS ESI** (m/z): [M]$^+$ calculated. for C$_{56}$H$_{62}$InN$_2$OPTe, 1054.27033; found, 1054.26845. **IR** (ATR, neat): $\tilde{\nu}$= 2913 (s), 2851 (m), 1770 (w) 1650 (w), 1610 (w), 1557 (w), 1495 (m), 1433 (s), 1370 (m), 1310 (s), 1228 (w), 1175 (m), 1109 (w), 1078 (w), 1030 (m), 1014 (w), 846 (s), 801 (s), 767 (w), 733 (s), 695 (m), 662 (w) cm^{-1}.

Figure S19. ^{1}H NMR (THF-d$_8$, 600 MHz) spectrum of (2,6-Mes$_2$C$_6$H$_3$)$_2$InTeP(O)C(IMe$_4$) (**6**).

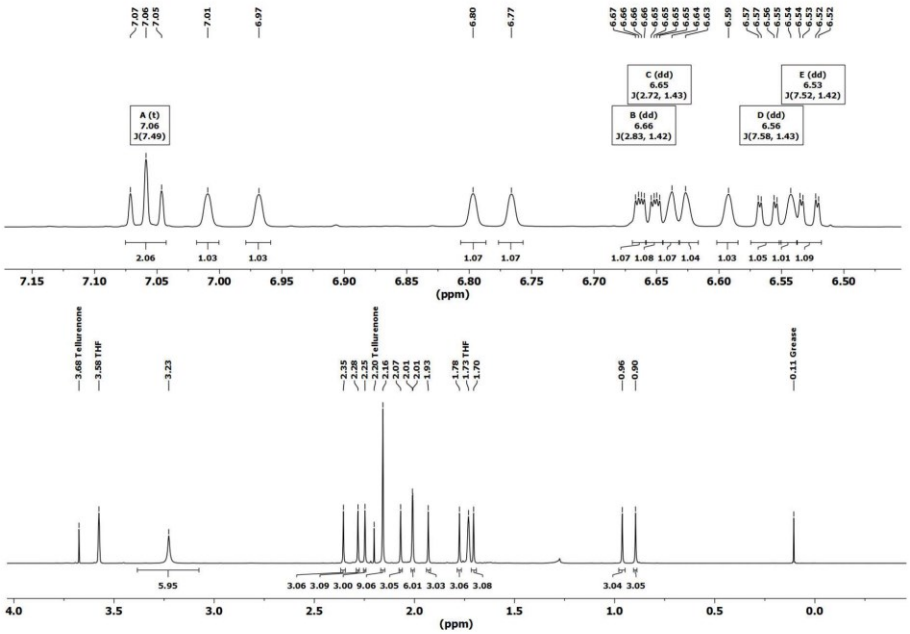

Figure S20. ^{1}H NMR (THF-d_8, 600 MHz) zoomed in spectrum of (2,6-$Mes_2C_6H_3$)$_2$InTeP(O)C(IMe_4) (**6**).

29

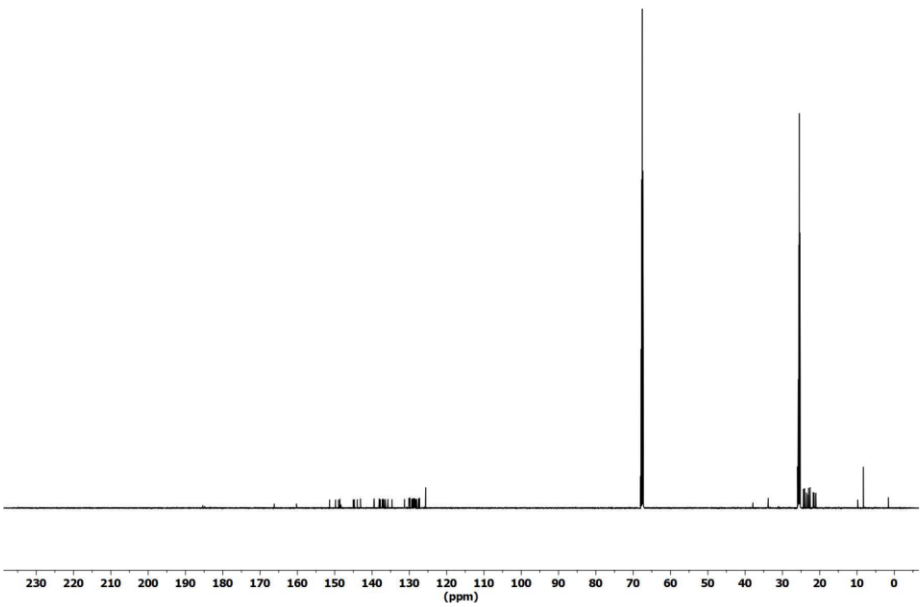

Figure S21. $^{13}C\{^{1}H\}$ NMR (THF-d_8, 151 MHz) spectrum of (2,6-$Mes_2C_6H_3$)$_2$InTeP(O)C(IMe_4) (**6**).

30

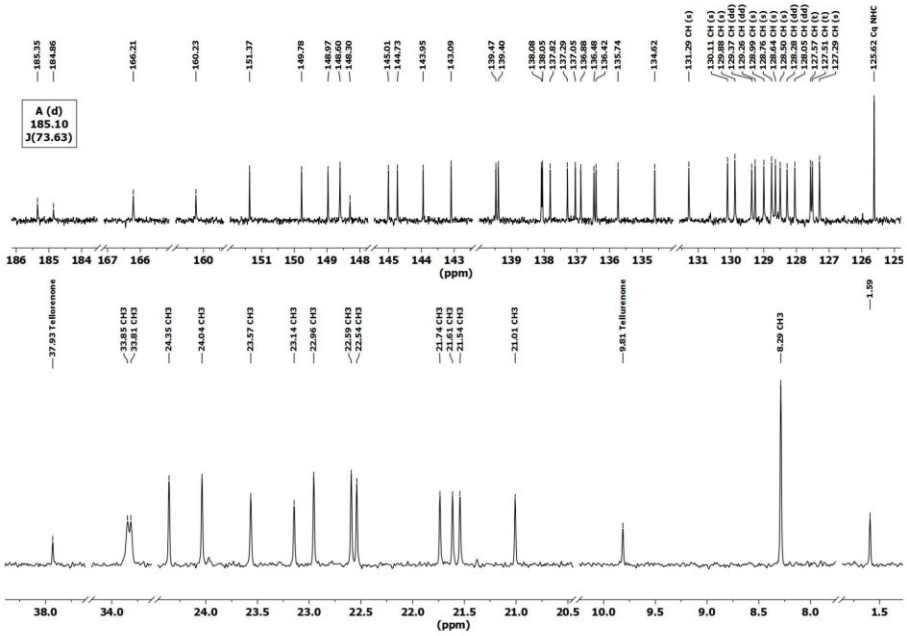

Figure S22. $^{13}C\{^{1}H\}$ NMR (THF-d_8, 151 MHz) zoomed in spectrum of (2,6-$Mes_2C_6H_3$)$_2$InTeP(O)C(IMe_4) (**6**).

31

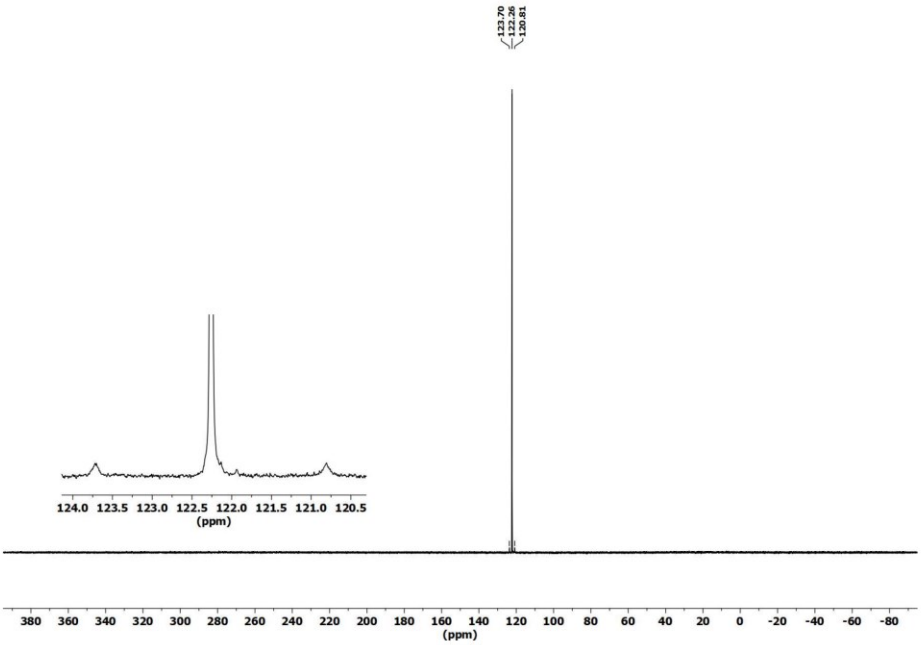

Figure S23. ^{31}P NMR (THF-d_8, 243 MHz) spectrum of (2,6-$Mes_2C_6H_3$)$_2$InTeP(O)C(IMe_4) (**6**)

32

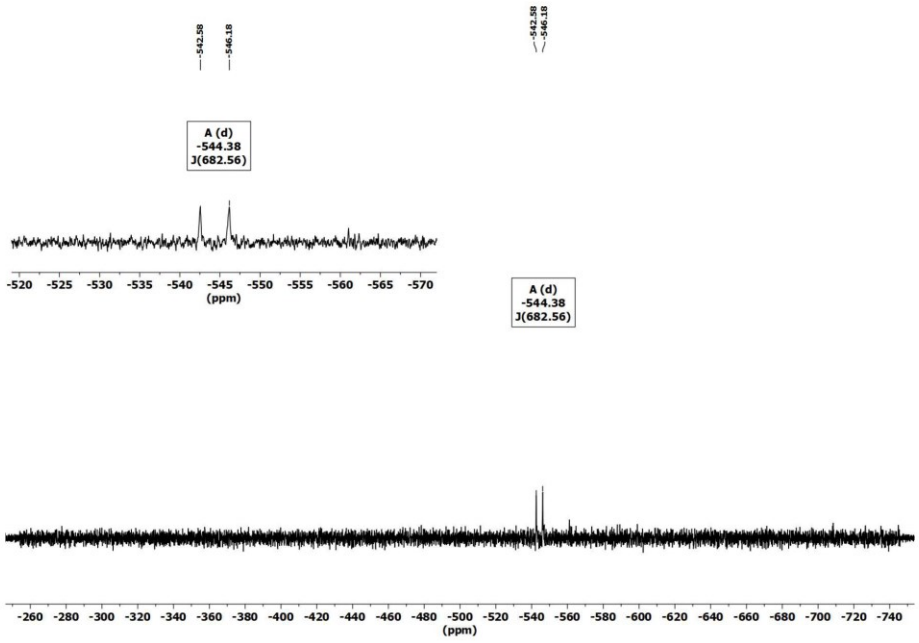

Figure S24. ^{125}Te NMR (THF-d_8, 189 MHz) spectrum of (2,6-$Mes_2C_6H_3$)$_2$InTeP(O)C(IMe$_4$) (**6**).

X-Ray diffraction studies

Single crystals suitable for X-Ray structure determination were grown from hot toluene solutions (**1**, **2**, **4**, **5** and **6**toluene) or by diffusion of *n*-hexane into a CH_2Cl_2 solutions (**3**). Intensity data were collected on a Bruker Venture D8 diffractometer at 100 K with graphite-monochromated Mo-Kα (0.7107 Å) radiation. All structures were solved by direct methods and refined based on F^2 by use of the SHELX program package as implemented in Olex2.[S5] All non-hydrogen atoms were refined using anisotropic displacement parameters. Hydrogen atoms attached to carbon atoms were included in geometrically calculated positions using a riding model. Crystal and refinement data are collected in Table S1. Figures were created using DIAMOND.[S6]

Table S1. Crystal data and structure refinement of **1-6.**

	1	**2**	**3**
Formula	$C_{49}H_{50}GaOP$	$C_{49}H_{50}InOP$	$C_{56}H_{62}GaN_2OP$
Formula weight, g mol^{-1}	755.58	800.68	879.76
Crystal system	Triclinic	triclinic	monoclinic
Crystal size, mm	0.24 × 0.13 × 0.12	0.21 × 0.12 × 0.07	0.18 × 0.15 × 0.09
Space group	$P\bar{1}$	$P\bar{1}$	$P2_1/n$
a, Å	10.4559(7)	10.6724(3)	11.0545(12)
b, Å	11.2875(7)	11.2002(4)	19.948(2)
c, Å	16.7900(10)	16.8476(5)	22.110(2)
α, °	88.711(2)	88.6950(10)	90
β, °	81.094(3)	80.3120(10)	98.272(3)
γ, °	82.517(3)	81.7330(10)	90
V, Å^3	1941.0(2)	1964.49(11)	4824.7(9)
Z	2	2	4
ρ_{calcd}, Mg m^{-3}	1.293	1.354	1.211
μ (Mo $K\alpha$), mm^{-1}	0.787	0.679	0.644
F(000)	796	832	1864
θ range, deg	2.17 to 36.38	2.21 to 33.28	2.12 to 25.00
Index ranges	–13 ≤ h ≤ 13	–16 ≤ h ≤ 16	–11 ≤ h ≤ 13
	–14 ≤ k ≤ 14	–17 ≤ k ≤ 17	–23 ≤ k ≤ 23
	–22 ≤ l ≤ 22	–25 ≤ l ≤ 25	–26 ≤ l ≤ 26
No. of reflns collected	51824	122752	27261
Completeness to θ_{max}	99.6%	99.9%	99.8%
No. indep. Reflns	9335	15094	8489
No. obsd reflns with($I>2\sigma(I)$)	7836	13210	6300
No. refined params	481	481	542
GooF (F^2)	1.074	1.039	1.101
R_1 (F) ($I > 2\sigma(I)$)	0.0518	0.0283	0.0803
wR_2 (F^2) (all data)	0.1335	0.0657	0.1585
Largest diff peak/hole, e Å^{-3}	1.709 / –1.543	0.686 / –0.477	1.206 / –1.149
CCDC number	2105254	2105255	2105256

Table S1. Cont.

4	**5**	**6**·toluene
$C_{56}H_{62}InN_2OP$	$C_{56}H_{62}GaN_2OPTe$	$C_{63}H_{70}InN_2OPTe$
924.86	1007.36	1144.60
monoclinic	monoclinic	monoclinic
0.32 × 0.23 × 0.16	0.47 × 0.15 × 0.11	0.25 × 0.20 × 0.14
$P2_1/n$	$P2_1/n$	$P2_1/n$
11.2294(5)	11.6850(8)	11.4267(10)
20.1471(12)	33.106(2)	28.438(3)
22.3970(12)	13.6771(12)	17.4895(14)
90	90	90
100.753(2)	110.903(2)	104.738(3)
90	90	90
4978.1(5)	4942.7(7)	5496.3(9)
4	4	4
1.234	1.354	1.383
0.546	1.208	1.022
1936	2072	2344
1.98 to 28.46	2.33 to 28.28	1.98 to 33.26
–13 ≤ h ≤ 13	–15 ≤ h ≤ 15	–13 ≤ h ≤ 17
–24 ≤ k ≤ 24	–44 ≤ k ≤ 44	–43 ≤ k ≤ 43
–27 ≤ l ≤ 27	–18 ≤ l ≤ 18	–26 ≤ l ≤ 26
91075	113392	95732
99.9%	99.8%	99.8%
9791	12243	21074
8776	10846	14438
582	575	575
1.294	1.178	1.022
0.0679	0.0521	0.0496
0.1345	0.1183	0.0842
0.674 / –1.362	1.121 / –1.843	0.717 / –0.629
2105257	2105258	2105259

Table S2. Calculated bond lengths and relative energies of (2,6-$Mes_2C_6H_3$)$_2$EPCO and (2,6-$Mes_2C_6H_3$)$_2$EOCP (E = B, Al, Ga, In, Tl).

Coord. mode	energy	delta	kJ mol^{-1}	d(E-P)	d(E-C)	d(E-O)	d(P-C)	d(C-O)
B-P-C-O	–2338.8817	–0.0029	–7.70	1.903	2.727	3.716	1.676	1.151
B-O-C-P	–2338.8788			3.951	2.457	1.390	1.546	1.275
Al-P-C-O	–2556.5002	–0.0086	–22.65	2.356	2.728	3.509	1.645	1.166
Al-O-C-P	–2556.4916			4.541	2.982	1.738	1.559	1.244
Ga-P-C-O	–4238.9190	–0.0202	–53.03	2.375	2.788	3.579	1.645	1.165
Ga-O-C-P	–4238.8988			4.236	2.830	1.922	1.565	1.249
In-P-C-O	–2504.3252	–0.0250	–65.53	2.579	2.950	3.708	1.641	1.169
In-O-C-P	–2504.3002			4.367	3.013	2.183	1.574	1.238
Tl-P-C-O	–2486.6805	–0.0234	–61.34	2.683	3.030	3.759	1.637	1.173
Tl-O-C-P	–2486.6571			4.453	3.141	2.374	1.583	1.226

Table S3. Dissociation of (2,6-$Mes_2C_6H_3$)$_2$EPCO into [(2,6-$Mes_2C_6H_3$)$_2$E]$^+$ and [PCO]$^-$.

E	[(2,6-$Mes_2C_6H_3$)$_2$E]$^+$	[(2,6-$Mes_2C_6H_3$)$_2$E]PCO	delta	kJ mol^{-1}
[PCO]$^-$	–454.6960			
B	–1884.0135	–2338.7095	–0.1722	–452.2
Al	–2101.6276	–2556.3236	–0.1766	–463.7
Ga	–3784.0489	–4238.7449	–0.1741	–457.2
In	–2049.4587	–2504.1546	–0.1705	–447.7
Tl	–2031.8282	–2486.5242	–0.1563	–410.5

Table S4. Calculated bond lengths and dissociation of (2,6-$Mes_2C_6H_3$)$_2$EP(O)C(IMe_4) into (2,6-$Mes_2C_6H_3$)$_2$EPCO and IMe_4 (E = B, Al, Ga, In, Tl).

E	energy	delta	kJ mol^{-1}	d(E-P)	d(E-C)	d(E-O)	d(P-C)	d(C-O)
IMe_4	-383.4438							
B	-2722.3925	-0.067	-175.7	2.074	2.149	1.555	1.709	1.344
Al	-2940.0211	-0.077	-202.3	2.411	2.377	1.862	1.720	1.334
Ga	-4622.4235	-0.061	-159.2	2.416	2.496	2.032	1.724	1.316
In	-2887.8199	-0.051	-133.6	2.592	2.707	2.281	1.730	1.303
Tl	-2870.1656	-0.041	-108.4	2.642	2.841	2.513	1.735	1.284

Computational methodology

Density functional theory (DFT) computations were performed in the gas-phase at the B3PW91/6-311+G(2df,p)[S7] level of theory using Gaussian09.[S8] For the In, Tl and Te atoms, effective core potentials (ECP28MDF, ECP60MDF)[S9] and corresponding cc-pVTZ basis set[S9] were utilized. Dispersion was taken account for by the empirical dispersion correction of Grimme.[S10] Subsequent normal mode analysis had to be skipped as it exceeded computational capacities. The wavefunction files were used for a topological analysis of the electron density according to the Atoms-In-Molecules space-partitioning scheme[16] using AIM2000,[S11] whereas DGRID[S12] was used to generate and analyze the Electron-Localizability-Indicator (ELI-D)[18] related real-space bonding descriptors applying a grid step size of 0.05 a.u. (0.12 a.u. for visualization). The NCI[17] grids were computed with NCIplot (0.1 a.u. grids).[S13] Bond paths are displayed with AIM2000, ELI-D and NCI figures are displayed with MolIso,[S14] and spin densities are displayed with GaussView. AIM provides a bond paths motif, which resembles and exceeds the Lewis picture of chemical bonding, disclosing all types and strengths of interactions. Additionally, it provides atomic volumes and charges. Analyses of the reduced density gradient, $s(\mathbf{r}) = [1/2(3\pi^2)^{1/3}]|\nabla\rho|/\rho^{4/3}$, according to the NCI method is used to visualize non-covalent bonding aspects. An estimation of different non-covalent contact types according to steric/repulsive ($\lambda_2 > 0$), van der Waals-like ($\lambda_2 \approx 0$), and attractive ($\lambda_2 < 0$) is facilitated by mapping the ED times the sign of the second eigenvalue of the Hessian ($\mathrm{sign}(\lambda_2)\rho$) on the *iso*-surfaces of $s(\mathbf{r})$. AIM and NCI are complemented by the ELI-D, which provides electron populations and volumes of bonding and lone-pair basins and is especially suitable for the analysis of (polar-)covalent bonding aspects.

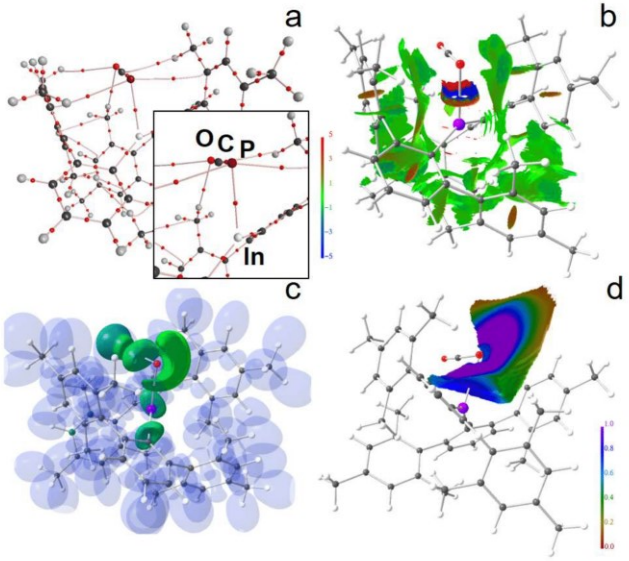

Figure S25. RSBI analysis of **2** (a) AIM bond paths motif, (b) NCI *iso*-surface at s(r) = 0.5, (c) ELI-D localization domain representation at *iso*-value of 1.3, (d) ELI-D distribution mapped on the In-P ELI-D basin.

Table S5. Calculated bond lengths of (2,6-$Mes_2C_6H_3$)$_2$ETeP(O)C(IMe_4)

E	d(E-P)	d(E-C)	d(E-O)	d(P-C)	d(C-O)	d(E-Te)
Ga	3.622	2.933	1.964	1.721	1.304	2.689
In	3.800	3.146	2.203	1.728	1.292	2.842

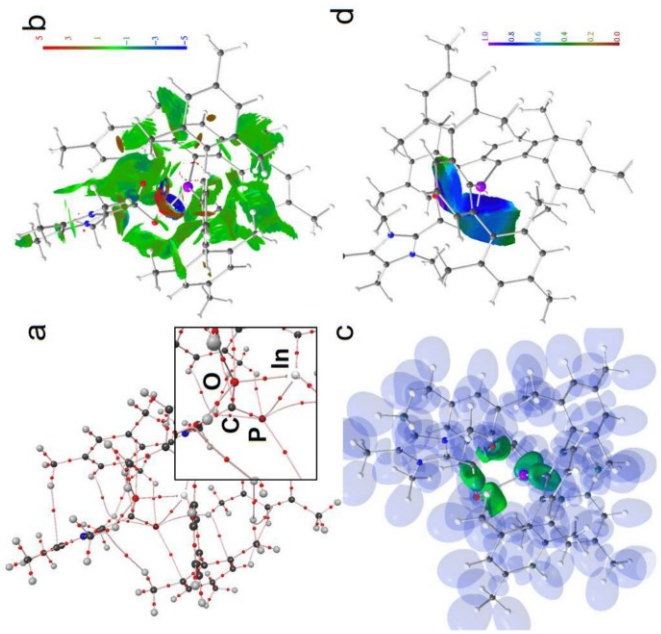

Figure S26. RSBI analysis of **4** (a) AIM bond paths motif, (b) NCI *iso*-surface at s(r) = 0.5, (c) ELI-D localization domain representation at *iso*-value of 1.3, (d) ELI-D distribution mapped on the In-P and In-O ELI-D basins.

41

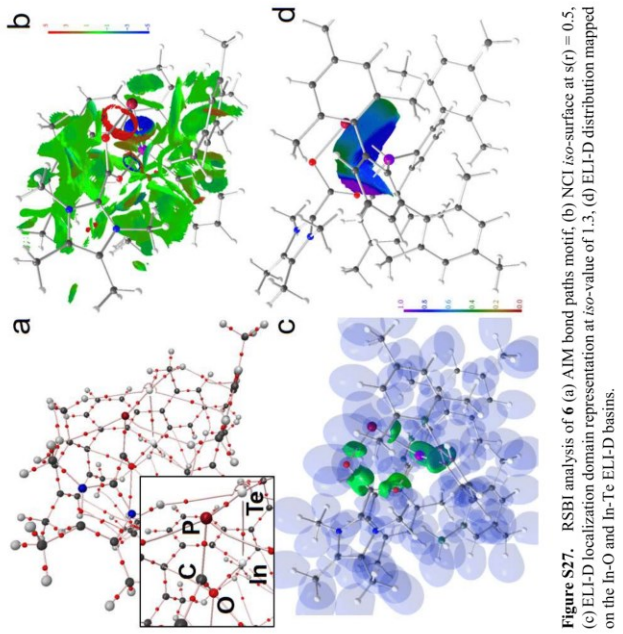

Figure S27. RSBI analysis of **6** (a) AIM bond paths motif, (b) NCI *iso*-surface at s(r) = 0.5, (c) ELI-D localization domain representation at *iso*-value of 1.3, (d) ELI-D distribution mapped on the In-O and In-Te ELI-D basins.

42

References

[S1] X.-W. Li, W. T. Pennington, G. H. Robinson, *Organometallics* **1995**, *14*, 2109-2111.

[S2] X.-W. Li, G. Robinson, W. T. Pennington, *Main Group Chem.* 1996, *1*, 301-307.

[S3] R. E. Schreiber, J. M. Goicoecha, *Angew. Chem. Int. Ed.* **2021**, *60*, 3759-3767.

[S4] A. J. Arduengo III, H. V. R. Dias, R. L. Harlow, M. Kline, *J. Am. Chem. Soc.* **1992**, *114*, 5530-5534.

[S5] O. V. Dolomanov, L. J. Bourhis, R. J. Gildea, J. A. K. Howard, H. Puschmann. *J. Appl. Cryst.* **2009**, *42*, 339–341.

[S6] K. Brandenburg, H. Putz, Crystal Impact GbR, Bonn **2012**.

[S7] (a) A. D. Becke, *J. Chem. Phys*. **1993**, *98*, 5648-5652. (b) J. P. Perdew, J. A. Chevary, S. H. Vosko, K. A. Jackson, M. R. Pederson, D. J. Singh, C. Fiolhais, *Phys. Rev*. B **1992**, *46*, 6671-6687.

[S8] Gaussian 16, Revision C.01, M. J. Frisch, G. W. Trucks, H. B. Schlegel, G. E. Scuseria, M. A. Robb, J. R. Cheeseman, G. Scalmani, V. Barone, G. A. Petersson, H. Nakatsuji, X. Li, M. Caricato, A. V. Marenich, J. Bloino, B. G. Janesko, R. Gomperts, B. Mennucci, H. P. Hratchian, J. V. Ortiz, A. F. Izmaylov, J. L. Sonnenberg, D. Williams-Young, F. Ding, F. Lipparini, F. Egidi, J. Goings, B. Peng, A. Petrone, T. Henderson, D. Ranasinghe, V. G. Zakrzewski, J. Gao, N. Rega, G. Zheng, W. Liang, M Hada, M. Ehara, K. Toyota, R. Fukuda, J. Hasegawa, M. Ishida, T. Nakajima, Y. Honda, O. Kitao, H. Nakai, T. Vreven, K. Throssell, J. A. Jr. Montgomery, J. E. Peralta, F. Ogliaro, M. J. Bearpark, J. J. Heyd, E. N. Brothers, K. N. Kudin, V. N. Staroverov, T. A. Keith, R. Kobayashi, J. Normand, K. Raghavachari, A. P. Rendell, J. C. Burant, S. S. Iyengar, J. Tomasi, M. Cossi, J. M. Millam, M. Klene, C. Adamo, R. Cammi, J. W. Ochterski, R. L. Martin, K. Morokuma, O. Farkas, J. B. Foresman, D. J. Fox, Gaussian, Inc., Wallingford CT, 2016.

[S9] K. A. Peterson, *J. Chem. Phys.* **2003**, *119*, 11099.

[S10] S. Grimme, J. Anthony, S. Ehrlich, H. Krieg, *J. Chem. Phys*. **2010**, *132*, 154104.

[S11] F. Biegler-König, J. Schönbohm, D. Bayles, *J. Comput. Chem*. **2001**, *22*, 545-559.

[S12] M. Kohout, *DGRID*-4.6 Radebeul, **2015**.

[S13] J. Contreras-García, E. Johnson, S. Keinan, R. Chaudret, J.-P. Piquemal, D. Beratan, W. Yang, *J. Chem. Theor. Comp.* **2011**, *7*, 625-632.

[S14] C. B. Hübschle, P. Luger, *J. Appl. Crystallogr*. **2006**, *39*, 901-904.

Zeitschrift für anorganische und allgemeine Chemie - Article

Kinetic Stabilization of Heavier Bis(*m*-terphenyl)pnictogen Phosphaethynolates

Daniel Duvinage,[a‡] *Marvin Janssen,*[a‡] *Enno Lork,*[a] *Hansjörg Grützmacher,*[b] *Stefan Mebs,*[*c]

Jens Beckmann[*a]

[a] Institut für Anorganische Chemie und Kristallographie, Universität Bremen, Leobener Straße 7, 28359 Bremen, Germany

[b] Laboratory of Inorganic Chemistry, ETH Zürich, Vladimir-Prelog-Weg 1-5/10, 8093 Zürich, Switzerland

[c] Institut für Experimentalphysik, Freie Universität Berlin, Arnimallee 14, 14195 Berlin, Germany

Supporting Information

Table of contents

* Correspondence to Jens Beckmann and Stefan Mebs (E-mail: j.beckmann@uni-bremen.de, stebs@physik.fu-berlin.de)

Zeitschrift für anorganische und allgemeine Chemie

Supporting Information

Kinetic Stabilization of Heavier Bis(*m*-terphenyl)pnictogen Phosphaethynolates

Daniel Duvinage[+], Marvin Janssen[+], Enno Lork, Hansjörg Grützmacher, Stefan Mebs,* and Jens Beckmann*

6.7 Kinetic Stabilization of Heavier Bis(*m*-terphenyl)pnictogen phosphaethynolates

Experimental procedures

General information

Unless otherwise stated, all reactions and manipulations were performed under inert atmosphere (argon) using anhydrous solvents. The starting materials (2,6-$Mes_2C_6H_3$)$_2$SbCl,[6] (2,6-$Mes_2C_6H_3$)$_2$BiCl,[7] [Na(1,4-dioxane)$_{2.5}$][PCO][3] and 1,2,3,4-tetramethylimidazol-2-ylidene, IMe_4,[4] were prepared following the published procedures. Anhydrous dichloromethane, hexane, tetrahydrofurane and toluene were collected from an SPS800 mBraun solvent purification system and stored over 4 Å molecular sieves. Dimethoxyethane was dried over CaH_2 and distilled over 4 Å molecular sieves for storage. Deuterated solvents were degassed and dried over 4 Å molecular sieves under argon.

NMR spectra were recorded at room temperature on a Bruker Avance 600 MHz spectrometer. ^{1}H, ^{13}C{^{1}H} and ^{31}P{^{1}H} spectra are reported on the δ scale (ppm) and are referenced against $SiMe_4$ and H_3PO_4 (85% in water). ^{1}H and ^{13}C{^{1}H} chemical shifts are reported relative to the residual peak of the solvent (C_6HD_5 7.16 ppm for C_6D_6 and C_4HD_7O: 1.71 ppm for THF-d_8) in the ^{1}H NMR spectra, and to the peak of the deuterated solvent (C_6D_6:128.06 ppm and THF-d_8: 67.21 ppm) in the ^{13}C{^{1}H} NMR spectra. The assignment of the ^{1}H and ^{13}C{^{1}H} resonance signals was made in accordance with the COSY, HSQC and HMBC spectra.

The ESI HRMS spectra were measured on a Bruker Impact II spectrometer. Acetonitrile or toluene/acetonitrile solutions (c =1·10^{-5} mol·L^{-1}) were injected directly into the spectrometer at a flow rate of 3 µL·min^{-1}. Nitrogen was used both as a drying gas and for nebulization with flow rates of approximately 5 L·min^{-1} and a pressure of 5 psi. Pressure in the mass analyzer region was usually about 1·10^{-5} mbar. Spectra were collected for 1 min and averaged. The nozzle-skimmer voltage was adjusted individually for each measurement.

IR spectra were recorded on a *Nicolet* Thermo iS10 scientific spectrometer with a diamond ATR unit. The absorption bands are reported in cm^{-1} with indicated relative intensities: s (strong, 0 – 33 % T); m (medium, 34 – 66 % T), w (weak, 67 – 100 % T), and br (broad).

UV-Vis spectra were measured on a VWR UV-1600PC Spectrometer.

NMR spectroscopy

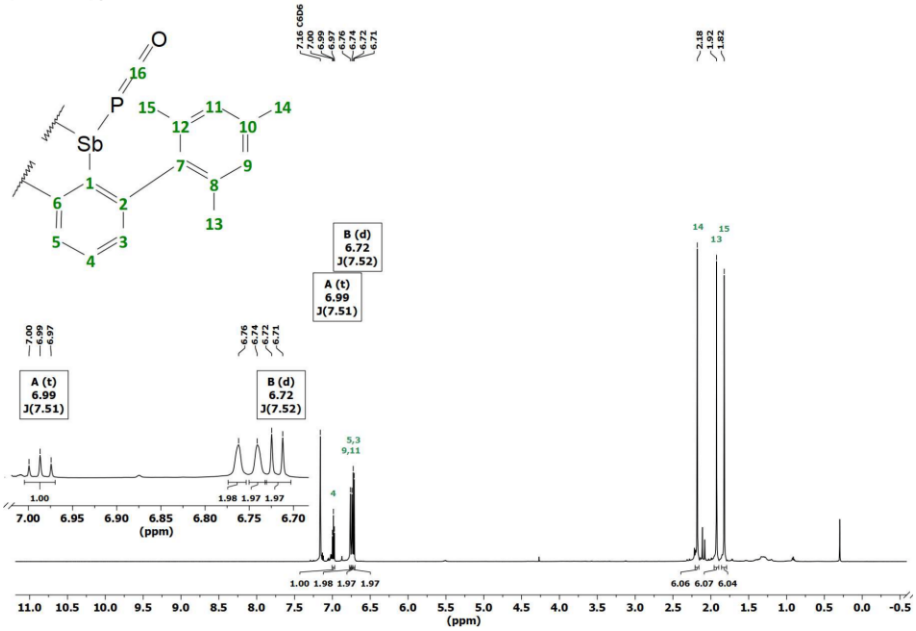

Figure S1. ^{1}H NMR (C_6D_6, 600 MHz) spectrum of (2,6-$Mes_2C_6H_3$)$_2$SbPCO (**1**).

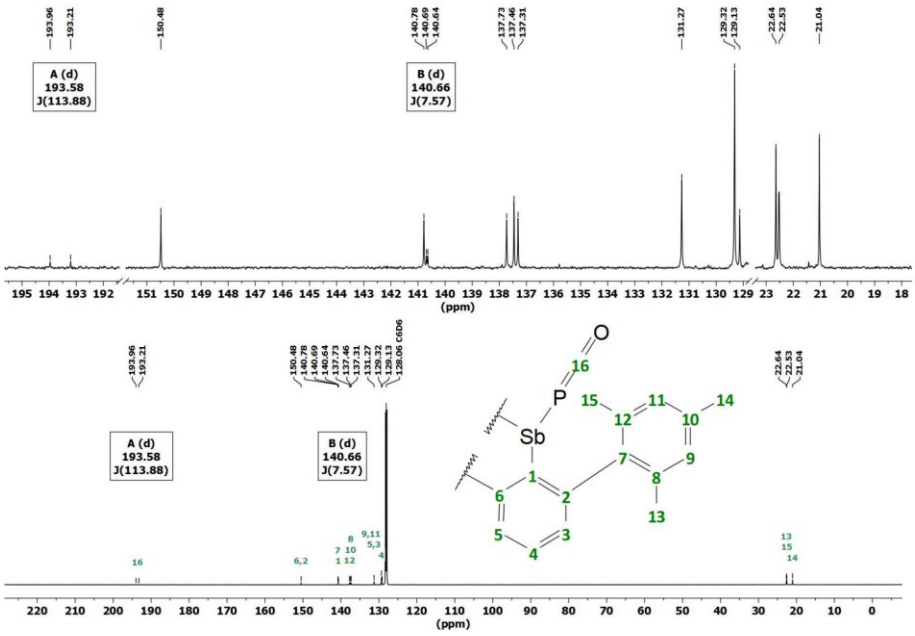

Figure S2. $^{13}C\{^{1}H\}$ NMR (C_6D_6, 151 MHz) spectrum of (2,6-$Mes_2C_6H_3$)$_2$SbPCO (**1**).

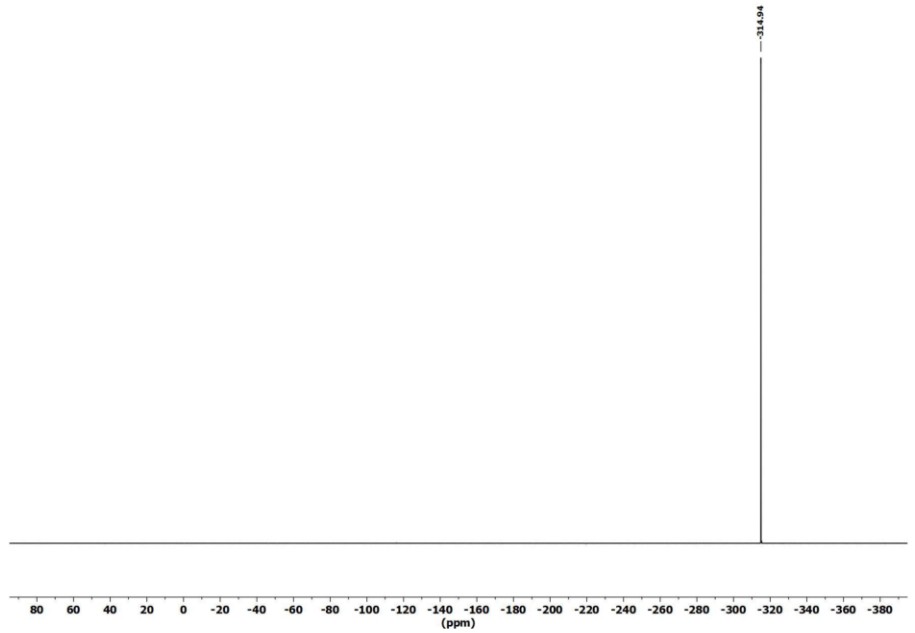

Figure S3. ^{31}P NMR (C_6D_6, 243 MHz) spectrum of (2,6-$Mes_2C_6H_3$)$_2$SbPCO (**1**).

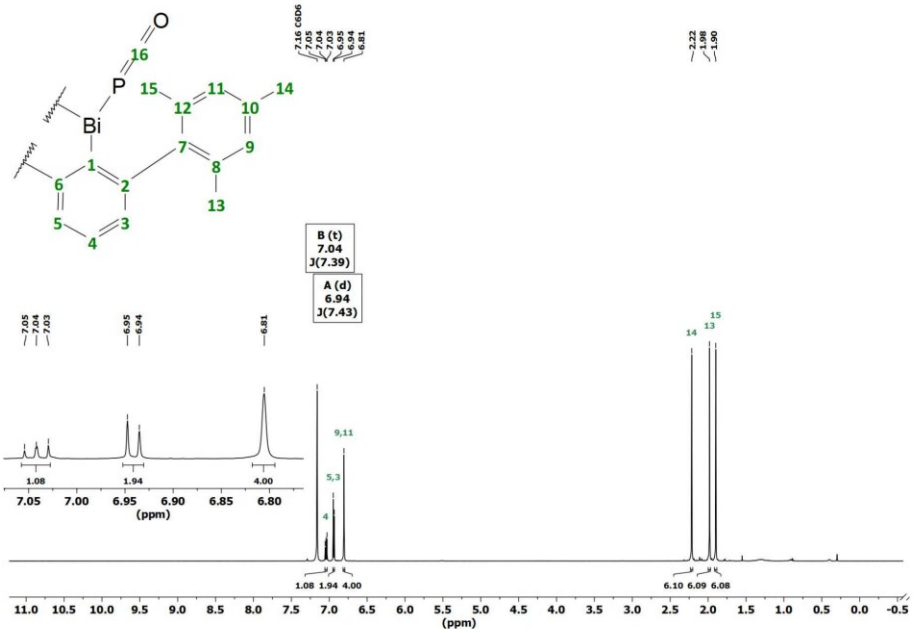

Figure S4. ^{1}H NMR (C_6D_6, 600 MHz) spectrum of (2,6-$Mes_2C_6H_3$)$_2$BiPCO (**2**).

6

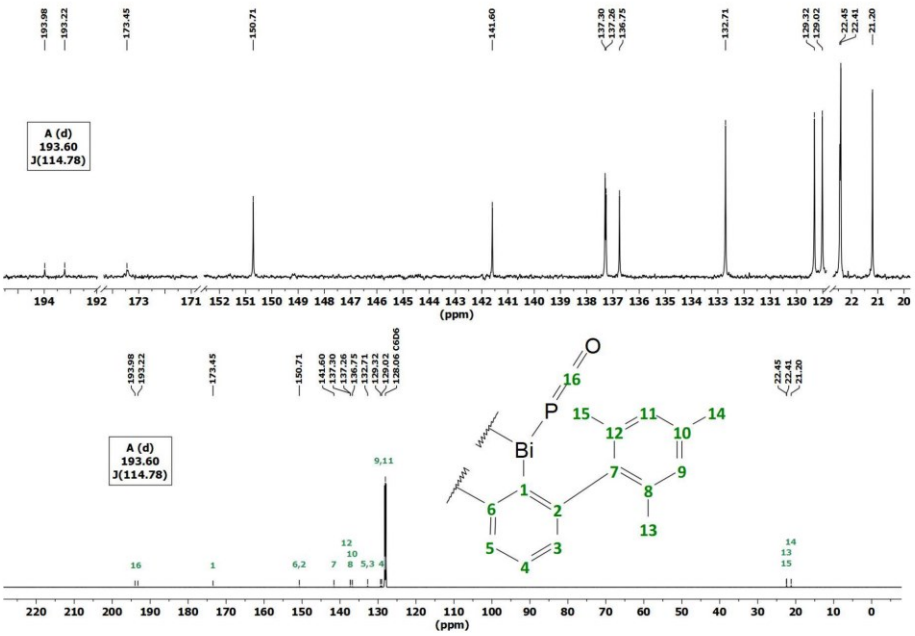

Figure S5. $^{13}C\{^{1}H\}$ NMR (C_6D_6, 151 MHz) spectrum of (2,6-$Mes_2C_6H_3$)$_2$BiPCO (**2**).

7

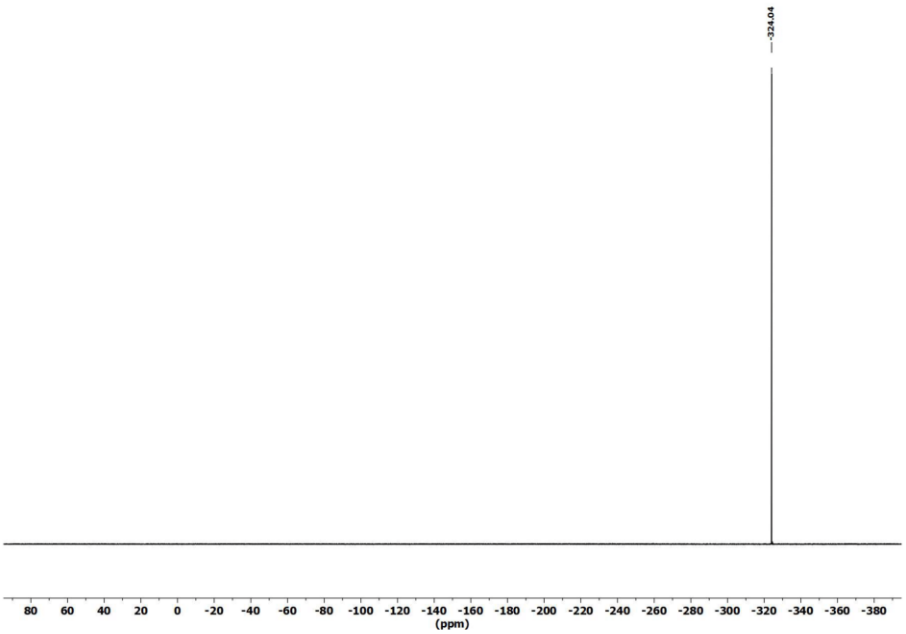

Figure S6. ^{31}P NMR (C_6D_6, 243 MHz) spectrum of (2,6-$Mes_2C_6H_3$)$_2$BiPCO (**2**).

8

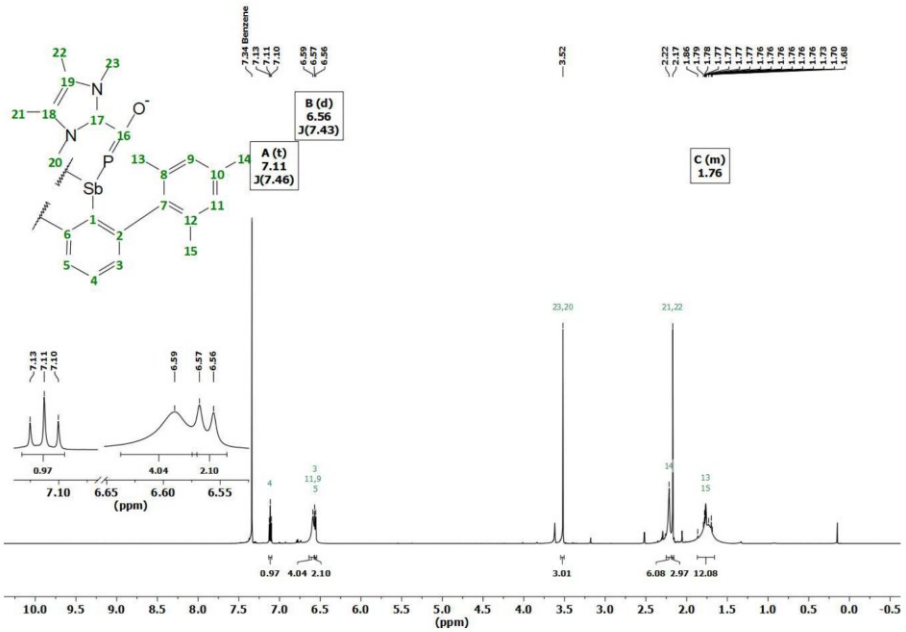

Figure S7. ^{1}H NMR (THF-d_8, 600 MHz) spectrum of (2,6-$Mes_2C_6H_3$)$_2$SbP(O)C(IMe$_4$) (**3**).

9

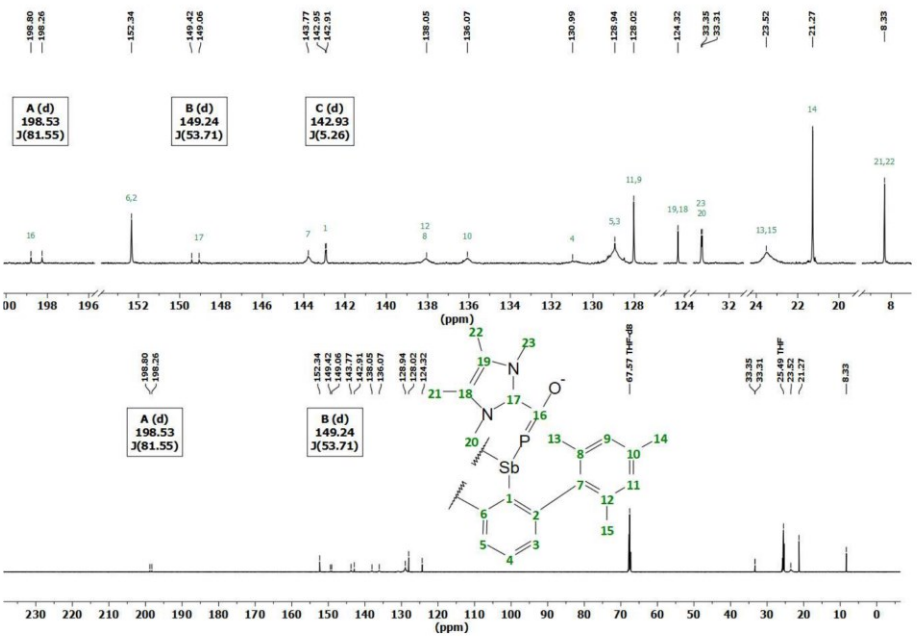

Figure S8. $^{13}C\{^{1}H\}$ NMR (THF-d8, 151 MHz) spectrum of (2,6-$Mes_2C_6H_3$)$_2$SbP(O)C(IMe_4) (**3**).

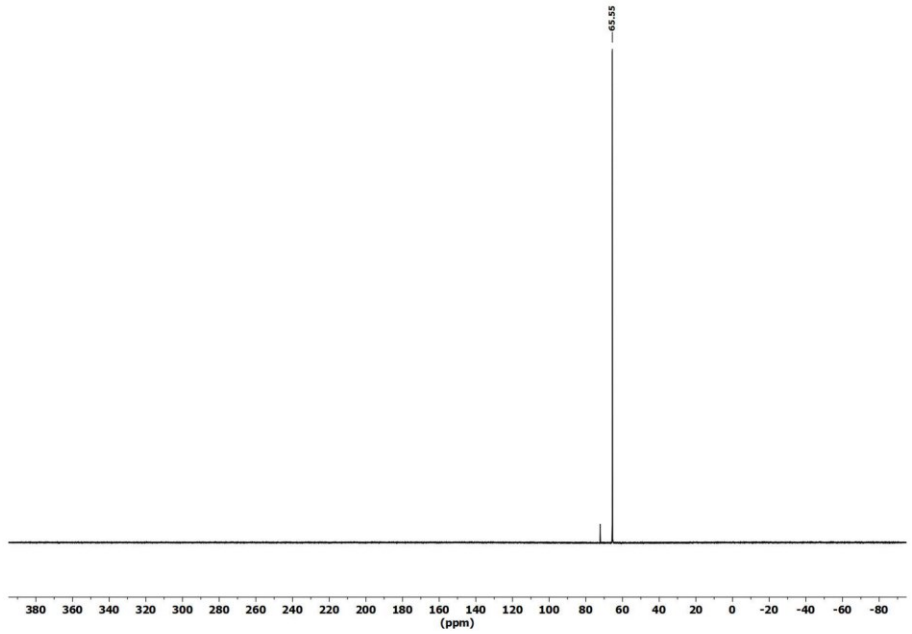

Figure S9. ^{31}P NMR (THF-d8, 243 MHz) spectrum of (2,6-$Mes_2C_6H_3$)$_2$SbP(O)C(IMe_4) (**3**).

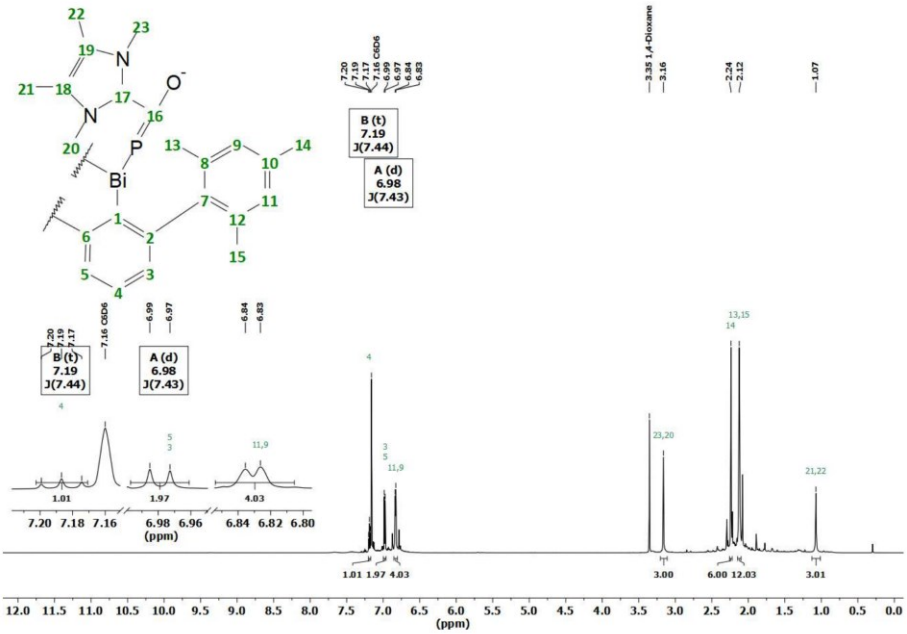

Figure S10. ^{1}H NMR (C_6D_6, 600 MHz) spectrum of (2,6-$Mes_2C_6H_3$)$_2$BiP(O)C(IMe_4) (**4**).

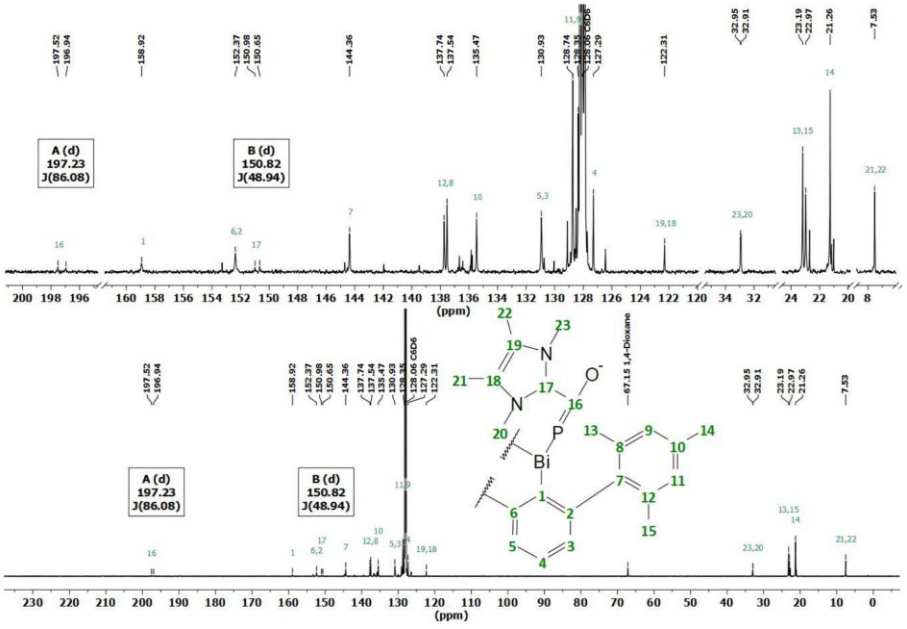

Figure S11. $^{13}C\{^{1}H\}$ NMR (C_6D_6, 151 MHz) spectrum of (2,6-$Mes_2C_6H_3$)$_2$BiP(O)C(IMe_4) (**4**).

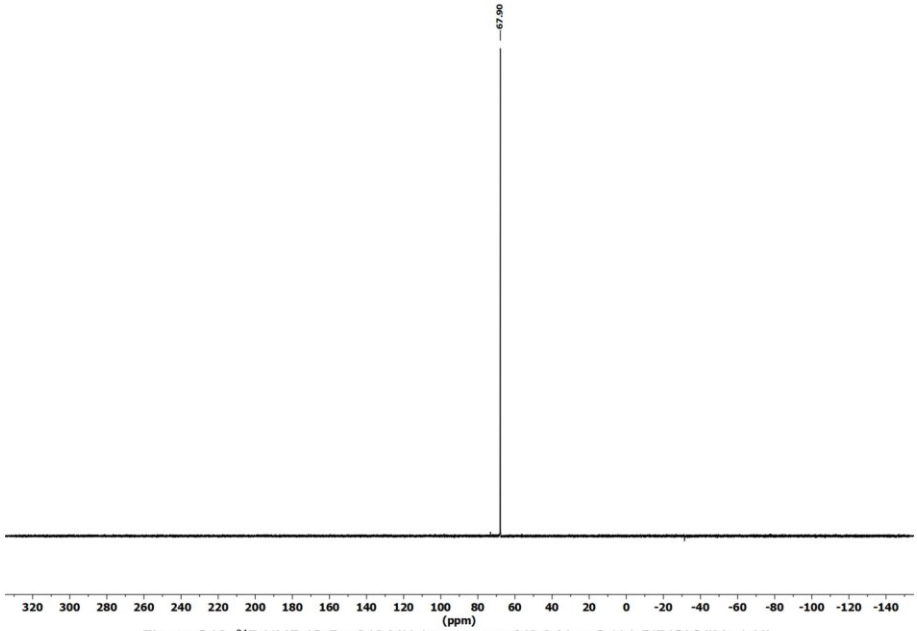

Figure S12. ^{31}P NMR (C_6D_6, 243 MHz) spectrum of (2,6-$Mes_2C_6H_3$)$_2$BiP(O)C(IMe$_4$) (**4**).

UV-Vis spectroscopy

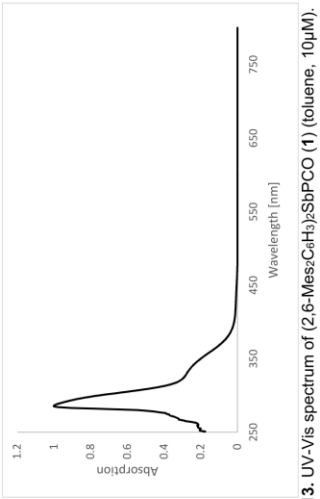

Figure S13. UV-Vis spectrum of (2,6-$Mes_2C_6H_3$)$_2$SbPCO (**1**) (toluene, 10μM).

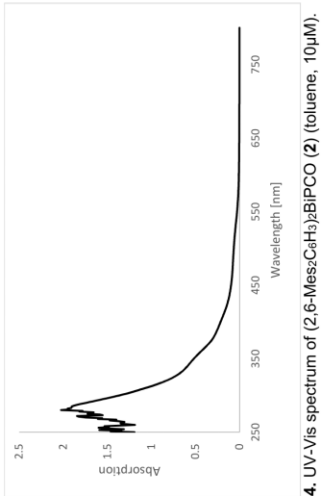

Figure S14. UV-Vis spectrum of (2,6-$Mes_2C_6H_3$)$_2$BiPCO (**2**) (toluene, 10μM).

X-ray crystallography

Intensity data of **1**, **2**, **3** and **4**·4 C_6H_6 was collected on a Bruker Venture D8 diffractometer at 100 K with graphite-monochromated Mo-Kα (0.7107 Å) radiation. All structures were solved by direct methods and refined based on F^2 by use of the SHELX program package as implemented in Olex 2.[S1,S2] All non-hydrogen atoms were refined using anisotropic displacement parameters. Hydrogen atoms attached to carbon atoms were included in geometrically calculated positions using a riding model. For **1**, disorder was resolved for Sb (97:3). For **2**, a twin refinement (BASF = 0.388(8)) was carried out and disorder was resolved for the BiPCO moiety (60:40). For **3**, diffuse electron density was accounted for using the SQUEZZE routine. For **4**·4 C_6H_6, a twin refinement (BASF = 0.0198(4) was carried out and disorder was resolved for the BiPCO moiety (70:30). Crystal and refinement data are collected in Tables S1. Figures were created using DIAMOND.[S3] Crystallographic data for the structural analyses have been deposited with the Cambridge Crystallographic Data Centre. Copies of this information may be obtained free of charge from The Director, CCDC, 12 Union Road, Cambridge CB2 1EZ, UK (Fax: +44-1223-336033; e-mail: deposit@ccdc.cam.ac.uk or http://www.ccdc.cam.ac.uk).

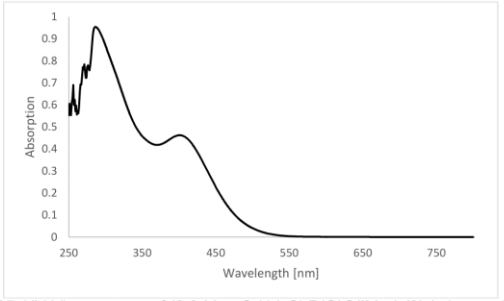

Figure S15. UV-Vis spectrum of (2,6-$Mes_2C_6H_3$)$_2$SbP(O)C(IMe$_4$) (**3**) (toluene, 10µM).

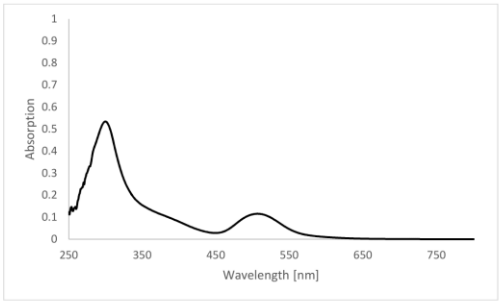

Figure S16. UV-Vis spectrum of (2,6-$Mes_2C_6H_3$)$_2$BiP(O)C(IMe$_4$) (**4**) (toluene, 10µM).

Table S1. Crystal data and structure refinement of **1** - **4**.

	1	**2**	**3**
Formula	$C_{49}H_{50}OPSb$	$C_{49}H_{50}BiOP$	$C_{56}H_{62}N_2OPSb$
Formula weight, g mol^{-1}	807.61	894.84	931.79
Crystal system	orthorhombic	monoclinic	triclinic
Crystal size, mm	0.05 × 0.11 × 0.13	0.14 × 0.18 × 0.27	0.09 × 0.13 × 0.36
Space group	Pccn	Cc	$P\bar{1}$
a, Å	18.8660(5)	10.8105(6)	11.4927(11)
b, Å	30.0224(8)	19.1965(14)	14.9684(14)
c, Å	14.2318(4)	19.6772(11)	14.9946(13)
α, °	90	90	97.268(3)
β, °	90	94.841(2)	91.313(3)
γ, °	90	90	93.800(3)
V, Å^3	8060.9(4)	4068.9(4)	2551.9(4)
Z	8	4	2
ρ_{calcd}, Mg m^{-3}	1.331	1.461	1.213
μ (Mo *Kα*), mm^{-1}	0.760	4.408	0.610
F(000)	3344	1800	972
θ range, deg	2.25 to 28.37	2.07 to 36.51	2.06 to 30.52
Index ranges	–25 ≤ h ≤ 25	–18 ≤ h ≤ 18	–16 ≤ h ≤ 16
	–40 ≤ k ≤ 40	–32 ≤ k ≤ 32	–21 ≤ k ≤ 21
	–18 ≤ l ≤ 19	–32 ≤ l ≤ 32	–21 ≤ l ≤ 21
No. of reflns collected	251433	202815	108773
Completeness to θ_{max}	99.9%	99.9%	99.9%
No. indep. Reflns	10075	19847	15598
No. obsd reflns with($I>2\sigma(I)$)	8045	16495	13716
No. refined params	490	519	566
GooF (F^2)	1.080	1.082	1.043
R_1 (F) ($I > 2\sigma(I)$)	0.0394	0.0439	0.0379
wR_2 (F^2) (all data)	0.0770	0.1089	0.0946
Largest diff peak/hole, e Å^{-3}	2.445 / –2.334	2.445 / –2.334	3.329 / –0.084
CCDC number	2127081	2127082	2127083

Table S1. Cont.

	4·4 C_6H_6
Formula	$C_{80}H_{86}BiN_2OP$
Formula weight, g mol^{-1}	1331.45
Crystal system	triclinic
Crystal size, mm	0.05 × 0.17 × 0.22
Space group	$P\bar{1}$
a, Å	10.6698(13)
b, Å	11.1211(14)
c, Å	29.429(4)
α, °	79.787(4)
β, °	79.742(4)
γ, °	79.085(3)
V, Å^3	3336.6(7)
Z	2
ρ_{calcd}, Mg m^{-3}	1.325
μ (Mo *Kα*), mm^{-1}	2.713
F(000)	1372
θ range, deg	2.07 to 36.51
Index ranges	–16 ≤ h ≤ 16
	–17 ≤ k ≤ 17
	–45 ≤ l ≤ 45
No. of reflns collected	103704
Completeness to θ_{max}	99.9%
No. indep. Reflns	25465
No. obsd reflns with($I>2\sigma(I)$)	20388
No. refined params	698
GooF (F^2)	1.220
R_1 (F) ($I > 2\sigma(I)$)	0.0780
wR_2 (F^2) (all data)	0.1414
Largest diff peak/hole, e Å^{-3}	2.348 / –3.349
CCDC number	2127084

Table S2 Molecular energies [hartrees, kJ mol^{-1}] and relevant distances [Å]

type	PCO	energy	delta	kJ mol^{-1}	d(E-P)	d(E-C)	d(E-O)
N	**P**-C-O	-2368.7399			1.753	2.627	3.655
	P-C-**O**	-2368.6468	-0.0931	-244.35	3.712	2.311	1.480
P	**P**-C-O	-2655.3751			2.224	2.701	3.539
	P-C-**O**	-2655.3351	-0.0400	-105.01	4.066	2.647	1.723
As	**P**-C-O	-4549.9070			2.354	2.808	3.621
	P-C-**O**	-4549.8607	-0.0464	-121.73	4.084	2.733	1.903
Sb	**P**-C-O	-2554.4354			2.554	2.964	3.743
	P-C-**O**						
Bi	**P**-C-O	-2528.8164			2.654	3.031	3.781
	P-C-**O**						

type	PCO-NHC	energy	delta	kJ mol^{-1}	d(E-P)	d(E-C)	d(E-O)
N-NHC	**P**-C-O	-2752.2431			1.748	2.712	2.928
	P-C-**O**	-2752.1283	-0.1149	-301.65	3.070	2.443	1.403
P-NHC	**P**-C-**O**	-3038.8113			2.106	2.296	1.633
As-NHC	**P**-C-O	-4933.3935			2.291	3.157	3.333
	P-C-**O**	-4933.3575	-0.0360	-94.60	3.192	2.740	1.845
Sb-NHC	**P**-C-O	-2937.9181			2.493	3.266	3.362
	P-C-**O**	-2937.8981	-0.0199	-52.29	2.806	2.803	2.131
Bi-NHC	**P**-C-O	-2912.2991			2.594	3.307	3.351
	P-C-**O**						

type	$[R_2E]^+$	$[R_2E]^+ + [PCO]^-$	delta	kJ mol^{-1}
PCO	-454.6960			
N	-1913.8472	-2368.5432	-0.20	-516.45
P	-2200.4646	-2655.1606	-0.21	-563.21
As	-4095.0029	-4549.6989	-0.21	-546.56
Sb	-2099.5401	-2554.2361	-0.20	-523.14
Bi	-2073.9285	-2528.6244	-0.19	-504.10

Computational Methodology. Starting from the solid-state molecular geometries density functional theory (DFT) computations were performed in the gas-phase at the B3PW91/6-311+G(2df,p)[S4] level of theory using Gaussian 16.[S5] For the Sb and Bi atoms, effective core potentials (ECP28MDF, ECP60MDF)[S6] and corresponding cc-pVTZ basis set[S6] were utilized. Dispersion was taken account for by the empirical dispersion correction of Grimme.[S7] Subsequent normal mode analysis had to be skipped as it exceeded computational capacities. The wavefunction files were used for a topological analysis of the electron density according to the Atoms-In-Molecules space-partitioning scheme[13] using AIM2000,[S8] whereas DGRID[S9] was used to generate and analyze the Electron-Localizability-Indicator (ELI-D)[15] related real-space bonding descriptors applying a grid step size of 0.05 a.u. (0.12 a.u. for visualization). The NCI[14] grids were computed with NCIplot (0.1 a.u. grids).[S10] Bond paths are displayed with AIM2000, ELI-D and NCI figures are displayed with MolIso,[S11] and spin densities are displayed with GaussView 6.1. AIM provides a bond paths motif, which resembles and exceeds the Lewis picture of chemical bonding, disclosing all types and strengths of interactions. Additionally, it provides atomic volumes and charges. Analyses of the reduced density gradient, $s(\mathbf{r}) = [1/2(3\pi^2)^{1/3}]|\nabla\rho|/\rho^{4/3}$, according to the NCI method is used to visualize non-covalent bonding aspects. An estimation of different non-covalent contact types according to steric/repulsive ($\lambda_2 > 0$), van der Waals-like ($\lambda_2 \approx 0$), and attractive ($\lambda_2 < 0$) is facilitated by mapping the ED times the sign of the second eigenvalue of the Hessian ($\mathrm{sign}(\lambda_2)\rho$) on the *iso*-surfaces of $s(\mathbf{r})$. AIM and NCI are complemented by the ELI-D, which provides electron populations and volumes of bonding and lone-pair basins and is especially suitable for the analysis of (polar-)covalent bonding aspects.

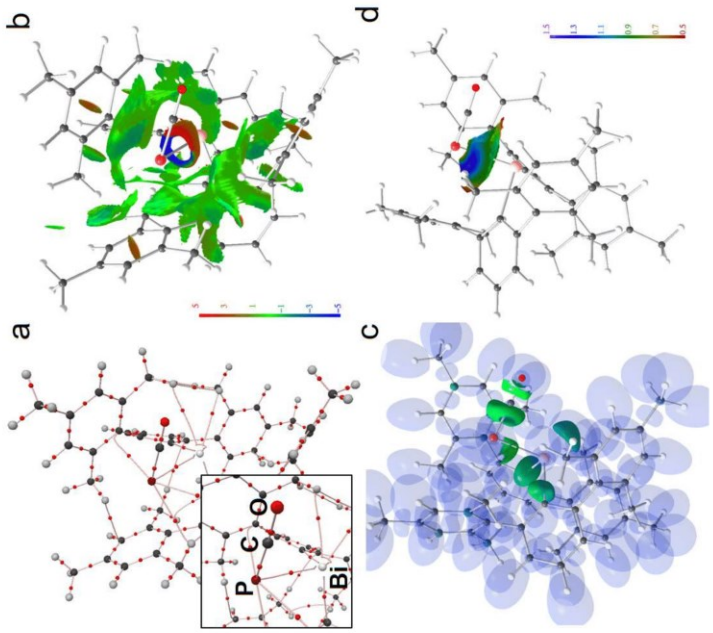

Figure S17. RSBI analysis of **2** (a) AIM bond paths motif, (b) NCI *iso*-surface at s(**r**) = 0.5, (c) ELI-D localization domain representation at *iso*-value of 1.3, (d) ELI-D distribution mapped on the Bi–P ELI-D basin.

22

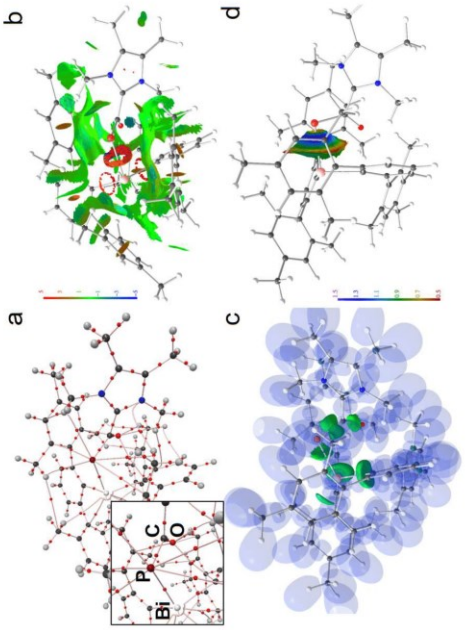

Figure S18. RSBI analysis of **4** (a) AIM bond paths motif, (b) NCI *iso*-surface at s(r) = 0.5, (c) ELI-D localization domain representation at *iso*-value of 1.3, (d) ELI-D distribution mapped on the Bi–P ELI-D basin.

23

Additional References

[S1] G. M. Sheldrick, A*cta Cryst.* **2008**, *A64*, 112-122.

[S2] O. V. Dolomanov, L. J. Bourhis, R. J. Gildea, J. A. K. Howard, H. Puschmann. *J. Appl. Cryst.* **2009**, *42*, 339–341.

[S3] K. Brandenburg, H. Putz, Crystal Impact GbR, Bonn **2012**.

[S4] (a) A. D. Becke, *J. Chem. Phys.* **1993**, *98*, 5648-5652. (b) J. P. Perdew, J. A. Chevary, S. H. Vosko, K. A. Jackson, M. R. Pederson, D. J. Singh, C. Fiolhais, *Phys. Rev*. B **1992**, *46*, 6671-6687.

[S5] Gaussian 16, Revision C.01, M. J. Frisch, G. W. Trucks, H. B. Schlegel, G. E. Scuseria, M. A. Robb, J. R. Cheeseman, G. Scalmani, V. Barone, G. A. Petersson, H. Nakatsuji, X. Li, M. Caricato, A. V. Marenich, J. Bloino, B. G. Janesko, R. Gomperts, B. Mennucci, H. P. Hratchian, J. V. Ortiz, A. F. Izmaylov, J. L. Sonnenberg, D. Williams-Young, F. Ding, F. Lipparini, F. Egidi, J. Goings, B. Peng, A. Petrone, T. Henderson, D. Ranasinghe, V. G. Zakrzewski, J. Gao, N. Rega, G. Zheng, W. Liang, M Hada, M. Ehara, K. Toyota, R. Fukuda, J. Hasegawa, M. Ishida, T. Nakajima, Y. Honda, O. Kitao, H. Nakai, T. Vreven, K. Throssell, J. A. Jr. Montgomery, J. E. Peralta, F. Ogliaro, M. J. Bearpark, J. J. Heyd, E. N. Brothers, K. N. Kudin, V. N. Staroverov, T. A. Keith, R. Kobayashi, J. Normand, K. Raghavachari, A. P. Rendell, J. C. Burant, S. S. Iyengar, J. Tomasi, M. Cossi, J. M. Millam, M. Klene, C. Adamo, R. Cammi, J. W. Ochterski, R. L. Martin, K. Morokuma, O. Farkas, J. B. Foresman, D. J. Fox, Gaussian, Inc., Wallingford CT, 2016.

[S6] K. A. Peterson, *J. Chem. Phys.* **2003**, *119*, 11099.

[S7] S. Grimme, J. Anthony, S. Ehrlich, H. Krieg, *J. Chem. Phys.* **2010**, *132*, 154104.

[S8] F. Biegler-König, J. Schönbohm, D. Bayles, *J. Comput. Chem.* **2001**, *22*, 545-559.

[S9] M. Kohout, *DGRID*-4.6 Radebeul, **2015**.

[S10] J. Contreras-García, E. Johnson, S. Keinan, R. Chaudret, J.-P. Piquemal, D. Beratan, W. Yang, *J. Chem. Theor. Comp.* **2011**, *7*, 625-632.

[S11] C. B. Hübschle, P. Luger, *J. Appl. Crystallogr.* **2006**, *39*, 901-904.

6.8 Synthesis and Single-Electron Oxidation of Bulky Bis(*m*-terphenyl)chalcogenides: The Quest for Kinetically Stabilized Radical Cations

Chemistry—A European Journal

Supporting Information

Synthesis and Single-Electron Oxidation of Bulky Bis(*m*-terphenyl)chalcogenides: The Quest for Kinetically Stabilized Radical Cations

Daniel Duvinage, Farzin Mostaghimi, Mattis Damrath, Julian Spils, Pascal Komorr, Danila S. Odintsov, Matvey Fedin, Leonid A. Shundrin,* Stefan Mebs,* and Jens Beckmann*

Table of Contents

Experimental procedures

General information

Unless otherwise stated, all reactions and manipulations were performed under inert atmosphere (argon) using anhydrous solvents. Reagents used in this work including $S(O)Cl_2$, $S(O)_2Cl_2$, $S(O)F_2$, $S(O)OMe_2$, SeO_2, TeO_2 and XeF_2 were obtained commercially and were used as received. SF_4 was obtained commercially (abcr) and used as received. The reagents SeF_4,[S1] TeF_4,[S2] 2,6-$Mes_2C_6H_3Li$ (Mes = 2,4,6-$Me_3C_6H_2$),[S3] (2,6-$Mes_2C_6H_3$)$_2$E (E = S, Se),[S4] (2,6-$Mes_2C_6H_3$)$_2Te_2$,[S5] K[B(C_6F_5)$_4$][S6] and IPrSF_2[S7] were prepared following the published procedure. Anhydrous dichloromethane (CH_2Cl_2), hexane, tetrahydrofuran (THF) and toluene were collected from a SPS800 mBraun solvent purification system and stored over 4 Å molecular sieves. Et_2O was dried by refluxing it over Na/benzophenone under argon atmosphere. Deuterated solvents were degassed and dried over 4 Å molecular sieves under argon.

Unless otherwise noted, NMR spectra were recorded at room temperature on a Bruker Avance 600 MHz spectrometer. ^1H, $^{13}C\{^1H\}$, ^{11}B, $^{11}B\{^1H\}$, ^{19}F NMR, ^{77}Se and ^{125}Te spectra are reported on the δ scale (ppm) and are referenced against $SiMe_4$ respectively. ^1H and $^{13}C\{^1H\}$ chemical shifts are reported relative to the residual peak of the solvent ($CDHCl_2$ 5.32 ppm for CD_2Cl_2, $CHCl_3$ 7.26 ppm for $CDCl_3$) in the ^1H NMR spectra, and to the peak of the deuterated solvent (CD_2Cl_2 53.84 ppm, $CDCl_3$ 77.16 ppm) in the $^{13}C\{^1H\}$ NMR spectra.[8] The assignment of the ^1H and $^{13}C\{^1H\}$ resonance signals was made in accordance with the COSY, HSQC and HMBC spectra. The labelling schemes are attached to the ^1H and ^{13}C spectra.

The ESI HRMS spectra were measured on a Bruker Impact II spectrometer. Acetonitrile or dichloromethane/acetonitrile solutions (c =1·10^{-5} mol·L^{-1}) were injected directly into the spectrometer at a flow rate of 3 µL·min^{-1}. Nitrogen was used both as a drying gas and for nebulization with flow rates of approximately 5 L·min^{-1} and a pressure of 5 psi. Pressure in the mass analyzer region was usually about 1·10^{-5} mbar. Spectra were collected for 1 min and averaged. The nozzle-skimmer voltage was adjusted individually for each measurement.

IR spectra were recorded on a *Nicolet* Thermo iS10 scientific spectrometer with a diamond ATR unit. The absorption bands are reported in cm^{-1} with indicated relative intensities: s (strong, 0 – 33 % T); m (medium, 34 – 66 % T), w (weak, 67 – 100 % T), and br (broad).

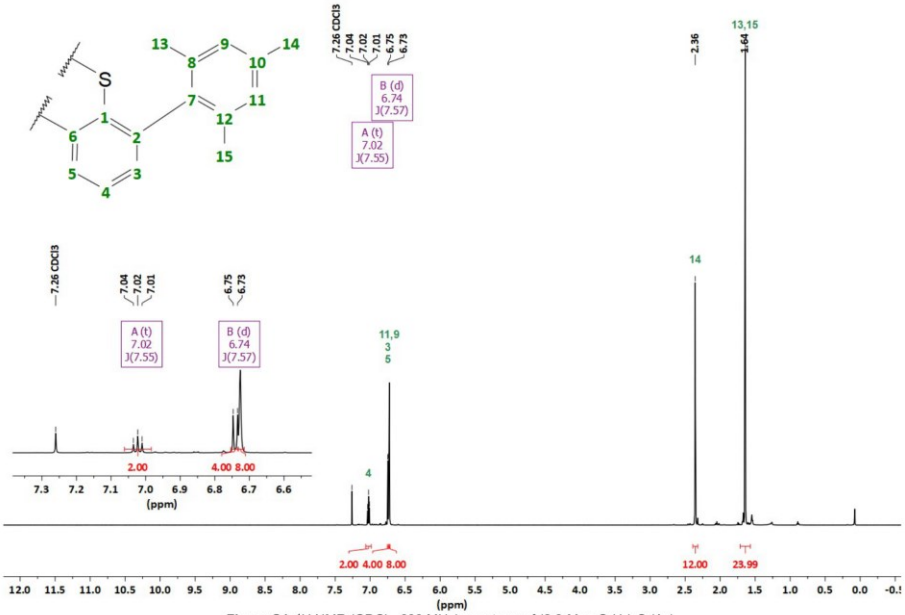

Figure S1. ^1H NMR ($CDCl_3$, 600 MHz) spectrum of (2,6-$Mes_2C_6H_3$)$_2$S (**1a**).

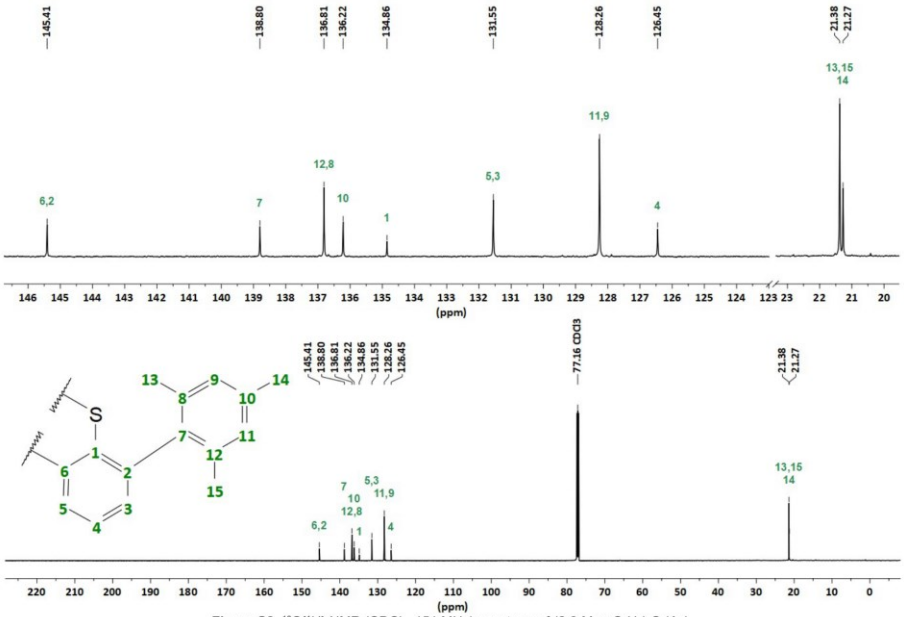

Figure S2. $^{13}C\{^{1}H\}$ NMR ($CDCl_3$, 151 MHz) spectrum of (2,6-$Mes_2C_6H_3)_2S$ (**1a**).

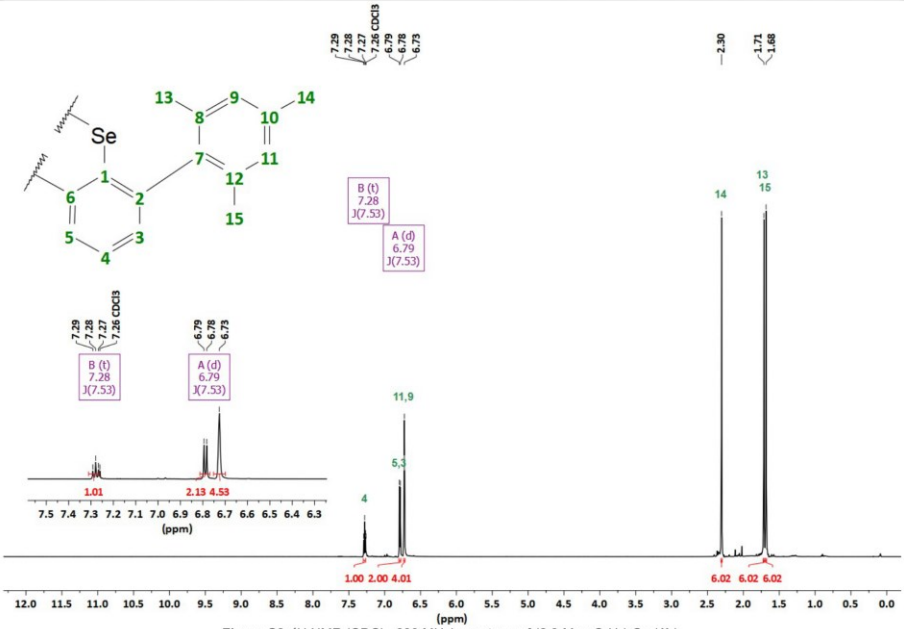

Figure S3. ^{1}H NMR ($CDCl_3$, 600 MHz) spectrum of (2,6-$Mes_2C_6H_3)_2Se$ (**1b**).

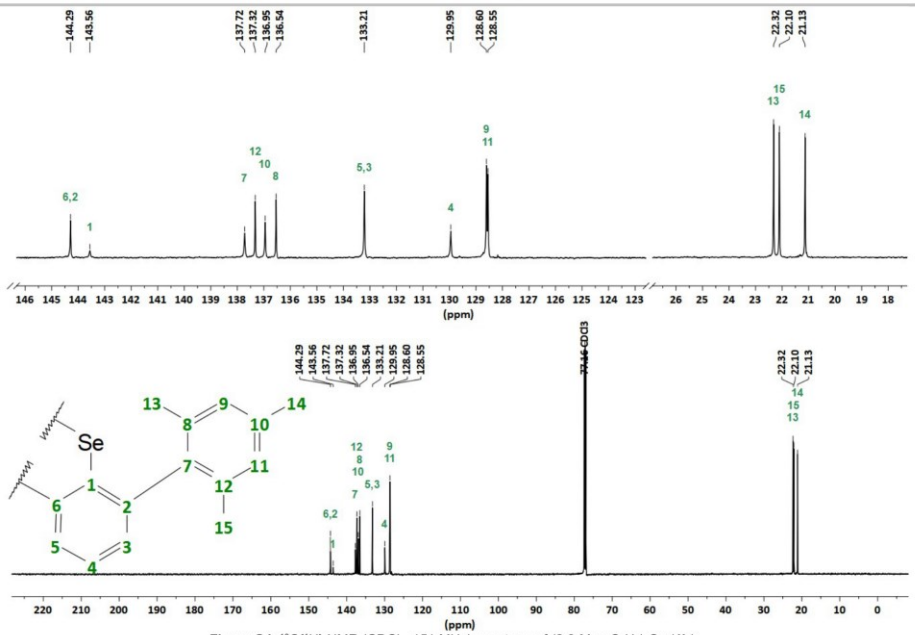

Figure S4. $^{13}C\{^{1}H\}$ NMR ($CDCl_3$, 151 MHz) spectrum of (2,6-$Mes_2C_6H_3$)$_2$Se (**1b**).

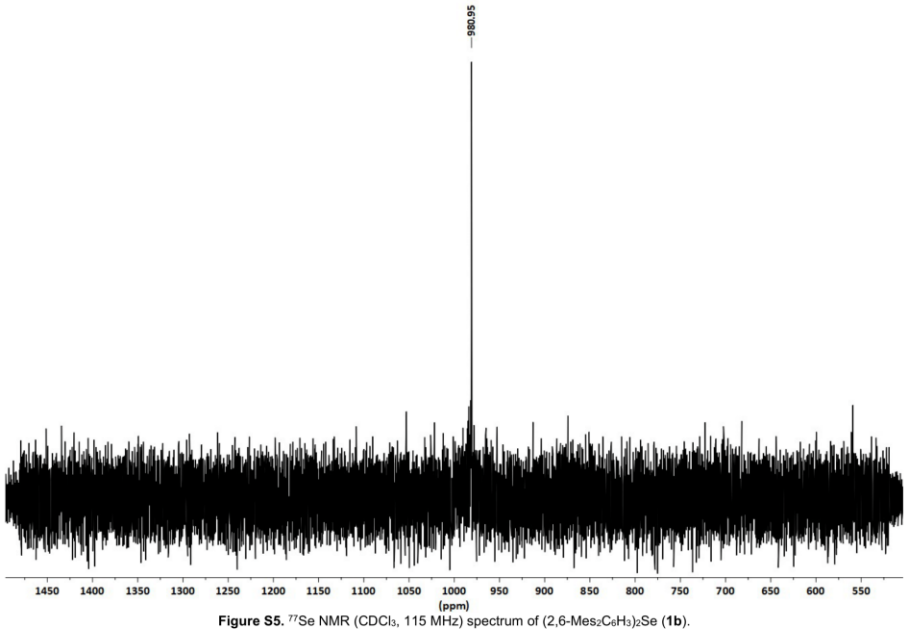

Figure S5. ^{77}Se NMR ($CDCl_3$, 115 MHz) spectrum of (2,6-$Mes_2C_6H_3$)$_2$Se (**1b**).

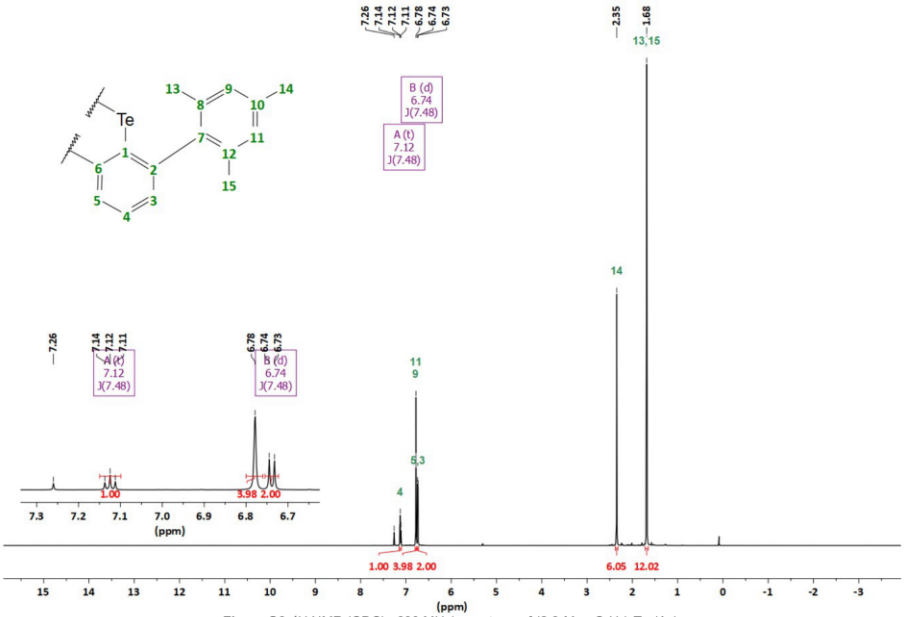

Figure S6. ^{1}H NMR ($CDCl_3$, 600 MHz) spectrum of $(2,6\text{-}Mes_2C_6H_3)_2Te$ (**1c**).

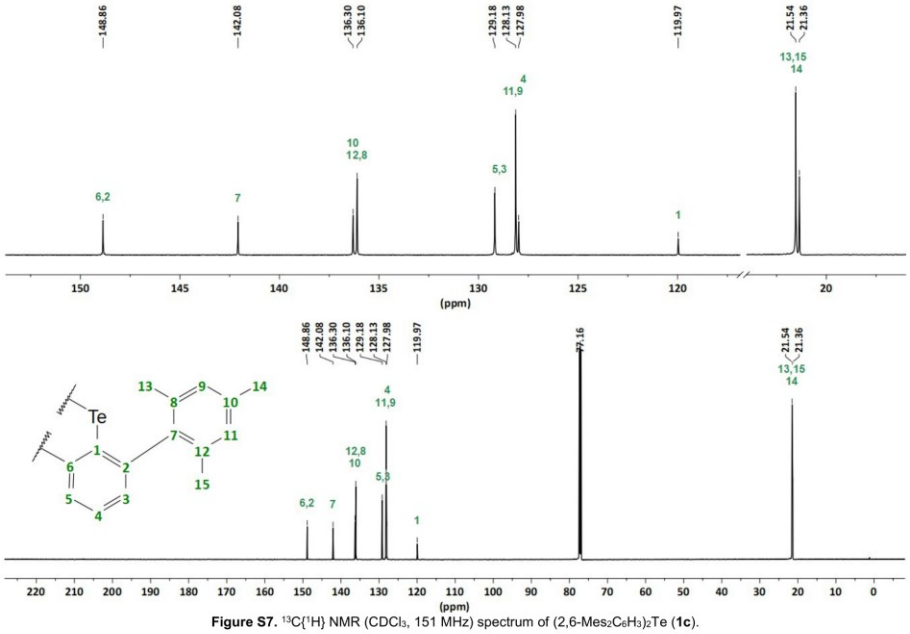

Figure S7. $^{13}C\{^{1}H\}$ NMR ($CDCl_3$, 151 MHz) spectrum of $(2,6\text{-}Mes_2C_6H_3)_2Te$ (**1c**).

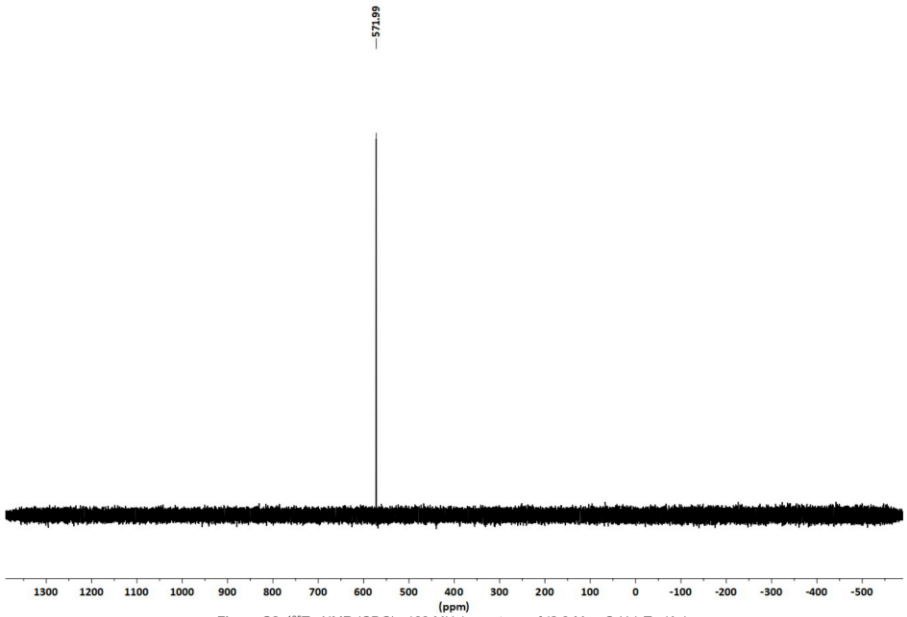

Figure S8. ^{125}Te NMR ($CDCl_3$, 189 MHz) spectrum of (2,6-$Mes_2C_6H_3$)$_2$Te (**1c**).

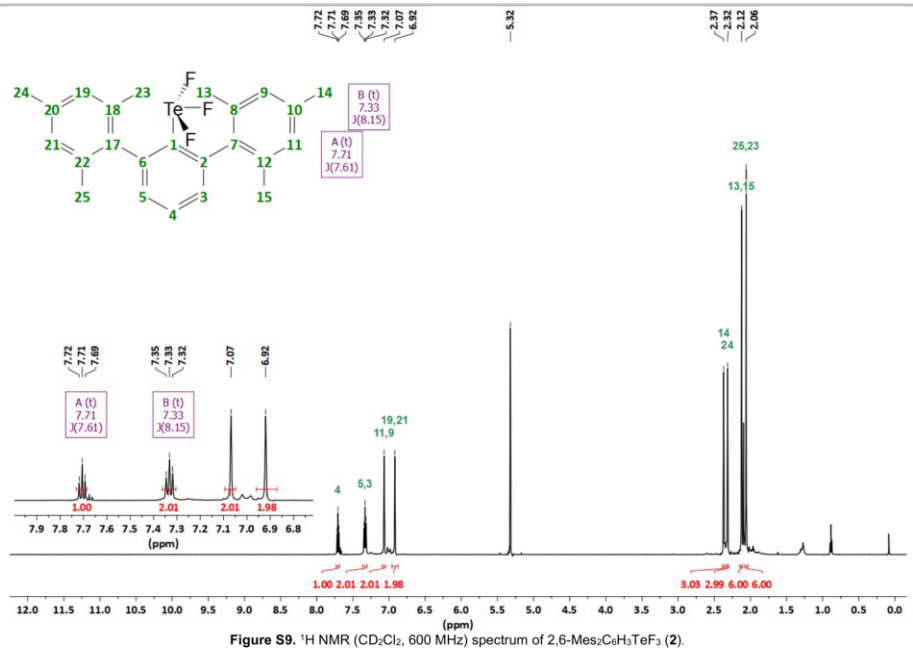

Figure S9. ^{1}H NMR (CD_2Cl_2, 600 MHz) spectrum of 2,6-$Mes_2C_6H_3TeF_3$ (**2**).

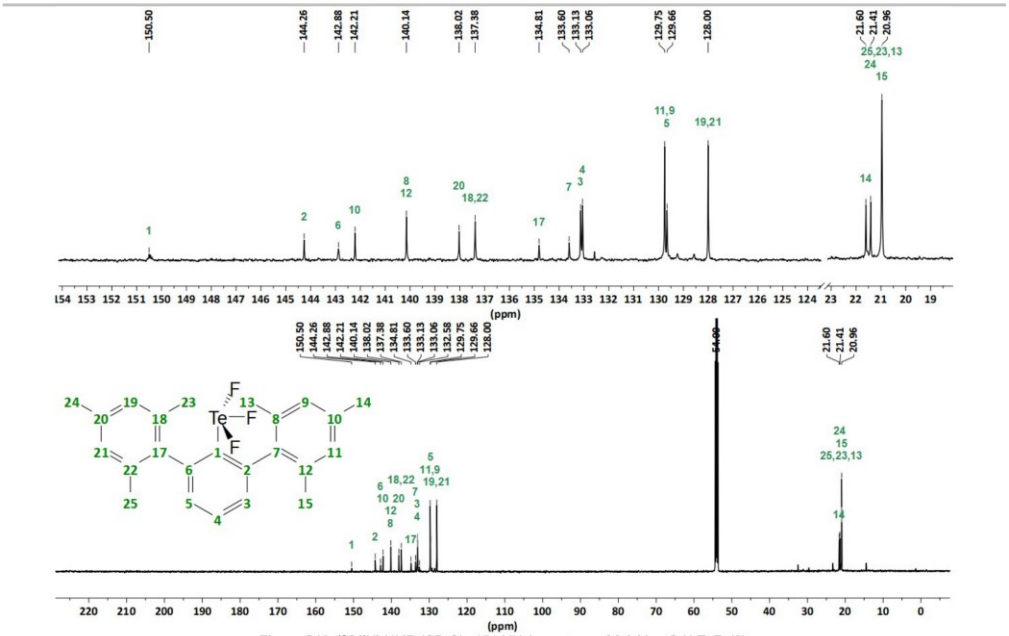

Figure S10. $^{13}C\{^{1}H\}$ NMR (CD_2Cl_2, 151 MHz) spectrum of 2,6-$Mes_2C_6H_3TeF_3$ (**2**).

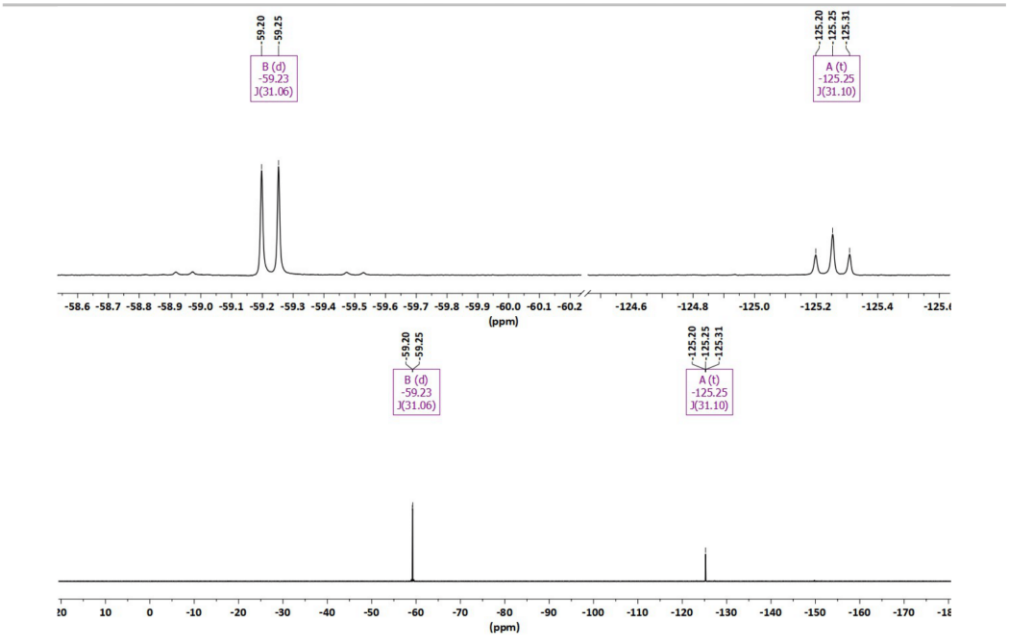

Figure S11. ^{19}F NMR (CD_2Cl_2, 565 MHz) spectrum of 2,6-$Mes_2C_6H_3TeF_3$ (**2**).

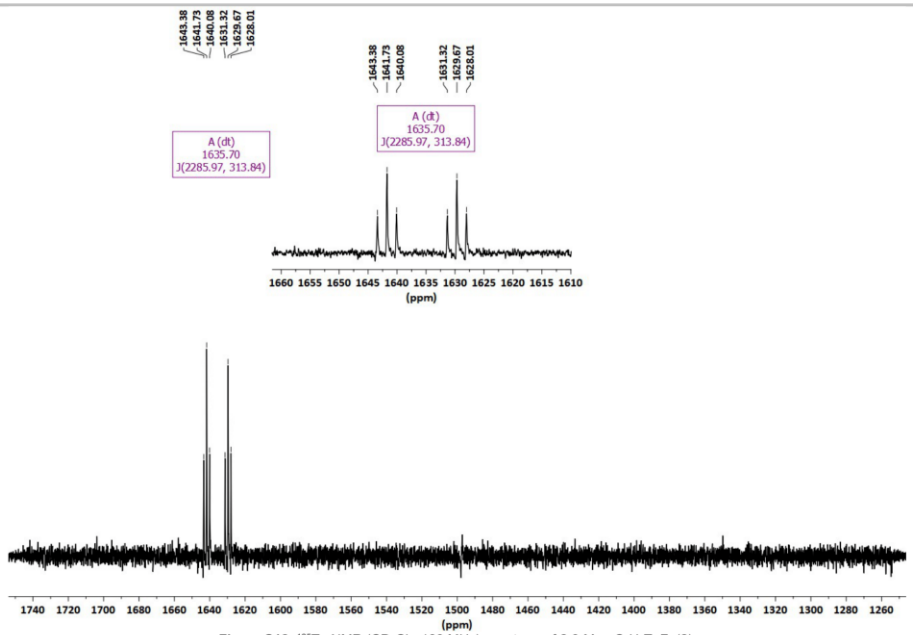

Figure S12. ^{125}Te NMR (CD_2Cl_2, 189 MHz) spectrum of 2,6-$Mes_2C_6H_3TeF_3$ (**2**).

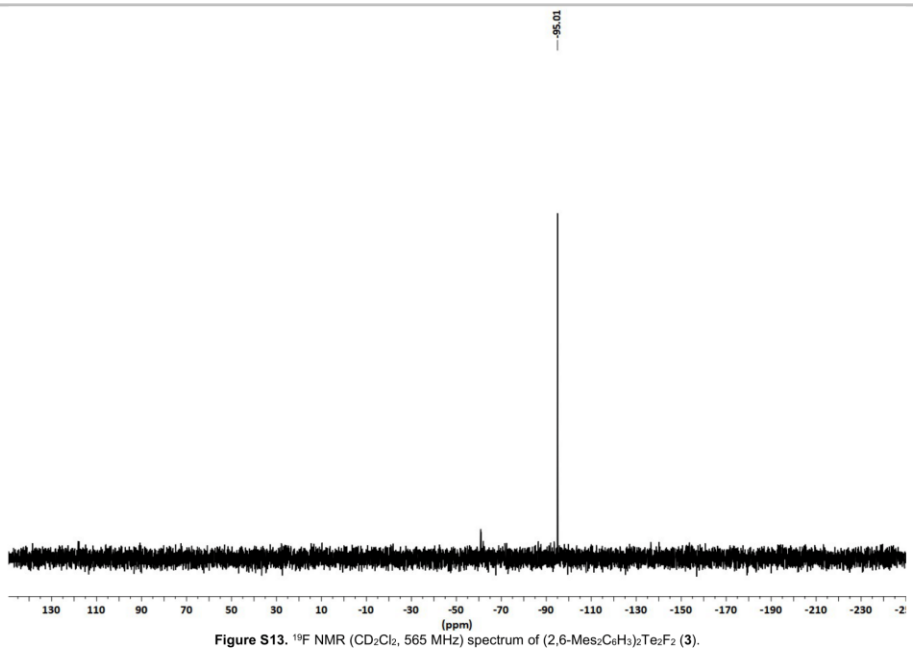

Figure S13. ^{19}F NMR (CD_2Cl_2, 565 MHz) spectrum of (2,6-$Mes_2C_6H_3)_2Te_2F_2$ (**3**).

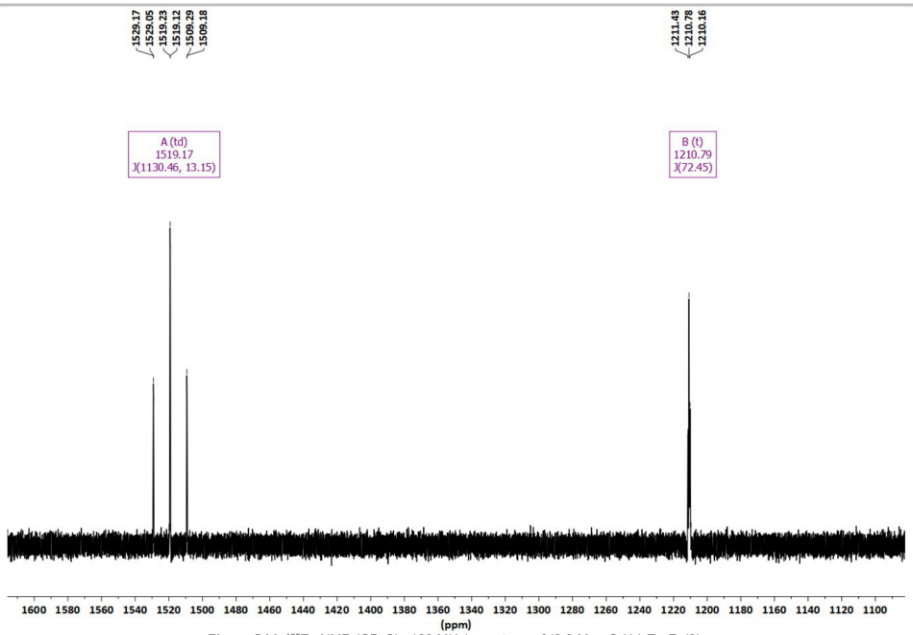

Figure S14. ^{125}Te NMR (CD_2Cl_2, 189 MHz) spectrum of (2,6-$Mes_2C_6H_3$)$_2Te_2F_2$ (**3**).

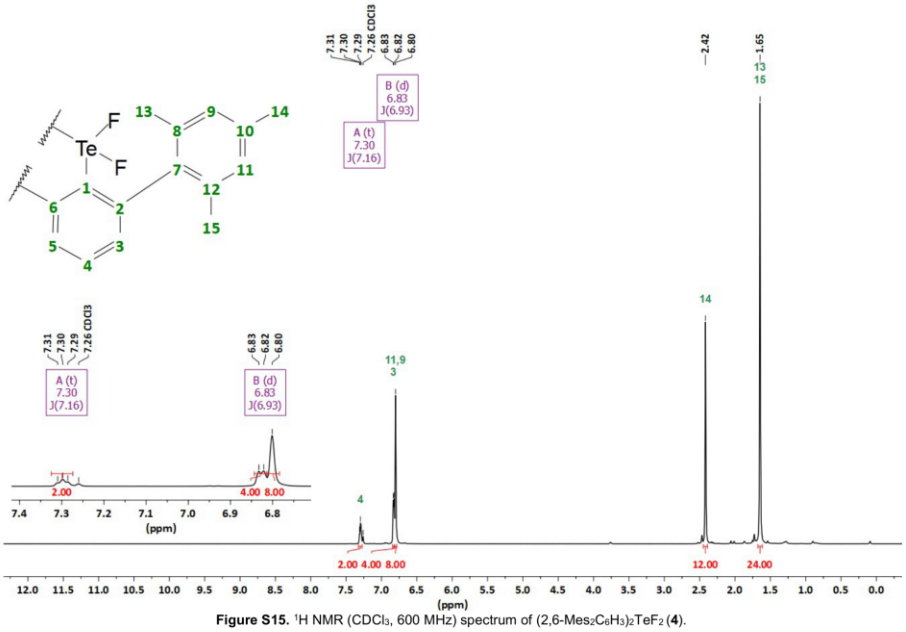

Figure S15. ^1H NMR ($CDCl_3$, 600 MHz) spectrum of (2,6-$Mes_2C_6H_3$)$_2TeF_2$ (**4**).

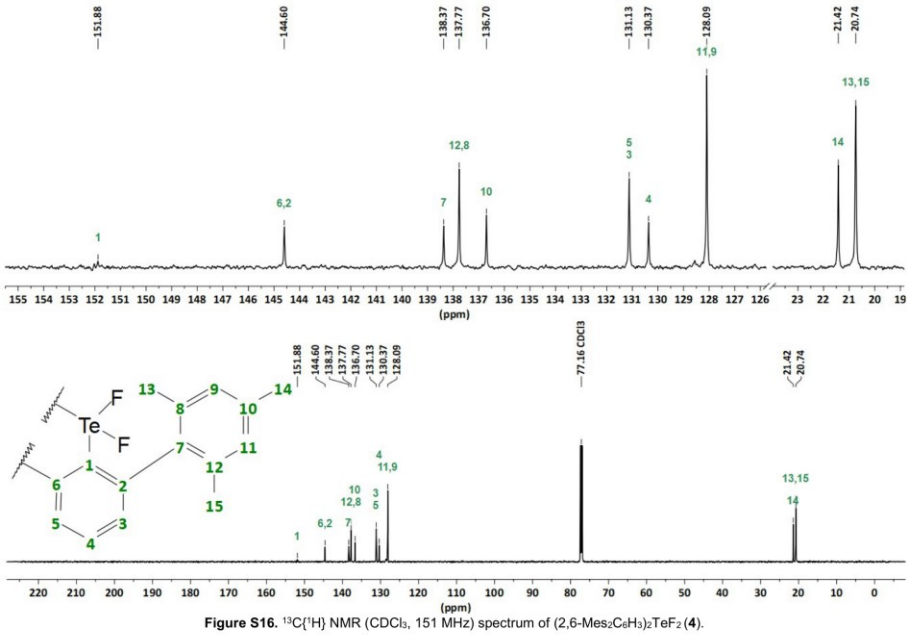

Figure S16. $^{13}C\{^{1}H\}$ NMR ($CDCl_3$, 151 MHz) spectrum of $(2,6\text{-}Mes_2C_6H_3)_2TeF_2$ (**4**).

18

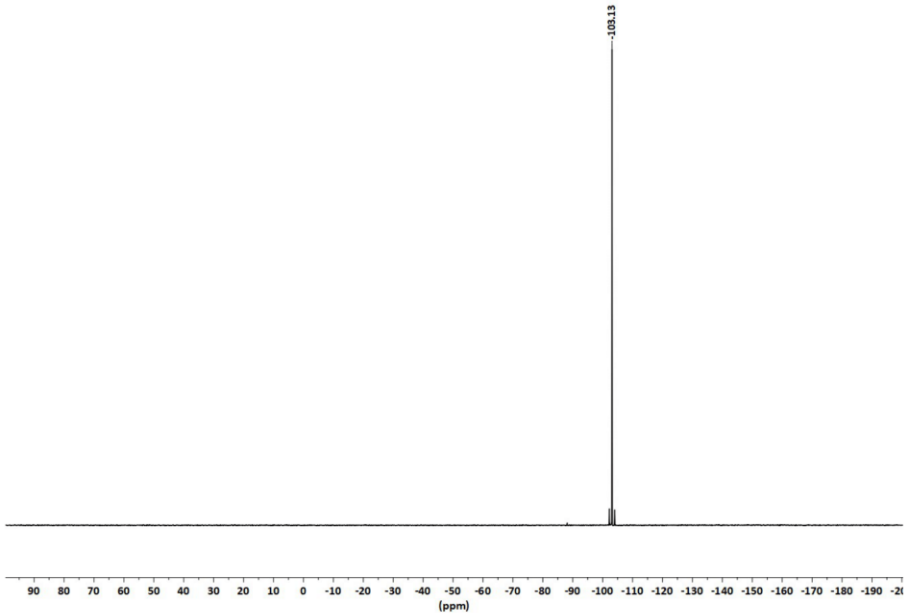

Figure S17. ^{19}F NMR ($CDCl_3$, 565 MHz) spectrum of $(2,6\text{-}Mes_2C_6H_3)_2TeF_2$ (**4**).

19

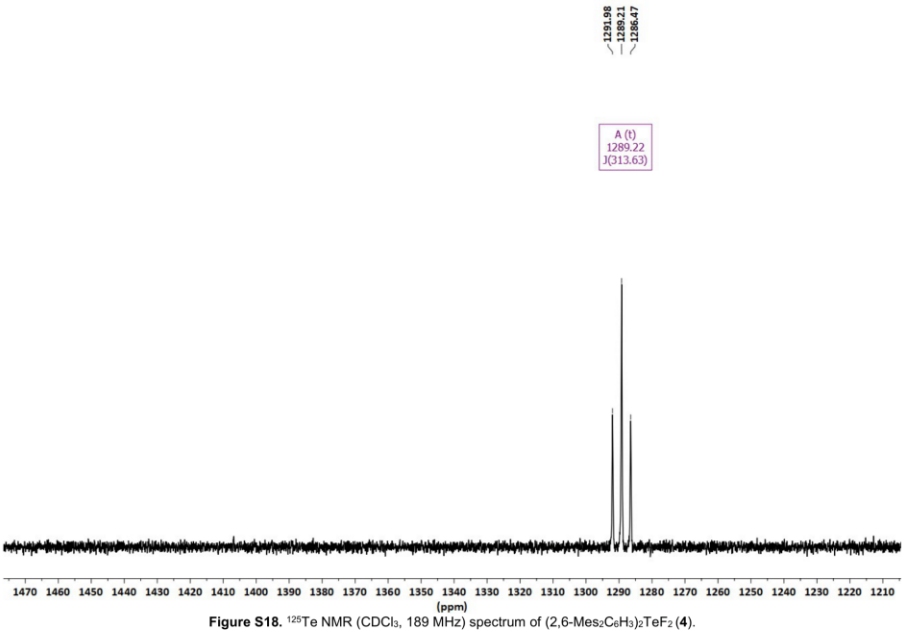

Figure S18. ^{125}Te NMR ($CDCl_3$, 189 MHz) spectrum of $(2,6\text{-}Mes_2C_6H_3)_2TeF_2$ (**4**).

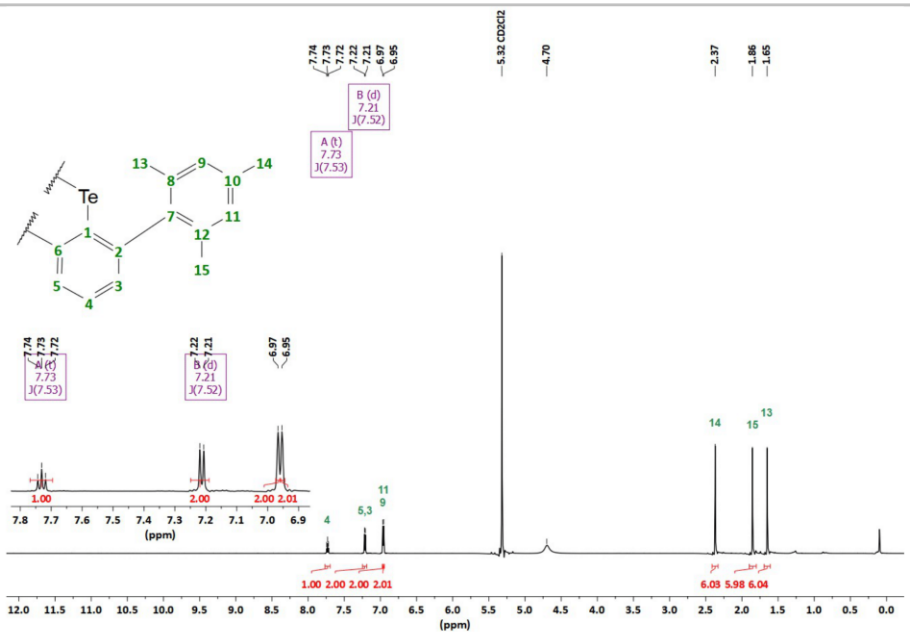

Figure S19. ^{1}H NMR (CD_2Cl_2, 600 MHz) spectrum of $[\mathbf{1c}]^{+}[B(C_6F_5)_4]^{-}$.

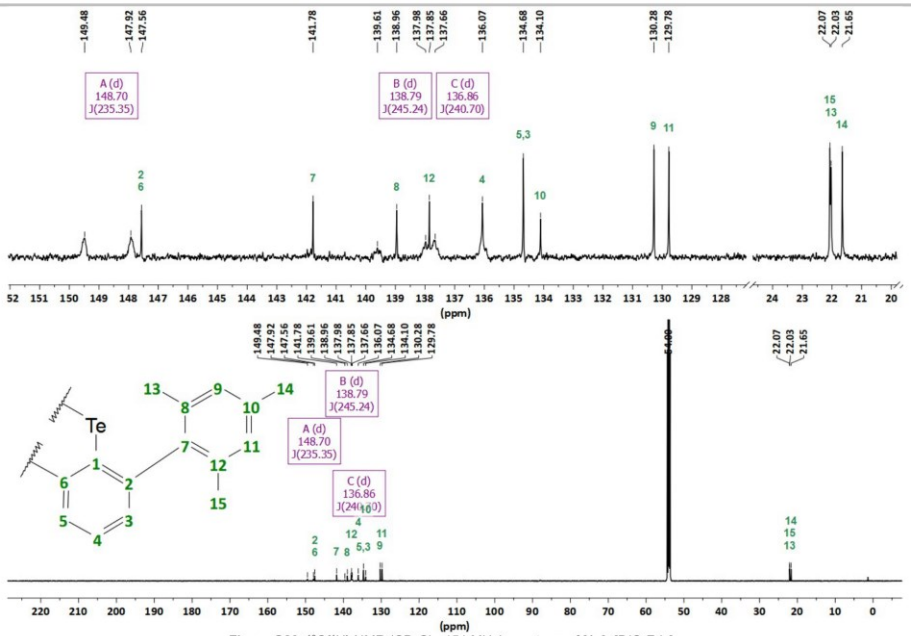

Figure S20. $^{13}C\{^{1}H\}$ NMR (CD_2Cl_2, 151 MHz) spectrum of [**1c**]$^{+}$[$B(C_6F_5)_4$]$^{-}$.

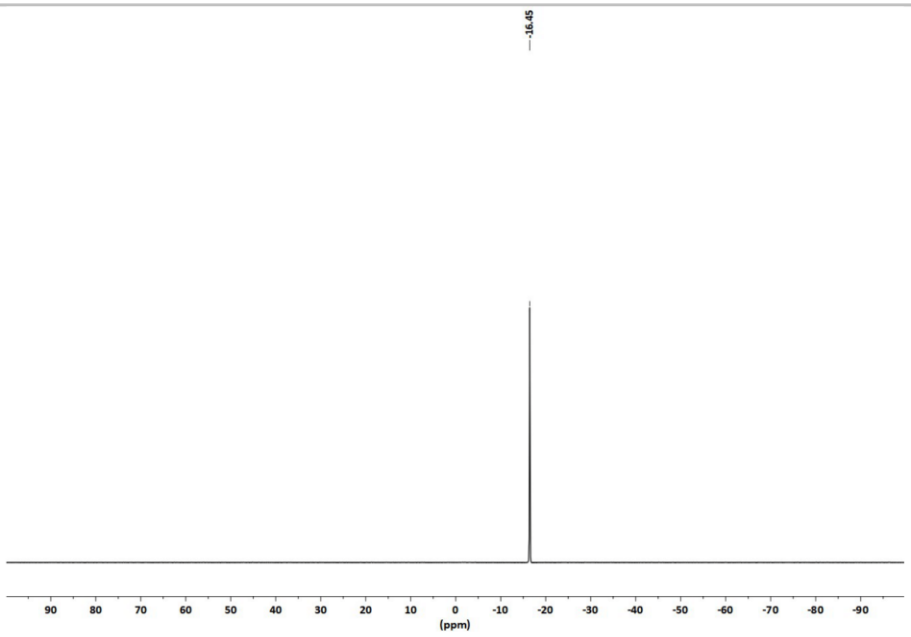

Figure S21. $^{11}B\{^{1}H\}$ NMR (CD_2Cl_2, 193 MHz) spectrum of [**1c**]$^{+}$[$B(C_6F_5)_4$]$^{-}$.

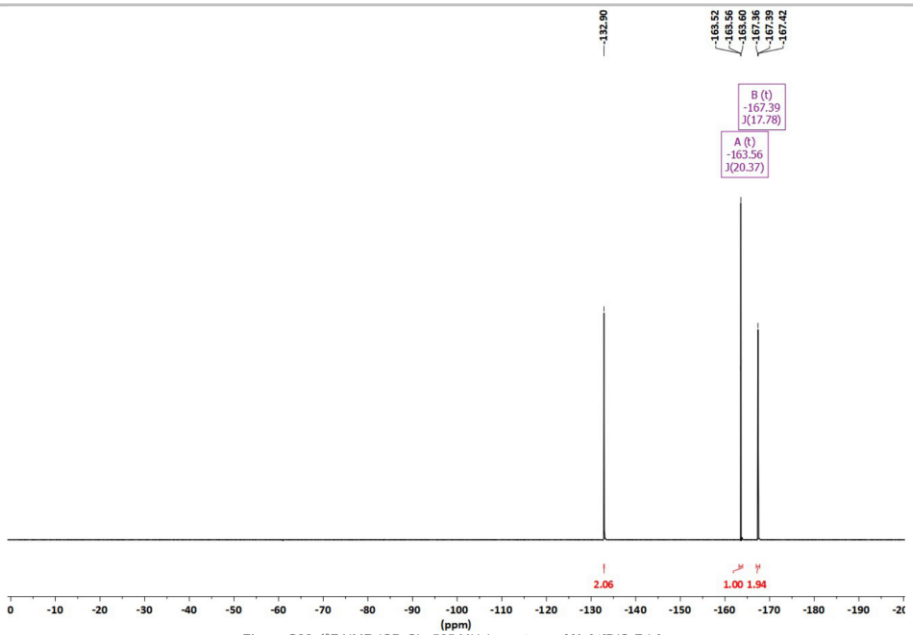

Figure S22. ^{19}F NMR (CD_2Cl_2, 565 MHz) spectrum of [**1c**]$^{++}$[$B(C_6F_5)_4$]$^-$.

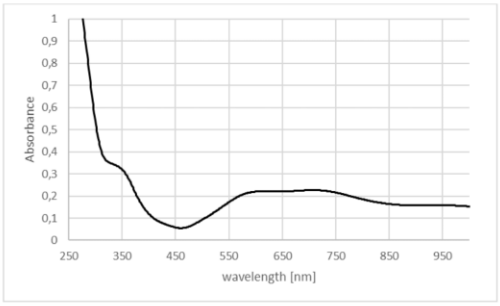

Figure S23. UV-Vis spectrum (CH_2Cl_2, 10µM) of [**1c**]$^{++}$[$B(C_6F_5)_4$]$^-$.

Synthesis and characterization of 2,6-Mes$_2$C$_6$H$_3$SCl

To a solution of (2,6-Mes$_2$C$_6$H$_3$)$_2$S$_2$ (173 mg, 250 µmol, 1.00 eq.) in THF (12 mL) SO_2Cl_2 (101 mg, 750 µmol, 3.00 eq.) was added at 0 °C. The solution was stirred for 4 hours at 0°C and slowly warmed up to room temperature and stirred overnight. The solvent was removed under reduced pressure and 2,6-Mes$_2$C$_6$H$_3$SCl was obtained as a yellow solid (190 mg, quant.)

Crystals suitable for X-ray diffraction experiments were obtained by diffusion of *n*-hexane into a solution of 2,6-Mes$_2$C$_6$H$_3$SCl in CH_2Cl_2.

^{1}H NMR (600 MHz, $CDCl_3$): δ = 7.62 (t, J = 7.6 Hz, 1H, H4), 7.23 (d, J = 7.6 Hz, 2H, H3 and H5), 6.98 (s, 4H, H9 and H11), 2.36 (s, 6H, H14), 2.01 (s, 12H, H13 and H15) ppm. **^{13}C NMR (151 MHz, $CDCl_3$):** δ = 148.7 (s, C2 and C6), 137.5 (s, C7), 137.2 (s, C10), 135.6 (s, C8 and C12), 132.9 (s, C4), 132.5 (s, C1), 130.0 (s, C3 and C5), 128.0 (s, C9 and C11), 21.2 (s, C14), 20.9 (s, C13 and C15) ppm.

HRMS ESI (m/z): no signal found in positive nor negative mode.

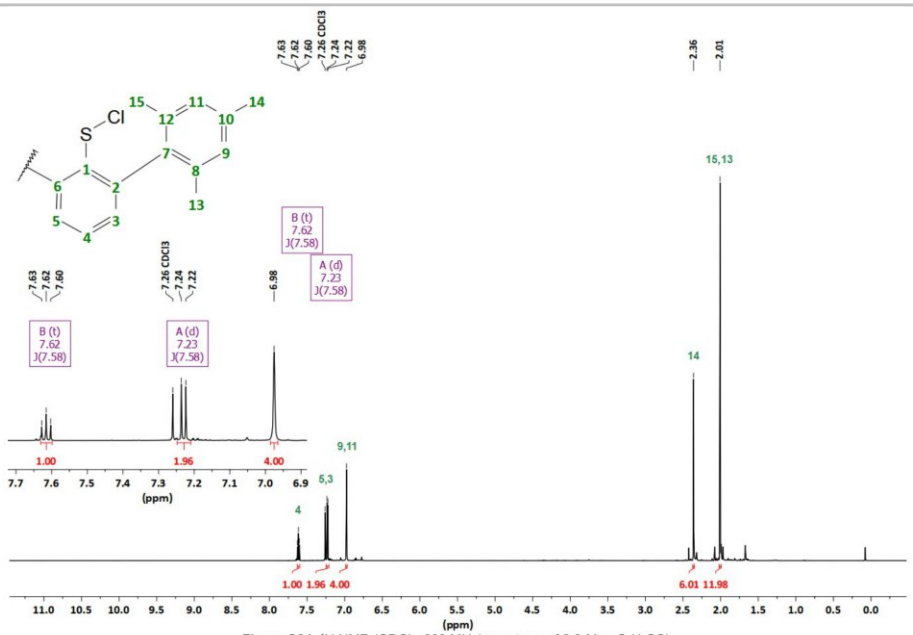

Figure S24. ^{1}H NMR ($CDCl_3$, 600 MHz) spectrum of 2,6-Mes$_2$C$_6$H$_3$SCl.

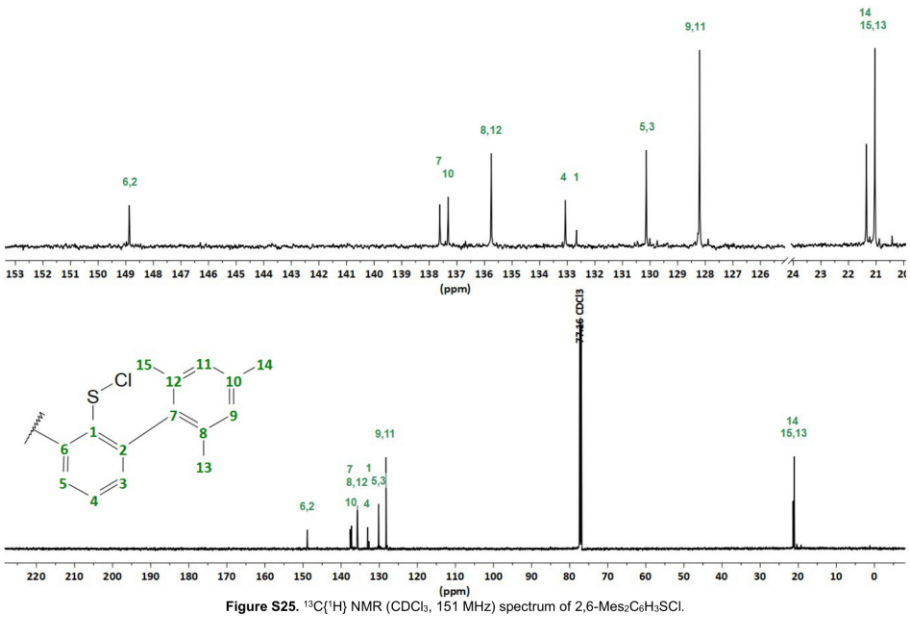

Figure S25. $^{13}C\{^{1}H\}$ NMR ($CDCl_3$, 151 MHz) spectrum of 2,6-$Mes_2C_6H_3SCl$.

Synthesis and characterization of 2,6-$Mes_2C_6H_3SeCl$

(2,6-$Mes_2C_6H_3$)$_2Se_2$ (196 mg, 250 µmol, 1.00 eq.) was dissolved in THF (12 mL) and cooled to 0 °C. To this, SO_2Cl_2 (101 mg, 750 µmol, 1.00 eq.) was added dropwise. The reaction mixture was stirred for an additional 4 hours at 0 °C and then slowly warmed up to room temperature and stirred for 18 hours. The solvent was removed under reduced pressure to obtain 2,6-$Mes_2C_6H_3SeCl$ as an orange solid (214 mg, quant.).

Crystals suitable for X-ray diffraction experiments were grown by diffusion of *n*-hexane into a solution of 2,6-$Mes_2C_6H_3SeCl$ in CH_2Cl_2.

^{1}H-NMR (600 MHz, $CDCl_3$): δ = 7.60 (t, J = 7.5 Hz, 1H, H4), 7.24 (d, J = 7.5 Hz, 2H, H3 and H5), 6.96 (s, 4H, H9 and H11), 2.36 (s, 6H, H14), 2.01 (s, 12H, H13 and H15) ppm. **^{13}C-NMR (151 MHz, $CDCl_3$):** δ = 148.9 (s, C2 and C6), 137.6 (s, C7), 137.3 (s, C10), 135.8 (s, C8 and C12), 133.1 (s, C4), 132.67 (s, C1), 130.1 (s, C3 and C5), 128.2 (s, C9 and C11), 21.4 (s, C14), 21.1 (s, C13 and C15) ppm. **^{77}Se-NMR (115 MHz, $CDCl_3$):** δ = 1023.9 ppm. **HRMS ESI (m/z):** no signal found in positive nor negative mode.

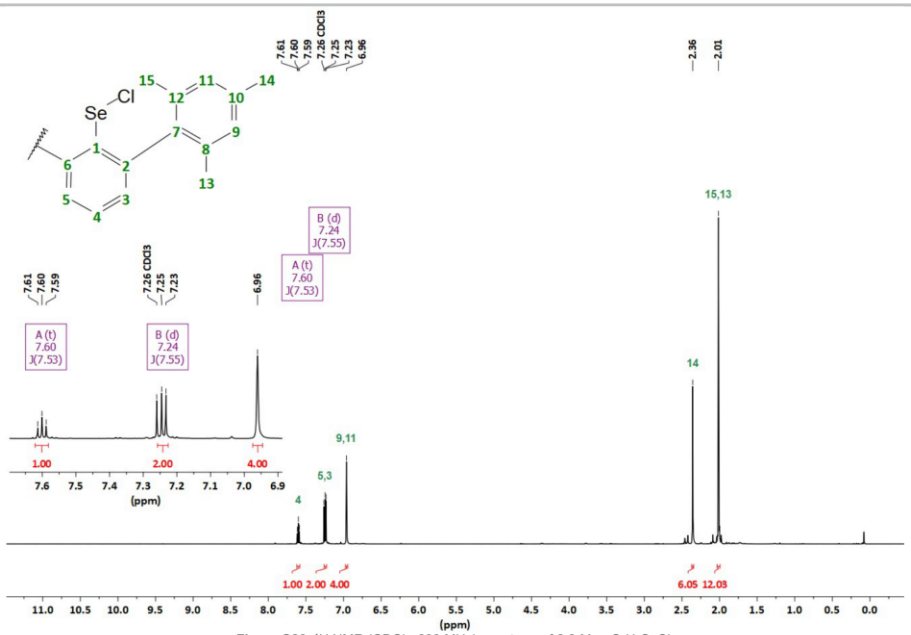

Figure S26. ^{1}H NMR ($CDCl_3$, 600 MHz) spectrum of 2,6-$Mes_2C_6H_3SeCl$.

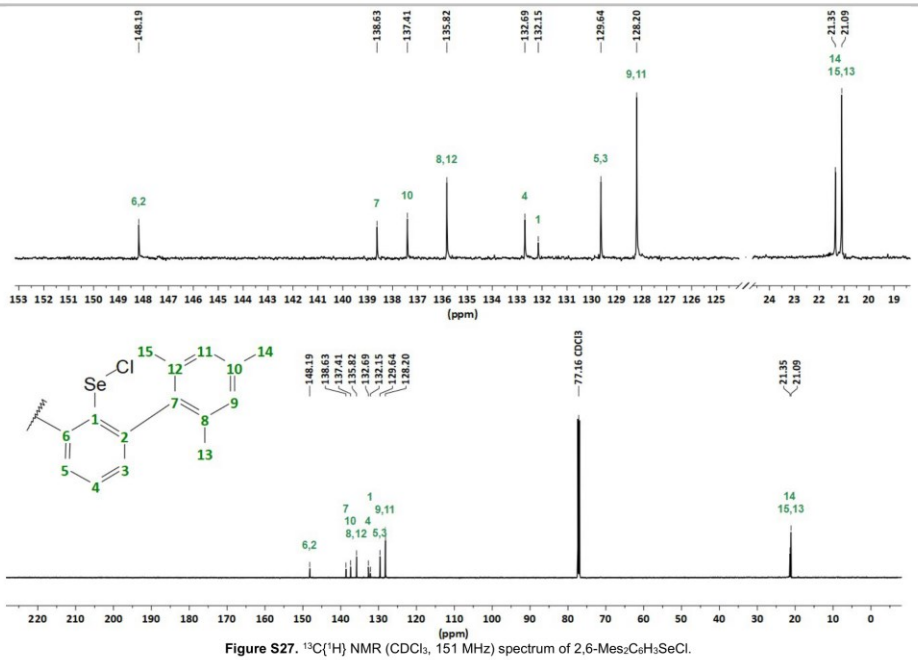

Figure S27. $^{13}C\{^{1}H\}$ NMR ($CDCl_3$, 151 MHz) spectrum of 2,6-$Mes_2C_6H_3SeCl$.

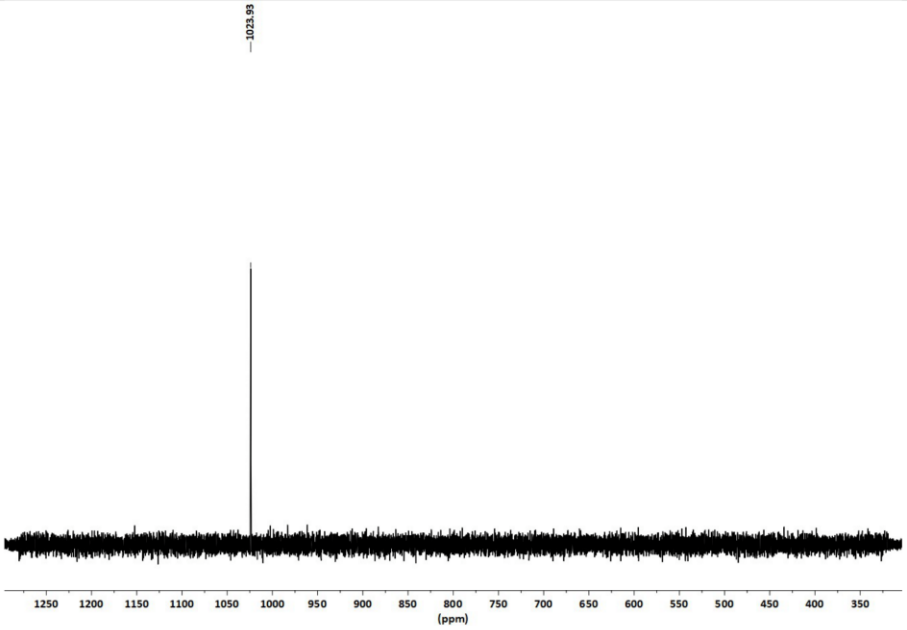

Figure S28. ^{77}Se NMR ($CDCl_3$, 115 MHz) spectrum of 2,6-$Mes_2C_6H_3SeCl$.

Synthesis and characterization of 2,6-$Mes_2C_6H_3S(O)F$

2,6-$Mes_2C_6H_3Li$ (1.60 g, 5.00 mmol, 1.00 eq.) was placed in a Schlenk tube, to this Et_2O (60 mL) was added and the solution was cooled to -78 °C. To this, thionyl fluoride (2.0 g, 23.2 mmol, 4.65 eq.) was condensed and the reaction was slowly warmed up to room temperature. After 18 hours, the solvent was removed under reduced pressure. The residual solid was dissolved in CH_2Cl_2 (40 mL) and worked up aqueous (3 x 20 mL). The solution was dried over anhydrous sodium sulfate and the solvent was removed under reduced pressure to yield 2,6-$Mes_2C_6H_3S(O)F$ as a colourless solid (1.65 g, 87%).

Crystals suitable for X-Ray diffraction measurements were grown by diffusion of n-hexane into a CH_2Cl_2 solution of 2,6-$Mes_2C_6H_3S(O)F$.

^{1}H NMR (600 MHz, $CDCl_3$): δ = 7.69 (t, $^3J(^1H-^1H)$ = 7.6 Hz, 1H, H4), 7.19 (d, $^3J(^1H-^1H)$ = 7.6 Hz, 2H, H3 and H5), 6.95 (s, 4H, H9 and H11), 2.34 (s, 6H, H14), 2.04 (s, 6H, H13), 2.03 (s, 6H, H15) ppm. **$^{13}C\{^1H\}$ NMR (151 MHz, $CDCl_3$)**: δ = 141.9 (s, C1), 141.5 (s, C2 and C6), 138.0 (s, C10), 136.8 (s, C8), 136.1 (s, C12), 133.9 (s, C4), 133.8 (s, C7), 130.9 (s, C3 and C5), 128.1 (s, C11), 128.0 (s, C9), 21.3 (s, C14), 20.9 (s, C15), 20.9 (s, C13) ppm. **^{19}F NMR (565 MHz, $CDCl_3$)**: δ = -4.2 (s) ppm. **HRMS ESI (m/z)**: $[M+Na]^+$ calculated. For $C_{24}H_{25}FNaOS$ 403.15078; found, 403.15023.

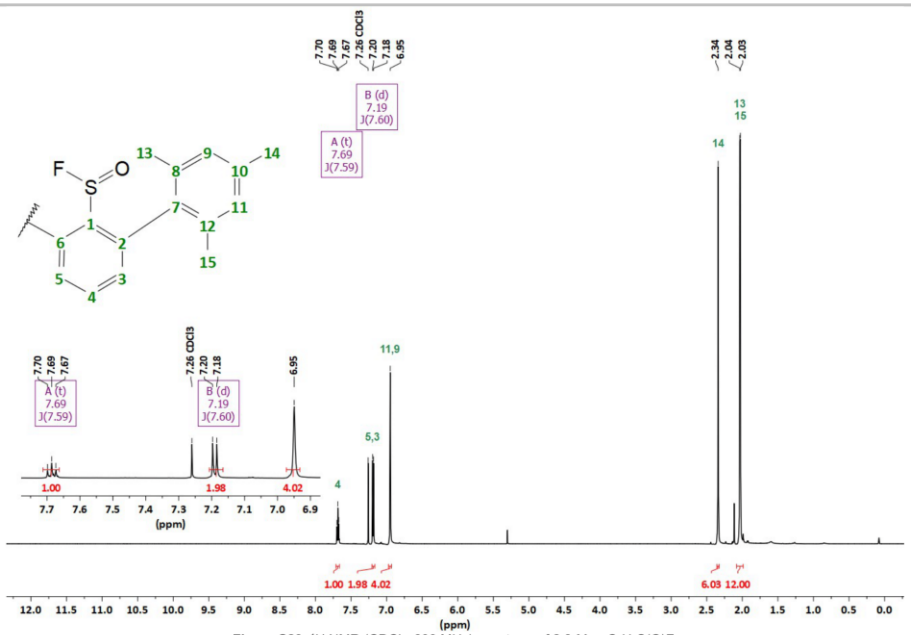

Figure S29. ^{1}H NMR ($CDCl_3$, 600 MHz) spectrum of 2,6-$Mes_2C_6H_3S(O)F$.

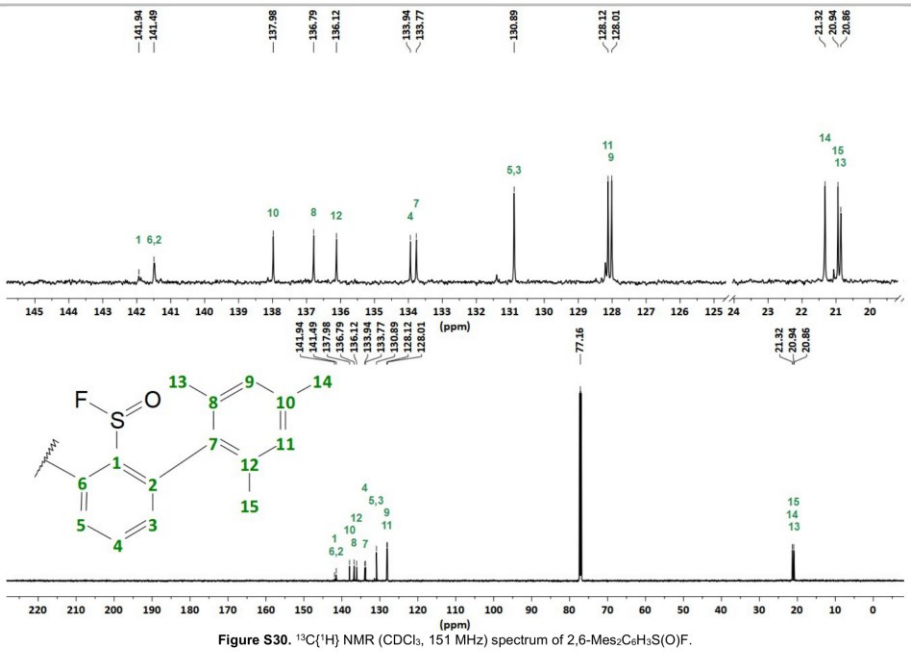

Figure S30. $^{13}C\{^{1}H\}$ NMR ($CDCl_3$, 151 MHz) spectrum of 2,6-$Mes_2C_6H_3S(O)F$.

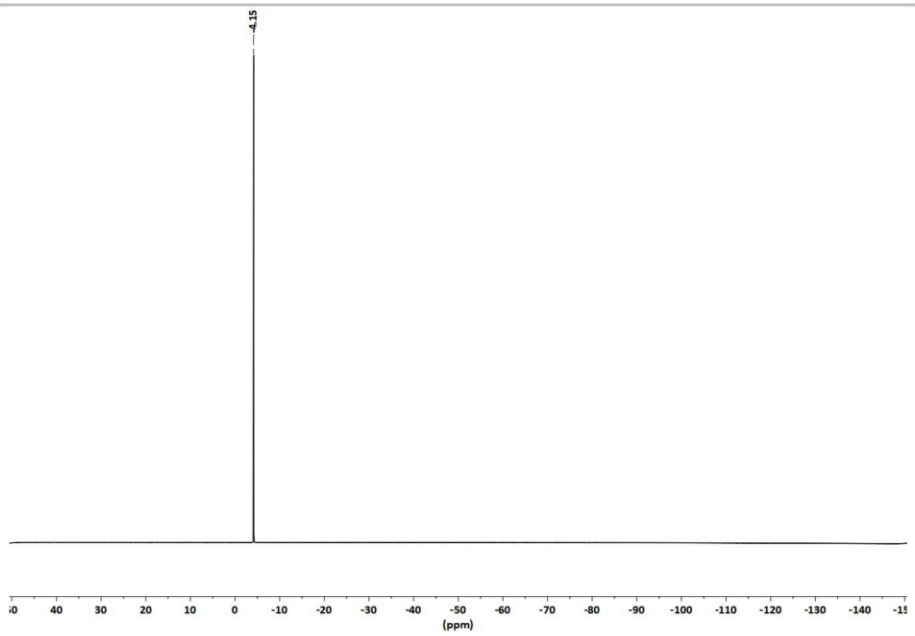

Figure S31. ^{19}F NMR ($CDCl_3$, 565 MHz) spectrum of 2,6-$Mes_2C_6H_3S(O)F$.

Synthesis and characterization of 2,6-$Mes_2C_6H_3S(O)Cl$

2,6-$Mes_2C_6H_3Li$ (320 mg, 1.00 mmol, 1.00 eq.) was placed in a Schlenk tube and dissolved in toluene (10 mL). The solution was cooled to -78 °C and to this, thionyl chloride (131 mg, 1.10 mmol, 1.10 eq.) was added and the reaction was slowly warmed up to room temperature and stirred for 18 hours. The solvent was removed under reduced pressure and the residue was dissolved in CH_2Cl_2 (15 mL) and filtered through a pad of celite. The solvent was removed under reduced pressure and the residue was washed with acetonitrile (2 x 5 mL) and *n*-hexane (2 x 5 mL) to yield 2,6-$Mes_2C_6H_3S(O)Cl$ as a colourless solid (194 mg, 49%).

2,6-$Mes_2C_6H_3S(O)Cl$ slowly decomposes in solution at room temperature into multiple species.

Crystals suitable for X-Ray diffraction measurements were grown by diffusion of *n*-hexane into a toluene solution of 2,6-$Mes_2C_6H_3S(O)Cl$ at -30 °C.

^1H NMR (600 MHz, $CDCl_3$): δ = 7.69 (t, $^3J(^1H\text{-}^1H)$ = 7.6 Hz, 1H, H4), 7.19 (d, $^3J(^1H\text{-}^1H)$ = 7.6 Hz, 2H, H3 and H5), 6.96 (s, 4H, H9 and H11), 2.35 (s, 6H, H14), 2.12 (s, 6H, H13), 2.04 (s, 6H, H15) ppm. **$^{13}C\{^1H\}$ NMR (151 MHz, $CDCl_3$):** δ = 143.4 (s, C1), 141.3 (s, C2 and C6), 138.1 (s, C10), 137.0 (s, C12), 135.6 (s, C8), 133.8 (s, C4), 133.3 (s, C7), 131.4 (s, C3 and C5), 128.2 (s, C9 and C11), 21.3 (s, C13 and C14), 21.1 (s, C15) ppm. **HRMS ESI (m/z):** $[M+Na]^+$ calculated. For $C_{24}H_{25}ClNaOS$ 419.12123; found, 419.12054.

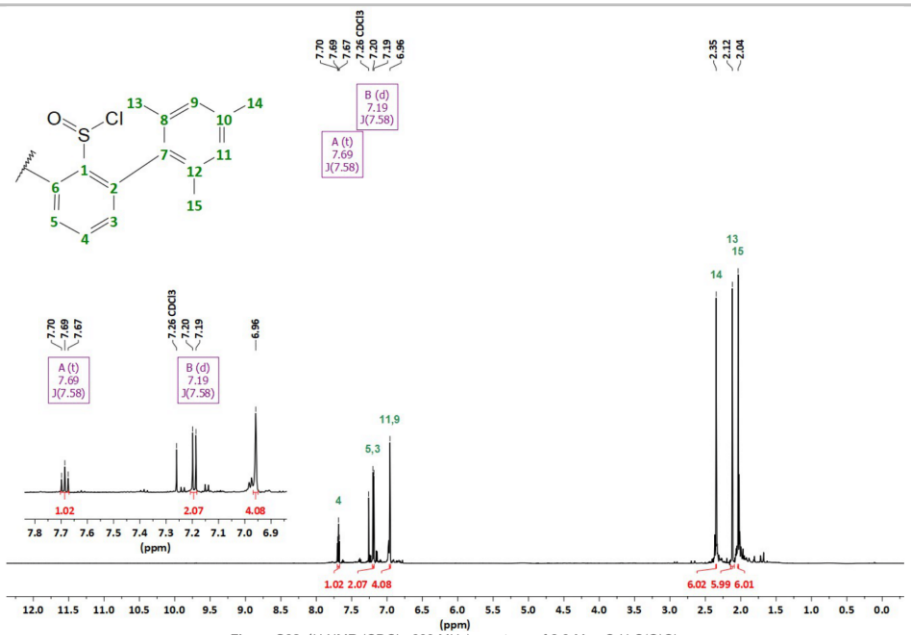

Figure S32. ^{1}H NMR ($CDCl_3$, 600 MHz) spectrum of 2,6-$Mes_2C_6H_3S(O)Cl$.

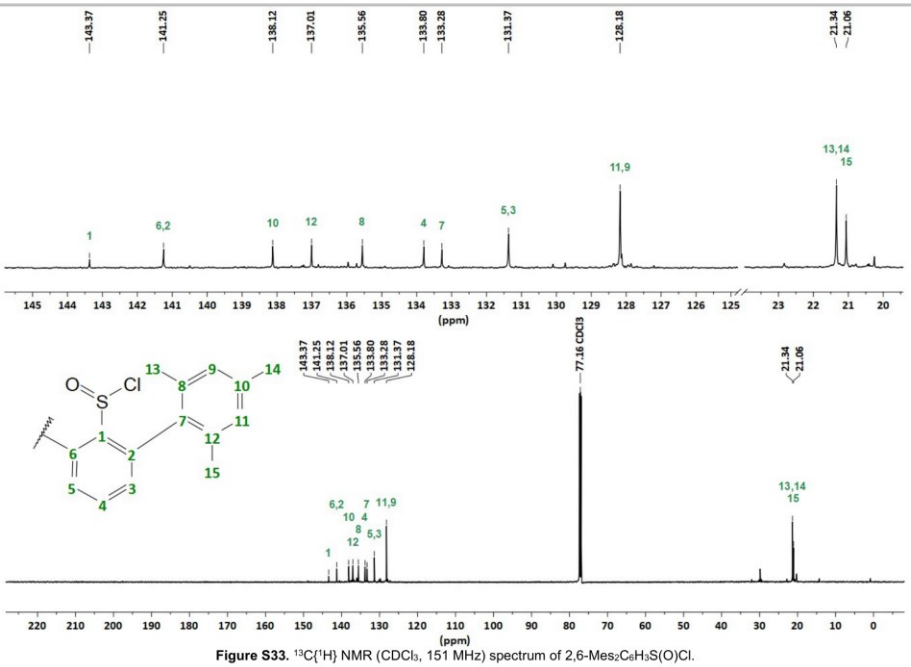

Figure S33. $^{13}C\{^{1}H\}$ NMR ($CDCl_3$, 151 MHz) spectrum of 2,6-$Mes_2C_6H_3S(O)Cl$.

Synthesis and characterization of 2,6-Mes$_2$C$_6$H$_3$S(O)OMe

To a solution of dimethyl sulfite (165 mg, 1.50 mmol, 1.00 eq.) in *n*-hexane (2 mL) a suspension of 2,6-Mes$_2$C$_6$H$_3$Li (320 mg, 1.00 mmol, 1.00 eq.) in *n*-hexane (5 mL) was added. The solution was stirred for 18 hours at room temperature. After this, water (5 mL) was added and the mixture was extracted with CH_2Cl_2 (3 x 10 mL). The combined organic phases were dried over sodium sulfate and the solvent removed under reduced pressure to yield 2,6-Mes$_2$C$_6$H$_3$S(O)OMe as a colourless solid (180 mg, 46%).

Crystals suitable for X-Ray diffraction measurements were grown by diffusion of n-hexane into a toluene solution of 2,6-Mes$_2$C$_6$H$_3$S(O)OMe.

^{1}H NMR (600 MHz, $CDCl_3$): δ = 7.61 (t, $^3J(^1H\text{-}^1H)$ = 7.6 Hz, 1H, H4), 7.13 (d, $^3J(^1H\text{-}^1H)$ = 7.6 Hz, 2H, H3 and H5), 6.96 (s, 4H, H9 and H11), 3.34 (s, 6H, H16), 2.36 (s, 6H, H14), 2.09 (s, 6H, H15), 2.03 (s, H13) ppm. **$^{13}C\{^1H\}$ NMR (151 MHz, $CDCl_3$):** δ = 141.3 (s, C1), 140.8 (s, C2 and C6), 137.2 (s, C10), 136.40 (s, C8), 135.9 (s, C12), 135.4 (s, C7), 132.2 (s, C4), 130.5 (s, C3 and C5), 127.9 (s, C11), 127.7 (s, C9), 55.4 (s, C16), 21.3 (s, C14), 20.9 (s, C15), 20.8 (s, C13) ppm. **HRMS ESI (m/z):** $[M\text{-}Me]^+$ calculated. For $C_{24}H_{25}O_2S$ 392.18088; found, 392.18045.

40

Figure S34. ^{1}H NMR ($CDCl_3$, 600 MHz) spectrum of 2,6-Mes$_2$C$_6$H$_3$S(O)OMe.

41

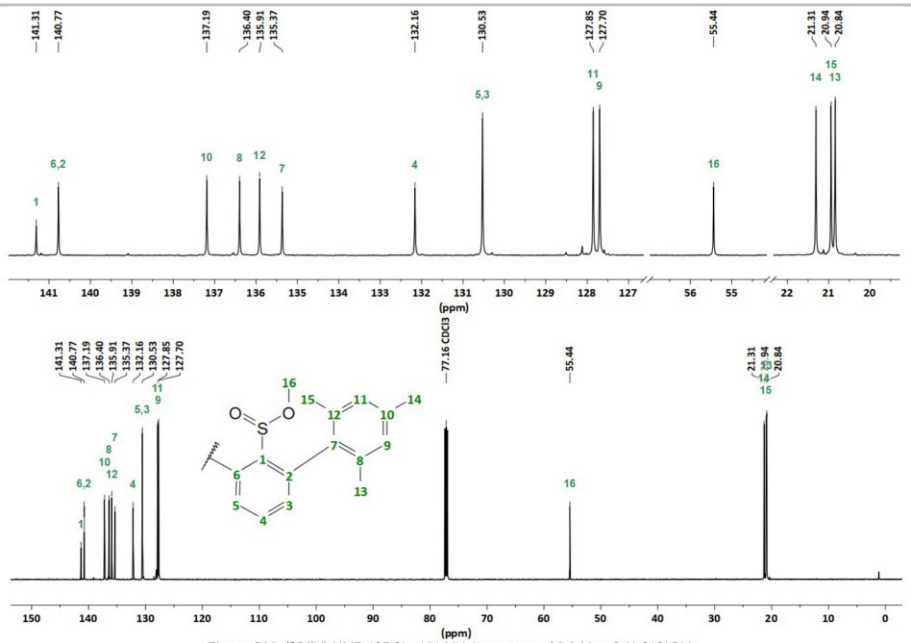

Figure S35. $^{13}C\{^{1}H\}$ NMR ($CDCl_3$, 151 MHz) spectrum of 2,6-$Mes_2C_6H_3S(O)OMe$.

Synthesis and characterization of (2,6-$Mes_2C_6H_3$)$_2$S(O)

2,6-$Mes_2C_6H_3S(O)F$ (571 mg, 1.50 mmol, 1.00 eq.) and 2,6-$Mes_2C_6H_3Li$ (481 mg, 1.50 mmol, 1.00 eq.) were placed in a Schlenk tube. To this *n*-hexane (15 mL) was added and the suspension was stirred for 48 hours at room temperature. After this, H_2O (10 mL) was added and extracted with CH_2Cl_2 (3 x 20 mL). The organic phase was dried over sodium sulfate and the solvent was removed under reduced pressure. The residual solid was washed with acetone (3 x 10 mL) to yield (2,6-$Mes_2C_6H_3$)$_2$S(O) as a colourless solid (600 mg, 59%).

Crystals suitable for X-Ray diffraction measurements were grown by slow cooling of a hot toluene solution of (2,6-$Mes_2C_6H_3$)$_2$S(O)

^{1}H NMR (600 MHz, $CDCl_3$): δ = 7.32 (t, $^3J(^1H\text{-}^1H)$ = 7.6 Hz, 1H, H4), 6.85 (d, $^3J(^1H\text{-}^1H)$ = 7.6 Hz, 2H, H3 and H5), 6.79 (s, 2H, H9), 6.77 (s, 2H, H11), 2.37 (s, 6H, H14), 1.77 (s, 6H, H13), 1.72 (s, 6H, H15) ppm. **$^{13}C\{^1H\}$ NMR (151 MHz, $CDCl_3$):** δ = 144.0 (s, C1), 143.2 (s, C2 and C6), 138.2 (s, C7), 137.3 (s, C12), 136.6 (s, C10), 136.5 (s, C8), 133.4 (s, C3 and C5), 129.7 (s, C4), 128.6 (s, C9), 128.4 (s, C11), 22.3 (s, C15), 22.0 (s, C13), 21.0 (s, C14), ppm. **HRMS ESI (m/z):** $[M+H]^+$ calculated. For $C_{48}H_{51}OS$ 675.36551; found, 675.36513. $[M+Na]^+$ calculated. For $C_{48}H_{50}NaOS$ 697.34746; found, 697.34674.

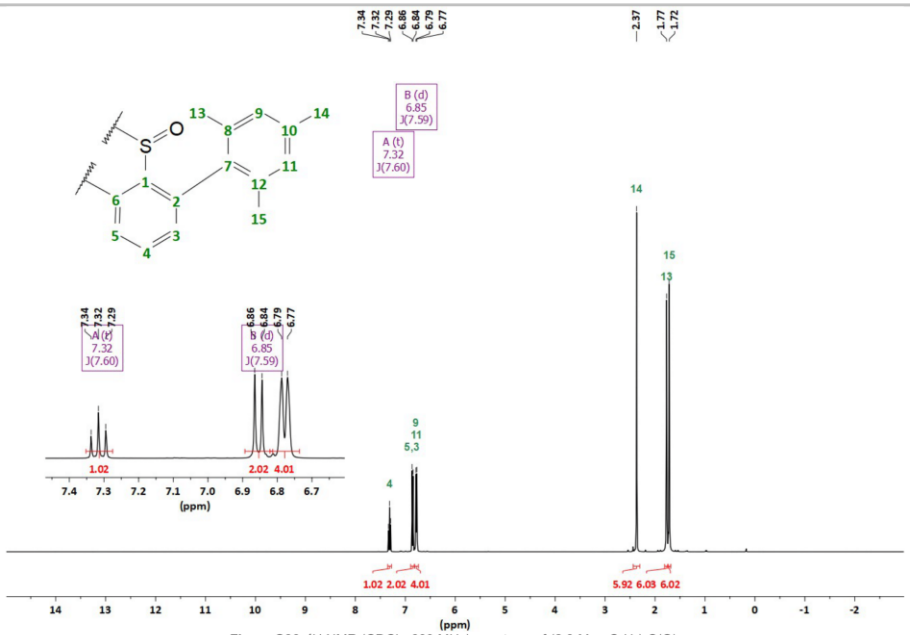

Figure S36. ^{1}H NMR ($CDCl_3$, 600 MHz) spectrum of $(2,6\text{-}Mes_2C_6H_3)_2S(O)$.

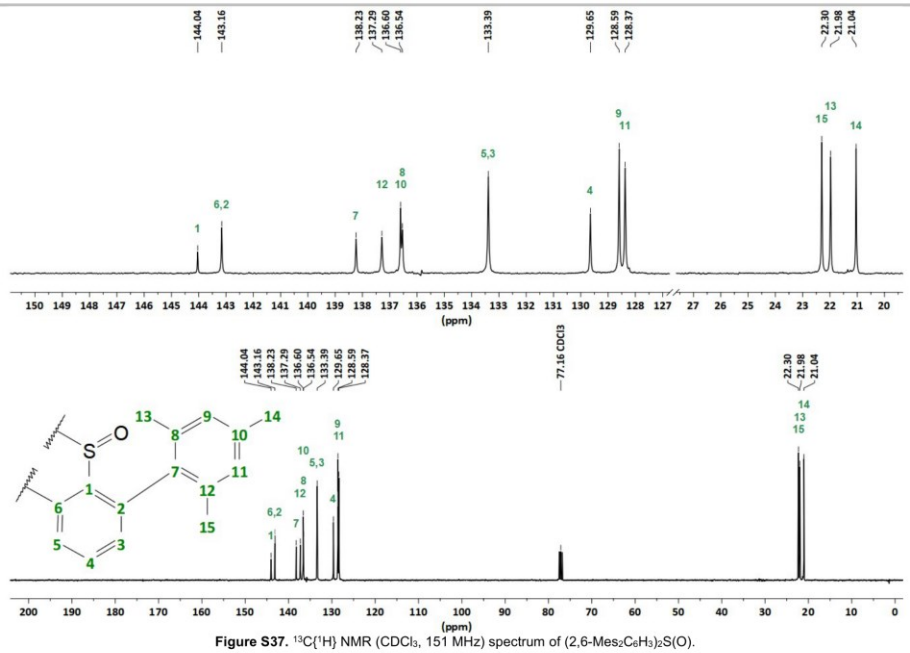

Figure S37. $^{13}C\{^{1}H\}$ NMR ($CDCl_3$, 151 MHz) spectrum of $(2,6\text{-}Mes_2C_6H_3)_2S(O)$.

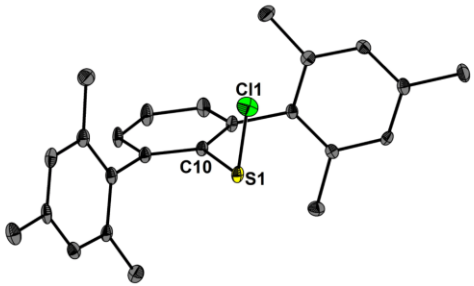

Figure S38. Molecular structure of 2,6-$Mes_2C_6H_3SCl$ showing 50% probability ellipsoids and the atomic numbering scheme. Selected bond parameters [Å, °]: S1-Cl1 2.0405(14), S1-C10 1.769(3), C10-S1-Cl1 103.33(13).

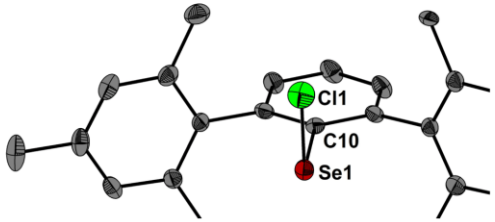

Figure S39. Molecular structure of 2,6-$Mes_2C_6H_3SeCl$ showing 50% probability ellipsoids and the atomic numbering scheme. Selected bond parameters [Å, °]: Se1-Cl1 2.1688(13), Se1-C10 1.924(3), C10-Se1-Cl1 100.55(11).

X-Ray diffraction studies

Single crystal X-ray diffraction data of **1a-c**, **2-4**, [**1c**]$^{+}$[$B(C_6F_5)_4$]$^{-}$, 2,6-$Mes_2C_6H_3SCl$, 2,6-$Mes_2C_6H_3SeCl$, 2,6-$Mes_2C_6H_3Se(O)OH$, 2,6-$Mes_2C_6H_3S(O)F$, $(2,6\text{-}Mes_2C_6H_3)_2S(O)$, 2,6-$Mes_2C_6H_3S(O)Cl$ and 2,6-$Mes_2C_6H_3S(O)OMe$ were collected on a Bruker Venture D8 diffractometer at 100 K with graphite-monochromated Mo-Kα (0.7107 Å) radiation. All structures were solved by direct methods and refined based on F^2 by use of the SHELX program package as implemented in Olex2.[S8,S9] All non-hydrogen atoms were refined using anisotropic displacement parameters. Hydrogen atoms attached to carbon atoms were included in geometrically calculated positions using a riding model. Disorder was resolved for **3** (split occupancies for F1 and F2, ratio 70:30), **4** (split occupancies for Te1, F1 and F2, ratio 70:30), 2,6-$Mes_2C_6H_3SeCl$ (split occupancies for Se2 and Cl2, ratio 82:18), 2,6-$Mes_2C_6H_3S(O)Cl$ (split occupancies for S1 and O1, ratio 62:38) and 2,6-$Mes_2C_6H_3S(O)OMe$ (split occupancies for S1, O1 and O2, ratio 60:40). Crystal and refinement data are collected in Tables S1-S5. Figures were created using DIAMOND.[S10] Crystallographic data for the structural analyses have been deposited with the Cambridge Crystallographic Data Centre. Copies of this information may be obtained free of charge from The Director, CCDC, 12 Union Road, Cambridge CB2 1EZ, UK (Fax: +44-1223-336033; e-mail: deposit@ccdc.cam.ac.uk or http://www.ccdc.cam.ac.uk).

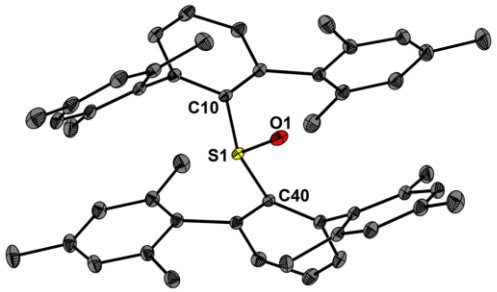

Figure S42. Molecular structure of (2,6-$Mes_2C_6H_3$)$_2$S(O) showing 50% probability ellipsoids and the atomic numbering scheme. Selected bond parameters [Å, °]: S1-O1 1.4836(15), S1-C10 1.8121(9), S1-C40 1.7978(9), C10-S1-C40 104.96(4).

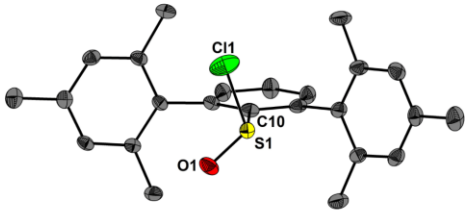

Figure S43. Molecular structure of 2,6-$Mes_2C_6H_3$S(O)Cl showing 50% probability ellipsoids and the atomic numbering scheme. Selected bond lengths [Å]: S1-O1 1.452(3), S1-Cl1 1.975(2), S1-C10 1.863(3).

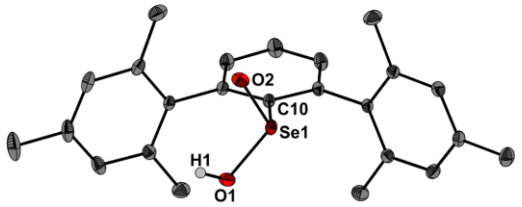

Figure S40. Molecular structure of 2,6-$Mes_2C_6H_3$Se(O)OH showing 50% probability ellipsoids and the atomic numbering scheme. Selected bond parameters [Å, °]: Se1-O1 1.7557(7), Se1-O2 1.6460(7), Se1-C10 1.9541(8), O1-Se1-O2 106.45(3), O1-Se1-C10 100.64(3), O2-Se1-C10 100.11(3).

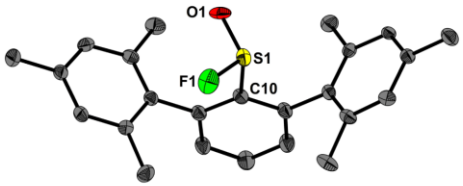

Figure S41. Molecular structure of 2,6-$Mes_2C_6H_3$S(O)F showing 50% probability ellipsoids and the atomic numbering scheme. Selected bond parameters [Å, °] S1-F1 1.5377(13), S1-O1 1.5275(18), S1-C10 1.818(3), F1-S1-O1 107.14(10), F1-S1-C10 100.47(7), O1-S1-C10 101.97(9).

Table S1. Crystal data and structure refinement of **1a** - **1c**.

	1a	**1b**	**1c**
Formula	$C_{48}H_{50}S$	$C_{48}H_{50}Se$	$C_{48}H_{50}Te$
Formula weight, g mol^{-1}	658.94	705.84	754.48
Crystal system	Monoclinic	Orthorhombic	Orthorhombic
Crystal size, mm	0.4 × 0.4 × 0.3	0.07 × 0.06 × 0.04	0.07 × 0.05 × 0.04
Space group	$P2_1/c$	Fdd2	Fdd2
a, Å	14.5411(13)	20.3777(4)	20.657(5)
b, Å	16.4008(15)	42.9059(8)	43.485(5)
c, Å	16.0294(16)	8.3558(2)	8.277(5)
α, °	90	90	90
β, °	101.681(4)	90	90
γ, °	90	90	90
V, Å^3	7343.6(6)	7305.7(3)	7435(5)
Z	4	8	8
ρ_{calcd}, Mg m^{-3}	1.169	1.283	1.348
μ (Mo *Kα*), mm^{-1}	0.119	1.061	0.833
F(000)	1416.0	2976	3120
θ range, deg	2.48 to 30.51	2.68 to 29.87	2.18 to 37.57
Index ranges	–20 ≤ h ≤ 20	–28 ≤ h ≤ 28	–35 ≤ h ≤ 35
	–23 ≤ k ≤ 23	–60 ≤ k ≤ 60	–74 ≤ k ≤ 74
	–22 ≤ l ≤ 22	–11 ≤ l ≤ 11	–14 ≤ l ≤ 14
No. of reflns collected	128371	206200	150801
Completeness to θ_{max}	99.9%	99.9%	99.9%
No. indep. Reflns	11437	5367	9813
No. obsd reflns with ($I>2\sigma(I)$)	9457	5144	9507
No. refined params	642	228	228
GooF (F^2)	1.027	1.030	1.123
R_1 (F) ($I > 2\sigma(I)$)	0.0421	0.0514	0.0156
wR_2 (F^2) (all data)	0.1116	0.1264	0.0404
Largest diff peak/hole, e Å^{-3}	0.42/ –0.28	2.43 / –1.83	0.36 / –0.55
CCDC number	2215859	2215860	2215861

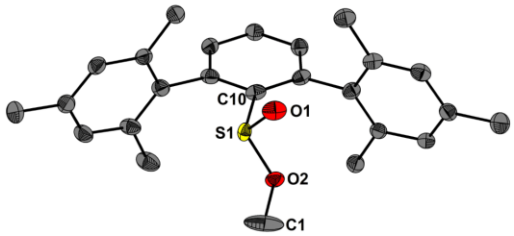

Figure S44. Molecular structure of 2,6-$Mes_2C_6H_3S(O)OMe$ showing 50% probability ellipsoids and the atomic numbering scheme. Selected bond lengths [Å]: S1-O1 1.457(4) S1-O2 1.639(4), S1-C10 1.828(2).

Table S3. Crystal data and structure refinement of **4,** 2,6-$Mes_2C_6H_3SCl$ and 2,6-$Mes_2C_6H_3SeCl$.

	4	TerSCl	TerSeCl
Formula	$C_{48}H_{50}F_2Te$	$C_{24}H_{25}ClS$	$C_{24}H_{25}ClSe$
Formula weight, g mol^{-1}	792.48	380.95	427.85
Crystal system	Orthorhombic	Monoclinic	Monoclinic
Crystal size, mm	0.24 × 0.24 × 0.23	0.17 × 0.15 × 0.12	0.17 × 0.15 × 0.07
Space group	Pbca	Pc	$P2_1/n$
a, Å	17.288(4)	8.2805(11)	13.3713(14)
b, Å	18.843(5)	17.675(2)	8.7732(10)
c, Å	23.608(6)	7.6299(8)	35.375(4)
α, °	90	90	90
β, °	90	113.518(4)	90.280(4)
γ, °	90	90	90
V, Å^3	7691(3)	1023.9(2)	4149.7(8)
Z	8	2	8
ρ_{calcd}, Mg m^{-3}	1.369	1.236	1.370
μ (Mo *Kα*), mm^{-1}	0.816	0.293	1.943
F(000)	3264.0	404.0	1760.0
θ range, deg	2.35 to 35.54	2.30 to 25.03	2.30 to 27.49
Index ranges	–28 ≤ h ≤ 28	–9 ≤ h ≤ 9	–16 ≤ h ≤ 17
	–30 ≤ k ≤ 28	–21 ≤ k ≤ 21	–11 ≤ k ≤ 11
	–33 ≤ l ≤ 38	–9 ≤ l ≤ 9	–45 ≤ l ≤ 45
No. of reflns collected	102341	20784	85330
Completeness to θ_{max}	99.7%	99.9%	99.9%
No. indep. Reflns	17560	3475	9523
No. obsd reflns with ($I>2\sigma(I)$)	12282	3384	7163
No. refined params	490	241	500
GooF (F^2)	1.011	1.070	1.046
R_1 (F) ($I > 2\sigma(I)$)	0.0438	0.0360	0.0571
wR_2 (F^2) (all data)	0.1000	0.0976	0.1538
Largest diff peak/hole, e Å^{-3}	1.00 / –1.07	1.05/ –0.19	2.36 / –0.71
CCDC number	2215865	2215866	2215867

Ter = 2,6-$Mes_2C_6H_3$

Table S2. Crystal data and structure refinement of [**1c**][$B(C_6F_5)_4$], **2** and **3**.

	[**1c**][$B(C_6F_5)_4$]	**2**	**3**
Formula	$C_{72}H_{50}BF_{20}Te$	$C_{24}H_{25}F_3Te$	$C_{48}H_{50}F_2Te_2$
Formula weight, g mol^{-1}	1433.53	498.04	920.08
Crystal system	Triclinic	Orthorhombic	Monoclinic
Crystal size, mm	0.26 × 0.18 × 0.17	0.22 × 0.21 × 0.19	0.22 × 0.22 × 0.21
Space group	P-1	$Cmc2_1$	$P2_1/c$
a, Å	12.2237(6)	22.9156(8)	13.0467(6)
b, Å	16.3099(8)	13.2929(8)	20.9767(10)
c, Å	16.5127(7)	6.7491(3)	15.2989(8)
α, °	80.957(2)	90	90
β, °	81.885(2)	90	101.516(2)
γ, °	81.536(2)	90	90
V, Å^3	3192.2(3)	2055.88(17)	4102.7(3)
Z	2	4	4
ρ_{calcd}, Mg m^{-3}	1.491	1.609	1.490
μ (Mo *Kα*), mm^{-1}	0.567	1.480	1.463
F(000)	1438.0	992.0	1840.0
θ range, deg	2.52 to 36.46	3.07 to 26.37	2.49 to 25.35
Index ranges	–20 ≤ h ≤ 20	–28 ≤ h ≤ 28	–15 ≤ h ≤ 15
	–27 ≤ k ≤ 27	–16 ≤ k ≤ 16	–25 ≤ k ≤ 25
	–26 ≤ l ≤ 27	–8 ≤ l ≤ 8	–18 ≤ l ≤ 18
No. of reflns collected	145501	17520	133969
Completeness to θ_{max}	99.4%	99.9%	99.9%
No. indep. Reflns	31095	2169	7519
No. obsd reflns with ($I>2\sigma(I)$)	26427	1987	6792
No. refined params	859	145	517
GooF (F^2)	1.037	1.057	1.265
R_1 (F) ($I > 2\sigma(I)$)	0.0349	0.0333	0.0394
wR_2 (F^2) (all data)	0.0864	0.0742	0.0833
Largest diff peak/hole, e Å^{-3}	0.71/ –0.61	0.43/ –0.50	0.46/ –0.90
CCDC number	2215862	2215863	2215864

Table S4. Crystal data and structure refinement of 2,6-$Mes_2C_6H_3Se(O)OH$, 2,6-$Mes_2C_6H_3S(O)F$ and (2,6-$Mes_2C_6H_3)_2S(O)$.

	TerSe(O)OH	TerS(O)F	$Ter_2S(O)$
Formula	$C_{24}H_{26}O_2Se$	$C_{24}H_{25}FOS$	$C_{48}H_{50}OS$
Formula weight, g mol^{-1}	425.41	380.50	674.94
Crystal system	Triclinic	Orthorhombic	Triclinic
Crystal size, mm	0.21 × 0.17 × 0.12	0.27 × 0.25 × 0.18	0.22 × 0.22 × 0.21
Space group	P-1	Pbca	P-1
a, Å	9.3079(3)	17.6275(4)	11.2455(4)
b, Å	10.9619(3)	7.7331(2)	13.3961(5)
c, Å	11.7302(3)	29.6996(7)	14.7559(5)
α, °	65.787(1)	90	64.784(1)
β, °	74.853(1)	90	68.817(1)
γ, °	69.006(1)	90	75.166(1)
V, Å^3	1009.87(5)	4048.51(17)	1861.42(12)
Z	2	8	2
ρ_{calcd}, Mg m^{-3}	1.399	1.249	1.204
μ (Mo *Kα*), mm^{-1}	1.875	0.179	0.123
F(000)	440.0	1616.0	724.0
θ range, deg	2.62 to 36.45	2.69 to 30.43	2.72 to 36.44
Index ranges	–15 ≤ h ≤ 15	–22 ≤ h ≤ 22	–18 ≤ h ≤ 18
	–18 ≤ k ≤ 18	–9 ≤ k ≤ 9	–22 ≤ k ≤ 22
	–19 ≤ l ≤ 19	–37 ≤ l ≤ 37	–24 ≤ l ≤ 24
No. of reflns collected	58700	117480	107138
Completeness to θ_{max}	99.8%	99.8%	99.8%
No. indep. Reflns	9874	4128	18178
No. obsd reflns with ($I>2\sigma(I)$)	9060	3591	14451
No. refined params	254	277	481
GooF (F^2)	1.067	1.069	1.040
R_1 (F) ($I > 2\sigma(I)$)	0.0238	0.0421	0.0467
wR_2 (F^2) (all data)	0.0644	0.1106	0.1332
Largest diff peak/hole, e Å^{-3}	0.60 / –0.44	0.28/ –0.27	0.58 / –0.33
CCDC number	2215868	2215869	2215870

Ter = 2,6-$Mes_2C_6H_3$

Table S5. Crystal data and structure refinement of 2,6-$Mes_2C_6H_3S(O)Cl$ and 2,6-$Mes_2C_6H_3S(O)OMe$.

	TerS(O)Cl	TerS(O)OMe
Formula	$C_{24}H_{25}ClOS$	$C_{25}H_{28}O_2S$
Formula weight, g mol^{-1}	396.95	392.53
Crystal system	Monoclinic	Orthorhombic
Crystal size, mm	0.29 × 0.28 × 0.17	0.31 × 0.24 × 0.23
Space group	Pc	$P2_12_12_1$
a, Å	8.2375(3)	7.8940(3)
b, Å	17.6188(7)	15.6172(5)
c, Å	7.8414(3)	17.1608(5)
α, °	90	90
β, °	113.844(1)	90
γ, °	90	90
V, Å^3	1040.93(7)	2115.62(12)
Z	2	4
ρ_{calcd}, Mg m^{-3}	1.266	1.232
μ (Mo *Kα*), mm^{-1}	0.295	0.171
F(000)	420.0	840.0
θ range, deg	2.94 to 27.50	2.37 to 28.34
Index ranges	–10 ≤ h ≤ 10	–10 ≤ h ≤ 10
	–22 ≤ k ≤ 22	–20 ≤ k ≤ 20
	–10 ≤ l ≤ 10	–22 ≤ l ≤ 21
No. of reflns collected	29286	23627
Completeness to θ_{max}	99.9%	99.9%
No. indep. Reflns	4726	5271
No. obsd reflns with ($I>2\sigma(I)$)	4526	4938
No. refined params	268	287
GooF (F^2)	1.047	1.090
R_1 (F) ($I > 2\sigma(I)$)	0.0357	0.0394
wR_2 (F^2) (all data)	0.0943	0.1110
Largest diff peak/hole, e Å^{-3}	0.54 / –0.28	0.25/ –0.33
CCDC number	2215871	2215872

Ter = 2,6-$Mes_2C_6H_3$

CV data, Cottrell and kinetic analysis of the ECO first stage of compound **1c** [(2,6-$Mes_2C_6H_3$)$_2$Te].

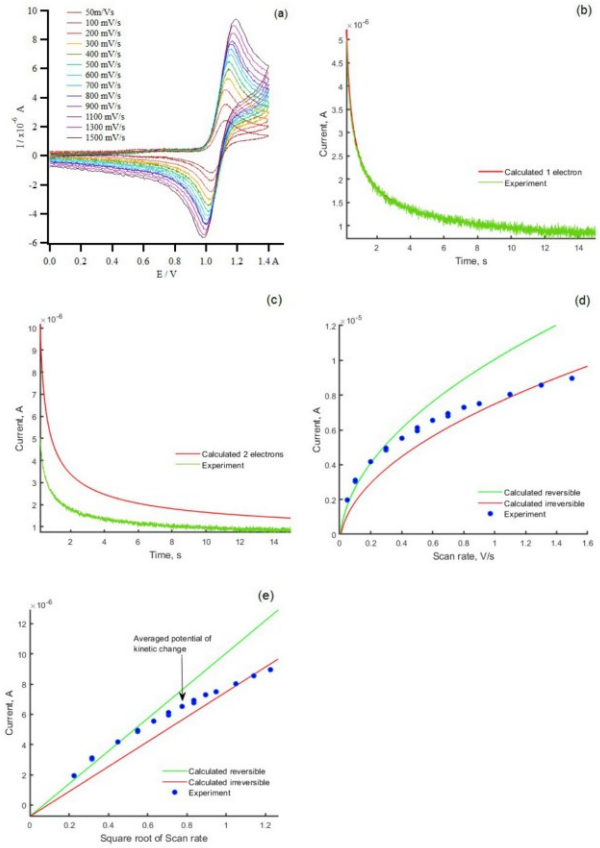

Figure S45. (a) CVs of **1c** in CH_2Cl_2 at various potential sweep rates (indicated by color), (b) experimental (green) and calculated (red) Cottrell curves for one-electron electrochemical oxidation process, (c) experimental

Electrochemical and Spectroelectrochemical characterization

Cyclic voltammetric (CV) experiments were performed in CH_2Cl_2 using a standard glass electrochemical cell with a solution volume of 6 mL equipped with a stationary Pt disc electrode (A = 0.0122 cm^2, calibrated using ferrocene as a standard). A Pt helix was used as an auxiliary electrode. A PG 310 USB potentiostat (HEKA Elektronik GmbH, Germany) was used for the measurements. The cell was connected to the potentiostat using a three-electrode circuit. Peak potentials were quoted with a reference to a saturated calomel electrode (SCE). A bridge with 0.1 M of supporting electrolyte in CH_2Cl_2 was used to connect the cell and SCE. The measurements were performed at 295 K. 0.1 M solution of *n*-Bu_4NBF_4 in CH_2Cl_2 was used as a supporting electrolyte in all CV and spectroelectrochemical experiments (see below). All CV curves were measured using triangular potential sweep.

The Cottrell's current curves for compounds **1a-c** were measured under the same experimental conditions as the CV experiments. At the beginning of all Cottrell experiments, the initial potential was held at 0.0 V (vs SCE) during 10s, and then pulsed increased up to 1.8 V for **1a**, 1.5 V for **1b**, 1.3 V for **1c**. The duration of Cottrell's measurements was 15 s in all cases. The experiments were carried out in two steps at the same potentials: the first step included a "blank" experiment without a depolarizer (**1a-1c**), the second step was carried out after the addition of a depolarizer. The resulting Cottrell curves were obtained as the difference between the second step curves and the "blank" curves. Analysis of Cottrell's curves, as well as the observed kinetics of reversibility/irreversibility of electrode processes, was done using the Matlab R2018B software.

Spectroelectrochemical measurements for **1c** were performed in CH_2Cl_2 solution (0.1 mM) at 295 K in the potential sweep range of 0.0> E> 2.0 V. A Honeycomb spectroelectrochemical Cell kit (USA) with an optical path of 0.16 cm was used for measurements. A platinum multi-cylindrical electrode was employed as a working electrode, and an Ag wire electrode was used as a pseudo reference electrode. All manipulations with the cell were performed under nitrogen in a glove box. The cell was connected to an Ellins 3-45X potentiostat (Electrochemical Instruments, Russia) via a three-electrode circuit and simultaneously to a UV-VIS-NIR spectrophotometer (Avantes) via a fiber optic line. UV-VIS-NIR spectra were recorded in a differential form ($D(\lambda) - D_{blank}(\lambda)$), where $D(\lambda)$ is the optical density at wavelength λ recorded during reduction, $D_{blank}(\lambda)$ is the spectrum of a neutral form of **1c** in CH_2Cl_2 recorded before oxidation. The potentiostat was synchronized with the spectrophotometer using the *ES8* software synchronized with the *AvaSoft 8.7* software. Both programs were used for the simultaneous acquisition of optical and electrochemical data in a mode of staircase cyclic potential sweep with a potential step of 0.5 mV/s. The final data analysis was carried out with the *Igor PRO 8.0* software.

Cyclic voltammograms of 1a – 1c, analysis of reversibility/irreversibility of electrochemical processes and determination of the number of transferred electrons.

CV data, Cottrell's and kinetic analysis of the ECO first stage of compound **1b** [(2,6-$Mes_2C_6H_3$)$_2$Se].

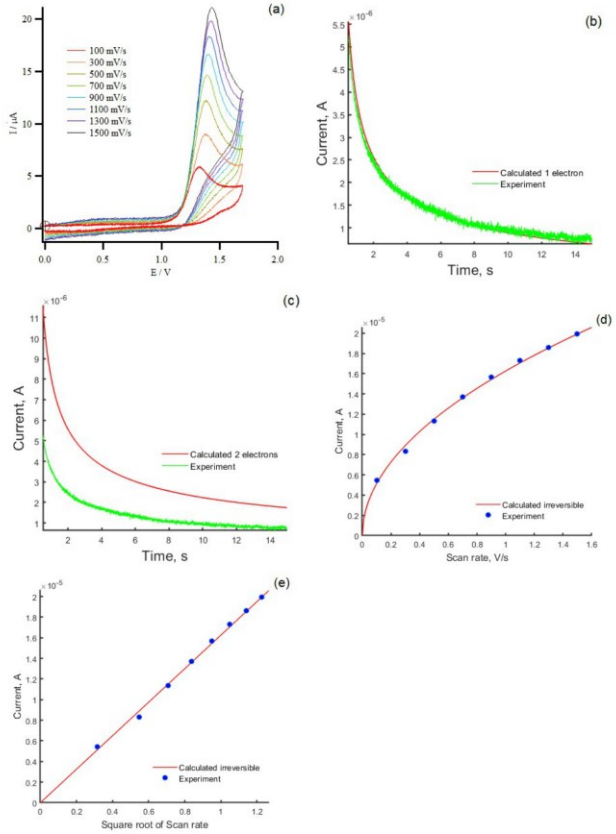

Figure S46. (a) CVs of **1b** in CH_2Cl_2 at various potential sweep rates (indicated by color), (b) experimental (green) and calculated (red) Cottrell curves for **ONE**-electron electrochemical oxidation process, (c) experimental (green) and calculated (red) Cottrell curves for two-electron electrochemical oxidation process, (d) experimental dependence of the 1st oxidation peak current on the potential sweep rate (blue circles) and the corresponding

(green) and calculated (red) Cottrell curves for two-electron electrochemical oxidation process, (d) experimental dependence of the 1st oxidation peak current on the potential sweep rate (blue circles) and the corresponding theoretical curves for reversible (green curve) and irreversible (red curve) processes, (e) experimental dependence of the 1st oxidation peak current on the square root of potential sweep rate (blue circles) and the corresponding theoretical lines for reversible (green line) and irreversible (red line) processes.

*(Bulk concentration C_0(**1c**)= 1.31 mM, Calculated diffusion coefficient D(**1c**)= 6.5±0.2·10^{-6} cm^2/c, Calculated electron transfer coefficient for equation (3) is α=0.45)*

Figure S45(b) demonstrates an excellent description of the experimental current response at a potential of 1.3 V (vs SCE) using the Cottrell equation, assuming **ONE**-electron process for the first ECO stage of **1c:**

$$I(t)=\frac{nFAC_0D^{1/2}}{\pi^{1/2}t^{1/2}} \quad (1)$$

where n is the number of transferred electrons, F is the Faraday constant, A is the area of the working electrode, C_0 is the bulk concentration of the depolarizer, D is the corresponding diffusion coefficient, and t is time.

If to assume n=2 (Figure S45(c)), then the corresponding description of the experimental Cottrell curve fails.

Figure S45(d) demonstrates the change in the electron transfer kinetics of the first one-electron stage ECO **1c** from a reversible process at low potential sweep rates (ν) to an irreversible process.

For a reversible process, the dependence of the peak current on the potential sweep rate is described by the well-known Randles-Sevcik equation[S11]:

$$I_p = 0.4463\ nFAC_0\left(\frac{nF\nu\ D}{RT}\right)^{1/2} \quad (2)$$

where I_p is the current at the peak maximum, n is the number of electrons transferred in the redox event, A is the electrode area in cm^2, F is the Faraday constant in C·mol^{-1}, D is the diffusion coefficient in cm^2/s, C_0 is the concentration of the depolariser in mol/cm^3, ν is the potential sweep rate in V/s, R is the gas constant in J·K^{-1}·mol^{-1}, T is the temperature in K.

For an irreversible n-electron process, the corresponding dependence I_p(ν) has the following form:

$$I_p = 0.496\ n_1FAC_0D^{1/2}(n_2\alpha)^{1/2}\left(\frac{F}{RT}\right)^{1/2}\nu^{1/2} \quad (3)$$

where n_1 is the total number of electrons transferred in the process, n_2 is the number of electrons in the limiting stage, α is the electron transfer coefficient, all other values have their usual meaning.

The kinetic analysis of electron transfer using the same values of C_0 and D as in the Cottrell experiment showed a reversible one-electron ECO of **1c** in the range of potential sweep rates 0.05<ν<0.3 V s^{-1}, the transition to an irreversible process (in this case, n_1=n_2=1) at intermediate sweep rates 0.3< ν<1.3 V s^{-1} and to an irreversible process at higher ν (Figures S45(d,e)).[S12] The described kinetic analysis indicates three cases of electron transfer during ECO **1c** in CH_2Cl_2: reversible, intermediate and irreversible. These processes are related to the rate of mass transport, as described in ref. S12 in the reversible regime, the electron transfer rate is greater than the rate of mass transport, both rates become comparable in the intermediate regime (Figure S45(e)), and in the irreversible regime, the electron transfer rate is smaller than the rate of mass transport. These observations indicate a rather slow ionization rate of compound **1c** in CH_2Cl_2 with the formation of the long-lived radical cation **1c**$^{+\bullet}$ (for EPR results, see below).

CV data, Cottrell's and kinetic analysis of the ECO first stage of compound **1a** [(2,6-$Mes_2C_6H_3)_2S$].

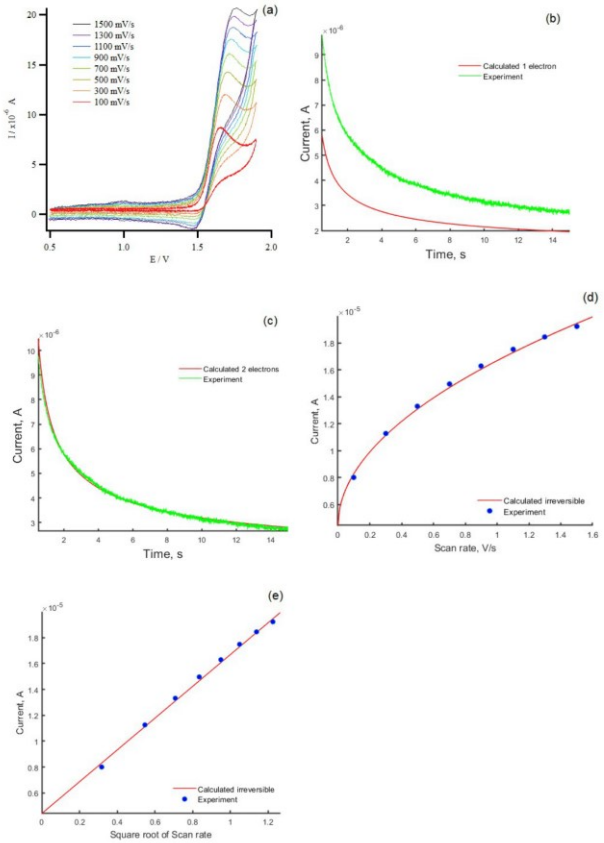

Figure S47. (a) CVs of **1a** in CH_2Cl_2 at various potential sweep rates (indicated by color), (b) experimental (green) and calculated (red) Cottrell curves for one-electron electrochemical oxidation process, (c) experimental (green) and calculated (red) Cottrell curves for **TWO**-electron electrochemical oxidation process, (d) experimental

theoretical curve for irreversible (red curve) processes, (e) experimental dependence of the 1st oxidation peak current on the square root of potential sweep rate (blue circles) and the corresponding theoretical line for irreversible (red line) processes.

*(Bulk concentration C_0(**1b**)= 2.55 mM, Calculated diffusion coefficient D(**1b**)= 6.8±0.4·10^{-6} cm^2/c, Calculated electron transfer coefficient for equation (3) α=0.48)*

Figure S46(b) demonstrates a good description of the experimental current decay measured at a potential of 1.5 V (vs SCE) using the Cottrell equation assuming a **ONE**-electron process for the first stage of ECO **1b**. If we take n=2 (Figure S46(c)), then the corresponding description of the experimental Cottrell curve fails. This fact proves that ECO **1b** is an EC-process leading to an unstable radical cation 1b$^{+\cdot}$. Kinetic analysis of electron transfer using the dependence of the peak's current in the CV of **1b** on the potential sweep rate showed a one-electron irreversible process in accordance with equation (3), for which n1, n2=1 and α=0.48 (Figure S46(c,d)). The corresponding half-wave potential was determined approximately using the differences of E_{onset} and $E_{1/2}$ potentials for compounds **1a** and **1c** (0.068 V, 0.070 V, respectively, and the averaged value is 0.069 V). For **1a** and **1c**, the corresponding $E_{1/2}$ values can be accurately calculated from the corresponding CVs (Figures S47(a), S45(a)) Assuming this difference is the same for **1b**, the corresponding $E_{1/2}$ value was estimated to be 1.22 V (vs SCE).

We would like to note that the irreversible ECO of **1b** in CH_2Cl_2 leads to contamination of the working electrode's surface, probably, due to the adsorption of products formed as a result of [**1b**]$^{+\cdot}$ decomposition. The contamination revels in the deviation of the corresponding CV's shape in the second and subsequent cycles of potential sweep. To avoid this phenomenon, a 5-second bubbling of the working electrode space with dry argon was used before each cycle of potential sweep.

3D UV-VIS-NIR spectroelectrochemical data on the ECO of **1c**

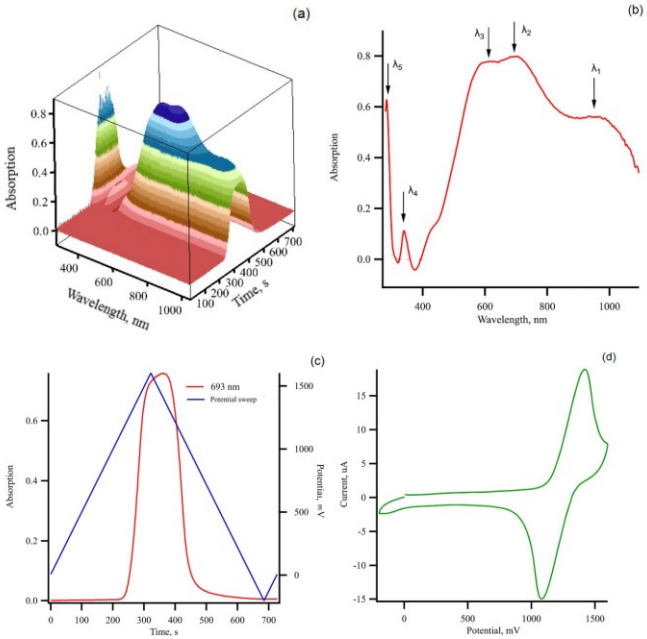

Figure S48. (a) 3D UV-VIS-NIR spectroelectrochemical surface of **1c** oxidation in CH_2Cl_2, (b) optical absorption spectrum of radical cation [**1c**]$^{+\bullet}$ obtained at maximum absorption intensity (360 s of electrolysis), (c) kinetic profile of the spectroelectrochemical surface at 693 nm (λ_2, left axis) and the corresponding potential sweep (right axis), (d) macro-electrolysis curve obtained in a 3D spectroelectrochemical experiment. (C_0(**1c**)= 1 mM in CH_2Cl_2, 0.1 M of nBu_4NBF_4 in CH_2Cl_2 was used as a supporting electrolyte, Pt multi-cylindrical electrode was used as a working electrode, and an Ag wire was used as a pseudo-reference electrode.)

The optical spectrum obtained at maximum intensity (Figure S48(b)) in the "differential mode" is characterized by a region of "transparency" in the wavelength range 299 <λ< 436 nm. The spectrum has an intense absorption in the visible and near IR region (436 <λ< 1100 nm), and the shape of the spectrum is in a good agreement with the optical spectrum of [**1c**]$^{+\bullet}$ obtained by oxidation of **1c** with XeF_2 (Figure S23). The estimated extinction coefficients at the selected optical absorption wavelengths (Figure S48(b)) are listed in Table S6.

dependence of the 1st oxidation peak current on the potential sweep rate (blue circles) and the corresponding theoretical curves for irreversible (red curve) processes, (e) experimental dependence of the 1st oxidation peak current on the square root of potential sweep rate (blue circles) and the corresponding theoretical curves for irreversible (red line) processes.

*(Bulk concentration C_0(**1a**)= 1.76 mM, Calculated diffusion coefficient was found D(**1a**)= $8.0\pm0.2\cdot10^{-6}$ cm^2/c, Calculated electron transfer coefficient for equation (3) α=0.45)*

If to assume n=1 (Figure S47(b)), then the corresponding description of the experimental Cottrell curve fails. Figure S47(c) shows an excellent description of the experimental current response at a potential of 1.8 V (vs SCE) using the Cottrell equation assuming a **TWO**-electron process for the first stage of ECO **1a.** This fact proves that ECO **1a** is an EEC-process with two collapsing CV-waves and an unstable dication [**1a**]$^{2+}$. By comparison of the CVs of compounds **1a** and **1c** at *normalized to 1mM* bulk concentrations of these depolarizers (Fig. 3, main text) it shows an approximately 2:1 ratio of the first peak currents in CVs of **1a** and **1c**. Kinetic analysis of the electron transfer using the dependence of the peak's current in the CV of **1a** on the potential sweep rate showed a two-electron irreversible process in accordance with equation (3), for which n_1=2, n_2=1 and α=0.45 (Figure S47(c,d)), which is the same as for **1c** in the irreversible regime (Figure S47(d)). Increasing the potential sweep rates leads to the appearance of a cathode peak on CVs of **1a** at potential sweep rates ν>500 mV/s (Figure S47(a)), which makes it possible to determine the corresponding $E_{1/2}$= 1.08 V.

Note that the found diffusion coefficient of **1a** is the highest among all compounds indicating a smaller Stokes radius of compound **1a** due to the smallest size of the S atom compared to the Se and Te atoms.

Electron paramagnetic resonance spectroscopy

All EPR measurements were done on a Bruker Elexsys E580 spectrometer at X-band (9.7872 GHz). The spectrometer was equipped with an Oxford Instruments temperature control system (4-300 K). Continuous wave (CW) EPR measurements were carried out in conditions avoiding modulation broadening and microwave saturation at T=40 K. Pulse EPR measurements were done at T=20 K using free induction decay (FID) detection in order to avoid artificial broadening of spectral lines. A microwave π-pulse of 500 ns length was used, and the FID was integrated over a 150-200 ns time window. In order to compare FID-detected and CW EPR spectra, pseudomodulation with the 0.5 mT amplitude has been applied to the former ones.

Simulations of anisotropic CW spectra were performed with the *Simfonia* (Bruker) program. When modeling, a uniform distribution of paramagnetic particles in all directions, (θ,ϕ)=(360, 360), was assumed.

Electrochemical generation of [1c]$^{\bullet+}$ for EPR studies

For EPR measurements, the radical cation [**1c**]$^{\bullet+}$ was obtained in two ways: by electrochemical generation (Figure S49) and by oxidation of telluride **1c** with XeF_2 in the presence of $K[B(C_6F_5)_4]$ in CH_2Cl_2.

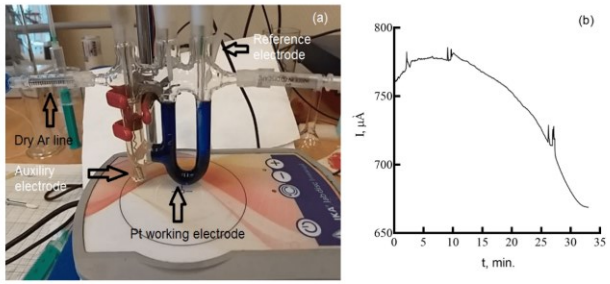

Figure S49. (a) Electrochemical H-cell used for the generation of radical cation [**1c**]$^{\bullet+}$ by ECO of 2 mM solution of **1c** in CH_2Cl_2 at a potential of 1.3 V using potentiostatic electrolysis (vs Ag wire pseudo-reference electrode), (b) current-time characteristic electrolysis.
(*The working volume of the cell was 6 ml, Pt wire was used as the working and auxiliary electrodes, an Ag wire was used as a pseudo-reference electrode, 0.1 M solution of n-BuNBF$_4$ in CH_2Cl_2 was used as a supporting electrolyte*)

After 34 min of electrolysis (Figure S49(b)), a dark blue solution of radical cation [**1c**]$^{\bullet+}$ with a counter-ion of $[BF_4]^-$ (Figure S49(a)) was carefully transferred from the working part of the H-cell into a quartz tube for EPR measurements in an Ar medium and then used for low-temperature EPR.

At low potential sweep rates, oxidative cyclic macroelectrolysis of **1c** (Figure S48(d)) and the corresponding optical absorption profile (Figure S48(c)) reveal good reversibility, which is in good agreement with the electron transfer kinetics obtained for ECO **1c** (Figure S45(c)).

Table S6. Estimated extinction coefficients[a] at the selected wavelengths obtained at maximum intensity of optical absorption spectrum of [**1c**]$^{\bullet+}$.

Maximum of absorption band[b]	Wavelength, nm	Optical absorption at 360 s	$\varepsilon(\lambda_i)$, M^{-1} cm^{-1}
$\lambda_{.10}$	951	0.561	3506
$\lambda_{.2}$	693	0.797	4981
$\lambda_{.3}$	613	0.778	4863
$\lambda_{.4}$	339	0.112	700
$\lambda_{.5}$	284	0.628	3925

[a] *Extinction coefficients were determined assuming complete one-electron oxidation of* ***1c*** *inside multi-cylindrical working electrode.*

[b] *The positions of* λ_i are shown in Figure S48(b).

The CW EPR spectrum of the $[\mathbf{1c}]^{\bullet+}[B(C_6F_5)_4]^-$ salt in frozen glassy CH_2Cl_2 (Figure S51) is characterized by very similar g-tensor components (Table S7), which indicate the same nature of paramagnetic species obtained by electrolysis and oxidation with XeF_2. Unlike $[(2,6\text{-}Mes_2C_6H_3Te)_2]^{\bullet+}$, no anisotropic hyperfine structure was observed for $[\mathbf{1c}]^{\bullet+}$ obtained by both methods of its generation under the experimental conditions used.

Table S7. Principle components of g-tensors and corresponding line widths of $[\mathbf{1c}]^{\bullet+}$ in frozen glassy CH_2Cl_2 at 40 K.

Particle / method of generation	g-tensor principle components			Linewidth / G		
	g_x	g_y	g_z	x	y	z
$[\mathbf{1c}]^{\bullet+}$/potentiostatic electrolysis[a]	1.9593	2.0455	2.2125	9.1	14.5	35.0
$[\mathbf{1c}]^{\bullet+}$ $[B(C_6F_5)_4]^-$ salt / oxidation of **1c** by XeF_2	1.9593	2.0455	2.2085	11.0	16.5	37.0

[a] The final solution of $[\mathbf{1c}]^{\bullet+}[BF_4]^-$ in CH_2Cl_2 obtained with a potentiostatic electrolysis contains also supporting electrolyte, n-Bu_4NBF_4.

We would like to mention an interesting phenomenon observed when detecting the spin-echo signal at 20 K. For the sample of $[\mathbf{1c}]^{\bullet+}$ obtained by potentiostatic electrolysis, a good intense spin-echo signal was observed at 20K, which makes it possible to measure the corresponding spin-echo –detected EPR spectrum of high quality (Figure S50). In contrast to this fact, an attempt to observe the spin-echo signal for a sample of $[(2,6\text{-}Mes_2C_6H_3)_2Te]^{\bullet+}[B(C_6F_5)_4]^-$ salt under the same experimental conditions was unsuccessful. Nevertheless, CW EPR spectra were observed for both samples, which indicate the same nature of the paramagnetic species (Table S7). On the other hand, the linewidths measured in EPR spectrum of the salt sample are noticeably larger than those of the electrochemically obtained $[\mathbf{1c}]^{\bullet+}$. This indicates a shorter spin relaxation time of the radical cation $[\mathbf{1c}]^{\bullet+}$ with the counterion $[B(C_6F_5)_4]^-$ and, as a consequence, the absence of a spin-echo signal.

A tentative explanation for this phenomenon is that $[\mathbf{1c}]^{\bullet+}[BF_4]^-$ obtained by electrolysis also contains a large amount of bulky n-Bu_4N^+ cations, which lead to additional spatial separation of paramagnetic species $[\mathbf{1c}]^{\bullet+}$ inside the frozen solution and an increase in the relaxation time. Contrary to that, paramagnetic species $[\mathbf{1c}]^{\bullet+}$ in a frozen salt solution ($[\mathbf{1c}]^{\bullet+}[B(C_6F_5)_4]^-$) are distributed closer to each other, due to missing bulky n-Bu_4N^+ cations which leads to a decrease in the relaxation time. It is also possible that the electrochemical generated radical cations $[\mathbf{1c}]^{\bullet+}$ are capable of forming some ion associates with BF_4^-. These associates are not formed in the solution obtained by chemical oxidation due to use of $[B(C_6F_5)_4]^-$ as a weakly coordinating anion.

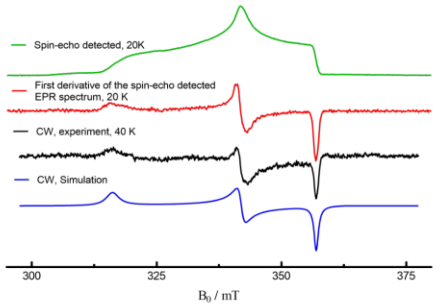

Figure S50. Spin-echo-detected EPR spectrum of electrochemically generated radical cation $[\mathbf{1c}]^{\bullet+}$ in frozen glassy CH_2Cl_2 at 20K (green), its first derivative obtained using the pseudo-modulation (red), continuous wave EPR spectrum of $[\mathbf{1c}]^{\bullet+}$ at 40 K (black) and its simulation (blue).

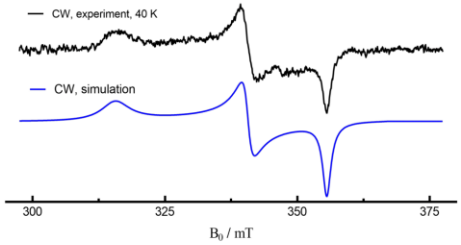

Figure S51. CW EPR spectrum of a solution of the radical cation salt $[(2,6\text{-}Mes_2C_6H_3)_2Te]^{\bullet+}[B(C_6F_5)_4]^-$, 1mM, in frozen glassy CH_2Cl_2 at 40K (black) and its simulation (blue).

For $[\mathbf{1c}]^{\bullet+}$ obtained by potentiostatic electrolysis, an intense spin—echo signal was observed at 20 K, which made it possible to measure the corresponding EPR spectrum using a pulsed method (Figure S50). The CW spectrum of $[\mathbf{1c}]^{\bullet+}$ was also observed at 40 K. This temperature turned out to be optimal for the CW experiment. The CW and spin-echo-detected EPR spectra of the electrochemically generated radical cation $[\mathbf{1c}]^{\bullet+}$ in frozen glassy CH_2Cl_2 are characterized by the g tensor with the principle components shown in Table S7.

Table S9. Frontier orbital energies of **1a-c**.

	no.				energy (a.u.)				gap		ΔE (a.u.)			
	α-H	α-L	β-H	β-L	α-H	α-L	β-H	β-L	α	β	α-H	α-L	β-H	β-L
1a	177	178			-0.209	-0.039			-0.170					
[1a]$^{\bullet+}$	177	178	176	177	-0.324	-0.154	-0.321	-0.284	-0.170	-0.037	-0.12	-0.12	-0.11	-0.25
[1a]$^{2+}$	176	177			-0.422	-0.395			-0.027		-0.10	-0.24		
1b	186	187			-0.203	-0.037			-0.166					
[1b]$^{\bullet+}$	186	187	185	186	-0.325	-0.148	-0.323	-0.277	-0.177	-0.046	-0.12	-0.11	-0.12	-0.24
[1b]$^{2+}$	185	186			-0.421	-0.391			-0.030		-0.10	-0.24		
1c	181	182			-0.188	-0.004			-0.184					
[1c]$^{\bullet+}$	181	182	180	181	-0.324	-0.153	-0.326	-0.262	-0.171	-0.064	-0.14	-0.15	-0.14	-0.26
[1c]$^{2+}$	180	181			-0.421	-0.380			-0.041		-0.10	-0.23		

α/β-H/L: alpha/beta-HOMO/LUMO

Table S10. Relevant geometric and ELI-D parameters of **1a-c**.

	Geometry			E–C bonding			LP(E)			
	d(E–C)	°(C–E–C)	d(E···C$_\pi$)	$N_{(ELI)}$	$V_{(ELI)}$	$\gamma_{(ELI)}$	$N_{(ELI)}$	$V_{(ELI)}$	$\gamma_{(ELI)}$	$Q_{(AIM)}$
1a	1.768	108.4	3.022	1.89	3.3	1.85	2.14	8.7	2.13	0.01
[1a]$^{\bullet+}$	1.755	107.7	2.937	2.02	3.6	1.86	1.86	7.4	2.03	0.29
[1a]$^{2+}$	1.761	106.0	2.958	2.02	3.6	1.86	1.88	7.4	2.03	0.22
1b	1.922	107.8	3.221	1.90	4.0	1.68	2.29	10.7	1.81	0.04
[1b]$^{\bullet+}$	1.912	113.3	2.955	2.00	4.4	1.77	1.94	8.6	1.73	0.55
[1b]$^{2+}$	1.909	110.3	2.966	2.03	4.3	1.77	1.93	8.4	1.71	0.59
1c	2.125	101.5	3.200	1.96	5.3	1.80	2.30	15.6	1.88	0.57
[1c]$^{\bullet+}$	2.121	119.2	2.946	2.11	6.9	1.75	1.86	10.9	1.58	0.95
[1c]$^{2+}$	2.115	114.0	2.835	2.14	7.3	1.62	1.73	10.3	1.53	1.03

N_{ELI} and V_{ELI} are electron populations and volumes of related ELI-D basins, γ_{ELI} is the ELI-D value at the attractor position

Computational data

Density functional theory (DFT) calculations (geometry optimizations in the gas-phase) were performed at the (U)B3PW91/6-311+G(2df,p)[S13, S14] level of theory using Gaussian09.[S15] For the Te atoms, an effective core potential (ECP28MDF)[S16] and corresponding cc-pVTZ basis set was utilized. Topological analysis of the electron density according to the Atoms-In-Molecules (AIM[S17]) space-partitioning scheme was conducted using AIM2000,[S18] whereas DGRID[S19] was used to generate and analyze the Electron-Localizability-Indicator (ELI-D[S20]) related real-space bonding descriptors (grid step size: 0.05 a.u.). The non-covalent interactions index (NCI[S21]) grids were computed with NCIplot.[S22] Bond paths are displayed with AIM2000,[S18] ELI-D and NCI figures are displayed with MolIso.[S23] AIM bond topology exceeds the Lewis picture of chemical bonding as it also includes weak secondary interactions, such as C–H···H–C and E···C$_\pi$, which is not only relevant for packing motifs in crystal structures but also for intra-molecular interactions. AIM also provides atomic basins, giving access to atomic/fragmental charges and volumes. In contrast, ELI-D provides basins of paired electrons, giving access to electron populations and volumes of bonding or lone-pair sections. Together AIM and ELI-D thus facilitate the determination of minute charge rearrangements following structural changes. NCI uncovers (extended) regions in space where non-covalent interactions occur, thereby greatly complementing AIM and ELI-D.

Table S8. First and second vertical and adiabatic ionization energies (IE) of **1a-c**.

	energy (a.u.)		ionization energy (kJ mol^{-1})	
	Optimized	single-point	vertical	adiabatic
1a	–2257.5589			
[1a]$^{\bullet+}$	–2257.3115	–2257.3080	658.8	649.6
[1a]$^{2+}$	–2256.9501	–2256.9397	1625.9	948.9
1b	–4260.9183			
[1b]$^{\bullet+}$	–4260.6779	–4260.6711	649.2	631.3
[1b]$^{2+}$	–4260.3173	–4260.3017	1618.9	946.8
1c	–2127.5349			
[1c]$^{\bullet+}$	–2127.3094	–2127.3018	612.1	592.2
[1c]$^{2+}$	–2126.9582	–2126.9386	1565.6	921.9

Table S11. AIM topological descriptors of the primary E–C bonds in **1a-c**.

	contact	d [Å]	d_1+d_2 [Å]	Δ(d)	d_1/d [%]	ρ(**r**) [eÅ^{-3}]	$\nabla^2\rho(\mathbf{r})$ [eÅ^{-5}]	ε	G/ρ(**r**) [a.u.]	H/ρ(**r**) [a.u.]
1a	S–C	1.768	1.769	0.000	0.52	1.32	-7.6	0.13	0.30	-0.70
[**1a**]$^{+\bullet}$	S–C	1.755	1.755	0.000	0.53	1.37	-8.3	0.12	0.29	-0.72
[**1a**]$^{2+}$	S–C	1.761	1.761	0.000	0.53	1.36	-8.1	0.13	0.29	-0.71
1b	Se–C	1.922	1.922	0.000	0.51	1.05	-3.4	0.10	0.39	-0.62
[**1b**]$^{+\bullet}$	Se–C	1.912	1.913	0.001	0.53	1.08	-4.1	0.09	0.36	-0.62
[**1b**]$^{2+}$	Se–C	1.909	1.910	0.000	0.53	1.09	-4.2	0.10	0.36	-0.63
1c	Te–C	2.125	2.125	0.000	0.51	0.82	-0.2	0.13	0.51	-0.52
[**1c**]$^{+\bullet}$	Te–C	2.121	2.123	0.002	0.52	0.83	-0.8	0.13	0.46	-0.53
[**1c**]$^{2+}$	Te–C	2.115	2.116	0.002	0.53	0.85	-1.2	0.11	0.43	-0.54

For all contacts, d_1 or d_2 are the distances of the chalcogen or carbon atom to the bond critical point (bcp), $\rho(\mathbf{r})_{bcp}$ is the electron density at the bcp, $\nabla^2\rho(\mathbf{r})_{bcp}$ is the corresponding Laplacian, ε is the bond ellipticity, $G/\rho(\mathbf{r})_{bcp}$ and $H/\rho(\mathbf{r})_{bcp}$ are the kinetic and total energy density over $\rho(\mathbf{r})_{bcp}$ ratios.

Table S12. AIM topological descriptors of the secondary E···C/H bonds in **1a-c**.

	contact	d [Å]	d_1+d_2 [Å]	Δ(d)	d_1/d [%]	ρ(**r**) [eÅ^{-3}]	$\nabla^2\rho(\mathbf{r})$ [eÅ^{-5}]	ε	G/ρ(**r**) [a.u.]	H/ρ(**r**) [a.u.]
1a	S···H29	2.612	2.620	0.008	0.61	0.09	1.1	0.37	0.70	0.12
1a	S···H47	2.791	2.800	0.009	0.62	0.08	0.8	0.25	0.63	0.10
[**1a**]$^{+\bullet}$	S···H29	2.631	2.653	0.022	0.60	0.09	1.1	0.80	0.72	0.12
[**1a**]$^{+\bullet}$	S···H47	2.872	2.889	0.018	0.61	0.06	0.7	0.47	0.67	0.13
[**1a**]$^{2+}$	S···C10	2.958	3.092	0.134	0.52	0.13	1.2	2.78	0.61	0.06
[**1a**]$^{2+}$	S···H29	2.612	2.649	0.036	0.60	0.10	1.3	1.44	0.75	0.12
[**1a**]$^{2+}$	S···H47	2.926	2.957	0.031	0.60	0.06	0.7	0.69	0.70	0.15
1b	Se···H29	2.913	3.077	0.164	0.57	0.08	1.1	0.16	0.79	0.15
1b	Se···H47	2.855	2.862	0.007	0.63	0.07	0.7	0.17	0.58	0.09
[**1b**]$^{+\bullet}$	Se···H29	2.730	2.748	0.018	0.61	0.09	1.0	0.74	0.69	0.12
[**1b**]$^{+\bullet}$	Se···H47	2.892	2.902	0.010	0.61	0.07	0.7	0.32	0.62	0.11
[**1b**]$^{2+}$	Se···H29	2.662	2.686	0.024	0.61	0.10	1.2	0.99	0.71	0.11
[**1b**]$^{2+}$	Se···H47	2.974	3.012	0.038	0.60	0.06	0.7	0.80	0.67	0.14
1c	Te···H29	2.984	2.986	0.003	0.62	0.06	0.6	0.35	0.63	0.11
1c	Te···H47	3.001	3.005	0.004	0.65	0.07	0.6	0.19	0.51	0.06
[**1c**]$^{+\bullet}$	Te···C10	2.948	2.951	0.003	0.54	0.15	1.3	1.09	0.61	-0.01
[**1c**]$^{+\bullet}$	Te···H29	2.965	2.981	0.016	0.62	0.07	0.7	1.00	0.62	0.11
[**1c**]$^{+\bullet}$	Te···H47	2.979	2.987	0.008	0.62	0.07	0.6	0.37	0.56	0.08
[**1c**]$^{2+}$	Te···C10	2.835	2.843	0.008	0.54	0.21	1.1	0.45	0.46	-0.08
[**1c**]$^{2+}$	Te···H29	2.823	2.839	0.016	0.62	0.09	0.9	0.75	0.62	0.09
[**1c**]$^{2+}$	Te···H47	3.002	3.008	0.006	0.62	0.06	0.5	0.27	0.55	0.08

For all contacts, d_1 or d_2 are the distances of the chalcogen or C/H atom to the bond critical point (bcp), $\rho(\mathbf{r})_{bcp}$ is the electron density at the bcp, $\nabla^2\rho(\mathbf{r})_{bcp}$ is the corresponding Laplacian, ε is the bond ellipticity, $G/\rho(\mathbf{r})_{bcp}$ and $H/\rho(\mathbf{r})_{bcp}$ are the kinetic and total energy density over $\rho(\mathbf{r})_{bcp}$ ratios.

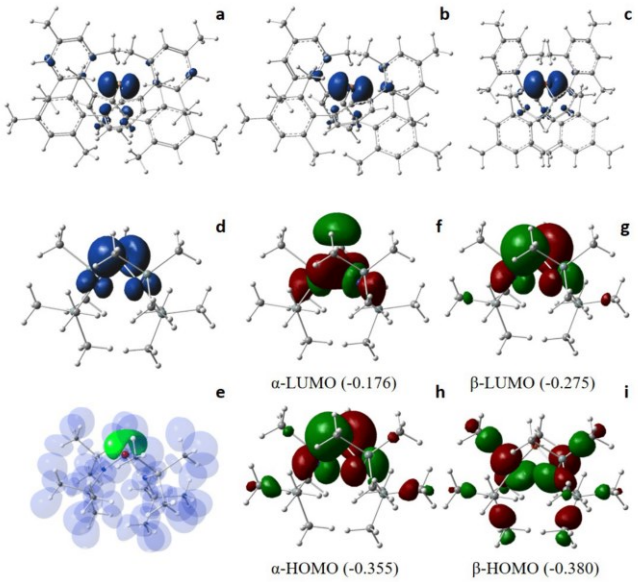

Figure S53. a-d) Spin densities of [**1a-c**]$^{++}$ and [{(Me$_3$Si)$_2$N}$_2$Te]$^{++}$ (φ = 0.005 a.u.), e) ELI-D representation (γ =1.4) of [{(Me$_3$Si)$_2$N}$_2$Te]$^{++}$, f-i) frontier orbitals of [{(Me$_3$Si)$_2$N}$_2$Te]$^{++}$.

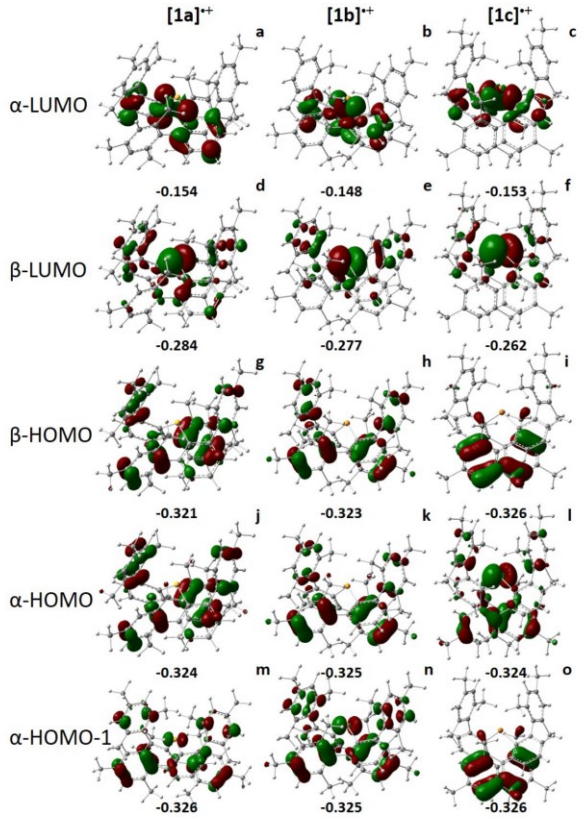

Figure S52. Frontier orbitals of [**1a-c**]$^{++}$.

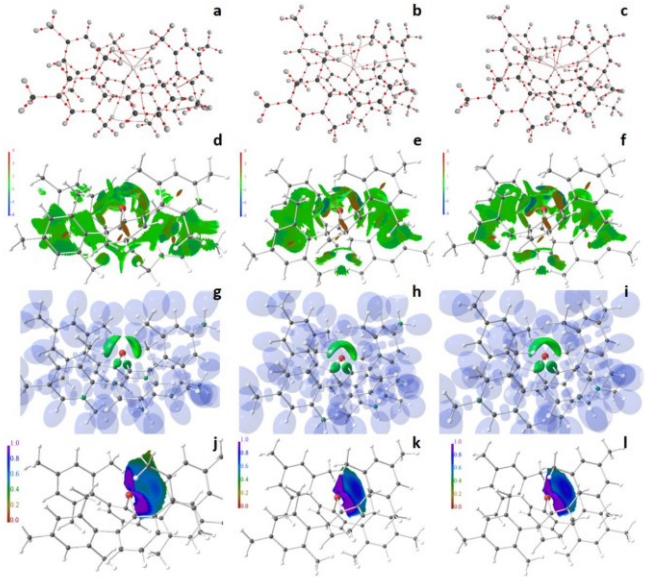

Figure S55. RSBI analysis of **1b**. (a-c) AIM bond paths motif, (d-f) NCI *iso*-surface at s(**r**) = 0.5, (g-i) ELI-D localization domain representation at *iso*-value of 1.4, (j-l) ELI-D distribution mapped on the lone-pair basin of the Se atom. Left column: **1b**, middle column: [**1b**]$^{+\bullet}$, right column: [**1b**]$^{2+}$.

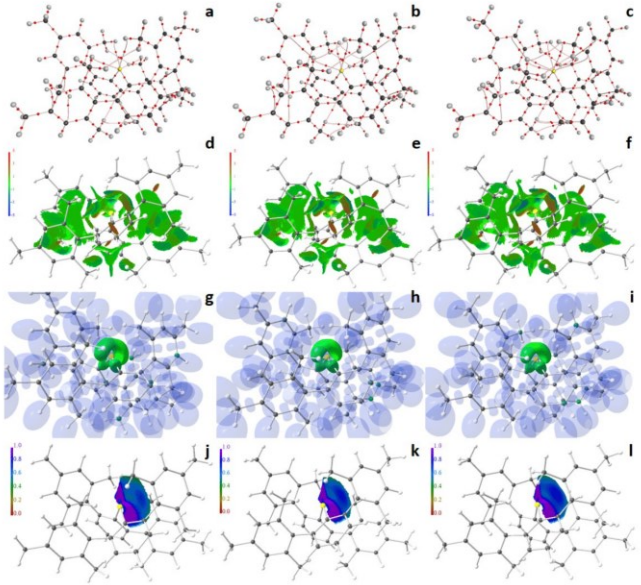

Figure S54. RSBI analysis of **1a**. (a-c) AIM bond paths motif, (d-f) NCI *iso*-surface at s(**r**) = 0.5, (g-i) ELI-D localization domain representation at *iso*-value of 1.4, (j-l) ELI-D distribution mapped on the lone-pair basin of the S atom. Left column: **1a**, middle column: [**1a**]$^{+\bullet}$, right column: [**1a**]$^{2+}$.

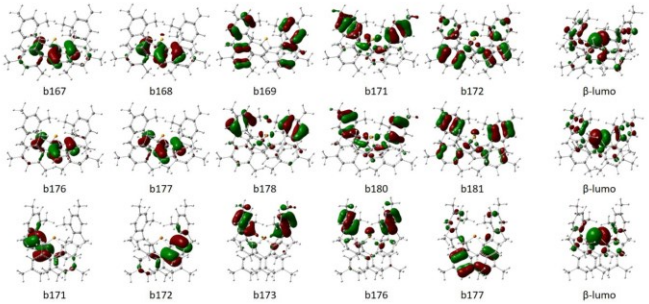

Figure S57. Frontier orbitals of [**1a-c**]$^{++}$ representing the UV/vis transitions.

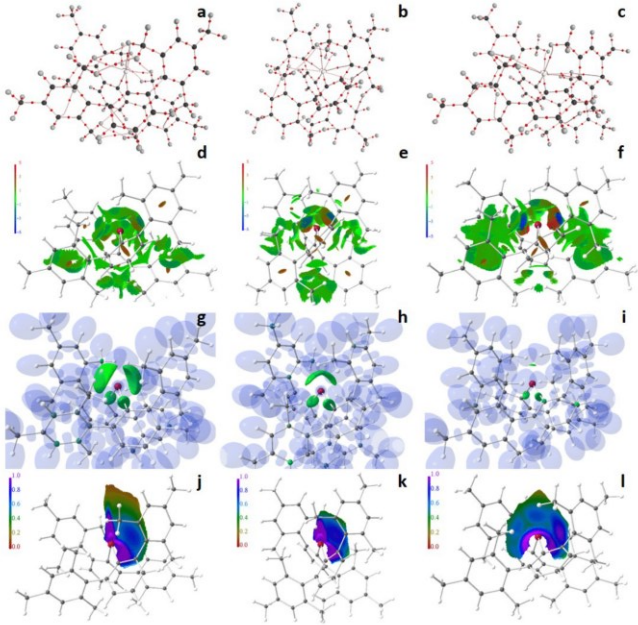

Figure S56. RSBI analysis of **1c**. (a-c) AIM bond paths motif, (d-f) NCI *iso*-surface at s(**r**) = 0.5, (g-i) ELI-D localization domain representation at *iso*-value of 1.4, (j-l) ELI-D distribution mapped on the lone-pair basin of the Te atom. Left column: **1c**, middle column: [**1c**]$^{++}$, right column: [**1c**]$^{2+}$.

Table S14. UV/vis transitions in [**1b**]$^{\cdot+}$.

	nm	f	s^2	from	to	contr.	%
1	2006.04	0.00490	0.759	183B	186B	0.18025	6.5
				185B	186B	0.97553	190.3
2	1664.63	0.00020	0.760	180B	186B	-0.10222	2.1
				184B	186B	0.99209	196.8
3	1514.84	0.00490	0.760	181B	186B	-0.16562	5.5
				183B	186B	0.96070	184.6
				185B	186B	-0.19834	7.9
4	1447.80	0.00770	0.760	180B	186B	-0.14617	4.3
				182B	186B	0.98752	195.0
5	1398.73	0.06060	0.758	175B	186B	-0.14280	4.1
				181B	186B	0.96818	187.5
				183B	186B	0.18157	6.6
6	1167.39	0.00800	0.759	180B	186B	0.97874	191.6
				182B	186B	0.14699	4.3
				184B	186B	0.10584	2.2
7	1067.62	0.00070	0.760	179B	186B	0.99023	196.1
8	958.61	0.01670	0.760	178B	186B	0.99192	196.8
9	745.91	0.00170	0.765	177B	186B	0.99556	198.2
10	733.75	0.00370	0.764	176B	186B	0.99471	197.9

Table S13. UV/vis transitions in [**1a**]$^{\cdot+}$.

	nm	f	s^2	from	to	contr.	%
1	3483.52	0.0038	0.759	172B	177B	0.24189	11.7
				176B	177B	0.96597	186.6
2	2404.86	0.0003	0.759	171B	177B	0.20238	8.2
				174B	177B	0.97874	191.6
3	2226.67	0.0099	0.759	172B	177B	0.31536	19.9
				175B	177B	0.94022	176.8
				176B	177B	-0.12415	3.1
4	1998.49	0.0026	0.759	171B	177B	-0.19313	7.5
				173B	177B	0.97708	190.9
5	1928.80	0.0454	0.758	166B	177B	0.10985	2.4
				172B	177B	0.90786	164.8
				175B	177B	-0.32681	21.4
				176B	177B	-0.22285	9.9
6	1581.91	0.0144	0.758	171B	177B	0.95349	181.8
				173B	177B	0.19656	7.7
				174B	177B	-0.19804	7.8
7	1226.21	0.0051	0.760	170B	177B	0.99222	196.9
8	1080.98	0.0150	0.760	169B	177B	0.99276	197.1
9	797.28	0.0069	0.764	166B	177B	0.12631	3.2
				168B	177B	0.98791	195.2
10	787.81	0.0018	0.763	167B	177B	0.99480	197.9

Additional references

[S1] K. Seppelt, D. Lentz, G. Klöter, C. J. Schack, In *Inorganic Syntheses*; John Wiley & Sons, Inc.: Hoboken, NJ, **1986**; p 27.

[S2] D. Lenz, H. Pritzkow K. Seppelt, *Inorg. Chem.* **1978**, *17*, 1926-1931.

[S3] K. Ruhlandt-Senge, J. J. Ellison, R. J. Wehmschulte, F. Pauer, P. P. Power, *J. Am. Chem. Soc.* **1993**, *115*, 11353-11357.

[S4] O. Mallow, M. A. Khanfar, M. Malischewski, P. Finke, M. Hesse, E. Lork, T. Augenstein, F. Breher, J. R. Harmer, N. V. Vasilieva, A. Zibarev, A. S. Bogomyakov, K. Seppelt, J. Beckmann, *Chem. Sci.* **2015**, *6*, 497-504.

[S5] J. Beckmann, M. Hesse, H. Poleschner K. Seppelt, *Angew. Chem. Int. Ed.* **2007**, *46*, 8277-8280.

[S6] P. Romanato, S. Duttwyler, A. Linden, K. K. Baldridge, J. S. Siegel, *J. Am. Chem. Soc.*, **2010**, *132*, 7828−7829.

[S7] P. Komorr, M. Olaru, E. Hupf, S. Mebs, J. Beckmann, *Chem. Eur. J.* **2022**, *28*, e202201023.

[S8] G. M. Sheldrick, *Acta Cryst.* **2008**, *A64*, 112-122.

[S8] O. V. Dolomanov, L. J. Bourhis, R. J. Gildea, J. A. K. Howard, H. Puschmann. *J. Appl. Cryst.* **2009**, *42*, 339–341.

[S9] K. Brandenburg, H. Putz, Crystal Impact GbR, Bonn **2012**.

[S11] A. J. Bard, L. R. Faulkner, Electrochemical Methods: Fundamentals and Applications (2nd ed.), John Wiley & Sons, 2001

[S12] D. A. C. Brownson, C. E. Banks, The Electrochemistry of Graphene. In: The Handbook of Graphene Electrochemistry. Springer, London. 2014.

[S13] A. D. Becke, *J. Chem. Phys.* **1993**, *98*, 5648-5652.

[S14] J. P. Perdew, J. A. Chevary, S. H. Vosko, K. A. Jackson, M. R. Pederson, D. J. Singh, C. Fiolhais, *Phys. Rev.* B **1992**, *46*, 6671-6687.

[S15] M. J. Frisch, G. W. Trucks, H. B. Schlegel, G. E. Scuseria, M. A. Robb, J. R. Cheeseman, G. Scalmani, V. Barone, B. Mennucci, G. A. Petersson, *Gaussian09*, revision D.01; Gaussian, Inc.: Wallingford, CT, 2010.

[S16] K. A. Peterson, D. Figgen, E. Goll, H. Stoll, M. Dolg, *J. Chem. Phys.* **2003**, *119*, 11113.

[S17] R. W. F. Bader, *Atoms in Molecules.* A Quantum Theory; Cambridge University Press: Oxford U.K., **1991**.

[S18] F. Biegler-König, J. Schönbohm, D. Bayles, *J. Comput. Chem.* **2001**, *22*, 545-559.

[S19] M. Kohout, *DGRID*-4.6 Radebeul, **2015**.

[S20] M. Kohout, *Int. J. Quantum Chem.* **2004**, *97*, 651-658.

[S21] E. R. Johnson, S. Keinan, P. Mori-Sanchez, J. Contreras-García, A. J. Cohen, W. Yang, *J. Am. Chem. Soc.* **2010**, *132*, 6498-6506.

[S22] J. Contreras-García, E. Johnson, S. Keinan, R. Chaudret, J.-P. Piquemal, D. Beratan, W. Yang, *J. Chem. Theor. Comp.* **2011**, *7*, 625-632.

[S23] C. B. Hübschle, P. Luger, *J. Appl. Crystallogr.* **2006**, *39*, 901-904.

Table S15. UV/vis transitions in [**1c**]$^{++}$.

	nm	f	s^2	from	to	contr.	%
1	1151.81	0.0013	0.763	176B	181B	-0.25790	13.3
				178B	181B	0.38357	29.4
				180B	181B	0.87972	154.8
2	1097.19	0.0061	0.763	176B	181B	-0.40275	32.4
				178B	181B	0.77754	120.9
				180B	181B	-0.46664	43.6
3	1089.46	0.0101	0.764	177B	181B	0.15913	5.1
				179B	181B	0.97959	191.9
4	1031.05	0.0208	0.763	176B	181B	0.86222	148.7
				178B	181B	0.48420	46.9
5	976.81	0.0014	0.763	175B	181B	0.12965	3.4
				177B	181B	0.97585	190.5
				179B	181B	-0.15661	4.9
6	795.24	0.0023	0.763	173B	181B	0.28804	16.6
				175B	181B	0.94659	179.2
				177B	181B	-0.11510	2.6
7	793.14	0.0021	0.762	174B	181B	0.99384	197.5
8	770.45	0.0322	0.762	173B	181B	0.95252	181.5
				175B	181B	-0.28502	16.2
9	620.33	0.0109	0.774	171B	181B	-0.65772	86.5
				172B	181B	0.74122	109.9
10	617.10	0.0008	0.774	171B	181B	0.74333	110.5
				172B	181B	0.66168	0.9